International scoping study of a future
Neutrino Factory and super-beam facility

RAL-TR-2007-019
IC/HEP/08-5
IPPP/08/45, DCPT/08/09

Physics at a future Neutrino Factory and super-beam facility

The ISS Physics Working Group

Editors:
S.F. King[1], K. Long[2], Y. Nagashima[3], B.L. Roberts[4], and O. Yasuda[5].

15th October 2007

[1] University of Southampton, School of Physics and Astronomy, Highfield, Southampton S017 1BJ, United Kingdom.
[2] Imperial College London, Blackett Laboratory, Department of Physics, Exhibition Road, London, SW7 2AZ, United Kingdom.
[3] Department of Physics, Osaka University, Toyonaka, Osaka 560-0043, Japan.
[4] Boston University, Department of Physics, 590 Commonwealth Avenue, Boston, MA 02215, USA
[5] Department of Physics, Tokyo Metropolitan University, Hachioji, Tokyo 192-0397, Japan.

A. Bandyopadhyay, S. Choubey, R. Gandhi, S. Goswami
Harish-Chandra Research Institute, Chhatnag Road, Jhunsi, Allahabad, 211 019, India

B.L. Roberts
Boston University, Department of Physics, 590 Commonwealth Avenue, Boston, MA 02215, USA

J. Bouchez
Service de Physique des Particules, CEA – Saclay, F-91191 Gif sur Yvette Cedex, France

I. Antoniadis, J. Ellis, G.F. Giudice, T. Schwetz
Department of Physics, CERN Theory Division, 1211 Geneva 23, Switzerland

S. Umasankar
Institute of Mathematical Sciences, Taramani, C.I.T. Campus, Chennai 600113, India

G. Karagiorgi, A. Aguilar-Arevalo, J. M. Conrad, M. H. Shaevitz
Department of Physics, Columbia University, New York, NY 10027, USA

S. Pascoli
University of Durham, Department of Physics, Ogen Center for Fundamental Physics, South Road, Durham, DH1 3LE, United Kingdom

S. Geer
Fermilab, Batavia, IL 60510-0500, USA

J.E. Campagne
LAL, Université Paris-Sud 11, Bâtiment 200, F-91898 Orsay cedex, France

M. Rolinec
Physik-Department T30d, Technische Universitaet Muenchen, James-Franck-Strasse, 85748 Garching, Germany

A. Blondel, M. Campanelli
Departement de Physique Nucleaire et Corpusculaire (DPNC), Universite de Geneve, Geneve, Switzerland

J. Kopp, M. Lindner
Max-Planck-Institut für Kernphysik, Saupfercheckweg 1, 69117, Heidelberg, Germany

J. Peltoniemi
Centre for Underground Physics in Pyhäsalmi, Universty of Oulu, Oulu, Finland

P.J. Dornan, K. Long, T. Matsushita, C. Rogers, Y. Uchida
Imperial College London, Blackett Laboratory, Department of Physics, Exhibition Road, London, SW7 2AZ, United Kingdon

M. Dracos
Centre de Recherches Nucleaire, Hautes Energies, Institut National de Physique Nucleaire et des Particules, Universite Louis Pasteur, Paris, France

K. Whisnant
Department of Physics and Astronomy, Iowa State University, Ames, IA 50011, USA

D. Casper, Mu-Chun Chen[6]
Department of Physics and Astronomy, University of California, Irvine, CA 92697, USA

B. Popov
Joint Institute for Nuclear Research, Joliot-Curie 6, 141980, Dubna, Moscow Region, Russia

J. Äystö
Jyvaskyla University, Finland

D. Marfatia
Department of Physics and Astronomy, University of Kansas, Lawrence, KS 66045, USA

Y. Okada, H. Sugiyama
Theory Group, KEK, 1-1 Oho, Tsukuba, Ibaraki 305-0801, Japan

K. Jungmann
KVI, Groningen, The Netherlands

J. Lesgourgues
Laboratoire de Physique Theorique, LAPTH, F-74941, Annecy-le-Vieux Cedex, France

M. Zisman
Lawrence Berkeley National Laboratory, Physics Division, 1 Cyclotron Road, 50R4049, Berkeley, CA 94720-8153 USA

M.A. Tortola
CFTP and Departamento de Fisica, Instituto Superior Tecnico. Av. Rovisco Pais, 1049-001 Lisboa, Portugal

A. Friedland
Los Alamos National Lab, P.O. Box 1663, Los Alamos, NM 87545, USA

S. Davidson
IPN de Lyon, Université Lyon 1, CNRS, 4 rue Enrico Fermi, Villeurbanne, F-69622 cedex France

[6] And Theoretical Physics Department, Fermilab, Batavia, IL 60510-0500, USA

S. Antusch[7], C. Biggio, A. Donini, E. Fernandez-Martinez, B. Gavela, M. Maltoni, J. Lopez-Pavon, S. Rigolin
Universidad Autonoma de Madrid, Facultad de Ciencias C-XVI, Departamento de Fisica Teorica (IFT), UAM-CSIC, Cantoblanco, Madrid 28049, Spain

N. Mondal
Tata Institute of Fundamental Research, School of Natural Sciences, Homi Bhabha Road, Mumbai 400005, India

V. Palladino
Università Federico II and INFN Napoli, Italy

F. Filthaut
Katholieke Universiteit Nijmegen, HEFIN - High Energy Physics Inst., P.O. Box 9010, NL-6500 GL Nijmegen, Netherlands

C. Albright[8]
Department of Physics, Northern Illinois University, DeKalb, IL 60115, USA

A. de Gouvea
Northwestern University 633 Clark Street Evanston, IL 60208, USA

Y. Kuno, Y. Nagashima
Department of Physics, Osaka University, Toyonaka, Osaka 560-0043, Japan

M. Mezzetto
Univ. di Padova, Dept. di Fisica, via Marzolo 8, I-35100 Padua, Italy

S. Lola
Department of Physics, University of Patras, GR-26100 Patras, Greece

P. Langacker
Department of Physics and Astronomy, University of Pennsylvania, Philadelphia, PA 19104

A. Baldini
INFN Pisa, Italy

H. Nunokawa
Departamento de Física, Pontifícia Universidade Católica Ddo Rio de Janeiro, C. P. 38071, 22452-970, Rio de Janeiro, Brazil

D. Meloni
INFN and Dipto. di Fisica, Università degli Studi di Roma "La Sapienza", P.le A. Moro 2, 00185, Rome, Italy

[7] and Max-Planck-Institut für Physik (Werner-Heisenberg-Institut), Föhringer Ring 6, 80805 München, Germany
[8] And Theoretical Physics Department, Fermilab, Batavia, IL 60510-0500, USA

M. Diaz
Departamento de Fisica, Universidad Catolica de Chile, Avenida Vicuna Mackenna 4860, Santiago, Chile

S.F. King
University of Southampton, School of Physics and Astronomy, Highfield, Southampton S017 1BJ, United Kingdom

K. Zuber
University of Sussex, Department of Physics and Astronomy, Falmer, Brighton, Sussex BN1 9QH, United Kingdom

A. G. Akeroyd
Department of Physics, National Cheng Kung University, Tainan 701, Taiwan

Y. Grossman
Department of Physics, Technion, Haifa 32000, Israel

Y. Farzan
Institute for Studies in Theoretical Physics and Mathematics, P.O. Box 19395-1795, Tehran, Iran

K. Tobe
Department of Physics, Tohoku University, Aoba-ku, Sendai, Miyagi 980-8578, Japan

Mayumi Aoki
Theory Group, Institute of Cosmic Ray Research, University of Tokyo, 5-1-5 Kashiwanoha, Kashiwa, Chiba 277-8582, Japan

H. Murayama
Institute for the Physics and Mathematics of the Universe, University of Tokyo, Kashiwa, Japan 277-8568
Berkeley Center of Theoretical Physics, University of California, Berkeley, CA 94720
Theoretical Physics Group, Lawrence Berkeley National Laboratory, MS 50A-5104, Berkeley, CA 94720

N. Kitazawa, O. Yasuda
Department of Physics, Tokyo Metropolitan University, Hachioji, Tokyo 192-0397, Japan

S. Petcov, A. Romanino
International School for Advanced Studies (SISSA/ISAS), via Beirut 2-4, I-34100 Trieste, Italy

P. Chimenti, A. Vacchi
INFN presso il Dipartimento di Fisica dell'Universit di Trieste, Via Valerio, 2, I - 34127 Trieste, Italia

A.Yu. Smirnov
Abdus Salam International Centre for Theoretical Physics Strada Costiera 11, I-34014 Trieste, Italy

E. Couce, J.J. Gomez-Cadenas, P. Hernandez, M. Sorel, J. W. F. Valle
Instituto de Física Corpuscular, IFIC, CSIC and Universidad de Valencia, Spain

P.F. Harrison
Department of Physics, University of Warwick, Coventry, Warwickshire, CV4 7AL, England

C. Lunardini
Institute for Nuclear Theory and Department of Physics, University of Washington, Seattle, WA 98195, USA

J.K. Nelson
Department of Physics, College of William and Mary, P.O. Box 8795, Williamsburg, VA 23187-8795, USA

V. Barger, L. Everett, P. Huber
Department of Physics, University of Wisconsin, 2506 Sterling Hall, 1150 University Avenue, Madison, WI 53706, USA

W. Winter
Universität Würzburg, Lehrstuhl fur Theoretische Physik II, Am Hubland, D-97074 Würzburg, Germany

W. Fetscher
ETH, Zürich, Switzerland

A. van der Schaaf
Physik-Institut der Universität Zürich, Switzerland

Executive summary

The international scoping study of a future Neutrino Factory and super-beam facility (the ISS) was carried by the international community between NuFact05, (the 7$^{\text{th}}$ International Workshop on Neutrino Factories and Superbeams, Laboratori Nazionali di Frascati, Rome, June 21–26, 2005) and NuFact06 (Ivine, California, 24–30 August 2006). The physics case for the facility was evaluated and options for the accelerator complex and the neutrino detection systems were studied. The principal objective of the study was to lay the foundations for a full conceptual-design study of the facility. The plan for the scoping study was prepared in collaboration by the international community that wished to carry it out; the ECFA/BENE network in Europe, the Japanese NuFact-J collaboration, the US Neutrino Factory and Muon Collider collaboration and the UK Neutrino Factory collaboration. STFC's Rutherford Appleton Laboratory was the host laboratory for the study. The study was directed by a Programme Committee advised by a Stakeholders Board. The work of the study was carried out by three working groups: the Physics Group; the Accelerator Group; and the Detector Group. Four plenary meetings at CERN, KEK, RAL, and Irvine were held during the study period; workshops on specific topics were organised by the individual working groups in between the plenary meetings. The conclusions of the study was presented at NuFact06. This document, which presents the Physics Group's conclusions, was prepared as the physics section of the ISS study group. More details of the ISS activities can be found at http://www.hep.ph.ic.ac.uk/iss/.

Neutrino oscillations are the sole body of experimental evidence for physics beyond the Standard Model of particle physics. The observed properties of the neutrino–the large flavour mixing and the tiny mass–are believed to be consequences of phenomena which occur at energies never seen since the Big Bang. Neutrino facilities to pursue the study of oscillation phenomena are therefore complementary to high-energy colliders and competitive candidates for the next world-class facilities for particle physics. Neutrino oscillations also provide a window on important issues in astrophysics and cosmology. Ongoing and approved experiments utilise intense pion beams (super-beams) to generate neutrinos. They are designed to seek and measure the third mixing angle θ_{13} of neutrino mixing matrix (the 'PMNS' matrix), but will have little or no sensitivity to matter-antimatter symmetry violation. Several neutrino sources have been conceived to reach high sensitivity and to allow the range of measurements necessary to remove all ambiguities in the determination of oscillation parameters. The sensitivity of these facilities is well beyond that of the presently approved neutrino oscillation programme. Studies so far have shown that the Neutrino Factory, an intense high-energy neutrino source based on a stored muon beam, gives the best performance over virtually all of the parameter space; its time scale and cost, however, remain important question marks. Second-generation super-beam experiments using megawatt proton drivers may be an attractive option in certain scenarios. Super-beams have many components in common with the Neutrino Factory. A beta-beam, in which electron neutrinos (or anti-neutrinos) are produced from the decay of stored radioactive ion beams, in combination with a second-generation super-beam, may be a competitive option.

The role of the ISS Physics Group was to establish the strong physics case for the various

proposed facilities and to find optimum parameters for the accelerator and detector systems from the physics point of view. The first objective of this report, therefore, is to try to answer the big questions of neutrino physics; questions such as the origin of neutrino mass, the role that neutrinos played in the birth of the universe, and what the properties of the neutrino can tell us about the unification of matter and force. These questions form the basis for the clarification of the physics cases for various neutrino facilities. Since it is not (yet) possible to answer these questions in general, studies have concentrated on more specific issues that may lead to answers to the big questions. In particular, studies have addressed such issues as:

1. The relevance of neutrino physics to the understanding of dark matter and dark energy, the connection between neutrino mass and leptogenesis and galaxy-cluster formation;

2. The connection of predictions at the grand-unification scale with low energy phenomena in the framework of see-saw mechanism and supersymmetric extensions of the Standard Model; and

3. The understanding of flavour and the connection between quarks and leptons, the possible existence of hidden flavour quantum numbers that may be connected with the small mixings among the quarks, the mass hierarchy of the quarks and charged leptons, and the relationship of these phenomena with the neutrino mass matrix.

The second objective of this report is to review the predictions of the various models for the physics that gives rise to neutrino oscillations and to review the associated phenomenology that is relevant for precision measurements of neutrino oscillations. For this purpose, we have evaluated the degree to which the various facilities, alone or in combination, can distinguish between the various models of neutrino mixing and determine optimum parameter sets for these investigations. A class of directly-testable predictions is afforded by the fact that the GUT and family symmetries result in relationships between the quark- and lepton-mixing parameters. These relationships can be cast in the form of sum rules. One example that can be used to discriminate amongst various models is:

$$\theta_{12}^{\Sigma} \equiv \theta_{12} - \theta_{13}\cos(\delta)\,,$$

where θ_{12}^{Σ} can be predicted in classes of flavour models while θ_{12} (the solar mixing angle) and $\theta_{13}\cos(\delta)$ (the product of the small mixing angle and the cosine of the CP violating phase) are measured experimentally. Another class of test is afforded by the investigation of the unitarity of the PMNS matrix. While the quark-mixing (CKM) matrix is constrained to be unitary in the Standard Model, the PMNS matrix, which originates from physics beyond the Standard Model, may not be exactly unitary; this is the case, for example, in see-saw models. The third class of the test is the existence of flavour-changing interactions that might appear at the production point, in the oscillation that occur during propagation, or at the point of detection. The possible strong correlations between lepton-flavour violation and neutrino oscillations are also discussed.

The potential of non-accelerator, long-baseline neutrino oscillation measurements were also considered. Significant improvements in the precision with which the solar parameters are known

could be made using a new long-baseline reactor experiment or by using gadolinium loading of the water in the Super-Kamiokande detector to increase its sensitivity to solar neutrinos. A large, underground, magnetised-iron detector could be used to improve the precision of the atmospheric mixing parameters, to determine the octant degeneracy, and to search for deviations from maximal atmospheric mixing.

The third, and key, objective of this report is to present the first detailed comparison of the performance of the various facilities. Using realistic specifications, we have estimated the likely performance, tried to find optimum combinations of facilities, baselines, and neutrino energies, and attempted to identify some staging scenarios. The cases considered are described in detail in the main report, only a brief summary is given here. Although the Neutrino Factory can achieve very large data samples with small backgrounds, it operates at energies considerably higher than the first oscillation peak ($E_{max}/\mathrm{GeV} = L/564$ km). Because of this, at intermediate values of θ_{13} ($10^{-3} \lesssim \sin^2 2\theta_{13} \lesssim 10^{-2}$) the Neutrino Factory with only one golden-channel ($\nu_e \rightarrow \nu_\mu$ and $\bar{\nu}_e \rightarrow \bar{\nu}_\mu$) detector (at, say, 4000 km) can not resolve all parameter degeneracies and the precision of the measurement of a particular parameter is reduced by correlations among the parameters. These problems can be resolved in one of three ways:

1. Placing a second detector at a different baseline (i.e. varying the ratio L/E);
2. Adding a detector sensitive to the silver channel ($\nu_e \rightarrow \nu_\tau$); or
3. Using an improved detector with lower neutrino-energy threshold and better energy resolution.

Possible configurations for each alternative, alone and in combination, were investigated to find an optimum performance of the Neutrino Factory. It was shown that a considerable reduction of parent muon-energy down to ~ 25 GeV is feasible without a significant loss of oscillation-physics output, provided a detector performance improved with respect to the one assumed in earlier studies can be achieved.

To make direct, quantitative comparisons of the various facilities, the GLoBES package was used. Three representative super-beam configurations were considered: the SPL, a super-beam directed from CERN to the Modane laboratory; T2HK, an upgrade of the J-PARC neutrino beam illuminating a detector close to Kamioka, and the WBB, a wide-band, on-axis beam from BNL or FNAL to a deep underground laboratory in the US. Each super-beam was assumed to illuminate a megaton-class water Cherenkov detector. The beta-beam options considered were the CERN baseline scheme in which helium and neon ions are stored with a relativistic γ of 100 and an optimised beta-beam for which $\gamma = 350$. Two Neutrino Factory options were considered: a conservative option with a single 50 kton detector sited at a baseline of 4000 km from a 50 GeV Neutrino Factory; and the optimised Neutrino Factory (see the full report) with two detectors, one at a baseline of 4000 km and the second at the magic baseline ($\sim 7500\ km$). The result of the comparisons may be summarised as follows: for the options considered, the Neutrino Factory has the best discovery reach for $\sin^2 2\theta_{13}$ followed by the beta-beam and the

super-beam, while the $\sin^2 2\theta_{13}$ reach for resolving the sign of the atmospheric mass difference is mainly controlled by the length of the baseline. For large values of θ_{13} ($\sin^2 2\theta_{13} \gtrsim 10^{-2}$), the three classes of facility have comparable sensitivity for the discovery of CP violation; the best precision on individual parameters being achieved at the Neutrino Factory using optimised detectors. The reduction of systematic uncertainties is the key issue at large θ_{13}; by reducing systematic uncertainties, the super-beam may be favourably compared with the conservative Neutrino Factory. For intermediate values of θ_{13} ($10^{-3} \lesssim \sin^2 2\theta_{13} \lesssim 10^{-2}$), the super-beams are outperformed by the beta-beam and the Neutrino Factory and the best CP coverage is achieved by the beta-beam. For small values of θ_{13} ($\sin^2 2\theta_{13} \lesssim 10^{-3}$), the Neutrino Factory out-performs the other options. Note, the comparisons are made using three performance indicators only ($\sin^2 2\theta_{13}$, the sign of mass hierarchy and the CP violating phase δ). If other physics topics, such as the search for e, μ, τ flavour anomalies, were to be emphasised, the relative performance may be different.

The final contribution to this report reviews the muon physics that can be performed with the intense muon beams that will be available at the Neutrino Factory. The study of rare, lepton-flavour violating processes in muon decay, and the search for a permanent electric-dipole moment of the muon, are complementary to precision studies of neutrino physics; often sensitive to the same underlying physics. The complementarity and the potential of a muon-physics programme at the Neutrino Factory is investigated. It will be important in the coming years to establish quantitatively the synergy between muon physics and the study of neutrino oscillations and to develop a plan for the co-existence of muon and neutrino programmes at the Neutrino Factory facility.

A significant amount of conceptual design work and hardware R&D is required before the performance assumed for each of the facilities can be realised. Therefore, an energetic, programme of R&D into the accelerator facilities and the neutrino detectors must be established with a view to the timely delivery of conceptual design reports for the various facilities.

Contents

1 Introduction

1.1 Neutrino In a Nutshell

Elusive, mysterious, yet abundant. Neutrinos are elementary particles, just like the electrons in our bodies. Neutrinos are so elusive that we don't feel ten trillions of them going through our body every second. They were discovered fifty years ago, but still pose many mysteries, defying our efforts to understand them due to their elusiveness. Yet neutrinos are the most numerous matter particles in the universe; there are about a billion neutrinos for every single atom.

Slowly we began to appreciate the important roles that neutrinos have played in shaping the universe as we see today. We already know that stars would not burn without neutrinos. Neutrinos played an important role in producing the various chemical elements that we need for daily life. Given that we (atoms) are completely outnumbered by neutrinos, it is quite certain that they played even more important roles.

There was a major surprise eight years ago when we discovered that neutrinos have a tiny, but non-zero, mass quite against the expectations of our best theory. This discovery opened up new important roles for neutrinos. We are all of a sudden grappling with new exciting questions about neutrinos that may lead to revolutionary understandings on how the universe came to be.

Because they have mass, neutrinos may have played an important role in shaping the galaxies, and eventually stars and planets. Neutrinos may actually be their own anti-particles; this may be the reason why the Universe did not end up empty but has atoms in it. Neutrinos seem to be telling us profound facts about the way matter and forces are unified, and how the three types of neutrino are related to each other; we have yet to decipher their message. In addition, neutrinos may actually be the reason why the universe exists at all.

We are only beginning to understand neutrinos and their roles in how the universe works. It will take many experimental approaches to get the full picture. A neutrino factory discussed here will most likely be an essential component of this programme.

1.2 Neutrino physics as part of the High Energy Physics Programme

The present is a very interesting time in the field of fundamental physics: over the past four decades, an impressive theoretical framework, the Standard Model, has been established. The Standard Model is capable of explaining how nature works at the smallest, experimentally-accessible distance scales; yet a handful of phenomena seem decisively to elude an explanation within the Standard Model and are therefore clues to a more fundamental understanding. These observations provide the only clues we have that our understanding of fundamental physics is incomplete. The experimental and theoretical pursuit of these clues drives the high energy physics programme and is likely to guide the bulk of the research in this area over the coming decades. In this brief sub-section, the forces currently driving research in fundamental physics are discussed and the possible interplay between the component parts of the research programme are

investigated; the objective being to establish the context within which the future experimental neutrino-physics programme must be developed.

Non-zero neutrino masses cannot be explained by the Standard Model. To allow for massive neutrinos, the Standard Model must be modified qualitatively. There are several distinct ways in which the Standard Model can be modified to accommodate neutrino mass, some of which will be discussed in detail in the next section. Our current experimental knowledge of the properties of the neutrino property does not allow us to choose a particular "new Standard Model" over all the others. We do not know, for example, whether neutrino masses are to be interpreted as evidence of new, very light, fermionic degrees of freedom (as is the case if the neutrinos are Dirac fermions), new, very heavy, degrees of freedom (as is the case if the canonical see-saw mechanism is responsible for tiny Majorana neutrino masses), or whether a more complicated electroweak-symmetry-breaking sector is required. To make progress, it is imperative that new probes of neutrino properties be vigorously developed. This is the main driving force of all experimental endeavours discussed in this study.

According to the Standard Model, the Lagrangian of nature is invariant under an $SU(3)_c \times SU(2)_L \times U(1)_Y$ local symmetry, but the quantum numbers of the vacuum are such that this gauge symmetry is spontaneously broken to $SU(3)_c \times U(1)_{\rm EM}$. The physics responsible for this electroweak-symmetry breaking is not known. The Standard Model states that electroweak symmetry breaking arises due to the dynamics of a scalar field – the Higgs field. While the Standard Model explanation for this phenomenon is in (reasonable) agreement with precision electroweak measurements, the definitive prediction – the existence of a new, fundamental scalar boson, the Higgs boson – has yet to be confirmed experimentally.

Even if the standard mechanism of electroweak symmetry breaking is realised in nature, our theoretical understanding of particle physics strongly hints at the possibility that there are more degrees of freedom at or slightly above the electroweak-symmetry-breaking scale (around 250 GeV). Furthermore, it is widely anticipated that these new degrees of freedom will serve as evidence of new organising principles; examples of such principles include supersymmetry and the existence of new dimensions of space.

The pursuit of the mechanism responsible for electroweak symmetry breaking is the driving force behind the current and the future high-energy-collider physics programme, which aims at exploring the high energy frontier. In the near future, the Large Hadron Collider (LHC) is expected to supplant the ongoing Tevatron collider as the highest energy particle accelerator in the world. It is widely expected that the LHC will reveal the mechanism of electroweak symmetry breaking and provide evidence of new heavy degrees of freedom. Anticipating the potential findings of the LHC-based experiments, the collider physics community is currently planning a high intensity, high precision, high energy electron collider – the International Linear Collider (ILC). The ILC should be able to study in detail the electroweak-symmetry breaking sector and reveal the properties of the new physics at the electroweak scale.

Finally, several very different but equally impressive measurements of the mass-energy budget of the Universe have revealed beyond reasonable doubt the existence of what is referred to

as 'dark matter'. After several years of observation, it is now clear that the Standard Model does not contain the degrees of freedom necessary to explain the dark matter. Other than its gravitational properties, very little is known about dark matter. It could consist of weakly interacting fundamental particles, but it may also consist of very heavy, very weakly interacting states, or more exotic objects. Experimental searches for dark matter are currently among the highest priorities of the fundamental physics research programme. Experiments that are sensitive to dark matter vary from direct-detection experiments, to neutrino telescopes, to gamma-ray observatories. The hope is that the pursuit of the dark-matter clue will not only reveal the existence of a new form of matter but will also provide other clues that will allow a more satisfying understanding of the composition of the universe and its behaviour in the first instants after the Big Bang to be developed.

On top of the dark-matter problem, we are now faced with a seemingly deeper puzzle – the existence of dark energy. We are still far from properly decoding what this puzzle means, and it is not clear how progress will be made towards resolving this most mysterious issue. New experiments are being devised to study in more detail the properties of dark energy. The results of these experiments may play a large role in modifying our picture of how nature works at its most fundamental level.

The different probes discussed above not only address different clues regarding new fundamental physics, but also complete and complement one-another. The amount of synergy among the different experiments cannot be over emphasised. Consider the following examples of such synergies:

1. While new physics at the electroweak scale is usually best studied using a high energy collider, there are several new-physics phenomena that will only manifest themselves in neutrino experiments, including new light, very-weakly-coupled degrees of freedom that could be related to dark matter or dark energy;

2. The knowledge of neutrino properties is essential for the understanding of certain dark-matter searches (for example those performed using neutrino telescopes);

3. A high-energy collider may provide the only means of studying in any detail the property of dark matter particles; and

4. A proper understanding of the origin of neutrino mass can only be obtained after the mechanism of electroweak-symmetry breaking is properly understood.

It is important to bear in mind that we do not know what the next set of clues will be, or where they will come from. It may turn out, for example, that neutrino experiments provide our only handle on grand unification and other types of very high energy physics, or that astrophysical searches for the properties of dark energy will reveal a direct window on quantum gravity. Or it may turn out that collider experiments will be able to study directly string-theoretical effects (this may be the case if there really are large extra dimensions). Only a comprehensive pursuit of the questions that we can formulate today will allow us to reach the next stage in understanding

fundamental physics – and ask a new set of more fundamental, deeper questions tomorrow. In this sense, we perceive the physics discussed here to be on equal footing with other studies of fundamental importance to our field, including the direct searches for dark matter, satellite missions that will measure the acceleration of the universe, or collider experiments at the energy frontier. These are all different, complementary ways of addressing the different questions that we cannot answer given our current understanding of fundamental physics.

1.3 Implications and opportunities

Fundamental fermions, are classified in three generations, each generation containing six quarks (two flavours, three colours) and two leptons. The measured properties of these particles exhibit a clear 'horizontal' hierarchy in which the mass of fermions carrying the same Standard Model quantum numbers increases with generation number. Within a generation, the fermion properties also exhibit 'vertical' patterns, for example, the sum of the electric charge of the members of a particular generation is zero. The quarks come in three colour varieties, the source of the strong force. Under the weak force, both the quarks and the leptons within a particular generation transform as a doublet. In contrast to the general expectation, the mixing angles among lepton flavours have turned out to be different to the quark-mixing angles. Many of the properties of the neutrino are unique, not shared by the other fundamental fermions. Firstly, it has neither colour nor electric charge, hence is the only fundamental fermion that feels solely the weak force in addition to the gravitational force. This fact becomes important when cosmological impact of the neutrino is discussed. Secondly, neutrino masses are tiny compared to the masses of all other fundamental fermions. Thirdly, the neutrino could be a Majorana particle; a fermion which cannot be distinguished from its own antiparticle[9].

The physics of flavour seeks to provide an explanation of these observed patterns. The vertical patterns noted above can be explained in 'Grand Unified Theories' (GUTs) in which the fermions are assigned to representations of a large symmetry group such as $SO(10)$. The horizontal, or family patterns, can be explained by assuming a family symmetry such as $SU(3)_{\text{family}}$. Some models that incorporate GUT and family symmetries with super-symmetric extensions come within the realm of string theories that incorporate extra dimensions. Understanding the symmetry structure seems to be a promising strategy to arrive at a description of the physics of flavour.

Neutrino oscillations are a phenomenon in which the neutrino changes flavour as it propagates. It was predicted by Pontecorvo [2, 3] and Maki, Nakagawa and Sakata [4] and the first clear evidence for neutrino oscillations was presented by Super-Kamiokande in 1998 in observations of the zenith angle distributions of atmospheric neutrinos [5]. The first indication, however, dates back as early as 1970, when the Homestake group detected a deficit in the solar-neutrino flux compared to that predicted by the Standard Solar Model [6]. The long-standing "solar

[9] The observation of double beta-decay processes in which no neutrino is produced would imply that the neutrino is its own antiparticle [1].

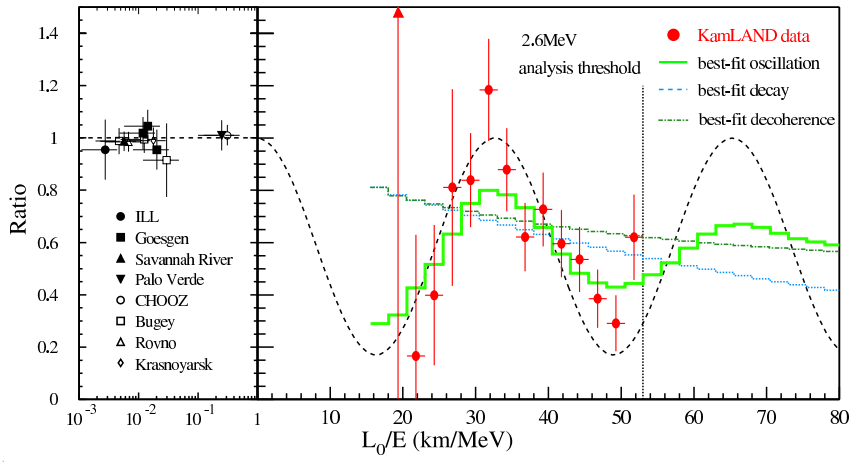

Figure 1: The ratio of the measured to the predicted neutrino flux is plotted as a function of L/E. The anti-electron-neutrino contribution to the reactor neutrino flux measured by the KamLAND collaboration [8] is shown. (Figure courtesy of K. Inoue)

neutrino puzzle" was finally proved to be a result of oscillations by SNO in 2001 [7]. The first observation of neutrino oscillations from terrestrial neutrino sources was obtained by KamLAND by measuring the energy spectrum of neutrinos produced in nuclear reactors [8]. The result of the KamLAND measurement, shown in figure 1, exhibits the expected oscillatory behaviour and constitutes compelling evidence for neutrino oscillations [9].

Neutrino oscillations occur because of flavour mixing and the tiny, but different, masses of the neutrinos. The see-saw mechanism, the most attractive and promising scheme to explain the tiny mass, requires the presence of very heavy Majorana neutrinos. In such models, neutrino oscillations are a consequence of the physics which pertains at an extremely large energy scale. See-saw models are able to explain the striking difference between the quark- and lepton-mixing angles in a natural way. If the heavy Majorana neutrino is abundant in the early Universe and decays preferentially into matter leptons in a CP violating process, then the lepton asymmetry would be converted into a baryon asymmetry a split second later during the electroweak era. This process is referred to as "leptogenesis" and is a primary theory to explain our matter universe. The neutrino is the most abundant of the matter fermions in the Universe; with a billion neutrinos for each of the other known matter particles, only the ubiquitous photon is more abundant. Hence, the tiny neutrino mass could contribute a non-negligible fraction of the dark matter and is known to play an important role in the formation of large-scale structure in the Universe.

Because of its direct connection with phenomena at energies never seen since the Big Bang, the precise determination of the masses and mixing angles of the 3 families of neutrino is a unique window onto these early times and provides a path to the possible unification of all forces. Measurements of neutrino oscillations can be used to determine the three mixing angles and the CP violating phase of the lepton-mixing matrix (the PMNS, Pontecorvo-Maki-Nakagawa-Sakata matrix) and two mass-squared differences. Examining neutrino oscillations is a most direct way to distinguish between the various possible theories of the physics of flavour and to understand

the origin of neutrino mass. It is also a logical place to seek for the origin of the CP violation.

Taking a different perspective, ever since Pauli's 1931 prediction, the unveiling of the properties of the neutrino has always heralded a new epoch in the history of elementary particle physics. Including the neutrino as a player of beta decay, Fermi formulated the first successful theory of weak interactions. The absence of right-handed neutrinos has manifested itself as the 'V-A' structure of the weak interaction and the pursuit of its origin lead to the discovery of the chiral gauge theory which forms the foundation of modern particle theories. The realisation of intense neutrino beams immediately resulted in the discovery of the neutral current, establishing the unification of the electroweak interactions. The ability of neutrino interactions to distinguish flavour and handedness has been extensively utilised in deep inelastic interactions to clarify the structure of the nucleon and to establish the asymptotic freedom of QCD. The recent discovery of neutrino oscillations could be regarded as another epoch-making observation. So far it is the only experimental evidence for, and a vital clue to, the physics beyond the Standard Model. Both the mysteries, and the brilliant record, of the neutrino can be attributed to its unique and characteristic insensitivity to both the strong and the electromagnetic forces. There are ample reasons to believe that this asset remains valid in uncovering the veils that surround the neutrino. Neutrino facilities to pursue oscillation phenomena are complementary to high-energy colliders and are competitive candidates for the next world-class facilities for particle physics.

1.4 Precision measurements and sensitive searches

Experimentally, there are several different approaches to elucidate the properties of the neutrino. In this report we concentrate mainly on accelerator-based facilities illuminating massive, underground detectors. Other complementary means are also taken into account and are described in section 6. Among them, reactor-based oscillation experiments may play a crucial role in untangling the degeneracies inherent in oscillation measurements. Other techniques include double-beta decay, a unique tool to test the Majorana nature of the neutrino [1]. Massive, underground detectors, while serving as a far detector for the oscillation experiments, also have an important role in their own right as telescopes for neutrino astronomy and as a possible window on grand unified theories by way of searching for proton decay.

Theories that purport to explain neutrino oscillations have consequences for the properties of the charged leptons, such as flavour changing process in lepton decay or lepton-induced reactions. Considering that very intense muon beams will be available as a by-product of the Neutrino Factory, it is natural to include muon physics as an indispensable ingredient of the study. Section 7 discusses in detail the opportunities that high-statistics studies of the properties of the muon have to offer.

The present generation of neutrino-oscillation experiments [10–12], reviewed in section 2 below, are designed to measure the smallest neutrino mixing parameter if it is not 'too small'. They utilise intense pion beams (super-beams) to generate neutrinos. They are designed to seek and measure the third mixing angle θ_{13} of the PMNS matrix, but will have little or no sensitivity

to matter-antimatter symmetry violation. Several neutrino sources, including second generation super-beams, beta-beams, and the Neutrino Factory have been envisaged to reach high sensitivity and redundancy well beyond that which can be achieved in the presently-approved neutrino-oscillation programme. Section 5 reviews the detailed performance of each of these classes of facility and presents quantitative comparisons of the physics potential. Their essential features are briefly introduced below.

The super-beam is a natural extension of the conventional neutrino beam and the current and approved experiments are mostly of this type [13–23]. The neutrino beam is produced through pion and kaon decay and hence these facilities provide beams in which ν_μ and $\bar{\nu}_\mu$ dominate the neutrino flux. However, these beams also contain $\nu_e(\bar{\nu}_e)$ from kaon and muon decay which constitute an irreducible background for the oscillation signal $\nu_\mu(\bar{\nu}_\mu) \to \nu_e(\bar{\nu}_e)$. In addition, the selection of samples of ν_e $(\bar{\nu}_e)$ is prone to neutral current contamination. The principal source of systematic uncertainty arises from the fact that the spectral shape of the pions and kaons is not well known. In the second generation super-beam experiments, the emphasis is on large detector mass, i.e. the collection of large data samples, and on muon and electron particle identification. These detector solution most often adopted for second-generation super-beam experiments is the megaton-scale water Cherenkov counter. Liquid-argon detectors or large volume scintillator detectors have also been considered.

The beta-beam [24], in which electron neutrinos or (anti-neutrinos) are produced from the decay of stored radio-active ion beams, provides essentially background-free pure "golden-channel" $(\nu_e \to \nu_\mu)$, i.e. "the appearance of wrong-sign muons". Unlike the Neutrino Factory, the beta-beam does not need a magnetised detector, because there is no contamination from anti-neutrinos. This allows the beta-beam to use a very massive detector just as the second generation super-beam does [25, 26]. Simultaneous operation of the beta-beam and the second generation super-beam has also been considered [27]. The disadvantage of the beta-beam is lack of the "silver channel", the $\nu_e \to \nu_\tau$, transition for most of the case studied.

The Neutrino Factory [28,29], an intense high-energy neutrino source derived from the decay of a stored muon beam, has access to all channels of neutrino-flavour transition including the golden channel. However, to reject beam-induced muon-neutrino events requires that the detector be magnetised. This leads most naturally to the magnetised iron calorimeter design. Another unique feature of the Neutrino Factory is the possibility to observe the silver channel. This can be achieved using either emulsion based detectors or a magnetised liquid-argon time-projection chamber.

Studies [30–35] so far have shown that the Neutrino Factory gives the best performance over virtually all of the parameter space; its time scale and cost remain, however, important question marks. Super-Beams have many components in common with the Neutrino Factory. A beta-beam may be competitive with the Neutrino Factory in some parameter space, but, being relatively new in this field, needs further study to fully explore its capability.

There is an important issue common to all the facilities that must be borne in mind. A typical oscillation experiment, trying to determine the small mixing angle θ_{13} and the CP violating phase

δ, generally suffers from correlation/degeneracy problem, described in detail in section 2.4. These correlations and degeneracies reduce the sensitivity typically by one order of magnitude over that given by the statistical and systematic uncertainties. This happens because a canonical oscillation experiment measures only two transition rates, $P(\nu_\alpha \to \nu_\beta)$ and $P(\bar{\nu}_\alpha \to \bar{\nu}_\beta)$ and the expression for these probabilities is a quadratic function of two unknown variables, $\sin 2\theta_{13}$ and $\sin \delta$. Given two measured values at fixed energy, E, and baseline, L, the solution of the equations has an extra, fake, (θ_{13}, δ) solution which is referred as the intrinsic degeneracy. Our ignorance of the sign of Δm^2_{23} (the sign degeneracy), and the indistinguishability of θ_{23} from $\pi/2 - \theta_{23}$ (the octant degeneracy) results in a total eight-fold degeneracy. The problem can be resolved in one of three ways:

1. To place a second detector at different value of L/E;
2. To add a different channel (or to combine data from a complementary source, for example from a reactor experiments); and
3. To use an improved detector with lower threshold and better energy resolution.

Method (3) may be regarded as a variant of (1) from the physics point of view because it is essentially equivalent to widening the energy spectrum. This is the reason why the consideration of synergy among the proposed, as well as the current experiments, is particularly important in oscillation physics. More often than not, the combination of experiments of different design can achieve a sensitivity that far exceeds what a mere statistical gain would suggest. For instance, NOvA [16] expects to enhance its sensitivity by combining with a proposed reactor experiment and an upgraded version of NOvA [17, 18] proposes to put a second detector at a different off axis angle (i.e. energy). T2KK [19, 20], a variation of T2HK [13], proposes to split their megaton water detector in two and place one in Korea; a remedy using two different baselines (L=295 km and $\simeq$ 1050 km). The on-axis WBB [23, 36, 37], a very long-baseline wide-band beam from FNAL or BNL to Henderson or Homestake mine in the US, on the other hand, takes advantage of its wide spectrum to resolve the problem. It has also been shown that the combination of atmospheric-neutrino data with T2HK [38] or a low energy beta-beam [27] is extremely helpful in resolving the degeneracies related to the mass hierarchy and the octant degeneracy. These examples illustrate the importance of working towards the identification of an optimum combination of the various facilities.

For all detector concepts, there are important questions concerning cost, feasibility and time scales. In addition, there are design optimisations to be made, e.g. between energy and angle resolution, optimum baseline length and detector mass. The study of detector concepts for the near detector stations will be an important aspect of the neutrino physics because of its access to many reactions complementary to the oscillation process.

For the neutrino-physics community to arrive at a consensus on the best possible neutrino-oscillation programme to follow the present generation of experiments requires a detailed evaluation of the performance and cost of the various options and of the timescale on which each

can be implemented. Further R&D programmes into the accelerator systems and the neutrino detectors must be carried out.

1.5 What the study tried to achieve

The role of the Physics Group of the ISS study was to establish the strong physics case for the various proposed facilities and to find the optimum parameters of the accelerator facility and detector systems from physics point of view. The first objective of this report, therefore, is to try to identify the big questions of neutrino physics such as the origin of neutrino mass, the role of the neutrino in the birth of the universe, what the properties of the neutrino can tell us about the unification of matter and force. These questions lay down the basis for making the physics case for the various neutrino facilities. Since it is not (yet) possible to answer these questions in general, studies have concentrated on more specific issues that may lead to answers to the big questions. A class of directly-testable predictions is afforded by the fact that GUT and family symmetries result in relationships between the quark- and lepton-mixing parameters; such relationships can be cast in the form of sum rules.

The second objective was to look for possible clues of new physics in a 'bottom-up' approach. For this purpose, we have evaluated the degree to which the various facilities, alone or in combination, can distinguish between the various models of neutrino mixing and determined optimum parameter sets for these investigations. One example is to search for the existence of a sterile neutrino. Although the anomaly presented by LSND [39] was not confirmed by MiniBooNE [40], the question is important enough to be pursued further. The second example is the unitary triangle: while the CKM matrix in quark sector is constrained to be unitary in the Standard Model, the PMNS matrix originates from physics beyond the Standard Model and, in see-saw models, may not be exactly unitary. The third example is the existence of flavour-changing interactions that might appear at the production point, in the oscillation stage, or at the detection point. Possible strong correlations between lepton-flavour violation and neutrino oscillations were also discussed. Other approaches to the determination of the three-flavour parameters (i.e. non-accelerator based measurements) were also considered. For example, the possibility of a new long-baseline reactor experiment and the loading of the water in the Super-Kamiokande detector with gadolinium to improve the solar-neutrino parameters, or an large, underground, magnetised-iron detector to improve the atmospheric-neutrino parameters and to test for deviation from maximal-mixing and determine the octant degeneracy were also discussed.

The third, and the key, objective of this report is to present the first detailed comparison of the performance of the various facilities. Utilising realistic specifications, we have estimated likely performances, tried to find an optimum combination of facilities, baselines and neutrino energies, and to come up with some staging scenarios.

Although past studies have shown that the Neutrino Factory can be considered as an excellent, and perhaps as an ultimate, facility, many questions remain open. For instance, the performance of the Neutrino Factory at large θ_{13} ($\sin^2 2\theta_{13} \gtrsim 10^{-2}$) where most super-beam experiments work is only now being studied in detail [41]. A question that must therefore be asked is: "Can the

Neutrino Factory remain competitive if θ_{13} turns out to be large?". Another concern is the cost of the accelerator facility and the detector systems. One estimate [32] in previous studies gives a total cost of 1500 M\$ + 400 M\$ $\times$ $E/20$(GeV). Therefore, the second question is: "What is the minimum energy that will deliver the physics?". The Neutrino Factory operates at energies considerably higher than the first oscillation peak (E_{max}/GeV = L/564 km). The canonical operating condition in past studies has been to use a parent muon beam of 50 GeV and a 50 kton magnetised-iron detector at a distance of 3000 – 4000 km [42]. Because of its operation at high energy with a single detector, it suffers from the degeneracy problem at intermediate values of θ_{13} ($10^{-3} \lesssim \sin^2 2\theta_{13} \lesssim 10^{-2}$). It has been shown that remedies exist through the addition of either a second detector at the 'magic' baseline ($L \simeq 7500$ km) [43] or the silver channel [44]. Both of these solutions require the second detector. So, the third question is "Can a single-detector configuration with improved performance do any better, and if two detectors are unavoidable, which combination is the best?". In order to answer those questions, an extensive investigation in the parameter space ($E_\mu - L$) was carried out. Then, various combinations have been compared with the intention to identify both a conservative option and an improved set of detector configurations with possible staging.

Direct, quantitative comparison of the various facilities is a highlight of the study. The GLoBES package [45, 46] was used. Other codes, Valencia and Madrid, showed good agreement with GLoBES in a test using a single reference input. A realistic set of detector specifications and a precise normalisation of neutrino flux and cross sections were prepared. The comparisons are made for three performance indicators only ($\sin^2 2\theta_{13}$, the sign of mass hierarchy, and the CP violation phase δ). If other physics topics, such as $e, \mu - \tau$ flavour anomaly searches, are emphasised, the relative importance may be different.

The final contribution to this report reviews the muon physics that can be performed with the intense muon beams that will be available at the Neutrino Factory. The study of rare processes in muon decay and muon-electron and muon-nucleon scattering is complementary to precision studies of neutrino oscillations; often sensitive to the same underlying physics. The complementarity and the potential of a muon-physics programme at the Neutrino Factory is investigated. It will be important in the coming years to establish quantitatively the qualitative synergy between muon physics and the study of neutrino oscillations.

This report is organised as follows. First, in section 2, we give a review of the present generation of experiments, state what is needed to complete the picture and explain the degeneracy problem. Next we expand upon the physics motivation for the neutrino-oscillation programme in sections 3 and 4; section 3 contains a 'big-picture' description of neutrino physics addressing such questions as the origin of neutrino mass, extra dimensions, flavour symmetry, and the role of the neutrino in unification and in cosmology, while section 4 takes a phenomenological approach to consider how measurements of neutrino properties may provide clues to new physics through studies such as the search for sterile neutrinos, the investigation of the leptonic unitary triangle, and the search for non-standard interactions in the oscillation experiments. Section 5 deals with the physics potential of the proposed facilities: the super-beam; the beta-beam; and the Neutrino Factory. Direct comparison of various facilities is given here. Alternative experiments which

can complement the oscillation experiments are described in section 6. The final section 7 is devoted to muon physics.

2 The Standard Neutrino Model

2.1 Introduction

The "standard neutrino-mixing model" emerged as a result of the remarkable progress made in the past decade in the studies of neutrino oscillations. The experiments with solar, atmospheric, and reactor neutrinos [5–7, 47–55] have provided compelling evidences for the existence of neutrino oscillations driven by non-zero neutrino masses and neutrino mixing. Evidence for neutrino oscillations were also obtained in the long-baseline accelerator neutrino experiments K2K [56, 57] and MINOS [11].

We recall that the idea of neutrino mixing and neutrino oscillations was formulated in [2–4]. It was predicted in 1967 [58] that the existence of ν_e oscillations would cause a "disappearance" of solar ν_e on the way to the Earth. The hypothesis of solar-ν_e oscillations, which (in one variety or another) were considered from ∼1970 on as the most natural explanation of the observed [6, 47–50] solar-neutrino, ν_e, deficit (see, e.g., references [59–64]), has been convincingly confirmed in the measurement of the solar-neutrino flux through the neutral-current (NC) reaction on deuterium by the SNO experiment [7, 52–54], and by the first results of the KamLAND experiment [55]. The combined analysis of the solar-neutrino data obtained by the Homestake, SAGE, GALLEX/GNO, Super-Kamiokande, and the SNO experiments, and of the KamLAND reactor $\bar{\nu}_e$ data [55], established large mixing-angle (LMA), MSW oscillations [60,61] as the dominant mechanism giving rise to the observed solar-ν_e deficit (see, e.g., [65]). The Kamiokande experiment [47] provided the first evidence for oscillations of atmospheric neutrinos, ν_μ and $\bar{\nu}_\mu$, while the data from the Super-Kamiokande experiment made the case for atmospheric-neutrino oscillations convincing [5]. Indications for ν-oscillations were also reported by the LSND collaboration [39] but are dis-favoured by the recent MiniBooNE measurement [40].

Compelling confirmation of oscillations in (ν_μ, $\bar{\nu}_\mu$), and reactor, $\bar{\nu}_e$ was provided by L/E-dependence observed by Super-Kamiokande [9] and by the spectral distortion observed by the KamLAND and K2K experiments [8,57]. For the first time the data exhibit directly the effects of the oscillatory dependence on L/E and E characteristic of neutrino-oscillations in vacuum [66]. As a result of these developments, the oscillations of solar ν_e, atmospheric ν_μ and $\bar{\nu}_\mu$, accelerator ν_μ (at $L \sim 250$ km and $L \sim 730$ km) and reactor $\bar{\nu}_e$ (at $L \sim 180$ km), driven by non-zero ν-masses and ν-mixing, can be considered as practically established.

All existing ν-oscillation data, except the data of LSND experiment [39], can be described assuming three-neutrino mixing in vacuum. Let us recall that in the LSND experiment indications for $\bar{\nu}_\mu \to \bar{\nu}_e$ oscillations with $(\Delta m^2)_{\rm LSND} \simeq 1$ eV^2 were obtained. The minimal four-neutrino-mixing scheme which could incorporate the LSND indications for $\bar{\nu}_\mu$ oscillations is disfavoured

by the existing, long-baseline data [67] and by the recent MiniBooNE data [40]. The ν-oscillation explanation of the LSND results is possible assuming five-neutrino mixing [68].

The three-neutrino mixing scheme will be referred to in what follows as the "Standard Neutrino Model" (SνM). It is the minimal neutrino mixing model which can account for the oscillations of solar (ν_e), atmospheric (ν_μ and $\bar{\nu}_\mu$), reactor ($\bar{\nu}_e$) and accelerator (ν_μ) neutrinos. In the SνM, the (left-handed) fields of the flavour neutrinos ν_e, ν_μ and ν_τ in the expression for the weak charged lepton current are linear combinations of fields of three neutrinos ν_j, $j = 1, 2, 3$, having definite mass m_j:

$$\begin{pmatrix} \nu_{e\mathrm{L}} \\ \nu_{\mu\mathrm{L}} \\ \nu_{\tau\mathrm{L}} \end{pmatrix} = U_{\mathrm{PMNS}} \begin{pmatrix} \nu_{1\mathrm{L}} \\ \nu_{2\mathrm{L}} \\ \nu_{3\mathrm{L}} \end{pmatrix} = \begin{pmatrix} U_{e1} & U_{e2} & U_{e3} \\ U_{\mu 1} & U_{\mu 2} & U_{\mu 3} \\ U_{\tau 1} & U_{\tau 2} & U_{\tau 3} \end{pmatrix} \begin{pmatrix} \nu_{1\mathrm{L}} \\ \nu_{2\mathrm{L}} \\ \nu_{3\mathrm{L}} \end{pmatrix} \tag{1}$$

where U_{PMNS} is the Pontecorvo-Maki-Nakagawa-Sakata (PMNS) neutrino mixing matrix [2–4], $U_{\mathrm{PMNS}} \equiv U$. The PMNS mixing matrix can be parametrised by 3 angles, and, depending on whether the massive neutrinos ν_j are Dirac or Majorana particles, by 1 or 3 CP-violation (CPV) phases [69–72]. In the standard parameterisation (see, e.g., [73]), U_{PMNS} has the form:

$$U_{\mathrm{PMNS}} = \begin{pmatrix} c_{12}c_{13} & s_{12}c_{13} & s_{13}e^{-i\delta} \\ -s_{12}c_{23} - c_{12}s_{23}s_{13} & c_{12}c_{23} - s_{12}s_{23}s_{13}e^{i\delta} & s_{23}c_{13} \\ s_{12}s_{23} - c_{12}c_{23}s_{13}e^{i\delta} & -c_{12}s_{23} - s_{12}c_{23}s_{13}e^{i\delta} & c_{23}c_{13} \end{pmatrix} \mathrm{diag}(1, e^{i\alpha/2}, e^{i\beta/2}) \,, \tag{2}$$

where $c_{ij} = \cos\theta_{ij}$, $s_{ij} = \sin\theta_{ij}$, the angles $\theta_{ij} = [0, \pi/2]$, $\delta = [0, 2\pi]$ is the Dirac CPV phase and α, β are two Majorana CP-violation phases [69–72]. One can identify $\Delta m^2_{\odot} = \Delta m^2_{21} > 0$ with the neutrino mass squared difference responsible for the solar-neutrino oscillations. In this case $|\Delta m^2_{\mathrm{A}}| = |\Delta m^2_{31}| \cong |\Delta m^2_{32}| \gg \Delta m^2_{21}$ is the neutrino mass-squared difference driving the dominant atmospheric-neutrino oscillations, while $\theta_{12} = \theta_{\odot}$ and $\theta_{23} = \theta_{\mathrm{A}}$ are the solar and atmospheric neutrino mixing angles, respectively. The angle θ_{13} is the so-called "CHOOZ mixing angle" – it is constrained by the data from the CHOOZ and Palo Verde experiments [74, 75].

Let us recall that the properties of Majorana particles are very different from those of Dirac particles. A massive Majorana neutrino χ_k with mass $m_k > 0$ can be described (in local quantum field theory) by a 4-component, complex spin-1/2 field, $\chi_k(x)$, which satisfies the Majorana condition:

$$C\,(\bar{\chi}_k(x))^{\mathrm{T}} = \xi_k\,\chi_k(x), \quad |\xi_k|^2 = 1\,, \tag{3}$$

where C is the charge conjugation matrix. The Majorana condition is invariant under proper Lorentz transformations. It reduces by two the number of independent components in $\chi_k(x)$.

The condition (3) is invariant with respect to $U(1)$ global gauge transformations of the field $\chi_k(x)$ carrying a $U(1)$ charge Q, $\chi_k(x) \to e^{i\alpha Q}\chi_k(x)$, only if $Q = 0$. As a result and in contrast to the Dirac fermions: i) the Majorana particles χ_k cannot carry non-zero additive quantum

numbers (lepton charge, etc.); and ii) the Majorana fields $\chi_k(x)$ cannot "absorb" phases. This is the reason why the PMNS matrix contains two additional CP-violating phases in the case when the massive neutrinos ν_k are Majorana fermions [69], $\nu_k \equiv \chi_k$. It follows from the above that the Majorana-neutrino field, $\chi_k(x)$, describes the two spin states of a spin 1/2, absolutely-neutral particle, which is identical with its antiparticle, $\chi_k \equiv \bar{\chi}_k$. If CP-invariance holds, Majorana neutrinos have definite CP-parity, $\eta_{CP}(\chi_k) = \pm i$:

$$U_{CP}\ \chi_k(x)\ U^{-1}_{CP} = \eta_{CP}(\chi_k)\ \gamma_0\ \chi_k(x'), \quad \eta_{CP}(\chi_k) = \pm i\ . \tag{4}$$

It follows from the Majorana condition that the currents $: \bar{\chi}_k(x) O^i \chi_k(x) : \equiv 0$, for $O^i = \gamma_\alpha$; $\sigma_{\alpha\beta}$; $\sigma_{\alpha\beta}\gamma_5$. This means that Majorana neutrinos cannot have non-zero $U(1)$ charges and intrinsic magnetic- and electric-dipole moments. Dirac fermions can possess non-zero lepton charge and intrinsic magnetic- and electric dipole-moments [10].

The existing data allow a determination of $\Delta m^2_{\odot}$, $\sin^2\theta_{12}$, and of $|\Delta m^2_{\rm A}|$, $\sin^2 2\theta_{23}$ with a relatively good precision (see, e.g. [77–79] and subsections 2.2.1 and 2.2.2). For the best fit values we have: $\Delta m^2_{\odot} = 8.0 \times 10^{-5}$ eV^2, $\sin^2\theta_{12} = 0.30$, $|\Delta m^2_{\rm A}| = 2.5 \times 10^{-3}$ eV^2, $\sin^2 2\theta_{23} = 1$. Thus, $\Delta m^2_{\odot} \ll |\Delta m^2_{\rm A}|$. It should be noted, however, that the sign of $\Delta m^2_{\rm A}$ is not fixed by current data. The present atmospheric-neutrino data is essentially insensitive to θ_{13}, satisfying the upper limit on $\sin^2\theta_{13}$ obtained in the CHOOZ experiment [80]. The probabilities of survival of solar ν_e and reactor $\bar{\nu}_e$, relevant for the interpretation of the solar neutrino, KamLAND and CHOOZ neutrino oscillation data, depend on θ_{13} in the case of interest, $|\Delta m^2_{31}| \gg \Delta m^2_{21}$:

$$P^{3\nu}_{\rm KL} \cong \sin^4\theta_{13} + \cos^4\theta_{13}\left[1 - \sin^2 2\theta_{12}\sin^2\tfrac{\Delta m^2_{21}{\rm L}}{4E}\right],$$

$$P^{3\nu}_{\rm CHOOZ} \cong 1 - \sin^2 2\theta_{13}\sin^2\tfrac{\Delta m^2_{31}{\rm L}}{4{\rm E}},$$

$$P^{3\nu}_{\odot} \cong \sin^4\theta_{13} + \cos^4\theta_{13}\ P^{2\nu}_{\odot}(\Delta m^2_{21}, \theta_{12}; N_e\cos^2\theta_{13}),$$

where $P^{2\nu}_{\odot}$ is the solar ν_e survival probability [81–83] corresponding to 2-ν oscillations driven by Δm^2_{21} and θ_{12}, in which the solar e^- number density N_e is replaced by $N_e\cos^2\theta_{13}$ [84], $P^{2\nu}_{\odot} = \bar{P}^{2\nu}_{\odot} + P^{2\nu}_{\odot\,\rm osc}$, $P^{2\nu}_{\odot\,\rm osc}$ being an oscillating term [81–83] and

$$\bar{P}^{2\nu}_{\odot} = \frac{1}{2} + (\frac{1}{2} - P')\cos 2\theta^m_{12}\ \cos 2\theta_{12}, \tag{5}$$

[10] Let us add, finally, that Majorana neutrinos have in addition to the standard propagator (formed by the neutrino field and its Dirac conjugate field), *two non-trivial non-standard (Majorana)* propagators. If $\nu_j(x)$ in equation (1) are massive Majorana neutrinos, the process of $(\beta\beta)_{0\nu}$-decay, $(A, Z) \to (A, Z+2) + e^- + e^-$, for example, can proceed by exchange of virtual neutrinos ν_j due to the one of these Majorana propagators. For Dirac fermions, the two analogous non-standard propagators are identically equal to zero. For further detailed discussion of the properties of Majorana neutrinos (fermions) see, e.g., [62, 76].

$$P' = \frac{e^{-2\pi r_0 \frac{\Delta m^2_{21}}{2E}} \sin^2\theta_{12} - e^{-2\pi r_0 \frac{\Delta m^2_{21}}{2E}}}{1 - e^{-2\pi r_0 \frac{\Delta m^2_{21}}{2E}}}. \quad (6)$$

Here $\bar{P}^{2\nu}_{\odot}$ is the average probability [81–83, 85, 86], P' is the "double exponential" jump probability [81–83], r_0 is the scale-height of the change of N_e along the ν-trajectory in the Sun [81–83, 87–89], and θ^m_{12} is the mixing angle in matter, which in the vacuum limit coincides with θ_{12}. In the LMA solution region of interest, ${P^{2\nu}_{\odot}}_{\rm osc} \cong 0$ [89]. Performing a combined analysis of the solar-neutrino, CHOOZ, and KamLAND data, one finds [77–79]: $\sin^2\theta_{13} < 0.040$ at 99.73% C.L.

It follows from the results described above that the atmospheric-neutrino mixing is close to maximal, $\theta_{23} \cong \pi/4$, the solar-neutrino mixing angle $\theta_{12} \cong \pi/3$, and the CHOOZ angle $\theta_{13} < \pi/15$. Correspondingly, the pattern of neutrino mixing is drastically different from that of the quark mixing. A comprehensive theory of flavour and of neutrino mixing must be capable of explaining this remarkable difference. The current theoretical ideas about the possible origin of the pattern of neutrino mixing are reviewed in Section 3.

As we have seen, the fundamental parameters characterising the SνM are: i) the 3 angles θ_{12}, θ_{23}, θ_{13}; ii) depending on the nature of massive neutrinos ν_j - 1 Dirac (δ), or 1 Dirac + 2 Majorana (δ, α, β), CP-violation phases; and iii) the 3 neutrino masses, m_1, m_2, m_3. This makes 9 additional parameters in the Standard Model of particle interactions.

It is convenient to express the two larger neutrino masses in terms of the third mass and the measured $\Delta m^2_{\odot} = \Delta m^2_{21} > 0$ and $\Delta m^2_{\rm A}$. We have remarked earlier that the atmospheric-neutrino, K2K, and MINOS data do not allow one to determine the sign of $\Delta m^2_{\rm A}$. This implies that, if we identify $\Delta m^2_{\rm A}$ with $\Delta m^2_{31(2)}$ in the case of 3-neutrino mixing, one can have $\Delta m^2_{31(2)} > 0$ or $\Delta m^2_{31(2)} < 0$. The two possible signs of $\Delta m^2_{\rm A}$ correspond to two types of ν-mass spectrum:

- *Normal ordering*: $m_1 < m_2 < m_3$, $\Delta m^2_{\rm A} = \Delta m^2_{31} > 0$, $m_{2(3)} = (m^2_1 + \Delta m^2_{21(31)})^{\frac{1}{2}}$; and
- *Inverted ordering* [11]: $m_3 < m_1 < m_2$, $\Delta m^2_{\rm A} = \Delta m^2_{32} < 0$, $m_2 = (m^2_3 + \Delta m^2_{23})^{\frac{1}{2}}$, $m_1 = (m^2_3 + \Delta m^2_{23} - \Delta m^2_{21})^{\frac{1}{2}}$.

Depending on the values of the lightest neutrino mass, $\min(m_j)$, the neutrino mass spectrum can also be:

- *Normal Hierarchy (NH)*: $m_1 \ll m_2 \ll m_3$, $m_2 \cong (\Delta m^2_{\odot})^{\frac{1}{2}} \sim 0.009$ eV, $m_3 \cong |\Delta m^2_{\rm A}|^{\frac{1}{2}} \sim 0.05$ eV;

[11] In the convention we use (called A), the neutrino masses are not ordered in magnitude according to their index number: $\Delta m^2_{31} < 0$ corresponds to $m_3 < m_1 < m_2$. We can also always number the neutrinos with definite mass in such a way that [90] $m_1 < m_2 < m_3$. In this convention (called B), we have in the case of inverted-hierarchy spectrum: $\Delta m^2_{\odot} = \Delta m^2_{32}$, $\Delta m^2_{\rm A} = \Delta m^2_{31}$. Convention B is used, e.g., in [73, 91].

- *Inverted Hierarchy (IH)*: $m_3 \ll m_1 < m_2$, with $m_{1,2} \cong |\Delta m^2_{\rm A}\ |^{\frac{1}{2}} \sim 0.05$ eV; or

- *Quasi-Degenerate (QD)*: $m_1 \cong m_2 \cong m_3 \cong m_0$, $m_j^2 \gg |\Delta m^2_{\rm A}\ |$, $m_0 \gtrsim 0.10$ eV.

One of the principal goals of the future studies of neutrino mixing is to determine the basic parameters of the SνM and to test its validity.

The possibilities of measuring with high precision the basic parameters of SνM $\Delta m^2_{\odot}$, $\sin^2\theta_{\odot}$ $|\Delta m^2_{\rm A}\ |$, $\sin^2 2\theta_{23}$, $\sin^2\theta_{13}$, of determining sgn(Δm^2_{31}) and of searching for the effects of CP-violation due to the Dirac phase δ, in neutrino oscillation experiments, will be discussed in detail below. It is well-known that the neutrino-oscillation experiments are not sensitive to the absolute scale of neutrino masses. Information on the absolute neutrino-mass scale, or on $\min(m_j)$, can be derived in ^{3}H β-decay experiments and from cosmological and astrophysical data (see sections 2.2.4 and 3.4.1.2). The most stringent upper bounds on the $\bar{\nu}_e$ mass and on the sum of neutrino masses will be discussed briefly in sections 2.2.4 and 3.4.2. These bounds lead to the conclusion that neutrino masses satisfy $m_j \lesssim 1$ eV and thus are much smaller than the masses of the charged leptons and quarks. A comprehensive theory of neutrino mixing should be able to explain this enormous difference between the neutrino and charged-fermion masses. The theoretical aspects of the problem of neutrino mass generation and of the smallness of neutrino masses are reviewed in section 3.1.

Neutrino-oscillation experiments are also insensitive to the nature – Dirac or Majorana, of massive neutrinos and, correspondingly, to the two CP-violating, Majorana phases in the PMNS matrix [69,92] since the latter do not enter into the expressions for the probabilities for neutrino oscillations. The only realistic experiments which could verify that the massive neutrinos ν_j are Majorana particles are, at present, the neutrinoless double-beta ($(\beta\beta)_{0\nu}$-) decay experiments. The physics potential of these experiments is discussed in section 2.2.4. Even if massive neutrinos are proven to be Majorana fermions, measuring the Majorana CP phases would be extremely challenging. It is quite remarkable, however, that the Majorana CP-violating phase(s) in the PMNS matrix, through leptogenesis (see section 3.4.2, may result in the baryon asymmetry of the Universe [93–95].

The existing data on neutrino oscillation, as we will see, allow a determination of $\Delta m^2_{\odot}$, $\sin^2\theta_{\odot}$, $|\Delta m^2_{\rm A}\ |$, and $\sin^2 2\theta_{23}$, at 3σ with an uncertainty of approximately $\sim$12%, $\sim$24%, $\sim$28% and $\sim$15%, respectively. These parameters can, and very likely will, be measured with much higher accuracy in the future: the indicated 3σ errors in the determination, for instance, of $\Delta m^2_{\odot}$ and $\sin^2\theta_{\odot}$, can be reduced to [96–98] 4% and 10%, as will be reviewed below. "Near" future experiments with reactor $\bar{\nu_e}$ can improve the current sensitivity to the value of $\sin^2\theta_{13}$ by a factor of between 5 and 10. The type of neutrino-mass spectrum, i.e. sgn(Δm^2_{31}), can be determined by studying the oscillations of neutrinos and antineutrinos, say, $\nu_\mu \leftrightarrow \nu_e$ and $\bar{\nu}_\mu \leftrightarrow \bar{\nu}_e$, in which matter effects are sufficiently large. If $\sin^2 2\theta_{13} \gtrsim 0.05$ and $\sin^2\theta_{23} \gtrsim 0.50$, information on sgn$(\Delta m^2_{31})$ might be obtained in atmospheric neutrino experiments by investigating the effects of the sub-dominant transitions $\nu_{\mu(e)} \to \nu_{e(\mu)}$ and $\bar{\nu}_{\mu(e)} \to \bar{\nu}_{e(\mu)}$ of atmospheric neutrinos

which traverse the Earth [99–101]. For $\nu_{\mu(e)}$ (or $\bar{\nu}_{\mu(e)}$) crossing the Earth's core, new types of resonance-like enhancement of the oscillation probabilities may take place due to the mantle-core constructive-interference effect (neutrino oscillation length resonance (NOLR)) [102–105]. As a consequence of this effect, the corresponding $\nu_{\mu(e)}$ (or $\bar{\nu}_{\mu(e)}$) transition probabilities can be maximal [103–105]. For $\Delta m^2_{31} > 0$, the neutrino transitions $\nu_{\mu(e)} \to \nu_{e(\mu)}$ are enhanced, while for $\Delta m^2_{31} < 0$ the enhancement of antineutrino transitions $\bar{\nu}_{\mu(e)} \to \bar{\nu}_{e(\mu)}$ takes place, which might allow to determine $\mathrm{sgn}(\Delta m^2_{31})$.

It should be emphasised that the CP-violation in the lepton sector is one of the most challenging frontiers in future studies of neutrino mixing. The experimental searches for CP-violation in neutrino oscillations can help answer fundamental questions about the status of CP-symmetry in the lepton sector at low energy. The observation of leptonic CP-violation at low energies will have far reaching consequences. It can shed light, in particular, on the possible origin of the baryon asymmetry of the Universe. As was realised recently [93, 94], the CP-violation necessary for the generation of the baryon asymmetry can be due exclusively to the Dirac (and/or Majorana) CP-violating phase in the PMNS matrix. Thus, there can be a direct relation between low energy CP-violation in the lepton sector, observable, e.g., in neutrino oscillations, and the matter-antimatter asymmetry of the Universe. These results underline the importance of understanding the status of the CP-symmetry in the lepton sector and, correspondingly, of the experiments aiming to measure the CHOOZ angle θ_{13} and of the experimental searches for CP-violation in neutrino oscillations.

2.2 Review of the present generation of experiments

2.2.1 Solar and reactor neutrino experiments

Measurements of the solar-neutrino flux were the first to indicate that neutrinos undergo flavour oscillations. The first indications that the solar-neutrino flux was smaller than that predicted by the Standard Solar Models came from Davis' experiment at Homestake (USA) [6]. The results of this experiment, have been confirmed by a series of solar neutrino experiments, the SAGE experiment in Russia [48], the Gallex and GNO experiments in Italy [106,107], the Kamiokande and Super-Kamiokande (SK) in Japan [51,108] and finally by the Sudbury Neutrino Observatory (SNO) in Canada [7, 52–54, 109]. In particular, the neutral current (NC) to charged current (CC) ratio from the SNO data in 2002 [52] established the presence of an active neutrino flavour other than ν_e in the observed solar neutrino flux at the 5.3σ level, putting to rest any doubt about the existence of flavour oscillations of solar neutrinos. Further evidence was provided by the statistically powerful NC data from the salt phase of the SNO experiment [54, 109]. The cumulative result of solar neutrino data, collected from different experiments over a period of more than four decades, culminated in the emergence of the 'Large Mixing Angle' (LMA) solution as the most favoured explanation of the solar neutrino problem.

Figure 2 shows the confidence level contours in the $\Delta m^2_{21} - \sin^2\theta_{12}$ plane, allowed from the global analysis of all solar neutrino data combined [77, 110, 111]. To illustrate the effect of the

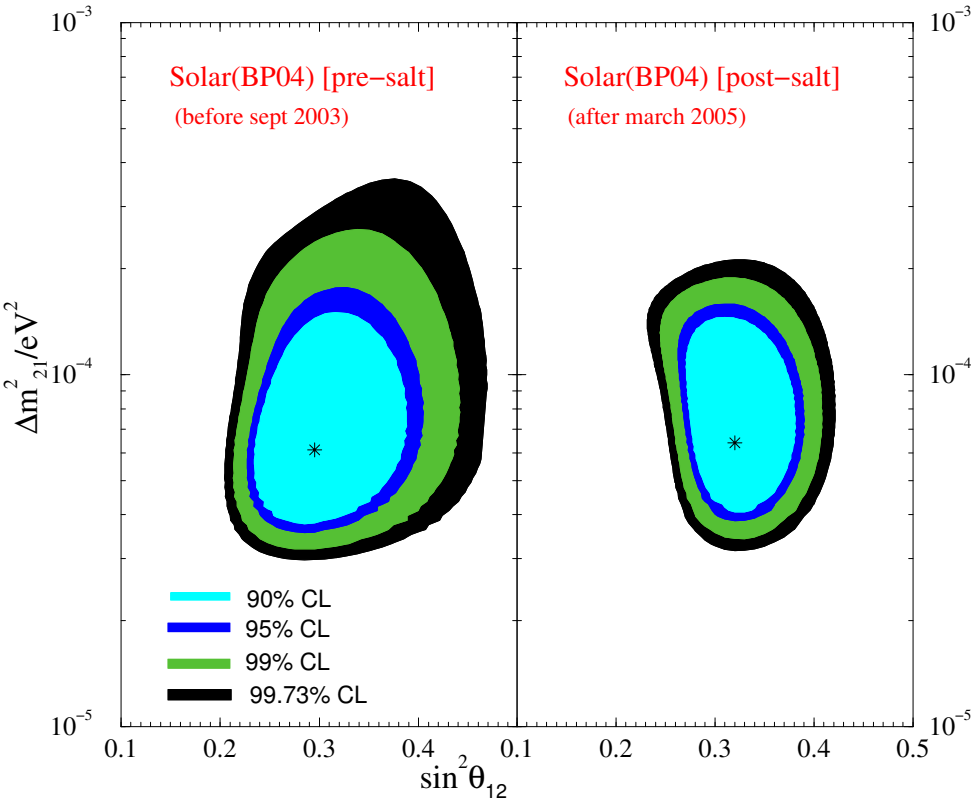

Figure 2: The 90%, 95%, 99% and 99.73% C.L. contours (for two degrees of freedom (dof)) show the allowed areas from the global analysis of the solar neutrino data with (right-hand panel) and without (left-hand panel) the SNO salt phase data. Taken with kind permission of International Journal of Modern Physics from figure 1 in reference [111]. Copyrighted by World Scientific Publishing Company.

results from the salt phase data from SNO, the figure shows in the right-hand and left-hand panels, the allowed areas obtained with and without the salt phase SNO results respectively. The high statistics NC to CC ratio in SNO salt data, causes the shrinking of the allowed regions. In particular, the upper bound on both Δm^2_{21} and $\sin^2\theta_{12}$ is seen to improve remarkably.

The KamLAND reactor anti-neutrino experiment in Japan [8, 55], specifically designed to test the LMA region of the solar neutrino parameter space, presented its first results in 2002, confirming the LMA solution [55]. The higher statistics data from this experiment released in 2004 [8] not only confirmed the observed depletion of the reactor antineutrinos from the first results [55], but for the first time unambiguously showed the existence of an L/E dependence in its positron spectrum, confirming that the observed $\overline{\nu}_e$ flavour oscillations were indeed due to neutrino mass and mixing.

Figure 3 [110, 111] shows the impact of the first and second set of data from the KamLAND experiment on the solar neutrino oscillation parameter space. The current 3σ allowed range of Δm^2_{21} and $\sin^2\theta_{12}$ obtained in the analysis of Bandyopadhyay *et al.* [77, 110, 111] is given in

Data set used	Range of Δm^2_{21}	Spread in Δm^2_{21}	Range of $\sin^2\theta_{12}$	Spread in $\sin^2\theta_{12}$
only solar	$(3.3-18.4)\times10^{-5}$ eV^2	69%	$0.24-0.41$	26%
solar + 766.3 Ty KL	$(7.2-9.2)\times10^{-5}$ eV^2	12%	$0.25-0.39$	22%
solar(SNO3) + 766.3 Ty KL	$(7.2-9.2)\times10^{-5}$ eV^2	12%	$0.26-0.37$	18%
solar(SNO3) + 3KTy KL	$(7.6-8.6)\times10^{-5}$ eV^2	6%	$0.26-0.36$	16%

Table 1: The 3σ allowed ranges (1 dof) and % spread of Δm^2_{21} and $\sin^2\theta_{12}$ obtained using current and expected future data from the current generation of solar neutrino and KamLAND experiments.

Table 1 along with their corresponding "spread" defined as:

$$\text{spread} = \frac{\mathscr{P}_{max} - \mathscr{P}_{min}}{\mathscr{P}_{max} + \mathscr{P}_{min}} \times 100 \ , \tag{7}$$

where $\mathscr{P}_{min}$ and $\mathscr{P}_{max}$ are the minimum and maximum allowed values of the parameter $\mathscr{P}$ at 3σ. The allowed regions were derived on the assumption of CPT invariance and that θ_{13} is negligible. Also given in Table 1 are the bounds on Δm^2_{21} and $\sin^2\theta_{12}$ that are expected to be obtained when additional data from the running SNO and KamLAND experiments becomes available. For SNO, the analysis assumes that the third and final phase of the experiment will measure the same NC and CC rates as the salt phase, but with reduced errors of 6% and 5% respectively [112]. For KamLAND, the prospective 3 kTy data is simulated at $\Delta m^2_{21} = 8.0\times10^{-5}$ eV^2 and $\sin^2\theta_{12} = 0.3$ and a systematic error of 5% is assumed. Better measurement of charged-current (CC) and neutral-current (NC) rates in SNO is expected to improve the limits on $\sin^2\theta_{12}$. The sensitivity of the KamLAND experiment to the shape of the reactor-induced $\overline{\nu}_e$ positron spectrum, gives the experiment a tremendous ability to constrain Δm^2_{21}. However, we can see from table 1, KamLAND is not as sensitive to the mixing angle θ_{12} [98,113]. The uncertainty in Δm^2_{21} is expected to reduce to 6% at 3σ with 3 kTy of data from KamLAND. The uncertainty in $\sin^2\theta_{12}$ is expected to improve after the phase-III results from SNO to 18% at 3σ. This would improve to about 16% if the SNO phase-III projected results are combined with the 3 kTy simulated data from KamLAND. However, we note that even with the combined data from phase-III of SNO and 3 kTy statistics from KamLAND, the uncertainty on $\sin^2\theta_{12}$ would stay well above the 10-15% level at 3σ.

In our discussion so far, we have assumed the mixing angle θ_{13} to be zero. If θ_{13} is allowed to vary freely, then the allowed regions obtained are those shown in figure 4 [114]. Note that this figure shows only the 2σ contours and uses the confidence-level definition appropriate for one degree of freedom. The data do not exclude the possibility that $\theta_{13} = 0$. The KamLAND experiment places an upper bound on the value of θ_{13} by taking into account the neutrino energy spectrum as well as the absolute rate. By lowering the value of θ_{12}, the anti-correlation between θ_{12} and θ_{13} can be used to explain the KamLAND rate data for a wide range of values of θ_{13}. In contrast, the KamLAND data on the positron energy spectrum can be explained only for a certain range of θ_{12}. This imposes an upper limit on the allowed value of θ_{13}. For the solar neutrinos, the upper limit on θ_{13} comes mainly from the difference in the θ_{12}–θ_{13} anti-correlation between the low- and high-energy end of the solar-neutrino spectrum. The tension between the

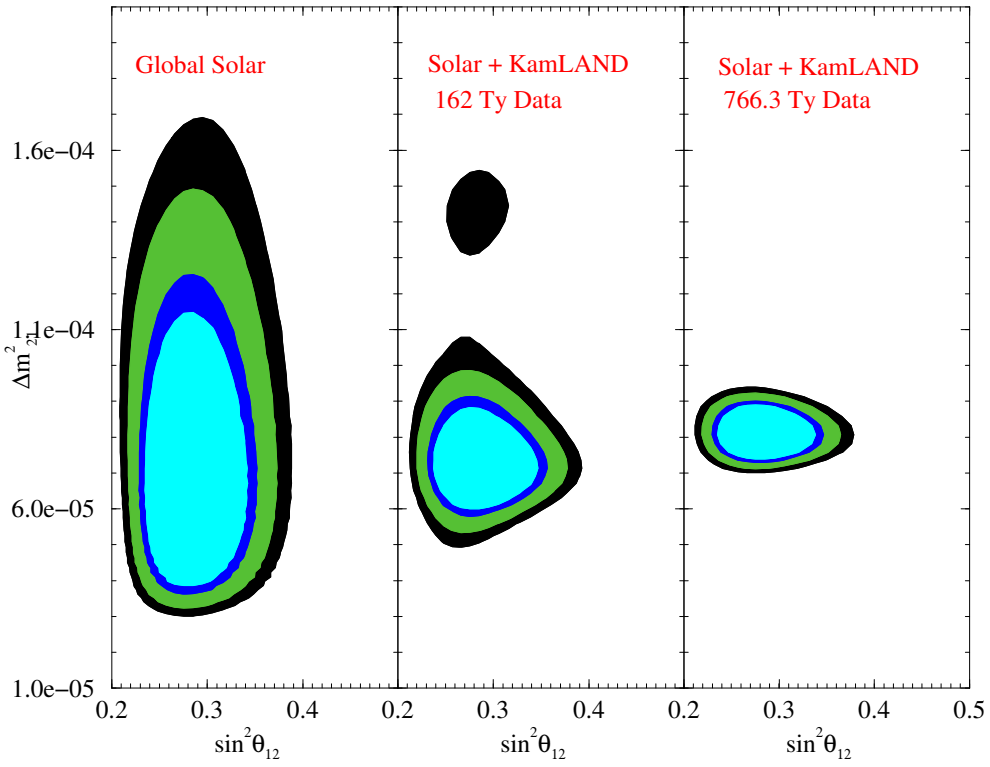

Figure 3: The 90%, 95%, 99% and 99.73% C.L. contours (2 dof) show the allowed areas from the global analysis of the solar neutrino data (left-hand panel) and solar neutrino data combined with the first KamLAND results [55] (middle panel) and second KamLAND results [8] (right-hand panel). Taken with kind permission of International Journal of Modern Physics from figure 2 in reference [111]. Copyrighted by World Scientific Publishing Company.

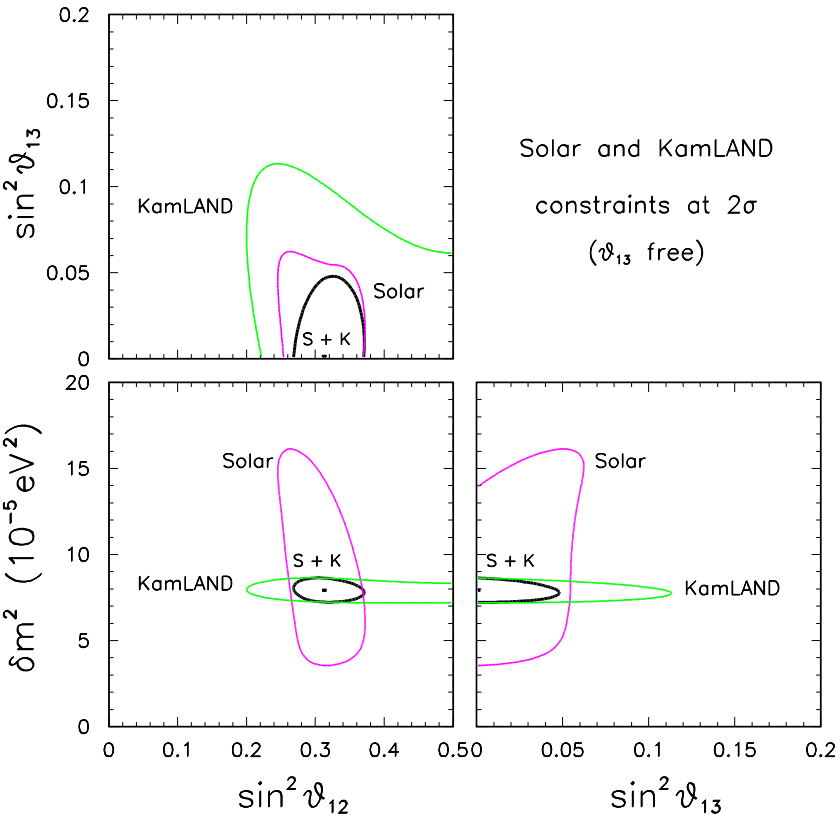

Figure 4: Three flavour analysis of solar and KamLAND data (both separately and in combination) in the ($\Delta m^2_{21} (\equiv \delta m^2)$, $\sin^2\theta_{12}$, $\sin^2\theta_{13}$). The contours show the 2σ allowed regions corresponding to $\Delta\chi^2 = 4$. Taken with kind permission of Progress in Particle and Nuclear Physics from figure 14 in reference [114]. Copyrighted by Elsevier Science B.V.

low energy solar neutrino data from SAGE, GALLEX, and GNO and the high energy ^8B data from SK and SNO, results in a reasonably tight upper bound on θ_{13} [97,115]. Together, the data from solar-neutrino experiments and KamLAND put a rather stringent limit of $\sin^2\theta_{13} > 0.05$ at 2σ [114].

2.2.2 Atmospheric neutrino experiments

The parameters Δm^2_{32} ($\approx \Delta m^2_{31}$) and $\sin^2\theta_{23}$ are constrained by the zenith-angle dependence of the atmospheric-neutrino data obtained by the Super-Kamiokande experiment (SK) [5, 116]. The results from the earlier Kamiokande [117, 118], MACRO [119, 120], and Soudan-2 [121] experiments are in agreement with the SK data. Figure 5 [116] shows the allowed areas in the Δm^2_{31}–$\sin^2 2\theta_{23}$ parameter space, from a two-generation analysis. The allowed regions are obtained by fitting both the zenith-angle data [116] and the L/E dependent data [9] from SK.

The values of Δm^2_{31} and $\sin^2 2\theta_{23}$ are also constrained by the results from the K2K [57] and MINOS [11] long-baseline experiments. While K2K has finished its run, MINOS has declared its first results in the summer of 2006. Both K2K and MINOS results are consistent with the SK

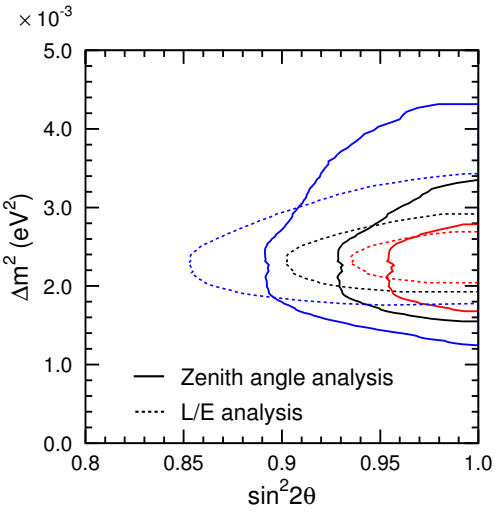

Figure 5: The 68% (red lines), 90% (black lines) and 99% (blue lines) C.L. (2 dof) allowed oscillation parameter regions obtained in two-generation framework by the SK collaboration. The solid lines are with the analysis of the zenith angle binned data, while the dashed lines are obtained using the L/E binned analysis. Taken with kind permission of the Physical Review from figure 42 in reference [116]. Copyrighted by the American Physical Society.

atmospheric neutrino data, and while the allowed range of values for $\sin^2 2\theta_{23}$ is still controlled mainly by the SK atmospheric data, the results from the long-baseline experiments have an impact on the allowed range of values for Δm^2_{31}.

Figure 6 [67] shows the projected allowed areas obtained from a full three-generation analysis of the global data from all solar, atmospheric, long-baseline, and reactor-neutrino experiments. Filled regions correspond to allowed areas with the latest MINOS [11] and SNO [109] results, while the hollow regions correspond to the allowed areas obtained without these updates. In the $\Delta\chi^2$ versus parameter curves in the figure, the solid lines are for the full data set, while the dashed lines are without the new SNO [109] and MINOS [11] results. The impact of the MINOS data on the allowed values of Δm^2_{31} is clearly visible. The best-fit for Δm^2_{31} shifts to a larger value compared to that obtained from the SK atmospheric-neutrino data alone. The range of allowed values for Δm^2_{31} is also significantly changed. While the upper bound on Δm^2_{31} is hardly affected, the lower limit on this parameter is considerably improved. The current limits on all the oscillation parameters can be directly read from this figure.

Figure 7 shows the 90% C.L. upper limit on θ_{13} and how it depends on the different data sets. One can note from this figure that the bound from the solar+KamLAND combined analysis is comparable to the one obtained using the atmospheric+K2K+MINOS results. The 90%(3σ)

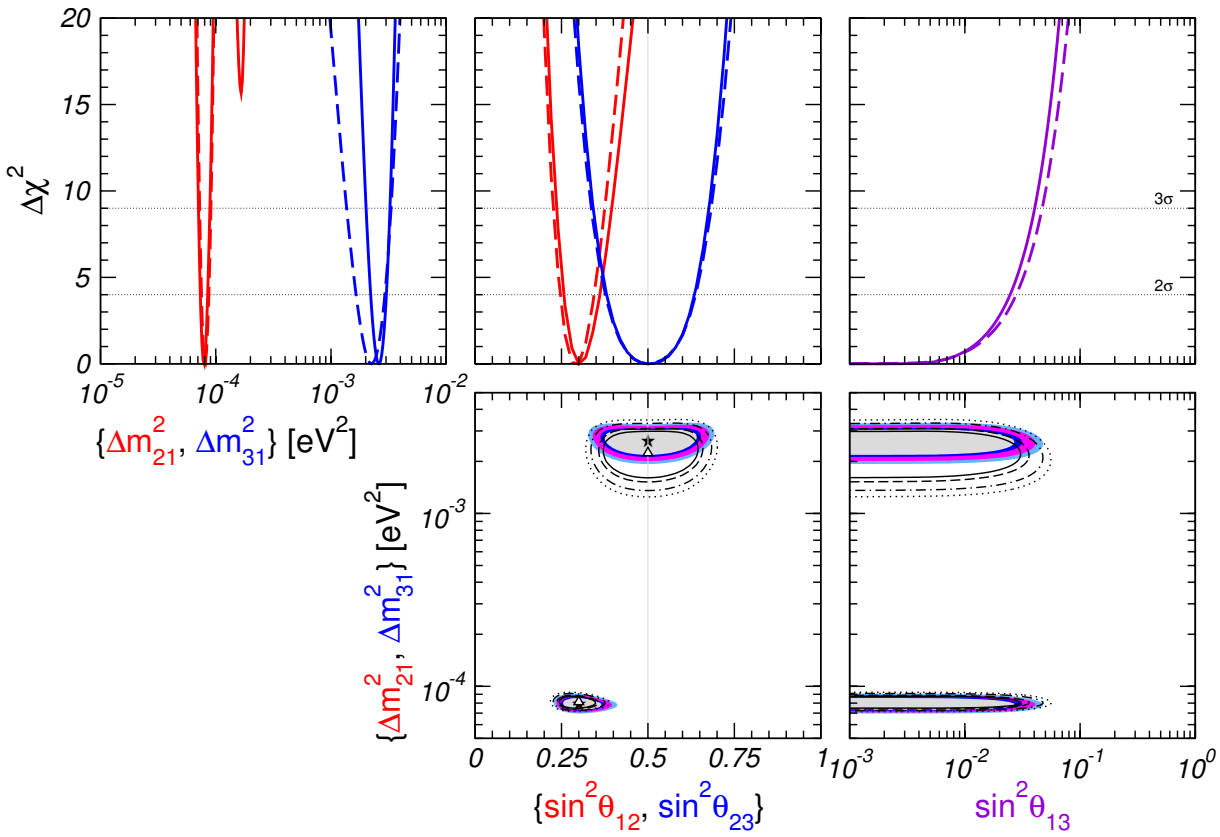

Figure 6: Projections of the allowed regions from the global oscillation data at 90%, 95%, 99%, and 3σ C.L. for 2 dof for various parameter combinations. Also shown is $\Delta\chi^2$ as a function of the oscillation parameters $\sin^2\theta_{12}, \sin^2\theta_{23}, \sin^2\theta_{13}, \Delta m^2_{21}, \Delta m^2_{31}$, minimized with respect to all undisplayed parameters. Dashed lines and empty regions correspond to the global analysis before this update, while solid lines and colored regions show our most recent results. Taken with kind permission of New Journal of Physics from figure 12 in reference [67]. Copyrighted by Deutsche Physikalische Gesellschaft & Institute of Physics

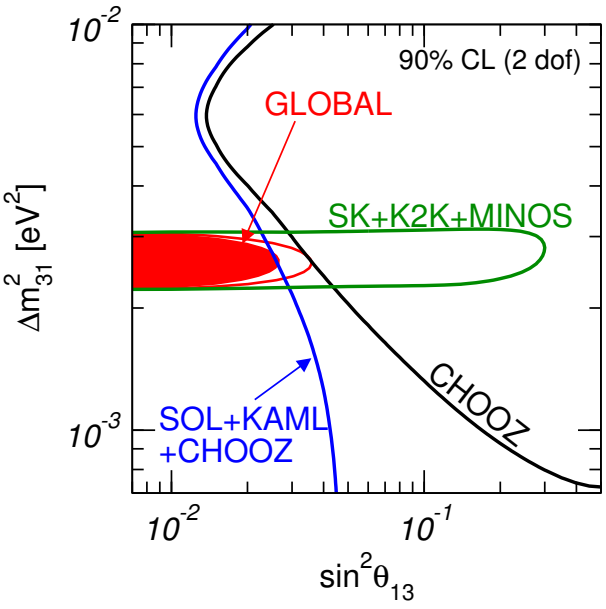

Figure 7: 90% C.L. upper bound on $\sin^2\theta_{13}$ (2 dof) from the combination of all neutrino oscillation data as a function of Δm^2_{31}. Taken from figure C2 in [67] (v6).

bounds (1 dof) on $\sin^2\theta_{13}$ from an analysis of different sets of data read as [67]

$$: \sin^2\theta_{13} \leq \begin{cases} 0.033\ (0.071) & (\text{solar} + \text{KamLAND}) \\ 0.026\ (0.054) & (\text{CHOOZ} + \text{atmospheric} + \text{K2K} + \text{MINOS}) \\ 0.020\ (0.040) & (\text{global data}) \end{cases} \tag{8}$$

The best-fit values and allowed range of values of the oscillation parameters at different C.L. obtained by Maltoni *et al.* in [67] are shown in Table 2.

parameter	best fit	2σ	3σ	4σ
Δm^2_{21} [10^{-5} eV^2]	7.9	7.3–8.5	7.1–8.9	6.8–9.3
Δm^2_{31} [10^{-3} eV^2]	2.6	2.2–3.0	2.0–3.2	1.8–3.5
$\sin^2\theta_{12}$	0.30	0.26–0.36	0.24–0.40	0.22–0.44
$\sin^2\theta_{23}$	0.50	0.38–0.63	0.34–0.68	0.31–0.71
$\sin^2\theta_{13}$	0.000	≤ 0.025	≤ 0.040	≤ 0.058

Table 2: Best-fit values, 2σ, 3σ, and 4σ intervals (1 dof) for the three–flavour neutrino oscillation parameters from global data including solar, atmospheric, reactor (KamLAND and CHOOZ) and accelerator (K2K and MINOS) experiments.

2.2.3 Long-baseline neutrino-oscillation experiments

In 1962, just a few years after neutrinos were observed directly for the first time using the intense flux generated in a nuclear reactor [122], the AGS proton accelerator at Brookhaven was

used to show that a second generation of neutrinos exists [123]. In this experiment, a 15 GeV proton beam impinged on a beryllium target, producing pions, which decayed into muons and neutrinos. 13.5m of steel separated the volume where the pions decayed and the spark chambers detected the muons created by the neutrinos penetrating the steel.

Today, the same fundamental principles are used to study the phenomenon of neutrino oscillations. The energies of the neutrinos are fixed at a GeV or more due to the production mechanism, therefore, to probe the oscillations first seen in atmospheric neutrinos, the distances between neutrino source and target have stretched to hundreds of kilometres, giving rise to their collective name of long-baseline (LBL) neutrino-oscillation experiments.

At the time of writing, two such experiments, K2K and MINOS, have demonstrated that neutrinos disappear from their muon neutrino beams in a way that is consistent with neutrino oscillations. A third LBL beam, providing neutrinos with energies running up to of tens of GeV, has just started operating from CERN to Gran Sasso. This facility will test whether the ν_μ-disappearance signals are actually accompanied by conversions of ν_μ into ν_τ, by looking for tau production in a beam that is originally free of tau neutrinos.

The K2K (KEK-to-Kamioka) experiment was formally proposed in 1995 [124], after the first indications of oscillations were seen in Kamiokande, IMB, and Soudan-II atmospheric neutrino data, but before the confirmation by Super-Kamiokande, and indeed before the completion of the 50 kt water Cherenkov detector.

K2K had a baseline of 250km, and the muon-neutrino energy was a GeV or so. The beam was created from a 12 GeV proton beam, the hadrons from which were focussed in a horn-shaped electromagnetic volume to increase the beam intensity. A dedicated detector complex, with a 1 kt water Cherenkov tank, fine-grained detectors, and a muon ranger, was located 100 m from the end of the pion-decay volume, and measured the beam before it started oscillating on its way to Kamioka. Super-Kamiokande was used as the far detector, and the first beam-induced neutrino event was observed in the summer of 1999.

Five and a half years after commissioning, K2K running ended late in 2004. The final oscillation analysis [10] was performed using a data set corresponding to 0.922×10^{20} protons on target. The estimated beam spectra for different neutrino types are shown in figure 8. 112 beam-originated neutrino events were observed, where the expected number in the absence of oscillations was $158.1^{+9.2}_{-8.6}$. Of these events, 58 were single-ring muon-like events fully-contained within the Super-Kamiokande detector. The energies and directions of the muons in fully-contained events can be reconstructed, and because of the simple kinematics of the charged-current quasi-elastic (CCQE) events that make up much of the cross section around 1 GeV, it is possible to estimate the energy of the incoming neutrinos. Such a spectrum is shown in figure 8, for the 58 events, with unoscillated and best-fit oscillated curves, normalised to the number of events seen. These results support maximal mixing, with best-fit two-neutrino oscillation parameters of $\sin^2 2\theta = 1$ and $\Delta m^2 = 2.8\times10^{-3}\mathrm{eV}^2$. The 90% C.L. range for Δm^2 at $\sin^2 2\theta = 1$ is between 1.9 and 3.5 $\times10^{-3}\mathrm{eV}^2$.

The MINOS (Main Injector Neutrino Oscillation Search) experiment was also proposed in

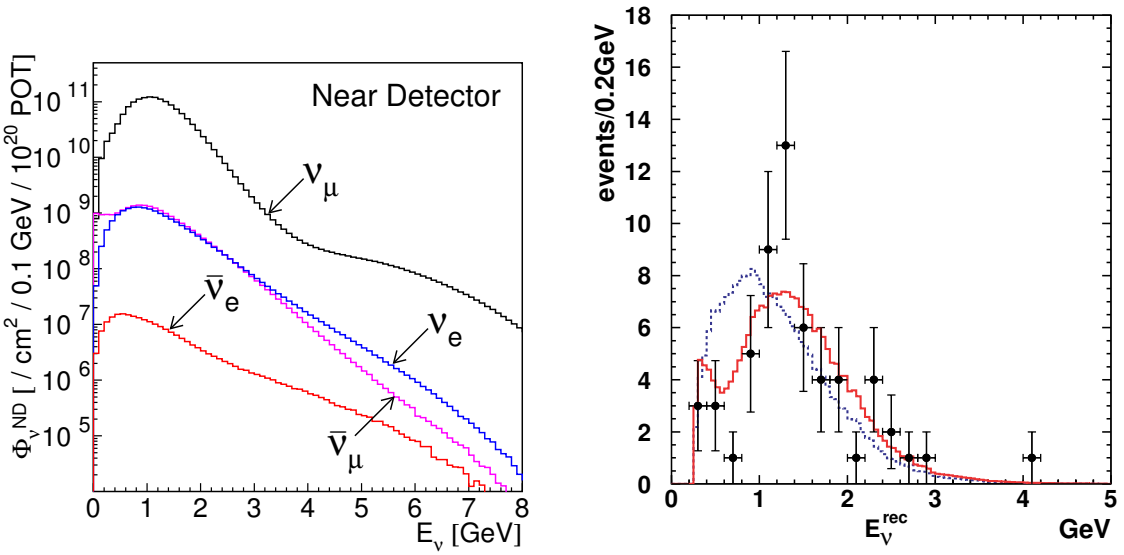

Figure 8: Left: The energy spectrum for each type of neutrino at the K2K Near Detector, estimated by MC simulations. The neutrino beam consists of 97.3% muon neutrinos. Right: The 58 fully-contained muon-like single-ring events, out of the 112 beam-originated neutrino events in K2K. The muon energies and directions can be reconstructed for these events, allowing their parent neutrino energies to be estimated under the assumption that they are from quasi-elastic interactions. The solid line is the best fit spectrum with neutrino oscillation and the dashed line is the expectation without oscillation, both normalised to the number of events seen [10]. Both figures taken with kind permission of Physical Review from figures 6 and 43 in referencefrom [10]. Copyrighted by the American Physical Society.

1995, with a neutrino beam pointed from Fermilab to the Soudan mine in Minnesota, with a baseline of 735 km. The beam has a system of movable focussing horns to allow the beam energy spectrum to be altered. Three different spectra are shown in the upper plot in figure 9. Both near and far detectors consist of a steel and plastic-scintillator sandwich structure, the performance of which was studied in detail in test beam work at CERN [125].

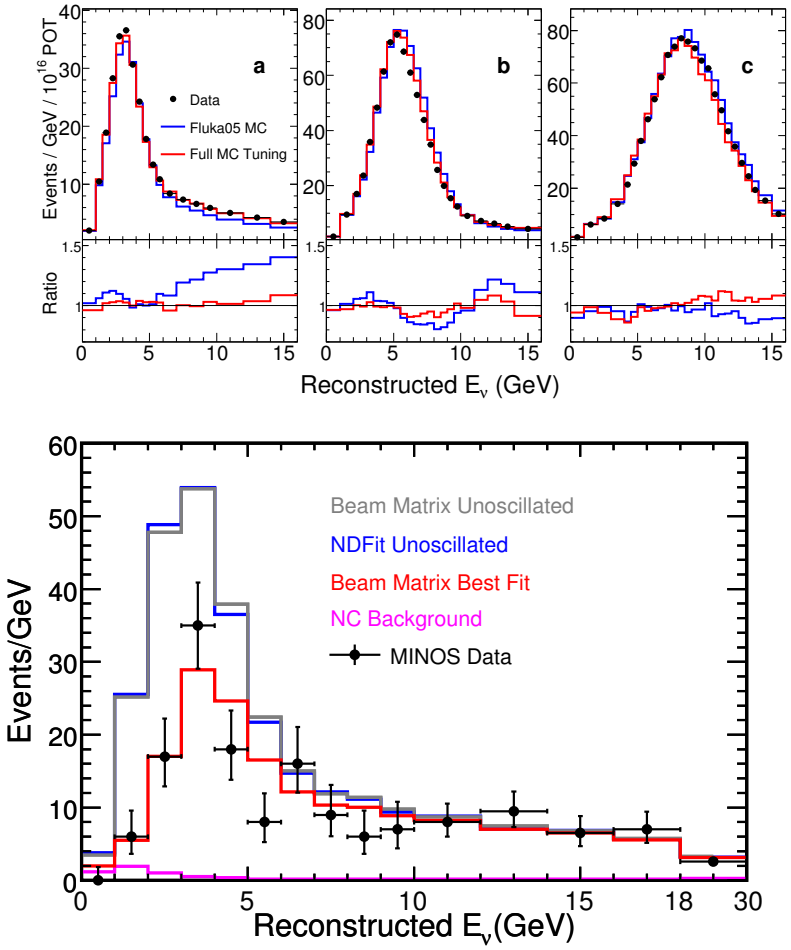

Figure 9: Top: MINOS neutrino beam spectra at the Near Detector, for three beam configurations. Bottom: The final far detector spectrum and predicted distributions, after the first full year of MINOS running (1.27×10^{20} protons on target) [11]. Two different methods of near-to-far extrapolation are shown for the unoscillated spectrum. Both figures taken from with kind permission of Physical Review Letters from figures 2 and 3 in [11]. Copyrighted by the American Physical Society.

The experiment started running in the spring of 2005, and within a year had gathered data corresponding to 1.27×10^{20} protons on target. The data are shown in the lower plot in figure 9. The MINOS results support maximal mixing, with best fit parameters of $|\Delta m^2_{32}| = 2.74^{+0.44}_{-0.26} \times 10^{-3}\text{eV}^2$ and $\sin^2 2\theta_{23} > 0.87$ at 68% C.L. The oscillation parameters from the K2K and MINOS experiments, together with results from Super-Kamiokande are shown in figure 10. MINOS will run for five years, with the goal of accumulating 16×10^{20} protons on target. This data set should improve our knowledge of the oscillation parameters substantially. Both the experiments

described here are linked, if only indirectly, to future projects to make precision measurements of the oscillation parameters and to probe the third mixing angle. These projects, T2K and NOνA, are discussed below.

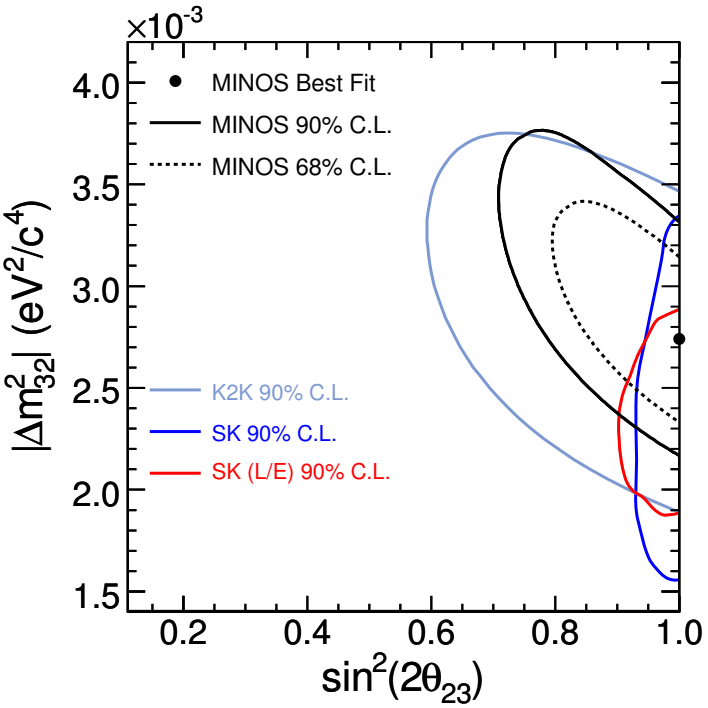

Figure 10: Confidence intervals from the MINOS experiment [11]. Results from K2K [57] and Super-K [9, 116] are also shown. Taken with kind permission of Physical Review Letters from figure 4 in [11]. Copyrighted by the American Physical Society.

2.2.4 $0\nu\beta\beta$ Experiments

Establishing whether the neutrino is a Dirac or a Majorana fermion is of fundamental importance for understanding the origin of neutrino masses and mixing (see, e.g., [126]). Let us recall that the neutrinos, ν_j, with definite mass, m_j, will be Dirac fermions if particle interactions conserve some additive lepton number, e.g., the total lepton number $L = L_e + L_\mu + L_\tau$. If no lepton number is conserved, the neutrinos will be Majorana fermions (see, e.g., [62]). The heavy neutrinos are predicted to be Majorana in nature by the see-saw mechanism [127], which also provides an attractive explanation of the smallness of neutrino masses and, through the leptogenesis theory [128], of the observed baryon asymmetry of the Universe. The observed patterns of neutrino mixing and of neutrino mass-squared differences driving the solar and the dominant atmospheric-neutrino oscillations, can be related to massive Majorana neutrinos and the existence of an approximate symmetry in the lepton sector corresponding to the conservation of the non-standard lepton number $L' = L_e - L_\mu - L_\tau$ (see, e.g., [129]).

The only experiments which have the potential of establishing the Majorana nature of massive neutrinos are the $(\beta\beta)_{0\nu}$-decay experiments searching for the process $(A, Z) \to (A, Z{+}2){+}e^{-}{+}e^{-}$ (for reviews see, e.g., [62, 130–134]). The observation of $(\beta\beta)_{0\nu}$-decay and the measurement of the corresponding half-life with sufficient accuracy, would not only be a proof that total lepton number is not conserved, but might also provide unique information on: i) the type of neutrino-mass spectrum; ii) the absolute scale of neutrino masses; and iii) the Majorana CP-violating phases in the neutrino mixing matrix [69–71, 73, 90, 91, 135–153].

If the ν_j are Majorana fermions, obtaining information about the Majorana CP phases in $U_{\rm PMNS}$ will be remarkably difficult [73, 135, 151, 154, 155]. In a large class of supersymmetric theories which include the see-saw neutrino-mass-generation mechanism, the phases α and β can affect significantly the predictions for the rates of lepton-flavour violating (LFV) decays such as $\mu \to e + \gamma$, $\tau \to \mu + \gamma$, etc. (see, e.g., [156–158]).

Under the assumptions of massive, Majorana neutrinos, three-neutrino mixing, and $(\beta\beta)_{0\nu}$-decay being generated solely through the (V-A) charged-current weak interaction mediated by the exchange of the three Majorana neutrinos, the $(\beta\beta)_{0\nu}$-decay amplitude has the form (see, e.g., [73, 135]): $A(\beta\beta)_{0\nu} \cong <m> M$, where M is the corresponding nuclear matrix element (NME) which does not depend on the neutrino mixing parameters, and:

$$\langle m \rangle = \left| m_1 |U_{\rm e1}|^2 + m_2 |U_{\rm e2}|^2 e^{i\alpha} + m_3 |U_{\rm e3}|^2 e^{i\beta} \right| , \tag{9}$$

is the effective Majorana mass in $(\beta\beta)_{0\nu}$-decay, $|U_{\rm e1}|{=}c_{12}c_{13}$, $|U_{\rm e2}|{=}s_{12}c_{13}$, $|U_{\rm e3}|{=}s_{13}$. In the case of CP-invariance one has [159–162], $\eta_{21} \equiv e^{i\alpha}{=}\pm 1$, $\eta_{31} \equiv e^{i\beta}{=}\pm 1$; $\eta_{21(31)}$ being the relative CP-parity of Majorana neutrinos $\nu_{2(3)}$ and ν_1.

Information on the absolute scale of neutrino masses can be derived in ^{3}H β-decay experiments [163, 164] and from cosmological and astrophysical data. The most stringent upper bounds on the $\bar{\nu}_e$ mass were obtained in the Troitzk [163] and Mainz [164] experiments:

$$m_{\bar{\nu}_e} < 2.3{\rm eV} \quad \text{at } 95\% \text{ C.L.} \tag{10}$$

We have $m_{\bar{\nu}_e} \cong m_{1,2,3}$ in the case of the QD ν-mass spectrum. The KATRIN experiment [164] is planned to reach a sensitivity of $m_{\bar{\nu}_e} \sim 0.20$ eV, i.e. it will probe the region of the QD spectrum. The CMB data of the WMAP experiment, combined with data from large-scale structure surveys (2dFGRS, SDSS), lead to a limit on the sum of ν_j masses (see, e.g., [165, 166]):

$$\sum_j m_j \equiv \Sigma < (0.4\text{–}1.7)\ {\rm eV} \quad \text{at } 95\% \text{ C.L.} \tag{11}$$

Data on weak lensing of galaxies, combined with data from the WMAP and PLANCK experiments, may allow Σ to be determined with an uncertainty of ~ 0.04 eV [167,168]. It proves convenient to express [169,170] the three neutrino masses in terms of $\Delta m^2_{\odot}$ and $\Delta m^2_{\rm A}$, measured in neutrino-oscillation experiments, and the absolute neutrino-mass scale determined by $\min(m_j)$ [73, 132–135]. In both the normal- and the inverted-hierarchy, one has: $\Delta m^2_{\odot} {=} \Delta m^2_{21} > 0$, $m_2{=}(m_1^2 + \Delta m^2_{\odot})^{\frac{1}{2}}$. For normal ordering, $\Delta m^2_{\rm A} {=} \Delta m^2_{31} > 0$ and $m_3{=}(m_1^2 + \Delta m^2_{\rm A})^{\frac{1}{2}}$, while if

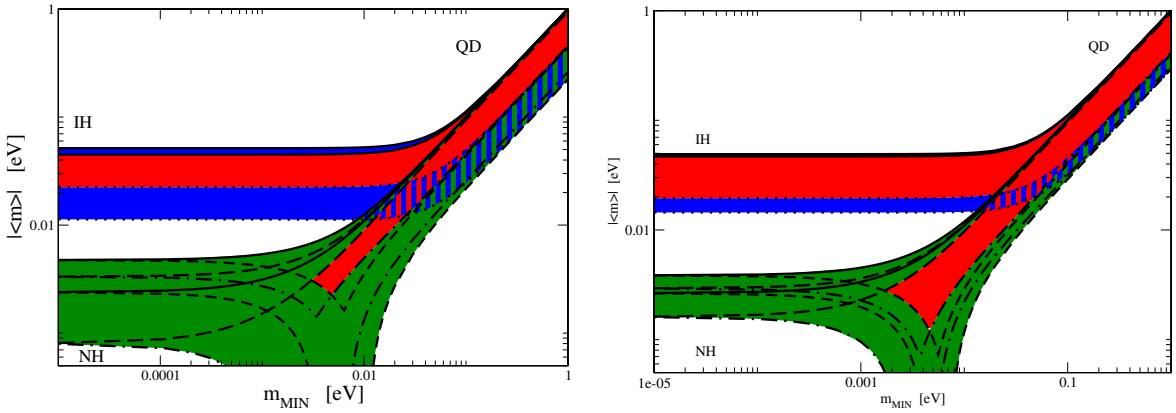

Figure 11: The value of $\langle m\rangle$ as a function of $min(m_j)$, obtained using i) the 95% C.L. allowed ranges of $\Delta m^2_{\odot}$, $|\Delta m^2_{\rm A}|$, $\sin^2\theta_{\odot}$ and $\sin^2\theta_{13}$ (left panel), and ii) prospective 2σ uncertainty in $\langle m\rangle$, corresponding to input 1-σ experimental errors in $\Delta m^2_{\odot}$ $\Delta m^2_{31}$and $\sin^2\theta_{\odot}$ of 2%, 2% and 4% and $\sin^2\theta_{13} = 0.010 \pm 0.006$ (right panel). The best fit values and the 2σ ranges used in the analysis are given in equations (2.1) - (2.4) in [170]. The regions shown in red/grey correspond to violation of CP-symmetry. Taken with kind permission of Physical Review from figures 1 and 2 in reference [170]. Copyrighted by the American Physical Society.

the spectrum is with inverted ordering, $m_{\rm MIN}$=m_3, $\Delta m^2_{\rm A}$ =$\Delta m^2_{23} > 0$ and m_1=$(m_3^2 + \Delta m^2_{\rm A} - \Delta m^2_{\odot}\ )^{\frac{1}{2}}$. Thus, given $\Delta m^2_{\rm A}$, $\Delta m^2_{\odot}$, $\theta_{\odot}$ and θ_{13}, $\langle m\rangle$ depends on $\min(m_j)$, Majorana phases α, β and the type of ν-mass spectrum.

The problem of obtaining the allowed values of $\langle m\rangle$ given the constraints on the parameters following from neutrino-oscillation data, and, more generally, of the physics potential of $(\beta\beta)_{0\nu}$-decay experiments, was first studied in [169, 170] and subsequently in [132–134]. Detailed analyses were performed more recently in [151–153, 170]. The results are illustrated in Fig.11. The main features of the predictions for $\langle m\rangle$ are [73, 91, 135, 141, 142] (figure 11, left panel):

1. For the NH spectrum, $\langle m\rangle \cong |\sqrt{\Delta m^2_{\odot}}\ s^2_{12} + \sqrt{\Delta m^2_{\rm A}}\ s^2_{13} e^{i(\alpha-\beta)}| \lesssim 0.005$ eV;

2. For the IH spectrum, $\langle m\rangle \cong \sqrt{|\Delta m^2_{\rm A}|}(1-\sin^2 2\theta_{\odot}\sin^2\frac{\alpha}{2})^{\frac{1}{2}}$, thus $\langle m\rangle \lesssim \sqrt{|\Delta m^2_{\rm A}|} \lesssim 0.055$ eV and $\langle m\rangle \gtrsim \sqrt{|\Delta m^2_{\rm A}|}\cos 2\theta_{\odot} \gtrsim 0.013$ eV, the bounds corresponding to the values α=0; π; and

3. For the QD spectrum, $\langle m\rangle \cong m_0(1-\sin^2 2\theta_{\odot}\sin^2\frac{\alpha}{2})^{\frac{1}{2}}$, $m_0 \gtrsim \langle m\rangle \gtrsim m_0\cos 2\theta_{\odot} \gtrsim 0.03$ eV, with $m_0 \gtrsim 0.1$ eV, $m_0 < 2.3$ eV [164] or $m_0 \lesssim 0.5$ eV [165, 166].

For the IH (QD) spectrum we have: $\sin^2(\alpha/2) \cong (1-\langle m\rangle^2/\tilde{m}^2)/\sin^2 2\theta_{\odot}$, $\tilde{m}^2$=$|\Delta m^2_{\rm A}|$ (m_0^2). Thus, a measurement of $\langle m\rangle$ (and m_0 for QD spectrum) can allow to determine α.

Many experiments have searched for $(\beta\beta)_{0\nu}$-decay [130]. The best sensitivity was achieved in Heidelberg-Moscow ^{76}Ge experiment [171]: $\langle m\rangle$ <(0.35 - 1.05) eV (90% C.L.), where a factor of 3 uncertainty in the relevant NME (see, e.g., [172–174]) is taken into account. The IGEX collaboration has obtained [175]: $\langle m\rangle$ < (0.33 - 1.35) eV (90% C.L.). A positive signal at >3σ, corresponding to $\langle m\rangle = (0.1 - 0.9)$ eV, is claimed to be observed [176]. Two experiments, NEMO3 (with ^{100}Mo and ^{82}Se) [177] and CUORICINO (with ^{130}Te) [178], designed to reach a

sensitivity to $\langle m \rangle \sim$ of $\langle m \rangle \sim (0.2--0.3)$ eV, published first results: $\langle m \rangle < (0.7--1.2)$ eV [177] and $\langle m \rangle < (0.2 - -0.9)$ eV [178] (90% C.L.), where estimated uncertainties in the NME are accounted for. Most importantly, a number of projects aim at sensitivity of $\langle m \rangle \sim$(0.01–0.05) eV [179]: CUORE (^{130}Te), GERDA (^{76}Ge), SuperNEMO (^{100}Mo), EXO (^{136}Xe), MAJORANA (^{76}Ge), MOON (^{100}Mo), XMASS (^{136}Xe), CANDLES (^{48}Ca), etc. These experiments will probe the region corresponding to IH and QD spectra and test the positive result claimed in [176].

The existence of significant lower bounds on $\langle m \rangle$ in the cases of IH and QD spectra [91], which lie either partially (IH spectrum) or completely (QD spectrum) within the range of sensitivity of the next generation of $(\beta\beta)_{0\nu}$-decay experiments, is one of the most important features of the predictions of $\langle m \rangle$. These minimal values are given, up to small corrections, by $\Delta m^2_{\rm A} \cos 2\theta_\odot$ and $m_0 \cos 2\theta_\odot$. According to the combined analysis of the solar- and reactor- neutrino data [77,79,180] including the latest SNO and KL results: i) the possibility of $\cos 2\theta_\odot = 0$ is excluded at $\sim 6\sigma$; ii) the best fit value of $\cos 2\theta_\odot$ is $\cos 2\theta_\odot = 0.38$; and iii) at 95% C.L. one has for $\sin^2 \theta_{13} =$ 0 (0.02), $\cos 2\theta_\odot \gtrsim 0.28$ (0.28). The quoted results on $\cos 2\theta_\odot$ together with the range of possible values of $|\Delta m^2_{\rm A}|$ and m_0, lead to the significant and robust lower bounds on $\langle m \rangle$ in the cases of the IH and the QD spectrum [91,143–145]. At the same time one can always have $\langle m \rangle = 0$ in the case of spectrum with (partial) normal hierarchy [141, 142]. As figure 11 indicates, $\langle m \rangle$ cannot exceed ~ 6 meV for the NH neutrino mass spectrum. This implies that $max(\langle m \rangle)$ in the case of the NH spectrum is considerably smaller than $\min(\langle m \rangle)$ for the IH and the QD spectra. This makes it possible that information about the type of neutrino-mass spectrum may be obtained from a measurement of $\langle m \rangle \neq 0$ [91]. In particular, a positive result in the future generation of $(\beta\beta)_{0\nu}$-decay experiments with $\langle m \rangle > 0.01$ eV would imply that the NH spectrum is strongly disfavored (if not excluded). Prospective experimental errors in the values of the oscillation parameters (figure 11, right panel), in $\langle m \rangle$ and the sum of neutrino masses, and the uncertainty in the relevant NME [172–174], can weaken but do not invalidate these results [141–145, 151].

As figure 11 indicates, a measurement of $\langle m \rangle \gtrsim 0.01$ eV would either: i) determine a relatively narrow interval of possible values of the lightest ν-mass $m_{\rm MIN}$; or ii) would establish an upper limit on $m_{\rm MIN}$. If an upper limit on $\langle m \rangle$ is experimentally obtained below 0.01 eV, this would lead to a significant upper limit on $m_{\rm MIN}$.

The possibility of establishing CP- violation in the lepton sector due to Majorana CPV phases has been studied in [73, 135, 154, 155] and in much greater detail in [141, 142, 151]. It was found that it is very challenging: it requires quite accurate measurements of $\langle m \rangle$ (and of m_0 for QD spectrum), and holds only for a limited range of values of the relevant parameters. More specifically [141,142,151], establishing at 2σ CP-violation associated with Majorana neutrinos in the case of QD spectrum requires, for $\sin^2 \theta_\odot = 0.31$ in particular, a relative experimental error on the measured value of $\langle m \rangle$ and m_0 smaller than 15%, a "theoretical uncertainty" $F \lesssim 1.5$ in the value of $\langle m \rangle$ due to an imprecise knowledge of the corresponding NME, and value of the relevant Majorana CPV phase α typically within the ranges of $\sim (\pi/4 - 3\pi/4)$ and $\sim (5\pi/4 - 7\pi/4)$ (figure 11, right-hand panel).

The knowledge of the NMEs with sufficiently small uncertainty is crucial for obtaining quantitative information on the neutrino-mixing parameters from a measurement of $(\beta\beta)_{0\nu}$-decay

half-life. Possible tests of the NME calculations are discussed in [181].

2.3 Completing the picture

The measurements of the neutrino-oscillation parameters reviewed above hint at new interactions present at an extremely large mass scale, Λ. In scattering experiments, for example at hadron or lepton colliders, these new interactions are suppressed by powers of Λ. In contrast, neutrino oscillations are widely believed to be a direct consequence of the physics at the large mass scale; hence, measurements of neutrino oscillations probe physics at a uniquely high mass scale. The measurements reviewed above have established the presence of neutrino oscillations and have determined a number of relevant parameters. To complete the picture, a dedicated experimental programme is required; the elements of this experimental programme are [182]):

- The search for neutrinoless double-beta decay, to establish whether neutrinos are Majorana particles [183, 184];
- The determination of the neutrino-mass scale by direct measurement (see for example [185]) or through cosmology (see for example [186, 187]);
- The determination of the neutrino-mass hierarchy by combining neutrino-oscillation measurements with the results of direct neutrino-mass measurements and searches for $0\nu\beta\beta$ decay;
- The determination of the small mixing angle θ_{13} through measurements of the sub-dominant neutrino oscillations;
- The precise determination of the mixing angle θ_{23} to seek to establish whether θ_{23} is maximal;
- The search for leptonic CP violation in neutrino oscillations; and
- The search for sterile light neutrinos through the observation of a third mass-squared difference in neutrino oscillations. The resent measurements from MiniBooNE [40] dis-favour a sterile-neutrino interpretation of the LSND results [188].

2.3.1 Bounds on θ_{13} from approved experiments

The present generation of long-baseline oscillation experiments (K2K [10] at KEK, MINOS [11] at the NuMI beam and ICARUS [189] and OPERA [12] at the CNGS beam, see table 3), are expected to measure $\sin^2 2\theta_{23}$ and $|\Delta m^2_{31}|$ with a precision of $\sim 10\%$, if $|\Delta m^2_{31}| > 10^{-3}$ eV^2. These experiments could, in principle, measure θ_{13} through $\nu_\mu \to \nu_e$ oscillations even though they are not optimized for such a measurement. MINOS is expected to reach a sensitivity of $\sin^2\theta_{13} \leq 0.02$ at a confidence level (CL) of 90% in 5 years [11]. The main limitation of the MINOS experiment is the poor electron-identification efficiency of the detector. Thanks to the high density and high granularity of the emulsion cloud chamber (ECC) structure, the

Neutrino facility	Proton momentum (GeV/c)	L (km)	E_ν (GeV)	pot/yr (10^{19})
KEK PS [10]	12	250	1.5	2
FNAL NuMI [192]	120	735	3	20÷ 34
CERN CNGS [193]	400	732	17.4	4.5÷ 7.6

Table 3: Main parameters for present long-baseline neutrino beams

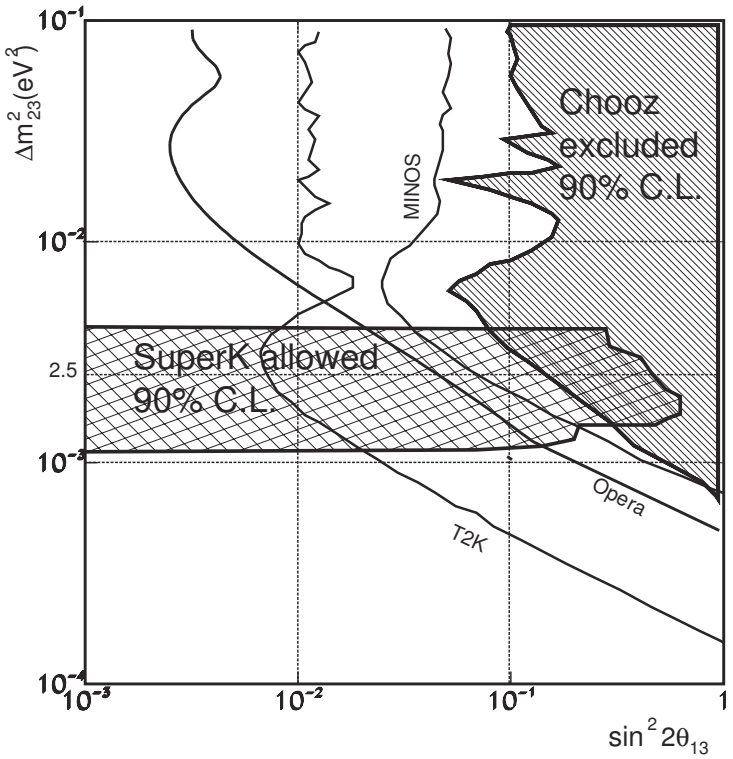

Figure 12: Expected θ_{13}-sensitivity (in vacuum and for $\delta_{CP} = 0$) for MINOS, OPERA and for the next T2K experiment, compared to the CHOOZ exclusion plot. Taken from reference [194].

OPERA detector is better suited for electron detection and can reach $\sin^2\theta_{13} \leq 0.015$ at 90% CL (for $\Delta m^2_{31} = 2.5 \times 10^{-3}$ eV^2), after five years exposure to the CNGS beam at nominal intensity [190, 191].

The θ_{13}-sensitivity of the present LBL experiments (including the T2K, that will be discussed in more detail below) is shown in figure 12. The sensitivity of such experiments to θ_{13} is limited by the power of the proton driver and by the ν_e contamination of the beam. In particular, the CNGS beam, which has been optimised for τ production, has a mean energy about ten times larger than the first $\nu_\mu \to \nu_e$ oscillation peak at a baseline of 732 Km.

Another approach to search for non-vanishing θ_{13} (and the θ_{23}-octant [195]) is to look at $\overline{\nu}_e$ disappearance using reactor neutrinos. The relevant oscillation probability is:

$$P(\bar{\nu}_e \to \bar{\nu}_e) \simeq 1 - \sin^2 2\theta_{13} \sin^2\left(\frac{\Delta m^2_{31} L}{4E}\right) + \ldots, \tag{12}$$

which does not depend on θ_{23} or δ_{CP}. At the baselines relevant for reactor-neutrino experiments, the dependence of the oscillation probability on Δm^2_{21} and θ_{12} is negligible. Therefore, this approach allows an unambiguous measurement of θ_{13} free of correlations and degeneracies (see section 2.4), though it requires a very precise knowledge of the absolute flux. The Double-Chooz experiment [196, 197] will employ a near and far detector, located at baselines of 0.2 Km and 1.05 Km respectively. Both detectors will be based on gadolinium-loaded liquid scintillator with a fiducial mass of 10.16 tonne. Antineutrinos will be detected using the delayed coincidence of the positron from the inverse β-decay and the photons from neutron capture. The direct comparison of the event rates in the two detectors will allow the cancellation of many of the systematic errors. After 5 years of data taking, this experiment will reach a θ_{13}-sensitivity of $\sin^2\theta_{13} \leq 0.0025$ at 90% CL. Another reactor experiment has been recently proposed in Japan [198]. This experiment has an expected sensitivity of $\sin^2\theta_{13} \leq 0.0038$ at 90% CL.

Present LBL and reactor-neutrino experiments can not address the other issues raised above; the baselines are too short to take advantage of matter effects required to identify the mass hierarchy, and they are not designed to look for CP-violation.

2.4 Degeneracies and correlations

We will follow reference [199] to introduce the degeneracy problem. Other approaches have been proposed in references [195, 200–204].

2.4.1 Appearance channels: $\nu_e \to \nu_\mu, \nu_\tau$ and $\nu_\mu \to \nu_e$

It was originally pointed out in reference [205] that a measurement of the appearance probability $P(\nu_\alpha \to \nu_\beta) = P_{\alpha\beta}$ for a neutrino-oscillation experiment with a fixed baseline (L) and energy (E) can not be used to determine uniquely the oscillation parameters. Indeed, taking $(\bar{\theta}_{13}, \bar{\delta})$ as the 'true' values, the equation

$$P_{\alpha\beta}(\bar{\theta}_{13}, \bar{\delta}) = P_{\alpha\beta}(\theta_{13}, \delta) \tag{13}$$

has a continuous number of solutions. The locus of points in the (θ_{13}, δ) plane satisfying this equation is called an 'equiprobability' curve. As can be seen from figure 13(left), the strong correlation between θ_{13} and δ [206] defines a strip in the (θ_{13}, δ) plane compatible with $P_{\alpha\beta}(\bar{\theta}_{13}, \bar{\delta})$.

Consider now an experiment that can measure both neutrino (+) and antineutrino (−) appearance oscillation probabilities, at the same L/E. The system of equations:

$$P^{\pm}_{\alpha\beta}(\bar{\theta}_{13}, \bar{\delta}) = P^{\pm}_{\alpha\beta}(\theta_{13}, \delta) \tag{14}$$

describes two equiprobability curves, see figure 13(right). The system has two solutions: the input pair $(\bar{\theta}_{13}, \bar{\delta})$ and a second, (L/E)-dependent, point. The 'continuum degeneracy' has been

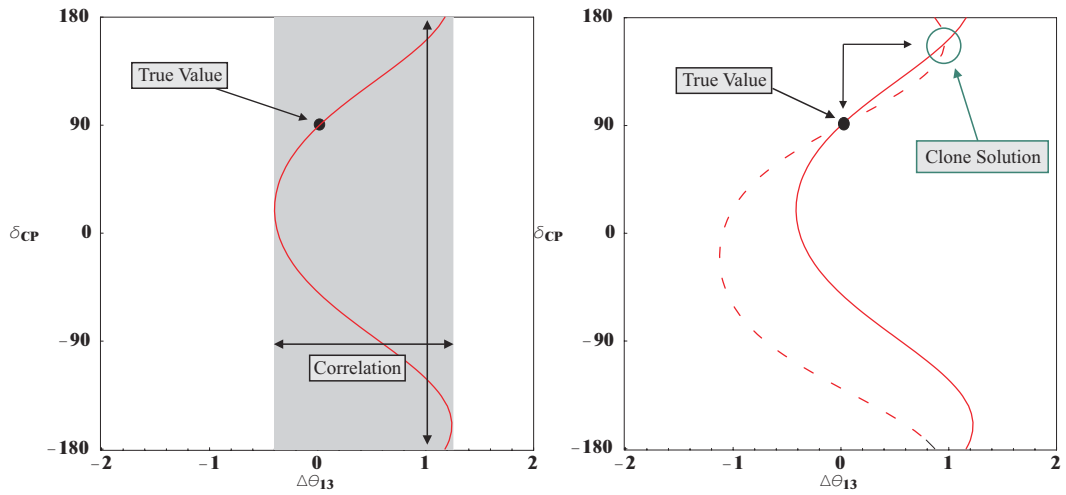

Figure 13: Correlation of θ_{13} and δ: Left: if only neutrinos (or antineutrinos) are measured: continuum degeneracy; Right: if both neutrinos (full line) and antineutrinos (dashed line) are measured: twofold degeneracy. Taken with kind permission of Nuclear Physics B Proceedings Supplements from figures 1 and 2 in reference [207]. Copyrighted by Elsevier Science B.V.

solved, but a discrete ambiguity in the measurement of the physical values of θ_{13} and δ is still present; the 'intrinsic degeneracy' or 'intrinsic clone' [205].

More information is needed to solve the intrinsic degeneracy. This information can be obtained either by making independent measurements at different values of L/E or by making use of independent oscillation channels. The value of L/E may be varied, for example, by measuring the Neutrino Factory beam at a number of baselines [205] and [208], by varying the neutrino-beam energy at a beta-beam facility [209], or by measuring precisely the neutrino-energy spectrum in a liquid-argon detector [210]. In figure 14(left) it can be seen that experiments with different baselines have intrinsic clones in different regions of the (θ_{13}, δ) plane. If the clones are well separated, the degeneracy can be solved. The equiprobability curves for the two oscillation channels $\nu_e \to \nu_\mu$ and $\nu_e \to \nu_\tau$ measured at a particular L/E are shown in figure 14(right). The figure shows that the intrinsic clones for the two channels appear in different regions of the parameter space, making it possible to resolve the intrinsic degeneracy.

Two other sources of ambiguities are also present [200, 211, 212]:

- Atmospheric-neutrino experiments measure ν_μ disappearance or $\nu_\mu \to \nu_\tau$ appearance for which the leading terms in the expressions for the oscillation probabilities depend quadratically on Δm^2_{13}, therefore the sign of Δm^2_{13} is not known [213]; and

- At leading order, the oscillation probabilities for ν_μ, ν_e disappearance and $\nu_\mu \to \nu_\tau$ appearance depend upon $\sin^2 2\theta_{23}$. Therefore only the difference of θ_{23} from 45° (maximal mixing) is known, i.e. it is not known whether θ_{23} is smaller or greater than 45°.

As a consequence, future experiments must measure the two continuous variables θ_{13} and δ as

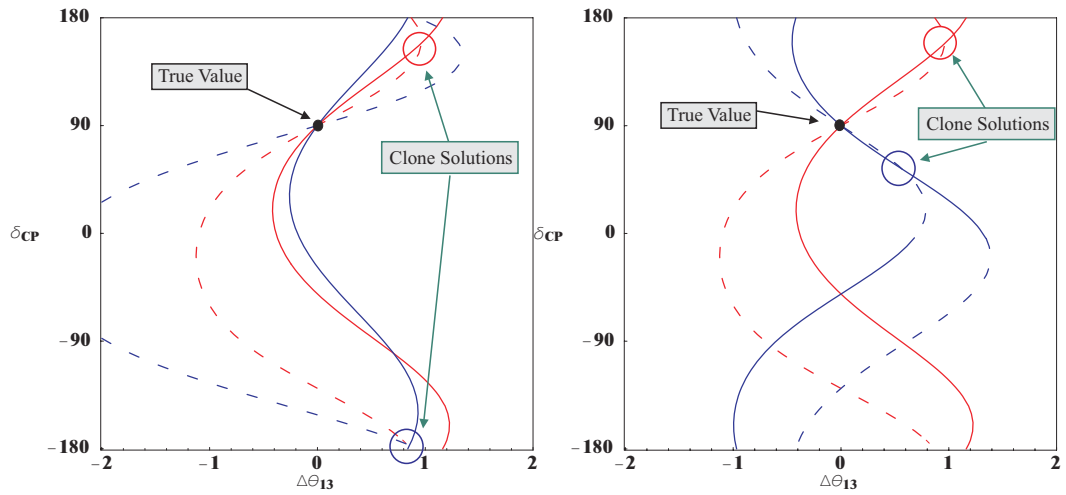

Figure 14: Solving the intrinsic degeneracy using: Left: same oscillation channel, but two different baselines; Right: same L/E, but two different oscillation channels (i.e. golden and silver). Taken with kind permission of Nuclear Physics B Proceedings Supplements from figures 3 and 4 in reference [207]. Copyrighted by Elsevier Science B.V.

well as the two discrete variables:

$$s_{atm} = \text{sign}[\Delta m^2_{23}]\,, \qquad s_{oct} = \text{sign}[\tan(2\theta_{23})]\,. \tag{15}$$

These two variables assume the values ± 1 depending on the sign of Δm^2_{23} ($s_{atm} = 1$ for $m^2_3 > m^2_2$ and $s_{atm} = -1$ for $m^2_3 < m^2_2$) and θ_{23} ($s_{oct} = 1$ for $\theta_{23} < \pi/4$ and $s_{oct} = -1$ for $\theta_{23} > \pi/4$). Therefore, taking into account the present ignorance on the neutrino masses and mixing matrix, equation (14) must be rewritten, more precisely, as:

$$P^{\pm}_{\alpha\beta}(\bar{\theta}_{13}, \bar{\delta}; \bar{s}_{atm}, \bar{s}_{oct}) \;=\; P^{\pm}_{\alpha\beta}(\theta_{13}, \delta; s_{atm} = \bar{s}_{atm}; s_{oct} = \bar{s}_{oct})\,, \tag{16}$$

where $\bar{s}_{atm}$ and $\bar{s}_{oct}$ have been included as input parameters in addition to $\bar{\theta}_{13}$ and $\bar{\delta}$. In equation (16) we have implicitly assumed that the sign of Δm^2_{23} and the octant for θ_{23} are unknown. The following systems of equations should be considered:

$$\begin{aligned} P^{\pm}_{\alpha\beta}(\bar{\theta}_{13}, \bar{\delta}; \bar{s}_{atm}, \bar{s}_{oct}) \;&=\; P^{\pm}_{\alpha\beta}(\theta_{13}, \delta; s_{atm} = -\bar{s}_{atm}; s_{oct} = \bar{s}_{oct}) && (17)\\ &=\; P^{\pm}_{\alpha\beta}(\theta_{13}, \delta; s_{atm} = \bar{s}_{atm}; s_{oct} = -\bar{s}_{oct}) && (18)\\ &=\; P^{\pm}_{\alpha\beta}(\theta_{13}, \delta; s_{atm} = -\bar{s}_{atm}; s_{oct} = -\bar{s}_{oct})\,. && (19) \end{aligned}$$

These new sets of equiprobability systems arise when we equate the measured probability (l.h.s.) with the theoretical probabilities obtained including one of the three possible wrong guesses of s_{atm} and s_{oct} (r.h.s.).

Solving the four systems of equations (16)–(19) will yield the true solution plus additional 'clones', forming an eightfold-degeneracy [212]. These eight solutions are respectively:

- The true solution and its intrinsic clone, obtained solving the system in equation (16);

- The Δm^2_{23}-sign clones (hereafter called 'sign' clones) of the true and intrinsic solution, obtained solving the system in equation (17);
- The θ_{23}-octant clones (hereafter called 'octant' clones) of the true and intrinsic solution, obtained solving the system in equation (18); and
- The Δm^2_{atm}-sign θ_{23}-octant clones (hereafter called 'mixed' clones) of the true and intrinsic solution, obtained solving the system in equation (19).

Notice, however, that transition probabilities are not the experimentally measured quantities. Experimental results are given in terms of the number of charged leptons observed in a specific detector. For the Neutrino Factory 'golden channel' ($\nu_e \to \nu_\mu$), for example, one counts the number of muons with charge opposite to the charge of the muons circulating in the storage ring. If the detector can measure the final state lepton and hadron energies with enough precision, events can be grouped in energy bins of width ΔE. The number of muons in the i^{th} energy bin for the input pair $(\bar{\theta}_{13}, \bar{\delta})$, for a parent muon energy $\bar{E}_\mu$, is given by:

$$N^i_{\mu^\mp}(\bar{\theta}_{13}, \bar{\delta}) \;=\; \left\{ \frac{d\sigma_{\nu_\mu(\bar{\nu}_\mu)}(E_\mu, E_\nu)}{dE_\mu} \otimes P^\pm_{e\mu}(E_\nu, \bar{\theta}_{13}, \bar{\delta}) \otimes \frac{d\Phi_{\nu_e(\bar{\nu}_e)}(E_\nu, \bar{E}_\mu)}{dE_\nu} \right\}_{E_i}^{E_i + \Delta E_\mu} \tag{20}$$

where $\otimes$ stands for a convolution integral, N^i is the number of events in bin i, E_ν is the neutrino energy, E_μ is the scattered muon energy, $\sigma_{\nu_m u(\bar{\nu}_\mu)}$, is the neutrino charged-current scattering cross section, and Φ is the neutrino flux. Solving the following systems of equations, for a given energy bin and fixed input parameters $(\bar{\theta}_{13}, \bar{\delta})$:

$$\begin{aligned}
N^i_{\mu^\pm}(\bar{\theta}_{13}, \bar{\delta}; \bar{s}_{atm}, \bar{s}_{oct}) &= N^i_{\mu^\pm}(\theta_{13}, \delta; s_{atm} = \bar{s}_{atm}, s_{oct} = \bar{s}_{oct}) && (21)\\
&= N^i_{\mu^\pm}(\theta_{13}, \delta; s_{atm} = \bar{s}_{atm}, s_{oct} = -\bar{s}_{oct}) && (22)\\
&= N^i_{\mu^\pm}(\theta_{13}, \delta; s_{atm} = -\bar{s}_{atm}, s_{oct} = \bar{s}_{oct}) && (23)\\
&= N^i_{\mu^\pm}(\theta_{13}, \delta; s_{atm} = -\bar{s}_{atm}, s_{oct} = -\bar{s}_{oct})\,, && (24)
\end{aligned}$$

yields the eight solutions corresponding to the i-th bin.

The existence of unsolved degeneracies results in a loss of sensitivity to the unknowns $\theta_{13}, \delta, s_{atm}$ (see below). The best way to solve the degeneracies is to perform a set of complementary measurements; experiments must have different baselines, good energy resolution, and access to different channels. There is no 'synergy' in experiments at the same L/E measuring the same channel [214]. A method to look for optimal combinations of measurements based on solving the set of systems of equations (21)–(24) has been presented in reference [199]. Most of the previous considerations also apply to the T-conjugated transition $\nu_\mu \to \nu_e$ and to $\nu_e \to \nu_\tau$ (the Neutrino Factory 'silver channel').

2.4.2 Disappearance channels: $\nu_\mu \to \nu_\mu$

An independent measurement of the atmospheric parameters θ_{23} and Δm^2_{23} can be made via the ν_μ-disappearance channel using a conventional neutrino beam or the Neutrino Factory.

It is expected that this kind of measurement will reduce the error on the atmospheric-mass difference to less than 10% with a few years of data if $\Delta m^2_{23} \geq 2.2 \times 10^{-3}$ eV^2 [215]. The expected error on the atmospheric angle depends on the value of θ_{23} itself, the smallest error being achieved for large, but non-maximal, mixing [216]. It is interesting to study in detail the parameter correlations and degeneracies that affect this measurement and that can induce large uncertainties. The vacuum-oscillation probability expanded to the second order in the small parameters θ_{13} and $(\Delta_{12}L/E)$ [213] is:

$$\begin{aligned} P(\nu_\mu \to \nu_\mu) &= 1 - \left[\sin^2 2\theta_{23} - s^2_{23} \sin^2 2\theta_{13} \cos 2\theta_{23}\right] \sin^2\left(\frac{\Delta_{23}L}{2}\right) \\ &\quad - \left(\frac{\Delta_{12}L}{2}\right) \left[s^2_{12} \sin^2 2\theta_{23} + \tilde{J} s^2_{23} \cos\delta\right] \sin(\Delta_{23}L) \\ &\quad - \left(\frac{\Delta_{12}L}{2}\right)^2 \left[c^4_{23} \sin^2 2\theta_{12} + s^2_{12} \sin^2 2\theta_{23} \cos(\Delta_{23}L)\right], \end{aligned} \tag{25}$$

where $\tilde{J} = \cos\theta_{13} \sin 2\theta_{12} \sin 2\theta_{13} \sin 2\theta_{23}$ and $\Delta_{23} = \Delta m^2_{23}/2E$, $\Delta_{12} = \Delta m^2_{12}/2E$. The dominant contribution comes from first term in the first parenthesis which is symmetric under $\theta_{23} \to \pi/2 - \theta_{23}$. This symmetry is lifted by the other terms which introduce a mild CP-conserving δ-dependence, albeit through sub-leading effects which are very difficult to isolate.

Since the $s_{atm} = \text{sign}(\Delta m^2_{23})$ is unknown, two systems of equations must be solved:

$$N^{\pm}_{\mu\mu}(\bar{\theta}_{23}, \Delta m^2_{atm}; \bar{s}_{atm}) = N^{\pm}_{\mu\mu}(\theta_{23}, |\Delta m^2_{23}|; \bar{s}_{atm})\,; \tag{26}$$

and

$$N^{\pm}_{\mu\mu}(\bar{\theta}_{23}, \Delta m^2_{atm}; \bar{s}_{atm}) = N^{\pm}_{\mu\mu}(\theta_{23}, |\Delta m^2_{23}|; -\bar{s}_{atm})\,, \tag{27}$$

where $\bar{s}_{atm}$ is the physical mass hierarchy. For non-maximal $\bar{\theta}_{23}$, four different solutions are obtained. For $|\Delta m^2_{23}| \sim \Delta m^2_{atm}$ equation (26) yields two solutions, the input value $\theta_{23} = \bar{\theta}_{23}$ and $\theta_{23} \simeq \pi/2 - \bar{\theta}_{23}$. The second solution is not exactly $\theta_{23} = \pi/2 - \bar{\theta}_{23}$ due to the small θ_{23}-octant asymmetry; Two more solutions from equation (27) at a different value of $|\Delta m^2_{23}|$ are also present [217]. In equation (25) we can see that changing the sign of Δm^2_{23} makes the second term positive; a change that must be compensated with an increase in $|\Delta m^2_{23}|$ to give $P^{\pm}_{\mu\mu}(\Delta m^2_{atm}; \bar{s}_{atm}) = P^{\pm}_{\mu\mu}(|\Delta m^2_{23}|; -\bar{s}_{atm})$.

The result of a fit to the disappearance-channel data at the T2K phase I experiment is shown in figure 15 for three different values of the atmospheric mass difference $\Delta m^2_{23} = (2.2, 2.5, 2.8) \times 10^{-3}$ eV^2. Fixed values of the solar parameters have been used, $\Delta m^2_{12} = 8.2 \times 10^{-5}$ eV^2; $\theta_{12} = 33^\circ$. For maximal mixing, $\theta_{23} = 45^\circ$, figure 15 (left), two solutions are found at 90 % CL when both choices of s_{atm} are considered. On the other hand, using a non-maximal atmospheric angle $\theta_{23} = 41.5^\circ$ ($\sin^2\theta_{23} = 0.44$) four degenerate solutions are found, figure 15(right). In general, a two-fold or four-fold degeneracy must be discussed in the disappearance channel.

Notice how the disappearance sign clones appear at a value of $|\Delta m^2_{23}|$ higher than the input value. This is expected from equation (25); the shift in the vertical axis is a function of θ_{13} and δ which, in this case, has been kept fixed at $\theta_{13} = 0^\circ = \delta$. The degeneracy can be softened or solved by using detectors at baselines long enough that matter effects can be exploited [218].

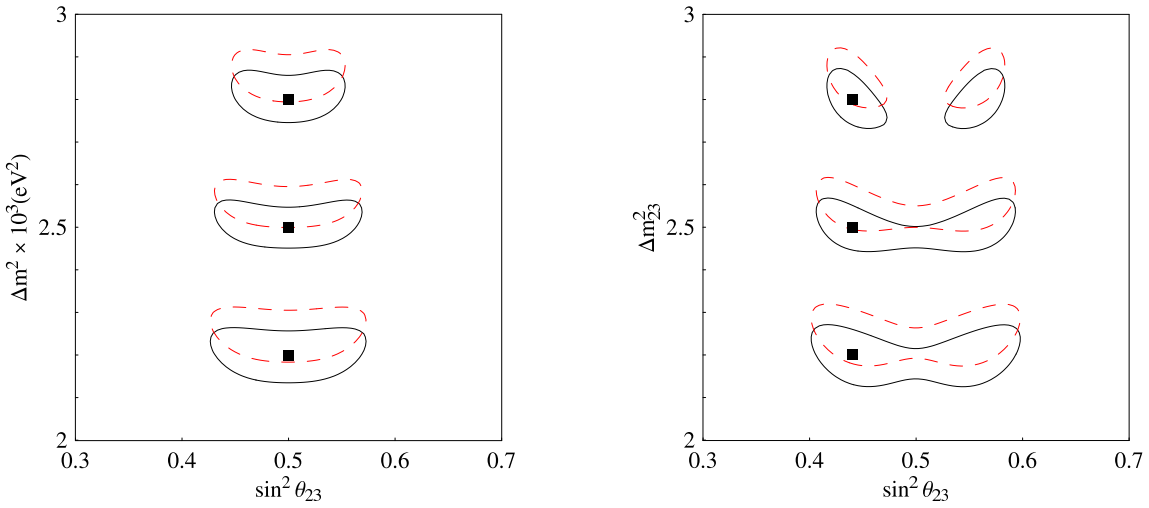

Figure 15: The sign degeneracy at T2K-I; left: $\theta_{23} = 45°$; right: $\theta_{23} = 41.5°$. Taken with kind permission of Nuclear Physics B from figure 4 in reference [218]. Copyrighted by Elsevier Science B.V.

2.4.3 A matter of conventions

It is useful to open here a short parenthesis to address a problem that arose recently concerning the 'physical' meaning of the variables used to fit the 'atmospheric' mass difference, Δm^2_{atm}. Notice, first of all, that the experimentally measured solar-mass difference Δm^2_{sol} can be unambiguously identified with the three-family parameter $\Delta m^2_{12} = m^2_2 - m^2_1$. This is not true for the experimentally measured atmospheric mass difference Δm^2_{atm}. Since the sub-leading solar effects are, at present, barely seen in atmospheric neutrino experiments we can define the three-family parameter to be used in the fits in a number of ways: by using $\Delta m^2_{23} = m^2_3 - m^2_2$; $\Delta m^2_{13} = m^2_3 - m^2_1$; or $\Delta m^2 = \left(\Delta m^2_{23} + \Delta m^2_{13}\right)/2$ [219]. A good description of the data will be obtained with either choice. When measurements of the atmospheric mass-squared difference with a precision at the level of 10^{-4} eV^2 are available, however, the different choices of the fitting parameter will give different results.

This effect can be observed in figure 16, where the three choices introduced above are compared. The three panels show the 90% CL contours resulting from a fit to the experimental data corresponding to the input value, $\Delta m^2_{atm} = 2.5 \times 10^{-3}$, in normal hierarchy, but fitted using in turn Δm^2_{23} (left panel), Δm^2_{13} (middle panel) and Δm^2 (right panel). It can be seen that the contour corresponding to the normal hierarchy, $s_{atm} = \bar{s}_{atm}$, is always located around the input value. On the other hand, the contour obtained for the inverted hierarchy is located above, below, or on top of the input value depending on the choice of fitting variable. This is a consequence of the fact that the difference between each of the possible choices is $O(\Delta m^2_{12})$.

For three-family mixing, three 'frequencies' can be defined, the shortest being the solar-oscillation frequency (unambiguously related to the mass difference Δm^2_{12}). In the case of the normal hierarchy, the middle frequency is related to Δm^2_{23} and the longest one to Δm^2_{13}. In the case of the inverted hierarchy these two frequencies are interchanged and the middle frequency

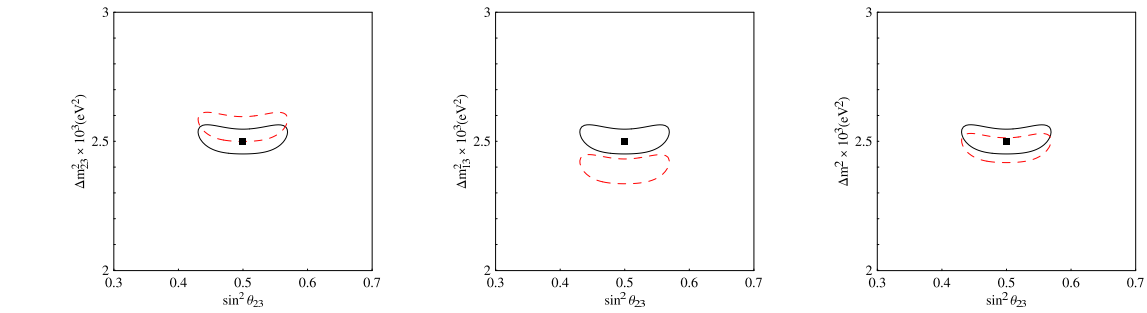

Figure 16: Different choices of the three-family "atmospheric" mass difference; left: Δm^2_{23}; middle: Δm^2_{13}; right: Δm^2. Taken with kind permission of Nuclear Physics B from figure 5 in reference [218]. Copyrighted by Elsevier Science B.V.

will be related to Δm^2_{31} and not to Δm^2_{32}. For this reason, it has been suggested that the analysis of the normal and inverted hierarchies should be presented using variables which maintain the ordering of the oscillation frequencies.

2.4.4 Disappearance channels: $\nu_e \to \nu_e$

A beta-beam or Neutrino Factory can exploit the ν_e-disappearance channel to measure the solar parameters $\Delta m^2_{12}, \theta_{12}$ or θ_{13} in a degeneracy-free environment. The ν_e-disappearance probability does not depend on δ or on θ_{23}. The θ_{13} measurement is, therefore, not affected by $(\theta_{13} - \delta)$ correlations or the s_{oct} ambiguity. The $\nu_e \to \nu_e$ matter-oscillation probability, expanded at second order in the small parameters θ_{13} and $(\Delta m^2_{12} L/E)$, is [220]:

$$P^{\pm}_{ee} = 1 - \left(\frac{\Delta_{23}}{B_{\mp}}\right)^2 \sin^2(2\theta_{13}) \sin^2\left(\frac{B_{\mp} L}{2}\right) - \left(\frac{\Delta_{12}}{A}\right)^2 \sin^2(2\theta_{12}) \sin^2\left(\frac{A L}{2}\right) , \qquad (28)$$

where $\Delta_{23} = \Delta m^2_{23}/2E$, $\Delta_{12} = \Delta m^2_{12}/2E$, $A = \sqrt{2} G_F N_e$, and $B_{\mp} = |A \mp \Delta_{23}|$. This equation describes reasonably well the behaviour of the transition probability in the energy range covered by the beta-beam facilities presently considered. Two sources of ambiguities are still present in ν_e-disappearance measurements, s_{atm} (for large values of θ_{13}, i.e. in the 'atmospheric' region) and the $\theta_{13} - \theta_{12}$ correlation (for small values of θ_{13}, i.e. in the 'solar' region). A beta-beam could in principle improve the precision with which the solar parameters are known through ν_e disappearance measurements. This is not the case for a beta-beam facility in which the neutrino energy of ~ 100 MeV is matched to a baseline of ~ 100 km. For such a facility, at large θ_{13}, the second term in equation (28) dominates over the last term. On the other hand, for small θ_{13} the statistics is too low to improve upon the present uncertainties on θ_{12} and Δm^2_{12} (note that the energy and baseline of the low-γ beta-beam has not been chosen to perform this task). It has been shown that if systematic errors cannot be controlled to better than at 5%, the beta-beam disappearance channel does not improve the CHOOZ bound on θ_{13} [217].

Equation (28) can also be applied to reactor-neutrino experiments which aim at a precise measurement of θ_{13} in a 'degeneracy-free' regime. For the typical baseline and energy of a reactor experiment (e.g., $L = 1.05$ km and $\langle E_\nu \rangle = 4$ MeV for the Double-Chooz proposal [196, 197])

we can safely consider antineutrino propagation in vacuum. As a consequence, no sensitivity to s_{atm} is expected at these experiments, since $B_{\mp} \to \Delta_{23}$ for $\Delta_{23} \gg A$. It is very difficult for reactor experiments to test small values of θ_{13}, and thus the $\theta_{13} - \theta_{12}$ correlation (significant only in the "solar" region) can also be neglected.

3 Implications for new physics and cosmology

Neutrino mass is the first example of physics beyond the Standard Model. The extreme smallness of neutrino masses, compared to charged fermion masses, and the large mixing angles, are both mysteries that make more acute the flavour problem in the Standard Model: why are there three families of quarks and leptons with the masses and mixings that are observed? Although there are many ideas concerning the underlying mechanism by which neutrino mass is generated, at present none of the proposed mechanisms have any experimental foundation; to make real progress more data is required. The neutrino masses and mixings are as fundamental as those of the quarks, yet the precision with which the neutrino-mixing parameters are known is very poor when compared to the precision of the quark parameters. Some of the neutrino parameters, such as the reactor angle and the CP-violating phase, have yet to be measured, and the sign of the atmospheric mass-squared difference is undetermined. If neutrino are Dirac fermions, then neutrino masses may arise in a manner similar to that which generates the masses of the other charged fundamental fermions. However, if neutrinos are Majorana particles, then the mass-generation mechanism may be quite different. These issues, which have profound implications for particle physics and cosmology, will be discussed in detail in this section.

3.1 The origin of small neutrino mass

This section will address the implications of see-saw mechanisms, supersymmetry and R-parity violation, extra dimensions, string theory, and TeV scale mechanisms for small neutrino masses on the properties of the neutrinos.

3.1.1 See-Saw mechanisms

The charged-fermion spectrum already contains quite strong hierarchies with the electron mass being a few million times smaller than the top-quark mass. Neutrino masses are also very small compared to charged-fermion masses, with the atmospheric neutrino mass being a few million times smaller than the electron mass. Such severe fermion mass hierarchies demand some explanation. One simple approach is based on the see-saw mechanism and its generalisation to include the charged-fermion masses by Froggatt and Nielsen [221]. The idea is that all Yukawa couplings are of order unity, but lowest order Yukawa couplings to Higgs fields are forbidden by some symmetry; neutrino masses are further suppressed by the fact that right-handed neutrinos are very heavy. Small effective Yukawa couplings and small Majorana masses are then generated

at higher order, suppressed by ratios of vacuum expectation values (vevs) to heavy field masses. The see-saw mechanism thus provides a convincing explanation for the smallness of neutrino masses. Here we review its simplest form, the type I see-saw mechanism and its generalisation to the type II see-saw mechanism.

Before discussing the see-saw mechanism, the different types of neutrino mass that are possible will be reviewed. So far we have been assuming that neutrino masses are Majorana masses of the form:

$$m^{\nu}_{LL}\overline{\nu_{\rm L}}\nu^{\rm C}_{\rm L} \tag{29}$$

where $\nu_{\rm L}$ is a left-handed neutrino field and $\nu^{\rm C}_{\rm L}$ is the CP conjugate of a left-handed neutrino field, in other words a right-handed anti-neutrino field. Majorana masses imply lepton-number violation. Note that lepton-number violation is forbidden by gauge invariance at the renormalisation level in extensions of the Standard Model in which the Higgs sector only contains doublets. The simplest version of the see-saw mechanism assumes that Majorana-mass terms are generated through the interactions of the right-handed neutrinos [127, 222, 223].

If we introduce right-handed neutrino fields then there are two sorts of additional neutrino mass terms that are possible: additional Majorana masses of the form:

$$M_{\rm RR}\overline{\nu_{\rm R}}\nu^{\rm C}_{\rm R} \ + \text{hermitian conjugate} \ , \tag{30}$$

where $\nu_{\rm R}$ is a right-handed neutrino field, $\nu^{\rm C}_{\rm R}$ is the CP conjugate of a right-handed neutrino field, in other words a left-handed antineutrino field; and Dirac masses of the form:

$$m^{\nu}_{\rm LR}\overline{\nu_{\rm L}}\nu_{\rm R} \ + \text{hermitian conjugate} \ . \tag{31}$$

Such Dirac mass terms conserve lepton number, and are not forbidden by electric-charge conservation.

Once this is done, the types of neutrino mass described in equations (30), (31) (but not equation (29) since we do not assume direct mass terms, e.g. from Higgs triplets, at this stage) are permitted, and we have the mass matrix:

$$\left(\begin{array}{cc} \overline{\nu_{\rm L}} & \overline{\nu^{\rm C}_{\rm R}} \end{array} \right) \left(\begin{array}{cc} 0 & m^{\nu}_{\rm LR} \\ m^{\nu T}_{\rm LR} & M_{\rm RR} \end{array} \right) \left(\begin{array}{c} \nu^{\rm C}_{\rm L} \\ \nu_{\rm R} \end{array} \right) \ + \text{hermitian conjugate} \ . \tag{32}$$

Since the right-handed neutrinos are electroweak singlets, the Majorana masses of the right-handed neutrinos, $M_{\rm RR}$, may be orders of magnitude larger than the electroweak scale. In the approximation that $M_{\rm RR} \gg m^{\nu}_{\rm LR}$ the matrix in equation (32) may be diagonalised to yield effective Majorana masses of the type in equation (29):

$$m^{\nu}_{\rm LL} = -m^{\nu}_{\rm LR}M^{-1}_{\rm RR}m^{\nu T}_{\rm LR} \ . \tag{33}$$

The effective left-handed Majorana masses, $m^{\nu}_{\rm LL}$, are naturally suppressed by the heavy scale, $M_{\rm RR}$. In a one-family example, if we take $m^{\nu}_{\rm LR} = M_W$ and $M_{\rm RR} = M_{\rm GUT}$, then we find

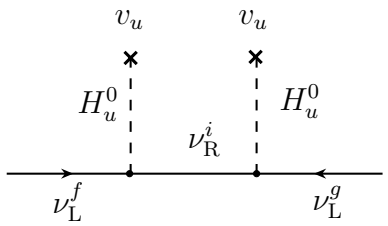

Figure 17: Diagram illustrating the type I see-saw mechanism.

$m^\nu_{\rm LL} \sim 10^{-3}$ eV which looks good for solar neutrinos. Atmospheric neutrino masses would require a right-handed neutrino with a mass below the GUT scale.

With three left-handed neutrinos and three right-handed neutrinos the Dirac masses, $m^\nu_{\rm LR}$, are a 3×3 (complex) matrix and the heavy Majorana masses, $M_{\rm RR}$, form a separate 3×3 (complex, symmetric) matrix. The light effective Majorana masses $m^\nu_{\rm LL}$ are also a 3×3 (complex symmetric) matrix and continue to be given by equation (33) which is now interpreted as a matrix product. From a model-building perspective the fundamental parameters which must be input into the see-saw mechanism are the Dirac mass matrix $m^\nu_{\rm LR}$ and the heavy right-handed neutrino Majorana mass matrix $M_{\rm RR}$. The light effective left-handed Majorana mass matrix $m^\nu_{\rm LL}$ arises as an output according to the see-saw formula in equation (33).

The version of the see-saw mechanism discussed so far is sometimes called the type I see-saw mechanism. It is the simplest version of the see-saw mechanism, and can be thought of as resulting from integrating out heavy right-handed neutrinos to produce the effective dimension-5 neutrino mass operator:

$$-\frac{1}{4}(H_{\rm u} \cdot L^T)\,\kappa\,(H_{\rm u} \cdot L)\ , \tag{34}$$

where the dot indicates the $\mathrm{SU}(2)_{\rm L}$-invariant product, and:

$$\kappa = 2\,Y_\nu M_{\rm RR}^{-1} Y_\nu^T\ , \tag{35}$$

with Y_ν being the neutrino Yukawa couplings and $m^\nu_{\rm LR} = Y_\nu v_{\rm u}$ with $v_{\rm u} = \langle H_{\rm u}\rangle$. The type I see-saw mechanism is illustrated diagrammatically in figure 17.

In models with a left-right symmetric particle content such as minimal left-right symmetric models, Pati-Salam models, or Grand Unified Theories (GUTs) based on SO(10), the type I see-saw mechanism is often generalised to a type II see-saw (see e.g. [70, 224–227]), where an additional direct mass term, $m^{\rm II}_{\rm LL}$, for the light neutrinos is present.

With such an additional direct mass term, the general neutrino mass matrix is given by:

$$\left(\begin{array}{cc} \overline{\nu_{\rm L}} & \overline{\nu_{\rm R}^{\rm C}} \end{array}\right) \left(\begin{array}{cc} m^{\rm II}_{\rm LL} & m^\nu_{\rm LR} \\ m^{\nu T}_{\rm LR} & M_{\rm RR} \end{array}\right) \left(\begin{array}{c} \nu_{\rm L}^{\rm C} \\ \nu_{\rm R} \end{array}\right). \tag{36}$$

Under the assumption that the mass eigenvalues $M_{{\rm R}i}$ of $M_{\rm RR}$ are very large compared to the components of $m^{\rm II}_{\rm LL}$ and $m_{\rm LR}$, the mass matrix can approximately be diagonalised yielding

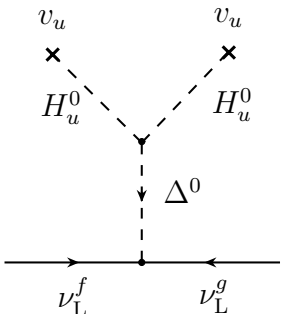

Figure 18: Diagram leading to a type II contribution $m_{\rm LL}^{\rm II}$ to the neutrino mass matrix via an induced vev of the neutral component of a triplet Higgs Δ.

effective Majorana masses:

$$m_{\rm LL}^{\nu} \approx m_{\rm LL}^{\rm II} + m_{\rm LL}^{\rm I}\,, \tag{37}$$

with :

$$m_{\rm LL}^{\rm I} \approx -m_{\rm LR}^{\nu}\, M_{\rm RR}^{-1}\, m_{\rm LR}^{\nu T}\,, \tag{38}$$

for the light neutrinos.

The direct mass term, $m_{\rm LL}^{\rm II}$, can also provide a naturally small contribution to the light-neutrino masses if it stems, e.g., from a see-saw suppressed induced vacuum-expectation value. We will refer to the general case, where both possibilities are allowed, as the II see-saw mechanism. Realising the type II contribution by generating the dimension-5 operator in equation (34) via the exchange of heavy Higgs triplets of $\mathrm{SU(2)_L}$ is illustrated diagrammatically in figure 18.

3.1.2 Supersymmetry and R-parity Violation

Another example of the origin of small neutrino masses is R-parity violating supersymmetry (SUSY) (for a review see [228]). Here, the left-handed neutrinos mix with neutralinos after SUSY breaking, leading to small, loop suppressed, Majorana masses. The masses depend on the SUSY mass spectrum. Should SUSY be discovered, and the mass spectrum determined, at high-energy colliders, the theory could be used to predict the Majorana masses.

In any supersymmetric extension of the Standard Model it is possible to introduce interactions that break R-parity, defined as $R = (-1)^{3B+L+2S}$ [229], where L, B, and S are the lepton number, baryon number, and spin, respectively. The interactions that can contribute to the neutrino masses must also violate lepton number, and are given by [230]:

$$W_{RpV} = \varepsilon_{ab}\left[\tfrac{1}{2}\lambda_{ijk}\widehat{L}_i^a\widehat{L}_j^b\widehat{R}_k + \lambda'_{ijk}\widehat{L}_i^a\widehat{Q}_j^b\widehat{D}_k + \epsilon_i\widehat{L}_i^a\widehat{H}_u^b\right] \tag{39}$$

The trilinear R-Parity violating (TRpV) parameters λ_{ijk} and λ'_{ijk} are dimensionless Yukawa couplings that violate lepton number keeping baryon number conserved. The baryon number violating interactions (of the form $\frac{1}{2}\lambda'' UDD$) can also be included, leading to proton decay. The

present limit on the lifetime of the proton [231] leads to stringent constraints on products of λ couplings, although such constraints can be relaxed in the case of Split Supersymmetry [232].

The bilinear R-Parity violating (BRpV) parameters, ϵ_i, induce sneutrino vacuum expectation values v_i, as well as mixing between particles and sparticles. In particular, neutrinos mix with neutralinos forming a set of seven neutral fermions F_i^0. A low energy see-saw mechanism induces the tree-level neutrino-mass matrix [233]:

$$\boldsymbol{M}_\nu^{(0)} = -m \cdot \mathcal{M}_{\chi^0}^{-1} \cdot m^T = \frac{M_1 g^2 + M_2 g'^2}{4\det(\mathcal{M}_{\chi^0})} \begin{bmatrix} \Lambda_1^2 & \Lambda_1\Lambda_2 & \Lambda_1\Lambda_3 \\ \Lambda_1\Lambda_2 & \Lambda_2^2 & \Lambda_2\Lambda_3 \\ \Lambda_1\Lambda_3 & \Lambda_2\Lambda_3 & \Lambda_3^2 \end{bmatrix} , \tag{40}$$

where $\mathcal{M}_{\chi^0}$ is the Minimal Supersymmetric Standard Model (MSSM) (for a review see [234]) neutralino mass matrix and the parameters $\Lambda_i \equiv \mu v_i + \epsilon_i v_d$ are proportional to the sneutrino vevs in the basis where the ϵ_i terms are rotated away from the superpotential. Note that if this is done BRpV reappears in the soft terms [235].

The tree-level neutrino mass matrix has only one non-zero eigenvalue, equal to the trace of the matrix in equation (40), and therefore proportional to $|\vec{\Lambda}|^2$. If the above tree-level contribution dominates over one-loop graphs, the square of this eigenvalue would be equal to the atmospheric mass-squared difference, $\Delta m^2_{31} \approx m_3^{(0)2}$, and the atmospheric and reactor angles would be given by $\tan^2\theta_{23}^{(0)} \approx \Lambda_2^2/\Lambda_3^2$ and $\tan^2\theta_{13}^{(0)} \approx \Lambda_1^2/(\Lambda_2^2+\Lambda_3^2)$ respectively. Without one-loop corrections, the solar mass-squared difference and the solar angle remain undetermined.

Once the one-loop corrections are included [236] the symmetry of the neutrino mass matrix in equation (40) is broken and thus the solar mass squared difference is generated radiatively. The one-loop corrected neutrino-mass matrix has the general form:

$$M_{ij}^\nu = A\Lambda_i\Lambda_j + B(\epsilon_i\Lambda_j + \epsilon_j\Lambda_i) + C\epsilon_i\epsilon_j \ , \tag{41}$$

where $A^{(0)} = (g^2 M_1 + g'^2 M_2)/4\det(\mathcal{M}_{\chi^0})$ is the only non-zero coefficient at tree-level. In BRpV most particles contribute in loops to the neutrino mass matrix. An important loop is the one involving bottom quarks and squarks, which is shown in figure 19. The external arrows represent the flow of lepton number, while the internal ones show the flow of the bottom-quark electric charge, and the cross signals a mass insertion. The complete dashed line represents a single scalar propagator corresponding to the heavy bottom squark $\tilde{b}_2$, with the full circles pictorially showing the component of this mass eigenstate in left and right sbottoms. The external lines are the neutrino states which define the basis used to write the neutrino mass matrix in equation (40). The open circles pictorially represent the component of these neutrinos in higgsinos and indicates the place where R-Parity is violated. A similar graph with the light sbottom, $\tilde{b}_1$, is obtained replacing $c_{\tilde{b}} \to -s_{\tilde{b}}$ and $s_{\tilde{b}} \to c_{\tilde{b}}$. The sum of these two graphs contributes to the coefficient C in the following way:

$$C^{(\tilde{b})} = -\frac{N_c m_b}{16\pi^2\mu^2} h_b^2 \sin(2\theta_{\tilde{b}})\ \Delta B_0^{\tilde{b}_1\tilde{b}_2} \ , \tag{42}$$

where $N_c = 3$ is the number of colours, and we have defined:

$$\Delta B_0^{\tilde{b}_1\tilde{b}_2} \equiv B_0(0; m_b^2, m_{\tilde{b}_2}^2) - B_0(0; m_b^2, m_{\tilde{b}_1}^2) \approx -\ln(m_{\tilde{b}_2}^2/m_{\tilde{b}_1}^2) \ . \tag{43}$$

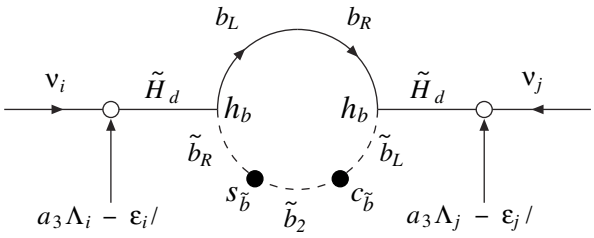

Figure 19: Pictorial representation of the bottom-sbottom loops contributing to the neutrino mass matrix, with Rp violated bilinearly in the open circles.

The result in equation (42) can be understood with the help of the graph presented above. It is proportional to the bottom-quark mass due to the mass insertion, and to the square of the bottom Yukawa coupling due to the vertices. The sbottom mixing contributes with the factor $\sin(2\theta_{\tilde{b}})$, and the higgsino-neutrino mixing accounts for the factor $\epsilon_i\epsilon_j/\mu^2$, where the ϵ parameters have been factored out from C. The contribution is finite because Veltman functions [237] from $\tilde{b}_2$ and $\tilde{b}_1$ are subtracted from each other. The contribution to the B parameter can be obtained using $B^{(\tilde{b})} = -a_3\mu C^{(\tilde{b})}$, with $a_3 = v_u(g^2M_1 + g'^2M_2)/4\det(\mathcal{M}_{\chi^0})$, as can be inferred from the neutralino-neutrino mixing shown in the graph. There is also a contribution $A^{\tilde{b}}$, but it is in general a small correction to $A^{(0)}$.

There are similar loops with charged scalars S_i^+ (charged Higgs bosons mixing with charged sleptons [238]) together with charged fermions F_j^+ (charginos mixing with charged leptons [239]). Among these are the charged Higgs and stau contributions which have the same form as that given in equation (42) with the replacements $b \to \tau$, $\tilde{b} \to \tilde{\tau}$, and taking $N_c = 1$. There are also loops with neutral scalars S_i^0 (neutral Higgs bosons mixing with sneutrinos [240]) together with the neutral fermions F_j^0 mentioned above.

BRpV can successfully be embedded in supergravity [241], although with non-universal ϵ_i terms at the GUT scale (as well as bilinear soft terms B_i, associated to ϵ_i). By definition, the coefficients A, B, and C in equation (41) depend exclusively on the universal scalar mass m_0, gaugino mass $M_{1/2}$, and trilinear parameter A_0 at the GUT scale, and the values of $\tan\beta$ and μ at the weak scale. In figure 20 we see the region of the $m_0 - M_{1/2}$ plane consistent with neutrino experimental data, for fixed values of the BRpV parameters $\epsilon_1 = -0.0004$, $\epsilon_2 = 0.052$, $\epsilon_3 = 0.051$ GeV, and $\Lambda_1 = 0.022$, $\Lambda_2 = 0.0003$, $\Lambda_3 = 0.039$ GeV^2 [242]. In this scenario, the solar mass-squared difference strongly limits the universal gaugino mass from above and below. Large values of the universal scalar mass are limited mainly by the atmospheric mass-squared difference.

This model can be tested at colliders, and the main signal that differentiates it from the MSSM is the decay of the lightest neutralino which decays only in RpV modes. In the scenario of figure 20 the neutralino mass is 99 GeV and decays to an on-shell W, satisfying:

$$\frac{B(\chi_1^0 \to We)}{B(\chi_1^0 \to W\mu)} = \frac{\Lambda_1^2}{\Lambda_2^2} \,. \tag{44}$$

Such ratios can be directly related to neutrino mixing angles [243].

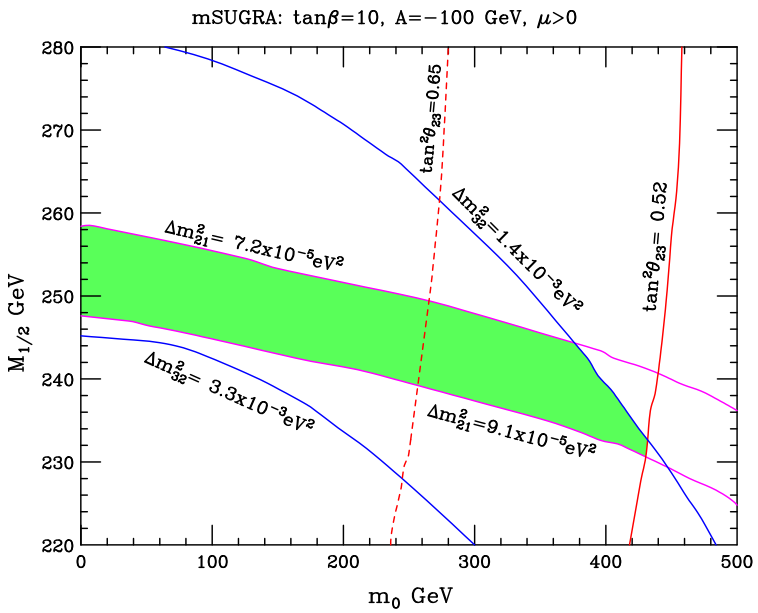

Figure 20: Region of parameter space where solutions satisfy all experimental constraints. Taken with kind permission of the European Physical Journal from figure 6 in reference [242]. Copyrighted by Springer Berlin/Heidelberg.

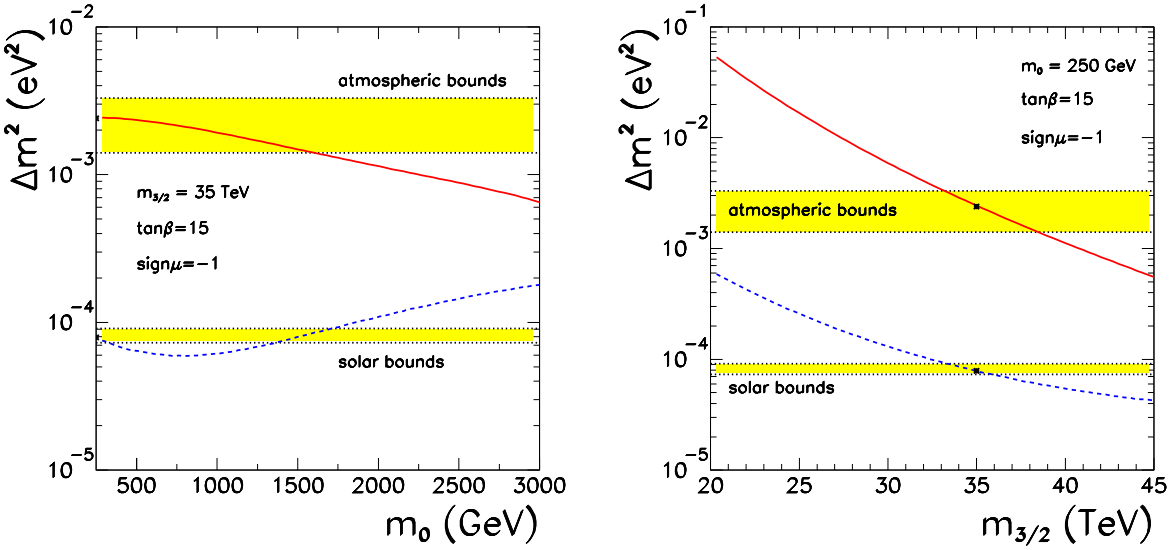

Figure 21: Atmospheric and solar mass-squared differences as a function of susy masses in AMSB. Taken with kind permission of Physical Review from figures 1 and 3 in reference [244]. Copyrighted by the American Physical Society.

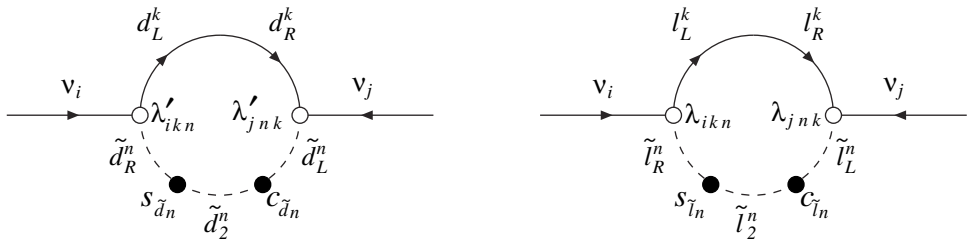

Figure 22: Pictorial representation of the fermion-sfermion loops contributing to the neutrino mass matrix, with Rp violated trilinearly in the open circles.

Other scenarios have been studied, for example Anomaly Mediated Super-Symmetry Breaking (AMSB) [245], and Gauge Mediated Supersymmetry Breaking [246], and Split Supersymmetry [247]. In the case of AMSB we see in figure 21 how the solar and atmospheric mass-squared differences depend on the universal scalar and gaugino masses, for fixed values of the BRpV parameters $\epsilon_1 = -0.015$, $\epsilon_2 = -0.018$, $\epsilon_3 = 0.011$ GeV, and $\Lambda_1 = -0.03$, $\Lambda_2 = -0.09$, $\Lambda_3 = -0.09$ GeV^2.

TRpV interactions do not contribute to neutrino masses at tree-level [248]. The one-loop contributions to these diagrams are given by the diagrams shown in figure 22. The convention for the graphs is the same as before. Analogous graphs are obtained for the light scalars $\tilde{d}_1^n$ and $\tilde{l}_1^n$ with the replacement $c_{\tilde{d}_n} \to -s_{\tilde{d}_n}$ and $s_{\tilde{d}_n} \to c_{\tilde{d}_n}$. The mixing angles are:

$$\sin(2\theta_{\tilde{d}_n}) = \frac{2(M^{\tilde{d}\,2}_{LR})_n}{M^{\tilde{d}\,2}_{Ln} - M^{\tilde{d}\,2}_{Rn}}\,, \qquad \sin(2\theta_{\tilde{l}_n}) = \frac{2(M^{\tilde{l}\,2}_{LR})_n}{M^{\tilde{l}\,2}_{Ln} - M^{\tilde{l}\,2}_{Rn}}\,. \tag{45}$$

The contribution to the neutrino mass matrix due to TRpV is:

$$(\Delta M^{\nu}_{ij})^{\lambda'} = \frac{N_c}{16\pi^2} \sum_{kn} \left(\lambda'_{ikn}\lambda'_{jnk} + \lambda'_{ink}\lambda'_{jkn}\right) \sin(2\theta_{\tilde{d}_n})\, m_{d_k} \Delta B_0(0; m^2_{d_k}; m^2_{\tilde{d}_n})\,. \tag{46}$$

Note that the contribution to the neutrino mass matrix is symmetric in the indices i and j [249]. A similar contribution holds for leptons and sleptons inside the loop, replacing λ' by λ couplings. In the approximation where only particles of the third generation contribute inside the loops, the shift to the neutrino mass matrix from TRpV is:

$$(\Delta M^{\nu}_{ij})^{TRpV} = D\lambda'_{i33}\lambda'_{j33} + E\lambda_{i33}\lambda_{j33}\,, \tag{47}$$

which can be added to equation (41). In this way, BRpV and TRpV, together or separated, can explain the neutrino masses and oscillations observed in experiments.

3.1.3 Extra Dimensions

The basic gauge-theoretic way to account for small neutrino masses is to ascribe them to the violation of lepton number by adding to the SM an effective dimension-five operator $\mathcal{O} = \lambda LHLH$ [250] (see figure 23). The favourite scenario realising this idea is the "see-saw" mechanism, which

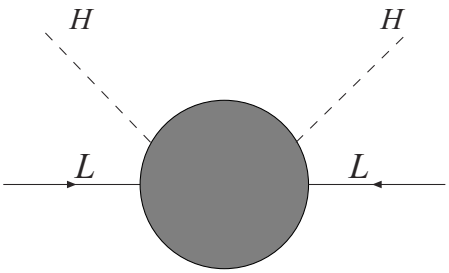

Figure 23: Dimension five operator responsible for neutrino mass. L denotes any of the three lepton doublets and H is the SM scalar doublet.

requires the presence of singlet "right"-handed neutrinos, which mix with the ordinary SU(2) doublet "left"-handed neutrinos [251]. The suppression of the neutrino masses results from the structure of the full mass matrix [70, 252]. In the simplest versions of this mechanism the mass of the extra states should be about ten orders of magnitude larger than the electroweak scale.

Recently, there have been a number of attempts to explain neutrino oscillations in theories with large internal dimensions and a low fundamental scale [253–257]. A convenient, perturbatively-calculable framework is type I string theory with D-branes. The SM is then localised on a stack of D-branes, transverse to some large extra dimensions, where gravity propagates. D-brane models offer a novel scenario to account for neutrino masses [258–263]; right-handed neutrinos are assumed to propagate in the bulk while left-handed neutrinos, being a part of the lepton doublet, live on the SM branes. As a result, the Dirac neutrino mass is naturally suppressed by the bulk volume. Adjusting this volume, so that the string scale lies in the TeV range, leads to tiny neutrino masses compatible with current experimental data.

Indeed, the relation between the string scale, M_s, and the four-dimensional Planck mass, M_P, is:

$$M_P^2 = \frac{8}{g^4} V_b M_s^2 \ , \tag{48}$$

where g is the SM gauge coupling and V_b is the volume of the bulk in string units. The simplest way to introduce a right-handed neutrino is to identify it with an open string excitation on some (stack of) brane(s) extended in the bulk. Moreover the SM Higgs and lepton doublets must come from open strings stretched between the SM and bulk branes and thus, living at their intersection, they couple to the bulk neutrino state. More precisely, its kinetic term is:

$$S_{kin} = V_b \int d^4x \sum_m \left\{ \bar{\nu}_{Rm} \partial\!\!\!/ \nu_{Rm} + \bar{\nu}^c_{Rm} \partial\!\!\!/ \nu^c_{Rm} + \frac{m}{R} \nu_{Rm} \nu^c_{Rm} + c.c. \right\} \ , \tag{49}$$

where the sum is extended over all Kaluza-Klein (KK) excitations, denoted collectively by m. For simplicity we assumed a toroidal compactification for n extra dimensions of common radius R, with $V_b = (2\pi R)^n$ in string units. The two states ν_R and ν^c_R correspond to the left and right four-dimensional (4d) components of the higher-dimensional spinor. The zero-mode ν_{R0} will be identified with the right-handed-neutrino state, while ν^c_{R0} may be projected out from the spectrum by an orbifold projection and is not relevant for our purposes.

The interaction of the bulk neutrino with the localised Higgs and lepton doublets reads:

$$S_{int} = \lambda \int d^4x H(x) L(x) \nu_R(x, y = 0)\,, \tag{50}$$

where it has been assumed that the SM brane stack is localised at the origin of the bulk and the coupling, λ, is in general of order g^2 (λ is equal to g^2 in the simplest 3-brane realisation of the SM). By expanding ν_R in KK modes, one gets the mass terms:

$$S_{mass} = \frac{\lambda v}{\sqrt{V_b}} \sum_m \nu_L \nu_{Rm}\,, \tag{51}$$

where v is the Higgs expectation value, $\langle H \rangle = v$. Note that the apparent mixing of ν_L with all KK excitations can be neglected since its strength (51) is much smaller than the KK mass $gv/R^{n/2} << 1/R$, or equivalently $gv << R^{n/2-1}$, which is valid for any $n \geq 2$. As a result, the right-handed neutrino is essentially the zero mode ν_{R0} and taking into account the normalisation of its kinetic term (49), one obtains a Dirac neutrino mass, $m_\nu \nu_L \nu_{Rm}$, with:

$$m_\nu \simeq \frac{\lambda v}{\sqrt{V_b}} \simeq \frac{\sqrt{8}\lambda}{g^2}\, v \frac{M_s}{M_p}\,, \tag{52}$$

which is of the order of 10^{-3} to 10^{-2} eV for $M_s \sim 1 - 10$ TeV.

The extra dimensional neutrino-mass suppression mechanism described above can be destabilized by the presence of a large Majorana neutrino-mass term. Indeed, in the absence of any protecting symmetry, the lepton-number-violating dimension-5 effective operator in figure 23 will be present. This would lead, in the case of TeV-string-scale models, to an unacceptable Majorana mass term of the order of a few GeV. Even if we manage to eliminate this operator in some particular model, higher-order operators would also give unacceptably large contributions, since in low-scale gravity models the ratio between the Higgs vacuum expectation value and the string scale is of order $\mathcal{O}(1/10 - 1/100)$.

An elegant way to avoid this problem was suggested in reference [264]. It consists of assuming that the bulk sector, where the SM singlet states live, is eight-dimensional. There is, however, a general theorem that states that in eight dimensions there can be no massive Majorana spinor [265–268]. Moreover, further unwanted large L-violating contributions to neutrino masses could be prevented by imposing lepton-number conservation leaving only the Dirac mass (52). Indeed, lepton number often arises as an anomalous abelian gauge symmetry associated to the $U(1)_b$ of the bulk (stack of) brane(s), possibly in a linear combination with other $U(1)$'s [269,270]. The anomaly is canceled by shifting an axion field from the closed string (Ramond-Ramond) sector [271, 272]. As a result, the gauge boson becomes massive, while lepton number remains unbroken as an effective global symmetry in perturbation theory [273]. The gauge coupling, g_b, of the bulk $U(1)_b$ gauge boson is extremely small since it is suppressed by the volume of the bulk V_b:

$$\frac{1}{g_b^2} = \frac{1}{g^2} V_b = \frac{g^2}{8} \frac{M_P^2}{M_s^2}\,, \tag{53}$$

where in the second equality we used equation (48). It follows that $g_b \simeq 10^{-16} - 10^{-14}$ for $M_s \sim 1 - 10$ TeV. Such a theory would lead to light Dirac neutrino masses, in contrast with general four-dimensional gauge-theoretic expectations which lead to Majorana neutrinos [251].

If the $U(1)_b$ gauge boson is light, it would be copiously produced in stellar processes, leading to supernova cooling through energy loss in the bulk of extra dimensions. There are strong constraints coming from supernova observations. Note that the corresponding process is much stronger than the production of gravitons because of the non-derivative coupling of the gauge-boson interaction [259]. In fact, for the case of n large transverse dimensions of common radius R, satisfying $m_A, R^{-1} << T$ with m_A the gauge boson mass and T the supernova temperature, the production rate, P_A, is proportional to:

$$P_A \sim g_b^2 \times [R(T - m_A)]^n \times \frac{1}{T^2} \simeq \frac{T^{n-2}}{M_s^n}\,, \tag{54}$$

where the factor $[R(T - m_A)]^n$ counts the number of KK excitations of the $U(1)_b$ gauge boson with mass less than T. This rate can be compared with the corresponding graviton production:

$$P_G \sim \frac{1}{M_P^2} \times (RT)^n \simeq \frac{T^n}{M_s^{n+2}}\,, \tag{55}$$

showing that for $n = 2$ (sub)millimeter extra dimensions, it is unacceptably large, unless the bulk gauge boson acquires a mass $m_A \gtrsim 10$ MeV. For $n \geq 3$, the supernova bound becomes much weaker and m_A may be much smaller [274]. Such a light gauge boson can mediate short distance forces within the range of table-top experiments that test Newton's law at very short distances [275–278].

These theories also lead to novel ways to generate neutrino oscillations. The interaction term in equation (50) involves in general all left-handed neutrinos and additional Higgs doublets:

$$\sum_{i=1}^{3} \lambda_i L_i H_i \nu_R \;\rightarrow\; \sum_{i=1}^{3} \lambda_i\, v_i\, \nu_{iL}\, \nu_R\,, \tag{56}$$

where i is a generation index and for each generation i, H_i is one of the possible available Higgs doublets H_d or H_u, providing also masses to down or to up quarks, with $v_i = \langle H_i \rangle$ the corresponding vev. The above couplings give mass to one linear combination of the weak eigenstates ν_{iL}, while the other two remain massless. The mass is given by equation (52) with λv replaced by $\sqrt{\sum_{i=1}^{3} \lambda_i^2 v_i^2}$. The right-handed neutrino, being a bulk state, has a tower of KK excitations. The mixing of these states with the ordinary neutrinos may have an impact upon neutrino oscillations.

3.1.3.1 The effect of extra dimensions

The most important features of the data on neutrino oscillations that are relevant for the present discussion are:

1. The existence of spectral distortions indicative of neutrino oscillations;

2. The solar mixing angle is large but significantly non-maximal;

3. The atmospheric best-fit mixing angle is maximal;

4. Both solar and atmospheric oscillation data strongly as well as the recent MiniBoone data [40] disfavour the presence of sterile neutrino states in the channel to which the relevant neutrino is oscillating.

There are several discussions in the literature [258–263] regarding neutrino masses and oscillations in the context of extra dimensions. Most of these discussions are restricted to the case of an effectively one-dimensional bulk. This simple one-dimensional bulk picture is not realistic [279], as it is at odds with the current global status of neutrino-oscillation data given in reference [67] and described above. Indeed, such a picture violates at least one of the four points mentioned above. In addition there is also a serious theoretical problem, since one-dimensional propagation of massless bulk states gives rise to linearly growing fluctuations which, in general, yield large corrections to all couplings of the effective field theory, destabilizing the hierarchy [280].

In the case of a two-dimensional bulk the situation is significantly improved [270]. Indeed, there is enough structure to describe both solar and atmospheric oscillations by introducing a single bulk-neutrino pair, using essentially the two lowest frequencies of the neutrino-mass matrix: the mass of the zero mode (equation (52)), arising via the electroweak Higgs phenomenon, which is suppressed by the volume of the bulk, and the mass of the first KK excitation. The former is used to reproduce the solar-neutrino data. The later is used to explain atmospheric-neutrino oscillations, which have a higher oscillation frequency, with an amplitude which is enhanced due to logarithmic corrections of the two-dimensional bulk [280]. One can see, however, that at least condition (4) above is violated, as there is a significant sterile component at least in one of the channels of neutrino conversion, corresponding to the KK excitations of the bulk right-handed neutrino, and this is highly disfavoured by the global fits of neutrino oscillations [67].

One way out is to introduce three bulk neutrinos and explain the observed neutrino oscillations in the traditional way [281]. In this case, ν_R in equation (56) would carry a generation index i and all left-handed neutrinos would acquire Dirac-type masses with the zero modes of the bulk states. Moreover, the effect of KK mixing can be suppressed by appropriately decreasing the size of the extra dimensions and thus increasing the value of the string scale. Thus, in this limit one would obtain the generic case of three Dirac neutrinos, and the lepton-mixing matrix depends on precisely three angles and one CP phase, as the quark-mixing matrix. Correspondingly, the oscillation pattern is "generic" without special predictions. Having Dirac instead of Majorana neutrinos can be experimentally tested by searching for the existence of processes like $0\nu\beta\beta$.

On the other hand, "extra-dimensional" signatures may be present in oscillations at a subleading level, as non-standard interactions (see [251] for a short discussion). The Neutrino Factory will provide an interesting laboratory to probe for the possible presence of such effects.

3.1.4 String Theory

There has been relatively little work on the implications of superstring theories for neutrino masses. However, it is known that some of the ingredients employed in Grand Unified Theories and other four-dimensional models may be difficult to implement in known types of constructions. For example, the chiral supermultiplets that survive in the effective four-dimensional field theory are generally bi-fundamental in two of the gauge-group factors (including the case of fundamental under one factor and charged under a $U(1)$) for lowest-level heterotic constructions; or either bi-fundamental, adjoint, antisymmetric, or symmetric for intersecting brane constructions. This makes it difficult to break the GUT symmetry, and even more so to find the high-dimensional Higgs representations (such as the **126** of $SO(10)$) usually employed in GUT models for neutrino and other fermion masses. Thus, it may be difficult to embed directly many of the models, especially GUT models involving high-dimensional representations rather than higher-dimensional operators, in a string framework. Perhaps more likely is that the underlying string theory breaks directly to an effective four-dimensional theory including the Standard Model and perhaps other group factors [282]. Some of the aspects of grand unification, especially in the gauge sector, may be maintained in such constructions. However, the GUT relations for Yukawa couplings are often not retained [283–285] because the matter multiplets of the effective theory may have a complicated origin in terms of the underlying string states. Another difference is that Yukawa couplings in string-derived models may be absent due to symmetries in the underlying string construction, even though they are not forbidden by any obvious symmetries of the four-dimensional theory, contrary to the assumptions in many non-string models. Finally, higher-dimensional operators, suppressed by inverse powers of the Planck scale, are common.

Much activity on neutrino masses in string theory occurred following the first superstring revolution. In particular, a number of authors considered the implications of an E_6 subgroup of the heterotic $E_8 \times E_8$ construction [283, 286–288]. Assuming that the matter content of the effective theory involves three **27**s, one can avoid neutrino masses altogether by fine-tuned assumptions concerning the Yukawa couplings [283]. However, it is difficult to implement a canonical type I see-saw. Each **27** contains two Standard Model singlets, which are candidates for right-handed neutrinos, and for a field which could generate a large Majorana mass for the right-handed neutrinos if it acquires a large vacuum expectation value and has an appropriate trilinear coupling to the neutrinos. However, there are no such allowed trilinear couplings involving three **27**s (this is a reflection of the fact that the **27** does not contain a **126** of the $SO(10)$ subgroup). E_6 string-inspired models were constructed to get around this problem by invoking additional fields not in the **27** [285,289] or higher-dimensional operators [288], typically leading to extended versions of the see-saw model involving fields with masses or vevs at the TeV scale.

Similarly, more recent heterotic and intersecting brane constructions, e.g., involving orbifolds and twisted sectors, may well have the necessary fields for a type I see-saw, but it is again required that the necessary Dirac Yukawa couplings and Majorana masses for the right-handed neutrinos be present simultaneously. Dirac couplings need not emerge at the renormalisable

level, but can be of the form:

$$\langle S'_1 \cdots S'_{d-3} \rangle N L H_u / M_{\rm PL}^{d-3} \ , \tag{57}$$

where the S'_i are Standard Model singlets which acquire large expectation values ($d = 3$ corresponds to a renormalisable operator). Similarly, Majorana masses can be generated by the operators:

$$\langle S_1 \cdots S_{n-2} \rangle N N / M_{\rm PL}^{n-3} \ . \tag{58}$$

Whether such couplings are present at the appropriate orders depends on the underlying string symmetries and selection rules, which are often very restrictive. It is also necessary for the relevant S and S' fields to acquire the large expectation values that are needed, presumably without breaking supersymmetry at a large scale. Possible mechanisms involve approximately flat directions of the potential, e.g., associated with an additional $U(1)'$ gauge symmetry [290, 291], string threshold corrections [292–294], or hidden sector condensates [295].

There have been surprisingly few investigations of neutrino masses in explicit semi-realistic string constructions. It is difficult to obtain canonical Majorana masses in intersecting brane constructions [296] because there are no interactions involving the same intersection twice. Two detailed studies [269, 270] of non-supersymmetric models with a low string scale concluded that lepton number was conserved, though a small Dirac mass might emerge from a large internal dimension. Large enough internal dimensions for the supersymmetric case may be difficult to achieve, at least for simple toroidal orbifolds.

There are also difficulties for heterotic models. An early study of Z_3 orbifolds yielded no canonical Dirac neutrino Yukawa couplings [286] at low order. Detailed analyses of free-fermionic models and their flat directions were carried out in [295, 297] and [298, 299]. Both studies concluded that small Majorana masses could be generated if one made some assumptions about dynamics in the hidden sector. In [295,297] the masses were associated with an extended see-saw involving a low mass scale. The see-saw found in [298, 299] was of the canonical type I type, but in detail it was rather different to GUT-type models. A see-saw was also claimed in a heterotic Z_3 orbifold model with E_6 breaking to $SU(3) \times SU(3) \times SU(3)$ [300]. A recent study of Z_6 orbifold constructions found Majorana-type operators [301], but (to the order studied) the S_i fields did not have the required expectation values when R-parity is conserved.

In [302] a large class of vacua of the bosonic Z_3 orbifold were analysed with emphasis on the neutrino sector to determine whether the minimal type I see-saw is common, or if not to find possible guidance to model building, and possibly to get clues concerning textures and mixing if examples were found. Several examples from each of 20 patterns of vacua were studied, and the non-zero superpotential terms through degree 9 determined. There were a huge number of D-flat directions, with the number reduced greatly by the F-flatness condition. Only two of the patterns had Majorana mass operators, while none had simultaneous Dirac operators of low enough degree to allow neutrino masses larger than 10^{-5} eV. (One apparently successful model was ruined by off-diagonal Majorana mass terms.) It is not clear whether this failure to obtain a minimal see-saw is a feature of the particular class of construction, or whether it is suggesting

that string constraints and selection rules might make string vacua with minimal see-saws rare. Systematic analyses of the neutrino sector of other classes of constructions would be very useful.

There are other possibilities for obtaining small neutrino masses in string constructions, such as extended see-saws [295, 297] and small Dirac masses from higher dimension operators [291]. Small Dirac neutrino masses in models with anisotropic compactifications motivated by type I strings [303] have been discussed recently in [304]. The possibility of embedding type II see-saw ideas (involving Higgs triplets) in heterotic string constructions was considered in [305]. It is possible to obtain a Higgs triplet of $SU(2)$ with non-zero hypercharge in a higher level construction (in which $SU(2) \times SU(2)$ is broken to a diagonal subgroup). In this case, because of the underlying $SU(2) \times SU(2)$ symmetry the Majorana mass matrix for the light neutrinos should involve only off-diagonal elements (often with one of the three off-diagonal elements small or vanishing). This leads to phenomenological consequences very different from those of triplet models that have been motivated by grand unification or bottom-up considerations, including an inverted hierarchy, two large mixings, a value of U_{e3} induced from the charged-lepton mixings that is close to the current experimental lower limit, and an observable neutrinoless double-beta decay rate. This string version of the triplet model is a top-down motivation for the $L_e - L_\mu - L_\tau$-conserving models that have previously been considered from a bottom-up point of view [306], but has the advantage of allowing small mixings from the charged-lepton sector. A recent study indicates that it may also be possible to generate a type II see-saw in intersecting D6-brane models involving $SU(5)$ grand unification, although the examples constructed are not very realistic [307].

These comments indicate that string constructions may be very different from traditional grand unification or bottom-up constructions, mainly because of the additional string constraints and symmetries encountered. Versions of the minimal see-saw (though perhaps with non-canonical family structure) are undoubtedly present amongst the large landscape of string vacua, though perhaps they are rare. One point of view is to simply focus on the search for such string vacua. However, another is to keep an open mind about other possibilities that may appear less elegant from the bottom-up point of view but which may occur more frequently in the landscape.

3.1.5 TeV scale mechanisms for small neutrino masses

Neutrino mass may arise in a class of non-SUSY models via $L = 2$ scalar-lepton-lepton Yukawa interactions. The Lagrangian can be written generically as follows:

$$-\mathcal{L}^{yuk} = f_{ij} H^{++} l_i l_j + g_{ij} H^{+} l_i \nu_j + h_{ij} H^0 \nu_i \nu_j + \text{hermitian conjugate} \, . \tag{59}$$

Here $H^{\pm\pm}, H^{\pm}$ and H^0 are doubly-charged, singly-charged and neutral scalars respectively which originate from an $SU(2)_{L,R}$ isospin singlets ($I = 0$) or triplets ($I = 1$). Each scalar is assigned $L = 2$. The charged leptons ($l^{\pm}$) and neutrinos (ν) may be of either chirality. Four examples of models which utilise various terms in $\mathcal{L}^{yuk}$ to generate neutrino mass are listed below:

- *The left-right symmetric model*: TeV scale breaking of $SU(2)_R$ via the right-handed scalar triplet vacuum expectation value which gives rise to a TeV scale see-saw mechanism [308];

- *Higgs Triplet Model*: Tree-level neutrino mass for the observed neutrinos proportional to $SU(2)_L$ triplet scalar vev (no right-handed neutrino) [309];

- *Zee model*: Radiative neutrino mass at 1-loop via $SU(2)_L$ singlet scalar $H^{\pm}$ [310]; and

- *Babu model*: Radiative neutrino mass at 2-loop via $SU(2)_L$ singlet scalars $H^{\pm\pm}$ and $H^{\pm}$ [311].

All the above models can provide TeV-scale mechanisms of neutrino mass generation consistent with current neutrino-oscillation experiments. New particle discovery (e.g. $Z', W', H^{\pm\pm}$) at the Large Hadron Collider (LHC) is also a possibility if $M_{Z'}, M_{W'} < 3-4$ TeV, $M_{H^{\pm\pm}} < 1$ TeV. Precision measurements of the neutrino-mass matrix at a Neutrino Factory would provide valuable information on the Yukawa couplings f, g, h. Such couplings also induce lepton-flavour violating (LFV) decays (e.g. $\mu \to eee, \mu \to e\gamma$) [62, 312], which might also form part of the research programme at a Neutrino Factory. Importantly, any signal for $\mu \to e\gamma$ from the MEG experiment can be interpreted in the above models. The first pair of models above can accommodate any value of $\sin\theta_{13}$ and any of the currently allowed mass hierarchies, normal (NH), inverted (IH) and degenerate (DG). The second pair of models above are more predictive for $\sin\theta_{13}$ and accommodate specific neutrino mass hierarchies. A distinctive feature of all the models is the synergy between precision measurements of oscillation parameters (at a Neutrino Factory), LFV decays of μ and τ, and direct searches for the $L = 2$ scalars, all of which involve the couplings f, g, h.

Left-Right Symmetric Model

The left-right (LR) symmetric model [313] is an extension of the Standard Model based on the gauge group $SU(2)_R \otimes SU(2)_L \otimes U(1)_{B-L}$. The LR-symmetric model has many virtues, e.g.:

- The restoration of parity as an original symmetry of the Lagrangian which is broken spontaneously by a Higgs vev; and

- The replacement of the arbitrary SM hypercharge Y by the theoretically more attractive $B - L$.

Although the Higgs sector is arbitrary, a theoretically and phenomenologically appealing way to break the $SU(2)_R$ gauge symmetry is by invoking Higgs isospin-triplet representations. Such a choice conveniently allows the implementation of a low energy see-saw mechanism for neutrino masses. A right-handed neutrino is required by the $SU(2)_R$ gauge group and leptons are assigned to multiplets with quantum numbers $(T_L, T_R, B-L)$:

$$L_{iL} = \begin{pmatrix} \nu_i' \\ l_i' \end{pmatrix}_L : (1/2 : 0 : -1)\,, \; L_{iR} = \begin{pmatrix} \nu_i' \\ l_i' \end{pmatrix}_R : (0 : 1/2 : -1)\,. \tag{60}$$

Here $i = 1, 2, 3$ denotes generation number. The Higgs sector consists of a bidoublet Higgs field, Φ, and two triplet Higgs fields, Δ_L and Δ_R:

$$\begin{aligned}
\Phi &= \begin{pmatrix} \phi_1^0 \phi_2^+ \\ \phi_1^- \phi_2^0 \end{pmatrix} : (1/2 : 1/2 : 0) \ , \\
\Delta_L &= \begin{pmatrix} \delta_L^+/\sqrt{2} \delta_L^{++} \\ \delta_L^0 - {\delta_L}^+/\sqrt{2} \end{pmatrix} : (1 : 0 : 2) \ , \\
\Delta_R &= \begin{pmatrix} \delta_R^+/\sqrt{2} \delta_R^{++} \\ \delta_R^0 - {\delta_R}^+/\sqrt{2} \end{pmatrix} : (0 : 1 : 2) \ .
\end{aligned} \tag{61}$$

The vevs for these fields are as follows:

$$\langle \Phi \rangle = \begin{pmatrix} \kappa_1 & 0 \\ 0 & \kappa_2 \end{pmatrix} \frac{1}{\sqrt{2}}, \ \langle \Delta_L \rangle = \begin{pmatrix} 0 & 0 \\ v_L & 0 \end{pmatrix} \frac{1}{\sqrt{2}} \ , \ \langle \Delta_R \rangle = \begin{pmatrix} 0 & 0 \\ v_R & 0 \end{pmatrix} \frac{1}{\sqrt{2}} \ . \tag{62}$$

The gauge groups $SU(2)_R$ and $U(1)_{B-L}$ are spontaneously broken at the scale v_R. Phenomenological considerations require $v_R \gg \kappa = \sqrt{\kappa_1^2 + \kappa_2^2} \sim \frac{2M_{W_1}}{g}$. The vev v_L does not play a role in the breaking of the gauge symmetries and is constrained to be small ($v_L < 8$ GeV) in order to comply with the measurement of $\rho = M_Z^2 \cos^2 \theta_W / M_W^2 \sim 1$. The Lagrangian responsible for generating neutrino mass is as follows:

$$-\mathcal{L} = \bar{L}_L (y_D \Phi + \tilde{y}_D \tilde{\Phi}) L_R + i y_M (L_L^T C \tau_2 \Delta_L L_L + L_R^T C \tau_2 \Delta_R L_R) + \text{hermitian conjugate} \ , \tag{63}$$

where y_M is a 3×3 Majorana-type Yukawa coupling matrix. Expanding the terms proportional to y_M results in a Lagrangian of the form of equation (59) with $y_M = f = \sqrt{2} g = h$. The 6×6 mass matrix for the neutrinos can be written in the block form:

$$M_\nu^{LR} = \begin{pmatrix} M_L & m_D \\ m_D^T & M_R \end{pmatrix} \ . \tag{64}$$

Each entry is given by

$$m_D = \frac{1}{\sqrt{2}} (y_D \kappa_1 + \tilde{y}_D \kappa_2) \, ; \ \ M_R = \sqrt{2} h v_R ; \ \ M_L = \sqrt{2} h v_L . \tag{65}$$

The neutrino mass matrix is diagonalised by a 6×6 unitary matrix V as $V^T M_\nu V = M_\nu^{diag} = \text{diag}(m_1, m_2, m_3, M_1, M_2, M_3)$, where m_i and M_i are the masses for neutrino mass eigenstates. The small neutrino masses m_i are generated by the Type II see-saw mechanism. Obtaining eV scale neutrino masses with $h = \mathcal{O}(0.1 - 1)$ requires M_L (and consequently v_L) to be at the eV scale. In LR-model phenomenology, with $v_R \sim$ TeV, it is customary to arrange the Higgs potential such that $v_L = 0$ [314]. In this case the masses of the light neutrinos arise from the Type I see-saw mechanism and are approximately $m_i \sim m_D^2 / M_R$. In order to realise the low-energy ($\sim \mathcal{O}(1 - 10)$ TeV) scale for the right-handed Majorana neutrinos, the Dirac mass term, m_D, should be $\mathcal{O}$ (MeV), which for $\kappa_2 \sim 0$ corresponds to $y_D \sim 10^{-6}$ (i.e. comparable in magnitude to the electron Yukawa coupling). The LR model with v_R of order a TeV predicts lepton-flavour violating (LFV) decays of the muon and tau mediated by $H^{\pm\pm}$ with a rate $\sim |hh|^2 / M_{H^{\pm\pm}}^4$ [315], and a rich phenomenology in direct searches at the LHC.

Higgs Triplet Model

In the Higgs Triplet Model (HTM) [70], [316] [12] a single $I = 1$, $Y = 2$ complex $SU(2)_L$ triplet Δ_L (see equation (62)) is added to the SM with the Yukawa coupling:

$$iy_M(L_L^T C\tau_2 \Delta_L L_L) + \text{hermitian conjugate} \ . \tag{66}$$

Expanding equation (66) results in equation (59) with $y_M = f = \sqrt{2}g = h$. No right-handed neutrino is introduced, and the light neutrinos receive a Majorana mass proportional to the left-handed triplet vev (v_L) leading to the following neutrino mass matrix:

$$\mathcal{M}_\nu^{HTM} = \sqrt{2} v_L h_{ij} \ . \tag{67}$$

The presence of a trilinear coupling $\mu \Phi^T i\tau_2 \Delta_L^\dagger \Phi$ (where Φ is the SM Higgs doublet with vev v) in the Higgs potential ensures a non-zero $v_L \sim \mu v^2/M^2$, where M is the mass of the triplet scalars. Taking M to be at the TeV scale results in $v_L \sim \mu$. From equation (67) it is apparent that the HTM does not provide predictions for the elements of $\mathcal{M}_\nu$ but instead accommodates the observed values (as does the LR model). However, combining accurate measurements of the neutrino oscillation parameters with any signals in LFV processes involving the muon or the tau [317] and/or direct observation of $H^{\pm\pm}$ [318] would enable this mechanism of neutrino mass generation to be tested. From equation (67) h_{ij} is directly related to the neutrino masses and mixing angles as follows:

$$h_{ij} = \frac{1}{\sqrt{2} v_L} V_{\text{PMNS}} diag(m_1, m_2, m_3) V_{\text{PMNS}}^T \ . \tag{68}$$

Observation of LFV decays of the muon for example at MEG and/or of the tau (at a Super B Factory) together with discovery of $H^{\pm\pm}$ (at LHC) would permit measurements of h_{ij}. A Neutrino Factory would greatly reduce the experimental error in the right-hand side of equation(68) and allow the above identity in the HTM to be checked precisely.

One loop radiative mechanism via a singly-charged, singlet scalar (Zee model)

A singly-charged, singlet scalar is added to the Two Higgs Doublet Model (2HDM) extension of the SM. Neutrino mass is generated radiatively via a 1-loop diagram figure 24a in which the mixing between the charged singlet and doublet scalars (proportional to a trilinear coupling μ) is crucial [310]. The relevant Lagrangian is:

$$\mathcal{L}^{Zee} = g_{ab} \left(L_{aL}^{Ti} C L_{bL}^{j} \right) \epsilon_{ij} H^+ + \sum_{i=1,2} y_k \overline{L}_L H_i l_R + \text{hermitian conjugate} \ , \tag{69}$$

where y_k is the Yukawa coupling of the doublet H_k to the leptons. If only one of the Higgs doublets couples to leptons (referred to as the "minimal Zee model") the resulting neutrino mass matrix is symmetric with vanishing diagonal elements:

$$\mathcal{M}_\nu^{Zee} = \begin{pmatrix} 0 & m_{e\mu} & m_{e\tau} \\ m_{e\mu} & 0 & m_{\mu\tau} \\ m_{e\tau} & m_{\mu\tau} & 0 \end{pmatrix} \tag{70}$$

[12] The model of [309] contains a triplet majoron and was excluded by LEP data. A viable extension of the HTM which contains a singlet majoron (referred to as the "123" model) was introduced in ref. [252].

where [312]

$$m_{ij} = g_{ij}(m_{l_j}^2 - m_{l_i}^2)\mu F \frac{1}{16\pi^2}\frac{1}{m_{S_1}^2 - m_{S_2}^2}\ln\frac{m_{S_1}^2}{m_{S_2}^2} \tag{71}$$

and m_{l_i} are the charged lepton masses, M_{S_i} are the charged scalar masses and $F = \cot\beta$ ($\tan\beta$) for Type I (II) couplings of the doublets to the leptons. The above mass matrix predicts the solar angle to be almost maximal, which is now ruled out at the 6σ level (see section 2.2.1). However, allowing both Higgs doublets to couple to the leptons (the "general Zee model") leads to non-zero diagonal elements in $\mathcal{M}_\nu^{Zee}$ [319]. The non-maximal solar angle can then be accommodated, $\sin\theta_{13} \neq 0$ is expected, and an inverted hierarchical neutrino mass pattern is predicted.

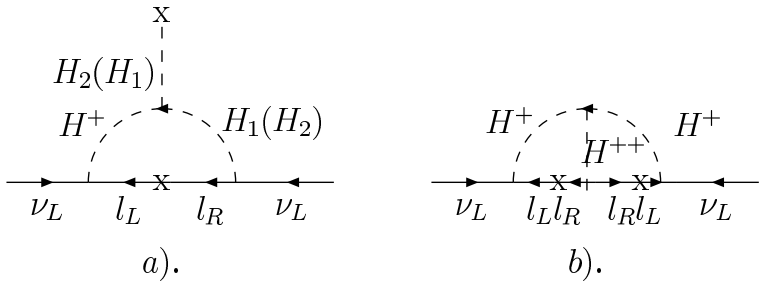

Figure 24: Diagram for neutrino mass generation in a) Zee model, and b) Babu model

Two loop radiative mechanism via singly and doubly-charged, singlet scalars (Babu model)

$SU(2)_L$ singlet charged scalars $H^{\pm\pm}$ and $H^\pm$ are added to the SM Lagrangian [311] with the following Yukawa couplings:

$$\mathcal{L} = \; f_{ab}\left(l_{aR}^T C l_{bR}\right) H^{++} + g_{ab}\left(L_{aL}^{Ti} C L_{bL}^j\right)\epsilon_{ij} H^+ \; + \text{hermitian conjugate}\,. \tag{72}$$

No right-handed neutrino is introduced. A Majorana mass for the light neutrinos arises at the two loop level (figure 24b) in which the lepton number violating trilinear coupling $\mu H^\pm H^\pm H^{\pm\pm}$ plays a crucial role. The explicit form for $\mathcal{M}_\nu$ is as follows:

$$\mathcal{M}_\nu^{Babu} = \zeta \times \begin{pmatrix} \epsilon^2\omega_{\tau\tau} + 2\epsilon\epsilon'\omega_{\mu\tau} + \epsilon'^2\omega_{\mu\mu}\,, & \epsilon\omega_{\tau\tau} + \epsilon'\omega_{\mu\tau} - \epsilon\epsilon'\omega_{e\tau} - \epsilon'^2\omega_{e\mu}\,, & -\epsilon\omega_{\tau\tau} - \epsilon'\omega_{\mu\mu} - \epsilon^2\omega_{e\tau} - \epsilon\epsilon'\omega_{e\mu} \\ . & \omega_{\tau\tau} - 2\epsilon'\omega_{e\tau} + \epsilon'^2\omega_{ee}\,, & -\omega_{\mu\tau} - \epsilon\omega_{e\tau} + \epsilon'\omega_{e\mu} + \epsilon\epsilon'\omega_{ee} \\ . & . & \omega_{\mu\mu} + 2\epsilon\omega_{e\mu} + \epsilon^2\omega_{ee} \end{pmatrix}, \tag{73}$$

where $\epsilon = g_{e\tau}/g_{\mu\tau}$, $\epsilon' = g_{e\mu}/g_{\mu\tau}$, $\omega_{ab} = f_{ab}m_a m_b$ (m_a, m_b are charged lepton masses) and ζ is given by:

$$\zeta = \frac{8\mu g_{\mu\tau}^2 \tilde{I}}{(16\pi^2)^2 m_{H^\pm}^2}\,. \tag{74}$$

Here $\tilde{I}$ is a dimensionless quantity of $\mathcal{O}(1)$ originating from the loop integration. The expression for $\mathcal{M}_\nu$ involves 9 arbitrary couplings. Since the model predicts one massless neutrino (at the

two-loop level), quasi-degenerate neutrinos are not permitted and only normal-hierarchy (NH) and inverted-hierarchy (IH) mass patterns can be accommodated. The g couplings (contained in ϵ and ϵ') are directly related to the elements of $\mathcal{M}_\nu$, and thus would be obtained precisely at a Neutrino Factory. In the scenario of NH, $\epsilon \approx \epsilon' \approx \tan\theta_{12}/\sqrt{2}$ and $\sin\theta_{13}$ is close to zero. Since $\epsilon, \epsilon' < 1$ one may neglect those terms in $\mathcal{M}_\nu$ which are proportional to the electron mass (i.e. $\omega_{ee}, \omega_{e\mu}, \omega_{e\tau}$). This simplification leads to the following prediction: $f_{\mu\mu} : f_{\mu\tau} : f_{\tau\tau} \approx 1 : m_\mu/m_\tau : (m_\mu/m_\tau)^2$. In the case of IH, large values are required for $\epsilon, \epsilon'(> 5)$, and thus neglecting $\omega_{ee}, \omega_{e\mu}, \omega_{e\tau}$ in $\mathcal{M}_\nu$ may not be entirely justified. However, if such terms are neglected then the above prediction for the ratio of $f_{\mu\mu} : f_{\mu\tau} : f_{\tau\tau}$ also holds approximately for the case of IH. A lower bound on $s_{13} > 0.05$ can also be derived. If the 2-loop diagram is solely responsible for the generation of the neutrino mass matrix the Babu model requires $g, f_{\mu\mu} \sim 10^{-2}$. Such relatively large couplings may lead to observable rates for LFV decays of muons and taus.

3.2 Unification and Flavour

A survey of the theoretical models that have been developed to explain the physics of flavour is presented in this section. Measurables that can be used to distinguish between the various models is also presented. These measurables include the mixing angles themselves and combinations of mixing angles, the latter are referred to as 'sum rules'. This section also contains a discussion of lepton-flavour violation.

3.2.1 Model survey

To understand the origin of the postulated forms of the Yukawa matrices, one must appeal to some sort of Family symmetry, $G_{\rm Family}$. In the framework of the see-saw mechanism, new physics beyond the Standard Model is required to cause lepton-number conservation to be violated and to generate right-handed neutrino masses at around the GUT scale. This is exciting since it implies that the origin of neutrino masses is related to a GUT symmetry group $G_{\rm GUT}$, which unifies the fermions within a family. Putting these ideas together leads to the development of a framework for physics beyond the SM which is based on $N = 1$ super-symmetry with commuting GUT and Family symmetry groups, $G_{\rm GUT} \times G_{\rm FAM}$. There are many possible candidate GUT and Family symmetry groups. Unfortunately the model dependence does not end there; the details of the symmetry-breaking vacuum plays a crucial role in specifying the model and in determining the masses and mixing angles. These models may be classified according to the particular GUT and Family symmetry that is assumed.

It may be possible to use precise measurements of the oscillation parameters to distinguish between different models. A survey of over sixty neutrino-mass models has been performed. The survey included:

- Models with assumptions about the structure of the mixing matrix ('texture' assumptions);
- Models based on lepton symmetries such as A_4, S_3, or $L_e - L_\mu - L_\tau$; and

- Models based on GUT symmetries such as $SU(5)$, flipped $SU(5)$, $SO(10)$, E_6, or $E_8 \times E_8$.

These models are reviewed briefly below with emphasis on how the different predictions arise from different symmetry-breaking patterns. A detailed, tabulated summary of the predictions for all three angles with references to models that have been included in our survey can be found in reference [320].

Models with Lepton Symmetries based on $\mu - \tau$ Symmetry

The maximal (or near maximal) mixing observed in atmospheric neutrinos strongly suggests a $\mu - \tau$ symmetry in the neutrino-mass matrix. There are two ways to realise the $\mu - \tau$ symmetry which give rise to maximal mixing in the atmospheric-neutrino sector, $\theta_{23} = \frac{\pi}{4}$ [321]. The first possibility is of the following form:

$$M_\nu \simeq \begin{pmatrix} 0 & 0 & 0 \\ 0 & 1 & 1 \\ 0 & 1 & 1 \end{pmatrix} , \tag{75}$$

which gives rise to the normal mass hierarchy. In this case, when the $\mu - \tau$ symmetry is exact, the 1-3 mixing angle vanishes, $\sin\theta_{13} = 0$. In addition, the mass splitting in the solar neutrino sector vanishes, $\Delta m^2_{12} = 0$. Non-vanishing Δm^2_{12} can be generated in a $\mu - \tau$ symmetric way by adding small parameters of the order of $\mathcal{O}(\epsilon \ll 1)$,

$$M_\nu \simeq \frac{\sqrt{\Delta m^2_{13}}}{2} \begin{pmatrix} c\epsilon & d\epsilon & d\epsilon \\ d\epsilon & 1+\epsilon & -1 \\ d\epsilon & -1 & 1+\epsilon \end{pmatrix} , \tag{76}$$

where the coefficients c and d are of order 1. This leads to,

$$\theta_{13} = 0,\ \theta_{23} = \frac{\pi}{4},\ \tan 2\theta_{12} \simeq \frac{2\sqrt{2}d}{(1-c)} , \tag{77}$$

and the parameter ϵ is fixed by the ratio of Δm^2_{13} and Δm^2_{12} as:

$$\epsilon = \frac{4}{1 + c + \sqrt{(c-1)^2 + 8d^2}} \sqrt{\frac{\Delta m^2_{12}}{\Delta m^2_{13}}} . \tag{78}$$

In order to generate non-zero θ_{13}, the $\mu - \tau$ symmetry has to be broken. How the symmetry breaking occurs dictates the size of the θ_{13} angle. The $\mu - \tau$ symmetry breaking also causes θ_{23} to differ from $\frac{\pi}{4}$, i.e. the mixing is no longer maximal. The breaking of the $\mu - \tau$ symmetry can generally be parametrised as:

$$M_\nu \simeq \frac{\sqrt{\Delta m^2_{13}}}{2} \begin{pmatrix} c\epsilon & d\epsilon & b\epsilon \\ d\epsilon & 1+a\epsilon & -1 \\ b\epsilon & -1 & 1+\epsilon \end{pmatrix} , \tag{79}$$

Table 4: Predictions for θ_{13} and for the deviation $(\theta_{23} - \pi/4)$ in models with softly broken $\mu - \tau$ symmetry for different symmetry breaking directions. This table is taken from reference [321].

symmetry breaking	θ_{13}	$\theta_{23} - \frac{\pi}{4}$
none	0	0
$\mu - \tau$ sector only	$\sim \Delta m^2_{12}/\Delta m^2_{13}$	$\lesssim 8^o$
e-sector only	$\sim \sqrt{\Delta m^2_{12}/\Delta m^2_{13}}$	$\lesssim 4^o$
dynamical	$\sim \sqrt{\Delta m^2_{12}/\Delta m^2_{13}}$	large

where the parameter a is of order unity. If the breaking is introduced in the e-sector, that is, $a = 1$, $b \neq d$, one then has:

$$\epsilon = \frac{4}{\sqrt{1+8d^2}}\sqrt{\frac{\Delta m^2_{12}}{\Delta m^2_{13}}}, \quad \tan 2\theta_{12} \simeq \frac{2(b+d)}{(1-c)}\,, \tag{80}$$

and a non-vanishing θ_{13} angle:

$$\theta_{13} = (b-d)\sqrt{\frac{\Delta m^2_{12}}{\Delta m^2_{13}}}\,. \tag{81}$$

A non-vanishing deviation of the atmospheric mixing angle from $\frac{\pi}{4}$ can exist with magnitude $\frac{\pi}{4} - \theta_{23} \sim \mathcal{O}(\epsilon^2)$. The breaking of the $\mu - \tau$ symmetry can also be introduced in the $\mu - \tau$ sector. This is characterised by $a \neq 1$ and $b = d$. In this case, the parameter ϵ is related to Δm^2_{12} and Δm^2_{13} by:

$$\epsilon = \frac{4}{c + \frac{1}{2}(1+a) + \sqrt{(c - \frac{1}{2}(1-c))^2 + 8d^2}}\sqrt{\frac{\Delta m^2_{12}}{\Delta m^2_{13}}}\,. \tag{82}$$

Thus, the predictions for $\sin\theta_{13}$ and $\pi/4 - \theta_{23}$ strongly depend on the symmetry-breaking pattern. Table 4 summarises the predictions for θ_{13} and for $\frac{\pi}{4} - \theta_{23}$ for various symmetry-breaking scenarios.

The inverted mass hierarchy can be obtained when the neutrino mass matrix is of the form:

$$M_\nu \simeq \begin{pmatrix} 0 & 1 & 1 \\ 1 & 0 & 0 \\ 1 & 0 & 0 \end{pmatrix}\,. \tag{83}$$

This mass matrix has an enhanced $L_e - L_\mu - L_\tau$ symmetry [322, 323] and is a special case of the following mass matrix:

$$M_\nu \simeq \sqrt{\Delta m^2_{13}}\begin{pmatrix} 0 & \sin\theta & \cos\theta \\ \sin\theta & 0 & 0 \\ \cos\theta & 0 & 0 \end{pmatrix}\,. \tag{84}$$

In the exact $L_e - L_\mu - L_\tau$ symmetric limit, this leads to the following predictions [322]:

$$\Delta m^2_{12} = 0, \quad \theta_{13} = 0, \quad \theta_{12} = \frac{\pi}{4}, \quad \sin^2 2\theta_{23} = \sin^2 2\theta \quad . \tag{85}$$

Since $\theta_{12} \neq \frac{\pi}{4}$, the $L_e - L_\mu - L_\tau$ symmetry has to be softly broken. The soft breaking of the $L_e - L_\mu - L_\tau$ symmetry can be introduced by adding small $e-e$, $\mu-\mu$, $\mu-\tau$ and $\tau-\tau$ couplings:

$$M_\nu \simeq \sqrt{\Delta m^2_{13}} \begin{pmatrix} z & \sin\theta & \cos\theta \\ \sin\theta & y & d \\ \cos\theta & d & x \end{pmatrix}, \qquad x,\ y,\ d \ll 1 \qquad . \tag{86}$$

For non-zero x, y and d, one has:

$$\sin^2 2\theta_{12} \simeq 1 - \left(\frac{\Delta m^2_{12}}{4\Delta m^2_{13}} - z \right)^2 . \tag{87}$$

The breaking of the $\mu - \tau$ symmetry can arise in the $\mu - \tau$ sector, *i.e.*, $\cos\theta = \sin\theta = 1/\sqrt{2}$ and $x \neq y$, which leads to:

$$\theta_{13} = \frac{1}{2}(x - y), \quad \frac{\Delta m^2_{12}}{\Delta m^2_{13}} = 2(x + y + z + d) \quad . \tag{88}$$

The breaking of the $\mu-\tau$ symmetry can also be introduced in the e-sector by having $\cos\theta \neq \sin\theta$ and $x = y$. This leads to $\theta_{13} \simeq -d\cos 2\theta_{23}$. In the inverted hierarchy case, the correlations among the neutrino-mixing angles is not as strong as in the normal-hierarchy case.

Single-RH neutrino dominance

Single-RH neutrino dominance (SRND), proposed in [324], can be implemented in many classes of model; it is therefore a mechanism rather than a model. SRND provides a natural way to generate large mixing angles. In the simplified case, with only the second and third families, the Dirac neutrino-mass matrix and RH Majorana neutrino-mass matrix are generally of the form:

$$M_D = \begin{pmatrix} \cdot & \cdot & \cdot \\ \cdot & a & b \\ \cdot & c & d \end{pmatrix}, \quad M_R = \begin{pmatrix} \cdot & \cdot & \cdot \\ \cdot & x & 0 \\ \cdot & 0 & y \end{pmatrix} \quad , \tag{89}$$

in the basis where the RH Majorana neutrino-mass matrix is diagonal. The effective light neutrino-mass matrix is then given by:

$$m_\nu = -M_D \cdot M_R^{-1} \cdot M_D^T = \begin{pmatrix} \cdot & \cdot & \cdot \\ \cdot & \frac{a^2}{x} + \frac{b^2}{y} & \frac{ac}{x} + \frac{bd}{y} \\ \cdot & \frac{ac}{x} + \frac{bd}{y} & \frac{c^2}{x} + \frac{d^2}{y} \end{pmatrix} . \tag{90}$$

If one RH neutrino dominates, that is, if $y \gg x$, then the sub-determinant in the $\mu - \tau$ block is roughly of the order $\sim m_2 \cdot m_3$. The normal hierarchy is obtained for $m_2 \ll m_3$. The atmospheric mixing angle is roughly given by $\tan\theta_{23} \sim (a/c)$. For $a \sim c$, large mixing angles

can arise naturally. The two-family case can be generalised to the three-family case when sequential dominance with three RH neutrinos is implemented [325].

Models with GUT Symmetries

Grand Unified Theories based on $SO(10)$ accommodate all 16 fermions (including the right-handed neutrinos) in a single spinor representation. Furthermore, $SO(10)$ provides a framework in which the see-saw mechanism arises naturally. Models based on $SO(10)$ combined with a continuous, or discrete, flavour symmetry group have been constructed to understand the flavour problem, especially the small neutrino masses and the large leptonic mixing angles. These models can be classified according to the family symmetry that is implemented as well as the Higgs representations introduced in the model. For reviews, see, for example, reference [326]. Phenomenologically, the resulting mass matrices can be either symmetric, lop-sided, or asymmetric.

Due to the product rule, $16 \otimes 16 = 10 \oplus 120_a \oplus 126_s$, the only Higgs particles that can couple to the matter fields at tree level are in the 10, $\overline{120}$, and $\overline{126}$ representations of SO(10). The Yukawa matrices involving the 10 and $\overline{126}$ are symmetric under interchange of family indices, while the matrix involving the $\overline{120}$ is anti-symmetric. The Majorana mass term for the RH neutrinos can arise either from a renormalisable operator involving the $\overline{126}$, or from a non-renormalisable operator that involves the 16s. The case of $\overline{126}$ has the advantage that R-parity is preserved automatically.

Two large mixing angles in the leptonic sector may arise in two ways:

1. *Symmetric mass textures:* This scenario is realised if $SO(10)$ is broken through the left-right symmetry-breaking route. In this case, both the large solar mixing angle and the maximal atmospheric mixing angle come from the effective neutrino-mass matrix. A characteristic of this class of models is that the predicted value for the $|U_{e\nu_3}|$ element tends to be larger than the value predicted by models in class (ii) below. This GUT-symmetry-breaking pattern gives rise to the following relations among various mass matrices:

$$M_u = M_{\nu_D}, \quad M_d = M_e \ , \tag{91}$$

up to some calculable, group-theoretical factors which are useful in obtaining the Jarlskog relations among masses for the charged leptons and down-type quarks when combined with family symmetries. The value of U_{e3} is predicted to be large, close to the sensitivity of current experiments. The prediction for the rate of $\mu \to e\gamma$ is about two orders of magnitude below the current experimental bound.

In a particular model constructed by Chen and Mahanthappa [327], the Higgs sector contains fields in 10, 45, 54, 126 representations, with the 10 and 126 breaking the electro-weak symmetry and generating fermions masses, and the 45, 54, 126 breaking the SO(10) GUT symmetry. The mass hierarchy can arise if there is an $SU(2)_H$ symmetry acting non-trivially on the first two generations such that the first two generations transform as a doublet and the third generation transforms as a singlet under $SU(2)_H$, which breaks down in two steps,

$SU(2) \overset{\epsilon M}{\to} U(1) \overset{\epsilon' M}{\to}$ 'nothing', $\epsilon' \ll \epsilon \ll 1$. The mass hierarchy is generated by the Froggatt-Nielsen mechanism [221]. The resulting mass matrices at the GUT scale are given by:

$$M_{u,\nu_{LR}} = \begin{pmatrix} 0 & 0 & \langle 10_2^+ \rangle \epsilon' \\ 0 & \langle 10_4^+ \rangle \epsilon & \langle 10_3^+ \rangle \epsilon \\ \langle 10_2^+ \rangle \epsilon' & \langle 10_3^+ \rangle \epsilon & \langle 10_1^+ \rangle \end{pmatrix} = \begin{pmatrix} 0 & 0 & r_2\epsilon' \\ 0 & r_4\epsilon & \epsilon \\ r_2\epsilon' & \epsilon & 1 \end{pmatrix} M_U \ , \tag{92}$$

$$M_{d,e} = \begin{pmatrix} 0 & \langle 10_5^- \rangle \epsilon' & 0 \\ \langle 10_5^- \rangle \epsilon' & (1,-3) \left\langle \overline{126}^- \right\rangle \epsilon & 0 \\ 0 & 0 & \langle 10_1^- \rangle \end{pmatrix} = \begin{pmatrix} 0 & \epsilon' & 0 \\ \epsilon' & (1,-3)p\epsilon & 0 \\ 0 & 0 & 1 \end{pmatrix} M_D \ . \tag{93}$$

The right-handed neutrino mass matrix is of the same form as $M_{\nu_{LR}}$:

$$M_{\nu_{RR}} = \begin{pmatrix} 0 & 0 & \left\langle \overline{126}_2'^0 \right\rangle \delta_1 \\ 0 & \left\langle \overline{126}_2'^0 \right\rangle \delta_2 & \left\langle \overline{126}_2'^0 \right\rangle \delta_3 \\ \left\langle \overline{126}_2'^0 \right\rangle \delta_1 & \left\langle \overline{126}_2'^0 \right\rangle \delta_3 & \left\langle \overline{126}_1'^0 \right\rangle \end{pmatrix} = \begin{pmatrix} 0 & 0 & \delta_1 \\ 0 & \delta_2 & \delta_3 \\ \delta_1 & \delta_3 & 1 \end{pmatrix} M_R \ . \tag{94}$$

Note that, since the $\overline{126}$-dimensional Higgs representation is used to generate the heavy Majorana neutrino-mass terms, R-parity is preserved at all energies. The effective neutrino mass matrix is:

$$M_{\nu_{LL}} = M_{\nu_{LR}}^T M_{\nu_{RR}}^{-1} M_{\nu_{LR}} = \begin{pmatrix} 0 & 0 & t \\ 0 & 1 & 1+t' \\ t & 1+t' & 1 \end{pmatrix} \frac{d^2 v_u^2}{M_R} \, , \tag{95}$$

and causes the atmospheric mixing angle to be maximal and the solar mixing angle to be large. The form of the neutrino mass matrix in this model is invariant under the see-saw mechanism. The value of U_{e3} is related to the ratio $\sim \sqrt{\Delta m_{12}^2 / \Delta m_{13}^2}$, which is predicted to be close to the sensitivity of current experiments. The prediction for the rate of $\mu \to e\gamma$ is about two orders of magnitude below the current experimental bound.

2. *Lopsided mass textures for charged fermions:* In this scenario, the large atmospheric-mixing angle comes from the unitary matrix that diagonalises the charged-lepton mass matrix. This scenario is realised in models with $SU(5)$ as the intermediate symmetry which gives rise to the so-called "lopsided" mass textures, due to the $SU(5)$ relation:

$$M_e = M_d^T . \tag{96}$$

Due to the lopsided nature of M_e and M_d, the large atmospheric neutrino mixing is related to the large mixing in the (23) sector of the RH charged-lepton diagonalisation matrix, instead of V_{cb}. Thus it explains why V_{cb} is small while $U_{\mu\nu_3}$ is large. The large solar mixing angle comes from the diagonalisation matrix for the neutrino mass matrix. Because the two large mixing angles come from different sources, the constraint on $U_{e\nu_3}$ is not as strong as in class (1). In fact, the prediction for $U_{e\nu_3}$ in this class of models tends to be quite small. On the

other hand, this mechanism also predicts an enhanced decay rate for the flavour-violating process $\mu \to e\,\gamma$ which is close to current experimental limit. As R-parity is broken by the vev of the 16 dimensional Higgs, a separate 'matter parity' must be imposed to distinguish the particles from their SUSY partners.

In a particular model constructed by Albright and Barr [328], the Higgs sector of the model contains Higgs particles in the $10, 16, 45$, with $\langle 16_{H_1} \rangle$ breaking $SO(10)$ down to $SU(5)$ and $\langle 16_{H_2} \rangle$ breaking the EW symmetry. The lopsided textures arise due to the operator $\lambda(16_i 16_{H_1})(16_j 16_{H_2})$ which gives rise to mass terms for the charged leptons and down quarks which satisfy the SU(5) relation $M_d = M_e^T$. When other operators are included, the lopsided structure of M_e results, provided the coupling σ is of order 1:

$$M_{u,\nu_{LR}} = \begin{pmatrix} \eta & 0 & 0 \\ 0 & 0 & (1/3,1)\epsilon \\ 0 & -(1/3,1)\epsilon & 1 \end{pmatrix} \cdot m_u \tag{97}$$

$$M_d = \begin{pmatrix} \eta & \delta & \delta^{'} e^{i\phi} \\ \delta & 0 & \sigma + \epsilon/3 \\ \delta^{'} e^{i\phi} & -\epsilon/3 & 1 \end{pmatrix} \cdot m_d, \quad M_e = \begin{pmatrix} \eta & \delta & \delta^{'} e^{i\phi} \\ \delta & 0 & -\epsilon \\ \delta^{'} e^{i\phi} & \sigma + \epsilon & 1 \end{pmatrix} \cdot m_d. \tag{98}$$

The large mixing in $U_{e,L}$ leads to the large atmospheric mixing angle. Meanwhile, because large mixing in $U_{e,L}$ corresponds to large mixing in $U_{d,R}$, the CKM mixing angles remain small. A unique prediction of the lopsided models is the relatively large branching ratio for LFV processes, e.g. $\mu \to e\gamma$. By considering a RH Majorana neutrino-mass term of the following form, a large solar mixing angle can arise for some choice of the parameters in $M_{\nu_{RR}}$, leading to a large value for the solar mixing angle:

$$M_{\nu_{RR}} = \begin{pmatrix} c^2\eta^2 & -b\epsilon\eta & a\eta \\ -b\epsilon\eta & \epsilon^2 & -\epsilon \\ a\eta & -\epsilon & 1 \end{pmatrix} \cdot \Lambda_R, \quad M_\nu^{eff} = \begin{pmatrix} 0 & -\epsilon & 0 \\ -\epsilon & 0 & 2\epsilon \\ 0 & 2\epsilon & 1 \end{pmatrix} \frac{m_u^2}{\Lambda_R}\,. \tag{99}$$

Models with renormalisation-group enhancements

It is possible to obtain large neutrino mixing angles through renormalisation-group evolution. Assuming that the CKM matrix and the leptonic mixing matrix are identical at the GUT scale, which is a natural consequence of quark-lepton unification, two large neutrino mixing angles can be generated by renormalisation-group evolution [329]. The only requirement for this mechanism to work is that the masses of the three neutrinos are nearly degenerate ($m_3 \gtrsim m_2 \gtrsim m_1$) and have the same CP parity. The one-loop renormalisation-group equation (RGE) of the effective left-handed Majorana neutrino mass operator is given by:

$$\frac{dm_\nu}{dt} = -\{\kappa_u m_\nu + m_\nu P + P^T m_\nu\}, \tag{100}$$

where $t \equiv \ln \mu$ and μ is the energy scale. In the MSSM, P and κ_u are given by:

$$P = -\frac{1}{32\pi^2}\frac{Y_e^\dagger Y_e}{\cos^2\beta} \simeq -\frac{1}{32\pi^2}\frac{h_\tau^2}{\cos^2\beta} diag(0,0,1) \equiv diag(0,0,P_\tau) \; ; \tag{101}$$

$$\kappa_u = \frac{1}{16\pi^2}\left[\frac{6}{5}g_1^2 + 6g_2^2 - 6\frac{Tr(Y_u^\dagger Y_u)}{\sin^2\beta}\right] \simeq \frac{1}{16\pi^2}\left[\frac{6}{5}g_1^2 + 6g_2^2 - 6\frac{h_t^2}{\sin^2\beta}\right] \; ; \tag{102}$$

respectively, where $g_1^2 = \frac{5}{3}g_Y^2$ is the $U(1)$ gauge coupling constant, Y_u and Y_e are the 3×3 Yukawa coupling matrices for the up quarks and charged leptons respectively, and h_t and h_τ are the t- and τ-Yukawa couplings. One can then follow the "diagonalise-and-run" procedure and obtain the RGEs at scales between $M_R \geq \mu \geq M_{SUSY}$ for the mass eigenvalues and the three mixing angles, assuming CP violating phases vanish:

$$\frac{d\, m_i}{dt} = -4P_\tau m_i U_{\tau\nu_i}^2 - m_i\kappa_u, \quad (i = 1,2,3) \; ; \tag{103}$$

$$\frac{d\, s_{23}}{dt} = -2P_\tau c_{23}^2(-s_{12}U_{\tau\nu_1}\nabla_{31} + c_{12}U_{\tau\nu_2}\nabla_{32}) \; ; \tag{104}$$

$$\frac{d\, s_{13}}{dt} = -2P_\tau c_{23}c_{13}^2(c_{12}U_{\tau\nu_1}\nabla_{31} + s_{12}U_{\tau\nu_2}\nabla_{32}) \; ; \tag{105}$$

$$\frac{d\, s_{12}}{dt} = -2P_\tau c_{12}(c_{23}s_{13}s_{12}U_{\tau\nu_1}\nabla_{31} - c_{23}s_{13}c_{12}U_{\tau\nu_2}\nabla_{32} + U_{\tau\nu_1}U_{\tau\nu_2}\nabla_{21}) \; ; \tag{106}$$

where $\nabla_{ij} \equiv (m_i + m_j)/(m_i - m_j)$. Because the leptonic-mixing matrix is identical to the CKM matrix, we have, at the GUT scale, the following initial conditions, $s_{12}^0 \simeq \lambda$, $s_{23}^0 \simeq \mathcal{O}(\lambda^2)$ and $s_{13}^0 \simeq \mathcal{O}(\lambda^3)$, where λ is the Wolfenstein parameter. When the masses m_i and m_j are nearly degenerate, ∇_{ij} approaches infinity. Thus it drives the mixing angles to become large. Starting with the values of $(m_1^0, m_2^0, m_3^0) = (0.2983, 0.2997, 0.3383)$ eV at the GUT scale, the solutions at the weak scale for the masses are $(m_1, m_2, m_3) = (0.2410, 0.2411, 0.2435)$ eV, which correspond to $\Delta m_{13}^2 = 1.1 \times 10^{-3}\text{eV}^2$ and $\Delta m_\odot^2 = 4.8 \times 10^{-5}\text{eV}^2$. The mixing angles predicted at the weak scale are $\sin^2 2\theta_{23} = 0.99$, $\sin^2 2\theta_{12} = 0.87$ and $\sin\theta_{13} = 0.08$. Because the masses are larger than 0.1 eV, they are testable at the present searches for the neutrinoless double beta decay.

Predictions for the Oscillation Parameters

In the literature, there are thirty models based on $SO(10)$, six models that utilise single-RH-neutrino dominance mechanism, five based on $L_e - L_\mu - L_\tau$ symmetry, ten based on S_3 symmetry, three on A_4 symmetry, one on $SO(3)$ symmetry, and three based on texture-zero assumptions. The predictions of these models for $\sin^2\theta_{13}$ are summarised in figures 25 and 26. In some models, a range of values (rather than a single value) is given for θ_{13}. If these values range over N bins for $\sin^2\theta_{13}$ in a particular model, a weight of $1/N$ is assigned for each bin. As a result, non-integer values for the number of models for some values of $\sin^2\theta_{13}$ can arise.

Figure 25 shows the histogram of the number of models for each $\sin^2\theta_{13}$ including all sixty models and one including only models that predict all three mixing angles. An observation one can draw immediately is that the predictions of $SO(10)$ models are larger than 10^{-4}, and the median value is roughly $\sim 10^{-2}$. Furthermore, $\sin^2\theta_{13} < 10^{-4}$ can only arise in models based on leptonic symmetries. However, these models are not as predictive as the GUT models, due

Table 5: A summary of the current experimental limit on θ_{13} and the reach of future experiments.

	$\sin^2 2\theta_{13}$	$\sin\theta_{13}$
current limit	10^{-1}	0.16
reactor	10^{-2}	0.05
conventional beam	10^{-2}	0.05
superbeam	3×10^{-3}	2.7×10^{-2}
neutrino factory	$(5 - 50) \times 10^{-5}$	$(3.5 - 11) \times 10^{-3}$

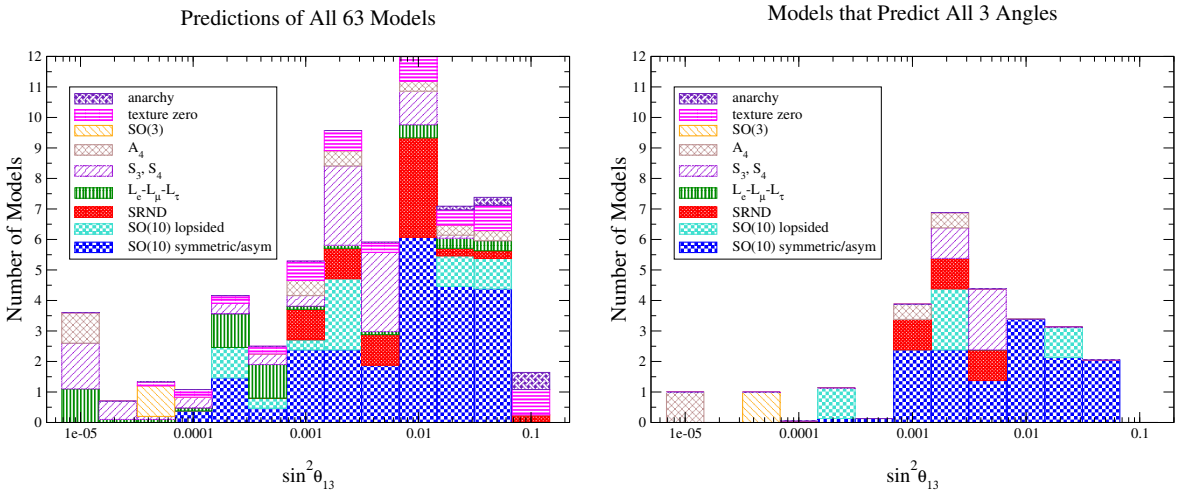

Figure 25: Histogram of the number of models for each $\sin^2\theta_{13}$. The diagram on the left includes all sixty models, while the diagram on the right includes only those that give predictions for all three leptonic mixing angles. Taken with kind permission of Physical Review from figures 1 and 2 in reference [320]. Copyrighted by the American Physical Society.

to the uncertainty in the charged-lepton mixing matrix. In this case, to measure θ_{13} will require a neutrino superbeam or the Neutrino Factory. In table 5 the reach of future experiments is summarised.

In figure 26, histograms of the number of models for each $\sin^2\theta_{13}$ value are shown for both normal and inverted neutrino-mass hierarchies. From these two diagrams, one finds that there are more models that predict the normal hierarchy than the inverted hierarchy. This could merely be a result of the theorists' prejudice for the model. What is more important is the correlation between the type of the hierarchy and the predicted values for θ_{13}. In the normal-hierarchy case, the predicted values tend to be larger, while in the inverted case, the distribution is quite uniform. The normal hierarchy arises in $SO(10)$ models with type-I see-saw, models with single-RH-neutrino dominance, and models based on $SO(3)$ and A_4 lepton symmetries, while the inverted hierarchy arises in models based on $L_e - L_\mu - L_\tau$, S_3, and S_4 lepton symmetries.

In conclusion, predictions for θ_{13} range from zero to the current experimental limit. For models based on GUT symmetries, the normal mass hierarchy can be generated naturally. The

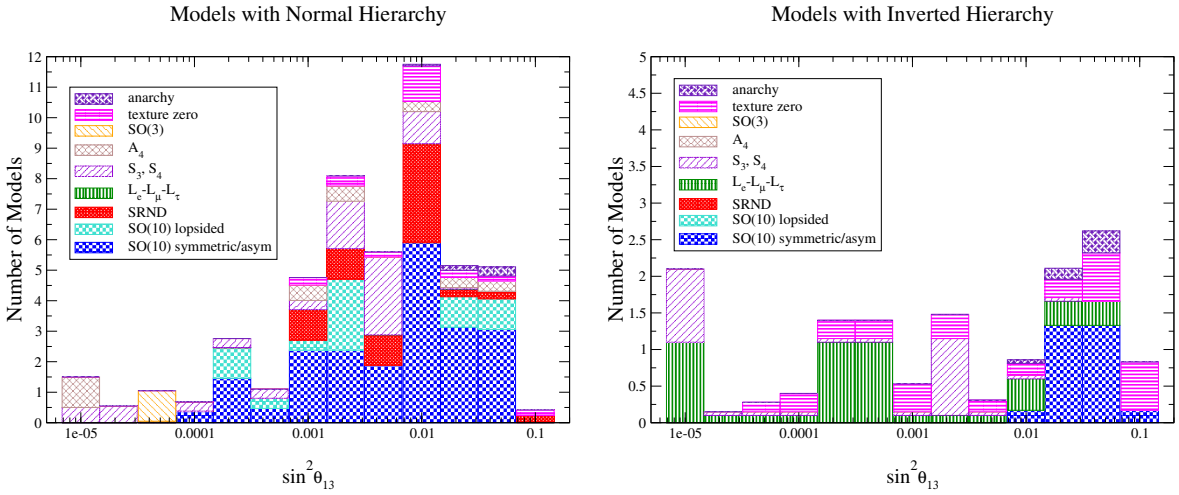

Figure 26: Histogram of the number of models for each $\sin^2\theta_{13}$. The diagram on the left includes models that predict normal mass hierarchy, while the diagram on the right includes models that predict inverted mass hierarchy. Taken with kind permission of Physical Review from figure 3 in reference [320]. Copyrighted by the American Physical Society.

inverted hierarchy may also be obtained in these models with a type-II see-saw, even though some fine-tuning is needed. Predictions for θ_{13} in these models tend to be large, with a median value $\sin^2\theta_{13} \sim 0.01$. On the other hand, models based on leptonic symmetries can give rise to inverted hierarchies and the predictions for θ_{13} can be quite small. Therefore, models based on lepton symmetries will be favoured if θ_{13} turns out to be tiny and the inverted hierarchy is observed. However, if θ_{13} turns out to be large, the two different classes would not be distinguishable. A precise measurement for the deviation of θ_{23} from $\pi/4$ can also be crucial for distinguishing different models. This is especially true for models based on lepton symmetries in which the deviation strongly depends on how the symmetry breaking is introduced into the models. Precision measurements are thus indispensable in order to distinguish different classes of models.

3.2.2 Sum Rules

In the previous section, the predictions of various models of neutrino masses have been reviewed. Many particularly attractive classes of models lead to interesting predictions for the neutrino-mass matrix m_ν, such as for instance tri-bimaximal or bimaximal mixing. Measurements of neutrino oscillation determine matrix elements of the neutrino-mixing matrix, $U_{\rm PMNS}$, which may be written as the product of $V_{\nu_{\rm L}}$, that diagonalises the neutrino-mass matrix and $V_{e_{\rm L}}$, which diagonalises the charged-lepton mass matrix, i.e. $U_{\rm PMNS} = V_{e_{\rm L}} V_{\nu_{\rm L}}^\dagger$. Often, the essential predictions of flavour models are hidden due to the presence of the charged lepton corrections. In many cases it can be shown that a combination of the measurable parameters θ_{12}, θ_{13}, and δ can be combined to yield a prediction for the 1-2 mixing of the neutrino-mass matrix [330, 331], i.e. to $\arcsin(\frac{1}{\sqrt{3}})$ for tri-bimaximal and $\frac{\pi}{4}$ for bimaximal mixing, for example. In an SO(3) family-symmetry model based on the see-saw mechanism with sequential dominance that predicts tri-

bimaximal mixing via vacuum alignment, such a 'sum rule' has been obtained in reference [330]. In reference [331], it has been shown that neutrino sum rules are not limited to one particular model, but apply to large classes of models under very general assumptions, to be specified below. Examples for sum rules with theory predictions of tri-bimaximal and bimaximal neutrino mixing, respectively, are [330–332]:

$$\theta_{12} - \theta_{13}\cos(\delta) \approx \arcsin\tfrac{1}{\sqrt{3}} \; ; \tag{107}$$

$$\theta_{12} - \theta_{13}\cos(\delta) \approx \tfrac{\pi}{4} \; . \tag{108}$$

Neutrino sum rules [330, 331] are thus a means of exploring the structure of the neutrino mass matrix in the presence of charged-lepton corrections and of testing whole classes of models. The sum rules, such as those of equations (107) and (108), can only be tested to high-enough precision in the most accurate experimental facilities such as the Neutrino Factory.

Charged-lepton corrections and sum rules

To illustrate the use of sum rules in testing theories of the neutrino-mass matrix in the presence of charged-lepton corrections, consider two examples, bimaximal [333] and tri-bimaximal [334] neutrino mixing, where the predicted neutrino-mixing angles are:

$$\begin{array}{llll} \theta_{12}^{\nu} = \pi/4, & \theta_{12}^{\nu} = \pi/4, & \theta_{13}^{\nu} = 0 & \text{for bimaximal neutrino mixing; and} \\ \theta_{12}^{\nu} = \arcsin(\frac{1}{\sqrt{3}}), & \theta_{12}^{\nu} = \pi/4, & \theta_{13}^{\nu} = 0 & \text{for tri-bimaximal neutrino mixing.} \end{array} \tag{109}$$

A similar, but physically different form, was proposed earlier [335]. The leptonic-mixing matrix is the product of $V_{\nu_{\rm L}}$ and $V_{e_{\rm L}}$, and therefore corrections to the predictions for the neutrino-mixing angles given in equations (109) arising from the charged-lepton mixing matrix must be evaluated to obtain estimates of the mixing angles that are accessible experimentally.

The charged-lepton corrections can be evaluated if it is assumed that the charged-lepton mixing matrix has a CKM-like structure, i.e. the charged-lepton mixing angles θ_{ij}^{e} are small and dominated by a 1-2 mixing θ_{12}^{e}. This is the case in many generic classes of flavour model in the context of GUTs in which quarks and leptons are assigned to representations of the unified gauge symmetries [330, 336, 337]. For $\theta_{13}^{\nu} = 0$, which is the case in the examples mentioned above, such charged-lepton corrections lead to the following PMNS mixing angles [331]:

$$\theta_{23} \approx \theta_{23}^{\nu} \; , \tag{110a}$$

$$\theta_{13} \approx \sin(\theta_{23}^{\nu})\,\theta_{12}^{e} \; , \tag{110b}$$

$$\theta_{12} \approx \theta_{12}^{\nu} + \cos(\theta_{23}^{\nu})\,\theta_{12}^{e}\cos(\delta) \; . \tag{110c}$$

The quantity δ which appears on the right-hand side of equation (110c) is the Dirac CP phase observable in neutrino oscillations. For bimaximal and tri-bimaximal mixing, this implies that $\theta_{23} \approx \pi/4$ and leads to the prediction $\theta_{13} \approx \frac{1}{\sqrt{2}}\theta_{12}^{e}$. Substituting the expressions for θ_{13} and θ_{23} into equation (110c) results in the following sum rules [330–332]:

$$\theta_{12} - \theta_{13}\cos(\delta) \approx \theta_{12}^{\nu} = \begin{cases} \frac{\pi}{4} & \text{for bimaximal neutrino mixing,} \\ \arcsin(\frac{1}{\sqrt{3}}) & \text{for tri-bimaximal neutrino mixing.} \end{cases} \tag{111}$$

Therefore, in the case of bimaximal or tri-bimaximal neutrino mixing, precise measurements of the leptonic mixing parameters θ_{13}, θ_{12}, and δ allow the prediction for θ^{ν}_{12} in equation (111) to be tested without assuming any particular value for θ^{e}_{12}.

More generally, if it is assumed that $\theta^{\nu}_{13} \approx 0$, $\theta^{e}_{13} \approx 0$ and $\theta^{e}_{23} \approx 0$, and assuming $\theta_{23} \approx \pi/4$, then [331]:

$$\theta_{12} - \theta_{13}\cos(\delta) \approx \theta^{\nu}_{12} \qquad (\theta^{\nu}_{12} \text{ from "}m_{\nu}\text{-theory black box"})\,; \text{and} \tag{112a}$$

$$\theta_{13} \approx \tfrac{1}{\sqrt{2}}\theta^{e}_{12} \qquad (\theta^{\mathrm{e}}_{12} \text{ from "GUT black box"}). \tag{112b}$$

A measurement of the combination of PMNS parameters:

$$\theta^{\Sigma}_{12} \equiv \theta_{12} - \theta_{13}\cos(\delta) \tag{113}$$

can be used to constrain the neutrino mixing θ^{ν}_{12} by means of the sum rule in equation (112a). In many unified flavour models, the Cabibbo angle, θ_C is related to θ^{e}_{12}; equation (112b), therefore, can be used to relate θ_{13} to θ_C. Hence, a precise measurement of θ_{13} may be used to test such GUT predictions.

Sum Rules and Sensitivities of Future Experiments

For θ^{Σ}_{12} to be used to discriminate between the various models, precise, independent measurements of θ_{12} and on $\theta_{13}\cos(\delta)$ are required, (for more details see [338]). θ_{12} can be measured using solar neutrinos or using the neutrinos generated in nuclear reactors; a comparison of these options indicates that the best precision on is obtained using the latter [97]. An experiment optimised for the measurement of θ_{12}, the 'Survival Probability MINimum' (SPMIN) experiment, has been proposed [97]. In this experiment a single detector is placed at a baseline of $\sim 60\,\mathrm{km}$ so that the first oscillation minimum is right in the middle of the neutrino energy spectrum. The dependence of the 2σ error on θ_{12} on the exposure in units of GW kt y is shown in figure 27. The following systematic uncertainties were considered: normalisation, 5%; beam tilt, 2%; energy scale, 0.5%, reactor power, 2%; and burn-up, 2%. At large exposures these systematic uncertainties are as large as the statistical uncertainty. The figure also shows the performance that would be obtained if the water in the Super-Kamiokande detector were doped with gadolinium to make the detector sensitive to neutrinos from the nuclear reactors in Japan [96]. Another alternative, LENA, a 40 kt liquid scintillator detector that has been proposed for the Frejus laboratory in France, would be sensitive to neutrinos produced in the French nuclear reactors [339]. These experiments would yield $2\,\sigma$ errors on θ_{12} of 2.6° and 1.35° respectively. The SPMIN experiment has a greater sensitivity than either of these proposals since the baseline has been chosen to be optimal.

Long-baseline experiments, which are sensitive to δ and θ_{13} but have little sensitivity to θ_{12}, must be used to determine θ^{Σ}_{12}. The precision with which θ^{Σ}_{12} can be determined, has been estimated under the assumption that θ_{12} has been measured in a reactor experiment. Three cases have been considered corresponding to $2\,\sigma$ errors on θ_{12} of $= 0.75°$, 1.35°, and 2.6° respectively. For comparison, note that the current error on θ_{12} is 5.6° [67]. To estimate the precision on the quantity θ^{Σ}_{12} the general procedure described in [340] has been followed. The analysis therefore

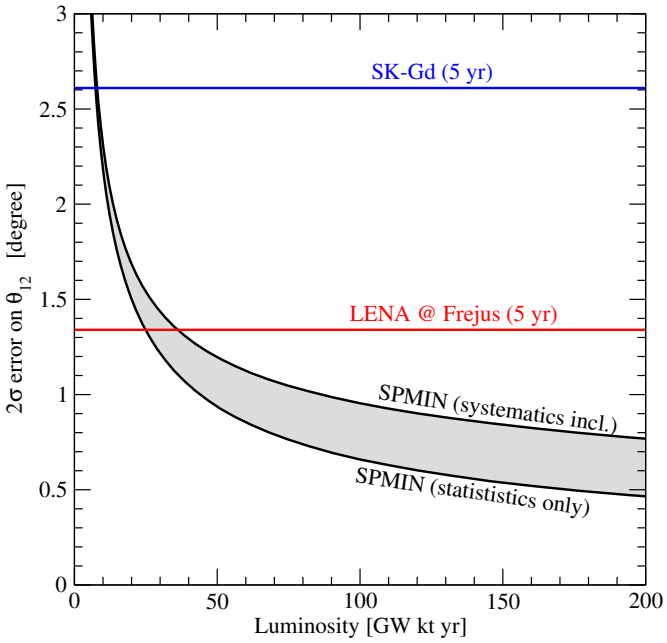

Figure 27: The $2\,\sigma$ error on θ_{12} as a function of the exposure for a so called SPMIN experiment.

includes the uncertainties on θ_{13} and δ, including correlations, as well as the uncertainties on θ_{12}, Δm^2_{21}, θ_{23}, Δm^2_{31} and the matter density. The inclusion of the correlation between θ_{13} and δ is crucial since the relevant oscillation probability contains terms which go as $\theta_{13}\sin\delta$ and $\theta_{13}\cos\delta$. However, the L/E dependence of these two terms is different and therefore experiments covering different L/E ranges may have very different sensitivities to θ_{12}^{Σ}. For these reasons the accuracy on the combination $\theta_{13}\cos\delta$ may be very different from the precision with which either θ_{13} or $\cos\delta$ can be determined individually.

Numerical estimates of the precision with which θ_{12}^{Σ} can be determined were made using the assumptions for the various oscillation parameters defined in section 5. The calculations are performed with GLoBES [45,46]. The cases considered are (see section 5.2): T2HK – an upgrade of the Japanese superbeam programme; SPL to Frejus – a European, CERN based superbeam facility; WBB – a US experiment employing a wide band neutrino beam; a conservative Neutrino Factory (NFC) and an optimistic Neutrino Factory NFO (as defined in section 5.4); and a $\gamma = 350$ β-beam (BB350) as described in [341] (see section 5.3).

Figure 28 shows the $3\,\sigma$ allowed interval in θ_{12}^{Σ} as a function of the true value of δ for $\sin^2 2\theta_{13} = 10^{-1}$. The plot shows three different experiments from left to right: SPL, T2HK, and WBB. All three have good sensitivity to θ_{12}^{Σ}. The presence of the mass-hierarchy-degenerate solutions (dashed lines) limits the usefulness of SPL and T2HK severely. These experiments are not able to distinguish between bimaximal and tri-bimaximal mixing (horizontal lines). This problem is absent for WBB for which the accuracy on θ_{12}^{Σ} is also somewhat better.

Figure 29 shows the results for: BB350, NFC, and NFO. Each of these experiments is unaffected by the mass-hierarchy degeneracy problem mentioned above for the large value of θ_{13}

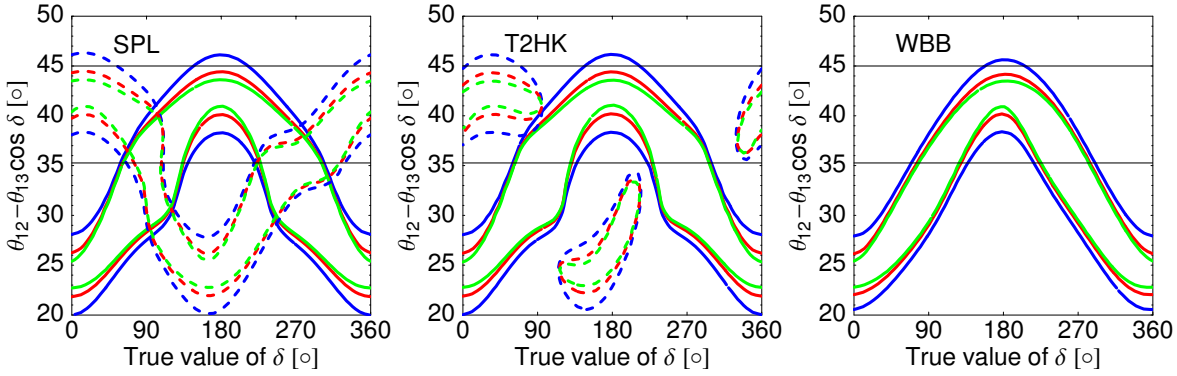

Figure 28: The $3\,\sigma$ allowed interval for the combination of physical parameters $\theta_{12}^{\Sigma} = \theta_{12} - \theta_{13}\cos(\delta)$ (defined in equation (113)) as a function of the true value of δ for $\sin^2 2\theta_{13} = 10^{-1}$. The left hand panel is for SPL, whereas the middle one is for T2HK and the right hand one for WBB. The dashed lines are for the $\mathrm{sgn}\Delta m^2_{31}$ degenerate solution. The colours indicate different errors on θ_{12}: blue – 2.8°, red – 1.35° and green – 0.75°. For the true value of θ_{12}, $\sin^2\theta_{12} = 0.3$ ($\theta_{12} = 33.12°$) has been used. The horizontal lines show the case of bimaximal and tri-bimaximal neutrino mixing. Taken with kind permission of the Journal of High Energy Physics from figure 2 in reference [338]. Copyrighted by SISSA.

considered. NFO offers the best sensitivity. The conservative Neutrino Factory option compares well to BB350, whereas the performance on δ and θ_{13} individually is much worse than for BB350 (see also section 5.4). The reason for this is that an experiment for which events are centred around the first oscillation maximum, such as a β-beam or a superbeam, is sensitive mainly to the $\theta_{13}\sin\delta$ term. The Neutrino Factory, however, produces the bulk of the events above the first oscillation maximum and thus is much more sensitive to the $\theta_{13}\cos\delta$ term.

So far, results for large θ_{13} only have been shown. However, the relative performance of the various options does not change very much with θ_{13}. In contrast, each of the options considered except the Neutrino Factory suffers from the mass-hierarchy degeneracy problem if θ_{13} is too small. For intermediate values of $\sin^2 2\theta_{13} \simeq 10^{-2}$ the accuracy of the measurement of θ_{12} is the dominating factor and the performance of the various experiments is similar if the mass-hierarchy problem is ignored. The true value of θ_{12} used in the plots is $\theta_{12} = 33.12°$ ($\sin^2\theta_{12} = 0.3$). For larger (smaller) values of true θ_{12}, the bands and islands in figures 28 and 29 are shifted up (down) accordingly. The performance of all experiments at large $\sin^2 2\theta_{13} = 10^{-1}$ is summarised in figure 30. An interesting observation from this figure is that the WBB performs second only to NFO. The NF is particularly well suited to the determination of the combination $\theta_{13}\cos\delta$, making this the machine of choice for testing the sum rule, even for large θ_{13}.

3.2.3 Cabibbo Haze in Lepton Mixing

As a step toward an explanation of the physics of flavour, a phenomenological approach was advocated recently in which parametrisations of the lepton-mixing matrix were developed as

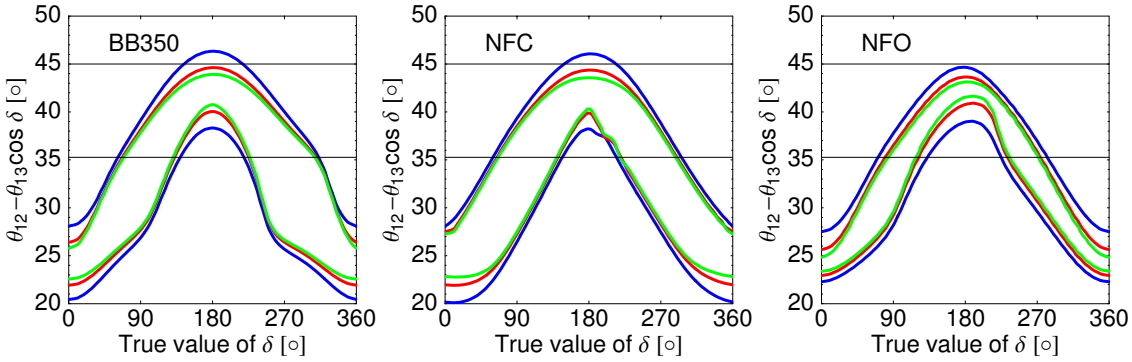

Figure 29: The $3\,\sigma$ allowed interval for the combination of physical parameters $\theta_{12}^{\Sigma} = \theta_{12} - \theta_{13}\cos(\delta)$ (defined in equation (113)) as a function of the true value of δ for $\sin^2 2\theta_{13} = 10^{-1}$. The left hand panel is for BB350, whereas the middle one is for NFC and the right hand one for NFO. The dashed lines are for the $\mathrm{sgn}\Delta m^2_{31}$ degenerate solution. The colours indicate different errors on θ_{12}: blue – 2.8°, red – 1.35° and green – 0.75°. For the true value of θ_{12}, $\sin^2\theta_{12} = 0.3$ ($\theta_{12} = 33.12^\circ$) has been used. The horizontal lines show the case of bimaximal and tri-bimaximal neutrino mixing. Taken with kind permission of the Journal of High Energy Physics from figure 2 in reference [338]. Copyrighted by SISSA.

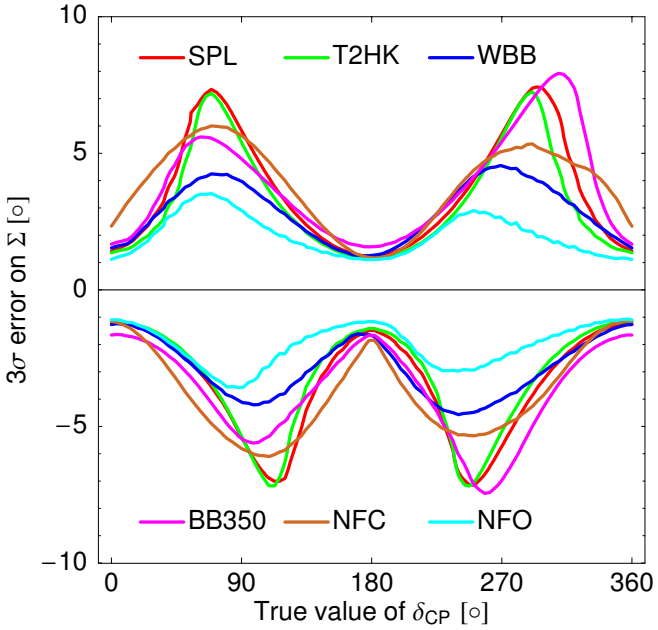

Figure 30: The $3\,\sigma$ error in degrees for θ_{12}^{Σ} as a function of the true value of δ for $\sin^2 2\theta_{13} = 10^{-1}$. The different coloured lines are for different experiments as given in the legend. The $\mathrm{sgn}\Delta m^2_{31}$ degenerate solution has been omitted. The error on θ_{12} is 0.75°.

an expansion in $\lambda \equiv \sin\theta_c \simeq 0.22$ in analogy with Wolfenstein's parametrisation of quark mixing [342–344]. In addition to its practical advantages for phenomenology, the Wolfenstein parametrisation hints at a guiding principle for flavour theory by providing a framework for examining quark mixing in the $\lambda \to 0$ limit. Quark-lepton unification implies that if Cabibbo-sized perturbations are present in the quark sector, such perturbations will also be manifest in the lepton sector. Due to the presence of large angles, however, the lepton-mixing matrix is unknown in the $\lambda \to 0$ limit (unlike the quark mixings, which vanish). Hence, if the limit of zero Cabibbo-angle is meaningful for theory, there is a 'Cabibbo haze' in lepton mixing, in which the initial or 'bare' values of the mixings are screened by Cabibbo-sized effects.

Cabibbo effects therefore represent deviations from bare mixings. They can be deviations from zero mixing (as in the quark sector); in this approach such effects are likely to represent the dominant source of θ_{13}. For θ_{23} and θ_{12} (and possibly θ_{13}), Cabibbo-sized perturbations represent deviations from (presumably large) non-zero initial values. Parametrisations are categorised according to the bare mixings and the structure of the allowed perturbations. Perturbations which are linear in λ yield shifts of $\lesssim \theta_c \simeq 13^\circ$, while $\mathcal{O}(\lambda^2)$ shifts are $\sim 3^\circ$. CP-violating phases can enter the $\mathcal{O}(\lambda)$ shifts but may only occur at sub-leading order, in which case the effective phase is suppressed and the size of θ_{13} does not dictate the size of CP-violating observables.

One aim of this approach is to obtain an efficient parametrisation of the lepton-mixing matrix in analogy to the Wolfenstein parametrisation for the quark-mixing matrix. However, current data is clearly consistent with many possible Wolfenstein-like parametrisations. One reason is that there is a wide range of possible bare mixing parameters and Cabibbo shifts, though some particular values may be singled out by well-motivated flavour theories. Another reason is the current precision of the data. Recast in terms of the Cabibbo angle, the error bar on θ_{12} is of $O(\lambda^2)$, while the uncertainties in θ_{23} and θ_{13} are of $O(\lambda)$. Although it is not possible to single out a particular parametrisation, the approach provides an organising principle for categorising the many top-down flavour models based on a λ expansion. The approach also provides a useful framework in which to interpret the results of future experiments, such as the programme to measure θ_{13}. Future facilities are expected to reach the $\mathcal{O}(\lambda^2)$ range, which will yield important insight into the nature of lepton mixing in the $\lambda \to 0$ limit.

The classification scheme proceeds as follows. Recall that the Wolfenstein parametrisation is based on the idea that the hierarchical quark mixing angles can be understood as a λ expansion, with:

$$\mathcal{U}_{\rm CKM} = 1 + \mathcal{O}(\lambda). \tag{114}$$

In the lepton sector, a similar parametrisation requires a λ expansion of the form :

$$\mathcal{U}_{\rm PMNS} = \mathcal{W} + \mathcal{O}(\lambda). \tag{115}$$

The starting matrix $\mathcal{W}$, which is dictated by the (unknown) underlying flavour theory, is then perturbed multiplicatively by a unitary matrix $\mathcal{V}(\lambda)$, which in turn is assumed to have a λ expansion:

$$\mathcal{V}(\lambda) = 1 + \mathcal{O}(\lambda). \tag{116}$$

For the quarks, the starting matrix is the identity matrix and the perturbation matrix takes the Wolfenstein form. For the leptons, the structure of the allowed perturbations depend on the details of $\mathcal{W}$. Due to Cabibbo haze, $\mathcal{W}$ can take different forms which are characterised by the number of large angles. For simplicity attention will be restricted here to the best-motivated scenario, in which the bare solar and atmospheric mixings, η_{12} and η_{23}, are non-zero and the bare θ_{13} vanishes (see [343] for a more general analysis). In this case $\mathcal{W}$ is of the form:

$$\mathcal{W} = \mathcal{R}_1(\eta_{23})\mathcal{R}_3(\eta_{12}) \equiv \begin{pmatrix} 1 & 0 & 0 \\ 0 & \cos\eta_{23} & \sin\eta_{23} \\ 0 & -\sin\eta_{23} & \cos\eta_{23} \end{pmatrix} \begin{pmatrix} \cos\eta_{12} & \sin\eta_{12} & 0 \\ -\sin\eta_{12} & \cos\eta_{12} & 0 \\ 0 & 0 & 1 \end{pmatrix} \mathcal{P}, \tag{117}$$

where $\mathcal{P}$ is a diagonal phase matrix of the form:

$$\mathcal{P} = \begin{pmatrix} e^{i\alpha_1} & 0 & 0 \\ 0 & e^{i\alpha_2} & 0 \\ 0 & 0 & e^{i\alpha_3} \end{pmatrix}, \tag{118}$$

which encodes the two physical Majorana CP-violating phases $\alpha_{12} \equiv \alpha_1 - \alpha_2$ and $\alpha_{23} \equiv \alpha_2 - \alpha_3$.

Unlike the quark sector, generically the perturbations do not commute with the starting matrix:

$$[\mathcal{W}\,,\,\mathcal{V}(\lambda)\,] \;\neq\; 0\;. \tag{119}$$

Hence, there are several possible implementations of Cabibbo shifts:

- *Right Cabibbo shifts.* The perturbations can be introduced as a multiplication of $\mathcal{V}(\lambda)$ on the right:

$$\mathcal{U}_{\rm PMNS} = \mathcal{W}\,\mathcal{V}(\lambda).; \tag{120}$$

- *Left Cabibbo shifts.* The perturbations can be implemented as a multiplication of $\mathcal{V}(\lambda)$ on the left:

$$\mathcal{U}_{\rm PMNS} = \mathcal{V}(\lambda)\,\mathcal{W}; \tag{121}$$

- *Middle Cabibbo shifts.* The perturbations can be sandwiched between the rotation matrices of $\mathcal{W}$:

$$\mathcal{U}_{\rm PMNS} = \mathcal{R}_1\,\mathcal{V}(\lambda)\,\mathcal{R}_3\mathcal{P}, \tag{122}$$

or

$$\mathcal{U}_{\rm PMNS} = \mathcal{R}_1\,\mathcal{V}(\lambda)\,\mathcal{R}_3\mathcal{P}. \tag{123}$$

To see that this encompasses all possibilities, recall that the assumption of Cabibbo haze is that the lepton-mixing matrix has a λ expansion:

$$\mathcal{U}_{\rm PMNS}(\lambda) = \sum_{n=0}^{\infty} \lambda^n W_n, \tag{124}$$

in which $W_0 \equiv \mathcal{W}$. This can be expressed as a right Cabibbo shift:

$$\mathcal{U}_{\rm PMNS}(\lambda) = \mathcal{W} \sum_{n=0}^{\infty} \lambda^n (\mathcal{W}^{-1} W_n) \equiv \mathcal{W}\mathcal{V}(\lambda), \tag{125}$$

with $\mathcal{V} = \sum_{n=0}^{\infty} \lambda^n (\mathcal{W}^{-1} W_n)$. It can also be expressed as a middle Cabibbo shift (dropping $\mathcal{P}$ for simplicity):

$$\begin{aligned} \mathcal{U}_{\rm PMNS}(\lambda) &= \mathcal{R}_1 \mathcal{R}_3 \mathcal{V}(\lambda); \\ &= \mathcal{R}_1 \left(\mathcal{R}_3 \mathcal{V}(\lambda) \mathcal{R}_3^{-1} \right) \mathcal{R}_3 \equiv \mathcal{R}_1 \mathcal{V}'(\lambda) \mathcal{R}_3. \end{aligned} \tag{126}$$

The generalisation to left shifts is straightforward. Note that since $\mathcal{V}$, by assumption, is given by:

$$\mathcal{V}(\lambda) = 1 + \sum_{i=1}^{\infty} \lambda^n V_n, \tag{127}$$

$\mathcal{V}'$ can also be written in an analogous form:

$$\mathcal{V}'(\lambda) = \mathcal{R}_3 \mathcal{V} \mathcal{R}_3^{-1} = 1 + \sum_{i=1}^{\infty} \lambda^n (\mathcal{R}_3 V_n \mathcal{R}_3^{-1}). \tag{128}$$

Hence, the decomposition into right, left, or middle shifts is meaningful for a specific choice of $\mathcal{V}$. To leading order in λ, $\mathcal{V}$ is assumed to be:

$$\mathcal{V} = \begin{pmatrix} 1 & a_1 \lambda & c_1 \lambda \\ -a_1^* \lambda & 1 & b_1 \lambda \\ -c_1^* \lambda & -b_1^* \lambda & 1 \end{pmatrix} + \mathcal{O}(\lambda^2), \tag{129}$$

which encompasses the Wolfenstein form ($a_1 = 1$, $b_1 = c_1 = 0$, and higher order terms $b_2 = A$ and $c_3 = A(\rho - \frac{1}{2} - i\eta)$, in self-evident notation), and allows for more general perturbations. Finally, as the shifts in the mixing angles are clearly dominated by perturbations linear in λ, it is useful to categorise models further as single, double, or triple shifts according to the number of such $\mathcal{O}(\lambda)$ perturbations in $\mathcal{V}$.

Given these ingredients, a systematic classification of possible models was presented in [342, 343], to which the reader is referred for further details. Here attention will be focused on one subset of examples. It is straightforward to obtain the following general results for the $O(\lambda)$ shifts in the mixing angles (including phases):

- *Right shifts*:

$$\begin{aligned}
\theta_{12} &= \eta_{12} + \lambda|a_1|\cos(\alpha_{12} + \phi_{a_1}) && (130)\\
\theta_{23} &= \eta_{23} + \lambda(\cos\eta_{12}|b_1|\cos(\alpha_{23} + \phi_{b_1}) - \sin\eta_{12}|c_1|\cos(\alpha_{12} - \alpha_{23} + \phi_{c_1})) && (131)\\
\theta_{13} &= \lambda|b_1 e^{i\alpha_{23}}\sin\eta_{12} + c_1 e^{i(\alpha_{12}-\alpha_{23})}\cos\eta_{12}|; && (132)
\end{aligned}$$

- *Left shifts*:

$$\begin{aligned}
\theta_{12} &= \eta_{12} + \lambda(\cos\eta_{23}|a_1|\cos\phi_{a_1} - \sin\eta_{23}|c_1|\cos\phi_{c_1}) && (133)\\
\theta_{23} &= \eta_{23} + \lambda|b_1|\cos\phi_{b_1} && (134)\\
\theta_{13} &= \lambda|\sin\eta_{23}a_1 + \cos\eta_{23}c_1|; && (135)
\end{aligned}$$

- *Middle shifts*:

$$\begin{aligned}
\theta_{12} &= \eta_{12} + \lambda|a_1|\cos\phi_{a_1} && (136)\\
\theta_{23} &= \eta_{23} + \lambda|b_1|\cos\phi_{b_1} && (137)\\
\theta_{13} &= \lambda|c_1|. && (138)
\end{aligned}$$

Each scenario displays distinct correlations between the Cabibbo shifts of the mixing angles. Note that certain shifts are sized by factors dependent on the bare-mixing parameters. In addition, the shifts in the mixing angles depend on the Majorana phases α_{12}, α_{23} only in the right Cabibbo shift scenario. The reason is that generically:

$$[\mathcal{P}\,,\,\mathcal{V}(\lambda)\,] \neq 0, \tag{139}$$

and hence the right shifts can be rewritten as follows:

$$\begin{aligned}
\mathcal{U}_{\rm PMNS} &= \mathcal{W}\mathcal{P}\mathcal{V}\\
&= \mathcal{W}(\mathcal{P}\mathcal{V}\mathcal{P}^{-1})\mathcal{P} \equiv \mathcal{W}\mathcal{V}_{\mathcal{M}}\mathcal{P}. && (140)
\end{aligned}$$

$\mathcal{V}_{\mathcal{M}}$ can be obtained from $\mathcal{V}$ through the replacements $a_i \to a_i e^{i\alpha_{12}}$, $b_i \to b_i e^{i\alpha_{23}}$, and $c_i \to c_i e^{i(\alpha_{12}-\alpha_{23})}$.

How might certain examples emerge from the viewpoint of flavour theory? One class of examples occur within grand unified models in which the fermion Dirac-mass matrices obey $SU(5)$ and $SO(10)$. GUT relations based on the simplest Higgs structures and the down-quark mass matrix is further assumed to be symmetric, such that $\mathcal{M}_d = \mathcal{M}_d^T \sim \mathcal{M}_e$ and $\mathcal{M}_u \sim \mathcal{M}_\nu$. In such models, the quark and lepton mixing matrices are related [345–348]:

$$\mathcal{U}_{\rm PMNS} = \mathcal{U}_{\rm CKM}^{\dagger}\,\mathcal{F}, \tag{141}$$

where $\mathcal{F}$ is a matrix which encodes the effects of the neutrino see-saw; in these models, $\mathcal{F}$ must contain two large angles. In the language of this classification scheme, this scenario is an example of a left Cabibbo single-shift model, in which $\mathcal{F}$ plays the role of $\mathcal{W}$ and $\mathcal{V}$ takes the

form of $\mathcal{U}_{\rm CKM}^{\dagger}$. Other possible examples include models based on quark-lepton complementarity, in which case $\mathcal{W}$ is a bimaximal-mixing matrix and $\mathcal{V}$ has $a_1 \neq 0$, $b_1 = 0$, and c_1 may or may not vanish depending on the details of the model. Different predictions for θ_{13} are implied in these cases depending on whether the model is a right, left, or middle Cabibbo shift model. Tri-bimaximal mixing scenarios are models in which $\mathcal{W}$ takes on the standard tri-bimaximal form, and $\mathcal{V}$ has $a_1 = b_1 = 0$ and c_1 may or may not be zero, with a range of predictions for θ_{13} depending on the shift scenario.

Turning now to the issue of CP violation, the parametrisations also display different predictions for the leptonic Dirac and Majorana phases, depending on the details of how and whether phases enter $\mathcal{W}$ and $\mathcal{V}$. Here, only Dirac-type CP violation is considered (as CP-violating observables sourced by Majorana phases are helicity suppressed and thus difficult to observe). For models in which $\mathcal{W}$ has two large angles (the reader is once again referred to [343] for a more general discussion), the invariant measure of Dirac CP violation:

$$\mathcal{J}_{\rm CP} = {\rm Im}(\mathcal{U}_{\alpha i}\mathcal{U}_{\beta j}\mathcal{U}^{*}_{\beta i}\mathcal{U}^{*}_{\alpha j}) \simeq \sin 2\theta_{12} \sin 2\theta_{23} \sin 2\theta_{13} \sin\delta, \tag{142}$$

vanishes in the $\lambda \to 0$ limit, and a non-zero value can be generated in two ways:

- *Complex $\mathcal{V}(\lambda)$:* $\mathcal{V}(\lambda)$ can be the source of CP-violating phases, which can be $\mathcal{O}(1)$ (as in the quark sector). Models can be categorised in terms of whether CP violation enters at leading or higher order in λ, and whether the effective leptonic phase is predicted to be $\mathcal{O}(1)$ or further suppressed;
- *Bare Majorana phases:* Majorana phases can also provide a source for Dirac CP violation once the Cabibbo-sized perturbations are switched on. For left and middle Cabibbo shifts, this does not occur. However, for right Cabibbo shifts it does, as such shifts encode $\mathcal{P}$ through the modification $\mathcal{V} \to \mathcal{V}_{\mathcal{M}}$.

Consider equation (141) as an illustrative example. If $\mathcal{V}$ is of the Wolfenstein form (complex $O(\lambda^3)$ terms), $\mathcal{J}_{\rm CP}$ is:

$$\mathcal{J}_{\rm CP} = \frac{1}{4} A\lambda^3 \eta \cos\eta_{23} \sin 2\eta_{23} \sin 2\eta_{12}. \tag{143}$$

Note that in this model, the shifts in the angles are given to $O(\lambda^2)$ by:

$$\theta_{12} = \eta_{12} - \lambda\cos\eta_{23}\,, \tag{144}$$

$$\theta_{23} = \eta_{23} - \lambda^2(A + \frac{1}{4}\sin 2\eta_{23}) \text{ and} \tag{145}$$

$$\theta_{13} = -\lambda\sin\eta_{23}\,. \tag{146}$$

The effective leptonic phase is $\delta \sim O(\lambda^2)$, in contrast to the $O(1)$ CKM phase. This suppression occurs because the phases in $\mathcal{V}$ arise in subdominant contributions to the mixing angles. Models with this feature demonstrate that while the magnitude of θ_{13} is clearly correlated with the prospects for the observability of lepton-sector CP violation, it is not the whole story because the CP-violating phase itself may be suppressed.

In summary, we are beginning to read the new lepton data, but there is much work to do before a satisfactory and credible theory of flavour is proposed. In the meantime, it is illustrative to examine the lepton sector through the lens of quark-lepton unification, and investigate parametrisations of the lepton-mixing matrix which include Cabibbo-sized effects. The approach emphasises the need for precision measurements, as present data are insufficient for singling out a particular parametrisation. Should the limit of zero Cabibbo mixing prove to be meaningful for theory, with improved data we may be able to see flavour patterns through the Cabibbo haze.

3.3 Lepton-flavour violation

Searching for lepton-flavour violation in charged-lepton decays is an important way to look for new physics beyond the Standard Model [349]. Since the early days of muon experiments, processes such as $\mu \to e\gamma$ have been searched for, and the absence of such processes has lead us to consider the separate conservation of electron and muon numbers. The discovery of two flavours of neutrino in 1962 at BNL indicated that lepton-flavour conservation is indeed realised in nature to a good degree of accuracy.

The situation has changed since the discovery of the neutrino oscillations. The separate conservation of each lepton number individually is likely violated. However, lepton-flavour violation can be observed in charged-lepton processes depends on how neutrino mass is generated. In the simple Dirac-neutrino, or the see-saw, framework, lepton-flavour violating processes in muon decays are suppressed by more than twenty orders of magnitude below the present experimental upper bounds. On the other hand, lepton-flavour violation becomes large, if some new particles or interactions exists at the TeV scale. Therefore, searching for lepton-flavour violation in muon and tau decay processes provides important information on the origin of the neutrino mass.

Lepton-flavour violation in three-muon processes

Among the various lepton-flavour violating processes, three-muon processes, $\mu \to e\gamma$, $\mu \to 3e$, and $\mu - e$ conversion in muonic atoms, are particularly important. The current experimental upper bound for $\mu \to e\gamma$ [350] is at the 10^{-11} level and about one order of magnitude smaller for the other two processes [351,352]. Although the $\mu - e$-conversion process has the smallest upper bound, the process which imposes the strongest constraints on the theoretical parameters depends on the model under consideration. Muonium-anti-muonium conversion is another process which violates the conservation of electron and muon numbers but conserves the total lepton number. This process is sensitive to new physics which changes the muon and electron numbers by two units. Upper bounds on the branching ratios of tau-lepton-flavour violating processes have been improved recently at KEK and the SLAC-B-factory experiments, and have reached the level of 10^{-7} and below depending on the decay mode in question [353–361]. Generally speaking, three-muon processes put stringent constraints on models that yield lepton-flavour violation and the study of correlations among the varous processes is useful to identify the correct model.

In near future, the MEG experiment is expected to improve the search-limit on the $\mu \to e\gamma$ process by more than two orders of magnitude. If lepton-flavour violation is discovered, the next steps will be to discover the nature of lepton-flavour violation and to distinguish between the different models. The following techniques can be used to do this:

- The ratio of the branching ratios of $\mu \to 3e$ ($\mu - e$ conversion) and $\mu \to e\gamma$ depends on what kinds of operator are responsible for lepton-flavour violation. In particular, if all three processes are generated by the same photonic-dipole-type operator, the following relations are hold:

$$B(\mu^+ \to e^+e^+e-) \sim 6 \times 10^{-3} B(\mu \to e\gamma), \quad (147)$$

$$\frac{\sigma(\mu^- Ti \to e^- Ti)}{\sigma(\mu^- Ti \to capture)} \sim 4 \times 10^{-3} B(\mu \to e\gamma). \quad (148)$$

  This is a good approximation, for example, for most supersymmetric models. On the other hand, if lepton-flavour violation is generated by tree-level processes, $\mu \to 3e$ and/or $\mu - e$ conversion, the branching fractions could be much larger than that of $\mu \to e\gamma$;

- Angular distributions in polarised muon decays provide information on the chiral and CP structures of lepton-flavour violating operators [362]. For the $\mu \to e\gamma$ search with a polarised μ^+, the $\mu^+ \to e^+_L\gamma$ and $\mu^+ \to e_R\gamma$ operators are distinguished by the angular distribution of the positron-momentum direction with respect to the initial muon-polarisation direction. The chiral structure carrys information on the origin of the lepton-flavour violating interaction. In supersymmetric models, for example, the chirality depends on whether the flavour mixing exists in the right- or left-handed slepton sector, and this distinction could provide very important clues to the interaction at the GUT scale; and

- In the $\mu - e$ conversion search, branching-ratio measurements of different atoms provides one means of discriminating between the different operators [363]. The atomic-number dependence of the $\mu - e$-conversion rate differs for different types of quark-level operators. For example, we can distinguish scalar, vector, and photon-dipole type operators by comparing branching fractions measured using different nuclei, for example a low-atomic-number nucleus such as aluminium and a heavy nucleus such as lead.

These techniques would provide information on different aspects of lepton-flavour violating interactions, and are the basic steps to required to clarify the nature of new interactions.

Supersymmetry and muon lepton-flavour violating processes

Among the new physics models explored by searches for lepton-flavour violation, supersymmetry is the most important. Since supersymmetry requires the introduction of a supersymmetric partner for each particle in the Standard Model, sleptons should exist. Mass terms for the slepton depend on supersymmetry-breaking terms, which do not have an a-priori relation with lepton mass terms. In fact, the flavour mixing in the slepton-mass matrix is strongly constrained

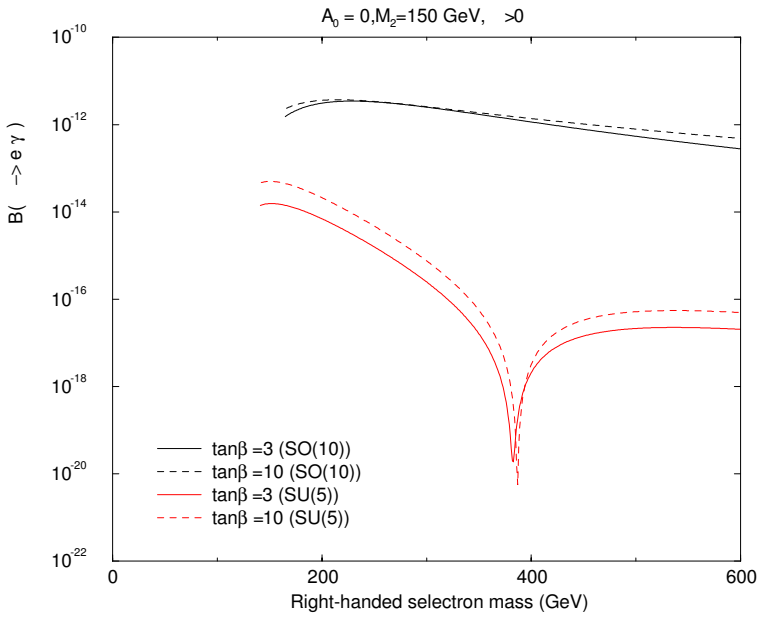

Figure 31: $\mu \to e\gamma$ branching ratios for SU(5) and SO(10) SUSY GUT. Adapted with permission of Reviews of Modern Physics from figures 8 and 13 in reference [349]. Copyrighted by the American Physical Society.

by the lepton flavour-violating processes. This is a part of the flavour problem in supersymmetric models, some mechanism is needed to suppress flavour-changing neutral-current processes in the quark and the lepton sectors. A solution to this problem is one of necessary conditions for a realistic supersymmetric model, and a variety of supersymmetry-breaking mechanisms are proposed. In principle, we will be able to identify the correct scenario by looking at the superparticle mass spectrum in energy frontier experiments at the LHC and the International Linear Collider.

Searches for lepton-flavour violating processes have a role to play in the determination of the off-diagonal elements of the slepton-mass matrix. The determination of these elements is particularly important because these elements carry information at very high energy scales such as the GUT scale and the see-saw neutrino scales [364, 365]. Even if we take a scenario where off-diagonal slepton terms are absent at the Planck scale, renormalisation effects due to large Yukawa coupling constants can induce sizable off-diagonal terms. In SUSY-GUT models, the large top Yukawa coupling constant a source of lepton-flavour violation because quarks and leptons are connected to each other above the GUT scale [366, 367]. A typical example is shown in figure 31 for SU(5) and S0(10) SUSY GUTs. The branching ratio is expected to be close to the current experimental upper limit for the SO(10) case.

In the supersymmetric see-saw model, a potentially large Yukawa coupling is provided by the neutrino Yukawa coupling constants. The off-diagonal term in the left-handed slepton-mass matrix is give by:

$$(m^2_{\tilde{l}_L})_{ij} \simeq -\frac{1}{8\pi^2}(y_\nu)^*_{ki}(y_\nu)_{kj} m_0^2 (3 + |A_0|^2) \ln(\frac{M_P}{M_R}), \tag{149}$$

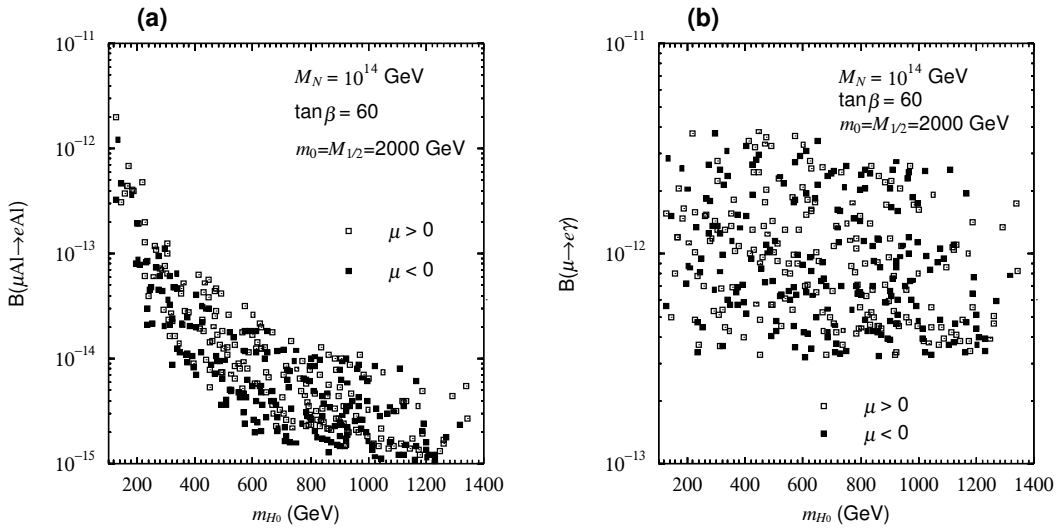

Figure 32: $\mu - e$ conversion branching ratio in aluminium nucleus and $\mu \to e\gamma$ branching ratio as a function heavy CP even Higgs boson mass in the supersymmetric see-saw model. Taken with kind permission of Physical Letters from figure 1 in reference [374]. Copyrighted by Elsevier B.V.

where M_P and M_R are the Planck mass and the right-handed neutrino mass respectively, m_0 is the universal scalar mass, A_0 is the universal triple-scalar-coupling constant for supersymmetry-breaking terms, and y_ν is the neutrino Yukawa coupling constant. Since the see-saw relation suggests that the Yukawa coupling is proportional to the square-root of M_R, the lepton-flavour violating branching ratio is proportional to M_R^2. Although the flavour structure of y_ν is not directly related to the flavour mixing in the PMNS matrix, it is natural to expect sizable off-diagonal elements from the large neutrino mixing. In fact, the $\mu \to e\gamma$ branching ratio can reach the experimental bound for $M_R = 0(10^{13}) - 0(10^{14})$ GeV [368–370].

There is an interesting special case which can be realised for a larger value of the ratio of the two Higgs vacuum expectation values ($\tan\beta$) [371–373]. In this case, supersymmetric loop corrections to the Higgs-lepton vertex can generate a large lepton-flavour violating coupling. As a result, heavy Higgs-boson exchange diagrams can be dominant, and the $\mu - e$ conversion process is enhanced relative to the $\mu \to e\gamma$ process [374]. An example is shown in figure 32. For a smaller heavy-Higgs-boson mass, the two branching ratios can be more similar. For the same parameter space, we can confirm that the dominant operator is of the scalar type from the atomic-number dependence of the $\mu - e$ conversion rate.

Other theoretical models

There are many new-physics models that predict sizable rates for muon lepton-flavour violating processes [349]. In many cases, the lepton-flavour violation is related to the physics of neutrino-mass generation, namely the interaction responsible for the neutrino mixings also induces lepton-flavour violation. This is the case for the supersymmetric see-saw model discussed above. Other examples are the Zee model [375], Dirac-type bulk neutrinos in the warped extra dimension [376], the triplet-Higgs model [317,377], and the non-supersymmetric left-right symmetric model [315,378,379]. Supersymmetric, with R-parity violation, can be considered to be in this category,

since neutrino masses can be generated from R-parity violating couplings [380]. Since each model introduces lepton-flavour violation in a different way, the phenomenological features can be quite different and measurements will provide important clues to identify the correct model of neutrino-mass generation.

The triplet-Higgs model provides a simple way to generate neutrino masses from a small triplet vacuum-expectation value. In this model, the triplet Higgs and lepton coupling generating neutrino mass also induces a doubly-charged Higgs boson and lepton coupling. The neutrino-mixing matrix has a direct relation to the doubly-charged-Higgs-boson coupling. Since the doubly-charged Higgs boson gives a tree-level contribution to the $\mu \to 3e$ process, this can dominate over the other two processes. On the other hand, the $\mu \to e\gamma$ and the $\mu - e$ conversion branching ratios become similar.

The left-right symmetric model also has the triplet-Higgs field. In this case, however, neutrino masses can be generated by the see-saw mechanism. The right-handed neutrino-mass term arises in association with $SU(2)_L \times SU(2)_R \times U(1)_{B-L}$ symmetry breaking to the Standard Model gauge groups. If this scale is close to the TeV scale, observable lepton-flavour violating effects are generated through the doubly-charged Higgs boson and lepton couplings. Unlike the triplet-Higgs model, the relationship between neutrino mixing and lepton-flavour violation is not straightforward. A generic feature is that the $\mu \to 3e$ branching ratio is larger by two orders of magnitude compared to the $\mu \to e\gamma$ and the $\mu - e$ conversion branching ratios.

In this way, muon lepton-flavour violating processes provide one way to explore physics beyond the Standard Model. This is particularly important because neutrino oscillations are clear evidence of new physics, and the origin of neutrino masses is still unknown. There are various scenarios for neutrino-mass generation, each with different features that may give rise to observable signals for lepton-flavour violation in charged-lepton processes. The experimental pursuit of $\mu \to e\gamma$, $\mu \to 3e$, and $\mu - e$ conversion is important if the origin of flavour mixing in the lepton sector is to be determined.

3.4 Cosmology

3.4.1 Neutrinos and Large Scale Structure

The observation of cosmological perturbations – such as Cosmic Microwave Background (CMB) anisotropies, or the large-scale density perturbations reconstructed, e.g., from the galaxy distribution in the Universe – are known to provide good measurements of many cosmological parameters. For instance, the spectrum of cosmological perturbations is very sensitive to the abundance of ultra-relativistic particles in the early Universe. This can be used to make a good estimate of the number of neutrinos which were in thermal equilibrium at that time, parametrised by an effective number, $N_{\rm eff}$. The standard scenario with three neutrino flavours and no other relativistic relics in the Universe (apart from photons) corresponds to $N_{\rm eff} = 3$, while scenarios with one light sterile neutrino originally in thermal equilibrium corresponds to

$N_{\rm eff} = 4$; relaxing the thermal equilibrium assumption, the last scenario would give $3 < N_{\rm eff} \leq 4$. Current cosmological bounds give $N_{\rm eff} = 3.8^{+2.0}_{-1.6}$ at 2σ [381–387], which is compatible with the standard scenario, but also with the presence of extra relativistic relics. Future experiments are expected to reach a 1σ sensitivity of 0.3 in approximately five years from now, and should be able to confirm the standard $N_{\rm eff} = 3$ cosmological scenario with better accuracy than Big Bang nucleosynthesis bounds. In the rest of this section, it will be assumed, for simplicity, that $N_{\rm eff} = 3$.

Neutrino masses are more difficult to measure than $N_{\rm eff}$ because they are too small to contribute more than $\sim 1\%$ of the current energy density of the Universe. Fortunately, the formation of structures (galaxies and clusters) during the matter-dominated epoch is quite sensitive even to small neutrino masses.

3.4.1.1 Impact of neutrinos on structure formation: theoretical predictions

The process of galaxy formation depends very much on the velocity dispersion of the components contributing to the matter of the Universe (for a review, see [388]). If all non-relativistic components (such as baryons and Cold Dark Matter, CDM) have a very small velocity dispersion the process of gravitational collapse reaches its maximal efficiency. The matter (or energy) density contrast starts from very small values in the early Universe, with Fourier modes $\delta_k = [\delta\rho_k/\bar{\rho}]$ of order 10^{-5}. On wavelengths corresponding today to the Large Scale Structure (LSS) of the Universe, the density contrast starts to be amplified during the radiation dominated epoch, but at a slow (logarithmic) rate. Efficient structure formation begins after the time of radiation-matter equality, when the photon pressure cannot resist the gravitational in-fall. At this point, the rate of linear structure formation is given by $\delta_k \propto a$, where a is the scale factor. This simple law is the result of a balance between gravitational collapse and the expansion of the Universe (which tends to increase all distances, and therefore to damp gravitational forces and to slow down structure formation). A crucial observation is that $\delta_k \propto a$ is a solution of the Einstein equation only under the condition that the same species contributes to both gravitational collapse and to the expansion (through the Friedmann law). This process brings δ_k from order 10^{-5} to order one, i.e. to the non-linear regime, starting with the smallest wavelengths. The non-linear evolution is very difficult to simulate numerically, but many current and future observations are based on large enough wavelengths or redshifts for probing the linear (or mildly non-linear) regime, for which theoretical predictions are well under control.

If neutrinos have a small mass (it will be assumed first, for simplicity, that only one species is massive), there will be a constant fraction of non-relativistic matter in the form of neutrinos between the time at which the neutrino became non-relativistic and today. Non-relativistic neutrinos have a much larger velocity dispersion than CDM particles, only two or three orders of magnitude smaller than the speed of light:

$$v \equiv \frac{\langle p \rangle}{m} \simeq \frac{3T_\nu}{m} \simeq 150(1+z)\left(\frac{1\,\mathrm{eV}}{m}\right)\mathrm{km\,s^{-1}}\ , \tag{150}$$

where $z = (a_0/a - 1)$ is the redshift. The neutrinos cannot cluster on scales smaller than the total distance over which they travel on average between the early Universe and today (this distance, called the free-streaming length, is insensitive to the precise choice of 'time zero'). Indeed, on such scales, the neutrinos experience free diffusion instead of being trapped inside gravitational potential wells. Therefore, we could expect naively that on scales smaller than the free-streaming scale, the density contrast δ_k of the total non-relativistic matter should be reduced by a fraction f_ν, where f_ν is the relative contribution of neutrinos to the total non-relativistic matter density. Fortunately, the effect is stronger than this since neutrinos not only do not participate in the gravitational collapse on small scales but neutrinos also slow down the growth of the density contrast of other matter components, CDM, and baryons.

The balance between gravity and expansion described above is broken in presence of neutrinos. On scales smaller than the free-streaming length, neutrinos do not participate in the gravitational collapse, but contribute to the expansion because their homogeneous background density appears in the Friedmann equation. So, massive neutrinos give rise to more expansion for the same amount of matter subject to gravitational clustering than would be the case if neutrinos were massless. As a consequence, the growth rate of the density contrast δ_k is reduced on those scales to $\delta_k \propto a^{1-(3/5)f_\nu}$. If the neutrino mass is very small, this reduction is tiny, but it accumulates over an extended period of time, so that today δ_k can be significantly smaller than in the massless case; typically the relative reduction is given by a factor $-4f_\nu$.

In total, the signature of massive neutrinos on the total matter power spectrum at redshift z, denoted $P(k,z) \equiv \langle|\delta_k(z)|^2\rangle$, is the sum of two effects:

1. As a function of k, the matter power spectrum $P(k,z)$ is step-like suppressed for wavelengths smaller than the free-streaming length (see figure 33). More precisely, for any observable redshift, what matters is the free-streaming length at the time of the non-relativistic transition, since $P(k,z)$ goes through a maximum when:

$$\lambda_{\rm nr} \simeq 350\ \Omega_{\rm m}^{-1/2} \left(\frac{1\,{\rm eV}}{m}\right)^{1/2} h^{-1}\,{\rm Mpc}\ , \tag{151}$$

   where $\Omega_m \simeq 0.3$ is the matter-density fraction today. The relative amplitude of the small-scale suppression today is well approximated by $-8f_\nu$. Note that no other cosmological parameters have such a step-like effect on $P(k,z)$; and

2. As a function of z or a, the matter power spectrum undergoes a different evolution on large scales (with $P(k,z) \propto a^2$) and small scales (with $P(k,z) \propto a^{2-(6/5)f_\nu}$). This is an absolutely unique effect of dark-matter particles with a large velocity dispersion, no other known ingredient can justify such a scale-dependent growth factor.

Note that both effects depend primarily on the total neutrino mass $M_\nu = \sum_i m_{\nu i}$ (summed over the three mass eigenstates):

$$f_\nu = \frac{\Omega_\nu}{\Omega_m} \simeq \frac{M_\nu}{14{\rm eV}}\ . \tag{152}$$

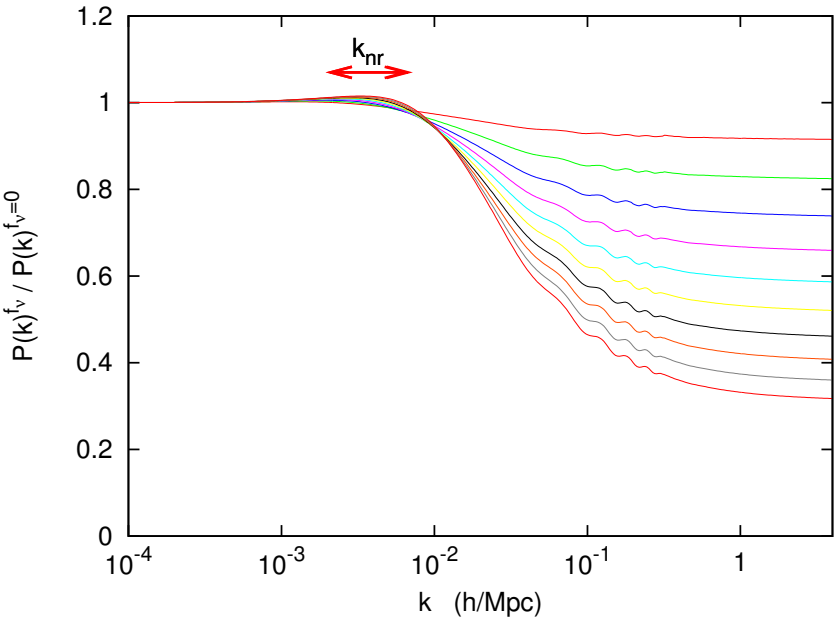

Figure 33: Ratio of the matter power spectrum including three degenerate massive neutrinos with density fraction f_ν to that with three massless neutrinos. The parameters $(\omega_{\rm m}, \Omega_\Lambda) = (0.147, 0.70)$ are kept fixed, and from top to bottom the curves correspond to $f_\nu = 0.01, 0.02, 0.03, \ldots, 0.10$. The individual masses m_ν range from 0.046 eV to 0.46 eV, and the scale $k_{\rm nr} = 2\pi/\lambda_{\rm nr}$ from $2.1 \times 10^{-3} h\,{\rm Mpc}^{-1}$ to $6.7 \times 10^{-3} h\,{\rm Mpc}^{-1}$ as shown on the top of the figure. Taken with kind permission of Physics Reports from figure 13 in reference [388]. Copyrighted by Elsevier Science B.V.

Since massive neutrinos have such distinct signatures on LSS, the total neutrino mass may, in principle, be extracted with a precision which depends upon:

- The statistical and systematic uncertainties of the experimental data; large uncertainties will result in a confusion between the effect of massive neutrinos and that of other cosmological parameters; and
- The priors that are considered acceptable for the underlying cosmological model.

3.4.1.2 Current bounds

Currently, the combination of up-to-date CMB and LSS data is compatible with the simplest version of the ΛCDM scenario, containing three species of massless neutrinos. Still, cosmological observations provide a stringent upper bound on the total neutrino mass. This bound is not unique since it depends on the exact data set considered and on the theoretical priors. The data sets used to determine the bound include CMB anisotropy measurements (from WMAP [389] and other experiments probing smaller angular scales). CMB anisotropies have a weak dependence on neutrino masses, but by accurately measuring other cosmological parameters CMB data plays a crucial role in reducing parameter degeneracies.

Current large-scale structure data consists of several types of complementary observations. One of them is the galaxy-galaxy two-point correlation function, best measured by the 2dF [390] and SDSS [391, 392] groups. This observable can be used over a range of scales and directly reflects the shape of the linear power spectrum predicted by the theory, modulo an unknown normalisation factor called the light-to-mass bias, the galaxy-galaxy correlation function probes the shape, but not the amplitude of the primordial spectrum. Therefore, an accurate determination of the shape of the spectrum is sufficient for detecting the characteristic step-like suppression caused by massive neutrinos. However, the galaxy-galaxy correlation function does not probe an extended range of scales; it is limited on small scales by the fact that it is difficult to compare the theory with the data for strongly non-linear scales $k > 0.2h^{-1}$Mpc; and it is limited on large scales by selection effects (i.e., if galaxies are too far from us, they are also too faint to be accurately sampled).

To complement this type of observation, the light-to-mass bias can be measured (for example by using higher-order correlations beyond the two-point correlation function). Determination of the light-to-mass bias is important for the determination of the neutrino mass because it fixes the amplitude of the matter power spectrum on small scales, while on large scales CMB experiments provide an accurate normalisation. The comparison of the two measurements provides some constraints on the step-like suppression caused by massive neutrinos.

Instead of being computed in three-dimensional space, the galaxy-galaxy two-point correlation function can be measured in angular space. This method offers greater sensitivity to the acoustic oscillations imprinted on the baryon density before photon decoupling. This type of data is usually called Baryonic Acoustic Oscillation (BAO) data. The latest BAO data, obtained by the SDSS collaboration [393], provides more precise constraints on cosmological parameters (including the neutrino mass) than can be obtained using the three-dimensional galaxy-galaxy power spectra at present.

Measurements of the matter power spectrum over a wide range of scales on both sides of the characteristic scale $\lambda_{\rm nr}$ are required for the determination of neutrino mass. Since the limitation on small scales is given by the transition to the non-linear regime, it would be very useful to measure the matter power spectrum at large redshift, i.e. far back in time, when the non-linear scales were confined to smaller wavelengths than today. This can be done using the Lyman-α forest data coming from a detailed analysis of quasar spectra, obtained for instance by the SDSS collaboration [394]. For each spectrum, one can identify a waveband corresponding to Lyman-α absorption along the line of sight; the wavelength at which the Lyman-α absorption band appears depends upon the redshift of the galaxy in question. The Lyman-α forest data is a tracer of matter fluctuations at redshifts in the range $2 < z < 3$, this is to be compared with current date on the galaxy-galaxy correlation function which spans redshifts in the range $0 < z < 0.2$. Therefore, Lyman-α forest data can probe very small scales which are strongly non-linear today, but were mildly non-linear at the time of the transition. The data can be related to the theoretical linear power spectrum. However, there is still some controversy about various aspects which might lead to an underestimation of systematic uncertainties.

A graphical summary is presented in figure 34, where the cosmological bounds found in the

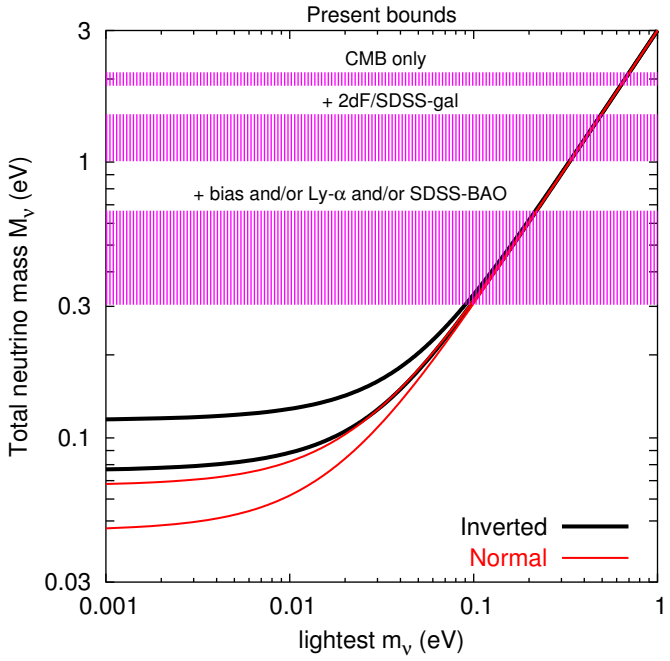

Figure 34: Various current upper bounds (2σ level) from cosmological data on the total neutrino mass, compared to the values in agreement with neutrino oscillation data (at the 3 σ level): for normal hierarchy, the total neutrino mass as a function of the lightest eigenstate mass is to be found between the two red lines; for inverted hierarchy, between the two black lines. Taken with kind permission of Physics Reports from figure 19 in reference [388]. Copyrighted by Elsevier Science B.V.

literature correspond to the horizontal bands. The three bands correspond to different types of data and the thickness of each band roughly describes the spread of values obtained by different authors [388] (see reference [395] for an update). The upper band corresponds to the constraints obtained from CMB data only. These bounds are very robust because the CMB probes the density contrast deep into the linear regime. The 2σ limits on M_ν derived from current CMB data range from 2 eV to 3 eV. The middle band includes three-dimensional measurements of the galaxy-galaxy correlation function in addition to CMB data. Here, the light-to-mass bias is left as a free parameter, so the data only measures the shape of the matter power spectrum. The corresponding robust and conservative bounds on the neutrino mass are in the range $0.9 - 1.7$ eV. Finally, the lower band includes data with more controversial systematic uncertainties, or for which the comparison between theory and observations is non-trivial and subject to caution, the light-to-mass bias determination and/or Lyman-α forest data and/or BAO angular spectrum. In this case, the 2σ upper limit on M_ν ranges typically from 0.2 to 0.9 eV. One can see from figure 34 that current cosmological data probe the region where the 3 neutrino states are degenerate, with a mass $M_\nu/3$. If one trusts the most aggressive combination of data sets (in particular, from Lyman-α forests), this region can be considered as entirely excluded by cosmological observations.

3.4.1.3 Future prospects

In order to improve the bounds on M_ν significantly, or to detect a non-zero value, it is necessary to observe large-scale structures both:

- On larger scales than today, in order to increase the lever-arm on the matter power spectrum towards large wavelengths, and also to reduce the statistical (sampling) error on all scales; and
- At higher redshift to probe smaller scales in the linear or mildly non-linear regime and thereby to increase the lever arm towards small wavelengths. In addition, measurements at high redshift are sensitive to the modified growth rate of density contrasts which are imprinted by neutrinos on small scales.

More precise CMB data would also be useful to constrain more strongly other cosmological parameters so further reducing parameter degeneracies.

The expected sensitivity of different cosmological data to M_ν is shown in figure 35. The figure also shows the values of M_ν which are allowed in two of the possible three-neutrino schemes (see reference [388] for details). The left-hand panel shows the expected sensitivity of future CMB and galaxy-redshift surveys. The Planck satellite will provide a measurement with a 2σ sensitivity of the order of 1 eV; the same data combined with the completed results of the SDSS galaxy redshift survey should reach 0.4 eV [396]. NASA is studying a number of projects with even better sensitivity and resolution, under the generic name of the 'Inflation Probe' [397]. Taking the sensitivity of one of these projects, CMBpol, as a benchmark, yields an expected sensitivity of 0.4 eV for CMBpol alone, and a sensitivity slightly better than 0.3 eV when the CMBpol data is combined with SDSS.

More spectacular improvements can be expected from weak lensing experiments, the goal of which is to deduce the surrounding gravitational potential and matter distribution from the distortion of the images of galaxies or from the anisotropy patterns in the CMB radiation itself. It would be impossible to estimate lensing effects by observing a single galaxy or a single CMB pixel. However, lensing distortions can be accurately deduced from a statistical analysis of many groups of galaxies or extended regions in CMB maps. CMB lensing measurements offer a unique opportunity to probe density contrasts at very high redshift (up to $z \sim 3$). However, galaxy weak lensing observations can reach a higher signal-to-noise ratio and can be used for tomography. By classifying the source galaxies in redshift bins, one can reconstruct the gravitational potential distribution at different redshifts, and follow the growth of perturbations as a function of redshift. This has been shown to be particularly useful for probing the neutrino-mass effect on small scales.

The right-hand pane of figure 35 shows the expected sensitivity of future CMB experiments such as Planck and CMBpol, including the lensing data extracted from the same experiment. The 2σ sensitivity to M_ν is as good as 0.3 eV and 0.07 eV respectively. These forecasts should be interpreted with care because it has been assumed that astrophysical foregrounds can be

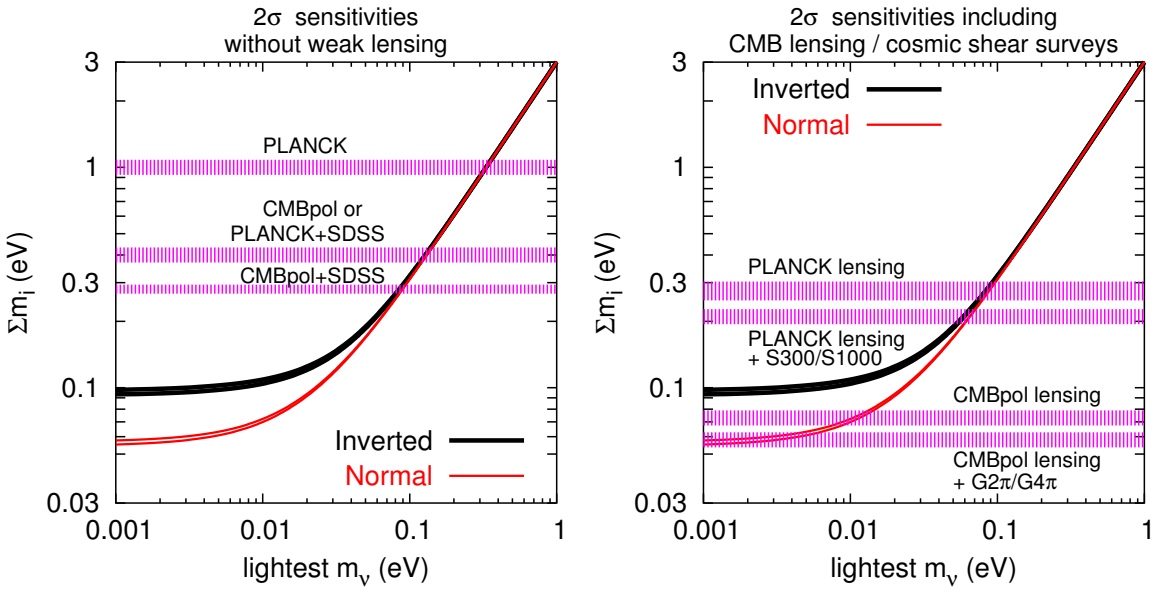

Figure 35: Forecast 2σ sensitivities to the total neutrino mass from future cosmological experiments, compared to the values in agreement with present neutrino oscillation data (assuming a future determination at the 5% level). Left: sensitivities expected for future CMB experiments (without lensing extraction), alone and combined with the completed SDSS galaxy redshift survey. Right: sensitivities expected for future CMB experiments including lensing information, alone and combined with future cosmic shear surveys. Here CMBpol refers to a hypothetical CMB experiment roughly corresponding to the Inflation Probe mission. Taken with kind permission of Physics Reports from figure 23 in reference [388]. Copyrighted by Elsevier Science B.V.

removed accurately from the CMB map. The improvement in sensitivity that can be obtained by adding data from galaxy weak-lensing surveys is also shown. S300/S1000 refers to experiments involving a spatial telescope scanning galaxies in a small region of the sky (300 to 1000 squared degrees). G2π/G4π refers to plausible ground-based experiments probing half of the sky or all of it. Such experiments are planned for the near future (see [167, 388] and references therein). The sensitivity of Planck plus S300/S1000 is of the order of 0.2 eV, while CMBpol combined with a full-sky galaxy scan would reach a 2σ sensitivity equal to the minimum value of M_ν in the case of normal hierarchy (of order 0.05 eV). The combination of measurements of the CMB with future galaxy-cluster surveys (derived from the same weak lensing observations as well as X-ray and Sunyaev–Zel'dovich surveys) should yield a similar sensitivity [398, 399].

3.4.2 Leptogenesis

The origin of the matter-antimatter asymmetry is one of the most important questions in cosmology. The presently observed baryon asymmetry is [389]:

$$Y_B = \frac{n_B - n_{\bar{B}}}{s} \simeq 6.1 \times 10^{-10} \,. \tag{153}$$

where Y_B is the baryon to photon ratio at recombination. In 1967 A. Sakharov suggested that the baryon density can be explained in terms of microphysical laws [400]. Three conditions need to be fulfilled: there must exist a mechanism by which baryon number conservation is violated; the conservation of C and CP must be violated; and there must be a period in which the Universe is out of thermal equilibrium. Several mechanism have been proposed to explain the baryon asymmetry, many of which are dis-favoured by cosmological or theoretical considerations.

Leptogenesis has emerged as a successful mechanism for explaining the origin of the baryon asymmetry of the Universe [128]. Assuming that $B - L$ is conserved both at the perturbative and the non-perturbative level, then if a net $B - L$ (for example a net lepton number) could be created, then the 'sphaleron' process would convert the net $B - L$ into a net baryon and lepton number of comparable magnitude. Leptogenesis is particularly appealing because it takes place in the context of see-saw models [127, 222, 223], which, naturally explain the smallness of neutrino masses. As discussed above, the see-saw mechanism requires the existence of heavy right-handed (RH) Majorana neutrinos, singlet with respect to the Standard Model gauge symmetry group. Introducing a Dirac neutrino mass term and a Majorana mass term for the right-handed neutrinos via the Lagrangian:

$$-\mathcal{L} = \overline{\nu_{Li}}\,(m_D)_{ij}\,N_{Rj} \,+ \frac{1}{2}\,\overline{(N_{Ri})^c}\,(M_R)_{ij}\,N_{Rj} \,, \tag{154}$$

leads, for sufficiently large M_R, to the well known see-saw formula for the low-energy neutrino mass matrix, m_ν [127, 222, 223]:

$$m_\nu \;\simeq -m_D\; M_R^{-1}\; m_D^T \,, \tag{155}$$

$$= U\; D_m\; U^T \,, \tag{156}$$

where terms of order $\mathcal{O}(M_R^{-2})$ have bee neglected, D_m is a diagonal matrix containing the masses $m_{1,2,3}$ of the three light massive Majorana neutrinos, and U is the unitary PMNS matrix.

The CP-violating and out-of-equilibrium decays of RH neutrinos produce a lepton asymmetry [128] that can be converted into a baryon asymmetry through anomalous electroweak processes [401, 402]. The requisite CP-violating decay asymmetry is caused by the interference of the tree-level contribution and the one-loop corrections in the decay rate of the heavy Majorana neutrinos, $N_i \to \Phi^- \, \ell^+$ and $N_i \to \Phi^+ \, \ell^-$:

$$\begin{aligned} \varepsilon_i &= \frac{\mathrm{d}\Gamma(N_i \to \Phi^- \, \ell^+) - \Gamma(N_i \to \Phi^+ \, \ell^-)}{\mathrm{d}\Gamma(N_i \to \Phi^- \, \ell^+) + \Gamma(N_i \to \Phi^+ \, \ell^-)} \\ &\simeq \mathrm{d} \frac{\mathrm{d}1}{\mathrm{d}8 \, \pi \, v^2} \sum_{j \neq i} \frac{\mathrm{Im}(m_D^\dagger m_D)_{ij}^2}{(m_D^\dagger m_D)_{ii}} \, \left(f(x_j) + g(x_j) \right) \, , \end{aligned} \tag{157}$$

where Φ and ℓ indicate the Higgs field and the charged leptons, respectively. Here $v \simeq 174$ GeV is the electroweak-symmetry-breaking scale and $x_j \equiv M_j^2 / M_i^2$. The functions f and g stem from vertex [128, 403–405] and from self-energy [406–410] contributions:

$$\begin{aligned} f(x) &= \sqrt{x} \left(1 - (1+x) \, \ln \left(\tfrac{\mathrm{d}1 + x}{\mathrm{d}x} \right) \right) \; ; \text{and} \\ g(x) &= \tfrac{\mathrm{d}\sqrt{x}}{\mathrm{d}1 - x} \, . \end{aligned} \tag{158}$$

For $x \gg 1$, i.e. for hierarchical heavy Majorana neutrinos, $f(x) + g(x) \simeq -\frac{3}{2\sqrt{x}}$. Under these assumptions, the baryon asymmetry is obtained via:

$$Y_B = a \, \frac{\kappa}{g^*} \, \varepsilon_1 \, , \tag{159}$$

where $a \simeq -1/2$ is the fraction of the lepton asymmetry converted into a baryon asymmetry [401, 402], $g^* \simeq 100$ is the number of massless degrees of freedom at the time of the decay, and κ is a efficiency factor that is obtained by solving the Boltzmann equations. Typically, one gets $Y_B \sim 6 \times 10^{-10}$ when $\varepsilon_1 \sim (10^{-6} - 10^{-7})$ and $\kappa \sim (10^{-3} - 10^{-2})$. Note that this estimate of Y_B is valid in the supersymmetric theories too [406–410].

The results reported so far are valid if the individual lepton flavours (which indicate the lepton-mass eigenstates at the temperature of leptogenesis) are effectively indistinguishable. Recently, it has been pointed out that if this assumption does not hold, the evolution of the lepton asymmetry in each flavour α, $Y_{L,\alpha}$, needs to be considered separately and the resulting final baryon asymmetry can be different from the one obtained from equation (159) [411]. Following reference [411], consider the case of hierarchical heavy neutrinos for which the generation of the lepton asymmetry is dominated by the decay of the lightest with mass M_1. The lepton-flavour asymmetry is proportional to the flavour CP-asymmetry, $\epsilon_{\alpha\alpha}$, of the decay of N_1 into the leptons of flavour α:

$$\epsilon_{\alpha\alpha} = \frac{1}{8\pi v^2} \frac{1}{(m_D^\dagger m_D)_{11}} \sum_j \mathrm{Im} \Big((m_D)_{\alpha 1} (m_D^\dagger m_D)_{1j} (m_D)_{\alpha j}^* \, \left(f(x_j) + g(x_j) \right) \Big) \, . \tag{160}$$

By solving the coupled Boltzmann equations for the asymmetries corresponding to the indistinguishable flavours, one obtains an efficiency factor for each flavour α. When computing the final baryon asymmetry, this flavour efficiency factor weights the decay asymmetries as $\varepsilon_{\alpha\alpha}$. If

$M_1 \lesssim 10^9$ GeV, the μ and τ Yukawa couplings are in equilibrium and the three flavours need to be considered separately. For 10^9 GeV $\lesssim M_1 \lesssim 10^{12}$ GeV, only the interactions mediated by the τ Yukawa coupling are in equilibrium and the problem reduces to an effective two-flavour case. Finally, if $M_1 \gtrsim 10^{12}$ GeV, the Yukawa interactions are all out of equilibrium and all flavours are indistinguishable. In this case, the results of one flavour are recovered.

In the MSSM, flavour effects are relevant for even larger temperature ranges [412]. Here, the one-flavour formulæcan only be applied for temperatures larger than $(1 + \tan^2\beta) \times 10^{12}$ GeV, since the squared charged-lepton Yukawa couplings in the MSSM are multiplied by this factor. Consequently, charged μ- and τ-lepton Yukawa couplings are in thermal equilibrium for $(1 + \tan^2\beta) \times 10^5$ GeV $\ll M_1 \ll (1 + \tan^2\beta) \times 10^9$ GeV and all flavours in the Boltzmann equations are to be treated separately. For $(1 + \tan^2\beta) \times 10^9$ GeV $\ll M_1 \ll (1 + \tan^2\beta) \times 10^{12}$ GeV, only the τ Yukawa coupling is in equilibrium and only the τ flavour is treated separately in the Boltzmann equations, while the e and μ flavours are indistinguishable.

Establishing a connection between the parameters at low energy (neutrino masses, mixing angles, and CP-violating phases), measurable in principle in present and future experiments, and at high energy (relevant in leptogenesis) has been intensively investigated. The number of parameters in the full Lagrangian of models which implement the see-saw mechanism is larger than the ones in the low-energy sector: in the case of three light neutrinos and three heavy ones, at high energy the theory contains, in the neutrino sector, 18 parameters of which 12 are real. At low energy only 9 are accessible - 3 angles, 3 masses and 3 phases. The decoupling of the heavy right-handed neutrinos implies the loss of information on 9 of the parameters required to specify the theory at high energy. This implies that reconstructing the high-energy parameters entering in the see-saw models from the measurement of the masses, angles, and CP-violating phases of m_ν depends on the specific model considered.

Using the weak basis in which both M_R and the charged-lepton mass matrix are real and diagonal, it is useful to parametrise the Dirac mass by the bi-unitary or the orthogonal parametrisations:

- *Bi-Unitary parametrisation:* The complex 3×3 Dirac mass matrix can be written in the form [413]:

$$m_D = U_L^\dagger \, m_D^{\rm diag} \, U_R \ , \tag{161}$$

  where U_L and U_R are unitary 3×3 matrices and $m_D^{\rm diag}$ is a real diagonal matrix. All the CP-violating phases are contained in U_L and U_R; and

- *Orthogonal parametrisation:* By using the see-saw formula, equation (155), we can express m_D as [156, 414]:

$$m_D = i \, U \, D_m^{1/2} \, R \, M_R^{1/2} \ , \tag{162}$$

  where D_m is the diagonal real matrix which contains the low-energy light neutrino masses, and R is a complex orthogonal matrix. R contains 3 real parameters and 3 phases.

The use of these parametrisations clarifies the dependence of leptogenesis and LFV charged-lepton decays, on the different parameters entering in m_D.

For leptogenesis, in the case of one effective flavour, the decay asymmetry ε_1 depends on the hermitian matrix $m_D^\dagger m_D$:

$$m_D^\dagger m_D = \begin{cases} U_R^\dagger \, (m_D^{\rm diag})^2 \, U_R \ , & \text{bi–unitary;} \\ M_R^{1/2} \, R^\dagger \, D_m \, R \, M_R^{1/2} \ , & \text{orthogonal.} \end{cases} \tag{163}$$

Notice that the PMNS unitary mixing matrix does not enter explicitly into the expression for the lepton asymmetry. However, it has been pointed out that if this approximation does not hold, single-flavour asymmetries need to be considered. In this case, the flavour CP asymmetry may be written:

$$\epsilon_{\alpha\alpha} = -\frac{3M_1}{16\pi v^2} \frac{{\rm Im}\Big(\sum_{\beta\rho} m_\beta^{1/2} m_\rho^{3/2} U^*_{\alpha\beta} U_{\alpha\rho} R_{\beta 1} R_{\rho 1}\Big)}{\sum_\beta m_\beta |R_{\beta 1}|^2} \ . \tag{164}$$

It is important to notice that in this case the lepton asymmetry depends also on the CP-violating phases in U. In the interesting case of R real, the asymmetry does not cancel out and will be determined by the values of the low-energy Dirac and Majorana CP-violating phases, which are measurable in principle in future experiments.

In the bi-unitary parametrisation, the neutrino mass matrix m_ν can be written as:

$$m_\nu = -U_L^\dagger \, m_D^{\rm diag} \, U_R \, M_R^{-1} \, U_R^T \, m_D^{\rm diag} \, U_L^* \ , \tag{165}$$

showing that the phases in U receive contributions from CP-violation both in the right-handed sector, responsible for leptogenesis, and in the left-handed one, which enters in lepton-flavour-violating processes. Due to the complicated way in which the high-energy phases and real parameters enter in m_ν, equation (165), if there is CP-violation at high energy, as required by the leptogenesis mechanism, we can expect in general to have CP-violation at low-energy, as a complete cancellation would require some fine-tuning or special forms of m_D and M_R.

More specifically, from equation (165), it can be seen that, in general, there is no one-to-one link between low energy CP-violation in the lepton sector and the baryon asymmetry; a measurement of the low-energy CP-violating phases does not allow the leptogenesis phase to be reconstructed. However, if the number of parameters in m_D is reduced, a one-to-one correspondence between high-energy and low-energy parameters might be established. For example, in certain classes of neutrino-mass models with sequential right-handed neutrino dominance, a strong link between the leptonic-CP violating phase, δ, and the CP-violation required for leptogenesis can be established, and flavour-dependent effects have a significant effect [412]. In other classes of models such strong links were not found. Links can also be achieved in models which allow for CP-violation. For example, this can be achieved in models which allow for CP-violation only in the right-handed sector, that is in U_R. It has been shown recently that, to the extent that the different flavours can be distinguished, leptogenesis depends only on the phases in the

PMNS mixing matrix, if R is real. Each model of neutrino mass generation should be studied separately in detail to establish the feasibility of the leptogenesis mechanism [415–422].

In conclusion, the observation of $(\beta\beta)_{0\nu}$-decay, implying the violation of the global lepton number (one of the main conditions for leptogenesis), and of leptonic CP-violation in neutrino oscillations and/or neutrinoless double-beta decay is crucial in understanding the origin of the baryon asymmetry. The observation of leptonic-CP violation itself would be a strong indication, though not a proof, that leptogenesis is the explanation for the observed baryon asymmetry of the Universe.

3.4.3 Neutrinos and Inflation

In the previous sections, we have seen that neutrinos may have played crucial roles in shaping the Universe of today (the large-scale structure) and in the removal of the anti-matter from the early Universe (leptogenesis). The neutrino may also may also be the key to the process of inflation by which the Universe went through a period of exponential growth. The 'stretching' of the Universe during inflation is held to explain the uniformity of the today's Universe.

In nearly all discussions about the birth of the Universe, it is assumed that the Universe was originally microscopically small. There is a good reason for this; communication between different parts of the Universe has a 'speed limit', the speed of light, c. No regions of space 'know' about other regions if they are separated by more than the distance $c\tau$ where τ is the age of the Universe at a particular moment. It is very difficult to conceive of a process that can create the Universe that is larger than $c\tau$. It is much more natural to think that the Universe was born small, but that there was a mechanism to stretch it to a macroscopic size later, much larger than that allowed by the assumed speed limit c.

Support for this view can be found in the CMB. The temperature of cosmic microwave background is the same, to better than one part in a hundred thousand or so, in every direction. The microwave photons from the different directions come from opposite ends of the Universe that could never have been in communication with each other. The CMB distribution reflects the temperature distribution of the early Universe. Therefore, the uniformity of the CMB implies that different regions of the early Universe, which are not necessarily causally connected, are nonetheless at the same temperature. This is the 'horizon problem': what is the mechanism which gave rise to such a uniform temperature distribution.

Another well-known problem is the 'flatness problem'. When the Universe was born, no known microphysics can determine what kind of space, namely the topology and the local curvature, should be chosen. At the time of big-bang nucleosynthesis (the best-tested aspect of the description of the early Universe when it was about a second to a minute old) the Universe must have been extremely flat at the level of 10^{-20}. This requirement becomes much stronger if we contemplate even earlier times. What mechanism squashed the Universe so flat?

Finally, the large-scale structure of the Universe discussed above suggests that the Universe originated from a small fluctuation in the energy density at the level of 10^{-5}, which somehow

appears to be correlated in different parts of the space – i.e., the initial density perturbation appears acausal. In addition, the spectrum of the fluctuation is nearly independent of the distance scales, suggesting that it was generated by some kind of self-replicating mechanism. The fluctuations themselves are Gaussian in nature.

Cosmological inflation is currently the only way to answer these profound questions and explain the empirical observations of the large-scale structure of the Universe [423, 424]. Inflation stretches the Universe exponentially from the microscopic size at its birth to a macroscopic size which leads to the vast Universe as observed today. At the same time, even a bumpy space gets flattened once it is exponentially stretched because what we see today is only a tiny portion of the entire space. Also, because the entire Universe originated from a small patch which was in communication, the sky in all directions must look the same. In a surprising way, quantum fluctuations in an exponentially expanding Universe soon become classical because the natural wave length exceeds the causally-connected region of space, and as the Universe keeps expanding it generates itself many times leading to a scale-invariant Gaussian spectrum of density fluctuations [425].

For concreteness, consider a simple model of inflation based on a scalar field (ϕ) with just a mass term, namely a quadratic potential [426]:

$$\mathcal{L} = \frac{1}{2}(\partial\phi)^2 - \frac{1}{2}m^2\phi^2. \tag{166}$$

Such a scalar field can drive inflation. The equation of motion of the scalar field is:

$$\ddot{\phi} + 3H\dot{\phi} + m^2\phi = 0, \tag{167}$$

while the expansion rate of the Universe $H = \dot{a}/a$, if dominated by this scalar field, is given by:

$$H^2 = \frac{8\pi}{3}G_N\frac{1}{2}(\dot{\phi}^2 + m^2\phi^2). \tag{168}$$

This coupled equation has a very simple solution if $\phi \gtrsim M_{Pl} = G_N^{-1/2}$. It can be shown that the $\ddot{\phi}$ and $\dot{\phi}^2$ in the above equations can be safely neglected (the 'slow-roll' condition). In this case equations (167) and (168) can be combined into a single equation:

$$3\sqrt{\frac{8\pi}{3}}\ \frac{1}{M_{Pl}}m\phi\dot{\phi} + m^2\phi = 0\ , \tag{169}$$

and hence:

$$\phi(t) = \phi(0) - \frac{mM_{Pl}}{\sqrt{24\pi}}t\ . \tag{170}$$

At the same time, the Universe expands as:

$$a(t) = a(0)\exp\left[\sqrt{\frac{4\pi}{3}}\frac{1}{M_{Pl}}\left(\phi(0)t - \frac{mM_{Pl}}{2\sqrt{24\pi}}\ t^2\right)\right]\ . \tag{171}$$

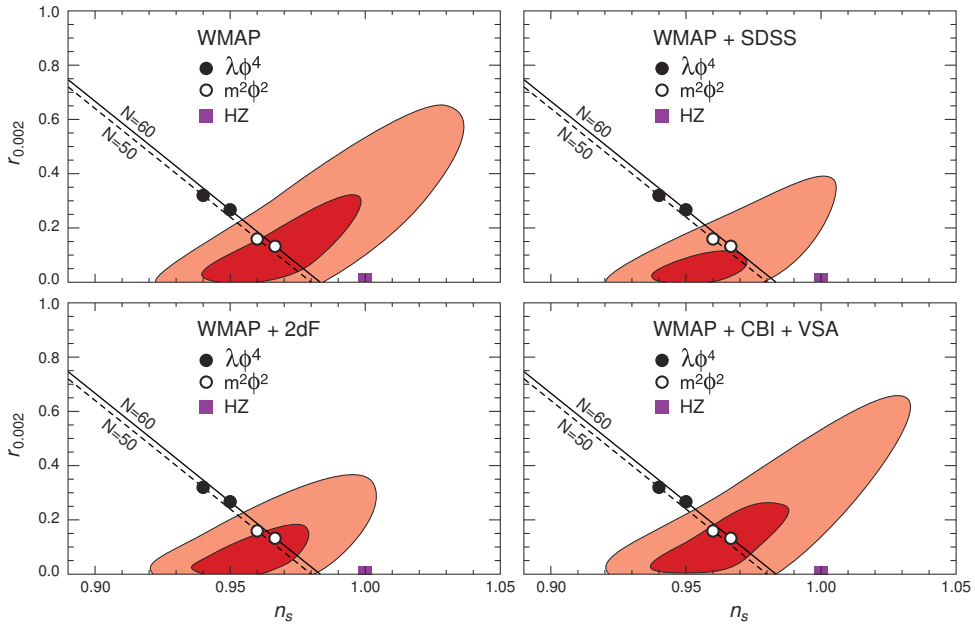

Figure 36: Global fits to the cosmological data versus predictions of simple inflation models [389]. Adapted with kind permission of the Astrophysical Journal Supplement Series from figure 14 in reference [389]. Copyrighted by the American Astronomical Society.

For $t \ll \phi(0)/(mM_{Pl})$ the second term in the parentheses can be ignored, and the expansion of the Universe is exponential. This way, the initial microscopic size of the Universe can be made macroscopically large. The curvature is squashed exponentially as $(a(0)/a(t))^2$ solving the flatness problem, and also the horizon problem by assuming that the e-folding is large enough ($\gtrsim 60$) so that the initial horizon contains the entire visible Universe of today.

To obtain the correct size of the density fluctuations, we need $m \simeq 2 \times 10^{13}$ GeV [427]. It is remarkable that the simple quadratic potential is consistent with available cosmological data, including the upper limit on the tensor component (see figure 36 [389]). A natural question from the particle physics point of view is what is this scalar field? The most likely candidate is a gauge singlet, to maintain the form of the potential against radiative corrections. There are no such fields within the Standard Model or its minimal supersymmetric extension.

However, the mass of the scalar required to generate the quadratic potential is similar to the mass of right-handed neutrinos required by the see-saw mechanism. The RH neutrinos are also naturally gauge singlets. It is therefore tempting to consider that neutrinos have something to do with inflation. If nature is supersymmetric, the right-handed neutrinos needed in the see-saw mechanism have superpartners (sneutrinos) which are scalar fields. The sneutrino potential is quadratic, making the right-handed sneutrinos candidates for the inflaton field [428]. Moreover, once the inflation is over, the right-handed sneutrino oscillates around the origin and decays, reheating the Universe to an ordinary thermal bath. This process is the same as that assumed in the discussion of leptogenesis above, and hence can generate the baryon asymmetry. Because the Universe is dominated by the right-handed neutrino at this point, leptogenesis is more efficient than conventional thermal leptogenesis. Using the available neutrino data and assuming

hierarchical spectrum of right-handed neutrinos, the resulting lepton asymmetry is given by:

$$\frac{n_L}{s} \simeq 1.5 \times 10^{-10} \frac{T_{RH}}{10^6 \text{ GeV}} \, \delta, \tag{172}$$

where δ is the CP violating phase in the neutrino mixing [429]. Interestingly, leptogenesis is possible with a relatively low reheating temperature $T_{RH} \sim 10^6$ GeV, low enough to avoid the cosmological problem of gravitinos even for the case of hadronic decay [430] which imposes strong constraints on thermal leptogenesis with hierarchical right-handed neutrinos [431, 432].

There is, however, an important issue to be addressed for the simple quadratic form of the potential to extend beyond the Planck-scale amplitude. In fact, supergravity tends to modify this form and requires a somewhat special Kähler potential to maintain the quadratic form [433] (see also [434, 435] for more recent discussions). The most important test of the quadratic potential is its prediction of the tensor component $r \simeq 0.15$. This relatively large tensor component will be probed in the near future by B-mode polarisation measurements of the cosmic microwave background [436]. An alternative scenario of sneutrino inflation, where a small r is predicted and which is therefore easily distinguishable from the above model, is hybrid inflation with a sneutrino inflaton field [437]. There is therefore an intriguing coincidence between the properties of scalar fields required to drive inflation, for the see-saw mechanism, and for leptogenesis. It points to a remarkable possibility that the neutrino is the mother of the Universe.

4 Effects of New Physics beyond the Standard Neutrino Model

Almost all experimental results to date are consistent with the Standard Neutrino Model (see section 2). These results are most often used to determine the parameters of the SνM. To go beyond the SνM, there are two complementary approaches. The first is the 'theoretical approach' in which models are constructed which solve one or more of the problems of the SνM, this was the approach taken in section 3. These models may predict new phenomena or predict small deviations from the results of the SνM. Present and future experiments may support, constrain, or contradict these models. The Standard Model itself was established in this way, the minimal super-symmetric standard model (MSSM) and other extension of the SM are expected to be tested in future experiments especially at the LHC [438]. The second approach is the 'phenomenological approach' in which possible effects of unknown physics are described in a model-independent way. Experiments may give constraints on these parameters, giving very important information for the development of a complete theoretical description. An example of this approach is the model-independent parameterisation of new physics effects in the vacuum polarisation of electroweak gauge bosons [439, 440]. The strong experimental constraints on the relevant parameters have allowed technicolor models to be rejected.

Neutrino experiments which are being carried out or are in preparation are optimised to measure precisely the parameters of the SνM. The second-generation neutrino facility, on the other hand, should be designed not only to determine these parameters but also to have sensitivity to signatures of physics beyond the SνM. In the following, the possibility of detecting various new-physics effects in neutrino oscillations will be discussed.

4.1 Sterile neutrinos

Neutrinos which have no Standard Model couplings are referred to as 'sterile'. They arise in many extensions of the SM which include singlet-fermion states and the corresponding mass eigenstates. The new sterile-neutrino states can mix with ordinary neutrinos and generate effects that may be observed in terrestrial, cosmological, and astrophysical experiments.

4.1.1 Theoretical issues

If sterile neutrinos are present, it is necessary to explain the origin of their masses and of the mixing with active neutrinos. Small masses and large mixings can arise, for example, via higher-dimensional operators in the superpotential [291] which induce an intermediate-scale expectation value, v_S, for a singlet field. The magnitude of v_S is between the electroweak scale and a large energy scale, M. The masses of the sterile neutrinos are found to be suppressed by powers of v_S/M. Sterile neutrinos with masses from 100 MeV to few GeV are required to generate the observed light-neutrino masses in theories with dynamic electroweak-symmetry breaking [441–444]. Models with 'mirror matter' contain mirror neutrinos which would be light for reasons similar to the reasons for which their ordinary partners are light [445–452]. The interactions between active and sterile neutrinos would be mediated by operators of the type $\nu\phi\nu'\phi'/M_P$, where the prime refers to the mirror world and M_P is the Planck mass. Singlet neutrinos could be the supersymmetric partners of the moduli field [453] or the singlets contained in representations of E_6 [454–456]. In these cases it can be argued that the singlet mass would be of order TeV^2/M_P, the TeV mass scale arising from supersymmetry breaking. Sterile neutrinos can easily be embedded in models based on extra dimensions, the sterile neutrinos can be new singlet fermions propagating in the bulk of a higher-dimensional theory with naturally small masses [457]. In addition, such theories predict a tower of Kaluza-Klein modes which can generate interesting observational signatures, neutrino oscillations in particular [458].

4.1.2 Phenomenology of light sterile neutrinos

Here we consider sterile neutrinos with masses up to a few eV that mix with ordinary neutrinos. The main signals for such sterile neutrinos arise in neutrino oscillations. The implications of the LSND measurements is postponed to section 4.1.5. A detailed discussion of the bounds summarised below is given in [67, 459].

Reactor- and accelerator-neutrino experiments

In these experiments active–sterile neutrino oscillations would take place, implying a reduction of the observed flux at the far detector. Reactor-neutrino experiments are sensitive to the mixing with ν_e, U_{es}. The CHOOZ and Bugey experiments put bounds as strong as $|U_{es}|^2 \lesssim 0.01$ for particular neutrino-mass ranges. Mixing of sterile neutrinos with ν_μ may be tested in accelerator experiments for which muon neutrinos are the dominant beam contribution at the source. Data

from the CDHS and CCFR disappearance experiments allow limits on $U_{\mu s}$ to be derived. In addition, appearance experiments sensitive to the transition $\nu_\mu \to \nu_e$ (KARMEN) and $\nu_\mu \to \nu_\tau$ (NOMAD and CHORUS) probe a combination of the mixing angles, $U_{\mu s}$, U_{es} and $U_{\mu s}$, $U_{\tau s}$, respectively. A combined analysis of recent data from Super-Kamiokande (SK), K2K, MACRO have yielded the constraint $|U_{\mu s}|^2 \lesssim 0.065$ at 99% C.L. [67].

Solar neutrino experiments and KamLAND

The data from these experiments can be used to constrain the mixing of sterile neutrinos with ν_e. The MSW enhancement of electron-neutrino oscillations, with its characteristic energy dependence, makes it possible to search for a sterile-neutrino component down to mass-squared differences as small as $\Delta m^2 \sim 10^{-8}$ eV^2. For large mixing angles, the search can be extended to masses as small as $\Delta m^2 \sim 10^{-12}$ eV^2. In some models sterile neutrinos produce effects at energies below an MeV; data from the SNO and SK experiments already dis-favour models which modify the energy distribution for neutrino energies greater than a few MeV. The low-energy ($E_\nu < 1$ MeV) region was accessible only to the Gallium experiments. In the future, Borexino will be able to test part of this interesting region through the analysis of, for example, diurnal or seasonal variations in the neutrino spectra.

Neutrinoless double-beta decay

Sterile neutrinos that are Majorana particles and mix with electron neutrinos would contribute to the effective Majorana mass on which the half-life of the double-beta-decay process depends. In particular, the effective mass would be:

$$| < m > | = \left| \sum_{i=1,2,3} m_i \; U_{ei}^2 + m_s \; U_{es}^2 \right|, \tag{173}$$

where m_i are the masses of the light, ordinary neutrinos and m_s indicates the mass of the sterile neutrino. Notice that $U_{es}^2 = |U_{es}|^2 \, e^{i\beta_s}$, where β_s is a Majorana CP–violating phase. Due to the presence of the Majorana phases the contributions in $| < m > |$ can be constructive or partially cancel [135]. A future measurement of $| < m > |$ with values outside the range predicted in the case of three light neutrinos might be a signal for the presence of sterile neutrinos.

4.1.3 Signatures of heavy sterile neutrinos

The signatures of sterile neutrinos with masses $m_s \gg 100$ eV depend strongly on the flavour with which the sterile neutrino mixes and on the sterile-neutrino mass [460]. For masses 30 eV $\lesssim m_N \lesssim 1$ MeV, the most sensitive probe is the search for kinks close to the end-point of β-decay spectra [461, 462]. The bounds are typically in the $|U_{es}|^2 \sim 10^{-2}$–10^{-3} range. For heavier masses, a very powerful probe of the mixing of a heavy neutrino with both ν_e and ν_μ are peak searches in leptonic decays of pions and kaons [461, 463]. A heavy neutrino can be produced in such decays and the lepton spectrum would show a monochromatic line at:

$$E_l = \frac{m_M^2 + m_l^2 - m_s^2}{2 m_M}, \tag{174}$$

where E_l and m_l are, respectively, the lepton energy and mass, and m_M is the meson mass. The mixing angle controls the branching ratio of this process and can be constrained by the height of the peak. Notice that these bounds are very robust because they rely only on the assumption that a heavy neutrino exists and mixes with ν_e and/or ν_μ. The limits for $|U_{es}|^2$ are as strong as 10^{-8}–few $\times 10^{-7}$ for masses around 100 MeV. For masses up to 34 MeV, the most stringent constraints on the mixing with muon neutrinos come from pion decays with $|U_{\mu s}|^2 \lesssim$ few 10^{-5}, while for higher masses kaon decays are used and lead to limits as strong as $|U_{\mu s}|^2 \lesssim 10^{-6}$ [464].

Another strategy to search for a heavy sterile neutrino is to look for the products of its decay. A sterile neutrino, ν_s, would be produced in every process in which active neutrinos are emitted, with a branching ratio depending on the mixing-matrix element $|U_{ls}|^2$. It would subsequently decay into neutrinos and other visible particles such as electrons, muons, and pions. Searches for the visible products were performed and were used to constrain the mixing parameters. These bounds are less robust than the ones previously discussed. In fact, if the dominant decay modes of the heavy neutrinos are into invisible particles, these bounds would be weakened, if not completely evaded. In reactors and in the Sun only low mass, $m_N <$ few MeV, heavy sterile neutrinos mixed with ν_e can be produced. The bounds, obtained by looking for decays into electron-positron pairs are, typically, $|U_{es}|^2 \lesssim 10^{-4}$. For higher masses, heavy sterile neutrinos mixed with $\nu_{e,\mu,\tau}$ can be produced in meson and vector bosons decays. There are two different types of experiments. In beam-dump experiments, ν_s are usually produced by the decay of mesons, π, K and D, and the detector is located far away from the production site. Alternatively, the production can happen in the detector itself. The limits depend strongly on the mass range. Typical values for the limits are: $|U_{es}|^2 \lesssim 10^{-9}$–$10^{-4}$, if $m_s \sim 0.02$ GeV – 0.4 GeV; $|U_{es}|^2 \lesssim 10^{-7}$–$10^{-6}$, if $m_s \sim 0.4$ GeV – 2 GeV; and $|U_{es}|^2 \lesssim$ few 10^{-5}, if $m_s \sim 2$ GeV – 80 GeV. Similar bounds hold for the mixing with ν_μ while $|U_{\tau s}|^2$ is constrained to be smaller than at most 10^{-5}. For a detailed review see references [460, 464].

If heavy, sterile neutrinos are Majorana particles, they would mediate $\Delta L = 2$ processes such as neutrinoless double beta-decay. New processes would be allowed and could also be resonantly enhanced for some mass ranges. A very sensitive probe of the mixing with muon neutrinos is given by the rare kaon decay $K^+ \to \pi^- \mu^+ \mu^+$ [465, 466], as well as the nuclear transition $\mu^- + (A, Z) \to \mu^+ + (A, Z-2)$ [467]. Heavy-quark meson decays, e.g. $D^+ \to K^-(\pi^-)\mu^+\mu^+$, were also studied [468]. Recently, bounds were obtained from the process $\Xi^- \to p\mu^-\mu^-$ [469,470].

4.1.4 Sterile neutrins and cosmology and astrophysics

Sterile neutrinos, if mixed with the active neutrinos, would be copiously produced in the early Universe and in astrophysical objects such as supernovae. Since the presence of sterile neutrinos would significantly affect the evolution of such events, it is possible to constrain sterile-neutrino models using astrophysical and cosmological observations ([187]).

4.1.4.1 Light, sterile neutrinos

If light, sterile neutrinos, with masses $m_s < 10$ eV, were produced in the early Universe, they would generate various effects. At Big Bang Nucleosynthesis (BBN), they would contribute to the energy density in relativistic particles, modifying the expansion rate of the Universe and consequently the n/p ratio. Different analyses have been performed and provide bounds on the number of neutrinos, typically $N_\nu \lesssim 3.24 \pm 1.2$ at 95% C.L. [471] (see also reference [459]). The presence of a neutrino asymmetry affects the reactions in which neutrinos are involved and could weaken the bounds quoted above. For a detailed recent analysis see, e.g., reference [472]. The number of relativistic degrees of freedom at photon decoupling can be probed by CMB observations and is constrained to be $N_\nu = 3 \pm 2$ [383, 384, 473].

Finally, light sterile neutrinos affect large-scale structure formation, making structures less clustered due to the free-streaming of these particles. Two parameters are relevant for these studies: the temperature at which these particles become non-relativistic, $T \sim m_s/3$; and the energy density, $\Omega_s h^2$. As the total energy-density in light degrees of freedom is constrained to be less than 1%, it is possible to put strong bounds on the mass of light-sterile neutrinos. Supernovæare also sensitive probes of the existence of sterile neutrinos [474,475]. The data from SN1987A strongly constrain the mixing angles, future experiments might allow these bounds to be strengthened. Sterile neutrinos would be produced in the core of supernovae and would escape carrying away a sizable fraction of the energy. The limit $|U_{ls}|^2 \lesssim 10^{-10}$ can be derived from such an analysis, while for large values of the mixing, $|U_{ls}|^2 \gtrsim 10^{-2}$, the sterile neutrinos would be effectively trapped and no bound applies. In addition, MSW oscillation in sterile neutrinos can take place for specific ranges of parameters and can modify the flux of electron anti-neutrinos. These bounds should be used with care as there is not yet a full understanding of the initiation and evolution of supernovae.

4.1.4.2 KeV sterile neutrinos

Sterile neutrinos with masses in the few-KeV range have been advocated as a source of dark matter [475–478]. Sterile neutrinos could have been produced via scattering-induced conversion of active neutrinos [475, 476]. In this case they would constitute a warm dark-matter candidate with interesting features for structure formation. A bound of $m_s > 10$ KeV applies in this case [479–481] from Lyman-α observations. In the presence of a large lepton asymmetry, the conversion can be resonantly enhanced and the resulting spectrum would be non-thermal, allowing for cool and cold dark matter as well [482]. Other mechanisms of production in which sterile neutrinos are colder than in the case of a thermal spectrum at structure formation allow the 10 KeV limit reported above to be relaxed down to masses as small as a few KeV [483, 484]. These massive neutrinos would decay into a neutrino and a photon, contributing to the diffuse extragalactic background radiation [485–488]. The observations typically exclude a large fraction of the parameter space required for dark matter. Future observations and in particular the Chandra X-ray observatory have the potential of strengthening these bounds or of detecting X-ray fluxes from clusters of galaxies. Weaker bounds on mixing angles and masses can also

be obtained from the contribution of sterile neutrinos to BBN and to the CMB. These bounds are not competitive with the ones from X-ray observations and structure formation. The decays of sterile neutrinos into photons could have affected star formation, as they can catalyse the production of molecular hydrogen and favour star formation [489]. Sterile neutrinos in the same mass and mixing ranges can explain the very high velocities of pulsars. In the presence of the strong magnetic fields of newly born neutron stars, they can be emitted asymmetrically generating a strong kick which boosts the star. The required values of the mixing angle are in the range 10^{-5}–10^{-4}, depending on the mass and on the type of conversion (resonant or non-resonant) of active-sterile neutrinos in the star core [490–492]. Larger values of the mixing angles are excluded by considerations similar to those which apply in the case of light neutrinos in supernovae.

4.1.4.3 MeV-GeV mass sterile neutrinos

Heavy sterile neutrinos, once produced in the early Universe, would decay rapidly into light particles; mainly neutrinos, electrons, and pions. They would affect the predictions of BBN for the abundance of light elements and in particular of ^{4}He [493]. The main effect would be to increase the energy density, leading to a faster expansion of the Universe and to an earlier freeze out of the n/p-ratio. In addition, the decay of ν_s into light neutrinos, in particular, ν_e, would modify the neutrino-energy spectrum and the equilibrium of the $n - p$ reactions. In principle, SN1987A data could also be used to exclude sterile neutrinos with mixing angles $10^{-7} \lesssim |U_{ls}|^2 \lesssim 10^{-2}$ and masses $m_s \lesssim T_{\rm core}$, where $T_{\rm core} = 30 - 80$ MeV is the temperature of the neutron star core. For masses larger than $T_{\rm core}$, the production of sterile neutrinos is suppressed by the Boltzmann factor. The emission of sterile neutrinos from the core depends on the mixing with active neutrinos and the emission history might be very complicated [475]. More detailed analyses should be performed for reliable bounds to be derived.

Notice that all the cosmological bounds quoted above depend on the density of sterile neutrinos in the early Universe. If they were not efficiently produced, these limits would be weakened or not apply at all. This is the case in the presence of mirror neutrinos with very small mass splittings or if there is a very late phase transition such that sterile and active neutrinos are unmixed at higher temperatures, or if the reheating temperature is as low as few MeV [494].

4.1.5 The LSND challenge[13]

The LSND experiment [188] at LANSCE in Los Alamos took data from 1993–1998 and observed an excess of $87.9 \pm 22.4 \pm 6.0$ events in the $\bar{\nu}_\mu \to \bar{\nu}_e$ appearance channel, corresponding to a transition probability of $P = (0.264 \pm 0.067 \pm 0.045)\%$, $\sim 3.3\sigma$ away from zero. To explain this signal with neutrino oscillations requires a mass-squared difference $\Delta m^2 \sim 1$ eV^2. Such a value is inconsistent with the mass-squared differences required by the solar and reactor experiments and that required by the atmospheric and long-baseline experiments within the SνM. Moreover, the KARMEN experiment at the neutron spallation source, ISIS, at the Rutherford Appleton Laboratory studied the same appearance channel ($\bar{\nu}_\mu \to \bar{\nu}_e$) between 1997 and 2001 at a slightly different baseline than LSND, but did not observe a positive signal [496]. A combined analysis of LSND and KARMEN data has been performed in reference [497].

The MiniBooNE experiment [498] at Fermilab has been designed to test the indication for oscillations reported by LSND. In April 2007 the Miniboone group announced the first oscillation analysis [40]. The results dis-favour the simplest sterile-neutrino schemes (the two flavour scheme as well as the (3+1)-scheme described in 4.1.5.3). However, the (3+2)-scheme, with two sterile neutrinos (section 4.1.5.5), can accommodate different oscillation patterns for ν and $\bar{\nu}$ (see section 4.1.5.6) and, as was shown in [495], the (3+2)-scheme is not dead at the time of writing since the Miniboone is yet to present $\bar{\nu}$ data. Until Miniboone announces a negative result for $\bar{\nu}$, therefore, the scenario which is described in sections 4.1.5.5 and 4.1.5.6 is still acceptable. Furthermore, even if Miniboone announces a negative result for $\bar{\nu}$ in the future, and even if schemes like (3+1) and (3+2) are dead, there still remains a possibility for sterile-neutrino scenarios in which the mixing angles are small enough to satisfy the Miniboone constraint, and the effect of these scenarios could be revealed as a violation of three-flavour unitarity in future neutrino experiments. Such scenarios are as probable as all other possibilities described in the rest of section 4 since there is no evidence as yet for any of them. So, from this point of view, it is useful to consider scenarios that seek to reconcile the evidence for $\bar{\nu}_\mu \to \bar{\nu}_e$ appearance from LSND with the other evidence for neutrino oscillations. In the following we discuss the difficulties that must be overcome if the LSND signal is to be explained by oscillations involving light sterile neutrinos.

[13] In April 2007 the Miniboone group announced the data [40] which disfavours the simplest sterile neutrino schemes (the two flavour scheme as well as the (3+1)-scheme described in 4.1.5.3). However, the (3+2)-scheme with two sterile neutrinos (section 4.1.5.5) can make a difference between ν and $\bar{\nu}$ (section 4.1.5.6) and as was shown by [495], the (3+2)-scheme is not dead at the time of writing since the Miniboone group hasn't published the $\bar{\nu}$ data yet. Until Miniboone announces the negative result for $\bar{\nu}$, therefore, the scenario which is described in sections 4.1.5.5 and 4.1.5.6 is still acceptable. Furthermore, even if Miniboone announces the negative result for $\bar{\nu}$ in the future, and even if the schemes like (3+1) and (3+2) are dead, there still remains a possibility for sterile neutrino scenarios whose mixing angles are small enough to satisfy the Miniboone constraint, and the effect of these scenarios could reveal as violation of three flavour unitarity in the future neutrino experiments. Such scenarios are as probable as all other possibilities described in the rest of the section 4 because none of the latter has ever been supported by any experiment so far. So also from that point of view, it is still useful to have the descriptions in 4.1.5.

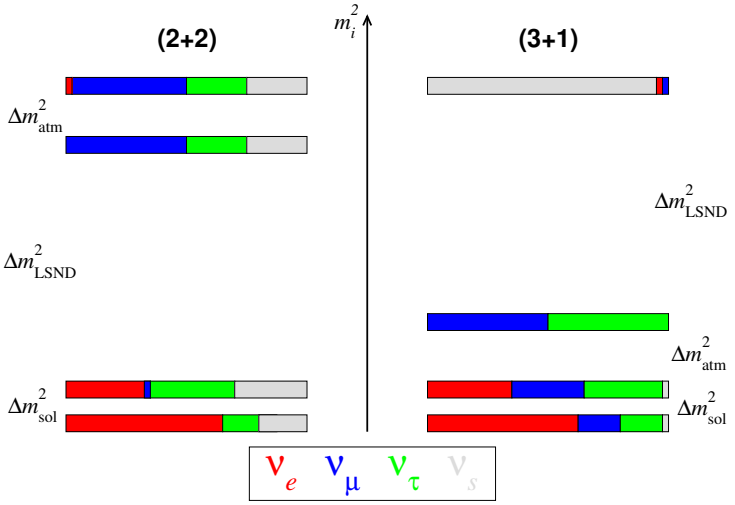

Figure 37: The two classes of four-neutrino mass spectra, (2+2) and (3+1).

4.1.5.1 Four-neutrino oscillations

Three mass-squared differences are required to accommodate all evidence for neutrino oscillations including that provided by LSND, the third mass-squared difference being significantly larger than the other two. A sterile neutrino with mass in the eV range must be introduced [499–501]. However, it turns out that in such four-neutrino models, it is not possible to arrange the mixing so as to accommodate all the data [67, 502, 503].

Four-neutrino schemes are usually divided into the two classes (3+1) and (2+2), as illustrated in figure 37. The (3+1) mass spectra can be considered as a small perturbation of the standard three-active-neutrino scenario. In this case, solar- and atmospheric-neutrino oscillations are explained mainly by active-neutrino oscillations, with mass-squared differences $\Delta m^2_{\rm SOL}$ and $\Delta m^2_{\rm ATM}$, and the fourth neutrino state separated by $\Delta m^2_{\rm LSND}$ contains just a small component of the electron- and muon-neutrino flavours to account for the LSND signal. In contrast, the (2+2) spectrum is intrinsically different from the standard three-active-neutrino scenario as the sterile neutrino must take part dominantly either in solar- or in atmospheric-neutrino oscillations, or in both.

Neglecting CP violation, neutrino oscillations in four-neutrino schemes are generally described by 9 parameters: 3 mass-squared differences and 6 mixing angles. A convenient parameterisation has been introduced in reference [504], in terms of $\Delta m^2_{\rm SOL}$, $\theta_{\rm SOL}$, $\Delta m^2_{\rm ATM}$, $\theta_{\rm ATM}$, $\Delta m^2_{\rm LSND}$, and $\theta_{\rm LSND}$. These 6 parameters are similar to the two-neutrino mass-squared differences and mixing angles and are directly related to the oscillations in the solar, atmospheric, and LSND experiments. For the remaining 3 parameters one can use η_s, η_e and d_μ. These quantities are defined by:

$$\eta_\alpha = \sum_i |U_{\alpha i}|^2 \quad \text{with } i \in \text{solar mass states; and} \tag{175}$$

$$d_\alpha = 1 - \sum_i |U_{\alpha i}|^2 \quad \text{with } i \in \text{atmospheric mass states;} \tag{176}$$

where $\alpha = e, \mu, \tau, s$. Note that in (2+2) schemes the relation $\eta_\alpha = d_\alpha$ holds, whereas in (3+1) η_α and d_α are independent. The physical meaning of these parameters is the following: η_α is the fraction of ν_α participating in solar oscillations, and $(1 - d_\alpha)$ is the fraction of ν_α participating in oscillations with frequency $\Delta m^2_{\rm ATM}$ (for further discussions and details of the approximations adopted see reference [504]).

4.1.5.2 (2+2): ruled out by solar and atmospheric data

The strong preference for oscillations into active neutrinos in solar and atmospheric oscillations leads to a direct conflict in (2+2) oscillation schemes [505, 506]. Thanks to recent solar neutrino data (in particular from the SNO-salt phase [54]) in combination with the KamLAND experiment, and Super-Kamiokande data on atmospheric neutrinos the tension in the data has become so strong that (2+2) oscillation schemes are essentially ruled out. The left panel of figure 38 shows the $\Delta\chi^2$ from solar-neutrino data as a function of η_s, the parameter describing the fraction of the sterile-neutrino participating in solar-neutrino oscillations. It is clear from the figure that the improved determination of the neutral-current-event rate from the solar ^{8}B flux implied by the salt enhanced measurement in SNO [54] substantially tightened the constraint on a sterile contribution; the 99% C.L. bound improves from $\eta_s \leq 0.44$ for pre-SNO-salt to $\eta_s \leq 0.33$ at the 99% C.L. Although KamLAND on its own is insensitive to a sterile neutrino contamination, it contributes indirectly to the bound because of the better determination of $\Delta m^2_{\rm SOL}$. The combined analysis leads to the 99% C.L. bound:

$$\eta_s \leq 0.25 \qquad \text{(solar + KamLAND)}. \tag{177}$$

In contrast, in (2+2) schemes atmospheric data prefer values of η_s close to 1. From the combined analysis of Super-Kamiokande atmospheric data, K2K and short-baseline (SBL) [496, 507, 508] neutrino data one obtains the bound $\eta_s \geq 0.75$ at 99% C.L., in clear disagreement with the bound from solar data. The middle panel of figure 38 shows the $\Delta\chi^2$ for solar data and for atmospheric+K2K combined with SBL data as a function of η_s. Note that the main effect comes from atmospheric+K2K data; SBL experiments contribute only marginally, as may be seen from the dashed line. From this figure we also see that the 'solar+KamLAND' and the 'atm+K2K+SBL' allowed domains overlap only at $\chi^2_{\rm PC} = 17.2$, i.e. at the 4.1σ level. In the middle panel of figure 38, the 'global' $\bar{\chi}^2$ function defined as [509]:

$$\bar{\chi}^2(\eta_s) \equiv \Delta\chi^2_{\rm SOL+KAM}(\eta_s) + \Delta\chi^2_{\rm ATM+K2K+SBL}(\eta_s) \tag{178}$$

is shown. In references [502, 509] a statistical method to evaluate the disagreement of different data sets used in a global analysis has been proposed. The 'parameter goodness of fit' (PG) makes use of the $\bar{\chi}^2$ defined in equation (178). The result, $\chi^2_{\rm PG} \equiv \bar{\chi}^2_{\rm min} = 26.1$, corresponds to exclusion of (2+2) mass schemes at the 5.1σ level. Sub-leading effects beyond the approximations adopted in [67] should not affect this result significantly [510].

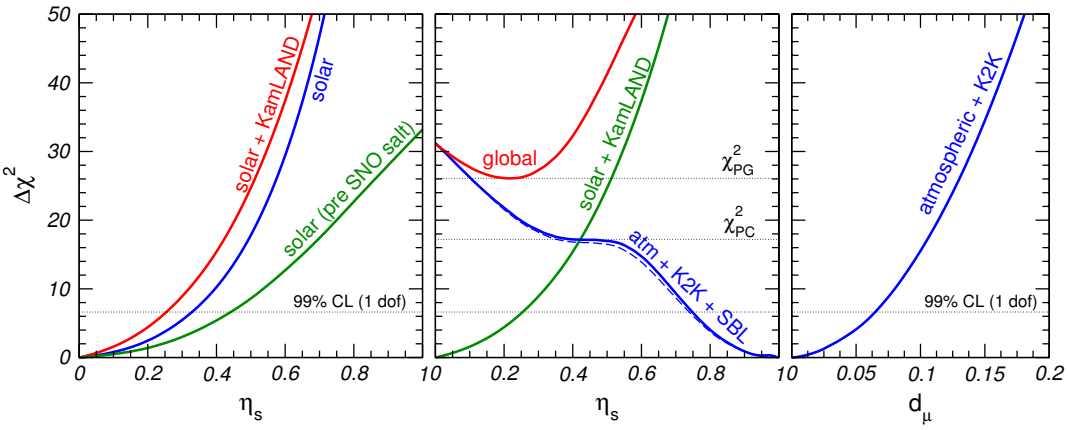

Figure 38: Left: $\Delta\chi^2$ as a function of η_s from solar data before the SNO salt-phase results, from current solar data, and from solar+KamLAND data. Middle: $\Delta\chi^2_{\rm SOL}$, $\Delta\chi^2_{\rm ATM+K2K+SBL}$ and $\bar{\chi}^2_{\rm global}$ as a function of η_s in (2+2) oscillation schemes. The dashed line corresponds to atmospheric and K2K data only (without SBL data). Right: $\Delta\chi^2_{\rm ATM+K2K}$ as a function of d_μ. Taken with kind permission of New Journal of Physics from figure 19 in reference [67]. Copyrighted by Deutsche Physikalische Gesellschaft & Institute of Physics.

4.1.5.3 (3+1): strongly dis-favoured by SBL data

It has been known for a long time that (3+1) mass schemes are dis-favoured by the comparison of SBL disappearance data [507, 508] with the LSND result [511–517]. The reason is that in (3+1) schemes the relation $\sin^2 2\theta_{\rm LSND} = 4\, d_e\, d_\mu$ holds, and the parameters d_e and d_μ (see equation (176)) are strongly constrained by ν_e and ν_μ disappearance experiments, leading to a double suppression of the LSND amplitude. In reference [514] it was shown that the up-down asymmetry observed in atmospheric μ events leads to an additional constraint on d_μ (see also reference [518]). The $\Delta\chi^2(d_\mu)$ from the fit to atmospheric+K2K data is shown in the right panel of figure 38, and one obtains the bound:

$$d_\mu \leq 0.065 \quad \text{at } 99\% \text{ C.L.} \tag{179}$$

Figure 39 shows the upper bound on the LSND oscillation amplitude, $\sin^2 2\theta_{\rm LSND}$, from the combined analysis of no-evidence (NEV) and atmospheric neutrino data [517]. Data from the Bugey [508], CDHS [507], KARMEN [496], and CHOOZ [519] experiments are included in the NEV data set; the NOMAD experiment [520] gives additional constraints in the region of high $\Delta m^2_{\rm LSND}$. From this figure one can see that the bound is incompatible with the signal observed in LSND at the 95% C.L. Only marginal overlap regions exist between the bound and global LSND data if both are taken at 99% C.L. Using only the decay-at-rest LSND data sample [497], the disagreement is even more severe. These results show that (3+1) schemes are strongly dis-favoured by SBL disappearance data.

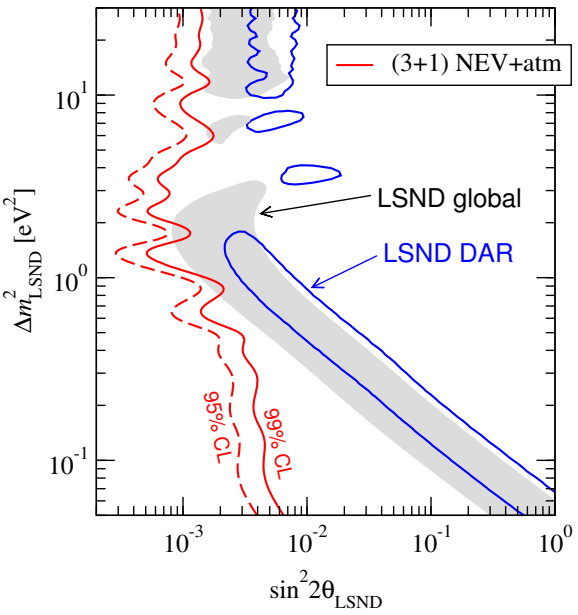

Figure 39: Upper bound on $\sin^2 2\theta_{\rm LSND}$ from NEV, atmospheric and K2K neutrino data in (3+1) schemes. The bound is calculated for each $\Delta m^2_{\rm LSND}$ using the $\Delta\chi^2$ for 1 dof Also shown are the regions allowed at 99% C.L. (2 dof) from global LSND data [188] and decay-at-rest (DAR) LSND data [497]. Taken with kind permission of New Journal of Physics from figure 20 in reference [67]. Copyrighted by Deutsche Physikalische Gesellschaft & Institute of Physics.

4.1.5.4 Global fit in four-neutrino schemes

The methods developed in [504] allow the oscillation data to be fit using the four-neutrino model. The result of such fits can be used to evaluate a goodness-of-fit statistic using the PG method [509], allowing the different hypotheses to be compared. The global oscillation data were divided into the four data sets SOL, ATM, LSND, and NEV and the PG method used to evaluate $\bar{\chi}^2$ [502]:

$$\begin{aligned} \bar{\chi}^2 &= \Delta\chi^2_{\rm SOL}(\theta_{\rm SOL}, \Delta m^2_{\rm SOL}, \eta_s) + \Delta\chi^2_{\rm ATM}(\theta_{\rm ATM}, \Delta m^2_{\rm ATM}, \eta_s, d_\mu) \\ &+ \Delta\chi^2_{\rm NEV}(\theta_{\rm LSND}, \Delta m^2_{\rm LSND}, d_\mu, \eta_e) + \Delta\chi^2_{\rm LSND}(\theta_{\rm LSND}, \Delta m^2_{\rm LSND})\,, \end{aligned} \tag{180}$$

where $\Delta\chi^2_X = \chi^2_X - (\chi^2_X)_{\rm min}$ (X = SOL, ATM, NEV, LSND), and $\bar{\chi}^2_{\rm min}$ is the minimum value of the $\bar{\chi}^2$. Table 6 shows the contributions of the four data sets to $\chi^2_{\rm PG} \equiv \bar{\chi}^2_{\rm min}$ for (3+1) and (2+2) oscillation schemes. As expected, the main contribution to $\chi^2_{\rm PG}$ in (3+1) schemes comes from SBL data due to the tension between LSND and NEV data in these schemes. For (2+2) oscillation schemes a large contribution to $\chi^2_{\rm PG}$ comes from solar and atmospheric data as discussed in Sec. 4.1.5.2. The contribution from NEV data in (2+2) comes mainly from the tension between LSND and KARMEN [497], which does not depend on the mass scheme. The parameter goodness of fit (PG) shown in the last column of table 6 is obtained by evaluating $\chi^2_{\rm PG}$ for four degrees of freedom [509]. This number of degrees of freedom corresponds to the four parameters $\eta_s, d_\mu, \theta_{\rm LSND}, \Delta m^2_{\rm LSND}$ describing the coupling of the different data sets.

The status of four-neutrino explanations of the LSND signal can be summarised as follows:

	SOL	ATM	LSND	NEV	$\chi^2_{\rm PG}$	PG
(3+1)	0.0	0.4	5.7	10.9	17.0	1.9×10^{-3} (3.1σ)
(2+2)	5.3	20.8	0.6	7.3	33.9	7.8×10^{-7} (4.9σ)

Table 6: Parameter goodness-of-fit (PG) and the contributions of different data sets to $\chi^2_{\rm PG}$ in (3+1) and (2+2) neutrino-mass schemes [67].

- Schemes of the (2+2) structure are ruled out at the $\sim 5\sigma$ level (PG of 7.8×10^{-7}) by the disagreement between the individual data sets. This result is very robust, independent of whether LSND is confirmed or disproved, and applies to all four-neutrino-mass models where two pairs of neutrino-mass states providing $\Delta m^2_{\rm SOL}$ and $\Delta m^2_{\rm ATM}$ are separated by a big mass gap;

- The explanation of the LSND effect within (3+1) schemes is dis-favoured at the $\sim 3\sigma$ level (PG of 0.19%). This result relies heavily on the null-result obtained from the SBL disappearance experiments Bugey and CDHS. Therefore, if the LSND appearance signal were to be confirmed by MiniBooNE, a (3+1) mass scheme should lead also to an observable signal for the ν_μ disappearance signal in MiniBooNE.

4.1.5.5 Five-neutrino oscillations

As a possible way out of the problems in four–neutrino schemes, a second sterile neutrino has been introduced in the analysis, and a five-neutrino mass scheme of the type (3+2) considered [68]. In a manner similar to the (3+1) scheme, the active neutrinos are contained mainly in the three lightest-mass states responsible for solar and atmospheric oscillations. the two states with masses in the eV range are available to explain the LSND effect. The disagreement between the data sets measured by the parameter goodness-of-fit is improved from 0.032% for the (3+1) scheme to 2.1% for the (3+2) scheme. The best fit point for the (3+2) scheme gives the mass-squared differences $\Delta m^2_{41} \simeq 0.9$ eV^2 and $\Delta m^2_{51} \simeq 22$ eV^2, but also solutions with only sub-eV masses are found [68].

Note that the possible conflicts of eV-scale sterile neutrinos with cosmology (see e.g. [521]), which already appear for four neutrinos, become more severe in the five-neutrino case and a non-standard cosmological model must be constructed. Moreover, the (3+2)-best-fit point found in [68] seems to be disfavoured also by atmospheric-neutrino data; as pointed out in [514], atmospheric neutrinos provide a constraint on the parameter d_μ (see equation (176)). In the (3+2) scheme this parameter is given by $d_\mu = |U_{\mu 4}|^2 + |U_{\mu 5}|^2$; with the best-fit values $U_{\mu 4} = 0.204$, $U_{\mu 5} = 0.224$ one obtains $d_\mu \approx 0.09$, in conflict with the bound given in equation (179) [68]. Figure 38 shows that this value of d_μ leads to a $\Delta\chi^2 \approx 12.5$ from atmospheric and K2K data, and hence is disfavoured at the 3.5σ level. Therefore, a re-analysis of the (3+2) scenario, including the constraint from atmospheric data, is required for this model to be considered viable.

4.1.5.6 Unconventional manifestations of leptonic-CP violation?

Neutrino models involving active/sterile neutrino mixing at the LSND [188] neutrino-mass-splitting scale via at least two sterile-neutrino states would open the possibility for further manifestations of leptonic-CP violation, including ones that could be measurable with neutrino-appearance experiments at short baselines [522].

For N neutrino species, there are, in general,$(N-1)$ independent mass splittings, $N(N-1)/2$ moduli of parameters in the unitary mixing matrix, and $(N-1)(N-2)/2$ Dirac CP-violating phases that may be observed in oscillations. In short-baseline (SBL) experiments that are sensitive only to $\nu_\mu \to \nu_{\not\mu}$, $\nu_e \to \nu_{\not e}$, and $\nu_\mu \to \nu_e$ transitions, the set of observable parameters is reduced considerably. First, oscillations due to atmospheric- and solar-mass splittings can be neglected or, equivalently, one can set $m_1 = m_2 = m_3$. Second, mixing-matrix elements that measure the τ-neutrino flavour fraction of the various neutrino mass eigenstates do not enter in the oscillation probability. In this case, the number of observable parameters is restricted to $(N-3)$ independent mass splittings, $2(N-3)$ moduli of mixing matrix parameters, and $(N-3)(N-4)/2$ CP-violating phases. Therefore, for the (3+2) sterile-neutrino models [68] that we wish to discuss here, that is for the $N = 5$ case, there are two independent mass splittings Δm^2_{41} and Δm^2_{51}, four moduli of mixing matrix parameters $|U_{e4}|$, $|U_{\mu 4}|$, $|U_{e5}|$, $|U_{\mu 5}|$, and one CP-violating phase. The convention used in the following for this CP-phase is:

$$\phi_{45} = arg(U^*_{\mu 5} U_{e5} U_{\mu 4} U^*_{e4}) \tag{181}$$

Under these assumptions, the relevant oscillation probabilities can be rewritten as:

$$P(\nu_\alpha \to \nu_\alpha) = 1 - 4[(1-|U_{\alpha 4}|^2 - |U_{\alpha 5}|^2)\cdot(|U_{\alpha 4}|^2 \sin^2 x_{41} + |U_{\alpha 5}|^2 \sin^2 x_{51}) + |U_{\alpha 4}|^2 |U_{\alpha 5}|^2 \sin^2 x_{54}] \text{ and} \tag{182}$$

$$\begin{aligned} P(\nu_\alpha \to \nu_\beta) = {} & 4|U_{\alpha 4}|^2 |U_{\beta 4}|^2 \sin^2 x_{41} + 4|U_{\alpha 5}|^2 |U_{\beta 5}|^2 \sin^2 x_{51} + \\ & 8|U_{\alpha 5}||U_{\beta 5}||U_{\alpha 4}||U_{\beta 4}| \sin x_{41} \sin x_{51} \cos(x_{54} + \phi_{45}) \end{aligned} \tag{183}$$

for $\alpha = \beta$ and $\alpha \neq \beta$, respectively. The formulas for antineutrino oscillations are obtained by substituting $\phi_{45} \to -\phi_{45}$.

We perform a combined analysis of SBL and atmospheric-neutrino data. The analysis uses the same seven SBL datasets as in reference [68], including results on ν_μ disappearance (from the CCFR84 [523] and CDHS [507] experiments), ν_e disappearance (from the Bugey [508] and CHOOZ [519] experiments), and $\nu_\mu \to \nu_e$ oscillations (from the LSND [188], KARMEN2 [496], and NOMAD [520] experiments). The assumptions used to describe SBL data are described in reference [68]. The atmospheric-neutrino constraints used in the analysis include 1489 days of Super-Kamiokande charged-current data [116], including the e-like and μ-like data samples of sub- and multi-GeV contained events, stopping events, and through-going upward-going muon events. The assumptions used to describe atmospheric data are described in Refs. [67, 524]. The atmospheric constraint also includes data on ν_μ disappearance from the long-baseline, accelerator-based experiment K2K [10].

Model	χ^2 $(d.o.f.)$	Δm^2_{41} (eV^2)	Δm^2_{51} (eV^2)	$\lvert U_{e4}\rvert$	$\lvert U_{\mu 4}\rvert$	$\lvert U_{e5}\rvert$	$\lvert U_{\mu 5}\rvert$	ϕ_{45}
CPC	141.4 (145)	0.92	24	0.132	0.158	0.066	0.159	0
CPV	140.8 (144)	0.91	24	0.127	0.147	0.068	0.164	1.8π

Table 7: Comparison of best-fit values for mass-splittings and mixing parameters for (3+2) CP-conserving and CP-violating models.

The purpose of this study is not only to determine what the allowed values of the SBL CP-violation phase ϕ_{45} are from existing SBL+atmospheric data, but also what the oscillation appearance probabilities in neutrino and anti-neutrino running modes are to be expected in the MiniBooNE experiment at Fermilab [525], in the context of (3+2) sterile neutrino models, and allowing for the possibility of CP violation. The MiniBooNE experiment took data in neutrino running mode between September 2002 and January 2006, at which point the experiment started its ongoing anti-neutrino run. Realistic estimates of the oscillation probabilities to be expected at MiniBooNE are used in the analysis, based on neutrino flux and cross-section expectations provided by the MiniBooNE Collaboration. In particular, the effect of "wrong sign" neutrinos in computing the expected oscillation probabilities, which have the effect of washing out CP-violating observables, is taken into account. This effect is non-negligible since as much as one third of the total interaction rate in anti-neutrino running mode is expected to be due to neutrinos rather than anti-neutrinos; on the other hand, the anti-neutrino contribution in neutrino running mode is expected to be much smaller.

From the upcoming MiniBooNE appearance measurements in neutrino and anti-neutrino running modes, the following CP-asymmetry observable, A_{CP}, could be extracted:

$$A_{CP} = \frac{p_{\rm BooNE} - \bar{p}_{\rm BooNE}}{p_{\rm BooNE} + \bar{p}_{\rm BooNE}} \, , \tag{184}$$

where we have defined the oscillation probability in neutrino (anti-neutrino) running mode as:

$$\overset{(-)}{p}_{BooNE} = \frac{\int dE \; [p(\nu_\mu \to \nu_e) \; \overset{(-)}{N_0}(\nu) + p(\bar{\nu}_\mu \to \bar{\nu}_e) \; \overset{(-)}{N_0}(\bar{\nu})]}{\int dE \; [\overset{(-)}{N_0}(\nu) + \overset{(-)}{N_0}(\bar{\nu})]} \, , \tag{185}$$

where E is the neutrino energy; $p(\nu_\mu \to \nu_e)$ and $p(\nu_{\bar{\mu}} \to \nu_{\bar{e}})$ are the oscillation probabilities given by equation (183), with $\phi_{45} = 0$ or π for the CP-conserving case, and $0 < \phi_{45} < 2\pi$ for the CP-violating case; $N_0(\nu)$ and $N_0(\bar{\nu})$ are the MiniBooNE neutrino and anti-neutrino full-transmutation rate distributions in neutrino-running mode (that is, muon neutrino and anti-neutrino fluxes multiplied by electron-neutrino and anti-neutrino cross-sections), and $\bar{N}_0(\nu)$ and $\bar{N}_0(\bar{\nu})$ are the neutrino and anti-neutrino full-transmutation rate distributions in anti-neutrino-running mode.

The main results of this study are given in table 7, and in figures 40 and 41. Table 7 shows the best-fit model parameters for CP-conserving and CP-violating (3+2) sterile neutrino models; figure 40 shows the oscillation probabilities to be expected at MiniBooNE in neutrino and anti-neutrino running modes (equation (185)), in a CP-violating, (3+2) scenario; and figure 41

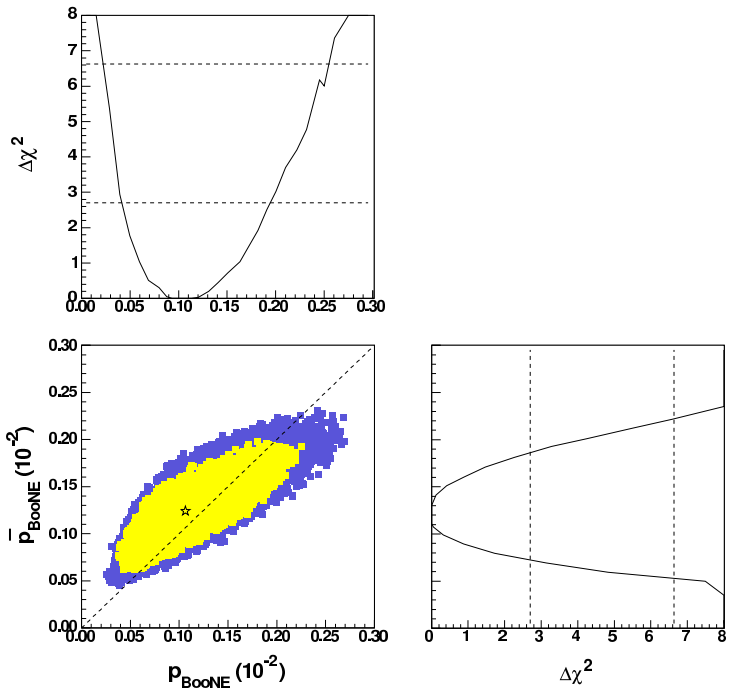

Figure 40: Expected oscillation probabilities at MiniBooNE in neutrino and anti-neutrino running modes, for CP-violating (3+2) models. The yellow (light grey) region corresponds to the 90% CL allowed region; the blue (dark grey) region corresponds to the 99% CL allowed region. Taken with kind permission of Physical Review from figure 4 in reference [522]. Copyrighted by the American Physical Society.

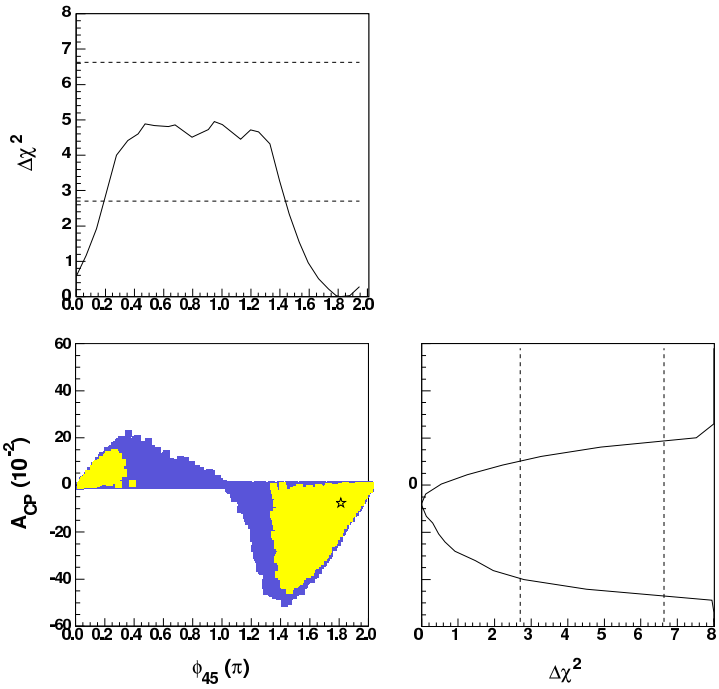

Figure 41: Current limits on the CP-violating phase ϕ_{45} from current short-baseline results, and CP asymmetry measurement expected at MiniBooNE, A_{CP}, as a function of ϕ_{45}. The yellow (light grey) region corresponds to the 90% CL allowed region; the blue (dark grey) region corresponds to the 99% CL allowed region. Taken with kind permission of Physical Review from figure 5 in reference [522]. Copyrighted by the American Physical Society.

shows the ϕ_{45} values (equation (181)) allowed by current SBL+atmospheric constraints, and the corresponding CP asymmetries expected at MiniBooNE (equation (184)), in this same scenario.

The results shown can be summarised as follows. First, we find that CP-violating, (3+2) models do not provide a significantly better description of short-baseline and atmospheric data, compared to CP-conserving, (3+2) models. On the other hand, even if only a small degree of CP violation is marginally preferred, we also find that existing data allow for all possible values for the single CP-violating phase that could be observed at short baselines in (3+2) models, at 99% C.L.. Finally, if leptonic-CP violation occurs and (3+2) sterile-neutrino models are a good description of the data, we find that differences as large as a factor of three between the electron (anti-)neutrino appearance probabilities in neutrino and anti-neutrino running modes at MiniBooNE, corresponding to $A_{CP} = -0.5$ in equation (184), are possible.

4.1.5.7 More exotic explanations of LSND

In view of these difficulties in finding an explanation of the LSND result, several alternative mechanisms have been proposed. Some of the proposed mechanisms involve speculative process such as: non-standard neutrino interactions; violation of CPT invariance; violation of Lorentz invariance; quantum decoherence; or mass-varying neutrinos [526]. Many of the proposed mechanisms are unable to accommodate all of the evidence for neutrino oscillations as well as the constraints from the NEV experiments. Mechanisms which seem to be in agreement with all present data are: the four-neutrino mass scheme plus CPT violation [527]; a model based on sterile neutrinos and large-extra dimensions [528]; and a model with a decaying sterile neutrino [529].

In reference [527], a four-neutrino scheme similar to (3+1) is considered. However, this model allows for different mixing matrices for neutrinos and anti-neutrinos, violating CPT invariance and therefore avoiding the constraints imposed by the NEV experiments. In reference [528], a new resonance effect is introduced by assuming 'short-cuts' for sterile neutrinos through rather particular extra dimensions. In contrast to such relatively exotic ideas, the scenario proposed in reference [529] involves a comparably 'modest amount' of non-standard physics. In this model a heavy neutrino, n_4, is introduced, with a small mixing with muon neutrinos of $|U_{\mu 4}|^2 \sim 0.01$, such that a small n_4 component is contained in the initial $\bar{\nu}_\mu$ beam produced in the LSND experiment. The n_4 decays into a scalar particle and a light neutrino, predominantly of the electron type, accounting in this way for the $\bar{\nu}_e$ appearance in LSND. Values of $gm_4 \sim$ few eV are required, where g is the neutrino-scalar coupling constant and m_4 is the heavy-neutrino mass. For example, one can take m_4 in the range from 1 keV to 1 MeV and $g \sim 10^{-6}$–10^{-3}, consistent with various bounds on such couplings. Unlike the case of (3+1) four-neutrino oscillation schemes, the decay model is in complete agreement with the constraints from SBL disappearance experiments. Testing the compatibility of LSND and all the null-result experiments, one finds a parameter goodness-of-fit PG = 4.6% for decay, which is slightly better than the PG = 2.1% obtained in reference [68] for the (3+2) five-neutrino oscillation scenario.

4.2 Mass Varying Neutrinos

Abundant cosmological data indicate that the expansion of our Universe is in an accelerating phase caused by a negative-pressure component called dark energy. Dark energy is troubling because the acceleration of the Universe is a very recent phenomenon in its expansion history. This 'cosmic coincidence' problem can be expressed as follows: why are the dark-matter and dark-energy densities comparable today, even though their ratio scales as $\sim 1/a^3$ (where a is the scale factor)? The coincidence that the scale of dark energy $(2 \times 10^{-3}$ eV$)^4$ is similar to the scale of the neutrino mass-squared difference squared ($[0.01$ eV$^2]^2$) was exploited recently to solve the coincidence problem [530]. The assumption was made that neutrinos couple to dark energy by in such a way as to make the dark-energy density a function of neutrino mass. The total energy density of neutrinos and dark energy was assumed to be constant, i.e. to be independent of neutrino mass. Under these assumptions, changes in the neutrino-energy density and the dark-energy density are correlated. Over a wide range of values of a, neutrino masses must vary so as to allow the total energy density remains constant.

A simple way to make the dark-energy density neutrino-mass dependent is to introduce a Yukawa coupling between a sterile neutrino, s, and a light, scalar field, ϕ, called the acceleron. At scales below the sterile-neutrino mass, a Lagrangian of the form:

$$\mathcal{L} = m_D \nu s + \lambda \phi s s + V_0(\phi)\,, \tag{186}$$

where ν is a Standard Model left-handed neutrino, leads to an effective potential for the acceleron (if neutrinos are non-relativistic) given by:

$$V = \frac{m_D^2}{\lambda \phi} n_\nu + V_0(\phi)\,. \tag{187}$$

Thus, the effective potential of the acceleron at late times receives a contribution equal to $m_\nu n_\nu$, where $m_\nu = m_D^2/(\lambda\phi)$ and n_ν are the active-neutrino mass and number density, respectively. More elaborate supersymmetric models of neutrino dark energy have been constructed in [531, 532].

Model-independent tests of neutrino dark energy are cosmological [530,533]. A strict relationship between the equation of state of the combined dark-energy neutrino fluid $w = p_{\rm nde}/\rho_{\rm nde}$ (where nde denotes neutrino dark energy) and neutrino mass is predicted to be [530]:

$$w = -1 + \frac{m_\nu n_\nu}{V}\,. \tag{188}$$

Further, since neutrino masses are predicted to scale with redshift approximately as a^3 in the non-relativistic regime, cosmological and terrestrial probes of neutrino mass could give conflicting results.

It has been argued that it is natural to expect couplings of the acceleron to quarks and charged leptons to be generated radiatively [534]. Moreover, Yukawa couplings of the acceleron to visible matter could be low energy manifestations of non-renormalisable operators arising

from quantum gravity. If the acceleron couples both to neutrinos and matter, it may be possible to investigate this scenario through neutrino oscillations [534, 535]. However, the coupling to matter is model-dependent. The effective neutrino mass in matter is altered by the interactions of the scalar which in turn modifies neutrino oscillations.

At low redshifts, the contribution to neutrino mass caused by the interactions of the acceleron with electrons and neutrinos is of the form [536]:

$$M = \frac{\lambda_\nu}{m_\phi^2}(\lambda_e n_e + \lambda_\nu(n_\nu^{C\nu B} + \frac{m_\nu}{E_\nu} n_\nu^{rel}))\,, \tag{189}$$

where λ_ν (λ_e) is the Yukawa coupling of the acceleron to the neutrino (the electron). In principle, ϕ has a mass, m_ϕ, that depends on n_e and the n_ν. This dependence is weak since the underlying assumption that has been made in obtaining equation (189) is that ϕ evolves adiabatically and remains at the minimum of its potential. The number density of the cosmic neutrino background in one generation of neutrinos and anti-neutrinos is $n_\nu^{C\nu B} \sim 112$ cm$^{-3} \sim 10^{-12}$ eV^3, the number density of relativistic neutrinos in the background frame is n_ν^{rel}, and the electron number density is n_e. We emphasise that m_ν is the neutrino mass in a background-dominated environment.

In terrestrial environments, and even for applications to solar neutrinos, the dominant contribution to the mass shift arises from the $\lambda_e n_e$ term. In this case, one can adopt a matter dependence of the form [536]:

$$M(n_e) = M^0 \left(\frac{n_e}{n_e^0}\right)^k\,, \tag{190}$$

where M^0 is the value at some reference density, n_e^0, and k parametrises a power-law dependence of the neutrino mass on density. In principle, M is expected to depend linearly on n_e, but, phenomenologically, one may allow k to deviate from unity. The choice of reference density is arbitrary. If the environment that neutrinos traverse has a constant density (e.g for passage through the earth's crust), then that density could be taken to be the reference density. If neutrino propagation is adiabatic (as in the sun), the reference density could be taken to be the density at which the neutrinos are produced. Implicit in the form of equation (190) is the assumption that the neutrino number density has a negligible effect on neutrino masses. Thus, it applies only in the current epoch when the cosmic neutrino background number density ($\mathcal{O}(10^{-12})$ eV^3) is tiny. At earlier epochs, the neutrino number density is orders of magnitude larger and must be taken into account. For example, in the era of Big Bang Nucleosynthesis (BBN), the neutrino number density is $\mathcal{O}(10^{30})$ eV^3. For the compatibility of mass-varying neutrinos (MaVaNs) with BBN see [537].

A simplifying assumption is that the heaviest neutrino has a mass of $\mathcal{O}(0.05)$ eV in the present epoch. As a result of their non-negligible velocities, the neutrino 'over-density' in the Milky Way from gravitational clustering can be neglected [538]. Then m_ν represents the masses of terrestrial neutrinos in laboratory experiments such as those measuring tritium beta decay. Note that cosmological bounds on the sum of neutrino masses of $\mathcal{O}(1)$ eV are inapplicable to MaVaNs. Consequently, the usual relationship between neutrino dark matter and neutrinoless

double beta decay is also rendered inapplicable [539]. Moreover, it was pointed out that if the acceleron couples to highly non-relativistic neutrino eigenstates, neutrino dark energy is unstable [540, 541]. The assumption that the background neutrino masses are small circumvents this instability problem.

For such light neutrinos, only model-dependent (neutrino oscillation) tests of the MaVaN scenario are viable because the model-independent (cosmological) tests become inoperable. There are two reasons for this:

- The effects of dark energy and a cosmological constant are almost the same in today's Universe; and
- If the light neutrinos do not cluster sufficiently, the local neutrino mass is the same as the background value, below the sensitivity of tritium beta-decay experiments. In this case, the high-redshift cosmological data (which should show no evidence for neutrino mass) and the data from tritium beta-decay experiments will be consistent.

It has been shown that oscillations of mass-varying neutrinos (that result in exotic matter effects of the same size as standard matter effects) lead to an improved agreement (relative to conventional oscillations) with solar-neutrino data while remaining compatible with KamLAND, CHOOZ, K2K, and atmospheric data [536]. MaVaN oscillations are perfectly compatible with solar data because the survival probability can change from a higher-than-vacuum value (at low energies) to $\sin^2\theta$ (at high energies) over a very narrow range of energies as shown in figure 42. An analysis of solar and KamLAND data concludes that the fit in the LMA-II region is improved; while the region is excluded at more than the 4σ C.L. in the standard oscillation analysis, it is allowed at the 98.9% C.L. for MaVaN oscillations [542].

Whether or not an explanation of solar-neutrino data requires MaVaN oscillations will be answered by experiments that will measure the survival probability of MeV and lower energy neutrinos. As shown in reference [545], other tests in reactor and long-baseline experiments emerge when the above scheme is embedded in a comprehensive model that can explain all the available neutrino-oscillation data, including the LSND anomaly, and a null MiniBooNE result. This model requires large values of $\sin^2 2\theta_{13}$ in the range $0.10 \lesssim \sin^2 2\theta_{13} \lesssim 0.30$. Such values are not inconsistent with the CHOOZ reactor constraint on $\bar{\nu}_e \to \bar{\nu}_e$ oscillations at the atmospheric scale ($L/E_\nu \simeq 250$ m/MeV) since the neutrino path in CHOOZ was primarily in air. The relevant limit is that provided by Palo Verde for which the neutrino path was through the ground; the Palo Verde limit is significantly weaker than that provided by CHOOZ. Such large values of $\sin^2 2\theta_{13}$, are likely to be measured in experiments such as Angra, Daya Bay, or KASKA for which most of the neutrino path is underground [546, 547]. These experiments will be sensitive to θ_{13} for $\sin^2 2\theta_{13} \geq 0.01$. However, Double-CHOOZ [196, 548], which should be sensitive to $\sin^2 2\theta_{13} \geq 0.03$, would see a null result since most of the neutrino path is in air. The MINOS experiment which is sensitive to $\sin^2 2\theta_{13} \geq 0.05$ at the 90% C.L. [549], should also see a positive signal in the $\nu_\mu \to \nu_e$ appearance channel.

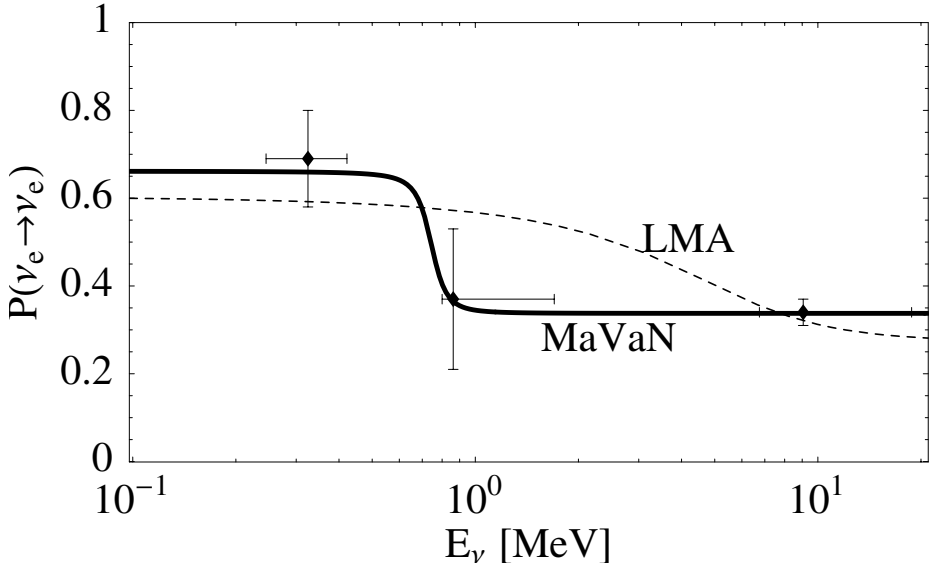

Figure 42: $P(\nu_e \to \nu_e)$ vs. E_ν for MaVaN oscillations (solid curve). The dashed curve corresponds to conventional oscillations with the best-fit solution to KamLAND data. The data points and the procedure to extract them can be found in [543, 544]. Taken with kind permission of Physical Review Letters from figure 2 in reference [536]. Copyrighted by the American Physical Society. Taken from reference [536].

The idea of using reactor experiments with different fractions of air and earth matter along the neutrino path to study MaVaN oscillations has been further explored in [550]. For $\sin^2 2\theta_{13} \gtrsim 0.04$, two reactor experiments with baselines of at least 1.5 km, one of which passes predominantly through air, the other through the earth, can constrain an oscillation effect which is different in air and matter at the level of a few percent. Neutrino super-beam experiments may probe mass-varying neutrinos in a controlled environment if the effects are large enough. It is worth investigating the sensitivity of long-baseline experiments to non-standard matter effects in MaVaN oscillations. A preliminary analysis can be found in reference [551].

4.3 CPT and Lorentz invariance violation

CPT, the product of charge conjugation, parity, and time reversal is one of the most fundamental symmetries in nature. CPT invariance has a number of profound implications; for example, it guarantees that the mass of particle and anti-particle are equal. Though there is no experimental evidence of CPT-invariance violation (CPTV), the presence of a small violation is compatible with all current data. On the other hand, CPTV and/or Lorentz-invariance violation (LIV) can arise in string theories [552–555]. CPTV is closely related to LIV and it has been shown that CPTV necessarily implies LIV [556].

The phenomenological consequences of CPTV and LIV in neutrino oscillations have been widely discussed [503, 527, 557–562, 562–565, 565, 566, 566, 567, 567–573]. In some cases, the phenomenological implications of the violation of the Equivalence Principle (EPV) in neutrino oscillations [574–578] is identical to that of LIV and therefore the two can be treated in a similar

fashion [579].

One of the possible implications of CPTV is that the masses and/or the mixings of neutrinos can be different from those of anti-neutrinos. In this case, oscillation probabilities for neutrinos would differ from those for anti-neutrinos even in the absence of CP violation or matter effects. CPTV has been suggested to reconcile LSND results with solar- as well as atmospheric-neutrino observations in the framework of three neutrino flavours [503, 558, 559]. Atmospheric neutrinos probe oscillations for both neutrino and anti-neutrino channels (though the contribution from neutrinos is dominant) whereas solar neutrinos probe only the neutrino channel. As a result, once CPTV is allowed solar and atmospheric oscillations can be described in terms of two mass squared differences $\Delta m^2_{\odot}$ and $\Delta m^2_{\rm atm}$ whereas atmospheric and LSND anti-neutrino oscillations were driven by $\Delta m^2_{\rm atm}$ and $\Delta m^2_{\rm LSND}$. However, in view of the KamLAND results [8, 55], this scenario is strongly dis-favoured, since KamLAND data are compatible with anti-neutrino oscillations also characterised by $\Delta m^2_{\odot}$ [561, 580].

In the presence of LIV, the maximum velocity which a particle can attain may differ from particle to particle. For neutrinos the implication could be that velocity is dependent on flavour. Mixing between flavour and velocity eigenstates will then lead to neutrino oscillations even if neutrinos are massless [570]. The possibility of resonant conversions in the massless-neutrino limit was first noted in the context of theories where neutrinos have non-standard interactions [581]. In such cases both the physics and the signatures are different from those expected when Lorentz invariance is violated [582].

4.3.1 Direct bounds on CPTV

Without assuming any underlying model, CPTV can be constrained by comparing the mixing parameters for neutrinos and anti-neutrinos [583]. The current bound on the difference between $\sin^2\theta_{12}$ for neutrino and $\sin^2\bar{\theta}_{12}$ for antineutrinos is rather weak [8, 55]. Even if it is assumed that $\bar{\theta}_{12}$ is in the first octant, $|\sin^2\theta_{12} - \sin^2\bar{\theta}_{12}| \lesssim 0.3$ at the 99.73% C.L. For mass-squared differences, the current bound [569] is $|\Delta m^2_{21} - \Delta\bar{m}^2_{21}| \leq 1.1\times10^{-4}\text{eV}^2$ at 99.73% C.L., where $\Delta\bar{m}^2_{21}$ is the mass squared difference of antineutrinos. For comparison, the bound on the difference between the neutrino and antineutrino θ_{23} mixing angle is $-0.41 \leq \sin^2\theta_{23} - \sin^2\bar{\theta}_{23} \leq 0.45$ [524] at the 99.73% C.L. level. For Δm^2_{32} there are two results: one from the Super-Kamiokande collaboration -1.9×10^{-2} eV$^2 \leq |\Delta m^2_{32}| - |\Delta\bar{m}^2_{32}| \leq 4.8\times10^{-3}$ eV^2 [584]; and the other from Gonzalez-Garcia et al. -10^{-2} eV$^2 \leq \Delta m^2_{32} - \Delta\bar{m}^2_{32} \leq 3.4\times10^{-3}$ eV^2 [524]; both at the 99.73% C.L. level.

4.3.2 CPTV/LIV Effect on conversion probability

Oscillations between two flavours, for example, between ν_μ and ν_τ in the presence of CPTV or LIV, can be described by the Hamiltonian [555, 585]:

$$\mathrm{H} \equiv \frac{\Delta m^2}{4E} \boldsymbol{U}_\theta \begin{pmatrix} -1 & 0 \\ 0 & 1 \end{pmatrix} \boldsymbol{U}_\theta^\dagger + \frac{\eta\, E^n}{2} \boldsymbol{U}_{\xi,\varphi} \begin{pmatrix} -1 & 0 \\ 0 & 1 \end{pmatrix} \boldsymbol{U}_{\xi,\varphi}^\dagger \,, \tag{191}$$

where Δm^2 is the mass-squared difference between the two neutrino mass eigenstates, η parametrises the size of the CPTV or LIV effect. Here, n is an integer where $n = 0$ corresponds to CPTV and LIV, $n = 1$ to LIV or EPV. The matrices $\boldsymbol{U}_\theta$ and $\boldsymbol{U}_{\xi,\varphi}$ are given by:

$$\boldsymbol{U}_\theta = \begin{pmatrix} \cos\theta & \sin\theta \\ -\sin\theta & \cos\theta \end{pmatrix} , \qquad \boldsymbol{U}_{\xi,\varphi} = \begin{pmatrix} \cos\xi & \sin\xi e^{\pm i\varphi} \\ -\sin\xi e^{\mp i\varphi} & \cos\xi \end{pmatrix} , \tag{192}$$

where φ is the non-vanishing relative phase. Note that $n = 0$ may also corresponds to the non-standard interaction case described in [581, 582].

If the CPTV or LIV strength is constant along the neutrino trajectory the survival probability takes the form [555, 585]:

$$P_{\nu_\mu \to \nu_\mu} = 1 - P_{\nu_\mu \to \nu_\tau} = 1 - \sin^2 2\Theta \, \sin^2 \left(\frac{\Delta m^2 L}{4E} \mathcal{R} \right) , \tag{193}$$

with

$$\sin^2 2\Theta = \frac{1}{\mathcal{R}^2} \left(\sin^2 2\theta + R_n^2 \sin^2 2\xi + 2R_n \sin 2\theta \sin 2\xi \cos\varphi \right) , \tag{194}$$

$$\mathcal{R} = \sqrt{1 + R_n^2 + 2R_n \left(\cos 2\theta \cos 2\xi + \sin 2\theta \sin 2\xi \cos\varphi \right)} \,, \tag{195}$$

$$R_n = \frac{\eta E^n}{2} \frac{4E}{\Delta m^2} \,, \tag{196}$$

where, for simplicity, CPTV or LIV scenarios which can be characterised by a unique parameter η have been assumed.

The $n = 0$ case can lead to CPTV and LIV by identifying $\eta = b_1 - b_2$ where the b_i are the eigenvalues of the Lorentz-violating CPT-odd operator [554, 555, 557]. The $n = 1$ case can lead to LIV by identifying $\eta = c_1 - c_2$ where the c_i are the maximal attainable velocities of ν_i [570]. This case is phenomenologically equivalent to EPV [579] for the constant gravitational potential through the identification $\eta = 2|\phi|(\gamma_1 - \gamma_2)$ where ϕ is the gravitational potential, assumed to be constant, and γ_i is the coupling of neutrinos to gravity [574, 575].

Atmospheric neutrino data can be used to constrain the possible CPTV, LIV, or EPV effects. For example, the following limits were derived in [524, 585]:

$$\eta = b_1 - b_2 \equiv \delta b \leq 5.0 \times 10^{-23} \text{ GeV} \,, \qquad \text{for CPTV, LIV } (n = 0) \tag{197}$$

$$\eta = (c_1 - c_2) \equiv \delta c/c \leq 1.6 \times 10^{-24} \,, \qquad \text{for VLI } (n = 1) \tag{198}$$

$$\eta = 2|\phi|(\gamma_1 - \gamma_2) \equiv 2|\phi|\Delta\gamma \leq 1.6 \times 10^{-24} \,, \qquad \text{for EPV } (n = 1) \tag{199}$$

4.3.3 Future Prospects

The bounds on the CPTV differences between neutrino and anti-neutrino mixing parameters at a future Neutrino Factory have been studied for a muon-beam energy of 50 GeV and a baseline of 7000 km [564]. Assuming a 10 kT detector and 10^{20} muon decays per year leads to the following bounds:

$$\frac{||\Delta m^2_{32}| - |\bar{\Delta m^2_{32}}||}{\frac{1}{2}(|\Delta m^2_{32}| + |\bar{\Delta m^2_{32}}|)} \lesssim 8 \times 10^{-3}\,; \text{and} \tag{200}$$

$$\frac{|\theta_{23} - \bar{\theta}_{23}|}{\frac{1}{2}(\theta_{23} + \bar{\theta}_{23})} \lesssim 4.2 \times 10^{-2}\,. \tag{201}$$

The bound on the CPTV effect is determined by the parameter δb through oscillation. For oscillation experiments with baselines shorter than ~ 1000 km and energy $\sim 1 - 2$ GeV, such as T2K [13] and NOvA [16], the existing bounds described in the previous section will not be improved. On the other hand, future neutrino-oscillation experiments at the Neutrino Factory with longer baseline, $L \gtrsim 3000$ km, and higher energy, $\langle E \rangle > 10$ GeV, are expected to improve the present bounds. Reference [557] estimates that the sensitivity on δb can be as small as $\sim 10^{-23}$ GeV for $L = 2900$ km for a 10 kt detector and 10^{19} muon decays.

4.4 Leptonic unitarity triangle and CP-violation

In the quark sector, the unitarity triangle has proved to be a very useful representation of mixing and CP-violation. Similarly, in the lepton sector, the unitarity triangle provides a convenient framework for a variety of analyses including: analysing the experimental results on lepton mixing; testing the unitarity of the mixing matrix and searching for new neutrino states; establishing the violation of the CP invariance and measuring the Dirac CP-violating phase δ; and searching for effects of new interactions of neutrinos.

In the following it will be assumed that there are only three neutrinos so that mixing may be described using a 3×3 unitarity matrix. In the standard parametrisation, $U = U_{23} I_\delta U_{13} I_\delta^\dagger U_{12}$, where U_{ij} are rotation matrices in the ij-plane, and $I_\delta \equiv \text{diag}(1, 1, e^{i\delta})$. The unitarity condition $UU^\dagger = I$ leads to three 'row equalities', $U_{\alpha i} U^*_{\beta i} = 0$, $\alpha \neq \beta$, or explicitly:

$$\begin{aligned} &U_{e1}U^*_{\mu 1} + U_{e2}U^*_{\mu 2} + U_{e3}U^*_{\mu 3} = 0, && (a)\\ &U_{e1}U^*_{\tau 1} + U_{e2}U^*_{\tau 2} + U_{e3}U^*_{\tau 3} = 0, && (b)\\ &U_{\tau 1}U^*_{\mu 1} + U_{\tau 2}U^*_{\mu 2} + U_{\tau 3}U^*_{\mu 3} = 0. && (c) \end{aligned} \tag{202}$$

In the complex plane, each term from the sums in equation (202) represents a vector. Equations (202) imply that the three terms appearing in each equation form a triangle, known as a 'unitarity triangle'. The expressions (202) also reflect the orthogonality of the flavour states; the corresponding triangles are called the flavour triangles, for example, equation (202)a describes the $e\mu$-triangle. The sides of triangle can be then enumerated by the mass eigenstates:

$$z_i \equiv U_{\alpha i} U^*_{\beta i}. \tag{203}$$

The unitarity condition $U^\dagger U = I$ leads to the 'column equalities' $\sum_\alpha U_{\alpha i} U^*_{\alpha j} = 0$, (for $i \neq j$). These equations also define triangles known as the mass state triangles.

The shape and area of the triangles are closely related to CP-violation in leptonic mixing. Indeed, the Dirac CP-violating phase vanishes if and only if the phases of all elements of the mixing matrix are factorisable: $U_{\alpha i} = e^{i(\sigma_\alpha + \gamma_i)}|U_{\alpha i}|$. In this case, $U_{\alpha i} U^*_{\beta i} = e^{i(\sigma_\alpha - \sigma_\beta)}|U_{\alpha i}||U_{\beta i}|$ and therefore the unitarity triangles shrink to segments. Recall that the CP-violating effects are determined by the Jarlskog invariant:

$$J_{CP} = \mathrm{Im}[U_{\alpha i} U^*_{\beta i} U^*_{\alpha j} U_{\beta j}] \,, \tag{204}$$

which in the standard parametrisation is given by:

$$J_{CP} = s_{12} c_{12} s_{23} c_{23} s_{13} c^2_{13} \sin\delta, \tag{205}$$

where $s_{12} \equiv \sin\theta_{12}$, etc. In particular, the invariant determines the CP-asymmetries in neutrino oscillations, $P(\bar\nu_\alpha \to \bar\nu_\beta) - P(\nu_\alpha \to \nu_\beta) \propto J_{CP}$. The area of the triangle, S, is related to the Jarlskog invariant. For the flavour triangle:

$$S = \frac{1}{2}|U_{\alpha i} U^*_{\beta i}||U_{\alpha j} U^*_{\beta j}| \sin\phi_{ij} \,, \tag{206}$$

where ϕ_{ij} is the angle between the sides i and j. Equations (204) and (206) can be combined to give:

$$S = \frac{1}{2} J_{CP}. \tag{207}$$

The relation 207 is the basis of the unitarity triangle method for measuring the CP-violating phase [586,587]. Reconstructing the unitarity triangle is an alternative to the direct measurement of the CP-asymmetries in transition probabilities $P(\bar\nu_\alpha \to \bar\nu_\beta) - P(\nu_\alpha \to \nu_\beta)$ [588–593].

4.4.1 Properties of the leptonic triangles

For very small 13 mixing, $\sin\theta_{13} \ll 0.15$, the unitarity triangles are of two forms:

- Triangles that include the element U_{e3} and therefore have one small side and two nearly equal sides: e.g., the $e\mu$-triangle in which $|z_1| \approx |z_2|$ and $|z_3| \approx s_{13}/\sqrt{2}$; and
- Triangles that do not include the U_{e3} element: e.g., the $\mu\tau$-triangle for which $|z_1| \approx 1/6 + O(s_{13})$, $|z_2| \approx 1/3$ and $|z_3| \approx -1/2 + O(s_{13})$.

For s_{13} saturating its upper bound, $s_{13} \sim 0.15$, the sides of the triangle can be of the same size.

Figure 43 shows examples of the $e\mu$-triangle constructed for $s_{12} = 0.56$, $s_{23} = 0.67$ (the best-fit values), $s_{13} = 0.15$, and for three different values of the CP-violating phase. The horizontal side is normalised to 1. Each scatter point represents the possible position of vertex if the

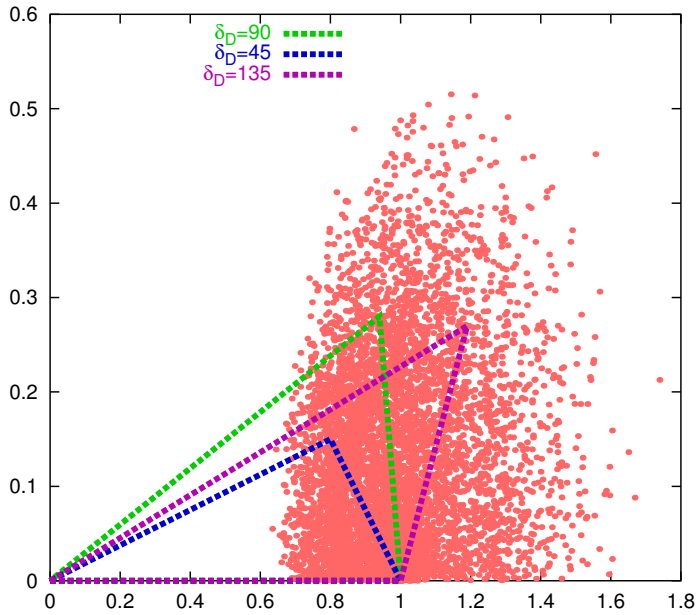

Figure 43: The unitarity $e\mu$-triangles. The horizontal side, $|U_{e1}U^*_{\mu 1}|$ is normalised to one. The triangles correspond to $s_{13} = 0.15$ and different values of δ. Each scatter point represents a possible position of vertex as the mixing parameters pick up random values within the present uncertainty ranges: $\sin^2\theta_{23} \in [0.36, 0.61]$, $\sin^2\theta_{12} \in [0.27, 0.37]$ and $\sin^2\theta_{13} \in [0, 0.031]$ and $\delta \in [0, 2\pi]$

values of mixing parameters pick up different values within the present uncertainty ranges: $\sin^2\theta_{23} \in [0.36, 0.61]$, $\sin^2\theta_{12} \in [0.23, 0.37]$ and $\sin^2\theta_{13} \in [0, 0.031]$ and δ varies between 0 and 2π. Some scatter points lie on the horizontal axis. This reflects the fact that with the present data it is not possible to establish CP-violation. Notice that despite the fact that s_{13} is relatively small, for a considerable portion of the scatter points, the sizes of the all three sides of the triangle are comparable. The triangles can take a particular form if the mass matrix, and consequently the mixing matrix, have a certain symmetry. The $\mu - \tau$ reflection symmetry defined as $\nu_\mu \to \nu^c_\tau$, $\nu_\tau \to \nu^c_\mu$, where the superscript c denotes the C-conjugation [594,595], leads to isosceles column-based triangles and congruent row-based $e\tau$- and $e\mu$-triangles.

4.4.2 Leptonic triangles and coherence of neutrino states

The charged-current (CC) coupling of neutrino mass eigenstate, ν_i, and the charged lepton, α, is given by $U_{\alpha i}$. As a result, by studying the CC interactions of a neutrino beam of pure mass eigenstates, we can derive the moduli of the mixing-matrix elements which give the sides of the unitarity triangle. Unfortunately, terrestrial neutrino beams are composed of flavour, rather than mass, eigenstates which are coherent combinations of the mass eigenstates. To create beams of neutrino-mass eigenstates it is necessary to destroy the coherence of the neutrino-flavour state produced through the weak interaction. There are several circumstances in which the coherence can be destroyed [587]:

- *Adiabatic conversion of the flavour neutrino state:* Suppose the neutrino flavour state, ν_α, is produced at densities much higher than the MSW-resonance density. Then, at the production point, the mixing in matter is strongly suppressed and ν_α practically coincides with one of the energy (or effective-mass) eigenstates in matter: $\nu_\alpha \approx \nu_{im}$. Suppose this state propagates to a region of small (zero) density. If the propagation is adiabatic, then $\nu_{im} \to \nu_i$ and at the exit from the matter layer, the beam will be pure ν_i. Such a situation is approximately realised for the high-energy (with $E_\nu > 10$ MeV) solar neutrinos; *i.e.,* ν_e produced in the center of the Sun is transformed into ν_2 at the surface;

- *Neutrino decay:* If the heavier neutrinos on their way to the detectors decay into the lightest neutrino (plus another light or massless particle), regardless of the original flavour composition, we will obtain a flux which is purely composed of the lightest mass eigenstate; and

- *Decoherence:* One can also use a beam of several mass eigenstates provided that they are *incoherent*. The rates of processes induced by such a beam will be determined by the moduli of matrix elements. The effective loss of coherence can occur due to divergence of the neutrino wave-packets over long distances or the averaging of oscillations.

The decay and the loss of coherence both require astronomical distances; moreover, the adiabatic conversion cannot be realised on distances smaller than the solar radius. Obtaining pure neutrino mass eigenstates therefore requires astrophysical sources of neutrinos and astrophysical methods. In section 6.4, we will discuss such methods.

To reconstruct the unitarity triangle, the absolute values of the elements of two rows (or equivalently two columns) in the mixing matrix must be measured. To reconstruct the $e\mu$-triangle, three quantities should be determined independently:

$$|U_{e1}U^*_{\mu1}|, \qquad |U_{e2}U^*_{\mu2}|, \qquad |U_{e3}U^*_{\mu3}|. \tag{208}$$

The form of the triangle depends on the, as yet unknown, value of $|U_{e3}|$. Assuming that only three neutrino species take part in the mixing and that there is no other source of CP-violation apart from the phases of the mass-matrix elements, one can use the two independent normalisation conditions:

$$\sum_{i=1,2,3} |U_{ei}|^2 = 1 \ , \qquad \sum_{i=1,2,3} |U_{\mu i}|^2 = 1 \ , \tag{209}$$

to determine the length of the sides of the $e\mu$-triangle. Thus, to find the sides of the $e\mu$-triangle it is enough to measure the moduli of the four mixing matrix elements:

$$|U_{e1}|, \quad |U_{\mu1}|, \quad |U_{e3}|, \quad |U_{\mu3}|. \tag{210}$$

To prove the CP violation, the following inequalities must be established:

$$|U_{e1}U^*_{\mu1}| \ < \ |U_{e2}U^*_{\mu2}| + |U_{e3}U^*_{\mu3}|;$$

$$|U_{e2}U^*_{\mu 2}| \;\; < \;\; |U_{e1}U^*_{\mu 1}| + |U_{e3}U^*_{\mu 3}|. \tag{211}$$

Using the present information on the absolute value of the matrix elements one can estimate the accuracy required. According to equation (211) the quantities:

$$A_1 \equiv -|U_{e1}||U_{\mu 1}| + |U_{e3}||U_{\mu 3}| + \sqrt{(1-|U_{e1}|^2-|U_{e3}|^2)(1-|U_{\mu 1}|^2-|U_{\mu 3}|^2)} \tag{212}$$

and:

$$A_2 \equiv |U_{e1}||U_{\mu 1}| + |U_{e3}||U_{\mu 3}| - \sqrt{(1-|U_{e1}|^2-|U_{e3}|^2)(1-|U_{\mu 1}|^2-|U_{\mu 3}|^2)} \tag{213}$$

are measures of CP violation; i.e., CP is conserved if either A_1 or A_2 is zero. Setting θ_{12} and θ_{23} to their best fit values ($\sin^2\theta_{12} = 0.315$ and $\sin^2\theta_{23} = 0.45$), θ_{13} close to the present upper bound ($U_{e3} = 0.15$), and taking a maximal Dirac phase, $\delta = 90^\circ$, we find $A_1 = 0.09$ and $A_2 = 0.10$.

Notice that $A_{1,2}$ can be negative if there is an extra neutrino and as a result the 3×3 active sub-matrix is not unitary. Equations (212) and (213) imply that, in order to establish CP-violation (non-zero values of $A_{1,2}$) the absolute errors, $\Delta|U_{\mu 3}|$, $\Delta|U_{e1}|$, $\Delta|U_{\mu 1}|$ and $\Delta|U_{\mu 3}U_{e3}|$ (regardless of the measurement method) should be smaller than a few percent even in the most optimistic case – namely, U_{e3} as large as possible and $\delta = 90^\circ$. This seems quite challenging specially in the case of $|U_{\mu 1}|$.

If $|U_{e3}|$ turns out to be very small, the sides proportional to $|U_{e3}|$ will be also tiny and it will be more difficult to reconstruct the $e\mu$-triangle and to check the inequalities (211). A similar situation occurs for the uc-triangle in the quark sector. In this connection, it was proposed in [596] to reconstruct the 12-triangle which is made up of $|U_{e1}U^*_{e2}|$, $|U_{\mu 1}U^*_{\mu 2}|$, and $|U_{\tau 1}U^*_{\tau 2}|$. Notice that although all the sides of the 12-triangle are comparable, in the limit of small s_{13}, the height of this triangle will be small. This creates another problem for measuring the area. Within the tri-bimaximal scenario, it may be simpler to reconstruct the 23-triangle (the triangle made up of $|U_{e3}U^*_{e2}|$, $|U_{\mu 3}U^*_{\mu 2}|$, and $|U_{\tau 3}U^*_{\tau 2}|$) [597,598]. Up to now, there is no direct information about the values of $|U_{\tau 1}|$ and $|U_{\tau 2}|$. Moreover, both the creation of intense ν_τ-beams and the detection of ν_τ seem to be difficult. Reconstructing the 23- and 12-triangles does not therefore seem very promising from a practical point of view. If we do not want to make any theoretical pre-assumptions about the mass texture, the $e\mu$-triangle seems to be a more promising option to reconstruct, especially if, for s_{13} close to the present upper bound, as demonstrated in figure 43, all the sides of the $e\mu$-triangle are comparable. Throughout the present analysis we therefore focus on the $e\mu$-triangle.

4.4.3 The unitarity triangle and oscillation experiments

In this section, we describe the set of oscillation measurements that have been suggested in [587] to determine the $e\mu$-triangle. Since the oscillation probabilities depend not only on the moduli of the mixing-matrix elements, but also on the unknown relative phases (δ_x), the strategy is to select configurations of oscillation measurements for which the dominant effect is determined by

moduli:

$$P_{\alpha\beta} = P_{\alpha\beta}(|U_{ei}|, |U_{\mu i}|) + \Delta P_{\alpha\beta}(\delta_x), \quad \alpha, \beta = e, \mu \ , \tag{214}$$

where $\Delta P \ll P$. The hierarchy of mass splittings:

$$\epsilon \equiv \frac{\Delta m^2_{12}}{\Delta m^2_{23}} \simeq 0.03 \ , \tag{215}$$

as well as the small $|U_{e3}|$ play a key role in this argument. The experimental setup must be chosen in such a way that the δ_x-dependent correction in (214) induced by the matter effect is suppressed. The product $|U^*_{e3}U_{\mu 3}|$, which is one side of the triangle, can be measured in studies of the $\nu_\mu \to \nu_e$ transitions driven by Δm^2_{32}. For this channel, in vacuum:

$$P_{\mu e} = 4|U^*_{e3}U_{\mu 3}|^2 \sin^2 \frac{\Delta m^2_{32} L}{4E} + \Delta P_{\mu e} \ , \tag{216}$$

where the correction $\Delta P_{\mu e}$ is due to non-zero Δm^2_{21}. In general, due to the matter effect it is not possible to write the transition probability in the simple form of equation (216) with $\Delta P_{\mu e} \ll P_{\mu e}$. The probability can however be reduced to the form (216) in two limiting cases [587]:

- The low-energy limit $E \ll E^R_{23}$ ($E^R_{23} \sim 6$ GeV is the resonance energy corresponding to the $2-3$ splitting) for which the matter correction is small;
- The short-baseline limit where 'vacuum mimicking' condition is satisfied [599, 600].

Unfortunately, neither of the proposed state-of-the-art long-baseline experiments, NoνA and T2K fulfill these requirements. As illustrated in figure 5 of [601], the transition probability for these setups is sensitive not only to $|U_{e3}||U_{\mu 3}|$ but also to the value of the CP-violating phase. Thus, the $|U_{\mu 3}U^*_{e3}|$ side should be determined by separately by measuring the values of $|U_{\mu 3}|$ and $|U_{e3}|$.

The four elements in equation (210) can be determined, in principle, as follows:

1. $|U_{e3}|$ can be measured by reactor experiments with a typical baseline of ~ 1 km. In these experiments the matter effect is negligible and the survival probability for $\bar{\nu}_e$ can be written:

   $$P_{ee} = 1 - 4(1 - |U_{e3}|^2)|U_{e3}|^2 \sin^2 \frac{\Delta m^2_{23} L}{4E} + \Delta P_{ee} \ . \tag{217}$$

   The relative correction is small, $\Delta P_{ee}/(1 - P_{ee}) < 2$ %, so $|U_{e3}|$ can be determined with O(1)% accuracy [587]. Experimental errors in the measurement of P_{ee} will dominate over ΔP_{ee}. If θ_{13} is close to the present upper bound, the next generation of reactor experiments will be able to measure it with a relative error of O(10)% [601–603]. The uncertainty in $A_{1,2}$ (defined in equations (212) and (213)) arising from $\Delta|U_{e3}|$ can be evaluated as:

   $$\Delta A_1 = \left[|U_{\mu 3}| - |U_{\mu 2}|\frac{|U_{e3}|}{|U_{e2}|}\right] \Delta|U_{e3}| \ \text{ and } \Delta A_2 = \left[|U_{\mu 3}| + |U_{\mu 2}|\frac{|U_{e3}|}{|U_{e2}|}\right] \Delta|U_{e3}| \ . \tag{218}$$

   Taking $|U_{e3}| \simeq 0.15$ and $\frac{\Delta|U_{e3}|}{|U_{e3}|} \simeq 10\%$ yields $\Delta A_{1,2}/A_{1,2} \simeq 20\%$.

2. The element $|U_{\mu 3}|$ can be measured in long-baseline ν_μ-disappearance experiments (one of the main motivations of which is to measure the mixing angle θ_{23} with high precision). For T2K and NoνA, the matter effect cannot be neglected since $\Delta m^2_{23}/E \sim \sqrt{2} G_F n_e$, however effects due to the solar mass splitting are unimportant. To an approximation of $\mathrm{O}(\Delta m^2_{12} L/2E) \sim 0.01$, the survival probability can be treated in the two-neutrino oscillation framework. The value of $\sin\theta_{23}$ (thus $|U_{\mu 3}| = s_{23} c_{13}$) can be extracted with accuracy of 4% or better [16];

3. The values of $|U_{e1}|$ and $|U_{e2}|$ can be obtained from the solar-neutrino data. Since the energy of solar neutrinos is low, to a good approximation, the matter effect on $|U_{e3}|$ can be neglected. Moreover, the solar-neutrino conversion driven by Δm^2_{31} produces only an averaged oscillation effect ($1 \ll \Delta m^2_{31} L/E_\nu$). In this case the survival probability reads [604, 605]:

$$P_{ee} = (1 - |U_{e3}|^2)^2 P_2(\tan^2\theta_{12}, \Delta m^2_{21}) + |U_{e3}|^4 \,, \tag{219}$$

where:

$$\tan^2\theta_{12} = \frac{|U_{e2}|^2}{|U_{e1}|^2} \,, \tag{220}$$

and P_2 is the two-neutrino survival probability determined from the solution of the two-neutrino-evolution equation with the oscillation parameters $\tan^2\theta_{12}$, Δm^2_{21} and the effective potential $(1-|U_{e3}|^2)V_e$. Analysis of solar-neutrino data alone cannot yield an uncertainty in $\sin^2\theta_{12}$ better than 19% at the 3σ C.L. [97], even if the *pp*-flux data with a 3% uncertainty is included.

For a reactor experiment with a large baseline (~ 100 km) such as KamLAND, P_{ee} is given by:

$$P_2 = 1 - \frac{4|U_{e1}|^2|U_{e2}|^2}{(1-|U_{e3}|^2)^2} \sin^2\frac{\Phi_{12}}{2} \,. \tag{221}$$

This opens up the possibility of measuring the value of $\sin\theta_{12}$ with high precision. Although the current experiment, KamLAND, cannot reach a precision better than 18% [97], if a reactor experiment with a baseline of 60 km, an exposure of ~ 60 GWkTy and a systematic error of 2% is constructed, $\sin^2\theta_{12}$ can be measured with an uncertainty of 6% at 3σ. Moreover, as shown in [606], combining data from KamLAND and Borexino will allow the uncertainty on $\sin^2 2\theta_{12}$ to be reduced to 5%. Then, using the measured value of $|U_{e1}|$, $|U_{e2}|$ and the normalisation condition, $|U_{e1}|^2 + |U_{e2}|^2 = 1 - |U_{e3}|^2$, $|U_{e1}|$ and $|U_{e2}|$ can be determined separately. In this way, $|U_{e1}|$ can be determined with relatively high precision leading to $(\Delta A_{1,2}) < A_{1,2}/5$ for $\delta \simeq 90^\circ$. Such an uncertainty is small enough to establish the CP-violation; and

4. The determination of $|U_{\mu 1}|$ (and/or $|U_{\mu 2}|$) is the most challenging part of the method. Note that in contrast to $|U^*_{e3} U_{\mu 3}|$, it is not possible to measure the combinations $|U^*_{e1} U_{\mu 1}|$ and $|U^*_{e2} U_{\mu 2}|$, directly from oscillation experiments. Indeed, in vacuum the $\nu_\mu \to \nu_e$ transition probability is determined by the product $Re\left[U^*_{\mu 1} U_{e1} U_{\mu 2} U^*_{e2}\right]$ which depends not only on the

absolute values of the matrix elements but also on their phases. Therefore one has to resort to the possibility of separately measuring $|U_{\mu 1}|$ and $|U_{\mu 2}|$. In fact, it is sufficient to measure a combination of $|U_{\mu 1}|$ and $|U_{\mu 2}|$ which differs from the normalisation condition (equation (209)). This requires an experiment sensitive to the Δm^2_{12} splitting which appears usually as a sub-dominant mode. To suppress the leading effect and the interference of the leading and sub-leading modes, the oscillations driven by Δm^2_{23} should be averaged out. This condition necessitates the following experimental configuration:

- The energy of the beam should be low: $E < 1$ GeV; and
- The baseline should be large, $L \gg 4E_\nu/\Delta m^2_{32}$.

Moreover, to avoid suppression of the sub-dominant mode the baseline, L, should be of the order of the oscillation length associated with the (1 - 2) splitting, $L \geq 2000$ km. Realisation of such a set-up is very challenging. The requirements listed above are fulfilled by the proposed Brookhaven to Homestake long-baseline experiment [607].

In summary, if $|U_{e3}|$ saturates the present bound ($|U_{e3}| \sim 0.1$), the results of the next generation of reactor experiments can be combined with the measurements of the ν_μ-survival probability in T2K and/or NoνA to determine $|U_{e3}|$ and $|U_{\mu 3}|$, and consequently the third side of the $e\mu$-triangle, with the required precision. Moreover, by combining the results of KamLAND and Borexino, or alternatively by constructing a reactor experiment with $L \sim 60$ km and an exposure of 60 GWkTy, one can determine $|U_{e1}|$ and $|U_{e2}|$ with sufficient accuracy to reconstruct the unitarity triangle. The main obstacle to the construction of the unitarity triangle is the precision measurement of $|U_{\mu 1}|$ and $|U_{\mu 2}|$ which requires a very-long-baseline experiment with a setup similar to the proposed Brookhaven to Homestake project [607].

The reconstruction of the unitarity triangle using measurements of neutrino mixing in matter has been considered in [596, 608, 609]. The area of the triangle will also be proportional to the CP-violating phase δ. However to extract information on the neutrino parameters, several different setups with distinct beam energies and matter densities are required which correspond to different 'triangles in matter'.

4.4.4 Leptonic unitarity triangle and future experiments

Figure (44) illustrates the possibility of establishing CP-violation by the triangle method for the realistic uncertainties which can be achieved after the next generation of experiments. The shown triangle corresponds to $s_{13} = 0.15$, $\delta_D = 90^\circ$ and the current best fit for the rest of the mixing parameters ($s_{23} = 0.67$ and $s_{12} = 0.56$). The horizontal side ($|U_{e1}U^*_{\mu 1}|$) is normalised to one. The scatter points show the position of the vertex of the triangle, when the moduli of the mixing matrix elements take random values around the central points $|U_{e1}| = 0.74$, $|U_{\mu 1}| = 0.42$, $|U_{e3}| = 0.15$ and $|U_{\mu 3}| = 0.67$ (which correspond to the mixing parameters above) within the future uncertainty ranges. To produce the scatter points, we have taken $\Delta|U_{e1}|/|U_{e1}| = 5\%$, $\Delta|U_{e3}|/|U_{e3}| = 10\%$ and $\Delta|U_{\mu 3}|/|U_{\mu 3}| = 3\%$ which correspond to the accuracy achievable

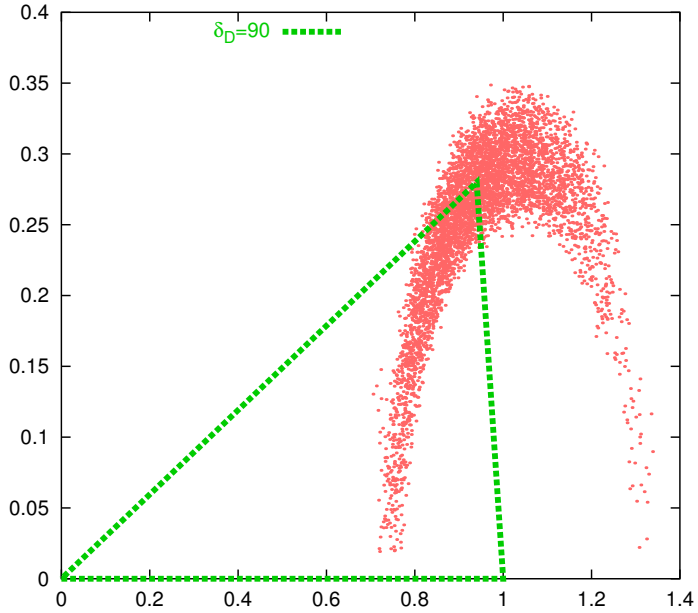

Figure 44: The $e\mu$-triangle taking $s_{13} = 0.15$, $\delta = 90^\circ$ and the best fit values $s_{23} = 0.67$ and $s_{12} = 0.56$. The $|U_{e1}U^*_{\mu 1}|$ side is normalised to one. Each scatter point represents the possible position of vertex when the moduli of mixing matrix elements pick up random values around $|U_{e1}| = 0.74$, $|U_{\mu 1}| = 0.42$, $|U_{e3}| = 0.15$ and $|U_{\mu 3}| = 0.67$ (which corresponds to the above mixing parameters) within the following uncertainty ranges: $\Delta|U_{e1}|/|U_{e1}| = 5\%$; $\Delta|U_{\mu 1}|/|U_{\mu 1}| = 10\%$; $\Delta|U_{e3}|/|U_{e3}| = 10\%$; and $\Delta|U_{\mu 3}|/|U_{\mu 3}| = 3\%$.

respectively by combined KamLAND and Borexino data analysis [606], reactor experiments [601], and T2K/NoνA [16]. We have taken an optimistic accuracy of $\Delta|U_{\mu 1}|/|U_{\mu 1}| = 10\%$. From this figure we observe that if the value of s_{13} is close to its present upper bound and δ_D is maximal, the uncertainties outlined above will be small enough to establish CP-violation.

The measurements described above can be complemented by those that can be made at the proposed super-beams and at a Neutrino Factory. While $|U_{\mu 1}|$ and $|U_{\mu 2}|$ can not be determined by these experiments, the triangle method can be considered as an alternative for resolving the eight-fold degeneracies which are encountered in the conventional methods of searching for the CP-violating phase [38, 214, 341, 610]. For example, none of the setups we have suggested to reconstruct the triangle is sensitive to $\mathrm{sgn}(\Delta m^2_{31})$ thus the triangle method can serve to resolve the $\mathrm{sgn}(\Delta m^2_{31})$ degeneracy.

4.4.5 Beyond three neutrinos

Deviation of the mixing matrix from unitarity may originate from violation of the universality of weak interactions due, for example, to mixing of neutrinos with heavy neutral leptons. This affects not only neutrino oscillations in vacuum and in matter but also the leptonic decays, for example through the existence of lepton-flavour violating decays [611]. The discovery of sterile neutrinos and their mixing with active neutrinos would imply violation of unitarity for active-neutrino mixing. In the case of four light neutrinos, the mixing can be represented in the form

of quadrangles. In this case, the number of Dirac CP-violating phases will increase to three. A classification of the unitarity quadrangles in the four-neutrino mixing scheme is given in [612]. Relations between the areas of the unitarity quadrangles and the re-phasing invariants of CP and T violation have been established. Also quadrangles in matter were studied in [596].

4.4.6 Constraints on unitarity

Neutrino oscillations constitute evidence for physics beyond the Standard Model. If new physics exists, it can manifest itself through unitarity violation in the Standard Model couplings, the complete theory being unitary and probability-conserving. In the quark sector, the search for deviations from unitarity of the CKM matrix is considered as a sensitive way to search for physics beyond the Standard Model. In the lepton sector unitarity violations can arise both from new physics at low energy – as in the case of the hypothetical existence of additional light sterile neutrinos – or at high energy – as in the case of the canonical see-saw mechanism [127,222,223,308], where light neutrino masses are generated through mixing with heavy, singlet, fermionic states. In the following we will discuss both possibilities.

To study mixing among active and sterile neutrinos, we consider the Standard Model field content plus N_s sterile neutrinos. The complete $(3+N_s)$-dimensional mixing matrix is unitary, but the 3×3 PMNS matrix is not since it is a sub-matrix. Probability conservation in the complete theory implies:

$$\sum_{y=e,\mu,\tau} P(\nu_x \to \nu_y) = 1 - P(\nu_x \to \nu_s)\,, \tag{222}$$

where $P(\nu_x \to \nu_s) \equiv P_{xs}$ is the oscillation probability into sterile neutrinos. Since neutral currents are sensitive to this sum, in principle a neutral-current measurement alone would be sufficient to determine P_{xs}. However, in a realistic detector mis-identifications of charged current and neutral current events, together with systematic uncertainties on neutrino interaction cross sections, complicate the analysis. In reference [613] the sensitivity of neutral-current measurements to the sterile content of a neutrino beam in a long-baseline oscillation experiment is studied. The performance that can be expected of the present and next generation of experiments (K2K, MINOS, and T2K) at 3σ sensitivity and the 90% C.L. exclusion limits for the sterile oscillation probability will be of order $0.10 - 0.15$.

To date, deviations from unitarity coming from the additional light neutrinos have been discussed. However, similar deviations can be generated by the presence of heavy neutrinos. This is the case, for instance, in the see-saw mechanism, where N_R right-handed neutrinos, with heavy Majorana masses, are added to the Standard Model. As before, the complete $(3+N_R)$-dimensional mixing matrix is unitary, while the 3×3 sub-matrix is not. The main difference with the light-neutrino case is that the mixing between the light and heavy states is minimal because the mass difference is so large. This case has been studied by many authors, both in general frameworks in which heavy fermions have been added to the Standard Model lagrangian [614–616] and in the specific neutrino context [617–620]. In particular, in reference [619]

CP violation in presence of non-unitarity induced by heavy neutrinos has been considered and an enhancement of the effect has been observed.

Deviations from unitarity can also be studied in an effective-theory approach, without the need for the introduction of new fermionic states. This can be done as long as the new physics resides at energies much larger than the electroweak scale, such that heavy fields can be integrated out. The low-energy effective lagrangian will generally contain corrections to the Standard Model couplings and a tower of non-renormalisable higher-dimensional operators suppressed by powers of the large energy scale, both of which can result in deviations from unitarity in the mixing matrices. In reference [611] deviations from unitarity of the leptonic mixing matrix are studied, in a minimal framework dubbed MUV (Minimal Unitarity Violation). In the MUV scheme sources of non-unitarity are allowed only in those terms of the Standard Model lagrangian involving neutrinos and only three flavours are considered, as in the standard case. It is always possible to go to a basis, the mass basis, where kinetic terms are diagonal and normalised and neutrino masses are diagonal too. Here the whole effect of new physics is encoded in the non-unitarity of the leptonic mixing matrix. In this framework, and taking a completely general mixing matrix, a large set of neutrino data, including oscillations and decays, is analysed, in order to see up to what point the measured elements of the mixing matrix arrange themselves in a unitary pattern.

The starting point is the Standard Model lagrangian, where the PMNS matrix is replaced by a generic matrix N, which relates the mass and flavour basis: $\nu_\alpha = N_{\alpha i}\nu_i$. Since N is not unitary, and since the mass basis is still orthonormal, the flavour basis is no longer orthogonal, and this gives rise to new physical effects. The oscillation probability now reads:

$$P_{\nu_\alpha\nu_\beta}(E,L) \equiv |\langle\nu_\beta|\nu_\alpha(L)\rangle|^2 \;=\; \frac{|\sum_i N^*_{\alpha i}\, e^{i\,P_i\,L}\, N_{\beta i}|^2}{(NN^\dagger)_{\alpha\alpha}(NN^\dagger)_{\beta\beta}}\,. \tag{223}$$

This formula is formally identical to the standard one, apart from a normalisation factor in the denominator. However, due to the non-unitarity of N, the oscillation probability at $L = 0$ is not zero, a phenomenon referred to as the 'zero-distance' effect:

$$P_{\nu_\alpha\nu_\beta}(E, L=0) \propto |(NN^\dagger)_{\beta\alpha}|^2\,. \tag{224}$$

The zero-distance effect, and the fact that oscillations in matter become non-diagonal, are the unique consequences of the non-unitarity of N on the phenomenology of neutrino oscillations. The non-unitarity of N also has consequences in other sectors. Since the electroweak couplings are modified, interactions involving the W and Z bosons are now sensitive to the elements of N. However, since it is not possible to tag experimentally neutrino mass eigenstates, in contrast to the quark sector, electroweak decays can only be used to determine sums of products of mixing-matrix elements. This information is extremely relevant in the determination of the moduli of the matrix elements.

The number of parameters required to specify N (9 moduli and 4 or 6 phases, depending on the Dirac or Majorana nature of neutrinos) is larger than in the unitary case. It is presently possible only to determine the moduli since all positive oscillation signals to date correspond to disappearance modes. The elements of the 'e-row' can be constrained using data from CHOOZ

[519], KamLAND [8], and SNO [109], together with the information on Δm^2_{23} resulting from an analysis of K2K data [56]. In contrast, less data is available that may be used to constrain the elements of the μ-row. Data from K2K and SuperKamiokande [116] can be used to determine $|N_{\mu 3}|$ and the combination $|N_{\mu 1}|^2 + |N_{\mu 2}|^2$. Putting all this information together, the following allowed 3σ ranges are obtained for the moduli of the elements of the leptonic mixing matrix:

$$|N| = \begin{pmatrix} 0.76 - 0.89 & 0.45 - 0.66 & < 0.37 \\ \left[\, \sqrt{|N_{\mu 1}|^2 + |N_{\mu 2}|^2} = \right. & 0.57 - 0.86 \,\right] & 0.57 - 0.86 \\ ? & ? & ? \end{pmatrix} . \tag{225}$$

Notice that using only oscillation experiments, and without assuming unitarity, only half of the elements can be determined. However, some information is also available from NOMAD [621], KARMEN [622], BUGEY [508], and the near detector at MINOS [623]. These experiments exploit the zero-distance effect (equation (224)) to provide constraints on $NN^\dagger$. Combining this information with equation (225), $|N_{\mu 1}|$ and $|N_{\mu 2}|$ can be disentangled.

In order to constrain all the elements of the mixing matrix, other data have to be considered. The decay widths for W and Z bosons are given by:

$$\Gamma(W \to \ell_\alpha \nu_\alpha) = \frac{G_F M_W^3}{6\sqrt{2}\pi} (NN^\dagger)_{\alpha\alpha} \quad ; \text{and} \quad \Gamma(Z \to \text{invisible}) = \frac{G_F M_Z^3}{12\sqrt{2}\pi} \sum_{\alpha,\beta} |(NN^\dagger)_{\alpha\beta}|^2 \,. \tag{226}$$

These relations allow the diagonal elements of $NN^\dagger$ to be constrained. Additional information can be obtained from ratios of the rate of decay of leptons, the W boson and the electroweak decays of pions.

The off-diagonal elements of $NN^\dagger$ can be constrained using rare charged-lepton decays such as $l_\alpha \to l_\beta \gamma$. The non-unitarity of N forbids the GIM cancellation of the constant term, and the branching ratio is approximated very accurately by:

$$\frac{\Gamma(\ell_\alpha \to \ell_\beta \gamma)}{\Gamma(\ell_\alpha \to \nu_\alpha \ell_\beta \overline{\nu}_\beta)} = \frac{100\alpha}{96\pi} \frac{|(NN^\dagger)_{\alpha\beta}|^2}{(NN^\dagger)_{\alpha\alpha}(NN^\dagger)_{\beta\beta}} \,. \tag{227}$$

Performing a global fit to all these electroweak data, the following values are obtained at the 90% CL:

$$|NN^\dagger| \approx \begin{pmatrix} 0.994 \pm 0.005 & < 7.0 \cdot 10^{-5} & < 1.6 \cdot 10^{-2} \\ < 7.0 \cdot 10^{-5} & 0.995 \pm 0.005 & < 1.0 \cdot 10^{-2} \\ < 1.6 \cdot 10^{-2} & < 1.0 \cdot 10^{-2} & 0.995 \pm 0.005 \end{pmatrix} . \tag{228}$$

Similar bounds can be inferred for $N^\dagger N$ proving that, in the MUV scheme, unitarity in the lepton sector is experimentally confirmed from data on weak decays with a precision better than 5%.

The elements of the mixing matrix obtained from the analysis of neutrino-oscillation experiments, equation (225), can now be combined with the unitarity constraints obtained from weak

decays, equation (228). The resulting mixing matrix in the MUV scheme is:

$$|N| = \begin{pmatrix} 0.75 - 0.89 & 0.45 - 0.65 & < 0.20 \\ 0.19 - 0.55 & 0.42 - 0.74 & 0.57 - 0.82 \\ 0.13 - 0.56 & 0.36 - 0.75 & 0.54 - 0.82 \end{pmatrix} . \tag{229}$$

All the elements are now significantly constrained to be rather close to those stemming from the usual unitary analysis [624]:

$$|U| = \begin{pmatrix} 0.79 - 0.88 & 0.47 - 0.61 & < 0.20 \\ 0.19 - 0.52 & 0.42 - 0.73 & 0.58 - 0.82 \\ 0.20 - 0.53 & 0.44 - 0.74 & 0.56 - 0.81 \end{pmatrix} . \tag{230}$$

In the future, improvements in the measurements of the matrix elements are expected, as well as improvements in the unitarity tests. On the one hand, the exploration of the appearance channels at future facilities, such as super-beams [13, 15, 16, 625], beta-beams [24], and the Neutrino Factory [28, 29], will permit the testing of the τ-row directly and the measurement of the phases of the mixing matrix, which up to now are completely unknown. On the other hand, improvements on the unitarity bounds are expected from the experiments looking for $\mu \to e\gamma$, but also from the bounds which can be obtained at a Neutrino Factory. In particular, since the bounds on rare τ decays are not likely to improve much, an improvement on the bounds on $(NN^\dagger)_{e\tau}$ and $(NN^\dagger)_{\mu\tau}$ could be obtained with an OPERA-like detector placed at a short baseline (100m) from a Neutrino Factory beam.

4.5 Non-standard interactions

Neutrino oscillation experiments probe lepton-flavour non-conservation, an effect which is not present in the Standard Model. In the Standard Model, the lepton sector exhibits a $U(1)^3$ flavour symmetry, i.e. electron, muon, and tau numbers are conserved guaranteeing that there are no leptonic flavour transitions. Neutrino masses break the symmetry $U(1)^3$; completely in the case of Majorana neutrino masses, or down to $U(1)_L$ in the case of Dirac masses. However, neutrino masses are not the only way in which the $U(1)^3$ symmetry may be broken. Non-standard interactions (NSIs) can also break the $U(1)^3$ symmetry and generate flavour transitions. The dependence of the neutrino-oscillation signal on source-detector distance and neutrino energy may be used to distinguish between the various possibilities.

Any interaction that cannot be diagonalised simultaneously with the weak interaction and the charged-lepton mass matrix breaks the $U(1)^3$ leptonic-flavour symmetry. A simple example is a new effective four Fermi-interaction that, in the basis where the charged-lepton-mass matrix and the W interaction are diagonal, is of the form $u\bar{d}\nu_e\bar{\nu}_\mu$. Such an interaction allows the $e - \mu$ transition even for massless neutrinos. Terms that break the lepton-flavour symmetry also generate flavour transition in processes that involve charged leptons, for example, $\tau \to \mu\gamma$. Thus, in principle, such processes can be used to probe the same physics as neutrino oscillation

experiments. When the only source of flavour breaking is neutrino mass, the effect in charged lepton processes is tiny due to the leptonic GIM mechanism. For example, the amplitude for $\tau \to \mu\gamma$ is suppressed by m_3^2/m_W^2 and thus $\mathrm{BR}(\tau \to \mu\gamma) \sim 10^{-50}$ which is out of reach.

The situation is different with NSIs. Here, the effect in charged lepton processes can be relatively large. The amplitude of the flavour transition in both the neutrino and the charged-lepton sectors are expected to be of the same order. Since experiments with charged leptons are in principle easier than those with neutrinos, it might seem that neutrino oscillation experiments will not be sensitive to NSIs. However, in oscillation experiments the effect of the NSI amplitude can be enhanced by interference with the standard oscillation amplitude [626, 627], an enhancement that is not present in charged-lepton processes. Roughly speaking, if the new physics amplitude is small, and parametrised by a small parameter ε, then the effect in oscillation experiments is $O(\varepsilon)$ while for charged leptons it is $O(\varepsilon^2)$. This enhancement makes the 'probing power' of neutrino oscillation experiments larger than one might naively expect.

Any neutrino-oscillation experiment can be divided into three phases: production; propagation; and detection. NSIs can affect any of these phases. In the following we consider the production and detection processes that are relevant to Neutrino Factories; an appearance experiment where neutrinos are produced in the process $\mu^+ \to e^+ \nu_\alpha \bar{\nu}_\mu$ and detected by the processes $\nu_\beta d \to \mu^- u$ and $\nu_\beta d \to \tau^- u$ and anti-neutrinos are produced and detected by the corresponding charge-conjugate processes. A new interaction of the form $\mu\bar{e}\nu_\tau\bar{\nu}_\mu$ would affect oscillation experiments that use neutrinos produced in muon decay. Similarly, interactions of the form $\mu\bar{\nu}_e u\bar{d}$ would affect the detection processes.

The effect on the propagation can come in two ways. In vacuum oscillations, it comes from flavour-violating wave-function normalisation; non-diagonal kinetic terms arise, which cannot be diagonalised simultaneously with the interaction of the W boson. Such effects are likely to be relatively small and are not discussed further [628]. The effect on propagation in matter can be large. For example, an interaction of the form $e\bar{e}\nu_\tau\bar{\nu}_\mu$ can generate $\mu - \tau$ transitions when neutrinos travel through a medium that contains electrons, such as the Earth or the Sun.

While NSIs can affect any of the three phases, they do not necessarily affect them all. The flavour structure of the new interactions that affect each phase are different. Consider the case of interactions that involve two quarks and two leptons; this kind of interaction affects both the detection and the propagation. Yet, at detection the interaction is charged current while during propagation the relevant interaction is neutral current. In many new-physics models these interactions are related, but this is not automatic. Purely leptonic interactions affect the production and propagation. Yet, in the production the charged leptons are the electron and the muon, while in propagation in matter both are electrons. In section 4.5.1 we concentrate on effects due to new physics in production or detection. In section 4.5.2 NSIs effects on the propagation are discussed.

4.5.1 Non-standard interactions in production and detection

Consider a model-independent parameterisation of new-physics effects on production and detection processes in neutrino oscillation experiments [626–630]. New physics in the source or the detector may be parameterised using two sets of four-fermion couplings: $(G^s_{\rm NP})_{\alpha\beta}$; and $(G^d_{\rm NP})_{\alpha\beta}$, where $\alpha, \beta = e, \mu, \tau$. Here $(G^s_{\rm NP})_{\alpha\beta}$ refers to processes in the source where a flavour eigenstate ν_β is produced in conjunction with an incoming charged lepton, α^-, or an outgoing α^+. $(G^d_{\rm NP})_{\alpha\beta}$ refers to processes in the detector where an incoming ν_β produces an α^-. While the $SU(2)_L$ gauge symmetry requires that the four-fermion couplings of the charged current weak interactions be proportional to $G_F\delta_{\alpha\beta}$, new interactions allow couplings with $\alpha \neq \beta$. Phenomenological constraints imply that the new interaction is suppressed with respect to the weak interaction, i.e.: $|(G^s_{\rm NP})_{\alpha\beta}| \ll G_F$; and $|(G^d_{\rm NP})_{\alpha\beta}| \ll G_F$.

In the SM, neutrino interactions have a Dirac $(V-A)(V-A)$ structure. Admitting non-standard interactions, massless neutrinos can have either the SM Dirac structure or a $(V-A)(V+A)$ structure. The effects of interactions of the form $(V-A)(V+A)$ at production or detection are suppressed by ratios of charged-lepton masses and are therefore very small and will be neglected [627].

In an appearance experiment where neutrinos are produced in the process $\mu^+ \to e^+\nu_\alpha\bar{\nu}_\mu$ and detected by the process $\nu_\beta d \to \ell^- u$ and anti-neutrinos are produced and detected by the corresponding charge-conjugate processes, the relevant couplings are $(G^s_{\rm NP})_{e\beta}$ and $(G^d_{\rm NP})_{\mu\beta}$. It is convenient to define small dimensionless quantities $\varepsilon^{s,d}_{\alpha\beta}$ as follows:

$$\begin{aligned}
\varepsilon^s_{e\beta} &\equiv \frac{(G^s_{\rm NP})_{e\beta}}{\sqrt{|G_F + (G^s_{\rm NP})_{ee}|^2 + |(G^s_{\rm NP})_{e\mu}|^2 + |(G^s_{\rm NP})_{e\tau}|^2}}\,; \text{and} \\
\varepsilon^d_{\mu\beta} &\equiv \frac{(G^d_{\rm NP})_{\mu\beta}}{\sqrt{|G_F + (G^d_{\rm NP})_{\mu\mu}|^2 + |(G^d_{\rm NP})_{\mu e}|^2 + |(G^d_{\rm NP})_{\mu\tau}|^2}}.
\end{aligned} \tag{231}$$

The assumption $|\varepsilon^{s,d}_{\alpha\beta}| \ll 1$ means that leading-order (linear) effects only need be considered. The leading effects from flavour-diagonal couplings are proportional to ε (flavour-diagonal)$\times\varepsilon$(flavour-changing) and can therefore be neglected.

Non-zero values of $\varepsilon^{s,d}_{\alpha\beta}$ can be generated if the three-by-three mixing matrix of the SνM is not unitary. For example, suppose that there exists a fourth neutrino-mass eigenstate ν_h which is heavy. If $m_h \gg m_\mu$, so that this mass eigenstate cannot be produced in muon decay, then:

$$\varepsilon^{d*}_{\ell e} + \varepsilon^s_{e\ell} \;\to\; -N_s^2 U_{eh} U^*_{\ell h}. \tag{232}$$

where $\ell = \mu, \tau$ and U_{eh} ($U_{\ell h}$) is the mixing between the heavy neutrino mass eigenstate and the electron (ℓ) neutrino and N_s is a normalisation factor given by:

$$N_s = (|U_{e1}|^2 + |U_{e2}|^2 + |U_{e3}|^2)^{-1/2} = (1 - |U_{eh}|^2)^{-1/2}. \tag{233}$$

If there are many heavy states, equations (232) and (233) must be modified to include an implicit summation over h.

The expression for the transition probability in neutrino-oscillation experiments may now be written as a function of the mixing-matrix parameters and the new-physics parameters. For simplicity, consider a two-generation framework (expressions for the three-flavour case can be found in [626]). The state (ν_e^s) that is produced in the source in conjunction with an e^+ and the state (ν_μ^d) that is tagged by μ^- production in the detector may be written in terms of the mass eigenstates as follows:

$$|\nu_e^s\rangle = \sum_i \left[U_{ei} + \varepsilon^s_{e\mu} U_{\mu i}\right] |\nu_i\rangle, \quad |\nu_\mu^d\rangle = \sum_i \left[U_{\mu i} + \varepsilon^d_{\mu e} U_{ei}\right] |\nu_i\rangle. \tag{234}$$

The transition probability, $P_{e\mu} = |\langle \nu_\mu^d | \nu_e^s(t)\rangle|^2$, where $\nu_e^s(t)$ is the time-evolved state that was purely ν_e^s at time $t = 0$, is then:

$$P_{e\mu} = \left| \sum_i e^{-iE_i t} \left[U_{ei} U^*_{\mu i} + \varepsilon^s_{e\mu} |U_{\mu i}|^2 + \varepsilon^{d*}_{\mu e} |U_{ei}|^2 \right] \right|^2 . \tag{235}$$

The results will be presented in terms of the following parameters:

$$\Delta m^2_{ij} \equiv m^2_i - m^2_j, \qquad \Delta_{ij} \equiv \Delta \frac{m^2_{ij}}{2E}, \qquad x_{ij} \equiv \frac{\Delta_{ij}\, L}{2} \, . \tag{236}$$

In the small-x limit, $P_{e\mu}$ may be expanded to second order in $x \equiv x_{12}$ and $\varepsilon \equiv \varepsilon^{d*}_{\mu e} + \varepsilon^s_{e\mu}$. In a basis in which the two-generation mixing matrix is real and is parameterised by one angle θ, the expression for $P_{e\mu}$ may be written:

$$P_{e\mu} = x^2 \sin^2 2\theta - 2x \sin 2\theta \, \Im(\varepsilon) + |\varepsilon|^2 \, . \tag{237}$$

The first term is the SνM piece, while the second and third terms arise only in the presence of new physics. The last term, which is a direct new-physics term, does not require oscillations and is very small. The second term is the most interesting one as it is an interference term between the direct new-physics amplitude and the SνM oscillation amplitude. There are two points to emphasise regarding this term:

1. It is linear in ε, and for $x \gg \varepsilon$ it is larger than the direct new physics term: the interference increases the sensitivity to the new physics; and

2. The interference is CP violating. This can be understood from the fact that it is linear in t, namely it is T odd. In order for it to be CPT even it must also be CP odd.

The interference term in equation (237) is CP violating and its effect can be sought through measurements of $P_{e\mu}$ and the transition probability of the CP-conjugate process, $P_{\bar{e}\bar{\mu}}$. A CP transformation of the Lagrangian takes the elements of the mixing matrix and the ε-terms into their complex conjugates. It is then straightforward to obtain the transition probability for anti-neutrino oscillations. It is interesting to define the CP asymmetry, $A_{\rm CP} = P_-/P_+$, where $P_\pm = P_{e\mu} \pm P_{\bar{e}\bar{\mu}}$. The CP-conserving rate P_+ is dominated by the SνM and is given by $P_+ = 8x^2_{31}|U_{e3}U^*_{\mu 3}|^2$. CP violation within the SνM ($P_-^{\rm S\nu M}$) is suppressed by both the small value

of $|U_{e3}|$ and the small mass-squared difference Δm^2_{21}. For short distances ($x_{21}, x_{31} \ll 1$) it is further suppressed since $P_-^{\mathrm{S}\nu\mathrm{M}} \propto L^3$. The new-physics term ($P_-^{\mathrm{NP}}$) does not suffer from the last two suppression factors, it does not require three generations, and it has a different dependence on the distance, $P_-^{\mathrm{NP}} \propto L$. $P_-^{\mathrm{S}\nu\mathrm{M}}$ and P_-^{NP} may be written:

$$A_{\mathrm{CP}}^{\mathrm{SM}} = -2x_{21}\Im\left(\frac{U_{e2}U^*_{\mu 2}}{U_{e3}U^*_{\mu 3}}\right), \qquad A_{\mathrm{CP}}^{\mathrm{NP}} = -\frac{1}{x_{31}}\Im\left(\frac{\varepsilon}{U_{e3}U^*_{\mu 3}}\right). \tag{238}$$

The apparent divergence of $A_{\mathrm{CP}}^{\mathrm{NP}}$ for small L is due to the approximations that have been used. Specifically, there is an $\mathcal{O}(|\varepsilon|^2)$ contribution to P_+ that is constant in L, namely $P_+ = \mathcal{O}(|\varepsilon|^2)$ for $L \to 0$. In contrast, $P_- = 0$ in the $L \to 0$ limit to all orders in $|\varepsilon|$.

Equation (238) leads to several interesting conclusions:

1. It is possible that, in CP-violating observables, the new-physics contributions compete with, or even dominate over, the SνM ones in spite of the weakness of the interactions ($|\varepsilon| \ll 1$);
2. The different distance dependence of $A_{\mathrm{CP}}^{\mathrm{SM}}$ and $A_{\mathrm{CP}}^{\mathrm{NP}}$ will allow, in principle, an unambiguous distinction to be made between new-physics contributions of the type described here and the contribution from lepton mixing; and
3. The $1/L$ dependence of $A_{\mathrm{CP}}^{\mathrm{NP}}$ suggests that the optimal baseline to observe CP violation from new physics is shorter than the one optimised for the SνM.

Since long-baseline experiments involve the propagation of neutrinos through the Earth, it is important to understand how matter effects affect these results. If a constant matter-density is assumed, then the matter contribution to the effective ν_e mass, $A = \sqrt{2}G_F N_e$, where N_e is the electron density, is constant. In general, any new interaction also generates a new non-diagonal contribution to the effective neutrino-mass matrix. Yet, since the new-physics effects are small, it is possible to treat the effect of new-physics at production or detection and the effect of new physics in the propagation separately.

The transition probability in matter is obtained by replacing the mass-squared differences, Δ_{ij}, and mixing angles, $U_{\alpha i}$, with their effective values in matter, Δ^m_{ij} and $U^m_{\alpha i}$. Considering only the two-generations and taking the small-x limit as before, the parameters x^m and θ^m may be defined by:

$$x^m = \frac{B}{\Delta}x, \qquad \sin 2\theta^m = \frac{\Delta}{B}\sin 2\theta, \tag{239}$$

where $B = \Delta - A$. From equation (237) it is clear that matter effects cancel at lowest order in x. Therefore, taking one higher order in x, the transition probability in matter, P^m, may be written:

$$P^m = P^v(1 \pm O(x^2)), \tag{240}$$

where P^v is the oscillation probability vacuum. Since matter in the Earth is not CP symmetric, its effect enters the oscillation formula for neutrinos and anti-neutrinos with opposite signs.

Therefore, in contrast to the case of vacuum oscillation, P_- will receive contributions from terms which would be CP conserving in vacuum and therefore A_{CP} will be non-zero even if there are no CP-violating amplitudes. In particular, a fake asymmetry can be related to the real part of ε.

The matter-related contribution to P_- may be denoted by $P_-^m \equiv P_-(A) - P_-(A=0)$ and, since the leading contributions to P_+ are the same as in the vacuum case, the matter-related contribution to $A_{\rm CP}$ may be written $A_{\rm CP}^m \equiv P_-^m/P_+$. The asymmetries for three neutrino generations in the small x_{31} limit assuming $|x_{12}/x_{13}| \ll |U_{e3}|$ are:

$$(A_{CP}^m)^{\rm SM} = \frac{2}{3}x_{31}^2\left(\frac{A}{\Delta_{31}}\right), \qquad (A_{CP}^m)^{\rm NP} = \frac{A}{\Delta_{31}}\Re\left(\varepsilon_{\mu e}^{d*} - \varepsilon_{e\mu}^{s}\frac{U_{e3}}{U_{\mu 3}^*}\right). \tag{241}$$

(more general results can be found in [626]). In equations (238) and (241):

1. Each of the four contributions has a different dependence on the distance. In the short-distance limit the asymmetries may be written:

$$(A_{\rm CP}^m)^{\rm SM} \propto L^2, \qquad A_{\rm CP}^{\rm SM} \propto L, \qquad (A_{\rm CP}^m)^{\rm NP} \propto L^0, \qquad A_{\rm CP}^{\rm NP} \propto 1/L. \tag{242}$$

   Thus, it is possible, in principle, to distinguish between the various contributions;

2. If the phases of the εs are of order 1, then the genuine CP asymmetry will be larger (at short distances) than that due to the matter effect; and

3. The search for CP violation in neutrino oscillations will allow us to constrain both $\Re(\varepsilon)$ and $\Im(\varepsilon)$.

A detailed study of the sensitivity of a future Neutrino Factory has not been carried out. Estimates indicated that $|\varepsilon| \sim 10^{-4}$ can be probed in a future Neutrino Factory [626, 627]. Of course, it is interesting to search for such effects without any specific new-physics framework in mind. In the following, however, we give several examples of specific new-physics models where large effects, $|\varepsilon| > 10^{-4}$, are possible [631].

Consider first left-right symmetric (LRS) models. These models are defined by extending the symmetry of the Standard Model to include right-handed electroweak interactions as follows:

$$G_{\rm LRS} = SU(3)_C \times SU(2)_L \times SU(2)_R \times U(1)_{B-L} \times D, \tag{243}$$

where D is a discrete symmetry that requires, among other constraints, $g_L = g_R$. Such models contain a scalar particle (Δ_L) with quantum numbers $\Delta_L(3,3,1)_{-2}$. The couplings of Δ_L to leptons are given by:

$$\begin{aligned}\mathcal{L}_{\Delta_L} &= f\bar{L}^c i\sigma_2\vec{\sigma}L\cdot\vec{\Delta}_L + \text{h.c.} \\ &= -\sqrt{2}f_{ij}\Delta_L^0\bar{\nu}_i^c P_L\nu_j + f_{ij}\Delta_L^-\left(\bar{\ell}_i^c P_L\nu_j + \bar{\ell}_j^c P_L\nu_i\right) + \sqrt{2}f_{ij}\Delta_L^{--}\bar{\ell}_i^c P_L\ell_j + \text{h.c.},\end{aligned} \tag{244}$$

where the 3×3 matrix f is symmetric in flavour space, $f_{ij}=f_{ji}$. The tree-level exchange of the Δ_L scalars lead to the following four-fermion vertices:

$$\begin{aligned}
\Delta_L^{--}-\text{exchange}: &\qquad \frac{f_{ij}f^*_{kl}}{m^2_{--}}(\bar{\ell}_k\gamma^\mu P_L\ell_i)(\bar{\ell}_l\gamma_\mu P_L\ell_j),\\
\Delta_L^{-}-\text{exchange}: &\qquad 2\frac{f_{ij}f^*_{kl}}{m^2_{-}}(\bar{\ell}_k\gamma^\mu P_L\ell_i)(\bar{\nu}_l\gamma_\mu P_L\nu_j),\\
\Delta_L^{0}-\text{exchange}: &\qquad \frac{f_{ij}f^*_{kl}}{m^2_{0}}(\bar{\nu}_k\gamma^\mu P_L\nu_i)(\bar{\nu}_l\gamma_\mu P_L\nu_j).
\end{aligned} \tag{245}$$

Effective couplings, $\varepsilon^s_{e\alpha}$, are induced in the decays $\mu^+\to e^+\nu_\alpha\bar{\nu}_\mu$, with $\alpha=\mu$ or τ, through Δ_L^- exchange in equation (245). (Note that the outgoing anti-neutrino must be a muon neutrino in order for the interference to take place.) Such contributions are proportional to:

$$2\frac{f_{e\mu}f^*_{\mu\alpha}}{m^2_-}(\bar{\mu}\gamma^\mu P_L e)(\bar{\nu}_\alpha\gamma_\mu P_L\nu_\mu). \tag{246}$$

Inspection of equation (246) indicates that an appropriate definition of the LRS-induced coupling that is relevant to muon decay is:

$$\frac{(G_\Delta)_{e\alpha}}{\sqrt{2}}=\frac{f_{e\mu}f^*_{\mu\alpha}}{2m^2_-}\quad\Longrightarrow\quad \varepsilon^s_{e\alpha}\equiv\frac{(G_\Delta)_{e\alpha}}{G_F}=4\frac{f_{e\mu}f^*_{\mu\alpha}}{g^2}\frac{m^2_W}{m^2_-}. \tag{247}$$

Bounds on $\varepsilon^s_{e\alpha}$ can be obtained from charged-lepton decays. If the Δ_L-scalar is heavy, the mass-squared splittings among its members, which break electroweak symmetry, are small and motivate the approximation $m_-\approx m_{--}$. Then, using data from $\mu\to e\gamma$ and from $\tau\to\mu\mu e$ to update tables 3 and 4 in [632], one obtains:

$$\varepsilon^s_{e\mu}\lesssim 2\times 10^{-5},\qquad\text{and}\qquad \varepsilon^s_{e\tau}\lesssim 2\times 10^{-3}, \tag{248}$$

indicating that $\varepsilon^s_{e\tau}$ can be large. Yet, it seems that models that saturate the bound have no particular motivation. In generic models $\varepsilon^s_{e\tau}$ is related to the ratio of the neutrino mass to the weak scale and thus is tiny. Of course, it may be possible to find models in which $\varepsilon^s_{e\tau}$ is not related to the smallness of the neutrino masses and is naturally large.

Supersymmetric (SUSY) models without R-parity also contain scalars with couplings to charged and neutral fermions [633]. The couplings of the scalars $\tilde{E}_i(1,1)_1$, where $i=1,2,3$ to leptons are given by:

$$\mathcal{L}_{\tilde{E}_i}=\lambda\bar{L}^c i\sigma_2 L\tilde{E}+\text{h.c.}\qquad\qquad =\lambda_{ijk}\tilde{E}^-_k\left(\bar{\ell}^c_i P_L\nu_j-\bar{\ell}^c_j P_L\nu_i\right)+\text{h.c.}.$$

The λ_{ijk} couplings are anti-symmetric in the flavour indices i,j, $\lambda_{ijk}=-\lambda_{jik}$ and, in particular, $\lambda_{eei}=\lambda_{\mu\mu i}=0$.

Tree-level exchange of the $\tilde{E}_i^-$ scalars leads to the following four fermions vertices:

$$2\frac{\lambda_{ijm}f^*_{klm}}{m^2_{\tilde{E}_m}}(\bar{\ell}_k\gamma^\mu P_L\ell_i)(\bar{\nu}_l\gamma_\mu P_L\nu_j). \tag{249}$$

The contributions from $\tilde{E}_i^-$ exchange in equation (249) to the decays $\mu^+ \to e^+\nu_\alpha\bar{\nu}_\mu$, with $\alpha = \mu$ or τ, are proportional to:

$$2\frac{\lambda_{e\mu i}\lambda^*_{\mu\alpha i}}{m^2_{E_i}}(\bar{\mu}\gamma^\mu P_L e)(\bar{\nu}_\alpha\gamma_\mu P_L\nu_\mu) \quad \Longrightarrow \quad \varepsilon^s_{e\alpha} \equiv \frac{(G_{\tilde{E}})_{e\alpha}}{G_F} = 4\frac{\lambda_{e\mu i}\lambda^*_{\mu\alpha i}}{g^2}\frac{m^2_W}{m^2_{E_i}}. \tag{250}$$

Due to the anti-symmetry of the λ_{ijm} couplings, $\varepsilon^s_{e\mu} = 0$. Tables 3 and 4 in [632] show that universality gives the strongest bound on $\varepsilon^s_{e\tau}$:

$$\varepsilon^s_{e\tau} \lesssim 6 \times 10^{-2}. \tag{251}$$

In general, only weak constraints on the values of the λ_{ijk} couplings in R-parity violating SUSY models can be obtained. In particular, the upper bound given above can be saturated in a generic model. The λ couplings, however, contribute to neutrino masses (see, for example, [634]. Unless there is fine-tuning, the bounds on neutrino masses imply $\varepsilon^s_{e\tau} \lesssim 10^{-3}$. Thus, large effects are possible even without fine-tuning. Of course, the bound in (251) can be saturated naturally in models with extra structure, such as horizontal symmetries [635].

NSIs arising in supersymmetric models with R parity were studied in [627,628]. Measurements of charged-lepton decays allow strong limits to be placed on NSI in SUSY models with R parity, implying that the relevant couplings are small. This class of model will not be discussed further here.

Finally, consider RS-type models [636] with right handed neutrinos in the bulk [637]. In such models bulk singlets are introduced with dimension-five mass terms. When these mass terms are of the order of the fundamental scale, the zero modes have very small couplings to the standard doublet neutrinos that are confined to the Planck brane. Thus, exponentially small Dirac neutrino masses are generated. In addition to the zero modes, the higher Kaluza-Klein modes couple to the doublet neutrinos. However, their wave functions are not small at the visible brane. Thus, their dimension-four Yukawa couplings (Y_5) are not particularly small, and large active-heavy mixing is expected. As a result of this mixing the effective 3×3 mixing matrix is not unitary, and this non-unitarity is equivalent to a new interaction in production or detection.

In order to have a viable model it is necessary to assume that the Y_5, are small. Note that this is a mild fine-tuning as the most natural values for these Yukawa couplings are $O(1)$. In this case, the mixing-matrix elements can be expanded in the small mixing angles and we have [637]:

$$|U_{i\alpha}|^2 \approx \frac{1}{2c_\alpha + 1}\,\frac{v_0^2|Y_5^{i\alpha}|^2}{k^2}\,, \tag{252}$$

where v_0 and k are fundamental mass parameters of the theory and $c_\alpha \equiv m^\alpha_{bulk}/k$ such that m^α_{bulk} are the bulk masses of the singlet fermions. In order to get neutrino masses in the range indicated by experiments, the parameter c_α has to be in the range of 1.1 to 1.5. Without any further input it seems natural to assume that all the mass parameters v_0, k and m^α_{bulk} take their naive values, and therefore:

$$|U_{i\alpha}| \sim |Y_5^{i\alpha}|, \tag{253}$$

up to coefficients of order unity. Since, by assumption, $|Y_5^{i\alpha}| \ll 1$, equation (232) yields:

$$\varepsilon_{\ell e} \equiv \varepsilon^{d*}_{\ell e} + \varepsilon^{s}_{e\ell} \sim Y_5^{e\alpha} Y_5^{*\ell\alpha}. \tag{254}$$

The light-heavy mixing angles can be bounded from several processes [376, 637]. The invisible width of the Z leads to the constraint:

$$|U_{eh} U_{\ell h}| \lesssim 10^{-2}. \tag{255}$$

Limits on the decays $\mu \to e\gamma$ and $\tau \to e\gamma$ lead to the following constraints [638]:

$$|U_{eh} U_{\tau h}| \lesssim 10^{-2}, \qquad |U_{eh} U_{\mu h}| \lesssim 10^{-4}\ ; \tag{256}$$

indicating that large effects are allowed for the tau case. For the muon channel the effects are not large but may still be observable.

Turning to the theoretical expectation for the mixing angles, naively, it might be expected that the light-heavy mixing should be of order unity. Yet, the Yukawa couplings may be rather small. Even so, the model seems to be more attractive for larger Y_5 and therefore for large mixing angles.

4.5.2 Non-standard interactions in propagation

4.5.2.1 Parameters and limits:

Non-standard neutrino interactions induced by new physics (NP) not yet observed at accelerator experiments presumably arise at scales $\Lambda_{\rm NP}$ much larger than the typical energy involved in future long-baseline experiments, $E \ll \Lambda_{\rm NP}$. At such energies the non-standard effects are conveniently described by effective interactions (operators) with dimension (D) 5 or more (in energy). The couplings of such operators involve inverse powers of the scale of the new physics that generates them. The effect of such operators at lower scales is suppressed by powers of $E/\Lambda_{\rm NP}$, where E is the typical energy of the experiment, so that it is only necessary to take into account the lowest dimensional interactions. The classic example is the Fermi interaction describing weak interactions at scales lower than the weak scale $\Lambda_{\rm EW}$. This four-fermion interaction has dimension 6 and its coupling $2\sqrt{2}G_F \sim 1/\Lambda^2_{\rm EW}$ involves two inverse powers of the scale $\Lambda_{\rm EW}$ at which the operator is generated, which makes the weak interactions weak at $E \ll \Lambda_{\rm EW}$.

The power of this 'effective' description of high-energy interactions is that: the effect of the most general high energy physics can be conveniently parameterised in terms of a (finite) set of operators only involving light fields, so that the knowledge of the physics above $\Lambda_{\rm NP}$ is not required; and the experimental identification of the operators actually present at low energy provides important information on the physics above $\Lambda_{\rm NP}$. Indeed, weak interactions were first parameterised in terms of generic four-fermion interactions. Unveiling the 'V-A' (left-handed) structure of those interactions was then crucial to the understanding of the renormalisable theory underlying them (the SM).

At present the only available firm evidence of a non-renormalisable remnant of higher energy physics is the $D = 5$ operator responsible for neutrino masses and mixings :

$$\frac{h_{ij}}{2\Lambda_L}(L_i H)(L_j H), \tag{257}$$

where L_i, $i = 1, 2, 3$ are the lepton doublets, H is the Higgs-doublet, and Λ_L is the lepton-number-violation scale at which the operator is generated. Once the Higgs gets a vacuum expectation value (vev), $\langle H \rangle = (0, v)^T$, that operator gives rise to Majorana neutrino masses $m^{\nu}_{ij} = -h_{ij}v^2/\Lambda_L$, which forces Λ_L to be near 10^{15} GeV for $h \sim 1$, not very far from the unification scale. The evidence for the existence of the operator in equation (257) is very strong, as the understanding of neutrino masses it provides is solid and general (the see-saw mechanism is just one example of a high-energy mechanism giving rise to such an operator [14]). However, such an operator has no significant effect on the neutrino-matter interaction in long-baseline experiments, as it is associated to the superheavy scale Λ_L. In order for new physics to have a measurable effect on the neutrino interactions in matter, a new effective interaction has to be associated to a scale not too much higher than the scale of the physics giving rise to the Standard Model interactions (matter effects), $\Lambda_{\rm EW} \sim G_F^{-1/2}$. At present there is no firm evidence at all of operators generated at such scale (which explains the variety of theoretical models available for the physics accessible at the LHC). In the following therefore, a general parameterisation of the possible operators relevant for neutrino interaction with ordinary matter is used.

Consider only those operators that arise at a scale much lower than Λ_L for which lepton number is conserved. The relevant interaction is then:

$$\sum_{\substack{f=e,u,d \\ \alpha,\beta=e,\mu,\tau}} 4\frac{G_F}{\sqrt{2}}\bar{\nu}_{\alpha L}\gamma^{\mu}\nu_{\beta L}\left(\epsilon^{f_L}_{\alpha\beta}\,\bar{f}_L\gamma_{\mu}f_L + \epsilon^{f_R}_{\alpha\beta}\,\bar{f}_R\gamma_{\mu}f_R\right) . \tag{258}$$

Since the scale at which this interaction arises is supposed to be not too far from the electroweak scale, its coupling may be parameterised by $G_F\epsilon$, where $\epsilon \sim (\Lambda_{\rm EW}/\Lambda_{\rm NP})^2$. equation (258) holds in a basis in which the kinetic terms are canonical and the charged-fermion masses are diagonal. The effect of the coherent forward scattering induced by equation (258) on neutrino propagation in an ordinary, neutral, unpolarised medium is encoded in the parameters [60, 646, 647]:

$$\epsilon = \sum_{f=e,u,d}\frac{n^f}{n_e}\epsilon^f = \epsilon^e + 2\epsilon^u + \epsilon^d + \frac{n_n}{n_e}(2\epsilon^d + \epsilon^u) , \tag{259}$$

where $\epsilon^f = \epsilon^{f_L} + \epsilon^{f_R}$, n_f is the number density of the fermion f in the medium crossed by the neutrinos (n_n for the neutron), and the flavour indices have been omitted. In Section 4.5.2.2 the signatures of the new interactions in terms of the $\epsilon_{\alpha\beta}$ parameters will be discussed, independent

[14] The operator in equation (257) accounts for essentially all high-energy mechanisms that generate neutrino masses. The only possible alternative is that the neutrino masses originate at or below the weak scale. The classic example is a Dirac mass term in the presence of an exactly conserved (at the perturbative level) lepton number. This possibility is less appealing because it needs tiny Yukawa couplings for the neutrinos of all the three families. The smallness of such Yukawas can however in turn be justified in terms of new symmetries appropriately broken [151, 309, 639–641] or extra-dimensional mechanisms [258, 259, 261–263, 457, 642–645].

of their origin. Constraints on the parameters are discussed here, focussing on the non-flavour-diagonal couplings.

A model-independent limit on $\epsilon_{\mu\tau}$ can be inferred from atmospheric-neutrino data [524, 648]. The limit is obtained on the hypothesis that the NP interactions only involve down quarks, $|\epsilon^d_{\mu\tau}| < 0.013$ at 90% C.L., corresponding to $|\epsilon_{\mu\tau}| \lesssim 0.4$. A recent combined analysis of Super-Kamiokande, K2K and MINOS data [649] also provides a bound on $\epsilon_{e\tau}$. In the limit in which $\epsilon_{ee} = \epsilon_{\tau\tau} = 0$, the analysis gives $|\epsilon_{e\tau}| \lesssim 0.5$. The latter limit could improve with future MINOS data. In [650] the limit $|\epsilon^{e_L,e_R}_{\alpha\beta}| \leq 0.53$ at 99%C.L is obtained from the $e^+e^- \to \nu\bar{\nu}\gamma$ cross section measurement at LEP. A stronger limit on $\epsilon_{\mu\tau}$ from neutrino-scattering experiments, $|\epsilon_{\mu\tau}| < 0.1$, is found in [651]. The latter also considers the limits from charged-lepton effects induced by loops involving the vertex in equation (258), which gives, in particular, $|\epsilon_{e\mu}| < 2 \cdot 10^{-3}$.

Stronger bounds can be obtained by relating the $\epsilon_{\alpha\beta}$ parameters to operators involving the charged leptons. The description of the effect of NSIs in neutrino propagation, equation (258), can be obtained in two steps. First, the general effective description just below the scale $\Lambda_{\rm NP}$, but above the weak scale, is written in terms of operators symmetric under the SM gauge group. Then, the operators are run to the weak scale and matched with the effective description below $\Lambda_{\rm EW}$ in terms of the operators in equation (258). The presence of the intermediate, $\mathrm{SU}(2)_L$ symmetric step is relevant as it relates the neutrino interactions in equation (258) to the interactions of their $\mathrm{SU}(2)_L$ charged lepton partners. However, this relation is complicated by the fact that $\mathrm{SU}(2)_L$ is broken. It is, in fact, possible to conceive of new physics affecting neutrinos but not charged leptons, see below. The amount of $\mathrm{SU}(2)_L$ breaking that can be tolerated is in turn bound by electroweak-precision tests performed at LEP.

Consider first the case in which $\mathrm{SU}(2)_L$ breaking is neglected and the operators in equation (258) originate from $\mathrm{SU}(2)_L$ invariant operators. Then, the experimental bounds on charged-lepton processes imply [652–654] :

$$\epsilon^e_{e\mu} \lesssim 10^{-6} \qquad \epsilon^e_{\mu\tau} \lesssim 3 \cdot 10^{-3} \qquad \epsilon^e_{e\tau} \lesssim 4 \cdot 10^{-3} \tag{260a}$$

$$\epsilon^{u,d}_{e\mu} \lesssim 10^{-5} \qquad \epsilon^{u,d}_{\mu\tau} \lesssim 10^{-2} \qquad \epsilon^{u,d}_{e\tau} \lesssim 10^{-2}\ . \tag{260b}$$

For example, the extension of the MSSM including three singlet, chiral neutrino fields (giving rise to a supersymmetric see-saw) can generate large misalignment between leptons and sleptons, in turn inducing non-standard interactions through one-loop diagrams involving the sleptons. $\mathrm{SU}(2)_L$ breaking is negligible in this case, so that the strong constraints in equation (260) hold and suppress the effects in neutrino propagation [628].

These limits can be evaded by taking into account $\mathrm{SU}(2)_L$ breaking. The extent to which the latter relaxes the limits depends on how the operator in equation (258) is generated and how $\mathrm{SU}(2)_L$ breaking enters. A general treatment should in principle be based on the most general effective lagrangian at the EW scale, including the effective contribution to the kinetic terms, along the lines of reference [650]. Such a general analysis is not available, but it is clear that the $\mathrm{SU}(2)_L$ symmetric limit is considerably weakened. This is supported by the analysis in [653, 654], where the case in which the operator in equation (258) is induced by the exchange

of new heavy bosons is considered. The effect of $\mathrm{SU}(2)_L$ breaking on the masses of such heavy bosons can relax the bounds from the charged-lepton sector in equation (260) by a factor of seven without a conflict with the electroweak-precision data. It is even possible to generate the neutrino operator in equation (258) without giving rise to any charged-lepton effects if the new physics (e.g. warped or flat extra-dimensions [655]) induces the operator:

$$4\frac{G_F}{\sqrt{2}}\varepsilon_{\alpha\beta}(HL_\alpha)^\dagger i\hat{\partial}(HL_\beta)\ . \tag{261}$$

The latter contributes to the neutrino wave function, but not to that of the charged lepton. The neutrino kinetic term must therefore be brought back to the canonical form by means of a non-unitary rotation. When acting on the standard Fermi interaction, the latter is rotated, inducing extra contributions in the form in equation (258) but leaving the charged-lepton sector completely unaffected. The ε parameters are therefore constrained mostly by neutrino experiments which give [655] $|\varepsilon_{e\mu}| < 0.05$, $|\varepsilon_{e\tau}| < 0.1$, $|\varepsilon_{\mu\tau}| < 0.013$. The couplings in equation (258) generated through this mechanism are [656] :

$$\epsilon^e_{\alpha\beta} = -\frac{1}{2}\Big(\varepsilon_{\alpha e}\delta_{\beta e} + \varepsilon_{e\beta}\delta_{\alpha e}\Big) + \Big(\frac{1}{2} - 2\sin^2\theta_W\Big)\varepsilon_{\alpha\beta} \tag{262a}$$

$$\epsilon^u_{\alpha\beta} = -\Big(\frac{1}{2} - \frac{4}{3}\sin^2\theta_W\Big)\varepsilon_{\alpha\beta} \qquad \epsilon^d_{\alpha\beta} = \Big(\frac{1}{2} - \frac{2}{3}\sin^2\theta_W\Big)\varepsilon_{\alpha\beta}\ . \tag{263}$$

so that the relevant parameters for the effects in neutrino propagation are:

$$\epsilon_{\alpha\beta} = -\frac{1}{2}\big(\varepsilon_{\alpha e}\delta_{\beta e} + \varepsilon_{e\beta}\delta_{\alpha e}\big) + \frac{1}{2}\frac{n_n}{n_e}\varepsilon_{\alpha\beta}\ . \tag{264}$$

Note that $\epsilon_{e\mu}$, $\epsilon_{\mu\tau}$, $\epsilon_{e\tau}$ are, in this case, suppressed by the relatively small factor $(n_n/n_e - 1)/2$. As a consequence, the bounds on $\epsilon_{\mu\tau}$, $\epsilon_{e\tau}$ are stronger than the ones from equation (260), despite the fact that bounds from the charged-lepton sector are, in this case, essentially irrelevant. The bound on $\epsilon_{e\mu}$ is, in contrast, weaker.

Finally, the limits on the impact of $\mathrm{SU}(2)_L$ breaking can be further weakened if the effect on the precision observables of each source of $\mathrm{SU}(2)_L$ breaking is considered separately or if it is assumed that the Higgs is light. In principle, the effects of two or more corrections (including the effect of a Higgs that is heavier than expected) on the SM fit to precision observables could in fact compensate each other, thus allowing stronger $\mathrm{SU}(2)_L$ breaking effects [651].

4.5.2.2 Effects on neutrino propagation

The possibility that new physics affects the neutrino transitions observed in solar [60, 652, 654, 657], atmospheric [648, 653, 658], LSND [659], and supernova [660] experiments has been widely studied in the literature since the seminal paper of Wolfenstein [60]. The effects of NSIs at production and decay are quite different from those that arise in the propagation between source and detector. This should make them relatively easy to disentangle. In fact, due to the geometrical L^{-2} suppression, the effects at production and detection are best studied at a smaller baseline L [626], whereas in the case of new interactions with matter the L^{-2} suppression is

compensated (up to a certain L) by the development of the oscillation. Moreover, the possibility of a peculiar growth with the neutrino energy opens up, which would give rise to a noticeable signature [656].

As in ordinary matter the rate of incoherent scattering is negligible, the effect of standard and non-standard interactions only shows up through the coherent forward-scattering effect. Such an effect is conveniently accounted for by the MSW potential term in the neutrino Schroedinger equation. The potential induced by $\nu_\alpha f \to \nu_\beta f$ forward scattering ($\alpha, \beta = e, \mu, \tau,\ f = e, u, d$) induced by the effective interaction in equation (258) can be parameterised as $V_{\alpha\beta} = \epsilon_{\alpha\beta} V = \sqrt{2}\epsilon_{\alpha\beta} G_F N_e$, where $V = \sqrt{2} G_F N_e$ is the MSW potential induced by the standard charged-current interactions, N_e is the electron number density and $\epsilon_{\alpha\beta} = \epsilon^*_{\beta\alpha}$ are the parameters defined in equation (259). In turn, the standard and non-standard MSW potentials can be reabsorbed in an energy-dependent redefinition of the neutrino mass-squared matrix, $M^2 \to M^2_{\rm eff} + \text{universal terms}$, where:

$$M^2_{\rm eff} = U \begin{pmatrix} 0 & 0 & 0 \\ 0 & \Delta m^2_{21} & 0 \\ 0 & 0 & \Delta m^2_{31} \end{pmatrix} U^\dagger + 2EV \begin{pmatrix} 1+\epsilon_{ee} & \epsilon_{e\mu} & \epsilon_{e\tau} \\ \epsilon^*_{e\mu} & \epsilon_{\mu\mu} & \epsilon_{\mu\tau} \\ \epsilon^*_{e\tau} & \epsilon^*_{\mu\tau} & \epsilon_{\tau\tau} \end{pmatrix} , \tag{265}$$

E is the neutrino energy, U is the PMNS mixing matrix in the usual parameterisation, and the flavour-universal terms do not play a role.

The possibility of observing the effect of non-universal diagonal terms, $\epsilon_{\alpha\alpha}$, has been considered in [661]. Such terms could arise, for example, from a violation of universality in $Z\nu\bar{\nu}$ couplings, in particular a correction to the $Z\nu_e\nu_e$ coupling, to be compensated in the bound from the Z invisible decay width by a corresponding correction to the $Z\nu_\tau\nu_\tau$ coupling. The effect of a non-universality at the level of 1% would amount in first approximation to an energy-dependent shift in the effective value of the θ_{23}. The possibility of observing such a shift depends on the true value of θ_{23} angle. The oscillation probability is proportional to $\sin^2 2\theta_{23}$, which is almost insensitive to a 1% shift in θ_{23}, for $\theta_{23} = \pi/4$. On the other hand, the shift might have a chance to be observed for example if $\sin^2 2\theta_{23} = 0.92$. This would require an experiment with neutrinos above the resonant energy and therefore a large enough baseline ($L \sim 10000\,\text{km}$), in such a way that the first oscillation peak is approached. Most analyses concentrate on the possibility of observing the effect of off-diagonal terms $\epsilon_{e\mu}$, $\epsilon_{\mu\tau}$, $\epsilon_{e\tau}$, and in particular on $\epsilon_{\mu\tau}$ and $\epsilon_{e\tau}$, since the bound on $\epsilon_{e\mu}$ is too strong for it to play any role.

Earlier work on the effect of non-vanishing $\epsilon_{\mu\tau}$, $\epsilon_{e\tau}$ on $\nu_\mu \to \nu_\tau$, $\nu_e \to \nu_\tau$ oscillations [662,663] assumed the presence of a τ detector with an efficiency $\eta \sim 0.3$ for observing ν_τ, $\bar{\nu}_\tau$. Moreover, the analyses were performed at fixed values of the oscillation parameters, in particular θ_{13} and the CP-violating phase δ. Later work [664, 665] carried forward the analysis by: focussing on the effect of $\epsilon_{e\tau}$ in $\nu_e \to \nu_\mu$ transitions, which can be detected through the easier wrong-sign-muon signal at a less ambitious muon detector; and by letting θ_{13} and δ vary. The latter might in fact have to be determined by the same experiments sensitive to $\epsilon_{e\tau}$, introducing an additional uncertainty on $\epsilon_{e\tau}$. At the same time, if the effect of a non-vanishing $\epsilon_{e\tau}$ is taken into account, the sensitivity to the oscillation parameters could worsen. This is indeed the case

if one considers the $\nu_e \to \nu_\mu$ transitions only. The wrong-sign-muon signal, however, is also due to $\nu_e \to \nu_\tau$ transitions producing a τ that then decays into a muon. This is important because the spectrum of the $\nu_e \to \nu_\tau$ transition can have a very peculiar behaviour in the presence of a sizable $\epsilon_{e\tau}$. Such a behaviour on the one hand enhances the $\nu_e \to \nu_\tau$ transitions at high energy (thus making the $\nu_e \to \nu_\tau$ contribution to the wrong-sign-muon signal important, sometimes even predominant) on the other hand it allows the effects of θ_{13} and $\epsilon_{e\tau}$ to be disentangled [656].

The presence of $\epsilon_{e\tau}$ effects can reduce the sensitivity of $\nu_e \to \nu_\mu$ transitions to θ_{13}. This is because an expansion in the small θ_{13} and $\epsilon_{e\tau}$ parameters gives $P(\nu_e \to \nu_\mu) \approx A s_{13}^2 + B s_{13}\epsilon_{e\tau} + C\epsilon_{e\tau}^2$, where A, B, C depend on the baseline, on the energy, and on the channel (neutrinos or anti-neutrinos) and $s_{13} = \sin\theta_{13}$. The total rate of $\nu_e \to \nu_\mu$-induced wrong sign muon events (obtained by convoluting A, B, C with the energy dependence of fluxes, cross-sections, efficiencies, etc.) then corresponds to an ellipse in the s_{13}–$\epsilon_{e\tau}$ plane, so that s_{13} and $\epsilon_{e\tau}$ cannot be disentangled by a single total-rate measurement only. It also turns out that using the spectral information as well does not help very much, as $\epsilon_{e\tau}$ does not modify the spectrum of $\nu_e \to \nu_\mu$ transitions significantly. On the other hand, combining measurements in the neutrino and anti-neutrino channels and combining measurements at different baselines helps to reduce the degeneracy, but the sensitivity to θ_{13} is still reduced by one order of magnitude [664]. The situation is even worse in the presence of new-physics effects in the production process. In this case the effect of a given θ_{13} (including its energy and baseline dependence) can be faked in both the neutrino and anti-neutrino channels by a proper combination of the NP parameters controlling the exotic production process and the matter effects [665]. A near detector, only sensitive to new effects at production, might help in this case.

The degeneracy can be resolved by taking into account the contribution of $\nu_e \to \nu_\tau$ transitions to the wrong-sign-muon signal. While the spectrum of $\nu_e \to \nu_\mu$ transitions is not significantly affected by $\epsilon_{e\tau}$, it turns out that the spectrum of $\nu_e \to \nu_\tau$ transitions can be. In order to have an intuitive picture of the basic features of the latter, and in general of all the $\epsilon_{\alpha\beta}$ parameters, consider first the approximation $\Delta m_{21}^2 = 0$, which is meaningful in the range of energies of interest. In this limit the mixing angle in vacuum θ_{12} becomes un-physical. We can also consider a phase convention for the neutrino fields in which the phases only appear in the ϵ parameters [15]. equation (265) then becomes:

$$M_{\rm eff}^2 = \Delta m_{31}^2 \begin{pmatrix} s_{13}^2 + (E/E_{\rm res})(1+\epsilon_{ee}) & s_{13}/\sqrt{2} + (E/E_{\rm res})\epsilon_{e\mu} & s_{13}/\sqrt{2} + (E/E_{\rm res})\epsilon_{e\tau} \\ s_{13}/\sqrt{2} + (E/E_{\rm res})\epsilon_{e\mu}^* & 1/2 + (E/E_{\rm res})\epsilon_{\mu\mu} & 1/2 + (E/E_{\rm res})\epsilon_{\mu\tau} \\ s_{13}/\sqrt{2} + (E/E_{\rm res})\epsilon_{e\tau}^* & 1/2 + (E/E_{\rm res})\epsilon_{\mu\tau}^* & 1/2 + (E/E_{\rm res})\epsilon_{\tau\tau} \end{pmatrix} , \tag{266}$$

where we also set $\theta_{23} = \pi/4$, $\cos\theta_{13}$, and $\cos 2\theta_{13} = 1$.

[15] While in the absence of non-standard interactions the CP-violating phase also becomes un-physical in the $\Delta m_{12}^2 = 0$ limit, in the general case it does not. In fact, the phase re-definition necessary to rotate δ away from the mixing matrix also acts on the non-diagonal new interactions. Therefore, if the ϵ parameters are real to start with, they acquire a phase δ once δ has been rotated away from the mixing matrix in vacuum. The phase has just moved from the mixing matrix in vacuum to the epsilon parameters.

The neutrino effective masses and mixings follow from the diagonalisation of $M^2_{\rm eff}$. In the limit in which the non-standard interactions are switched off, $\epsilon_{\alpha\beta} \to 0$, the usual expressions for the neutrino masses and mixings in the presence of matter are recovered, characterised by a resonant energy $E_{\rm res}$:

$$E_{\rm res} \simeq 10 \text{ GeV} \left(\frac{\Delta m^2_{31}}{2.5 \cdot 10^{-3} \text{ eV}^2}\right) \left(\frac{1.65 \,\text{g}\,\text{cm}^3}{\rho\, Y_e}\right) , \tag{267}$$

where ρ is the matter density and Y_e is the number of electrons per baryon in matter n_e/n_B. In particular, the characteristic suppression of the θ_{13}, θ_{12} mixing angles at energies higher than the resonance energy is recovered. This is because in the $E/E_{\rm res} \gg 1$ limit the large diagonal MSW term in $(M^2_{\rm eff})_{11}$ is enhanced, which suppresses the mixing. In particular, $\sin^2 2\theta^m_{13} \sim \sin^2 2\theta_{13}(E_{\rm res}/E)^2$, so that the transition probabilities decrease with E^2:

$$P(\nu_e \to \nu_\tau) \sim \left(\frac{E_{\rm res}}{E}\right)^2 \cos^2\theta_{23} \sin^2 2\theta_{13} \sin^2 \frac{LV}{2} \text{ ; and} \tag{268a}$$

$$P(\nu_e \to \nu_\mu) \sim \left(\frac{E_{\rm res}}{E}\right)^2 \sin^2\theta_{23} \sin^2 2\theta_{13} \sin^2 \frac{LV}{2} . \tag{268b}$$

Note also that the mass-squared difference in matter, $(\Delta m^2_{31})_m \sim 2EV$ grows with energy, canceling the $1/E$ dependence in the oscillating term of the probability.

The situation is completely different in the presence of non-standard, non-diagonal interactions; at least at very large energies $E \gg E_{\rm res}$. The non-diagonal elements now also get a contribution that grows with energy. As a consequence, at sufficiently large energy, matter effects will dominate in all the entries of $M^2_{\rm eff}$. Then: the effective mixing angles will be determined by matter effects only, thus providing a determination of the $\epsilon_{\alpha\beta}$ ratios; and the mixing angles become energy independent, i.e. they do not suffer from the high-energy suppression anymore. This is also true for the transition probabilities, the leading terms of which are given in the large $E/E_{\rm res}$ limit by the following simple expressions:

$$P(\nu_e \to \nu_\tau) \sim 4 \left|\epsilon_{e\tau} + \frac{E_{\rm res}}{E} c_{23} s_{13}\right|^2 \sin^2 \frac{LV}{2} \tag{269a}$$

$$P(\nu_e \to \nu_\mu) \sim 4 \left|\epsilon_{e\mu} + \frac{E_{\rm res}}{E} s_{23} s_{13}\right|^2 \sin^2 \frac{LV}{2} , \tag{269b}$$

where the leading $E_{\rm res}/E$ correction to the energy-independent amplitudes have been included. The oscillation probability reaches a constant value $4|\epsilon|^2 \sin^2(LV/2)$ at high energies.

The behaviour of the transition probabilities at sufficiently high energy is therefore drastically different in the presence of non-standard flavour-changing interactions. Note also that at a Neutrino Factory, the energy independent transition probability would be enhanced by the growth with energy of the neutrino flux and of the neutrino cross section, thus giving rise to a striking growth of the signal with energy. Of course, the interest of this observation depends on how large the 'sufficiently high' energy at which the energy-enhanced non-standard effect dominates. This in turn depends on the entry of the $M^2_{\rm eff}$ matrix under consideration. In order for the NP effects to emerge in the "atmospheric" 23 block in equation (266), the $E/E_{\rm res}$

enhancement must be very large, as the new $(E/E_{\rm res})\epsilon_{\mu\tau}$ effect competes with 1/2 and the limits on $\epsilon_{\mu\tau}$ are relatively severe. The situation is more promising in the 12 and 13 entries, where the vacuum matrix element is suppressed by $s_{13}/\sqrt{2}$, so that the new effect has a better chance to emerge. Particularly promising is the 13 entry, as values of $\epsilon_{e\tau}$ as large as 0.1 or more are not excluded (the limits on $\epsilon_{e\mu}$ are the most stringent). Note that due to the large ν_μ–ν_τ mixing, a large $\epsilon_{e\tau}$ would also affect the $\nu_e \to \nu_\mu$ transitions, but would not give rise, in this case, to an energy enhancement. This is because the large θ_{23} mixing communicating the effect of $\epsilon_{e\tau}$ to the $\nu_e \to \nu_\mu$ transition takes place at the atmospheric mass-squared difference Δm^2_{31}, which in the large $E_{\rm res}/E$ limit is subleading compared to the other mass-squared difference, $2EV$. This is also confirmed by equation (269) ($\epsilon_{e\tau}$ does not affect $P(\nu_e \to \nu_\mu)$ at the leading order in $E_{\rm res}/E$).

The $\epsilon_{e\tau}$ term exceeds the standard term at energies $E \gtrsim E_{\rm NP} = |s_{13}/(\sqrt{2}\,\epsilon)|E_{\rm res}$. The regime in which the new effects are comparable to the standard ones is therefore within the reach of a machine producing neutrinos of energy E_ν such that:

$$|\epsilon| \gtrsim \frac{|s_{13}|}{\sqrt{2}}\frac{E_{\rm res}}{E_\nu}\ . \tag{270}$$

At higher energies the non-standard effects start to dominate, and the transition probability becomes constant in energy. For example, at a machine producing neutrinos with an energy of 50 GeV, the new effects are at least comparable to the standard ones if $|\epsilon_{e\tau}| \gtrsim 0.007(|s_{13}|/0.05)$. Recall that $|s_{13}| = 0.05$ corresponds to $\sin^2 2\theta_{13} = 10^{-2}$, a value not very far from the present bound and well within the typical sensitivity of a Neutrino Factory.

To investigate the sensitivity to CP-violating phases, define $\epsilon = |\epsilon|e^{i\phi}$. The phase convention being considered is one in which the ϵ's are the only complex parameters. In an alternative convention, in which the δ phase has not been reabsorbed in ϵ, the physical phase would be $\delta - \phi$. equation (269) shows that in the high-energy limit, the probabilities depends on $\cos\phi$. This dependence is different in the neutrino and anti-neutrino channels, as the matter effects in the anti-neutrino channel have opposite sign. As a consequence, $\cos\phi$ could be determined together with $|\epsilon_{e\tau}|$. The absolute value $|\epsilon_{e\tau}|$ could in fact be determined in the high-energy regime, in which $|\epsilon_{e\tau}|$ dominates the transition amplitude. $\cos\phi$ could then be determined in the $E_\nu \sim E_{\rm NP}$ regime in which the interference between the standard and non-standard terms is maximal. If $\cos\phi > 0$, the two terms would interfere constructively in the neutrino channel and destructively in the anti-neutrino one, while if $\cos\phi < 0$, the two terms would be destructive for neutrinos and constructive for anti-neutrinos. The previous considerations hold of course provided that $E_{\rm NP} > E_{\rm res}$, or $|s_{13}/(\sqrt{2}\epsilon)| > 1$. For $E_{\rm NP} \lesssim E_{\rm res}$ the cancellation is spoiled by the Δm^2_{31} terms.

If the condition in equation (270) is met in at least a portion of the neutrino spectrum, the ν_τ spectrum shows a surprising enhancement at high energy. Direct τ detection is challenging and would require a very granular detector for τ identification. On the other hand, a coarse detector with only muon-charge-identification capability would not miss the peculiar feature of the signal, since the $\nu_e \to \nu_\tau$ channel contributes to the wrong-sign muon spectrum through

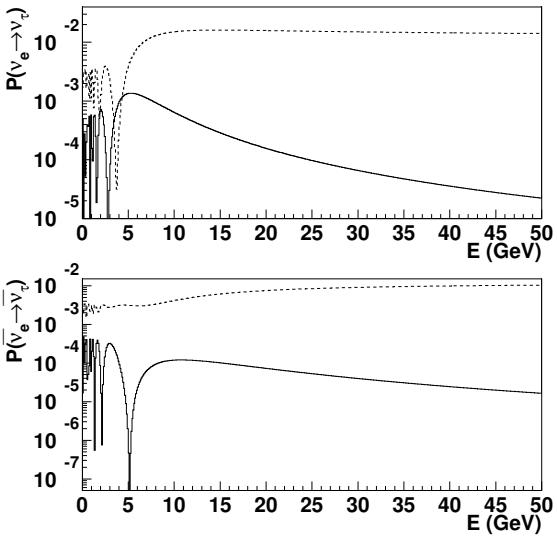

Figure 45: The $\nu_e \to \nu_\tau$ and $\bar{\nu}_e \to \bar{\nu}_\tau$ oscillation probabilities in the standard case (full line) and in the presence of new physics (dashed line), for $\sin^2 2\theta_{13} = 0.001$ and $\epsilon_{e\tau} = 0.07$. Adapted with kind permission of the Physical Review from figure 2 in reference [656]. Copyrighted by the American Physical Society.

$\tau \to \mu$ decay (B.R. $\approx 17\%$). Moreover, the unequivocal departure from the MSW prediction represents a clean signal and allows the effect to be separated from standard oscillations or from corrections due to the NSIs at production or detection. A detector capable of distinguishing electron-like from neutral-current-like events would also be sensitive to the large increase of the latter due to hadronic tau decays.

Consider now a specific, favourable, case with oscillation parameters $\theta_{23} = \pi/4$, $\Delta m^2_{31} = 3 \times 10^{-3}\text{eV}^2$, $\Delta m^2_{21} = 0\text{eV}^2$ and $\sin^2 2\theta_{13} = 0.001$ (the smaller the value of $\sin^2 2\theta_{13}$, the more visible the new physics effects). As for the ϵ parameters, the effect of $\epsilon_{e\mu}$ on oscillation probabilities is negligible, given the bounds discussed above. An $\epsilon_{\mu\tau}$ at the experimental bound could give rise to non-negligible effects [662] but not to the high-energy enhancement we are focussing on. We therefore set both $\epsilon_{e\mu} = 0$ and $\epsilon_{\mu\tau} = 0$ and we choose $\epsilon_{e\tau} = 0.07$.

The oscillation probability in matter in the standard case is compared to the oscillation probability in the presence of new physics in figure 45. While the standard oscillation probability decreases like $1/E_\nu^2$, in the presence of new physics the probability reaches a constant value at high energies larger than 10 GeV or so. The difference is striking at high energy. For anti-neutrinos, the same behaviour is observed at high energy, but a difference is noted at energies $E \sim E_{\text{NP}}$ or below. There, the two terms in the amplitude in equation (269a) are comparable and their relative sign is opposite for neutrinos and anti-neutrinos. As in the present example $\epsilon_{e\tau} > 0$, a suppression of the probability in the anti-neutrino channel is clearly visible. The difference between the two CP-conjugated channels at $E \sim E_{\text{NP}}$ represents a powerful tool to constrain the phase of $\epsilon_{e\tau}$. Note also that the behaviour at small E strongly depends on the $\Delta m^2_{21} = 0$ assumption, which has been kept for purposes of illustration.

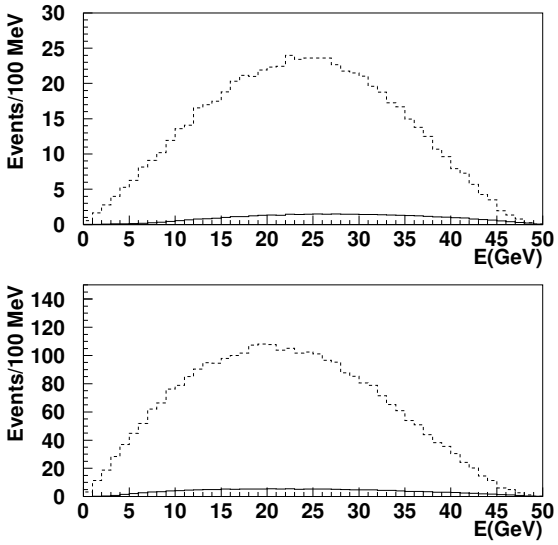

Figure 46: Spectrum of wrong-sign muon events in a neutrino factory as described in the text in the case of μ^- (upper plot) and μ^+ (lower plot) circulating in the storage ring. The full histogram corresponds to the standard case, the dashed histogram to the presence of new interactions. Taken with kind permission of the Physical Review from figure 4 in reference [656]. Copyrighted by the American Physical Society.

Consider now a Neutrino Factory with 10^{21} muon decays and a 40 kton detector with only muon identification capabilities, located at a distance of 3000 km from the accelerator. Given the significant enhancement of the $\nu_e \to \nu_\tau$ transition probability at high energy in the present example, we expect the effect to be visible in the wrong-sign muon spectrum due to $\tau \to \mu$ decays. The effect is indeed manifest in figure 46, where the spectrum of wrong-sign muon events in the standard case is compared to the spectrum in the presence of new physics. The large difference between the two cases is essentially due to τ decays. The wrong-sign muon signal due to $\nu_e \to \nu_\mu$ oscillations is in this case sub-leading in most of the energy range and is significant only at intermediate energies [664, 665].

4.5.3 Constraints on non-standard interactions from non-oscillation neutrino experiments

In this section, bounds on NSIs arising from experiments in which Standard Model parameters have been determined are presented [650, 651, 666]. These experiments include short-baseline neutrino experiments with which $\sin^2\theta_W$ was measured, LEP, and experiments used to measure weak decays. There are also constraints from oscillation and astrophysical experiments, which will be discussed in section 4.5.4. The four-fermion operators considered are of the form $(\bar{\nu}_\alpha \gamma \nu_\beta)(\bar{f}\gamma f)$, where f is an electron or a first-generation quark. These operators differ from those of section 4.5.1, in that they have two neutrino legs (of possibly different flavour), and the remaining two legs are first-generation fermions of the same type.

Consider non-standard, neutral current, neutrino interactions of the form of equation (258):

$$\mathcal{L}_{eff}^{NSI} = -\sum_{P,f,\alpha,\beta} \varepsilon_{\alpha\beta}^{fP} 2\sqrt{2} G_F (\bar{\nu}_\alpha \gamma_\rho L \nu_\beta)(\bar{f}\gamma^\rho P f) \,, \tag{271}$$

where f is a first-generation SM fermion (e, u or d), α, β are lepton flavour indices, and $P = L$ or R. The phase convention is such that $\varepsilon_{\alpha\beta}^{fP}$ is real (CP violation in the new interactions in included in sections 4.5.1 and 4.5.4. See also [626, 662]). As in equation (231), non-standard interactions are normalised as a perturbation away from $G_F \to G_F(1+\varepsilon)$. However, the indices used here on $\varepsilon_{\alpha\beta}^{fP}$ differ from equation (231): $P = L$ [R] is allowed in equation (271), which gives NSI of the form $(V-A)(V-A)$ [$(V-A)(V+A)$], and the fermions f are here restricted to be first generation of the same flavour. So, for instance, we do not constrain the interaction discussed in section 4.5.1, for example equation (246), because it changes the flavour of the charged lepton.

The four-fermion vertices of equation (271) can be generated by operators of dimension six, eight, and higher [650], with increasing powers of the Higgs-doublet vacuum-expectation value (vev). Due to Standard Model gauge symmetries, if equation (271) arises at dimension six, then a $(\bar{\ell}\gamma\nu)(\bar{f}\gamma f')$ operator arises with a coefficient of the same order [653]. As discussed in section 4.5.2, charged-lepton physics imposes tight constraints on the coefficients of such dimension-six operators. However at dimension eight, an operator as in equation (271) can appear at tree level without any charged-lepton counterpart [650]; the constraints summarised in this section apply in this case. Notice that at dimension eight, $\varepsilon \propto v^4/\Lambda^4$, where v is the Higgs vev and Λ the scale of new physics The bounds presented below have been derived on the assumption that only one operator is present at a time; the limits can be relaxed when several NSIs are considered simultaneously [651].

Non-standard interactions involving ν_e or ν_μ and either electrons or first-generation quarks, can be constrained by neutrino-scattering data. Such interactions would contribute to the neutral-current cross section, in neutrino-beam experiments which determine $\sin^2\theta_W$ by comparing the neutral-current and charged-current event rates. Neutrino-flavour-diagonal NSIs interfere with the SM amplitudes, so they contribute linearly. The flavour changing $\varepsilon_{\alpha\beta}^{fP}$, $\alpha \neq \beta$, contribute quadratically, as in equation (237). Bounds are obtained from the CHARM [667], CHARM II [668], LSND [669], and the NuTeV [670] experiments by requiring that the Standard Model + NSI contribution fit within the 90% C.L. experimental result. The Standard Model parameters are taken from other precision data, and the constraints are listed in table 8. NuTeV's results disagree with the Standard Model prediction, so in the table, the NSIs which could fit this discrepancy have non-zero values. If the NuTeV result is supposed to have some other explanation, this nonetheless gives an estimate of the sensitivity of the NuTeV data to NSI.

Bounds on the interactions in equation (271) can also be obtained from radiative corrections. W exchange between $\bar{\nu}$ and ν or f will generate effective interactions $(\bar{\ell}_\alpha \gamma_\rho L \ell_\beta)(\bar{f}\gamma^\rho P f)$ or $(\bar{\ell}_\alpha \gamma_\rho L \nu_\beta)(\bar{f}\gamma^\rho L f')$, where ℓ is a charged lepton. This Standard Model loop transforms the non-standard neutrino interaction to a charged-lepton interaction of strength $c \times 2\sqrt{2} G_F \varepsilon_{\alpha\beta}^{fP}$,

Table 8: Current 90 % CL limits, that can be set on the coefficients $2\sqrt{2}G_F\varepsilon$ of four fermion vertices involving two neutrinos and two first generation fermions. See equation (271) for the definition of ε. The limits marked with an asterisk, $^{*)}$, arise at one loop and are inversely proportional to $\log(\Lambda/m_W)$, taken $\gtrsim 1$. The superscript L, R of ε is the chiral projector $P = \{L, R\}$ in the operator.

vertex	current limits	experiment
$(\bar{e}\gamma^\rho Pe)(\bar{\nu}_\tau\gamma_\rho L\nu_\tau)$	$\lvert\varepsilon^{eP}_{\tau\tau}\rvert < 0.5$	$(Z \to \bar{e}e)^{*)}$
$(\bar{u}\gamma^\rho Pu)(\bar{\nu}_\tau\gamma_\rho L\nu_\tau)$	$\lvert\varepsilon^{uL}_{\tau\tau}\rvert < 1.4$, $\lvert\varepsilon^{uR}_{\tau\tau}\rvert < 3$	$(Z \to \bar{\nu}\nu)^{*)}$
$(\bar{d}\gamma^\rho Pd)(\bar{\nu}_\tau\gamma_\rho L\nu_\tau)$	$\lvert\varepsilon^{dL}_{\tau\tau}\rvert < 1.1$, $\lvert\varepsilon^{dR}_{\tau\tau}\rvert < 6$	$(Z \to \bar{\nu}\nu)^{*)}$
$(\bar{e}\gamma^\rho Pe)(\bar{\nu}_\mu\gamma_\rho L\nu_\mu)$	$\lvert\varepsilon^{eP}_{\mu\mu}\rvert < 0.03$	CHARM II
$(\bar{u}\gamma^\rho Pu)(\bar{\nu}_\mu\gamma_\rho L\nu_\mu)$	$\varepsilon^{uL}_{\mu\mu} = -0.0053 \pm 0.0032$, $\lvert\varepsilon^{uR}_{\mu\mu}\rvert < 0.006$	NuTeV
$(\bar{d}\gamma^\rho Pd)(\bar{\nu}_\mu\gamma_\rho L\nu_\mu)$	$\varepsilon^{dL}_{\mu\mu} = 0.0043 \pm 0.0026$, $\lvert\varepsilon^{dR}_{\mu\mu}\rvert < 0.013$	NuTeV
$(\bar{e}\gamma^\rho Pe)(\bar{\nu}_e\gamma_\rho L\nu_e)$	$-0.07 < \varepsilon^{eL}_{ee} < 0.1$, $-1 < \varepsilon^{eR}_{ee} < 0.5$	LSND
$(\bar{u}\gamma^\rho Pu)(\bar{\nu}_e\gamma_\rho L\nu_e)$	$-1 < \varepsilon^{uL}_{ee} < 0.3$, $-0.4 < \varepsilon^{uR}_{ee} < 0.7$	CHARM
$(\bar{d}\gamma^\rho Pd)(\bar{\nu}_e\gamma_\rho L\nu_e)$	$\lvert\varepsilon^{dL}_{ee}\rvert < 0.3$, $\lvert\varepsilon^{dR}_{ee}\rvert < 0.5$	CHARM
$(\bar{e}\gamma^\rho Pe)(\bar{\nu}_\tau\gamma_\rho L\nu_\mu)$	$\lvert\varepsilon^{eP}_{\tau\mu}\rvert < 0.4$	$(\tau \to \mu\bar{e}e)^{*)}$
	$\lvert\varepsilon^{eP}_{\tau\mu}\rvert < 0.1$	CHARM II
$(\bar{u}\gamma^\rho Pu)(\bar{\nu}_\tau\gamma_\rho L\nu_\mu)$	$\lvert\varepsilon^{uP}_{\tau\mu}\rvert < 0.05$	NuTeV
$(\bar{d}\gamma^\rho Pd)(\bar{\nu}_\tau\gamma_\rho L\nu_\mu)$	$\lvert\varepsilon^{dP}_{\tau\mu}\rvert < 0.05$	NuTeV
$(\bar{e}\gamma^\rho Pe)(\bar{\nu}_\mu\gamma_\rho L\nu_e)$	$\lvert\varepsilon^{eP}_{\mu e}\rvert < 5 \times 10^{-4}$	$(\mu \to 3e)^{*)}$
$(\bar{u}\gamma^\rho Pu)(\bar{\nu}_\mu\gamma_\rho L\nu_e)$	$\lvert\varepsilon^{uP}_{\mu e}\rvert < 7.7 \times 10^{-4}$	$(\mathrm{Ti}\mu \to \mathrm{Ti}e)^{*)}$
$(\bar{d}\gamma^\rho Pd)(\bar{\nu}_\mu\gamma_\rho L\nu_e)$	$\lvert\varepsilon^{dP}_{\mu e}\rvert < 7.7 \times 10^{-4}$	$(\mathrm{Ti}\mu \to \mathrm{Ti}e)^{*)}$
$(\bar{e}\gamma^\rho Pe)(\bar{\nu}_\tau\gamma_\rho L\nu_e)$	$\lvert\varepsilon^{eP}_{\tau e}\rvert < 0.8$	$(\tau \to e\bar{e}e)^{*)}$
	$\lvert\varepsilon^{eL}_{\tau e}\rvert < 0.4, \lvert\varepsilon^{eR}_{\tau e}\rvert < 0.7$	LSND
$(\bar{u}\gamma^\rho Pu)(\bar{\nu}_\tau\gamma_\rho L\nu_e)$	$\lvert\varepsilon^{uP}_{\tau e}\rvert < 0.7$	$(\tau \to e\pi)^{*)}$
	$\lvert\varepsilon^{uP}_{\tau e}\rvert < 0.5,$	CHARM
$(\bar{d}\gamma^\rho Pd)(\bar{\nu}_\tau\gamma_\rho L\nu_e)$	$\lvert\varepsilon^{dP}_{\tau e}\rvert < 0.7$	$(\tau \to e\pi)^{*)}$
	$\lvert\varepsilon^{dP}_{\tau e}\rvert < 0.5,$	CHARM

where:

$$c \simeq \frac{\alpha}{4\pi s_W^2} \ln\left(\frac{\Lambda}{m_W}\right) \approx 0.0027\,, \tag{272}$$

and Λ is a new-physics scale which may conservatively be taken to be $\sim$ TeV. Charged-lepton data can therefore constrain these NSI, even if the NSIs do not involve charged leptons at tree level.

The experimental bounds on $\mu \leftrightarrow e$ flavour change from the charged-lepton sector (e.g. $\mu \to 3e$, $\mu \to e$ conversion on titanium) are very strong. Despite the loop-suppression factor of equation (272), they give significant constraints on NSIs involving ν_μ and ν_e: $\varepsilon \lesssim 10^{-3}$, see table 8. The constraints from flavour-changing τ decays are weaker, $\varepsilon \lesssim 1$. The upper limits on the τ-decay branching ratios may improve in the future; the limits in table 8 scale as $\sqrt{BR}$, and are calculated from $BR(\tau \to \pi e) = BR(\tau \to \mu\bar{e}e) = 1.9 \times 10^{-7}$, and $BR(\tau \to e\bar{e}e) = 2.0 \times 10^{-7}$.

Constraints on the non-standard interactions $(\bar{\nu}_\tau \gamma_\rho L \nu_\tau)(\bar{f}\gamma^\rho P f)$ can be obtained from their loop contribution to Z decay. If the Z decays to $\bar{\nu}_\tau \nu_\tau$, which then become $\bar{e}e$ via the NSI $\varepsilon_{\tau\tau}^{eP}$, this contributes to the decay $Z \to \bar{e}e$. Or if the Z decays to $q\bar{q}$ ($q = u$ or d), which become $\bar{\nu}_\tau \nu_\tau$ via $\varepsilon_{\tau\tau}^{uP}$ or $\varepsilon_{\tau\tau}^{dP}$, this contributes to the invisible width of the Z. The Z decay branching ratios were measured at LEP to a precision $\sim \alpha_{em}/\pi$, and support the global fits to Standard Model parameters. This gives constraints of order $\varepsilon_{\tau\tau}^{fP} \sim 1$; see table 8. Better bounds on $\varepsilon_{\tau\tau}^{fP}$ can be found in section 4.5.4.

4.5.4 Oscillation experiments as probes of the NSI

The effective low-energy operators induced by non-standard interactions may appreciably modify the neutrino forward-scattering amplitude on electrons and nucleons, as a result affecting neutrino oscillations in matter. This makes neutrino-oscillation experiments a valuable low-energy tool in searching for physics beyond the Standard Model. As the precision of neutrino-oscillation experiments increases, they may begin to be regarded on the same footing as the existing precision low-energy tools, such as the measurements of $K - \bar{K}$ mixing, searches for flavour violating μ and τ decays, etc. In this section, a review of the sensitivity the existing neutrino-oscillation experiments, including solar, reactor, atmospheric, and accelerator neutrinos, to NSIs is presented.

4.5.4.1 NSI and oscillations: generalities

Regardless of their origin, at the low energies relevant to neutrino oscillations, NSIs are described by the effective low-energy, four-fermion Lagrangian:

$$L^{NSI} = -2\sqrt{2} G_F (\bar{\nu}_\alpha \gamma_\rho \nu_\beta)(\epsilon_{\alpha\beta}^{f\tilde{f}L} \bar{f}_L \gamma^\rho \tilde{f}_L + \epsilon_{\alpha\beta}^{f\tilde{f}R} \bar{f}_R \gamma^\rho \tilde{f}_R) + h.c. \tag{273}$$

Here $\epsilon_{\alpha\beta}^{f\tilde{f}L}$ ($\epsilon_{\alpha\beta}^{f\tilde{f}R}$) denotes the strength of the NSI between the neutrinos ν of flavours α and β and the left-handed (right-handed) components of the fermions f and $\tilde{f}$.

Not all of these parameters impact neutrino oscillations in matter. The propagation effects of NSI are, first of all, only sensitive to $\epsilon^{f\tilde{f}}_{\alpha\beta}$ when there is no flavour change of the background particle, $f = \tilde{f}$, as processes that change the flavour of the background fermion do not add up coherently [671]. Henceforth, the notation $\epsilon^{ffP}_{\alpha\beta} \equiv \epsilon^{fP}_{\alpha\beta}$ will be used. Secondly, only the vector component of the NSI enters, $\epsilon^{f}_{\alpha\beta} \equiv \epsilon^{fL}_{\alpha\beta} + \epsilon^{fR}_{\alpha\beta}$, with no sensitivity to the axial component. Therefore, the propagation and production/detection effects are sensitive to different combinations of the NSI parameters, and hence the corresponding measurements are complementary.

The matter piece of the oscillation Hamiltonian can be written (up to an irrelevant overall constant) as:

$$H^{3\times3}_{\rm mat} = \sqrt{2} G_F n_e \begin{pmatrix} 1+\epsilon_{ee} & \epsilon^*_{e\mu} & \epsilon^*_{e\tau} \\ \epsilon_{e\mu} & \epsilon_{\mu\mu} & \epsilon^*_{\mu\tau} \\ \epsilon_{e\tau} & \epsilon_{\mu\tau} & \epsilon_{\tau\tau} \end{pmatrix}, \tag{274}$$

where n_e is the number density of electrons in the medium. The epsilons here are the sum of the contributions from electrons (ϵ^e), up quarks (ϵ^u), and down quarks (ϵ^d) in matter: $\epsilon_{\alpha\beta} \equiv \sum_{f=u,d,e} \epsilon^f_{\alpha\beta} n_f/n_e$. Hence, unlike in the standard case ($\epsilon_{\alpha\beta} = 0$), the NSI-matter effects depend on the chemical composition of the medium, not only on the electron density, n_e.

The idea that non-standard neutrino interactions modify neutrino oscillations in matter has been around for many years. It is already clearly spelled out in the seminal paper by Wolfenstein [60] and has been elaborated by many authors ([581, 672, 673] and many others). While in the 1980's and 1990's the focus was mainly on NSI as an alternative to oscillations, in recent years the focus has shifted to using neutrino-oscillation data to measure neutrino interactions.

Because of the tight bounds on the parameters $\epsilon_{e\mu}$ and $\epsilon_{\mu\mu}$ (see Sect. 4.5.3), it makes sense to set them to zero while considering neutrino oscillations. Moreover, the parameters $\epsilon_{\mu\tau}$ will also be set to zero. This parameter was shown to be constrained ($\epsilon_{\mu\tau} < 10^{-1}$) by the two-flavour analysis of the atmospheric neutrino data [674]. Although a full 3-flavour analysis including $\epsilon_{\mu\tau}$ is yet to be done, there are arguments that suggest that the two-flavour bound may survive the generalisation to three flavours (unlike the corresponding bound on $\epsilon_{e\tau}$, see Sect. 4.5.4.3). Thus, only the effects of ϵ_{ee}, $\epsilon_{e\tau}$, and $\epsilon_{\tau\tau}$ will be considered. Even with this reduction, the parameter space of the problem is quite large: different assignments of the diagonal and off-diagonal NSI to electrons, and u and d quarks yield different dependences of the oscillation Hamiltonian on the chemical composition and different detection cross sections.

4.5.4.2 NSI and solar neutrinos

It is well known that the standard solar-neutrino analysis can be done with only two neutrino states: ν_e and ν'_μ, where the latter is a linear combination of ν_μ and ν_τ (The effect of the third state is to multiply the two-neutrino survival probability by $\cos^4\theta$. See, e.g. [114, 115] for recent data analyses.) This reduction involves performing a rotation in the $\mu - \tau$ sub-space by the atmospheric angle θ_{23} and taking the first two columns/rows of the mixing matrix. The

vacuum-oscillation Hamiltonian then takes the usual form:

$$H_{\rm vac}^{2\times 2} = \begin{pmatrix} -\Delta\cos 2\theta & \Delta\sin 2\theta \\ \Delta\sin 2\theta & \Delta\cos 2\theta \end{pmatrix}, \tag{275}$$

where $\Delta \equiv \Delta m^2/(4E_\nu)$ and Δm^2 is the mass splitting between the first and second neutrino mass states: $\Delta m^2 \equiv m_2^2 - m_1^2$.

It turns out (quite fortunately and unlike the atmospheric neutrino case, see section 4.5.4.3) that the two-neutrino reduction of the solar-neutrino analysis holds even when the matter interactions become non-standard. The corresponding matter contribution to the two-neutrino oscillation Hamiltonian can be written (once again, up to an irrelevant overall constant) as:

$$H_{\rm mat}^{NSI} = \frac{G_F n_e}{\sqrt{2}} \begin{pmatrix} 1+\epsilon_{11} & \epsilon_{12}^* \\ \epsilon_{12} & -1-\epsilon_{11} \end{pmatrix}, \tag{276}$$

where the quantities ϵ_{ij} $(i = 1, 2)$ depend on the original epsilons and on the rotation angle θ_{23}:

$$\epsilon_{11} = \epsilon_{ee} - \epsilon_{\tau\tau}\sin^2\theta_{23}, \qquad \epsilon_{12} = -2\epsilon_{e\tau}\sin\theta_{23}. \tag{277}$$

In equation (277) small corrections of order $\sin\theta_{13}$ or higher have been neglected. Equation (277) shows that the flavour-changing-NSI effect in solar-neutrino oscillations comes from $\epsilon_{e\tau}$, while the flavour-preserving-NSI effect comes from both ϵ_{ee} and $\epsilon_{\tau\tau}$.

A useful parameterisation is:

$$H_{\rm mat}^{NSI} = \begin{pmatrix} A\cos 2\alpha & Ae^{-2i\phi}\sin 2\alpha \\ Ae^{2i\phi}\sin 2\alpha & -A\cos 2\alpha \end{pmatrix}. \tag{278}$$

Here the parameters $A = A(x)$, α and ϕ are defined as follows:

$$\tan 2\alpha = |\epsilon_{12}|/(1+\epsilon_{11}), \qquad 2\phi = Arg(\epsilon_{12}), \qquad A = G_F n_e \sqrt{[(1+\epsilon_{11})^2 + |\epsilon_{12}|^2]/2}\ . \tag{279}$$

In the absence of NSIs, $A = G_F n_e/\sqrt{2}$, $\alpha = 0$, and the Hamiltonian (equation (278)) reduces to its standard form. The effect of α is to change the mixing angle in the medium of high density from $\pi/2$ to $\pi/2 - \alpha$. The angle ϕ (related to the phase of $\epsilon_{e\tau}$) is a source of CP violation. Solar-neutrino experiments, just like terrestrial-beam experiments [626, 656], are sensitive to its effects [675], while the atmospheric neutrinos are not (section 4.5.4.3).

To understand the basic physics of the sensitivity of solar neutrinos to NSI, first consider the electron-neutrino survival probability P_{ee} for the LMA-I solution in the standard case (no NSI). As shown in figure 47, P_{ee} varies across the solar-neutrino spectrum. On the low end (*pp* neutrinos), it approaches $\cos^4\theta + \sin^4\theta$. This is nothing but the (averaged) vacuum-oscillation value $1 - \sin^2 2\theta/2$. The low-energy solar neutrinos essentially are not affected by the presence of matter, even at the production point in the core ($\Delta m^2/2E_\nu \gg \sqrt{2}G_F n_e(r)$ for all r). On the high-energy end (^{8}B neutrinos), the survival probability approaches $\sin^2\theta$: the Hamiltonian at the production point is dominated by the matter term.

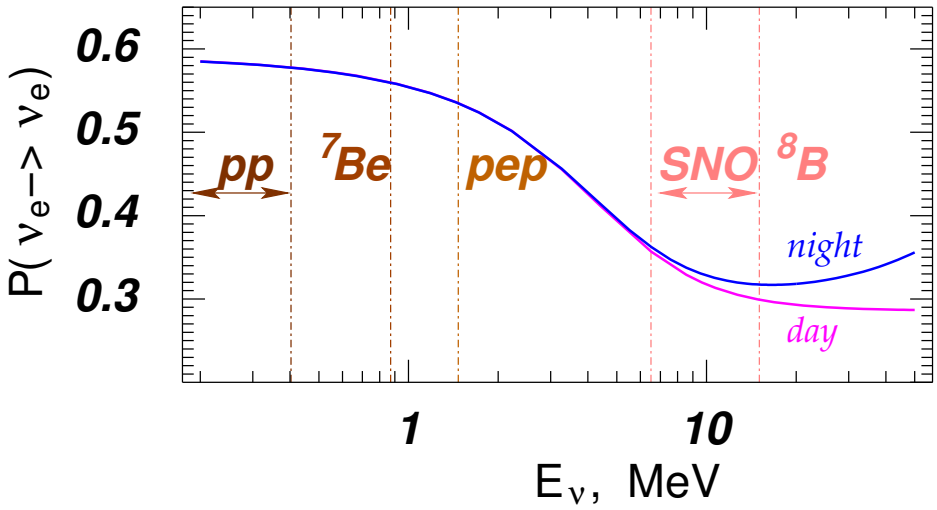

Figure 47: The electron neutrino survival probability and the day/night asymmetry as a function of energy for the LMA solution.

Between these two extremes lies the transition region where the matter potential at the production point and the kinetic terms guiding vacuum oscillations are comparable. It is natural to expect that this is the part of the solar-neutrino spectrum that would be most sensitive to the non-standard neutrino interactions.

Figure 48 confirms these expectations. It shows that the behaviour of P_{ee} in the transition region varies considerably with $\epsilon_{e\tau}$, both in amplitude and sign. Values of the order of 10^{-1} per quark can have a significant effect. In fact, some of the parameter space can already be excluded as the distortion of the spectrum at SNO would be unacceptably large. As an example, points with $\epsilon_{11} = 0$ and $\epsilon^u_{12} > 0.14$ are unacceptable at 90% C.L. (here $\epsilon^u_{\alpha\beta} = \epsilon^d_{\alpha\beta}$ is assumed) [675]. At the same time, possibilities such as curve 2 or 4 in the figure cannot presently be excluded. Clearly, an excellent way to probe this part of the parameter space would be to perform a high-statistics measurement of the ^{8}B-neutrino spectrum in the regime of low energies (< 6 MeV).

Note also that the day/night-asymmetry effect also changes in the presence of NSI. In particular, for certain values of the NSI parameters, the day/night asymmetry can be significantly reduced, as is clearly demonstrate by curve 4 in the bottom panel of figure 48. In this case, the LMA-0 solution, characterised by $\Delta m^2 \sim (1-2) \times 10^{-5}$ eV^2 and normally excluded by the solar data, becomes allowed. One way to obtain this solution is by choosing NSI such that the angle α (defined in equation (278)) becomes close to θ [675]. A choice can be made that is consistent with the atmospheric-neutrino constraints. Another way is by choosing the flavour-preserving NSI to cancel the standard matter term in the Earth [676]. The MSW effect in the Sun still happens in this scenario, because the Sun has a different chemical composition than the Earth. Lastly, we note that it is even possible to obtain a solution for $\theta > \pi/4$, the so-called LMA-D region [677] (in the 'dark side' [678, 679]). This requires quite large NSIs so that the sign of the matter effect in the Sun is reversed. For technical details, including approximate analytical expressions for P_{ee} and the day/night asymmetry, see [675].

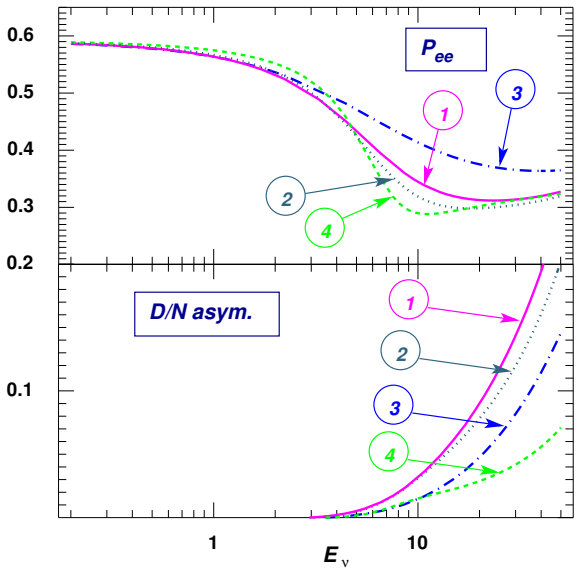

Figure 48: The electron neutrino survival probability and the day/night asymmetry as a function of energy for $\Delta m^2 = 7 \times 10^{-5}$ eV^2, $\tan^2\theta = 0.4$ and several representative values of the NSI parameters: (1) $\epsilon^u_{11} = \epsilon^d_{11} = \epsilon^u_{12} = \epsilon^d_{12} = 0$; (2) $\epsilon^u_{11} = \epsilon^d_{11} = -0.008$, $\epsilon^u_{12} = \epsilon^d_{12} = -0.06$; (3) $\epsilon^u_{11} = \epsilon^d_{11} = -0.044$, $\epsilon^u_{12} = \epsilon^d_{12} = 0.14$; (4) $\epsilon^u_{11} = \epsilon^d_{11} = -0.044$, $\epsilon^u_{12} = \epsilon^d_{12} = -0.14$. Recall that the parameters in equation (277) equal $\epsilon_{ij} = \epsilon^u_{ij} n_u/n_e + \epsilon^d_{ij} n_d/n_e$. Taken with kind permission of Physical Letters from figure 1 in reference [675]. Copyrighted by Elsevier B.V.

4.5.4.3 NSI and atmospheric neutrinos

On very general grounds, one expects the atmospheric neutrinos to be a very sensitive probe of NSI. The reason is the remarkable agreement between the Super-Kamiokande atmospheric-neutrino data and the predictions of the standard $\nu_\mu \to \nu_\tau$ oscillation scenario. The agreement is non-trivial: with only two parameters, Δm^2_{atm} and θ_{23}, it is possible to fit all presently available Super-Kamiokande data, spanning five orders of magnitude in energy, E_ν, and three orders of magnitude in baseline, L. It may be expected that the introduction of non-standard neutrino-matter interactions would change the oscillation pattern, breaking this beautiful fit.

Since the vacuum-oscillation Hamiltonian depends on the combination $\Delta m^2/E_\nu$, while the non-standard matter potential, $\sqrt{2}\epsilon_{\alpha\beta} G_F n_f$, is energy independent, the high-energy part of the data-set is generally expected to be most sensitive to non-standard interactions. The data in question are the stopping and through-going muon samples [680] and these should be first examined for NSI effects.

A simple estimate of the sensitivity could be obtained as follows. At very high energies, $E_\nu \gtrsim 50 - 100$ GeV, the vacuum-oscillation length, $\sim 4\pi E_\nu/\Delta m^2$, becomes greater than the size of the Earth. The standard oscillation mechanism predicts no oscillations for these neutrinos. If the $\epsilon_{\mu\tau}$ NSI is present, it will drive oscillations of the highest energy muon neutrinos, in conflict with the data. The simple criterion then is that the corresponding oscillation length in matter, $\sim \pi(\sqrt{2}\epsilon_{\mu\tau} G_F n_e)^{-1}$ be greater than the Earth's diameter. That yields $\epsilon_{\mu\tau} \lesssim 0.1$. Detailed

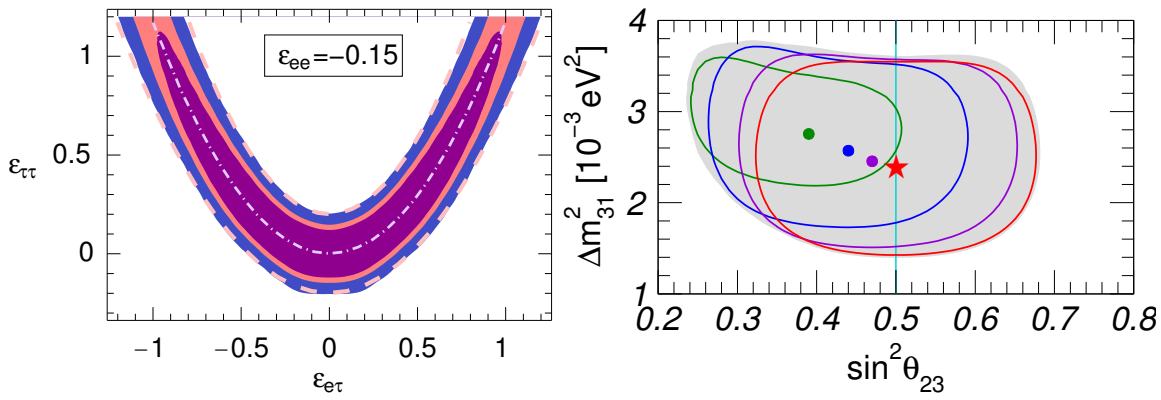

Figure 49: *Left panel*: A 2-D section ($\epsilon_{ee} = -0.15$) of the allowed region of the NSI parameters (shaded). The results are presented for $\Delta m^2_{\odot} = 0$, $\theta_{13} = 0$, and marginalised over θ and Δm^2. The dashed contours indicate our analytical predictions. See text for details. *Right panel*: The effect of the NSI on the allowed region and best-fit values of the oscillation parameters. Both figures taken with kind permission of the Physical Review from figures 1 and 2 in reference [681]. Copyrighted by the American Physical Society.

two-neutrino (ν_μ, ν_τ) numerical analysis [674] yields $\epsilon_{\mu\tau} \lesssim 0.08 - 0.12$ [16].

With $\epsilon_{\tau\tau}$, the argument is slightly different. At the highest energies, where vacuum oscillations are not operational, $\epsilon_{\tau\tau}$ has no effect. The effect appears at lower energies where vacuum oscillations are predicted to occur: $\epsilon_{\tau\tau}$ introduces diagonal splitting thus decreasing the effective mixing angle. Thus, one needs to compare $\sqrt{2}\epsilon_{\tau\tau} G_F n_e$ and $\Delta m^2/2E_\nu$ at $E_\nu \sim 20 - 30$ GeV, the highest energy at which an oscillation minimum is expected to occur for neutrinos traveling through the center of the Earth. This yields $\epsilon_{\tau\tau} \lesssim 0.2$, once again in reasonable agreement with the numerical two-neutrino analysis [674].

Clearly, these are very strong bounds; if they were to extend to $\epsilon_{e\tau}$, the NSI effects on solar neutrinos discussed in the previous sub-section would be excluded. It turns out, however, that this is not the case: when the analysis is properly extended to three flavours, one finds that very large values of both $\epsilon_{e\tau}$ and $\epsilon_{\tau\tau}$ are still allowed by the data.

This surprising result is illustrated in the left panel of figure 49 (taken from [681]), which shows a 2-D slice of the allowed region in the 3-D parameter space of ϵ_{ee}, $\epsilon_{e\tau}$, and $\epsilon_{\tau\tau}$. Order-one values for both $\epsilon_{e\tau}$ and $\epsilon_{\tau\tau}$ are allowed, in other words, the NSI can be as large as, or even larger than, the Standard Model neutrino interactions.

The contours presented in the left panel of figure 49 have been obtained by marginalising over Δm^2_{atm} and θ_{23}. The right panel of the figure shows what happens to the oscillation parameters as one moves along the parabolic direction of the allowed region away from the origin: the mixing angle becomes less than maximal, while the mass splitting increases. The good fit to the data is maintained at the expense of changing the oscillation parameters away from their standard values.

Both the shape of the allowed NSI region and the shift of the best-fit oscillation parameters

[16] Notice the difference in normalisations: our epsilons are normalised per electron, while [674] gives epsilons per d quark, resulting in a factor of ~ 4 apparent difference

can be understood physically. The allowed region is reasonably well described by the equations:

$$|1 + \epsilon_{ee} + \epsilon_{\tau\tau} - \sqrt{(1 + \epsilon_{ee} - \epsilon_{\tau\tau})^2 + 4|\epsilon_{e\tau}|^2}| \lesssim 0.4, \tag{280}$$

$$\cos^2\beta \gtrsim \tan^2\theta_{min}, \quad \cos^2\beta \geq \left[\frac{2\Delta m^2_{max}}{\Delta m^2_m} - 1\right]^{-1}, \tag{281}$$

where:

$$\tan 2\beta \equiv 2|\epsilon_{e\tau}|/(1 + \epsilon_{ee} - \epsilon_{\tau\tau}); \tag{282}$$

$$\Delta m^2_m \equiv \Delta m^2 \left[(\cos 2\theta(1 + \cos^2\beta) - \sin^2\beta)^2/4 + (\sin 2\theta \cos\beta)^2\right]^{1/2}; \tag{283}$$

and θ_{min} and Δm^2_{max} denote the smallest mixing and the largest mass splitting allowed by the low-energy data, $E \lesssim 1$ GeV, which are not affected by NSI. The derivation and discussion of these results are found in [649, 681, 682]. Under the conditions of equations (280) and (281), the high-energy atmospheric muon neutrinos undergo oscillations into a state that is a linear combination of ν_e and ν_τ, instead of purely into ν_τ as in the standard case. This fact, however, is unobservable because at the energies in question only the muon data is available. The low-energy neutrinos undergo 'normal' vacuum oscillations, since for them the vacuum-oscillation terms still dominate the Hamiltonian.

Notice that only the absolute value of $\epsilon_{e\tau}$ enters equations (280) to (283). Unlike solar neutrinos, for $\theta_{13} = 0$ atmospheric neutrinos are completely insensitive to the phase of this parameter, which can be explicitly seen also in figure 49. For $\theta_{13} \neq 0$ there is some sensitivity, but the effect is small [682].

4.5.4.4 Combined analysis of the atmospheric and K2K data

Although K2K by itself is not sensitive to the effects of the intervening matter because its baseline is too short (see section 4.5.5.1), the addition of the K2K oscillation data to the Super-Kamiokande atmospheric data does restrict the allowed NSIs. The reason behind this seemingly counter-intuitive result is that K2K, by measuring the 'true' vacuum oscillation parameters, restricts the range over which these parameters could be varied to compensate for the effects of the NSI, as described above. A typical impact of adding the K2K dataset is illustrated in figure 50.

Figure 51 shows the ranges of the NSI parameters allowed by the combined analysis of the atmospheric and K2K data. The different panels show sections of the 3-D region by contours of constant ϵ_{ee}. As before, in figure 49, the contours have been derived for $\theta_{13} = 0$, $\Delta m^2_{21} = 0$ and marginalised over θ_{23} and Δm^2_{23}. Since the results are symmetric around $\epsilon_{e\tau} = 0$, only positive values of this parameter are shown. The mass hierarchy is assumed to be inverted.

The same analysis, repeated for the case of normal mass hierarchy, is shown in figure 52. The difference between the two hierarchies is a sub-leading effect that is not described by equations (280) to (283). Figures 50, 51, 52 have been adapted from reference [682].

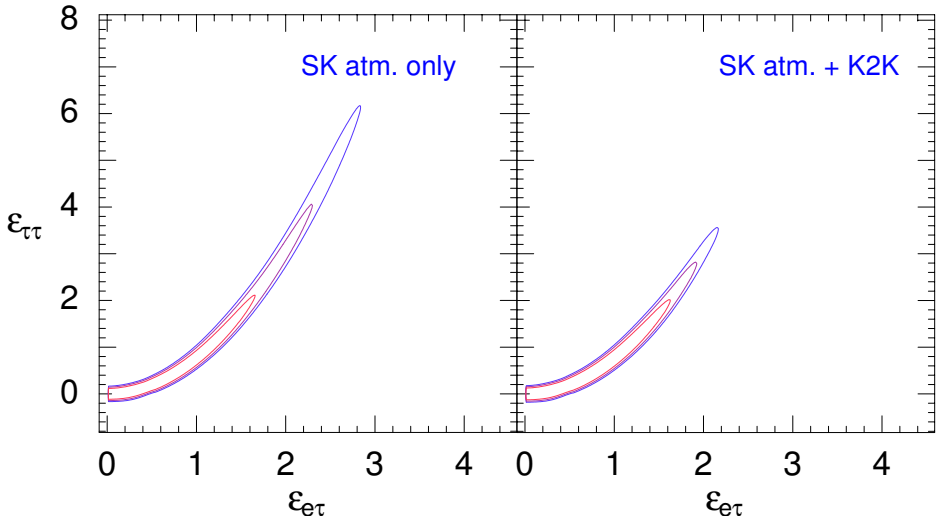

Figure 50: The role of K2K in constraining the allowed region of the NSI allowed by the atmospheric neutrino analysis. The value $\epsilon_{ee} = 0.3$ was chosen. Taken with kind permission of Physical Review from figure 4 in reference [682]. Copyrighted by the American Physical Society.

4.5.5 The role of MINOS

4.5.5.1 MINOS: first data release

The first question to address is whether NSIs can directly impact the neutrino oscillations observed by MINOS. To do this one has to compare the quantity $l_{ref} = (\sqrt{2}G_F n_e \epsilon)^{-1}$, characterising the NSI matter effect, with the baseline of the experiment. For the average density of the continental crust, $(\sqrt{2}G_F n_e)^{-1} \simeq 1.9 \cdot 10^3$ km; this number is nearly an order of magnitude greater than the baseline of K2K, 250 km, ensuring that K2K measures essentially the vacuum oscillation parameters. The situation for MINOS is less clear-cut: with the baseline of 735 km, it is sensitive to matter effects, although at the sub-dominant level.

At the low-statistics stage (0.97×10^{20} protons on target, 'MINOS I'), the subdominant matter effects at MINOS can be neglected. In this approximation, MINOS simply measures the vacuum oscillations parameters just as K2K does (see section 4.5.4.4). It turns out, however, that MINOS I does not add anything to constraining the NSI parameters. This can be understood from figure 53: the MINOS I dataset has very poor sensitivity in the direction in which the oscillation parameters Δm^2 and θ (here $\theta \equiv \theta_{23}$) change to compensate for the effects of the NSI (c.f. figure 49, right panel).

Indeed, the results of a detailed numerical fit, shown in figure 54 confirms this. The part of the allowed region in the oscillation-parameter space that arises because of the effect of the NSI (the part of the coloured region outside of the black contours) remains upon the addition of the data from MINOS I, implying that the NSI effect can still be compensated by the change of Δm^2 and θ. The fits shown in figures 51 and 52 are basically unchanged by the addition of MINOS data [649]. An updated dataset with 1.27×10^{20} protons on target has been recently

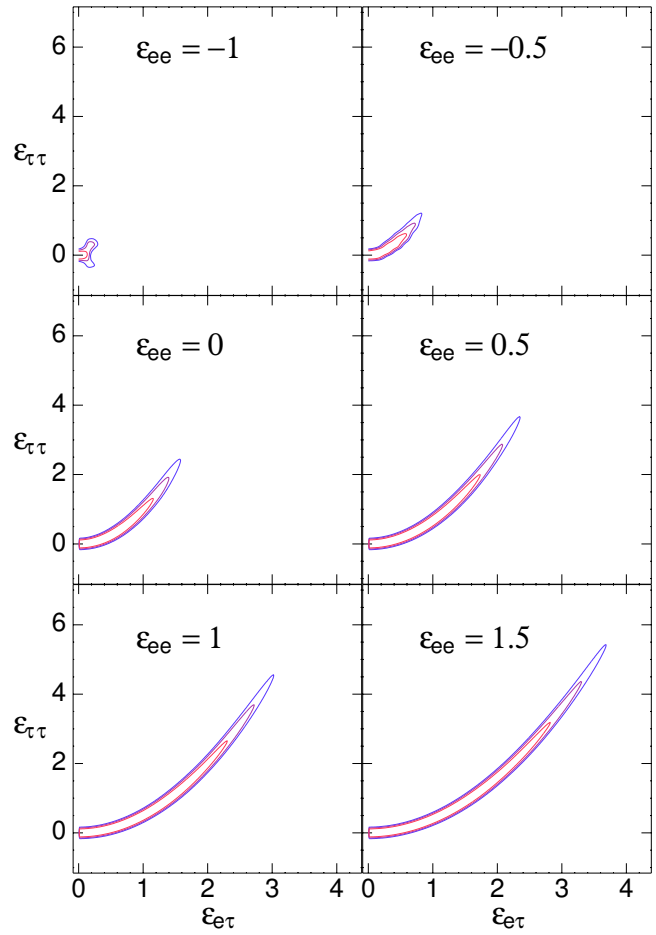

Figure 51: Ranges of the NSI parameters allowed by the combined analysis of the atmospheric and K2K data in the case of the inverted mass hierarchy. Taken with kind permission of Physical Review from figure 1 in reference [682]. Copyrighted by the American Physical Society.

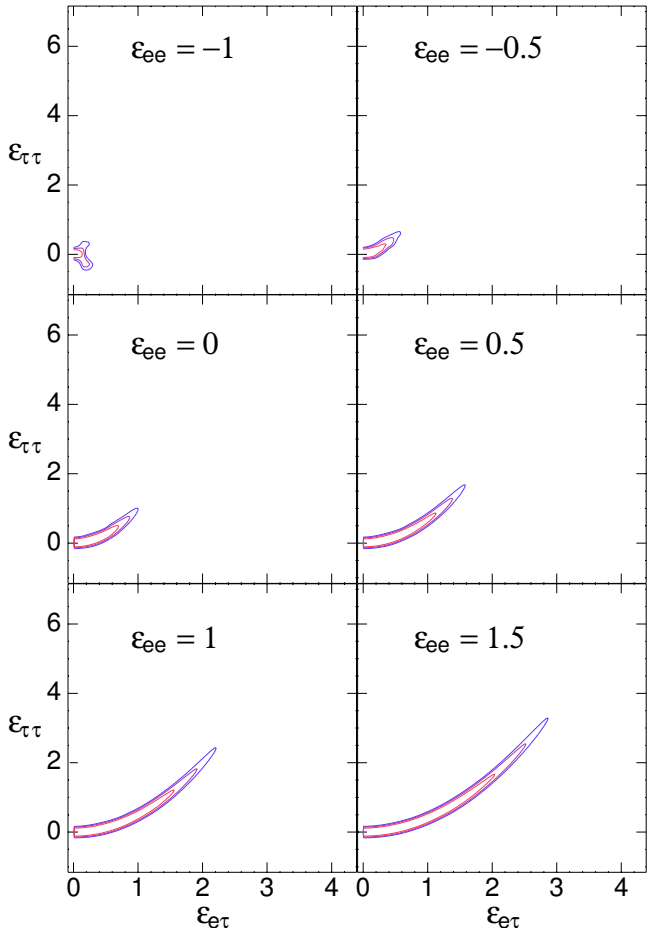

Figure 52: Same as figure 51 for normal mass hierarchy. Taken with kind permission of Physical Review from figure 6 in reference [682]. Copyrighted by the American Physical Society.

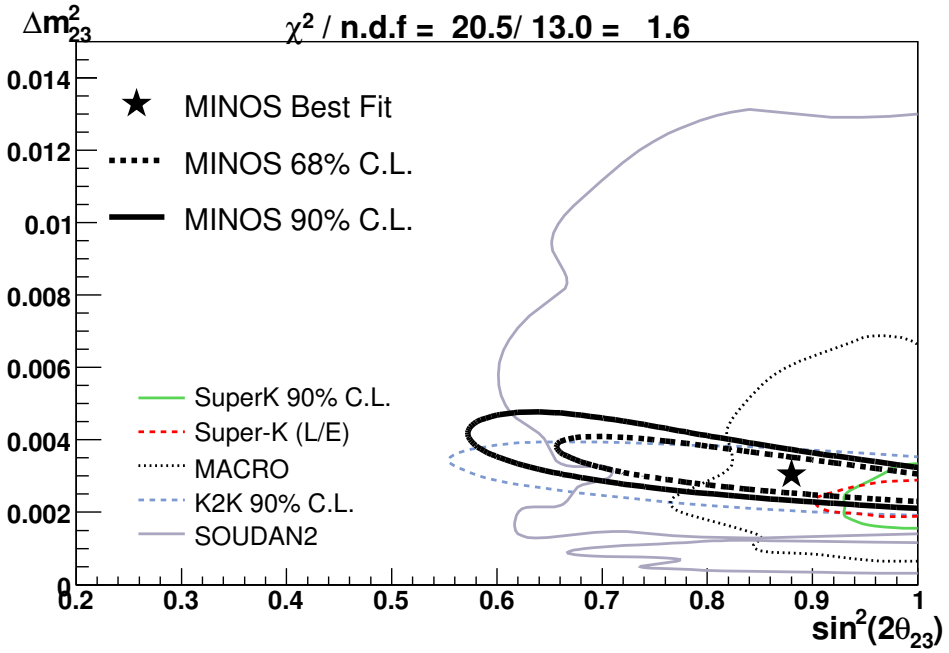

Figure 53: Neutrino oscillation parameters inferred from the analysis of the first MINOS data release. Other experiments are also included for comparison. Taken with kind permission of the MINOS Collaboration from [683].

released [11][17].

4.5.5.2 MINOS: projections for the future

The situation is expected to improve significantly as MINOS collects more data. Figure 55 (left panel) shows the projected sensitivity of MINOS with a data set corresponding to 25×10^{25} protons on target. Two scenarios, one corresponding to no NSI and one to large NSI (see the caption), are considered. In the second scenario, the experiment would measure oscillation parameters that are incompatible with those found from the atmospheric data under the assumption of the standard interactions. This incompatibility would indicate the need for new physics. The point $\epsilon_{ee} = \epsilon_{e\tau} = \epsilon_{\tau\tau} = 0$ would be excluded with confidence level (C.L.) higher than 99%. By the same token, in the first scenario, the compensation mechanism between the NSI and the vacuum parameters would be significantly constrained.

Similar results are obtained with a more modest increase of the MINOS statistics, to 16×10^{20} instead of 25×10^{20} protons on target. With this intermediate increase, the point $\epsilon_{ee} = \epsilon_{e\tau} = \epsilon_{\tau\tau} = 0$ in the second scenario would lie inside the 99% C.L. contour, but outside the 95% C.L. contour.

MINOS will also be able to search for flavour-changing NSI effects using the matter-induced

[17] **Note added**: Figure 53 is the preliminary result by the MINOS group, and the analysis described here was made as of September 2006. See reference [684] for the updated result with $3.36 * 10^{20}$POT.

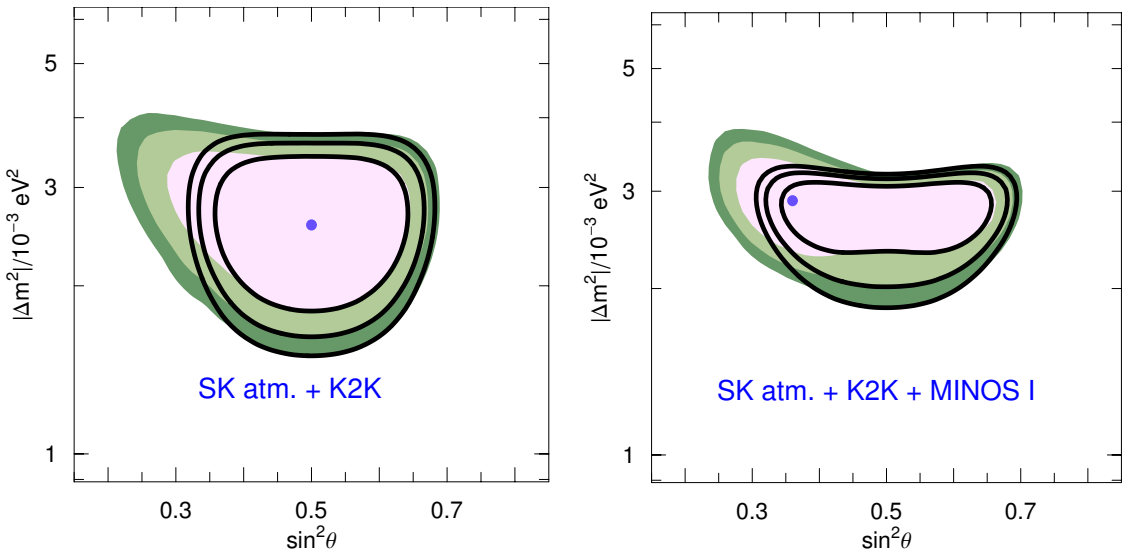

Figure 54: Regions in the space $\Delta m^2 - \sin^2\theta$ allowed by the global fit before (*left panel*) and after (*right panel*) the MINOS results, with purely standard interactions (contours) and with NSI (filled areas). For both cases we plot the regions allowed at 95%, 99% and 3σ confidence levels for 2 degrees of freedom. We have marginalised also over the sign of Δm^2 and took $-1 \leq \epsilon_{ee} \leq 1.6$, motivated by one of the accelerator bounds (see [681]). Both figures adapted with kind permission of Physical Review from figure 1 in reference [649]. Copyrighted by the American Physical Society.

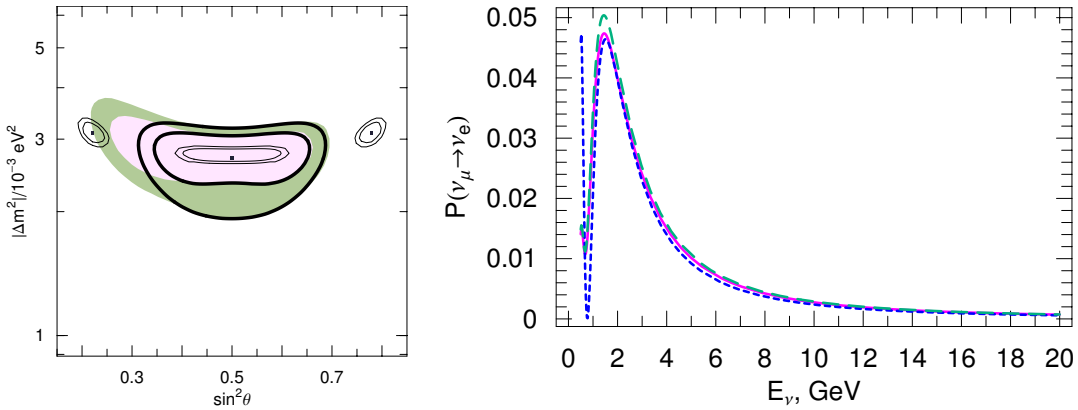

Figure 55: *Left panel*: Results of fits to simulated MINOS data with high statistics of 25×10^{20} protons on target (thin contours). The "data" were simulated for two sets of NSI and "true" oscillation parameters: (i) no NSI, $\sin^2\theta = 0.5$ and $\Delta m^2 = 2.7 \times 10^{-3}$, (ii) $\epsilon_{ee} = 0$, $\epsilon_{\tau\tau} = 0.81$, $\epsilon_{e\tau} = 0.9$, $\sin^2\theta = 0.27$ and $\Delta m^2 = 3.1 \times 10^{-3}$. The fits were done in both cases in the assumption of no NSI; 90% and 99% C.L. regions are shown. For reference, also shown are the regions allowed currently by all the data combined, at 90% and 99% C.L. with (filled area) and without NSI (thick contours), as in Fig. 54. *Right panel*: Conversion probability $P(\nu_\mu \to \nu_e)$ as a function of energy for (i) $\sin^2 2\theta_{13} = 0.07$, $\Delta m_{23} = 2.5 \times 10^{-3}$ eV^2, $\sin^2\theta_{23} = 1/2$ and standard neutrino interactions (short-dashed curve), vs. (ii) $\sin^2 2\theta_{13} = 0$, $\Delta m_{23} = 2.9 \times 10^{-3}$ eV^2, $\sin^2\theta_{23} = 0.36$ and $\epsilon_{ee} = 0$, $\epsilon_{e\mu} = 0.9$, $\epsilon_{\tau\tau} = 0.81$ (solid curve). The NSI and θ_{13} effects are nearly completely degenerate. Both figures taken with kind permission of Physical Review from figure 3 and4 in reference [649]. Copyrighted by the American Physical Society.

conversion $\nu_\mu \to \nu_e$ [649, 685]. Schematically, this conversion can be viewed in two steps:

$$\nu_\mu \overset{\Delta_{23},\theta_{23}}{\longrightarrow} \nu_\tau \overset{\epsilon_{e\tau}}{\longrightarrow} \nu_e. \tag{284}$$

The first step has already been observed by MINOS, with the largest conversion happening in the lower energy part of its spectrum ($1.5 - 2$ GeV). Correspondingly, ν_e production according to equation (284) is also expected to peak at low energy. The conversion probability $P(\nu_\mu \to \nu_e)$ as a function of energy is shown in figure 55 (right panel). One can see that the probability indeed peaks at low energies and, moreover, the effects of the NSI and θ_{13} are nearly completely degenerate [664]. Thus, if the conversion is observed, it will be necessary to break the degeneracy by some other means.

4.5.5.3 Summary

In summary, the least constrained NSI parameters, ϵ_{ee}, $\epsilon_{e\tau}$, and $\epsilon_{\tau\tau}$ are presently being probed by both solar- and atmospheric-neutrino experiments. Solar neutrino experiments, by themselves, already exclude some parts of the parameter space allowed by accelerator-based scattering experiments. At the same time, the available data leaves a lot of possibilities open. This is because the electron-neutrino survival probability as a function of energy is presently measured well only above the SNO/SK threshold of about 6 MeV. The crucial part of the spectrum below 5-6 MeV, where the transition from the matter-dominated to the vacuum oscillation regime occurs, is measured very poorly. This situation should change in the next decade, as Borexino, KamLAND (solar measurement), and other experiments come on line.

We have seen that atmospheric neutrinos, contrary to naive expectations, also allow large NSI, comparable to, or even exceeding, the strength of the Standard Model interactions. This happens because the effects of the NSI can be compensated by changing the oscillation parameters. This degeneracy is somewhat ameliorated, but not eliminated, by the inclusion of the K2K data. Moreover, the first data released by MINOS does not eliminate this degeneracy. Again, this situation is expected to be significantly improved in the future, as MINOS collects more data.

On the theoretical side, a lot of work on the implications of the current data on NSI remains to be done. For example, a combined study of the atmospheric- and solar-neutrino data has not yet been performed.

4.5.6 Complementarity of long- and short-baseline experiments for non-standard interactions

The combination of long- and short-baseline experiments is effective in distinguishing the oscillations due to θ_{13} and those due to the NSI. To see this, consider for simplicity the two-flavour scenario where the oscillation probability can be expressed analytically. The Hamiltonian for this case is:

$$U \begin{pmatrix} 0 & 0 \\ 0 & \frac{\Delta m^2}{2E} \end{pmatrix} U^\dagger + A \begin{pmatrix} 1+\epsilon_{ee} & \epsilon_{e\tau} \\ \epsilon_{e\tau} & \epsilon_{\tau\tau} \end{pmatrix}, \tag{285}$$

where $A \equiv \sqrt{2} G_F n_e$. The effective mass-squared difference Δm^2_M, the mixing θ_M and the oscillation probability $P(\nu_e \to \nu_\tau)$ at distance L in matter are given by:

$$\left(\frac{\Delta m^2_M L}{4E}\right)^2 = \left(\frac{\Delta m^2 L}{4E}\cos 2\theta - \frac{AL}{2}(1+\epsilon_{ee}-\epsilon_{\tau\tau})\right)^2 + \left(\frac{\Delta m^2 L}{4E}\sin 2\theta + AL\epsilon_{e\tau}\right)^2 \quad (286)$$

$$\sin 2\theta_M = \frac{\Delta m^2 \sin 2\theta + 4EA\epsilon_{e\tau}}{\Delta m^2_M} \text{ ; and} \quad (287)$$

$$P(\nu_e \to \nu_\tau) = \sin^2 2\theta_M \sin^2\left(\frac{\Delta m^2_M L}{4E}\right). \quad (288)$$

To have a large value of the oscillation probability $P(\nu_e \to \nu_\tau)$, large values for both $\sin^2 2\theta_M$ and $\sin^2\left(\Delta m^2_M L/4E\right)$ are required. Equation (288) implies: that the effect of the new physics in $\sin^2\left(\Delta m^2_M L/4E\right)$ appears in a form $AL(\epsilon_{ee}-\epsilon_{\tau\tau})$ or $AL\epsilon_{e\tau}$, so a large deviation of $\Delta m^2_M L/4E$ from the standard value $\Delta m^2 L/4E$ requires that $AL\epsilon_{\alpha\beta}$ be non-negligible irrespective of the neutrino energy E; and that, for the experiments with $|\Delta m^2|L/E \simeq \mathcal{O}(1)$, multiplying by L both the numerator and the denominator of equation (287), to obtain a non-trivial new-physics contribution to the mixing angle θ_M again demands that $AL\epsilon_{\alpha\beta}$ be non-negligible. These conditions imply that the baseline length has to be relatively large for the new-physics effect to affect both of the factors in the oscillation probability, since A can be roughly estimated as $A \simeq 1/(2000\text{km})$ with $\rho \simeq 3\text{g/cm}^3$. These features hold also in the case with three flavours.

The present and future generation of neutrino-oscillation experiments are designed mainly to probe neutrino oscillations with the atmospheric-neutrino mass-squared difference $|\Delta m^2_{\text{atm}}| \simeq 2.5 \times 10^{-3}\text{eV}^2$ and the typical neutrino energy, E, of each experiment satisfies $|\Delta m^2_{\text{atm}}|L/E \simeq \mathcal{O}(1)$. The baseline lengths, L, of these experiments, however, are quite different and, when $\epsilon_{\alpha\beta} \sim \mathcal{O}(1)$, only the experiments for which AL is non-negligible will have sensitivity to new physics. Reactor experiments, for which $AL \ll 1$, are insensitive to $\epsilon_{\alpha\beta}$. On the other hand, a reactor experiment has the advantage of having no backgrounds due to new physics in measurements of the standard oscillation parameters. For the T2K experiment, $AL \simeq 3/20$, so it has potential to see the new physics effect. MINOS, NOvA, T2KK, and a Neutrino Factory, since AL is larger, have greater potential to see the signal of $\epsilon_{\alpha\beta}$ [686, 687]. These effects can be seen in figure 56.

5 Performance of proposed future long-baseline neutrino oscillation facilities

5.1 Introduction

The precision with which the parameters of the Standard Neutrino Model have been determined in fits to neutrino-oscillation data is shown in figure 6 and summarised in table 2. Over the coming decade, the various long-baseline, reactor, solar, and atmospheric neutrino experiments that are in operation or in preparation will improve upon these results. In particular, the strong push to determine the small mixing angle will yield a measurement of θ_{13} if $\sin^2\theta_{13} > 0.1$ and

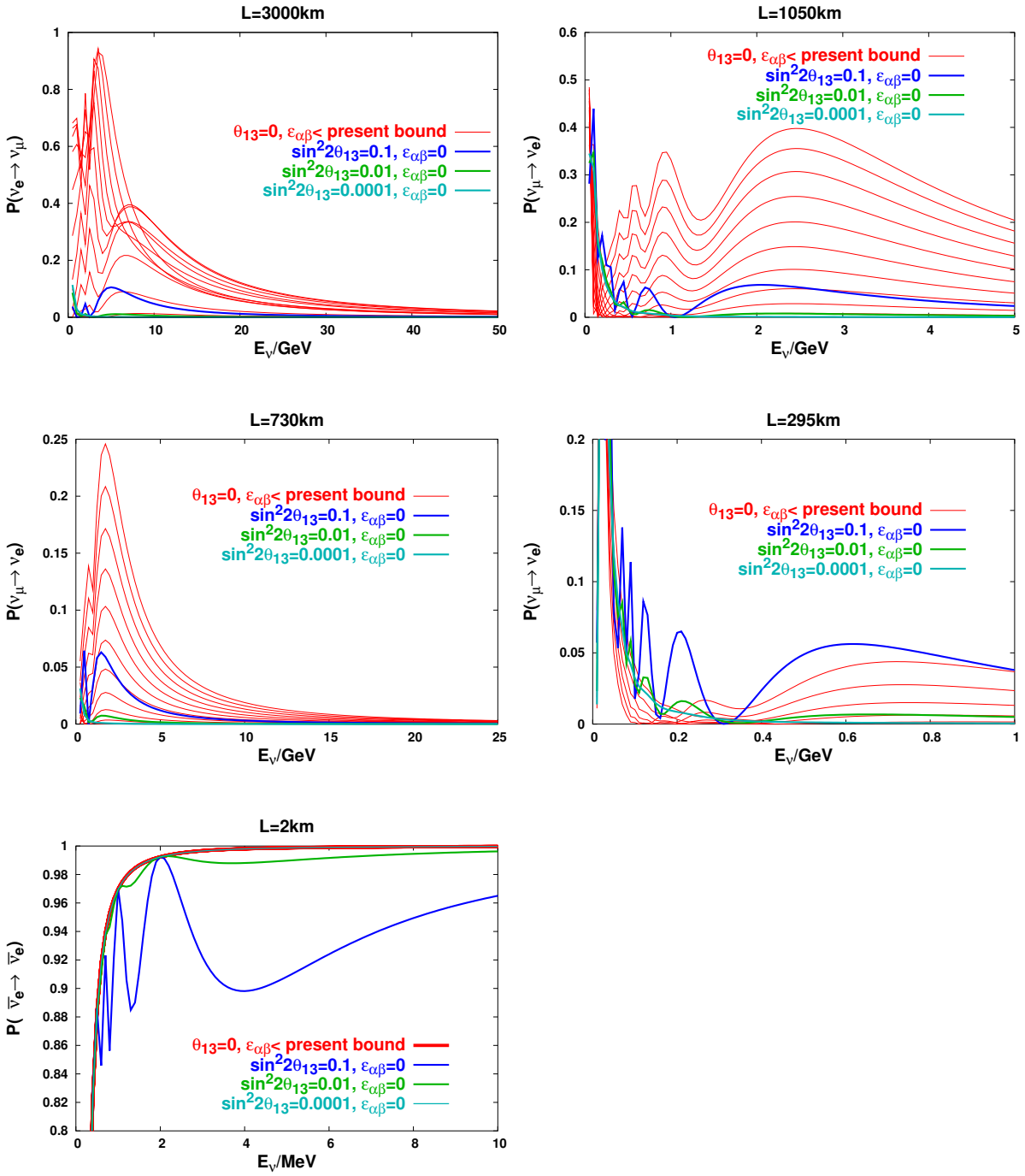

Figure 56: Effects of θ_{13} versus those of the NSI [685,688]: The oscillation probabilities with (red lines) or without (blue, green and light blue lines) the NSI are plotted for typical baseline lengths. The red lines are plotted for various values of $\epsilon_{ee}, \epsilon_{e\tau}, \epsilon_{\tau\tau}$ which are in the allowed region obtained by [682].

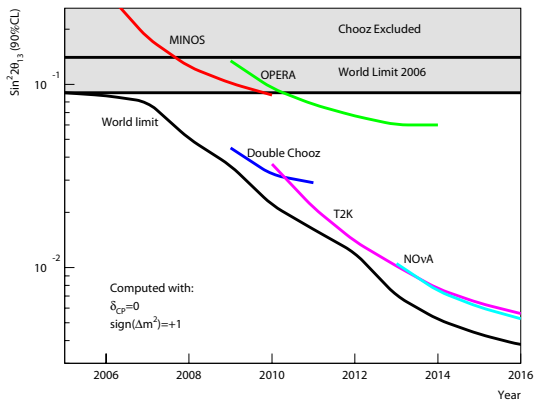

Figure 57: Projected evolution of the world limit on $\sin^2 2\theta_{13}$ at 90% CL. The anticipated impact of the MINOS, OPERA, T2K, and NOνA long-baseline neutrino-oscillation experiments are shown together with that of the Double Chooz reactor-neutrino experiment are shown. Taken with kind permission of the Editor from the Proceedings of the Neutrino Telescopes 2007 [689]. For a discussion of these experiments see section 2.

a substantially improved limit otherwise. Figure 57 shows the evolution of the upper limit on $\sin^2\theta_{13}$ that may be expected based on the performance claimed for the various experiments [689]. The sensitivity to the small mixing angle improves significantly as the data from each of the new experiments becomes available. By around 2016, the rate of improvement in the sensitivity of the neutrino-oscillation programme slows down and a new generation of high-flux facilities is required.

The new facility must offer the best possibility of observing leptonic-CP violation and of determining the mass hierarchy (sgn$\Delta(m^2_{32})$). The optimisation of the facility depends on the value of θ_{13}. If θ_{13} is large (such that $\sin^2 2\theta_{13} \gtrsim 0.01$) then it will have been measured, albeit with poor precision. In this case, the high-sensitivity facility is required to offer the best sensitivity to δ and (sgn$\Delta(m^2_{32})$). If θ_{13} is small (such that $\sin^2\theta_{13} \lesssim 0.01$) it is unlikely to have been measured and the facility will, in addition, be required to have the best possible sensitivity to θ_{13}.

At the same time, the new facility must aim at providing measurements of sufficient precision to inform the development of the theory of the physics of flavour. The status of the theoretical description of flavour is discussed in detail in section 3. Grand-unified theories typically provide relationships between the neutrino-mixing parameters and those of the quarks. For such relationships to be tested requires that the precision with which the neutrino-mixing parameters are determined matches that with which the quark-mixing parameters are known. At present the quark-mixing parameters are known at the percent level. This sets the standard; the high-precision neutrino-oscillation programme must deliver measurements of the neutrino-oscillation parameters at the percent level. To achieve this goal requires high-energy electron- and muon-neutrino beams and highly sensitive neutrino-detection systems.

Three types of facility have been proposed to provide the neutrino beams required to serve the high-sensitivity programme. The Neutrino Factory gives the best performance over most of the parameter. Second-generation super-conventional-beam experiments may be an attractive

option in certain scenarios. A beta-beam [24], in which electron neutrinos (or anti-neutrinos) are produced from the decay of stored radioactive-ion beams, in combination with a second-generation super-beam, may be competitive with the Neutrino Factory. The purpose of this chapter is to evaluate the physics performance of a second-generation super-beams, a beta-beam facility, and the Neutrino Factory and to present a critical comparison of their performance.

5.1.1 Definition of observables

The observables that will be examined in sections 5.2, 5.3, and 5.4, and compared in section 5.5 are defined below:

- *Number of degrees of freedom:* The number of degrees of freedom that are used to convert $\Delta\chi^2$-values into confidence levels must be clearly defined. In the literature several different approaches can be found, for example: in [217, 220] the CP-violation discovery potential is defined as the smallest (largest) value of "true" $|\delta|$ (as a function of "true" θ_{13}) for which the 3σ contour in the (θ_{13}, δ) plane of any of the degenerate solutions does reach either $\delta = 0$ ($\delta = \pi$; while in [208], the $\Delta\chi^2$ is marginalised over all parameters except δ and one degree of freedom is used. For definiteness, unless otherwise stated, we will use one degree of freedom throughout;

- *θ_{13}-sensitivity and θ_{13} discovery potential:* The θ_{13}-sensitivity as a function of "true" δ is the largest value of θ_{13} that fits the "true" value $\theta_{13} = 0$, after marginalisation over all parameters other than θ_{13}, once all possible wrong choices of $\mathrm{sgn}(\Delta m^2_{31})$ and of the θ_{23}-octant are taken into account.

  For the θ_{13} discovery potential, data are simulated for non-vanishing "true" θ_{13} and a given "true" δ. After marginalisation over all parameters other than θ_{13} and taking into account all possible wrong choices of $\mathrm{sgn}(\Delta m^2_{31})$ and of the θ_{23}-octant, if $\Delta\chi^2(\theta_{13} = 0) \geq 9$, the "true" θ_{13} is "discovered at 3σ";

- *CP discovery potential and sensitivity to maximal CP-violation:* To obtain the δ-discovery potential, data are simulated for "true" δ different from 0 and π and a given "true" θ_{13}. After marginalisation over all parameters other than δ and taking into account all possible wrong choices of $\mathrm{sgn}(\Delta m^2_{31})$ and of the θ_{23}-octant, if $\Delta\chi^2(\delta = 0)$ and $\Delta\chi^2(\delta = \pi)$ are both larger than 9, computed with respect to the absolute χ^2 minimum, the "true" δ is "discovered at 3σ".

  Sensitivity to maximal CP-violation, refers to the possibility that a "true" $\delta = \pm\pi/2$ from $\delta = 0$ or $\delta = \pi$ at a given CL as a function of some other parameter [206, 208];

- *Sensitivity to the sign of the atmospheric mass difference:* We have sensitivity to the "true" mass hierarchy if, when performing an hypothesis test, after marginalisation over all parameters and taking into account all possible choices of the θ_{23}-octant, we can exclude the wrong hierarchy at a given CL. The procedure is to draw a contour in the "true" (θ_{13}, δ) plane for the mass hierarchy under consideration. In most cases, a "true" normal hierarchy

will be discussed, since the inverted hierarchy gives qualitatively similar results. Note that, for the "true" inverted hierarchy anti-neutrinos are matter enhanced, thus compensating for the smaller cross-section with respect to neutrinos (see, for example, reference [690]);

- *θ_{23}–non-maximality discovery potential and sensitivity to the θ_{23}-octant:* Data are simulated for "true" θ_{23} different from $\pi/4$ and a given "true" Δm^2_{31}. After marginalisation over all parameters but θ_{23}, and taking into account all possible wrong choices of the sign of Δm^2_{31}, if $\Delta\chi^2(\theta_{23} = \pi/4) \geq 9$, the corresponding deviation from maximality is "discovered at 3σ".

  If $\theta_{23} \neq \pi/4$, we have sensitivity to the "true" θ_{23}-octant if, when performing an hypothesis test, after marginalisation over all parameters and taking into account all possible choices of the mass hierarchy, we can exclude the wrong octant at a given CL. The procedure is to draw a contour in the "true" (θ_{13}, δ) plane for the "true" octant under consideration;

- *Precision on θ_{13} and δ:* The precision on θ_{13} (δ) is the projection of the (marginalised) $\Delta\chi^2$ onto the $\sin^2 2\theta_{13}$ (δ) axis at a given CL. Remember that, for different choices of the hierarchy and of the θ_{23}-octant, several solutions can arise. In section 5.5, we also show our results as two-parameter contours in the $(\sin^2 2\theta_{13}, \delta)$ plane for a set of "true" input pairs; and

- *Precision on Δm^2_{31} and $\sin^2\theta_{23}$:* The precision on Δm^2_{31} (θ_{23}) is the projection of the (marginalised) $\Delta\chi^2$ onto the Δm^2_{31} ($\sin^2\theta_{23}$) axis at a given CL. Remember that, for different choices of the hierarchy, several solutions can arise.

  We will, in some cases, refer to the "Fraction of (true) δ" (or the "CP-fraction"). This is the fraction of the δ-parameter space, i.e. of $0 < \delta < 2\pi$) over which a facility has sensitivity to a given observable. For a graphical explanation of this procedure, see e.g. figure 3 of reference [691].

5.2 The physics potential of super-beams

5.2.1 The super-beam concept

Conventional neutrino beams from π-decay have, up to now, mainly been tuned for the study of ν_μ disappearance [10,11] or $\nu_\mu \to \nu_\tau$ appearance [12]. Such beams can be optimised for $\nu_\mu \to \nu_e$ searches. The design of such a facility, producing high intensity, low energy ν_μ and $\bar{\nu_\mu}$ beams, requires the development of new, high-power, proton accelerators delivering more intense proton beams on target. In the following, a super-beam is taken to be a conventional neutrino beam driven by proton driver with a beam power in the range 2 –5 MW.

The technology required for the super-beam is a development of that used today in long-baseline neutrino-oscillation experiments. Compared to beta-beam facilities or the Neutrino Factory, super-beams have the advantage that the required technology is relatively well known. The neutrino beam contains the dominant neutrino flavour (ν_μ if the capture system focuses π^+ into the decay channel) together with a small but unavoidable admixture of $\bar{\nu}_\mu$, ν_e and $\bar{\nu}_e$.

The presence of ν_e and $\bar{\nu}_e$ in the primary beam limits the super-beam sensitivity to $\nu_\mu \to \nu_e$ oscillations. The intrinsic ν_e contamination, which grows with increasing neutrino energy, must therefore be kept as low as possible. One way to achieve this is to arrange that the neutrino-beam axis is tilted by a few degrees with respect to the vector pointing from the source to the far detector (an off-axis beam). The kinematics of the two-body π-decay ensures that all pions above a given momentum produce neutrinos of similar energy at a given angle $\theta \neq 0$, with respect to the direction of the parent pion. The off-axis technique yields a low-energy beam of neutrinos with a small energy spread. Such neutrino beams have several advantages over the corresponding broad-band on-axis beams; the narrow-band low-energy beam allows energy cuts to be applied to reduce backgrounds and allows the L/E of the experiment to be tuned to the oscillation maximum. However, the off-axis neutrino flux is significantly smaller than the on-axis flux. Another way of reducing the ν_e background is suppressing the K^+ and K^0 production in the target.

5.2.2 T2K and T2HK

The T2K facility consists of a conventional neutrino beam driven by 50 GeV protons from the J-PARC proton synchrotron at a beam power of 0.75 MW. The neutrino beam will illuminate the Super-Kamiokande detector at a baseline of $L = 295$ km. The facility is presently under construction, data taking is scheduled to start in 2009 [13]. In the first year, the number of 'protons-on-target' (pot) is expected to be $\sim 10\%$ of the design value. The T2K neutrino beam line has been designed so that the off-axis angle can be varied between 2° and 3°. The off-axis angle will be chosen to maximise the sensitivity of the experiment to θ_{13} in the light of the most recent measurements of Δm^2_{31}.

An upgrade to the power of the J-PARC proton synchrotron to provide a 4 MW, 50 GeV proton beam is planned. This, together with the construction of a mega-Tonne (Mton) class, water Čerenkov detector (Hyper-Kamiokande) could provide enough events to compete with beta-beam and Neutrino Factory facilities if the mixing parameters are favourable. This upgraded version of T2K, T2HK or T2K-II, is considered below. Figure 58(left) shows the neutrino fluxes expected at Hyper-Kamiokande assuming a 2° off-axis angle.

It has been proposed to exploit the J-PARC neutrino beam with a second 100 Kton [20, 21] or 0.5Mton [19, 22] water Čerenkov detector in Korea. The second detector would be placed at a 0.5° [20, 21] or at a 2.5° [19, 22] off-axis angle for a baseline of $L = 1000$ km. This combination of two baselines would give significant sensitivity to the neutrino-mass hierarchy, reducing the degeneracy problem present in searches for leptonic CP-violation (see section 2.4.1).

5.2.3 The SPL

In the CERN super-beam project [14,625,692,693], the planned 4 MW Super-conducting Proton Linac (SPL) will deliver a 2.2 GeV proton beam on a mercury target to generate an intense

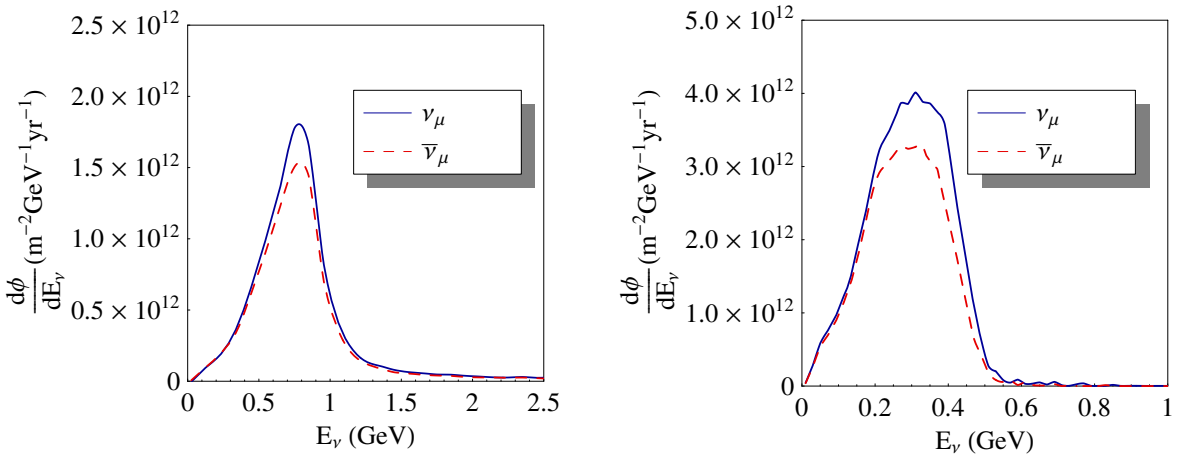

Figure 58: Left panel: T2HK fluxes at the Kamioka location (295 km baseline); Right panel: SPL fluxes at the Fréjus location (130 km baseline).

π^+ (π^-) beam focused by a magnetic horn into a short decay tunnel. As a result, an intense ν_μ ($\bar{\nu}_\mu$) beam will be produced, providing a flux $\phi \sim 3.6{\cdot}10^{11}\nu_\mu/\text{year}/\text{m}^2$ ($2.3{\cdot}10^{11}\bar{\nu}_\mu/\text{year}/\text{m}^2$), with an average energy of 0.27 (0.25) GeV aimed at a Mton-class, water Čerenkov detector at the Modane laboratory in the Fréjus area (a baseline of $L = 130$ km). The ν_e contamination from kaons will be suppressed by threshold effects and the resulting ν_e/ν_μ ratio ($\sim 0.4\%$) will be known to within 2%.

New developments show that the SPL potential could be improved by raising the SPL energy to 3.5 GeV [15], to produce more copious secondary mesons and to focus them more efficiently. This seems feasible if state-of-the-art RF cavities are used in place of the LEP cavities assumed in the 2.2 GeV design [694]. In this upgraded configuration the neutrino flux could be increased by a factor of 3 with respect to the 2.2 GeV configuration, with a slightly higher energy of 0.28 GeV. The fluxes that the 2.5 GeV configuration will produce are shown in figure 58(right).

5.2.4 NOνA

The NOνA experiment was proposed recently at FNAL to measure $\nu_\mu \to \nu_e$ oscillations with a sensitivity 10 times better than MINOS [16]. It consists of an upgraded NuMI Off-Axis neutrino beam with $E_\nu \sim 2$ GeV and a ν_e contamination of less than 0.5%. The baseline is $L = 810$ km with the detector sited 12 km ($\sim 0.85^\circ$) off-axis. If approved, the experiment could start data taking in 2011. The NuMI target will receive a 120 GeV/c proton beam with an expected intensity of $6.5{\cdot}10^{20}$ pot/year. The beam will be measured at a near and at a far detector, both 'totally active' liquid-scintillator detectors. With and a five-year run and a detector mass $\sim$ 30 Kton, NOνA will achieve a sensitivity to $\sin^2 2\theta_{13}$ comparable to that which T2K can achieve. The long baseline allows NOνA to make a measurement of $|\Delta m^2_{31}|$.

The possibility of exploiting NOνA together with a second detector at a different baseline to determine the mass hierarchy has been discussed [17, 18]. The potential of the increased data

volume provided by the NuMI beam instrumented with yet larger detectors, or detectors with larger detection efficiency, in conjunction with a possible NuMI upgrade has been studied [695]. However, as yet there is no well-developed proposal for a NOνA upgrade that is able to compete with other second generation super-beams such as T2HK or the SPL.

5.2.5 Wide-band super-beam

A wide-band beam has been proposed, sited at BNL and serving a very long baseline experiment [23, 36, 37, 691]. In this proposal, the 28 GeV AGS would be upgraded to 1 MW and a neutrino beam with neutrino energies in the range $0 - 6$ GeV could be sent to a Mton water Čerenkov detector at the Homestake mine at a baseline of 2540 km.

Wide-band beams possess the advantages of a higher on-axis flux and a broad energy spectrum. The latter allows the first and second oscillation nodes in the disappearance channel to be observed, providing a strong tool to solve the degeneracy problem. On the other hand, experiments served by wide-band beams must determine the incident neutrino energy with good resolution and eliminate the background from high energy tail of the spectrum.

Upgrades to the FNAL main injector after the end of the Tevatron programme are also under study and could provide a similar wide-band neutrino beam. The baseline in this case would be 1290 km. In the following, the flux obtained using 28 GeV protons and a 200 meter long decay tunnel will be used. For details of this spectrum see reference [37].

The combination of channels and spectral information of a long baseline wide-band beam experiment offers a promising means of solving parameter degeneracies. However, the very long baseline decreases the event rate at the far detector and reduces the sensitivity of the experiment to θ_{13} and CP-violation; the sensitivity of the experiment to θ_{13} and δ is somewhat smaller than that of T2HK or the SPL. Therefore, the following sections will focus on the performance of T2HK and the SPL. The performance of the wide-band beam will be discussed when considering the determination of the mass hierarchy, where the long baseline means that the wide-band beam out-performs T2HK and the SPL. The wide-band beam is a very interesting option to search for leptonic CP-violation, solving most of the degeneracies, if θ_{13} is large enough, i.e. $\sin^2 2\theta_{13} > 5 \times 10^{-3}$ ($\theta_{13} > 2^\circ$).

5.2.6 Physics at a super-beam facility

The first generation of neutrino super-beams, T2K and NOνA, will study the $\nu_\mu \to \nu_e$ channel which is sensitive to θ_{13} and δ. The experiments will start by running in neutrino mode. This has the advantage that a large data set can be accumulated relatively rapidly since the neutrino cross section is larger than the anti-neutrino cross section. Neutrino running alone, however, implies that the experiments have no sensitivity to δ. A second generation of upgraded super-beams, such as T2HK or the SPL, could follow. The extremely large data sets provided by these experiments would yield sensitivity to much smaller values of θ_{13}. These experiments could also

search for CP-violation by running with anti-neutrinos, if θ_{13} is large enough. In the rest of this section, the sensitivity to θ_{13} and δ of this second generation of super-beams will be considered.

The search for small θ_{13} in the $\nu_\mu \to \nu_e$ channel suffers from parametric degeneracies (see section 2.4.1). To alleviate this problem, and to improve significantly the measurement of the atmospheric parameters θ_{23} and Δm^2_{31} at these facilities, it is extremely useful to study ν_μ disappearance as well. Such measurements are also of importance in order to establish whether θ_{23} is maximal in order to discriminate between different mass models. The maximal-mixing-exclusion potential of the various super-beams will therefore also be investigated below.

5.2.7 The Water Čerenkov Detector

For small values of θ_{13}, a very large data set is required for the sub-leading $\nu_\mu \to \nu_e$ oscillation to be observed. The water Čerenkov is an ideal detector for this task since it is possible to construct a detector of very large fiducial mass in which the target material is also the active medium. The Čerenkov light is collected by photo-detectors distributed over the surface of the detector; the cost of instrumenting the detector, therefore, scales with the surface area rather than the fiducial mass. Mton-class, water Čerenkov detectors are therefore ideal when charge identification is not required and have been chosen for T2HK, the SPL, and the wide-band beam long-baseline experiment. Such a device could also be the ultimate tool for proton-decay searches and for the detection of atmospheric, solar, and supernovæneutrinos.

Charged leptons are identified through the detection of Čerenkov light in photo-multiplier tubes (PMTs) distributed around the vessel. The features of the Čerenkov rings can be exploited for particle identification. A muon scatters very little in crossing the detector, therefore, the associated Čerenkov ring has sharp edges. Conversely, an electron showers in the water, producing rings with 'fuzzy' edges. The total measured light can be used to give an estimate of the lepton energy, while the time measurement provided by each PMT allows the lepton direction and the position of the neutrino interaction vertex to be determined. By combining all this information, it is possible to reconstruct the energy, the direction, and the flavour of the incoming neutrino. It is worth noting that the procedure discussed above is suitable only for quasi-elastic events ($\nu_l n \to l^- p$). Indeed, for non-quasi-elastic events more particles are present in the final state that are either below the Čerenkov threshold or are neutral, resulting in a poor measurement of the total event energy. Furthermore, the presence of more than one particle above threshold produces more than one ring, spoiling the particle identification capability of the detector.

The water Čerenkov is a mature technology that has been demonstrated to be cost effective and to give excellent performance at low neutrino energies. A detector with a fiducial mass as large as 20 times that of Super-Kamiokande could be built and would be an optimal detector for neutrino beams with energies around or below 1 GeV [696]. There are three different proposals for such a detector, each of them exploited by a different super-beam. Hyper-Kamiokande [13] could be located at the Kamioka mine, at a distance of 295 km from J-PARC facility in Tokai. MEMPHYS [697], in the Fréjus area, could receive the SPL beam produced 130 km away at

CERN. The wide-band beam produced at BNL (FNAL) could aim at a detector in the Homestake mine [23] at 2540 km (1290 km).

5.2.8 Backgrounds and efficiencies

In a conventional super-beam experiment, the search for $\nu_\mu \to \nu_e$ ($\bar{\nu}_\mu \to \bar{\nu}_e$) is complicated by the $\nu_e(\bar{\nu}_e)$ contamination of the beam. In a water Čerenkov detector, the appearance, $\nu_e(\bar{\nu}_e)$, signal is detected by exploiting the high efficiency and high purity of the detector in identifying electrons and muons in low multiplicity interactions. In addition to the $\nu_e(\bar{\nu}_e)$ contamination of the beam, the main sources of background are the charged-current interactions of $\nu_\mu(\bar{\nu}_\mu)$ and the production of π^0s in neutral-current interactions. Even though the performance of water Čerenkov detectors is very well studied, there are few analyses of the efficiencies and backgrounds expected in the various super-beams considered here.

For T2HK, there is only the study reported in the letter of intent [13]. The expected signal- and background-event rates for the $\nu_\mu \to \nu_e$ channel are presented in table 2 of reference [13]. The expected efficiencies and fractional backgrounds have been extracted for several analyses from this table [27,38,218,340,698–700]. The signal efficiency, assumed to be constant, is 0.505. The various contributions to the background (N^{bg}), from the $\nu_e(\bar{\nu}_e)$ contamination in the beam (N_e^{CC}), π^0 production in neutral-current events (N^{NC}), and ν_μ charged-current interactions (N_μ^{CC} have the following weights:

$$N^{bg} = 7.5 \cdot 10^{-2} N_e^{CC} + 5.6 \cdot 10^{-3} N^{NC} + 3.3 \cdot 10^{-4} N_\mu^{CC} \tag{289}$$

The same efficiencies and backgrounds have been assumed for the $\bar{\nu}_\mu \to \bar{\nu}_e$ channel since no further information on this channel is available. The efficiencies and backgrounds are assumed to be flat since no energy dependence is presented. This is only an approximation and a more detailed description in terms of migration and background matrices as in [25, 341] would be desirable. For the spectral information, 20 bins of 40 MeV between 0.4 GeV and 1.2 GeV have been considered, convoluted with a Gaussian with $\sigma = 85$ MeV to account for the Fermi motion as in reference [340].

The situation is very similar in the case of the SPL. The only available study is that of reference [625], from which flat efficiencies and backgrounds can be extracted. The efficiencies quoted in [625] are 0.707 for the $\nu_\mu \to \nu_e$ channel and 0.671 for $\bar{\nu}_\mu \to \bar{\nu}_e$. The backgrounds, in a notation consistent with that used above, are:

$$N^{bg} = 4.4 \cdot 10^{-1} N_e^{CC} + 2.7 \cdot 10^{-3} N^{NC} + 4.6 \cdot 10^{-4} N_\mu^{CC} \text{ ; and} \tag{290}$$

$$\bar{N}^{bg} = 6.8 \cdot 10^{-1} N_e^{CC} + 4.4 \cdot 10^{-4} N^{NC} + 1.3 \cdot 10^{-3} N_\mu^{CC} \text{ .} \tag{291}$$

These numbers have been used in several different studies [27, 214, 217, 218, 220]. The fluxes obtained with the 2.2 GeV SPL proton beam have been assumed. No new analysis has been performed to obtain the fluxes of the upgraded 3.5 GeV SPL [15]. Again, an updated, and energy-dependent, description of the efficiencies and backgrounds would be desirable.

The SPL events have been divided into 5 bins of 200 MeV up to 1 GeV. For both the SPL and T2HK, a 440 Kton fiducial mass for the detector and 10 years running time have been assumed. The running time has been divided between the neutrino and anti-neutrino mode in such a way as to produce a roughly equal number of events for each channel. For both experiments, the rather optimistic value of 2% has been adopted for the systematic uncertainty. The less optimistic case of 5% systematic uncertainty is also presented. These errors are assumed to be uncorrelated between the various signal channels (neutrinos and anti-neutrinos), and between the signal and background samples.

For the wide-band beam long-baseline experiment, migration matrices for both the signal and the background channels have been computed [691] from a Monte Carlo simulation from the detector described in [701]. Following reference [691], a 300 Kton fiducial mass detector, 5 years neutrino running with 1 MW proton-beam power, and 5 years anti-neutrino running with a proton-beam power of 2 MW have been considered.

5.2.9 The super-beam performance

In the following, the performance of T2HK and the SPL super-beams is presented in terms of the θ_{13} and the CP-violation discovery potential, the sensitivity of the facility to the maximality of θ_{23}, the mass hierarchy, and the octant of θ_{23}. The precision with which the atmospheric parameters can be measured is also presented. To simulate the 'data', the following set of 'true values' for the oscillation parameters are adopted:

$$\begin{aligned} \Delta m^2_{31} &= +2.5 \times 10^{-3}\ \mathrm{eV}^2\,; \qquad & \sin^2\theta_{23} &= 0.5\,; \\ \Delta m^2_{21} &= 8.0 \times 10^{-5}\ \mathrm{eV}^2\,; \qquad & \sin^2\theta_{12} &= 0.3\,; \end{aligned} \tag{292}$$

and we include a prior knowledge of these values with a 1σ accuracy of 5% for θ_{12} and Δm^2_{21}. θ_{23} and Δm^2_{31} can be measured by these experiments and have been left free in the fits. These values and accuracies are motivated by recent global fits to neutrino oscillation data [67, 114], and they are always used except where explicitly stated otherwise.

5.2.10 The θ_{13} discovery potential

If the first generation of super-beam experiments do not demonstrate that θ_{13} is non-zero, then the second generation facility will be required to have a significantly improved sensitivity to this parameter. To assess the sensitivity of the proposed second-generation super-beams to θ_{13}, the following definition of the discovery potential is used. Data are simulated for a non-zero 'true' value of $\sin^2 2\theta_{13}$ and for a given true value of δ. If the $\Delta\chi^2$ of the fit to these data with $\theta_{13} = 0$ (marginalised over all parameters except θ_{13}) is larger than 9, the corresponding true value of θ_{13} is taken to be 'discovered' at 3σ. In other words, the 3σ-discovery limit as a function of the true δ is given by the true value of $\sin^2 2\theta_{13}$ for which $\Delta\chi^2(\theta_{13} = 0) = 9$. In general, tests must also be made for degenerate solutions in $\mathrm{sign}(\Delta m^2_{31})$ and the octant of θ_{23}.

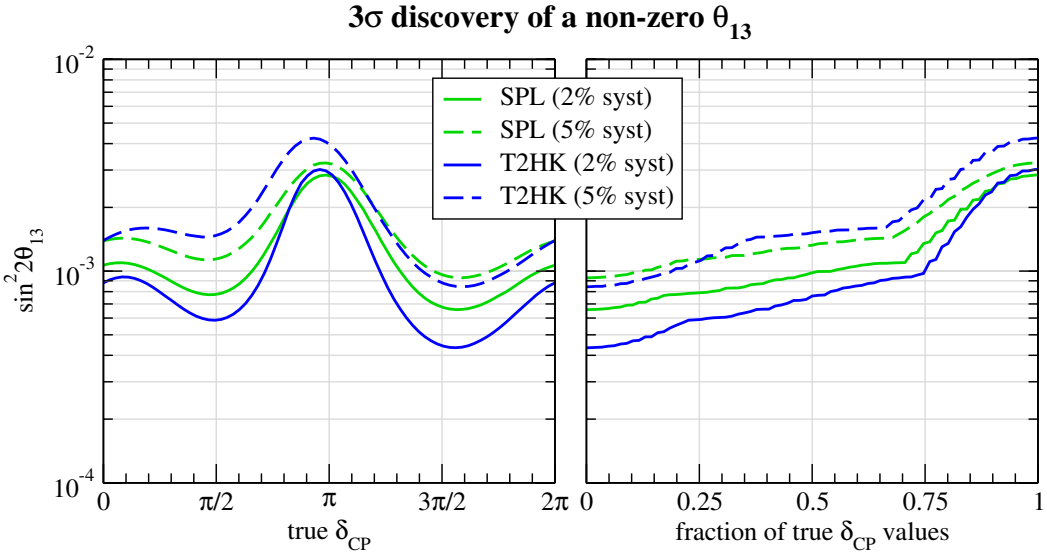

Figure 59: 3σ discovery sensitivity to $\sin^2 2\theta_{13}$ for the SPL and T2HK as a function of the true value of δ (left panel) and as a function of the fraction of all possible values of δ (right panel). Solid (dashed) lines are for 2% (5%) systematic errors. Adapted with kind permission of the Journal of High Energy Physics from figure 9 in reference [27]. Copyrighted by SISSA.

The discovery limits for the SPL super-beam and for T2HK are shown in figure 59. The performance of the two facilities is rather similar, and a discovery potential down to $\sin^2 2\theta_{13} \simeq 4 \times 10^{-3}$ is within reach for all possible values of δ. For certain values of δ (around $\delta = \pi/2$ or $3\pi/2$) the sensitivity is significantly improved, and discovery limits below $\sin^2 2\theta_{13} \simeq 10^{-3}$ are possible for a large fraction of all possible values of δ. The wide-band beam long-baseline experiment has a slightly lower sensitivity ranging from $\sin^2 2\theta_{13} \simeq 2 \times 10^{-3}$ to $\sin^2 2\theta_{13} \simeq 5 \times 10^{-3}$ (see figure 5 of reference [691]).

Figure 59 also illustrates the effect of systematic uncertainties on the θ_{13} discovery reach. The lower (solid) boundary of the band for each experiment corresponds to a systematic error of 2%, whereas the upper (dashed) boundary is obtained for a systematic uncertainty of 5%. These uncertainties include the (uncorrelated) normalisation uncertainties on the signal as well as the background; the dominant uncertainty is the uncertainty on the background. For the SPL, systematic uncertainties have a rather small impact on the sensitivity, whereas for the larger data set acquired by T2HK, the limit is more strongly affected.

5.2.11 CP-violation discovery potential

If θ_{13} is shown to be non-zero, then it becomes important to assess the leptonic CP-violation (CPV) discovery potential quantitatively, i.e. to assess the extent to which the proposed second-generation super-beam experiments can establish that δ differs from 0 or π. The CPV-discovery potential is evaluated as follows. Simulated data sets were produced for a range of assumed

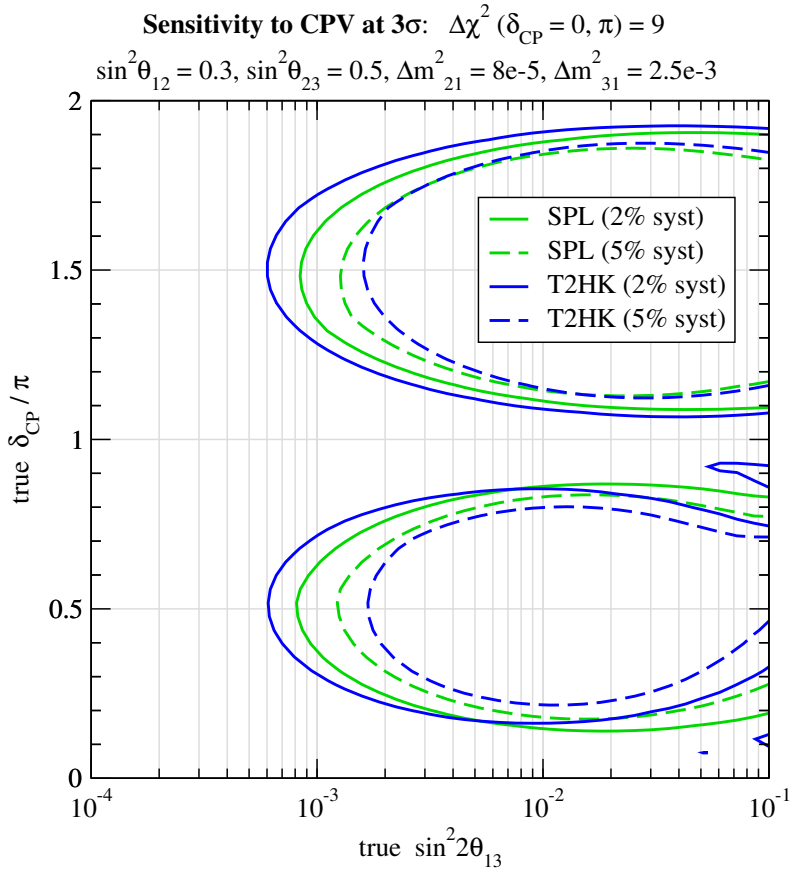

Figure 60: CPV discovery potential the SPL, and T2HK: for parameter values inside the ellipse-shaped curves CP conserving values of δ can be excluded at 3σ ($\Delta\chi^2 > 9$). Solid (dashed) lines are for 2% (5%) systematic errors. Adapted with kind permission of the Journal of High Energy Physics from figure 11 in reference [27]. Copyrighted by SISSA.

'true' values of $\sin^2 2\theta_{13}$ and δ. These data were then fitted using the CP-conserving values $\delta = 0$ and $\delta = \pi$, all other parameters being marginalised and the sign and octant degeneracies being taken into account. If no fit with $\Delta\chi^2 < 9$ is found, CP conservation can be excluded at 3σ confidence level for the chosen values of $\delta^{\rm true}$ and $\sin^2 2\theta_{13}^{\rm true}$.

The CPV discovery potential for the SPL super-beam, and for T2HK is shown in figure 60. As in the case of the θ_{13} discovery potential, the performance of the two facilities is comparable. For an assumed systematic uncertainty of 2%, maximal CPV (for $\delta^{\rm true} = \pi/2, 3\pi/2$) can be discovered at 3σ down to $\sin^2 2\theta_{13} \simeq 6 \times 10^{-4}$ for T2HK, and $\sin^2 2\theta_{13} \simeq 8 \times 10^{-4}$ for the SPL super-beam. The CPV discovery potential of the wide-band long-baseline super-beam would be limited to $\sin^2 2\theta_{13} \simeq 4 \times 10^{-3}$ (see the right panel of figure 7 in reference [691]). The best sensitivity to CPV is obtained for $\sin^2 2\theta_{13} \gtrsim 10^{-2}$, where, for a systematic uncertainty of 2%, CPV can be established for 75% of all possible values of δ. The figure shows the expected performance for systematic uncertainties of 2% and 5%. Again, T2HK is more strongly affected by the systematic uncertainties, out-performing the SPL super-beam for a 2% uncertainty but being out-performed by it for a 5% uncertainty.

The sensitivity maximum around $\sin^2 2\theta_{13} \simeq 10^{-2}$ can easily be understood from the oscillation probability. The interference term that allows the measurement of δ is suppressed by $\sin 2\theta_{13}$ and $\Delta m^2_{21} L/4E$ (see, for example equation (7) of reference [206]). There are two other leading terms in the probability, one suppressed by $\sin^2 2\theta_{13}$ and the other suppressed by $(\Delta m^2_{21}/4E)^2$. For $\sin 2\theta_{13} \simeq \Delta m^2_{21} L/4E$, the three terms in the oscillation probability will be of the same order of magnitude and the CP-violation signal will not be hidden by the other two terms. On the other hand, if $\sin 2\theta_{13}$ becomes too large or too small, one of the two CP-conserving terms dominates the interference term resulting in a loss of sensitivity. Indeed, for experiments built at the first peak of the atmospheric oscillation, $\sin 2\theta_{13} \simeq \Delta m^2_{21} L/4E$ for $\sin^2 2\theta_{13} \simeq 10^{-2}$. If the experiment operates at the second oscillation peak the larger $\Delta m^2_{21} L/4E$ will shift the maximum of the CP-violation sensitivity to larger values of $\sin^2 2\theta_{13}$, as can be seen in the right panel of figure 3 of reference [209].

5.2.12 Maximal θ_{23} exclusion potential

Experiments able to study the $\nu_\mu \to \nu_\mu$ oscillation can address the issue of the maximality of θ_{23} which is crucial to discriminate between different models of neutrino mass. The potential to exclude maximal θ_{23} has been computed in the following way: data are simulated for different true values of $\sin^2 \theta_{23}$, if the $\Delta\chi^2$ of the fit to these data with $\sin^2 \theta_{23} = 0.5$ (marginalised over all parameters except $\sin^2 \theta_{23}$) is larger than 9, then maximal mixing can be excluded at 3σ. Figure 61 shows that both T2HK and the SPL super-beam can measure at 3σ any deviation from maximal mixing larger than 10%. However, T2HK, with its better spectral information, out-performs the SPL, going down in sensitivity to deviations of 6% from maximal mixing. The importance of energy resolution in the disappearance channel to exclude maximal mixing is discussed in reference [218].

5.2.13 Sensitivity to the atmospheric parameters

The ν_μ disappearance channel available in super-beam experiments allows the atmospheric parameters $|\Delta m^2_{31}|$ and $\sin^2 \theta_{23}$ to be determined precisely (see, e.g., references [216, 218, 702] for recent analyses). Figure 62 illustrates the improved precision with which these parameters will be determined in future super-beam experiments. The figure shows the allowed regions at 99% CL for T2K, the SPL, and T2HK, where, in each case, five years of neutrino data are assumed. Table 9 gives the corresponding relative accuracies at 3σ for $|\Delta m^2_{31}|$ and $\sin^2 \theta_{23}$.

From the figure and the table it is evident that T2K and T2HK are very good at measuring the atmospheric parameters, only a modest improvement is possible with SPL with respect to T2K. T2HK provides excellent sensitivity to these parameters: for test-point 2, for example, sub-percent accuracies are obtained at 3σ. The disadvantage of the SPL with respect to T2HK is the limited spectral information. Because of the lower beam energy, nuclear Fermi motion is a severe limitation for energy reconstruction in the SPL super-beam, whereas in T2HK the somewhat higher energy allows an efficient use of spectral information in quasi-elastic events.

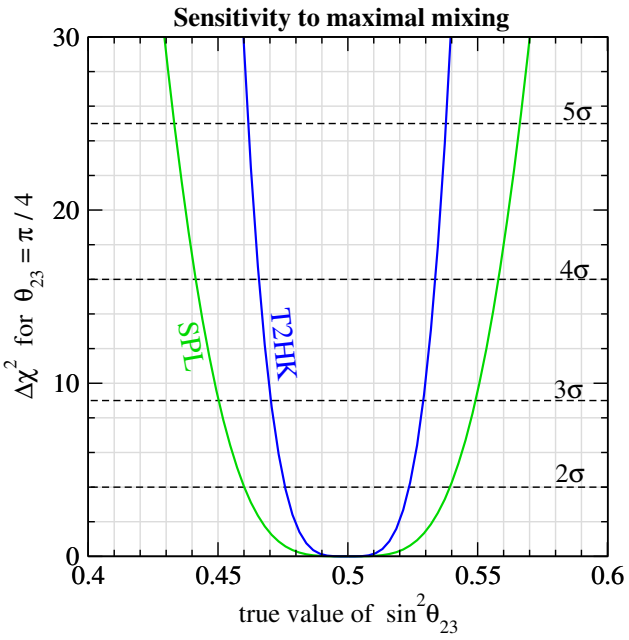

Figure 61: 3σ maximal mixing exclusion potential for the SPL and T2HK. The $\Delta\chi^2$ for maximal θ_{23} is shown as a function of the true value of $\sin^2\theta_{23}$.

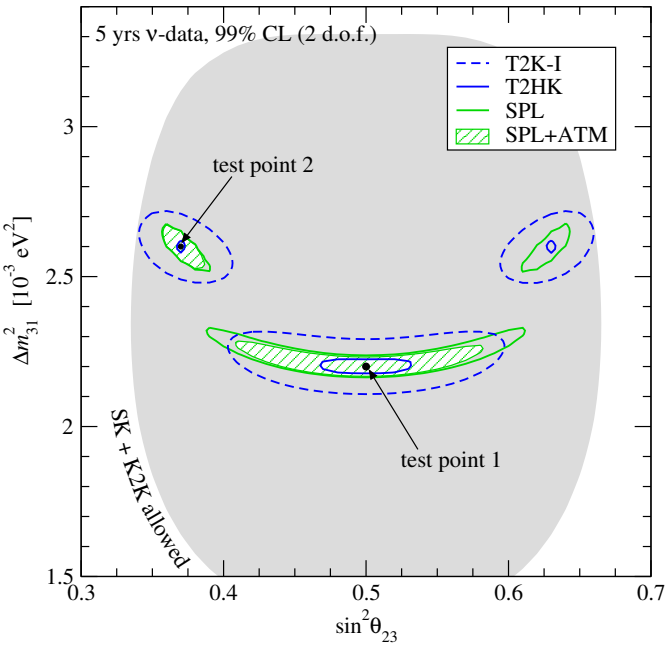

Figure 62: Allowed regions of Δm^2_{31} and $\sin^2\theta_{23}$ at 99% CL (2 d.o.f.) after 5 yrs of neutrino data taking for the SPL, T2K, and T2HK projects, and the combination of the SPL with 5 years of atmospheric-neutrino data in the MEMPHYS detector. For the true parameter values we use $\Delta m^2_{31} = 2.2\,(2.6) \times 10^{-3}$ eV^2 and $\sin^2\theta_{23} = 0.5\,(0.37)$ for the test point 1 (2), and $\theta_{13} = 0$ and the solar parameters as given in equation (292). The shaded region corresponds to the 99% CL region from present SK and K2K data [67]. Taken with kind permission of the Journal of High Energy Physics from figure 8 in reference [27]. Copyrighted by SISSA.

	True values	T2K	SPL	T2HK
Δm^2_{31}	$2.2 \cdot 10^{-3}$ eV^2	4.7%	3.9%	1.1%
$\sin^2\theta_{23}$	0.5	20%	22%	6%
Δm^2_{31}	$2.6 \cdot 10^{-3}$ eV^2	4.4%	3.0%	0.7%
$\sin^2\theta_{23}$	0.37	8.9%	4.7%	0.8%

Table 9: Accuracies at 3σ on the atmospheric parameters $|\Delta m^2_{31}|$ and $\sin^2\theta_{23}$ for 5 years of neutrino data from T2K, SPL, and T2HK for the two test points shown in figure 62 ($\theta_{13}^{\text{true}} = 0$). The accuracy for a parameter x is defined as $(x^{\text{upper}} - x^{\text{lower}})/(2x^{\text{true}})$, where x^{upper} (x^{lower}) is the upper (lower) bound at 3σ for 1 d.o.f. obtained by projecting the contour $\Delta\chi^2 = 9$ onto the x-axis. For the accuracies for test point 2 the octant-degenerate solution is neglected.

The effect of spectral information on the disappearance measurement is discussed in detail in reference [218].

For test point 1 (maximal mixing for θ_{23}), rather poor accuracies are obtained for $\sin^2\theta_{23}$ for T2K and the SPL ($\sim 20\%$), and only 6% for T2HK. The reason is that in the disappearance channel $\sin^2 2\theta_{23}$ (rather then $\sin^2\theta_{23}$) is measured. This translates into rather large errors for $\sin^2\theta_{23}$ if $\theta_{23} = \pi/4$ [216]. For the same reason it is difficult to solve the octant degeneracy. It can be seen that for test point 2, with a non-maximal value of $\sin^2\theta_{23} = 0.37$, the degenerate solution is still present around $\sin^2\theta_{23} = 0.63$ in each of the three experiments.

5.2.14 Sensitivities to the mass hierarchy and the θ_{23} octant

The determination of the mass hierarchy is a secondary goal for super-beams such as T2HK and the SPL which have too short a baseline to exploit the matter effects required to solve these degeneracies. Indeed, the sensitivity to the hierarchy of T2HK is limited to some favourable values of δ, while the SPL has no sensitivity whatsoever. However, the long baseline of the wide-band beam experiment gives significant sensitivity to the mass hierarchy. In figure 63, the discovery potential for a normal mass hierarchy is shown for two different baselines: 2500 km, roughly the baseline between BNL and Homestake; and 1300 km the distance between FNAL and Homestake. It can be seen that, for the 1300 km baseline, if $\sin^2 2\theta_{13} > 10^{-2}$, the mass hierarchy can be measured for any value of δ. The sensitivity is further increased to $\sin^2 2\theta_{13} > 8 \times 10^{-3}$ for the longer baseline.

As was shown above, neither experiment is sensitive to the octant of θ_{23}. However, as pointed out in references [703, 704], atmospheric-neutrino data may allow the octant of θ_{23} to be determined. If 5 years of atmospheric-neutrino data in MEMPHYS are added to the SPL super-beam data, the degenerate solution for test point 2 can be excluded at more than 5σ, as can be seen in figure 62, and hence the octant degeneracy is solved in this example. Of course, this way of measuring the octant works even better if atmospheric data taken with Hyper-Kamiokande are combined with T2HK data, see below.

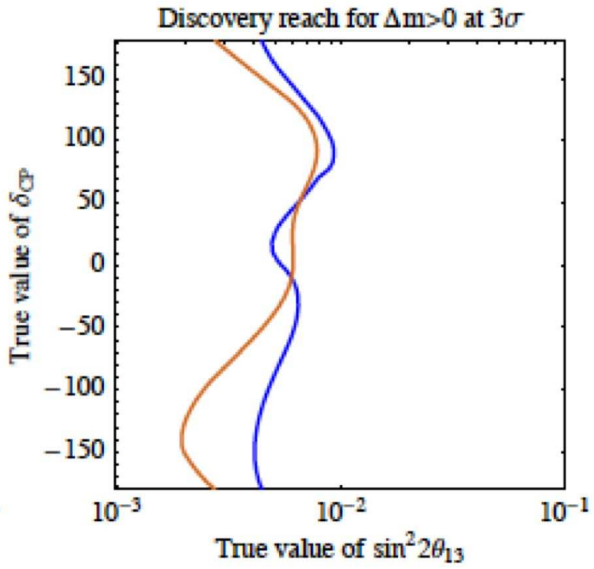

Figure 63: Sensitivity of the wide band beam long baseline experiment to the mass hierarchy at 3σ ($\Delta\chi^2 = 9$) as a function of the true values of $\sin^2 2\theta_{13}$ and δ. The blue (dark) curves are for $L = 1300$ km and the red (light) curves for $L = 2500$ km. The figure is taken from reference [23].

5.2.15 Combination with atmospheric neutrino measurements

Combining atmospheric-neutrino events to the long-baseline neutrino-beam data is an attractive method of resolving degeneracies [38]. If θ_{13} is sufficiently large, Earth matter effects in multi-GeV, e-like atmospheric-neutrino events are sensitive to the mass hierarchy [100, 102, 705]. Moreover, sub-GeV, e-like events provide sensitivity to the octant of θ_{23} [703, 704, 706] due to oscillations driven by Δm^2_{21} (see also reference [707] for a discussion of atmospheric neutrinos in the context of Hyper-Kamiokande). Following reference [38], the potential of the various second-generation super-beam experiments is investigated with the combined beam- and atmospheric-neutrino data set below. A general three-flavour analysis of atmospheric data is performed based on reference [704] and references therein. Fully-contained e-like and μ-like events (further divided into sub-GeV $p_l < 400$ MeV, sub-GeV $p_l > 400$ MeV, and Multi-GeV events) are included. In addition, partially-contained μ-like events, stopping muons, and through-going muons are considered. Each of these data samples is divided into 10 zenith angle bins.

Figure 64 shows how the combination of atmospheric plus long-baseline yields sensitivity to the sign of Δm^2_{31}. For the long-baseline data alone, the SPL super-beam has no sensitivity (because of the very small matter effects that arise in the relatively short baseline) and the sensitivity of T2HK depends strongly on the true value of δ. However, by including data from atmospheric neutrinos the mass hierarchy can be determined at the 3σ CL provided $\sin^2 2\theta_{13} \gtrsim 0.05 - 0.09$ for the SPL, and $\sin^2 2\theta_{13} \gtrsim 0.03 - 0.05$ for T2HK. Both experiments have the worst sensitivity around $\delta = \pi/2$, where the enhancement of the neutrino signal and the suppression of the anti-neutrino signal typical of the normal hierarchy is masked by the opposite effect of the CP-violating phase. Here, T2HK would only be able to exclude an inverted hierarchy if

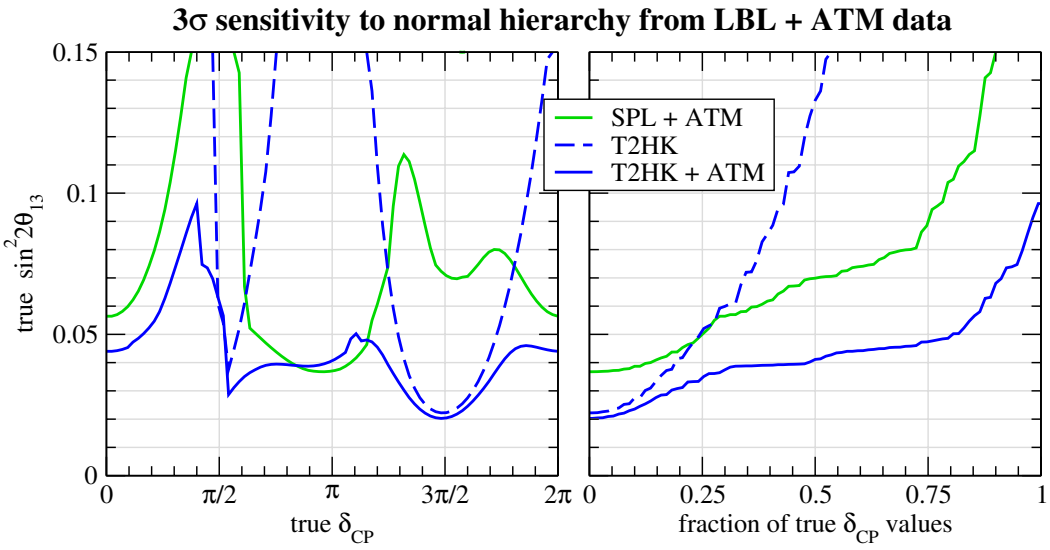

Figure 64: Sensitivity to the mass hierarchy at 3σ ($\Delta\chi^2 = 9$) as a function of the true values of $\sin^2 2\theta_{13}$ and δ (left panel), and the fraction of true values of δ (right panel). The solid curves are the sensitivities from the combination of the super-beams and atmospheric neutrino data, the dashed curves correspond to super-beam data only. Adapted with kind permission of the Journal of High Energy Physics from figure 16 in reference [27]. Copyrighted by SISSA.

$\sin^2 2\theta_{13} \gtrsim 0.1$ and the SPL loses its sensitivity altogether. Conversely there are maximums of the sensitivity around $\delta = 3\pi/2$, where δ enhances the neutrino signal and suppresses that of the anti-neutrino. Comparing figure 64 with figure 63 it is clear that, even when combined with atmospheric data, the sensitivity of T2HK and the SPL to the mass hierarchy is rather poor, being out-performed by the longer baseline wide-band beam experiment by an order of magnitude.

Figure 65 shows the potential of atmospheric plus long-baseline data to exclude the octant-degenerate solution. Since this effect is based mainly on oscillations driven by Δm^2_{21}, there is very good sensitivity even for $\theta_{13} = 0$; a non-zero value of θ_{13} improves the sensitivity in most cases [38]. From the figure one can see that both experiments can identify the true octant at 3σ for $|\sin^2\theta_{23} - 0.5| \gtrsim 0.05$.

5.2.16 Super-Beam associated with a beta-beam

A beta-beam could exploit the intense proton driver required to drive a super-beam and both facilities could illuminate the same far detector. The SPL in particular could be complemented by a low-γ beta-beam in the CERN design (see section 5.3). It is therefore interesting to study possible complementarities between the two facilities. The main difference between the two neutrino beams is the different initial neutrino flavour, ν_e ($\bar{\nu}_e$) for a beta-beam and ν_μ ($\bar{\nu}_\mu$) for a super-beam. This implies that at the near detector all relevant cross-sections can be measured. In particular, the near detector exposed to the beta-beam will measure the cross section for

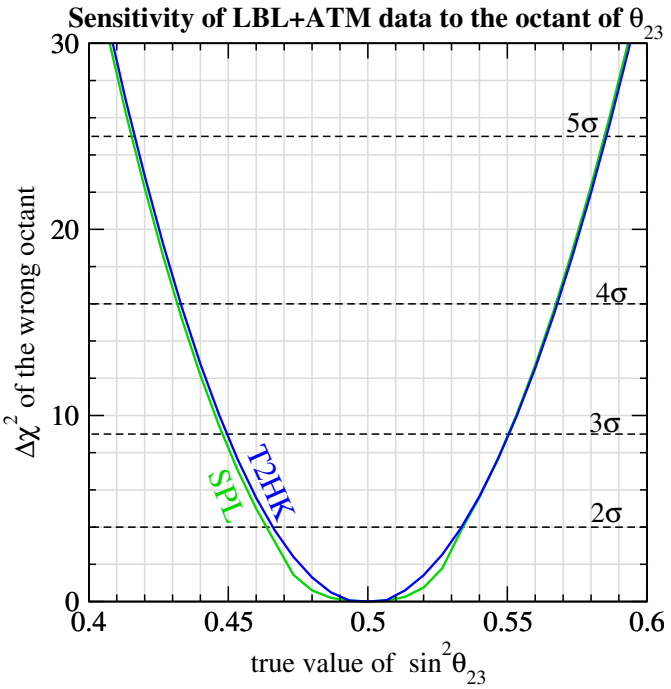

Figure 65: $\Delta\chi^2$ of the solution with the wrong octant of θ_{23} as a function of the true value of $\sin^2\theta_{23}$. A true value of $\theta_{13} = 0$ has been assumed. Adapted with kind permission of the Journal of High Energy Physics from figure 17 in reference [27]. Copyrighted by SISSA.

the SPL appearance search, and vice versa. If both experiments run with neutrinos and anti-neutrinos the following transition probabilities can be measured: $P_{\nu_e\to\nu_\mu}$, $P_{\bar\nu_e\to\bar\nu_\mu}$, $P_{\nu_\mu\to\nu_e}$, and $P_{\bar\nu_\mu\to\bar\nu_e}$. Tests of the T and CPT symmetries would thus be possible, in addition to CP-violation, since matter effects are very small because of the relatively short baseline.

However, if CPT symmetry is assumed, the beta-beam channels are redundant: the only gain in combining the two facilities is an increase in the size of the data set which does not help to solve the degeneracies [214]. Nevertheless, this also means that in principle all information can be obtained from neutrino data alone because of the relations $P_{\bar\nu_e\to\bar\nu_\mu} = P_{\nu_\mu\to\nu_e}$ and $P_{\bar\nu_\mu\to\bar\nu_e} = P_{\nu_e\to\nu_\mu}$. This implies that (time consuming) anti-neutrino running can be avoided. This is illustrated in figures 66 and 67. In figure 66 the θ_{13} discovery potential is shown for 5 years of neutrino data from the $\gamma = 100$ beta-beam and the SPL super-beam. Luminosities of $5.8 \cdot 10^{18}$ ($2.2 \cdot 10^{18}$) decays per year for ^{6}He (^{18}Ne) have been assumed. From the left panel it can be seen how each experiment plays the role an anti-neutrino run would have played the single-facility case. Combining these two data sets results in a slightly better sensitivity than 10 years (2ν+$8\bar\nu$) of T2HK data. In addition, figure 67 shows that the combination is also effective in searching for CPV, 5 years of neutrino data from the beta-beam and the SPL leads to a better sensitivity than 10 years of T2HK alone.

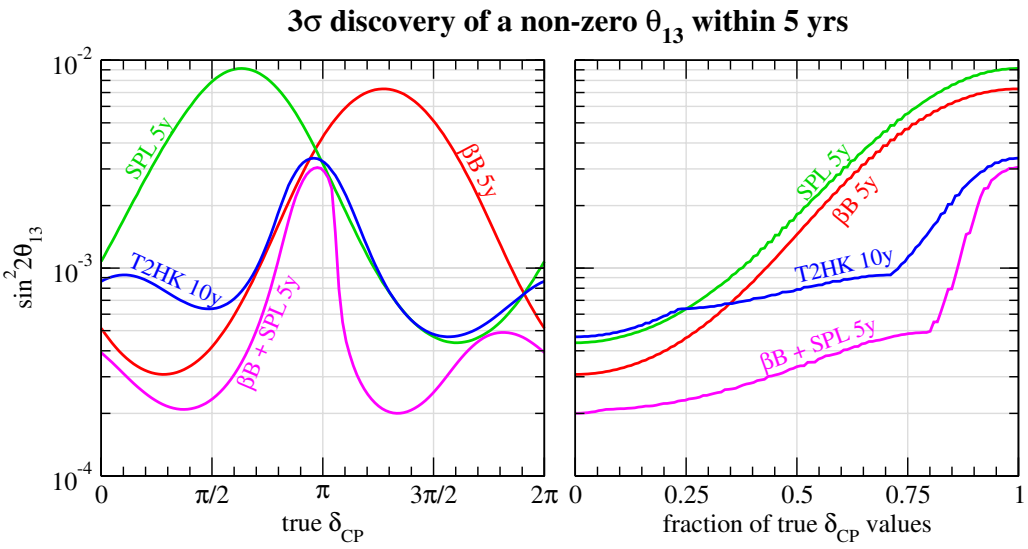

Figure 66: Discovery potential of a finite value of $\sin^2 2\theta_{13}$ at 3σ ($\Delta\chi^2 > 9$) for 5 yrs neutrino data from βB, SPL, and the combination of βB + SPL compared to 10 yrs data from T2HK (2 yrs neutrinos + 8 yrs anti-neutrinos). Taken with kind permission of the Journal of High Energy Physics from figure 14 in reference [27]. Copyrighted by SISSA.

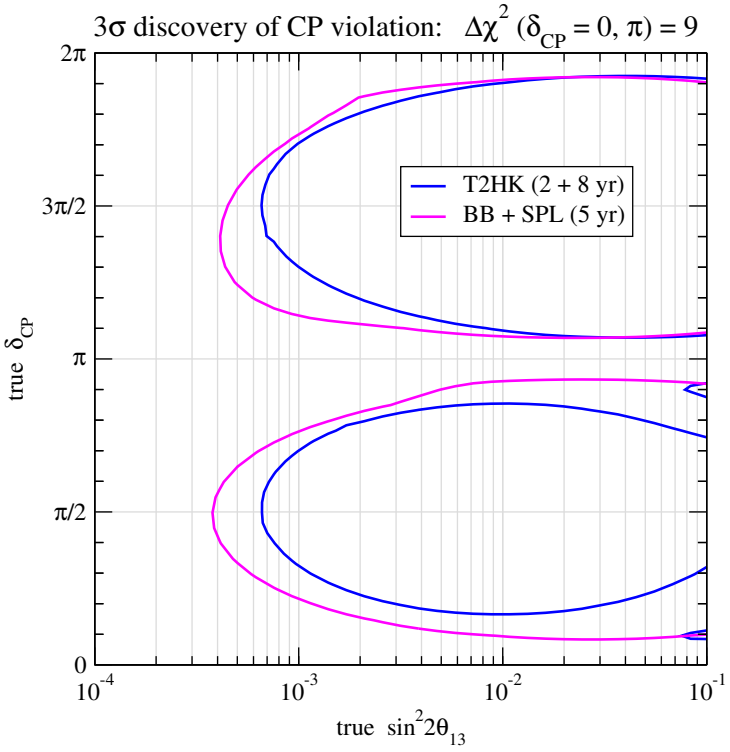

Figure 67: Sensitivity to CPV at 3σ ($\Delta\chi^2 > 9$) for combining 5 yrs neutrino data from βB and SPL compared to 10 yrs data from T2HK (2 yrs neutrinos + 8 yrs anti-neutrinos). Taken with kind permission of the Journal of High Energy Physics from figure 15 in reference [27]. Copyrighted by SISSA.

5.2.17 Super-Beam associated with the Neutrino Factory

As described in the section 5.4, the Neutrino Factory suffers acutely from the degeneracy problem because its energy and baseline are such that it operates far from the oscillation maximum. With its high energy and long baseline, the Neutrino Factory is ideal to tackle the problem of the sign degeneracies through matter effects. However, the fact that the oscillation peak occurs in the lowest energy bin with relatively low efficiency, causes the intrinsic degeneracy to spoil its sensitivity to CP-violation. Super-beams, with a completely different L/E and operating at the first oscillation maximum, do not suffer as badly from this degeneracy. On the other hand, the short baselines and lower energies favoured by super-beams strongly limit their ability to solve the sign degeneracy by exploiting matter effects. The combination of data from these two facilities can therefore be a very effective tool to solve the degeneracy problem. Furthermore, the intense pion beam that would produce the muons required for the Neutrino Factory beam might also be exploited as a super-beam source. Indeed, the 2.2 GeV SPL beam was originally conceived and optimised as the first stage of a Neutrino Factory project. Thus, in a Neutrino Factory a super-beam comes 'for free'. A Mton class water Čerenkov detector would still be needed to fully exploit its potential, though.

Detailed studies of the ability to solve the eightfold degeneracy by combining the Neutrino Factory and the SPL super-beam can be found in references [610, 708, 709]. An impressive synergy between the two facilities is found, lifting all the degenerate solutions for large fractions of the parameter space. However, a more detailed study fully including the systematics in the considered detectors is still required.

5.3 The physics potential of beta-beam facilities

A beta-beam [24] is produced from boosted, radioactive-ion decays and therefore is a pure ν_e or $\bar{\nu}_e$ beam. The flavour transitions that can, in principle, be studied in this facility are:

$$\begin{array}{lll} \nu_e \to \nu_\mu & \nu_e \to \nu_e & \nu_e \to \nu_\tau \\ \bar{\nu}_e \to \bar{\nu}_\mu & \bar{\nu}_e \to \bar{\nu}_e & \bar{\nu}_e \to \bar{\nu}_\tau. \end{array}$$

There are three variables that determine the properties of the facility: the type of ion used, and in particular the the end-point kinetic energy of the electron in the β-decay, E_0; the relativistic γ (energy divided by mass) of the ion; and the baseline, L. Once these parameters are fixed, the neutrino flux can be calculated precisely since the kinematics of β decay is very well known. In the laboratory frame, the neutrino flux, $\Phi^{\rm lab}$, is given by [25]:

$$\left.\frac{d\Phi^{\rm lab}}{dSdy}\right|_{\theta\simeq 0} \simeq \frac{N_\beta}{\pi L^2}\frac{\gamma^2}{g(y_e)} y^2(1-y)\sqrt{(1-y)^2 - y_e^2}\,; \tag{293}$$

where N_β is the number of ion decays per unit time, m_e is the mass of the electron, dS is the element of solid angle, $0 \leq y = \frac{E_\nu}{2\gamma E_0} \leq 1 - y_e$, and $y_e = m_e/E_0$; and:

$$g(y_e) \equiv \frac{1}{60}\left\{\sqrt{1-y_e^2}(2-9y_e^2-8y_e^4) + 15y_e^4 \log\left[\frac{y_e}{1-\sqrt{1-y_e^2}}\right]\right\}. \quad (294)$$

Note that the shape of the flux, and in particular the average (anti-)neutrino energy, is essentially constant for a particular γE_0 and that, if the number of decaying ions and the baseline are kept fixed, the flux increases with γ.

5.3.1 Beta-beam setups

The choice of isotope is a compromise between production yield, E_0, and lifetime. Isotopes should be sufficiently long-lived to avoid strong losses in the acceleration phase, but must decay fast enough to generate a neutrino beam of sufficient flux. Lifetimes of the order of 1 s are considered reasonable.

The following isotopes have been identified as good candidates: ^{6}He with $E_0 = 3506.7$ keV to produce $\bar{\nu}_e$ and ^{18}Ne with $E_0 = 3423.7$ keV to produce ν_e [24]. More recently two ions with larger E_0 have been also considered: ^{8}Li ($E_0 = 12.96$ MeV) and ^{8}B ($E_0 = 13.92$ MeV) [209,710]. At the same γ/L, the neutrino beams produced by the ions Li/B are typically at three to four times more energetic than those of He/Ne.

Optimisation of the γ factor and the baseline should take into account the following physics requirements:

- $L/\langle E_\nu \rangle$ should be near the first atmospheric maximum so that oscillation signals are as large as possible. For a particular ion, this means that L and γ have a constant ratio and therefore that the neutrino flux is constant;
- The neutrino energy should be above μ-production threshold;
- The neutrino energy should be large enough for a measurement of the spectral distortion to be used to resolve the intrinsic degeneracy;
- The baseline should be as long as possible to all the mass hierarchy to be determined through the observation of matter effects; and
- Event rate: increasing γ at fixed ion flux increases the neutrino energy and therefore the number of events since the neutrino cross sections increase with energy.

All these requirements point in the same direction: increasing the γ factor as much as possible and tuning the baseline to sit near the atmospheric-oscillation peak. Practical issues will lead to constraints on the maximum γ that can be achieved. If an existing accelerator infrastructure was developed to host a beta-beam, the γs which could be achieved for He and Ne are:

- *CERN-SPS:* $\gamma_{\rm He} = 150, \gamma_{\rm Ne} = 250$;
- *Refurbished SPS:* $\gamma_{\rm He} = 350, \gamma_{\rm Ne} = 580$;
- *Tevatron:* $\gamma_{{\rm He}} = 350, \gamma_{{\rm Ne}} = 580$; and
- *LHC:* $\gamma_{{\rm He}} \sim 2500, \gamma_{{\rm Ne}} \sim 4000$.

The γs that could be achieved for Li/B are $\gamma_{\rm Li/B} = 8/9\gamma_{\rm He/Ne}$.

For $\gamma_{\rm He} = 150$, bending magnets of 5 T and a useful decay length of 36%, the decay ring length is $\sim 6\,880$ m. If γ is increased and the bending magnets are the same, the decay ring should be scaled proportionally to maintain the same fraction of useful ion decays. The ions in the decay ring should be kept in small bunches in order to keep the machine duty-cycle small; this is required to keep the background from atmospheric neutrinos at a negligible level (see the discussion in section 5.3.8).

An appropriate long baseline site is also required. To reduce the background from cosmic muons, an underground location is preferable. Therefore, an additional constraint for the choice of baseline would be the availability of an appropriate site, preferably with an existing and underground laboratory. It should be noted that a detector for a beta-beam could be versatile enough to allow other data samples to be studied (for example: atmospheric neutrinos; supernova neutrinos; etc.). Fortunately a number of alternatives exist that roughly match the γs noted above.

5.3.2 The low-energy beta-beam: LE$\beta\beta$

A low-energy beta-beam, with average neutrino energies in the sub-GeV range, matches the distance from CERN to the Modane laboratory in the Frejus tunnel, $L = 130$ km. The nice feature of this option is that the appropriate γ could be achieved with the present CERN SPS. In the first proposal along these lines [711, 712], a $\gamma_{\rm He} = 60, \gamma_{\rm Ne} = 100$ was chosen so that the baseline would sit near the first atmospheric peak. It was then realised, in reference [25], that this was not optimal. The new standard choice is $\gamma_{He} = \gamma_{Ne} = 100$ [26]. In reference [341], a scan in γ was performed for this baseline, assuming a fixed ion flux, and the optimal γ was found to be $\gamma \geq 90 - 100$ and with little improvement for larger γ. The average neutrino energy is ~ 0.4 GeV, a little above the atmospheric peak at the CERN-Frejus baseline.

5.3.3 High-energy beta-beams: HE$\beta\beta$

Neutrino beams with average energies in the $1 - 1.5$ GeV range could reach the atmospheric peak at $L \sim 700$ km, matching the distance between CERN-Canfranc, CERN-Gran-Sasso or Fermilab-Soudan. Such a beam could be achieved in two ways:

(a) by using more powerful accelerators, such as a refurbished SPS or the Tevatron to increase $\gamma_{\rm He} = \gamma_{\rm Ne} = 350$ [25]

(b) by using higher E_0 ions such as Li/B at moderate $\gamma \sim 100$ that could be achieved also with the Fermilab Main Injector, but increasing significantly the number of decaying ions to compensate for the loss of flux [710, 713]

Even higher energy beta-beams have also been considered [25, 690]. If it were possible to accelerate the ions in LHC without significant additional losses, it would be possible to produce a beam with $\gamma = \mathcal{O}(1000)$. In this case, with a baseline of a few thousand kilometers, better sensitivity to matter effects and the sign of Δm^2_{31} would be achieved [25, 690]. The performance of such a setup will be presented below. However, such an increase in γ looks rather far-fetched at present and it is more likely that a greenfield scenario for the beta-beam would end up providing a higher intensity of ions [713] rather than larger boosts.

5.3.4 Ion production and ν fluxes

The only detailed studies on ion-production and acceleration performed up to now have concentrated on using the ISOLDE technique for ion production and the CERN PS and SPS for acceleration [714]. The EURISOL beta-beam group baseline assumes $\gamma = 100$ and a flux corresponding to 2.9×10^{18} He and 1.1×10^{18} Ne decays per year [715]. The goal is to achieve this performance without assuming modifications to the present CERN accelerators. No study has yet been performed for the Li/B option, so the ion flux assumed in this case should be considered as a goal. Since the ion production system would be common, it is reasonable to assume that a refurbished SPS could be used to accelerate ions to higher γ without further loses. More ions must be stored in the decay ring at higher γ since the ion lifetime is dilated, this may limit the neutrino flux. On the other hand, at higher γ the duty cycles that have been used in the baseline scenario to reduce the atmospheric background can be relaxed. Therefore, the fluxes noted above will be used for both the low- and the high-γ setups.

The neutrino fluxes at the detector location for the LE$\beta\beta$ and the HE$\beta\beta$ and the standard ion fluxes are shown in figure 68. As explained above, the shape of the flux depends only on the combination $2\gamma E_0$, which defines the end-point of the spectrum and therefore it is rather similar for the two HE$\beta\beta$ options. On the other hand, the absolute flux depends on the combination $(\gamma/L)^2$ and is therefore smaller for lower γ as can be seen by comparing the left and the right plots of figure 68; although they are very similar in shape, they differ by a factor 10 in absolute value. The properties of the various beta-beam setups are summarised in table 10.

Given the fact that proposals for new techniques by which the ion yield may be increased [713] have not yet been fully exploited, and on the assumption that a number of improvements to the present PS and SPS at CERN are likely to occur in the LHC-upgrade programme, it does not seem unreasonable to consider a greenfield scenario in which the number of ions is increased up to a factor 10 with respect to the baseline defined above. We will consider the reach of such an aggressive facility in section 5.3.19.

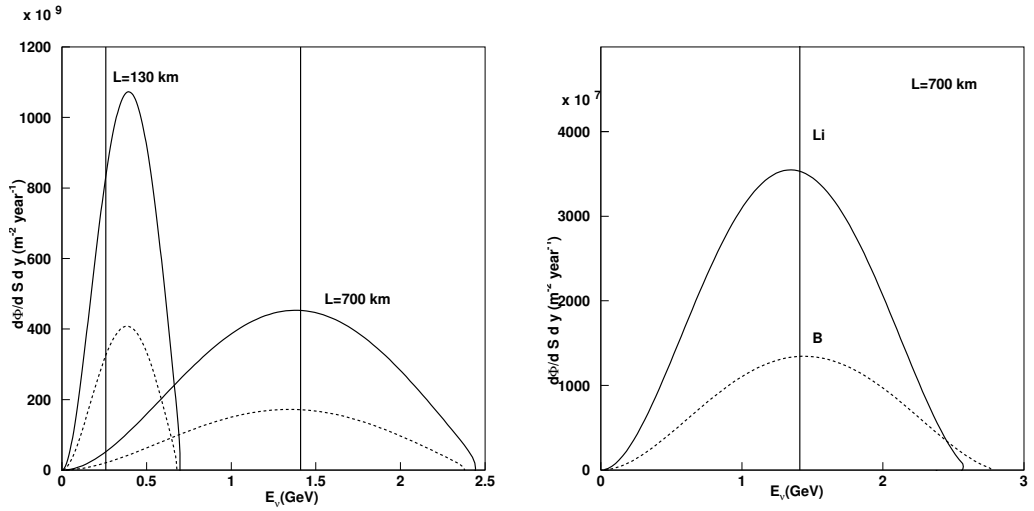

Figure 68: $\bar{\nu}_e$ (solid) and ν_e (dashed) fluxes as a function of the neutrino energy for He and Ne at $\gamma = 100, 350$ (left) and for Li and B at $\gamma = 100$ (right), assuming the number of decaying ions to be the standard one in all cases. The vertical lines correspond to the energy position of the atmospheric peak for $\Delta m^2_{13} = 0.0025$ eV^2.

Ion	γ	$L(km)$	$\bar{\nu}_e$ CC	ν_e CC	$\langle E_\nu \rangle (GeV)$
He/Ne	100	130	28.9	32.8	0.39/0.37
He/Ne	350	700	62.0	55.	1.35/1.3
Li/B	100	700	5.0	4.9	1.3/1.4

Table 10: Number of charged-current events per kton-year and average neutrino energy, in the absence of oscillation, for the different options and a number of decaying ions of $N_{He/\mathrm{Li}} = 2.9 \times 10^{18}\ year^{-1}$ and $N_{Ne/B} = 1.1 \times 10^{18}\ year^{-1}$.

5.3.5 Detector technology

The golden signals at a beta-beam facility are: a muon from the appearance channel; and an electron from the disappearance channel. The silver channel (τ production) is not open for most of the setups considered and has not been studied in any detail.

Since the beam, at source, is a pure flavour eigenstate, the principal uncertainties in the measured oscillation probabilities arise from uncertainties in the background rates and the precision with which the efficiencies can be determined. The main requirements for an optimal detector are, therefore, good particle identification (i.e. $\mu/e/\pi$ separation) and good neutrino-energy resolution. Several types of massive detector can be optimised to identify muons and electrons in the GeV range.

The fact that the beta-beam produces a pure ν_e (or $\bar{\nu_e}$) beam means that the golden (muon appearance) channel is free from the beam-generated 'wrong-sign muon' background that is present at the Neutrino Factory. This means that it is not necessary to magnetise the beta-beam detector; a significant advantage that the beta-beam has over the Neutrino Factory. Since magnetisation is not required, a very massive, water Čerenkov detector is an appropriate technology choice for the beta-beam. Such a detector has a broad physics potential beyond oscillation physics: proton decay; detection of neutrinos from supernovas; etc. It is hard to imagine that one can achieve megaton detector masses with a different type of technology.

Detectors that have been considered for the beta-beam to date include:

- A 500 kton fiducial water Čerenkov [25, 711, 712];
- A 50 kton NOvA-like detector [690]; and
- A 40 kton Iron calorimeter [716].

We will give some details of the performance of the first two options. Very recently a liquid argon TPC has also been discussed in the context of the beta-beam in reference [713]. We refer to this work for details.

5.3.6 Water Čerenkov

Water Čerenkovs are optimised to search for the quasi-elastic (QE), charged current (CC) events; it is not possible to measurement the hadronic energy and therefore it is possible to reconstruct the neutrino energy only for QE events. Figure 69 shows the signal-to-noise ratio for a megaton-year exposure as a function of γ (for fixed $\gamma/L \sim 0.5$) for a neutrino beam from Ne decays. The signal-to-noise ratio is defined in each energy bin (seven bins are considered in all setups between 200MeV and the end-point), the results for all bins are then added in quadrature. The expected improvement with γ slows down above $\gamma \sim 400$, because events at higher energies are likely to give more than one ring and therefore are not likely to be selected, while the background-selection

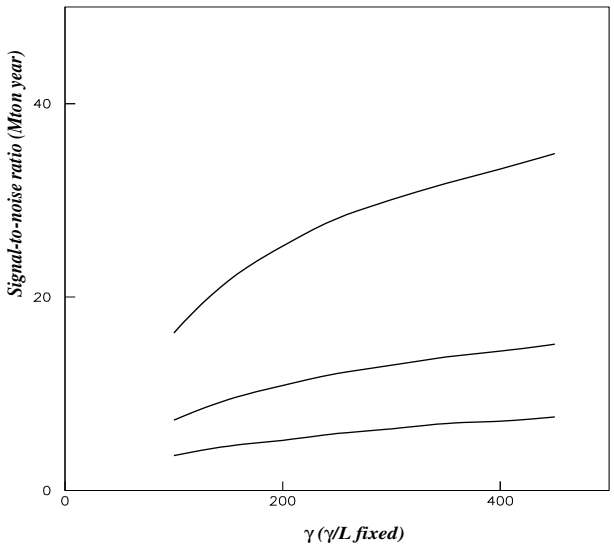

Figure 69: Signal to noise (i.e. square root of the signal plus background events add in quadrature for the different energy bins) for the appearance signal from Ne in units of one Mton-year as a function of γ, holding $\gamma/L \simeq 0.5$ fixed. The three curves correspond to $\theta_{13} = 8^\circ, 3^\circ$ and 1°.

efficiency continues to increase. The figure shows that there is little benefit from increasing γ above 300–400 using a water Čerenkov [341]. On the other hand, for lower γ this technology is probably close to optimal given the large mass that one could envisage for this type of detector.

Detailed Monte Carlo studies of a Super-Kamiokande-like detector have been performed to quantify the efficiencies and backgrounds for the μ-appearance signal. The signal selection cuts are essentially three:

- Single ring, contained events; and
- μ-like ring;
- Delayed ring: Michel electron from μ-decay.

The energy resolution for QE events is quite good, mainly limited by Fermi motion. However, the contamination from non-QE events, which increases with energy, introduces a shift between the true and reconstructed neutrino energies. In order to take into account this fact properly, migration matrices for efficiencies and backgrounds that allow for the 'migration' from true to reconstructed neutrino energy are used as first described in reference [25]. In the analysis presented below, reconstructed energy bins of 100 MeV for the LE$\beta\beta$ and 200 MeV for the HE$\beta\beta$ will be considered.

The main source of background are neutral current (NC) events with one positively-charged pion being produced through the Δ resonance. Negatively-charged pions are very much suppressed by the delayed-ring cut, because of the large absorption cross section for negative pions.

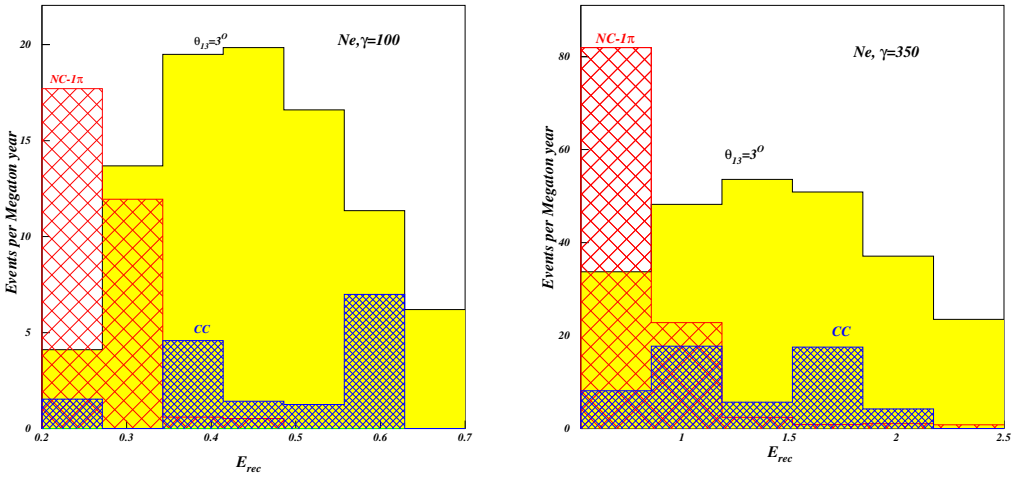

Figure 70: Reconstructed energy in a water Cerenkov per Megaton year for signal and NC and CC background (hatched) for the LE setup (left) and the HE one (right). The true values assumed are $\theta_{13} = 3^\circ$ and $\delta = 90^\circ$.

For the HE$\beta\beta$ setup, multi-pion events are also a significant source of background. In third place, a few charged current (CC) events, in which the electron ring goes undetected and a single pion is mis-identified as a muon, also survive the selection cuts. A more detailed analysis would be needed to see whether the presence of a low-energy electron in these events could be revealed by means of a more sophisticated reconstruction algorithm.

Figure 70 shows a comparison of the expected signal for $\theta_{13} = 3^\circ$ and $\delta = \pi/2$ (near the sensitivity reach of T2K-I) together with the different background contributions for each setup. The level of NC background is rather large, especially for the HE setup, but, owing to the very different kinematics of QE and NC events, the reconstructed neutrino energy for the NC events is strongly peaked at much lower values [25], making this background easily distinguished from the signal.

In the comparison plots which follow, a global normalisation uncertainty of 2% will be considered. This normalisation uncertainty is taken to include the fiducial-volume uncertainty. In addition, a 1% uncertainty in the ratio of neutrino to anti-neutrino cross sections, an optimistic assumption if the present knowledge of this ratio is taken into account. A dedicated neutrino cross-section-measurement programme using a near detector at the same facility would be required to reach such a precision. For the disappearance signal the uncertainty on the global normalisation is the most important, so we neglect background uncertainties and considered only the normalisation error.

5.3.7 NOνA-like detector

A totally-active, liquid-scintillator detector (TASD) á la NOνA has been considered in [690] for $\gamma \geq 500$. The main advantage of this technology is that the neutrino energy can be reconstructed

	Appearance		Disappearance	
	ν	$\bar{\nu}$	ν	$\bar{\nu}$
Signal efficiency	0.8	0.8	0.2	0.2
Background rejection	0.001	0.001	0.001	0.001
Signal error	2.5%	2.5%	2.5%	2.5%
Background error	5%	5%	5%	5%

Table 11: The signal efficiencies and background rejection respectively and the systematical errors for the various signals and backgrounds used in [690].

for non-QE events, which become dominant at higher energies, as well as for QE events. On the other hand, it may be difficult to build a detector of this type with a mass much larger than a few tens of kilotons. A fiducial mass of 50 kton will be assumed.

The detector performance has been studied in the NOνA proposal. Since the detector has been proposed for the conventional NUMI beam, the study considered only efficiencies and backgrounds for e-like events. These efficiencies and backgrounds are summarised in table 11. While assuming the same efficiencies and backgrounds for the μ signal might be conservative, as argued in [690], the physics is quite different and a detailed study of this detector for the beta-beam is essential for a reliable comparison to other technologies to be made.

The energy resolution is assumed to be a Gaussian with a width of $3\%/\sqrt{E}$ for muons and $6\%/\sqrt{E}$ for electrons and the background is conservatively assumed to have the same energy spectrum as the signal.

5.3.8 Atmospheric backgrounds

A very important source of background for all detector technologies are atmospheric-neutrino events. A detector like Super-Kamiokande will record approximately 120 $\nu_\mu + \bar{\nu}_\mu$ interactions per kiloton-year (including the disappearance of ν_μ into ν_τ).

There atmospheric background may be reduced in two ways. Firstly, the energy is often poorly reconstructed for these events since they come from all directions while the signal comes from the direction of the beam. The cut on the reconstructed energy to be within the range of energies produced by the beta-beam significantly reduces the background without affecting the signal efficiency. Secondly, selecting events for which the reconstructed neutrino direction is consistent with the beam also preferentially selects beam-induced events. While the neutrino direction cannot be measured directly, it is increasingly correlated with the observable lepton direction at high energies. A directional cut is more effective as γ increases, but is never perfectly efficient. For a similar signal efficiency, background rejection for the HE$\beta\beta$ was estimated in reference [341] to be a factor three better than for the LE$\beta\beta$.

Without imposing any directional cut, we show the ratio of the detector to atmospheric backgrounds in reconstructed-energy bins for the LE and HE setups in figure 71. Since the atmo-

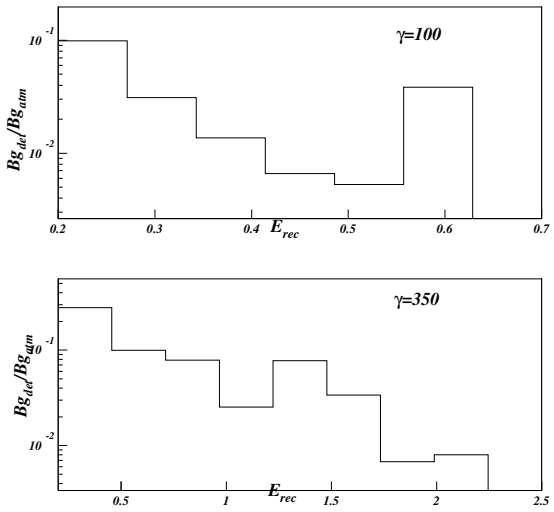

Figure 71: Ratio of ν background events coming from the detector misidentification to those coming from atmospheric neutrinos for the LE (up) and HE (down) setups. The statistics corresponds to a megaton year (10^7 sec).

spheric background can be measured with very good accuracy, the systematics associated to its subtraction are very small and therefore it would be sufficient if this ratio could be made of $\mathcal{O}(1)$. Such a rejection factor can be achieved by timing the parent ion bunches. It was estimated [712] that a rejection factor of 5×10^{-5} per bunch is feasible with bunches 10 ns in length. As already indicated in reference [341], this rejection power is an more than sufficient given the ratios shown in figure 71 which indicate that a global rejection of 10^{-2} is probably sufficient for the LE option and could be even relaxed further for the HE option. In the analysis presented below, the atmospheric background is assumed to be negligible.

5.3.9 Analysis of performance and optimisation

The following 'standard' setups will be compared directly:

- LE$\beta\beta$ with a 500 Mton fiducial Water Čerenkov;
- HE$\beta\beta$ with a 500 Mton fiducial Water Čerenkov: HE-a; and
- HE$\beta\beta$ with a 50 kton fiducial TASD: HE-b.

Further details of the experimental analyses can be found in references [26, 27, 341, 690]. The performance of these setups will be compared assuming the SνM and using the following central values for the known oscillation parameters:

$$\begin{aligned} \sin^2\theta_{23} = 0.44 \quad & \Delta m^2_{13} = +2.5 \times 10^{-3} eV^2 \\ \sin^2\theta_{12} = 0.3 \quad & \Delta m^2_{12} = 0.8 \times 10^{-4} eV^2 \,. \end{aligned} \tag{295}$$

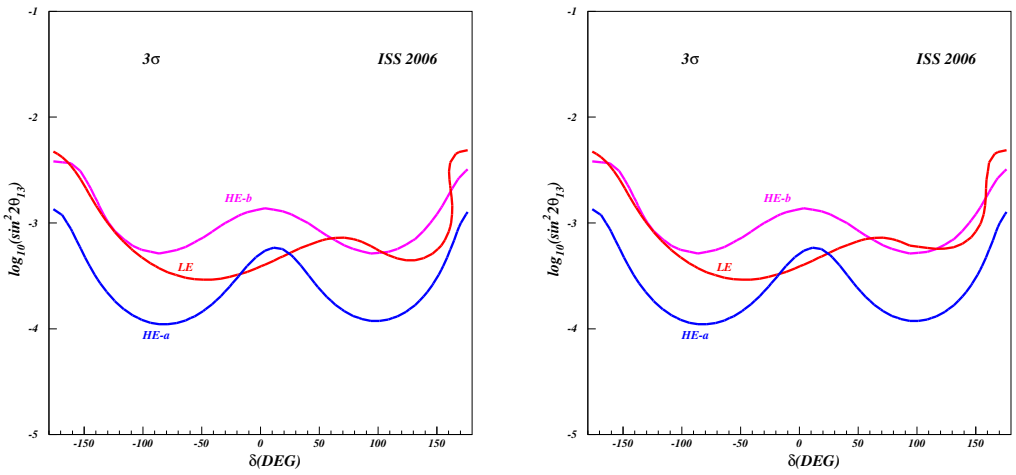

Figure 72: 3σ sensitivity to θ_{13} for the LE$\beta\beta$, HE$\beta\beta$-a, HE$\beta\beta$-b. The left plot does not include the discrete ambiguities and the right one does.

All the plots labeled $ISS2006$ assume these 'true' values, however this is not the case for all plots shown below.

5.3.10 Sensitivity to θ_{13}

In figure 72 we compare the sensitivity to $\theta_{13} \neq 0$ for the LE$\beta\beta$ and three HE$\beta\beta$ options using three types of detector. On the left plot only the intrinsic degeneracy is included, while the right plot also takes into account discrete ambiguities. Comparison of the left and right panels indicates that the effect of the discrete ambiguities is quite small. For the HE options, the bigger mass yields improved sensitivity as expected, while the LE option with a 500 kton detector slightly out-performs the HE-b option with a detect for which the fiducial mass is a factor 10 smaller.

5.3.11 Sensitivity to CP violation

The sensitivity to CP violation for the same setups is compared in figure 73. Again, the discrete ambiguities are not present in the left panel, but are taken into account in the the right panel. In the case of CP-violation sensitivity, the HE-a option out-performs the others, while the LE option is similar or slightly worse than HE-b. The sign ambiguity is directly responsible for the loss of sensitivity in a band at negative δ for the HE setups. This is a well-known effect that has also been observed in T2HK analyses (see for example reference [19]). A combination with another experiment/measurement to resolve the correlation between δ and the hierarchy is necessary. The different alternatives by which this can be done have not yet been explored.

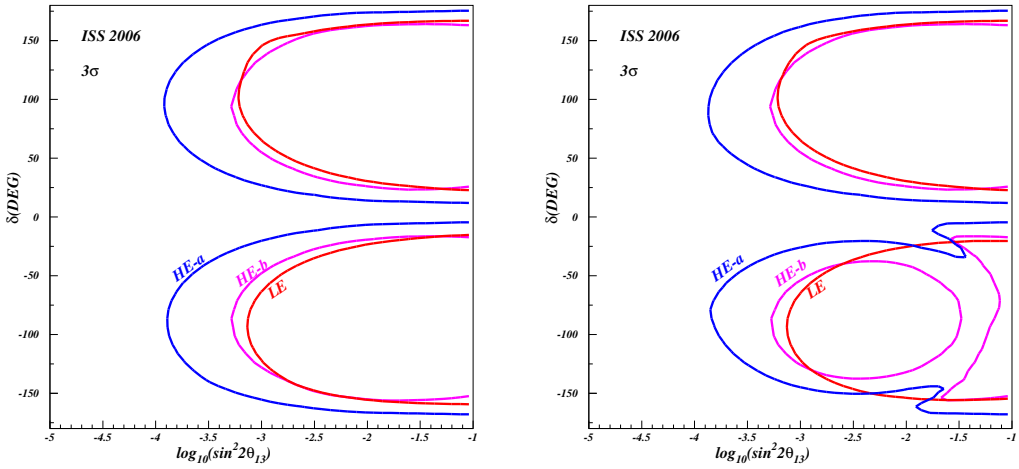

Figure 73: 3σ sensitivity to θ_{13} for the LE$\beta\beta$, HE$\beta\beta$-a, HE$\beta\beta$-b neglecting the discrete ambiguities (left) and including them (right).

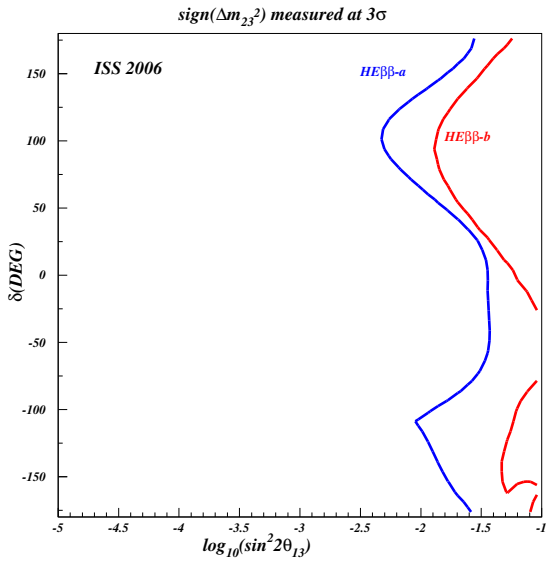

Figure 74: 3σ sensitivity to the normal mass hierarchy assuming for the HE$\beta\beta$-a and HE$\beta\beta$-b setups.

5.3.12 Sensitivity to the discrete ambiguities

The sensitivity to the sign of Δm^2_{23} for the HE options is compared in figure 74 (the sensitivity of the LE option is not shown since the short baseline makes fives it little or no sensitivity). The HE-a option again out-performs the HE-b option. The dependence on δ is very strong. Only for values of $\sin^2 2\theta_{13} > 0.03$ can the normal hierarchy be established at 3σ for any value of δ. A significant improvement can be made by combining the beta-beam data with atmospheric-neutrino data, this will be discussed in the next section.

The sensitivity to the octant of θ_{23} is extremely weak for the choice we have made of θ_{23} for all the setups. However, as we will see below this does not interfere with the measurement of θ_{13} and δ.

5.3.13 Measurement of θ_{13} and δ

The results from fitting the appearance and disappearance signals to extract the parameters (θ_{13} and δ), for the true values indicated by the stars ($\theta_{13} = 3^\circ$, $\delta = 90, -90, 0$) are shown in figure 75. The left panels correspond to the LE setup and the right panels to the HE-a option. The uncertainties on δ and θ_{13} are significantly larger for the LE$\beta\beta$ and in particular the eight-fold degeneracy is fully present in this case. The intrinsic degeneracy is resolved for the HE-a setup for all values of δ. The octant degeneracy remains in all cases for the HE-a setup, while the hierarchy and mixed degeneracies are resolved for $\delta = 90^\circ$.

5.3.14 Towards an optimal beta-beam setup

While the sensitivity of the setups considered above to CP violation and θ_{13} is comparable to the sensitivity that may be achieved at the Neutrino Factory, the ability to resolve the discrete degeneracies is rather limited. A number of ideas have been considered to improve the physics reach of beta-beams, particularly as regards the discrete ambiguities, these ideas will be discussed below.

5.3.15 Combination with atmospheric data

Any large detector that could be used for a beta-beam can provide more precise measurements of the atmospheric-neutrino flux. This is certainly the case for the water Čerenkov considered in setups LE$\beta\beta$ and HE$\beta\beta$-a for which the fiducial mass considered is twenty times larger than that of Super-Kamiokande. Also in the case of a much smaller detector, such as a magnetised iron calorimeter, the measurement of the neutrino and anti-neutrino fluxes could add valuable information on the oscillation parameters [717].

The physics potential that results from the combination of these measurements with those in a long-baseline experiment were first studied in reference [38], where the case of the T2HK super-beam was considered. More recently, the same analysis has been performed for the LE$\beta\beta$ [27]. In both cases, it has been found that for sufficiently large values of θ_{13}, the combination with atmospheric data is extremely helpful in resolving the discrete degeneracies related to the mass hierarchy and the θ_{23} octant. As we have seen, the LE$\beta\beta$ setup has no sensitivity to either, while the HE$\beta\beta$ options have some, δ-dependent, sensitivity.

The regions in which the sgnΔm^2_{31} can be established at 3σ by combining atmospheric-neutrino data with the LE$\beta\beta$ and the HE-a setup are shown in figure 76. The combination of the LE setup with atmospheric data results in a significant sensitivity to the hierarchy, although

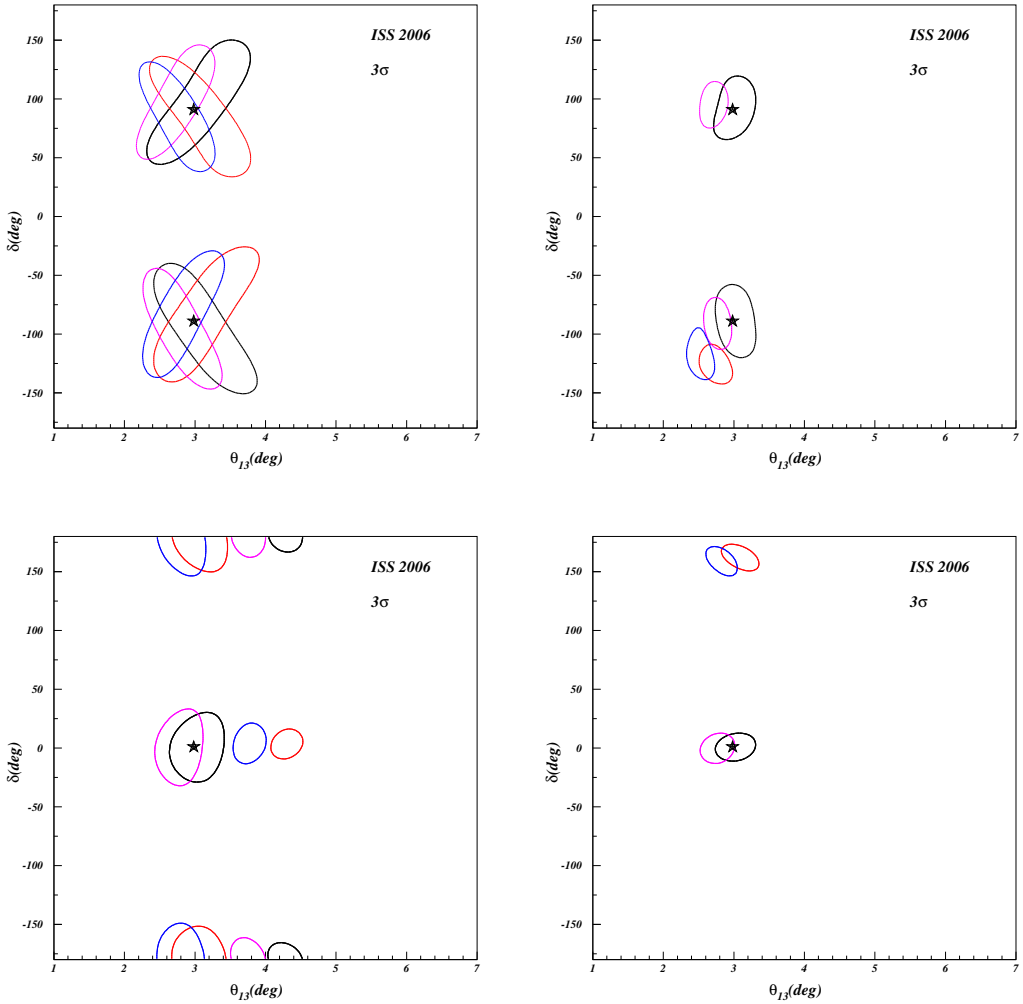

Figure 75: 3σ CL contours obtained in the LE$\beta\beta$ (left) and HE$\beta\beta$-a setup (right) for three values of the true parameters indicated by the stars. The solid black ellipses show the the intrinsic degeneracy, the pink ellipses the octant degeneracy, the red ellipses show the mass-hierarchy degeneracy, and the blue ellipse is the combined mass-hierarchy/octant degeneracy.

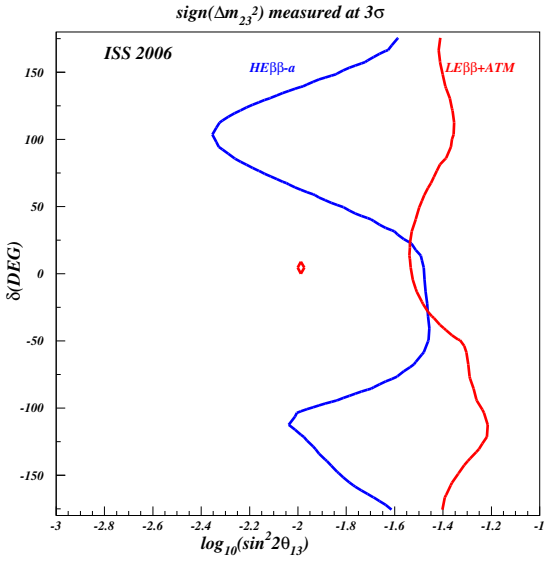

Figure 76: 3σ sensitivity to the normal mass hierarchy assuming for the HE$\beta\beta$-a and the LE$\beta\beta$ in combination with atmospheric data.

the combination does not improve the sensitivity of the HE-a setup. The combination with atmospheric data is also possible for all HE setups, this analysis has not yet been done. It is expected, however, that including the atmospheric data in this case will improve the sensitivity to the sgnΔm^2_{31} for those values of δ for which the sensitivity is poor and to improve the sensitivity to CP violation in the negative δ region in the right panel of figure 73.

Concerning the octant ambiguity, the combination of a LE$\beta\beta$ with atmospheric data has been shown not to improve the sensitivity that can be achieved using the atmospheric data alone [27]. It will be interesting to see whether, in the case of the HE$\beta\beta$ for which the sensitivity to the octant is better [341], the situation changes and there is some improvement as is in the case for the combination of the atmospheric data with other super-beams such as T2HK or the SPL.

5.3.16 An associated super-beam

In the first beta-beam scenario considered at CERN, the complex also included a conventional neutrino beam, the SPL super-beam, using the same baseline (CERN-Frejus) and detector (water Čerenkov) (see section 5.2. The advantage of having the two types of beam, is that, in addition to CP-conjugate transitions, T-conjugate and CPT-conjugate transitions could also be measured [711]. In particular, the comparison of the $\nu_e \rightarrow \nu_\mu$ and $\nu_\mu \rightarrow \nu_e$ oscillation probabilities is a T-odd observable and is therefore sensitive to δ.

Besides the theoretical interest of these measurements in the search for new physics, the determination of δ through such a T-odd measurement is advantageous from the experimental point of view because several systematic uncertainties would be cancelled. For example, the error on the Earth matter density is not relevant for this measurement.

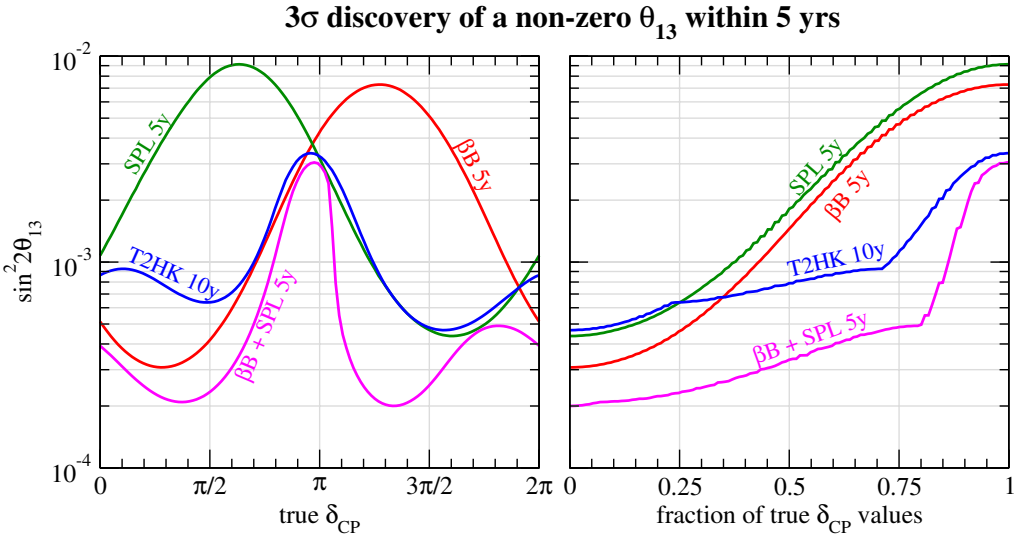

Figure 77: 3σ sensitivity to $\sin^2 2\theta_{13}$ for 5 years of run with a LE$\beta\beta$ (with twice the standard ion flux) and the SPL super-beam, compared with a 10 year run with T2HK (2 years neutrinos and 8 anti-neutrinos. Figure taken from reference [27]. The parameters are not the same as those in equation (295). Taken with kind permission of teh Journal of High Energy Physics from figure 14 in reference [27]. Copyrighted by SISSA.

The first analysis of the performance of a super-beam and beta-beam combination [711, 712] did not include spectral information and in this situation, given that the two $\langle E_\nu \rangle / L$ are very similar, it was clear that degeneracies, in particular the intrinsic, one would remain [214]. Later, the spectral information has been included and it has been shown that the SPL on its own is able to resolve the intrinsic degeneracy [27], however this is not the case for the LE$\beta\beta$ as we have seen.

A real synergy of both types of experiment has been explored recently [27]. The idea is to use only neutrino runs in both beams, which has the advantage that the cross sections are larger than for anti-neutrinos. In figure 77, the sensitivity to θ_{13} for this combination with a five-year run of both the SPL and beta-beam is shown to outperform a ten-year run of T2HK.

5.3.17 Combination of different ions

In reference [209], a combination of the beams produced by the four ions He/Ne/Li/B (the 'alternating-ion' scenario) with a γ below the present SPS limit has been considered. In this case, the baseline chosen was 630 km (CERN-Canfranc), which corresponds to the first atmospheric peak for the Li/B beam at $\gamma \sim 100$, while the He/Ne beam is close to the second peak for a similar γ. The ion fluxes are assumed to be the standard ones for Li/B as for He/Ne, so the total neutrino and anti-neutrino fluxes from all the ions are similar, but the shapes are quite different since the end-point values, E_0, differ (see section 5.3.1).

The main advantage of this combination over the LE$\beta\beta$ setup is the use of two different $L/\langle E_\nu \rangle$ which is a very powerful way of resolving degeneracies. In particular, the intrinsic degeneracy

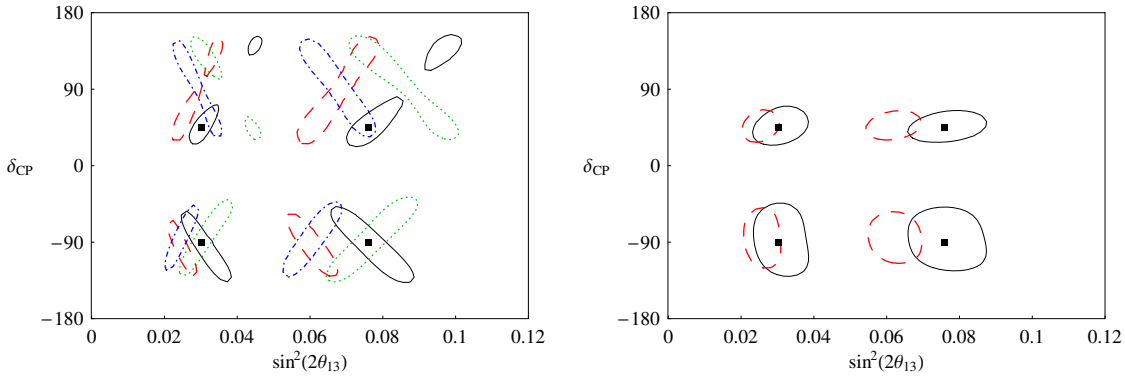

Figure 78: 90% contours for a LE$\beta\beta$ with $\gamma = 120$ (left) and an alternating ion scenario (right) both at $L = 630\ km$ (CERN-Canfranc). The true parameters are denoted with a thick black square. Figure taken from reference [209]. The parameters are not the same as those in equation (295). Taken with kind permission of Physical Letters from figure 2 in reference [209]. Copyrighted by Elsevier B.V.

which severely limits a precise determination of δ in the LE$\beta\beta$ setup is absent in the combination. This, however, is at the expense of having larger statistical uncertainties due to the smaller flux. Fits for (θ_{13}, δ) for a LE$\beta\beta$ with a slightly larger $\gamma = 120$ at $L = 130\ km$ and the combination of four ions at $L = 630\ km$ are compared in figure 78. The eight-fold degeneracy of the former is reduced to a two-fold degeneracy in the latter at 90%CL, only the octant ambiguity remains unresolved. The sensitivity of this combination to the hierarchy has also been shown to be very significant and much less dependent on δ than in the case of the HE-a setup. We therefore conclude that this combination outperforms the LE$\beta\beta$ if θ_{13} is not too small, within the reach of T2K phase I.

5.3.18 Higher γ ?

The possibility of using more powerful accelerators such as the LHC to achieve even higher γ has also been discussed. The increase in γ allows smaller detectors, optimised for events in the multi-GeV range, to be considered. The physics potential of a very high γ beta-beam with $\gamma \geq 1000$, but assuming the same ion flux, has been considered in [25,690]. In the first reference a $\sim$ 50kton idealised scintillator detector was assumed, while in the second the NOνA type detector discussed above was considered. The data-sample size is therefore improved very much with respect to the HE$\beta\beta$-a setup since the gain in γ is compensated by a decrease in the detector mass. The sensitivity to $\mathrm{sgn}\Delta m^2_{31}$ is compared for three beta-beams setups and the Neutrino Factory in figure 79. The conclusion of these studies is that going to such high γ improves the sensitivity to the hierarchy and therefore resolves the correlation of δ with $\mathrm{sgn}\Delta m^2_{31}$, so improving the sensitivity to CP violation.

A related idea has been proposed more recently in [718]. The goal is to arrive to the magic baseline ($L \sim 7\,500$ km [43] using ^{8}B and ^{8}Li ions with γ in the range 250–500; this could be achieved with a refurbished SPS at CERN pointing at the Indian Neutrino Observatory (INO) where a large magnetised iron calorimeter in the 50-100 kton range (ICAL) could be used as the

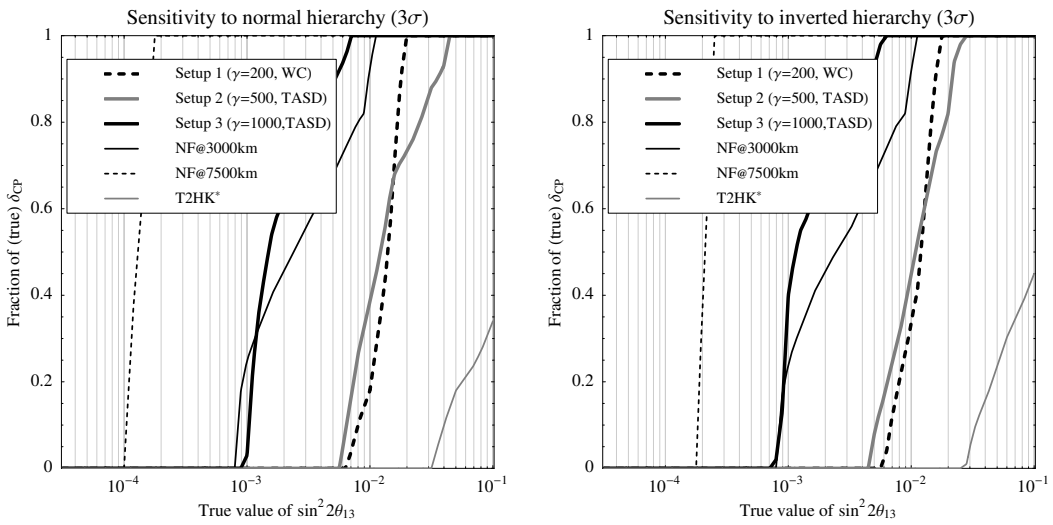

Figure 79: 3σ sensitivity to the normal mass hierarchy for different beta-beam setups including one with $\gamma = 1000$ combined with the same detector as in the HE-b setup discussed in the text. The Neutrino Factory setups are also included for comparison. Figure taken from reference [690]. The parameters are not the same as those in equation (295). Taken with kind permission of the Physical Review from figure 12 in reference [690]. Copyrighted by the American Physical Society.

far detector. For details of the potential of this setup see [718].

5.3.19 Higher fluxes ?

The standard ion fluxes that have been used in this study are based on the CERN design for a LE$\beta\beta$, using the present CERN SPS and PS and requiring a duty cycle of a few 10^{-3}. In the present design, a large fraction of the ions being produced are lost in the acceleration process and it is likely that a refurbished PS or SPS could eliminate some of the present losses. The refurbishing of these old machines is likely to be required to serve the LHC programme and, therefore, it is likely that further optimisations to increase the neutrino flux can be considered. Furthermore, an entirely new approach to producing the required unstable ions, using ionisation cooling, has been recently proposed in reference [710]. Although there remain many details to work out, this novel approach offers the possibility of increasing the ion-production yield by several orders of magnitude. The physics reach of such a beta-beam with such high fluxes would be outstanding and it is therefore of the upmost importance to explore possible optimisations that could be achieved with realistic improvements in the accelerators or/and the ion-production technique.

5.3.20 Monocromatic e-capture beams

Triggered by the beta-beam concept, a different type of neutrino beam has been proposed in reference [719]. The idea is to produce neutrinos from boosted ions that undergo an e-capture

Decay	$T_{1/2}$	E_ν (keV)	EC/β^+ (%)
^{148}Dy $\rightarrow$ ^{148}Tb	3.1 m	2062	96/4
^{150}Dy $\rightarrow$ ^{150}Tb	7.2 m	1397	99.9/0.1
^{152}Tm 2^- $\rightarrow$ ^{152}Er	8.0 s	4400	45/55
^{150}Ho 2^- $\rightarrow$ ^{150}Dy	72 s	3000	77/33

Table 12: *Decay properties of some rare-earth nuclei.*

transition, that is an atomic electron is captured by a proton, anti-neutrino beams cannot be produced this way. Kinematically it is a two-body decay and therefore the neutrino energy is well-defined and given by the difference between the initial and final nuclear mass energies minus the excitation energy of the final-state nucleus. Such transitions are usually dis-favoured, but there are a few nuclei (see table 12) for which the decay rate is significant.

The neutrino flux can easily be shown to be [719]:

$$\frac{d^2N_\nu}{dSdE} = \frac{1}{\Gamma}\frac{d^2\Gamma_\nu}{dSdE}N_{ions} \simeq \frac{\Gamma_\nu}{\Gamma}\frac{N_{ions}}{\pi L^2}\gamma^2\delta(E-2\gamma E_0), \tag{296}$$

where γ is the boost factor of the parent ion, E_0 is the neutrino energy in the laboratory frame, and Γ_ν/Γ is the e-capture branching fraction. The neutrino energy in the detector will be peaked at $2\gamma E_0$ and the requirement that the neutrino energy be reconstructed accurately in the detector can be relaxed. One can easily disentangle the different oscillation parameters by performing counting experiments at different values of γ.

As in the case of the beta-beam, a possible implementation of the concept would involve the use of EURISOL to produce the unstable ions, the SPS to accelerate them, and a decay ring. However, to allow electron capture to occur, we need to keep one electron bound to the ion's nucleus, partly ionised particles have a short vacuum life-time (even in a very good vacuum collisions with the few remaining atoms suffice to cause them rapidly to lose the remaining electron). The ion that has been proposed as optimal is ^{150}Dy, which could be accelerated in the CERN SPS up to a maximum γ of 195.

The main advantage of an electron-capture beam over a 'conventional' beta-beam, for a similar number of ion decays, is that all the intensity is peaked at the energy(ies) of interest. In a beta-beam the broad spectrum implies that many neutrinos will be produced at energies for which the dependence on δ is less pronounced, and/or the cross section is too low. It is also a excellent tool to discriminate against backgrounds of various types.

Even though no realistic study of the expected ion flux has yet been performed, an analysis of the performance of such a beam assuming an intensity of 10^{18} ions/year has been presented in [719, 720]. Using a 440 kton fiducial mass water Čerenkov located at a distance of 130 km (CERN-Frejus baseline), 5 years running time for each of $\gamma = 195$ and $\gamma = 90$, the precision in the determination of θ_{13} and δ that could be obtained is illustrated in figure 80. Due to the lack of a CP-conjugate observable, such as one would have with an anti-neutrino beam, all sensitivity to the CP phase is lost at a given γ. However, it is remarkable that the measurement of the

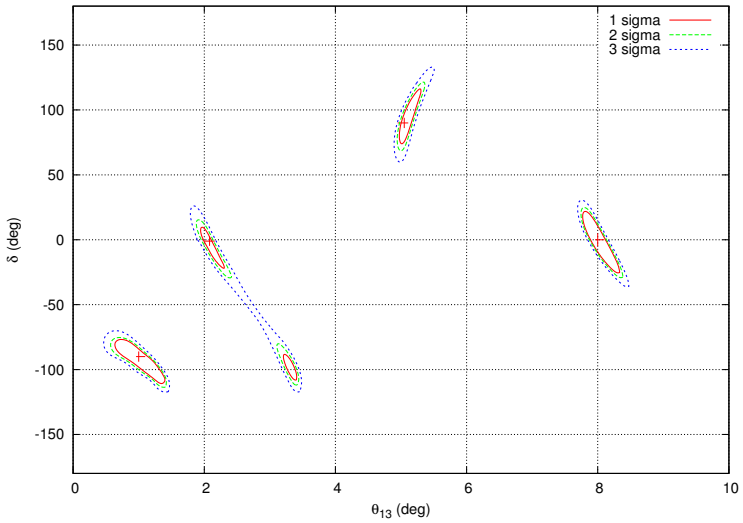

Figure 80: Combined fits of θ_{13} and δ for different central values of the parameters. The known parameters are not the same as those of equation (295). Figure taken from [720].

oscillation probabilities at two energies results in a significant sensitivity to δ. An alternative, that would improve the sensitivity to δ, would be to combine an e-capture beam with a standard beta-beam from ^{6}He using the same detector.

5.4 Optimisation and physics potential of a Neutrino Factory oscillation experiment

In a Neutrino Factory [28,29] muons are accelerated from an intense source to energies of several tens of GeV and injected into a storage ring with long straight sections. The muon decays $\mu^+ \to e^+ \nu_e \overline{\nu}_\mu$ and $\mu^- \to e^- \overline{\nu}_e \nu_\mu$ provide a very well known flux of neutrinos with energies up to the muon energy itself. Neutrino Factory designs have been proposed in Europe [33, 721], the US [30–32, 34, 35], and Japan [722]. The conclusion of these studies is that an accelerator complex capable of providing $\sim 10^{21}$ muon decays per year can be built. One of the most striking features of the Neutrino Factory is the precision with which the characteristics of all components of the beam would be known. The following effects were considered in reference [723]:

- Beam polarisation: with a polarimeter, the beam energy and energy spread can be measured and the degree to which the polarisation dependence of the neutrino flux affects the measured rates can be tested to high precision [724];
- Beam divergence and radiative corrections in muon decay [725];
- Absolute normalisation of the flux to be obtained from a beam monitor; and
- Absolute cross-section normalisation using the inverse-muon-decay reaction, $\nu_\mu e^- \to \mu^- \nu_e$, in the near detector. In principle, a normalisation of fluxes and cross-sections with a precision of 10^{-3} can be achieved.

$\mu^+ \to e^+ \nu_e \overline{\nu}_\mu$	$\mu^- \to e^- \overline{\nu}_e$	
$\overline{\nu}_\mu \to \bar{\nu}_\mu$	$\nu_\mu \to \nu_\mu$	disappearance
$\overline{\nu}_\mu \to \bar{\nu}_e$	$\nu_\mu \to \nu_e$	appearance (challenging)
$\overline{\nu}_\mu \to \bar{\nu}_\tau$	$\nu_\mu \to \nu_\tau$	appearance (atm. oscillation)
$\nu_e \to \nu_e$	$\bar{\nu}_e \to \bar{\nu}_e$	disappearance
$\nu_e \to \nu_\mu$	$\bar{\nu}_e \to \bar{\nu}_\mu$	appearance: "golden" channel
$\nu_e \to \nu_\tau$	$\bar{\nu}_e \to \bar{\nu}_\tau$	appearance: "silver" channel

Table 13: Oscillation processes in a Neutrino Factory.

Some of these features should also be present for a beta-beam, and for any facility in which a stored beam of well-defined optical properties is used to produce neutrinos. This is an important difference with respect to super-beams for which the precision with which the neutrino and anti-neutrino cross sections and fluxes are known is determined by the degree to which the particle-production spectra are known.

Twelve oscillation processes can be studied using the Neutrino Factory which and store beams of both positive and negative muons (see table 5.4). Neutrinos produced from the decay of positive and negative muons must not be confused. The required separation can be achieved by running the two polarities in turn or by careful timing if the two polarities are stored simultaneously. In order to take full advantage of this flavour-richness, the optimal detector should be able to perform both appearance and disappearance experiments, providing lepton identification and charge discrimination.

The search for $\nu_e \to \nu_\mu$ transitions (the 'golden channel') [206] appears to be particularly attractive at the Neutrino Factory. It can be studied in appearance mode, by looking for muons with charge opposite to that of the stored muon beam ('wrong-sing muons'), thus strongly reducing the dominant background ('right-sign muons'). The wrong-sign-muon channel yields an impressive sensitivity to $\sin^2\theta_{13}$ and sensitivity to the leptonic CP-violating phase, δ, down to very small values of θ_{13} [43,205,206]. For example, with two 40 Kton MINOS-like magnetised-iron detectors at two different baselines, exposed to beams of both polarity and 10^{21} muon decays, it will be possible to explore θ_{13} down to $\sin^2 2\theta_{13} \geq 1 \times 10^{-5}$ ($\theta_{13} \geq 0.1^\circ$) and to measure δ for most of the parameter space [205]. The relatively high energy of the neutrinos produced through the decay of high-energy stored muons implies that baselines of several thousand kilometers are needed for Neutrino Factory experiments. For such baselines, CP asymmetries are dominated by matter effects [588, 726, 727] that can be used to determine unambiguously $\mathrm{sign}(\Delta m^2_{31})$ for large enough θ_{13}.

The determination of (θ_{13}, δ) at the Neutrino Factory is not free of ambiguities; up to eight different regions of the parameter space can fit the same experimental data in the (θ_{13}, δ) plane. In order to solve these ambiguities, a single experimental measurement for a single neutrino beam is not enough. One possible solution to this problem is to combine detectors looking for 'golden' muons at different baselines (i.e., different L/E). A second possibility is to make use of the rich flavour content of the Neutrino Factory beam. The τ appearance channel ('silver

channel') [44,728] has been advocated as a powerful means of resolving ambiguities, if a detector capable of τ identification can be used. This can readily be understood since the δ-dependence of the silver and the golden channel are different, while the dependence of the two channels on matter effects and θ_{13} is similar. On the other hand, the ν_μ-disappearance channel is rather effective for large values of θ_{13} in measuring the θ_{23} octant [218]. A detector capable of measuring the charge of the electrons has been shown to allow the resolution of ambiguities by separating the events into several classes (right-sign muons, wrong-sign muons, electrons, and neutral currents) and performing a fine energy binning down to low energies. Such a possibility was first studied assuming the feasibility of a magnetised liquid-argon detector [729], and recently updated in reference [208]. R&D efforts for a liquid-argon detector embedded in a magnetic field are ongoing [730] (the first curved tracks were recently observed in a 10 litre liquid-argon TPC embedded in magnetic field [731]). A third possibility is an improved detector (with a much lower muon energy threshold) to look for 'golden muons' solving at the same time all the degeneracies.

This section is organised as follows: in section 5.4.1 the 'standard' Neutrino Factory setup is introduced and the different detectors are described; section 5.4.2 contains a review of the performance of the magnetised iron detector located at $L \sim 3000$ km from the source (i.e., the 'standard' setup) and of the problems that must be faced; in section 5.4.3 possible improvements to this setup are considered combining detectors at different baselines, channels (following table 5.4) and improving the 'standard' detector; in section 5.4.4 the main characteristics that are needed to use the Neutrino Factory at its best are addressed.

5.4.1 The Neutrino Factory setup

In the following, the 'standard' Neutrino Factory refers to a facility in which a 50 GeV stored-muon beam delivers a luminosity of 1×10^{21} muon decays per year. The total luminosity per muon polarity is taken as a given, independent of, for example, the specific choice of proton-driver beam power, storage-ring geometry, or the time spent running with a particular polarity. Notice that in the literature several different options have been considered for each of these [693]. Three detectors of different technologies, each specifically optimised to detect a particular signal, have been considered.

5.4.1.1 Magnetised Iron Detector (MID): the 'golden channel'

The most important signal at the Neutrino Factory is the 'golden channel', i.e. the appearance channel $\nu_e \to \nu_\mu$. The signal is tagged by 'wrong-sign muons', muons in the detector with charge opposite to that of the muons in the storage ring. In order to extract the signal from the dominant source of background, i.e. non-oscillated $\bar{\nu}_\mu$ (giving rise in the detector to a huge number of 'right-sign muons'), a magnetised detector is required. This requirement represents the most important difference between the detectors adopted for super-beam and beta-beam facilities and those needed to take full advantage of the Neutrino Factory. As a consequence,

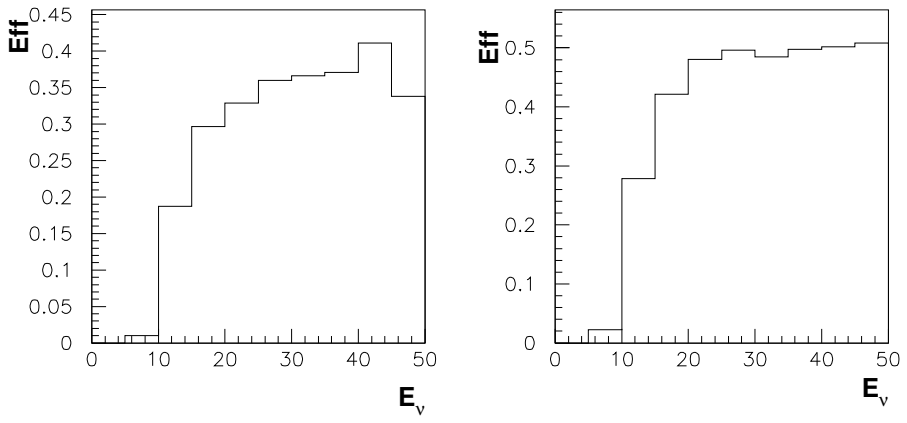

Figure 81: Signal efficiency at the magnetised iron detector for μ^+ (left panel) and μ^- (right panel) as a function of the neutrino energy. Taken with kind permission of Nuclear Physics B from figure 18 in reference [206]. Copyrighted by Elsevier Science B.V.

large, water Čerenkov detectors are dis-favoured and medium size magnetised detectors must be considered.

The reference detector, a 50 Kton magnetised iron calorimeter of the MINOS type, was optimised in reference [42] for the study of $\nu_e \to \nu_\mu$ oscillations. Tight kinematic cuts were applied to decrease the dominant and sub-dominant backgrounds (right-sign muons and charmed-meson decays). Such cuts, although strongly reducing the background, have the dis-advantage that a significant proportion of the signal with neutrino energy below 10 GeV is removed. This can be seen in figure 81, where the efficiencies of the golden channel in the magnetised iron detector with MINOS-like performance is shown. Measurements of the energy spectrum below 10 GeV, however, have been shown to be extremely important; the first oscillation peak for $L \sim 3000$ Km lies precisely in this energy range. For this reason, the Neutrino Factory is the single facility considered in this report most affected by degeneracies. The measurement of the spectrum both below and above the oscillation maximum has been shown to be crucial in the solution of many of the parametric degeneracies that compromise the (θ_{13}, δ)-measurement. The improvement in performance obtained by increasing the signal efficiency for neutrino energies below 10 GeV is considered in section 5.4.3.3.

Different treatments of the energy response of the detector can be found in the literature. For example, in reference [206] the energy resolution was assumed to be $0.2 \times E_\nu$. The effect of this finite energy resolution was taken into account by grouping the events in five bins of width $\Delta E_\nu = 10$ GeV. This approach is quite conservative especially at low energy where most of the oscillation signal is found. In reference [208] a finer binning was adopted, with a more detailed treatment of resolution effects. There are several differences between the treatment in reference [208] and that of reference [206]. First, the energy response of the detector is modeled by folding the raw-event distribution with a Gaussian resolution kernel of width $\sigma_E = 0.15 \times E_\nu$;

in this way, the results become independent of the bin width, provided that the binning is fine enough. Secondly, 43 bins of variable ΔE_ν were considered in the energy range $E_\nu \in [1, E_\mu]$ GeV. The bins were defined as follows: 18 bins of $\xi \times 500\,\mathrm{MeV}$; 10 bins of $\xi \times 1\,\mathrm{GeV}$; and 15 bins of $\xi \times 2\,\mathrm{GeV}$ from the lowest to the highest energy, where $\xi = (E_\mu - 1)/49$ is an overall scale factor ($\xi = 1$ corresponding to the 'standard' 50 GeV Neutrino Factory). The fast oscillations that arise at low energies and that can lead to 'aliasing' effects are averaged, at the probability level, over a width of 150 MeV [45, 46] for muon energies up to 100 GeV and baselines up to 9000 Km. This procedure has been tested, i.e. it has been verified that the χ^2-values do not change if a finer binning is chosen or if a different averaging procedure at the probability level is used.

The different procedures that have been adopted in the literature to account for the energy response of the detector could make, in principle, a significant difference in the results. This is especially true at the Neutrino Factory, where the parametric degeneracies play such a big role. Indeed, some of the degeneracies are energy dependent and can be solved if the detector considered has good energy resolution. For this reason the results obtained with the various binning procedures and efficiencies used in references [206] and [208] have been compared using GLoBES [45,46]. A point at $\sin^2 2\theta_{13} = 10^{-3}$ [$\theta_{13} = 1^\circ$] was chosen for this comparison since at these intermediate values the impact of degeneracies is, in general, largest. For the true solution the results obtained using the different procedures could not be distinguished. In contrast, for the intrinsic degeneracy a $\sim 30\%$ difference in the $\Delta\chi^2$ was observed. Such a difference, however, would also arise in other modification of the setup, such as, for example, the assumption of a different low-energy muon threshold or efficiency. The degeneracy is, nonetheless, always present at the 5σ level. Therefore, at the current level of accuracy in the detector simulation, there is no qualitative difference. In the context of improved detector simulations that will become available, however, it will be extremely important to describe accurately the detector response.

The results shown in below will be based on the treatment of references [208, 340], unless otherwise stated. For the wrong-sign muon signal, flat efficiencies of 0.45 (neutrinos) and 0.35 (anti-neutrinos) for energies in the range $E_\nu \in [20, 50]$ GeV are assumed. A linear rise of the efficiencies from the lower threshold (between 0 at 4 GeV) to their final value at 20 GeV is assumed. The energy resolution is treated as described above. The relatively high neutrino-energy threshold is the result of optimising for the purest possible sample of wrong-sign muons, thus selecting events with the highest possible energy. Indeed, the lower the muon energy, the higher the likelihood to mis-identify the muon charge or the nature of the event (charged current versus neutral current) becomes. As the average muon energy will decrease with the neutrino energy, we model the total, fractional background with the function βE_ν^{-2}, where $\beta = 10^{-3}$. Integrating from 4 GeV to 50 GeV, we fix the weight factor, β, by matching roughly the total fractional background obtained in reference [42]. The fractional backgrounds considered in the following are: 5×10^{-6} of the neutral current events; and 5×10^{-6} of the right-sign muon events.

It must be noted that this detector can also be used to look for $\nu_\mu \to \nu_\mu$ dis-appearance, providing a very good measurement of the atmospheric parameters θ_{23} and Δm^2_{31} and giving some handle on the 'octant degeneracy'. For the right-sign muon sample there is no need

to determine accurately the charge of the muon, since wrong-signs muons constitute only a negligible fraction of the sample. Therefore, the efficiencies and thresholds reported by MINOS [192], and a signal efficiency of 0.9 starting at 1 GeV are used. The backgrounds in this case are 10^{-5} of all neutral-current events and all wrong sign muon events. The latter are added directly to the signal.

For both channels we use a 2.5% systematic error on the signal and a 20% systematic error on the background normalisation. A different magnetised-iron calorimeter detector for a Neutrino Factory experiment has been described in reference [732].

5.4.1.2 Emulsion Cloud Chamber (ECC): the 'silver channel'

To soften the parametric degeneracy problem, it has been proposed to take advantage of the 'silver channel', i.e. $\nu_e \to \nu_\tau$ oscillations [44]. This is a unique feature of the Neutrino Factory, where the average neutrino energy is high enough to produce τ CC events; not even the highest γ beta-beam discussed above can look for this signal. The signal can be tagged looking for wrong-sign muons in coincidence with a τ-decay vertex, to distinguish them from golden channel wrong-sign muons. Therefore, a detector with muon-charge identification and vertex reconstruction is needed. Two technologies have been considered in the literature: liquid-argon detectors [729] and emulsion-cloud-chamber (ECC) techniques. The latter has been extensively studied for the OPERA detector that is under construction at the Gran Sasso laboratory, and a dedicated analysis to use this technique at the Neutrino Factory has been published in reference [728]. In [728], a 5 Kton ECC was considered and a detailed study of the main sources of background performed. In the following, the ECC will be considered as the standard detector to study the silver channel.

The various backgrounds to the silver-channel signal are presented in table 14. The ECC detector is assumed to have a fiducial mass of 5 Kton as in reference [728]. In addition, an overall signal efficiency of approximately 10%, chosen to reproduce the signal-event numbers from table 4 in reference [728], is assumed. The background rejection factors are taken from reference [728] as well and are summarised in table 14.

The energy resolution is assumed to be $20\% \times E$, implemented as in [208]. It is further assumed that silver-channel data-taking only occurs when μ^+ are stored (running with μ^- will produce very few silver events, due to the $\bar{\nu}_\tau N$ cross-section suppression). A 15% systematic uncertainty on the signal and a 20% systematic uncertainty on the background normalisation are assumed.

Notice that this detector can also be used to look for $\nu_\mu \to \nu_\tau$ appearance, i.e. precisely the purpose for which it is being built in the framework of the CNGS experiment. This channel can be useful to measure the atmospheric parameters, as well as the ν_μ dis-appearance channel discussed above. Other possible τ decay channels, such as decay into electrons or into hadrons, have not been considered as they would need a dedicated analysis and a totally different detector.

Background source	Rejection factor
Neutrino induced charm production	$10^{-8} \times (N_{CC}(\nu_e) + N_{CC}(\nu_\mu))$
Anti-neutrino induced charm production	$3.7 \cdot 10^{-6} \times N_{CC}(\bar{\nu}_\mu)$
$\tau^+ \to \mu^+$ decays	$10^{-3} \times N_{CC}(\bar{\nu}_\tau)$
μ matched to hadron track	$7 \cdot 10^{-9} \times N_{CC}(\bar{\nu}_\mu)$
Decay-in-flight and punch-trough hadrons	$6.97 \cdot 10^{-7} \times N_{NC} +$
	$+ 2.1 \cdot 10^{-8} \times N_{CC}(\nu_e)$
Large-angle muon scattering	$10^{-8} \times N_{CC}(\nu_\mu)$

Table 14: The background sources and rejection factors for the silver channel measurement in the μ^+-stored phase. From reference [728].

5.4.1.3 Liquid Argon Detector (LAr): the 'platinum' channel

In addition to the channels discussed above, $\nu_\mu(\bar{\nu}_\mu) \to \nu_e(\bar{\nu}_e)$ oscillations can be also observed at a Neutrino Factory. This channel, the 'platinum channel' (since the observation of a small number of events can be extremely valuable) is the T-conjugate of the golden channel. It is also its CP-conjugate, albeit with different matter effects. Combined with the golden channel, the platinum channel will help to resolve many of the correlations and degeneracies.

To take advantage of this channel, a detector that can identify the charge of the electrons (to reduce the dominant background from non-oscillated ν_e) is required. Electron charge identification has so far only been studied for a magnetised liquid-argon TPC [210]. A lower-energy detection threshold of 0.5 GeV was applied. In reference [210] it was pointed out that electrons and positrons of higher energy tend to shower early, which means that the track is short and the curvature is hardly measurable. Therefore, there may be an upper energy threshold above which it is no longer possible to measure the electron charge. The efficiency and the dominant backgrounds to the platinum channel in a liquid-argon detector are shown in figure 82.

In reference [208], the ν_e-appearance performance of the MINOS detector (which has been estimated in reference [734]) was adopted. An extra background corresponding to 1% of the non-oscillated ν_e was added to take into account the difference between the Neutrino Factory beam and the NuMI beam. The fractional background of this analysis is in agreement with that of reference [210].

The 'standard' platinum-channel detector is assumed to be liquid-argon TPC with a fiducial mass of 15 Kton. The signal efficiency, which is assumed to be energy independent, is taken to be 20% [210], and the background-rejection factors are summarised in table 15. Furthermore, the energy resolution is assumed to be $15\% \times E_\nu$. The upper threshold for the electron/positron-charge identification (CID) is assumed to be 7.5 GeV. The CID background is assumed to be 1% [210] and the other backgrounds are taken from reference [734].

In some of the figures of sections 5.4.3 and 5.4.4, however, the impact of an 'improved' platinum-channel detector is discussed. The 'improved' detector has the following character-

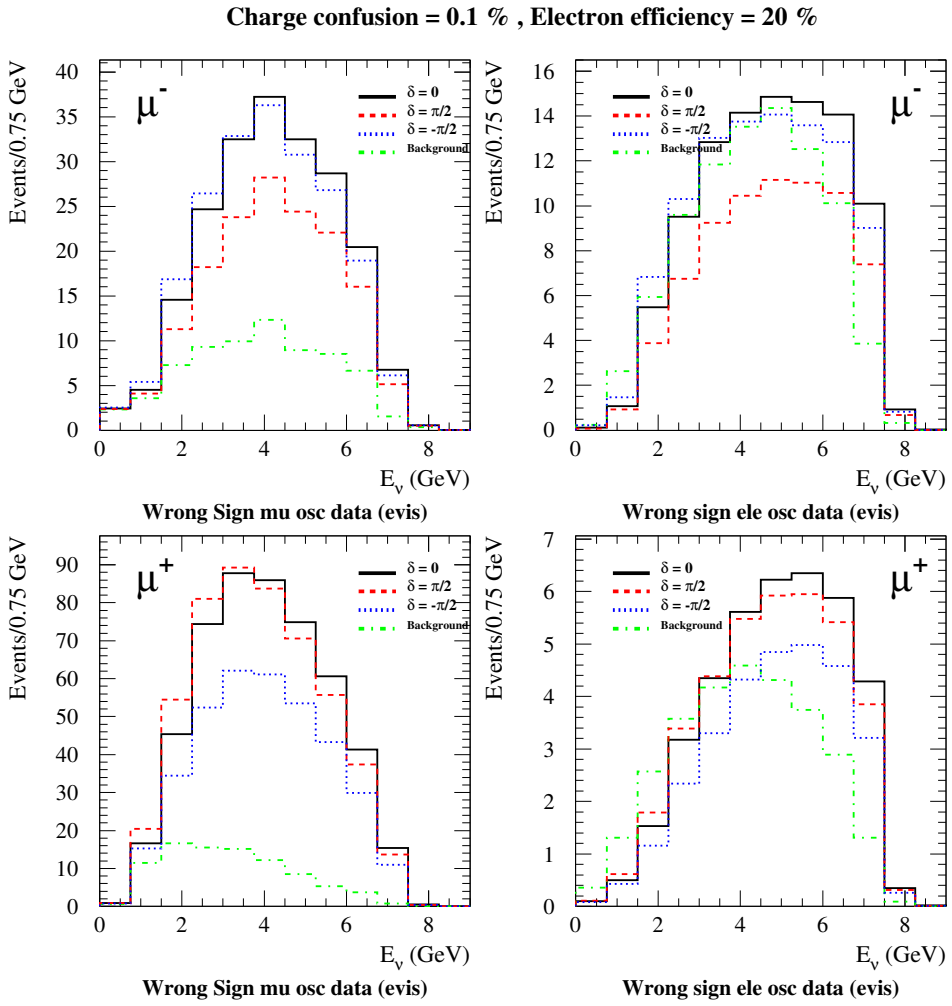

Figure 82: Visible energy distribution for wrong-sign muons (left panel) and wrong-sign electrons (right panel) normalised to 10^{21} muon decays. The electron efficiency ϵ_e is assumed to be 20% and charge confusion probability is set to 0.1%. Three sets of curves are represented, corresponding to $\delta = +\pi/2$ (dashed line), $\delta = 0$ (full line) and $\delta = -\pi/2$ (dotted line). The background contribution from tau decays is also shown. The other oscillation parameters are $\Delta m^2_{32} = 3 \times 10^{-3}$ eV^2, $\Delta m^2_{21} = 1 \times 10^{-4}$ eV^2, $\sin^2\theta_{23} = 0.5$, $\sin^2\theta_{12} = 0.5$ and $\sin^2 2\theta_{13} = 0.05$. Taken with kind permission of Nuclear Physics B from figure 18 in reference [733]. Copyrighted by Elsevier Science B.V.

Background source	Rejection factor
Muon dis-appearance	$10^{-3} \times N_{CC}(\nu_\mu)\,(N_{CC}(\bar{\nu}_\mu))$
Tau appearance	$5 \cdot 10^{-2} \times N_{CC}(\nu_\tau)\,(N_{CC}(\bar{\nu}_\tau))$
Neutral current reactions	$10^{-2} \times N_{NC}$
Wrong sign electron/positron	$10^{-2} \times N_{CC}(\bar{\nu}_e)\,(N_{CC}(\nu_e))$

Table 15: The background sources and rejection factors for the platinum channel measurement for the μ^--stored phase, while the brackets refer to the μ^+-stored phase. The numbers, besides the background from electron/positron CID, are taken from reference [734].

istics: a 50 Kton fiducial mass; an energy-independent signal efficiency of 40%; background-rejection factors as given in reference [734] extrapolated to higher energy; and CID background as for the standard setup. The CID upper energy threshold is varied continuously from 7.5 GeV to 50 GeV. The performance of this improved detector are labeled in the figures 'platinum*'.

Both for platinum and platinum* detectors a 2.5% systematic error on the signal and a 10% systematic error on the background normalisation have been assumed.

5.4.2 Physics potential of the golden channel

In this section, the physics potential of the standard golden-channel detector is presented. The $\nu_\mu \to \nu_\mu$ dis-appearance channel will be included in this section as well. Through this channel, an independent measurement of the atmospheric parameters is possible. This serves to reduce significantly the impact of the uncertainties induced by uncertainties in these parameters in the (θ_{13}, δ) measurement [220, 340].

Results will be presented following the definitions given in section 2.3. Most of the figures in this section are taken from reference [208], where the following input (or 'true') values were used:

$$\begin{aligned} \Delta m^2_{31} &= 2.2^{+1.1}_{-0.8} \cdot 10^{-3}\,\mathrm{eV}^2\,; \quad \sin^2\theta_{23} &= 0.5^{+0.18}_{-0.16}\,; \\ \Delta m^2_{21} &= 8.1^{+1.0}_{-0.9} \cdot 10^{-5}\,\mathrm{eV}^2\,; \quad \sin^2\theta_{12} &= 0.3^{+0.08}_{-0.07}\,; \\ \sin^2\theta_{13} &= 0^{+0.047}_{-0}\,; \quad \delta &= 0^{+\pi}_{-\pi}\,. \end{aligned} \tag{297}$$

The ranges represent the current 3σ allowed ranges (from reference [67] (see also references [77,735,736]), both choices of $\mathrm{sgn}(\Delta m^2_{31})$ are allowed. A 5% additional uncertainty on Δm^2_{21} and θ_{12} from solar experiments at the time that data from the Neutrino Factory becomes available is assumed [736]. Matter-density uncertainties at the level of 5%, uncorrelated between different baselines, have been included [737, 738]. Whenever discussing the octant degeneracy, the 'true value' of the atmospheric angle has been fixed to $\theta_{23} = 0.44$ (or 0.56) [114].

The precision with which many of the SνM observables can be measured strongly depend on the true values of $\sin^2 2\theta_{13}$ and δ. Hence, the results are presented in terms of two-dimensional plots in the (θ_{13}, δ) plane. Each point in the plot corresponds to a different input (θ_{13}, δ)

Performance indicator	L [km]	E_μ [GeV]
Three-flavour effects:		
$\sin^2 2\theta_{13}$ sensitivity	$\sim 7\,500$ ("magic baseline")	20-50
Mass hierarchy sensitivity	$\gtrsim 6\,000$	20-50
Max. CP violation sensitivity	$\sim 3\,000 - 5\,000$	> 30
Leading atmospheric parameters:		
Δm^2_{31} precision	$\gtrsim 3\,000$	$\gtrsim 40$
Deviation from maximal mixing (θ_{23})	$\gtrsim 3\,500 + 50 \cdot E_\mu/\text{GeV}$	$\gtrsim 20$
Optimisation for large $\sin^2 2\theta_{13}$:		
Mass hierarchy sensitivity	$> 1\,000$	> 10
CP violation sensitivity ($\Delta\rho = 1\%\,\bar{\rho}$)	$\sim 1\,500 - 5\,500$	20-50
CP violation sensitivity ($\Delta\rho = 5\%\,\bar{\rho}$)	$\sim 1\,500 - 2\,000$	20-50
	$\sim 4\,500 - 5\,500$	20-40

Table 16: Requirements for the near-optimal performance of our 'standard Neutrino Factory' (one individual experiment) for $\Delta m^2_{31} = 0.0022$ eV^2 for different performance indicators.

pair. Notice that, in all plots, the $\Delta\chi^2$ is marginalised over the external atmospheric and solar parameters, as well as over the matter density, to take into account fully the correlations among the various parameters.

The requirements for the optimisation of the standard Neutrino Factory are summarised in table 16. There are two very important results. No baseline performs optimally for all the observables considered, a 'shorter' baseline $L \sim 3\,000 - 5\,000$ km is needed to provide good sensitivity to CP-violation and for the precise determination of the leading atmospheric parameters; a longer baseline, $L \simeq 7\,500$ km, is required to give optimal sensitivity to $\sin^2 2\theta_{13}$, the mass hierarchy, and for the disentanglement of degeneracies in the CP-violation measurements. For the muon energies, we find that $E_\mu \gtrsim 20$ GeV is sufficient for most applications, and $E_\mu \sim 40$ GeV should be on the safe side. Therefore, we find that the main challenge for a Neutrino Factory will be the baseline, which can affect the physics potential much more than a muon energy lower than previously assumed.

5.4.2.1 θ_{13}-sensitivity

The $\Delta\chi^2$ function, marginalised over all parameters other than θ_{13}, for a fit to data from the golden-channel detector under the conditions described above is shown in figure 83. The left panel of figure 83 shows that the $\Delta\chi^2$ function has two minima, the first corresponding to the input value $\theta_{13} = 0$ and the second for $\sin^2 2\theta_{13} \geq 10^{-3}$ (the intrinsic degeneracy). If there is no signal (hypothesis $\sin^2 2\theta_{13} = 0$), the degeneracy will worsen the $\sin^2 2\theta_{13}$ sensitivity, since a fake solution with a relatively large $\sin^2 2\theta_{13}$ will still be consistent with $\sin^2 2\theta_{13} = 0$. Therefore, it is not possible to exclude rather large $\sin^2 2\theta_{13}$ values. It must be stressed that results at 3σ are strongly dependent on small changes in the luminosities, the external parameters or the setup.

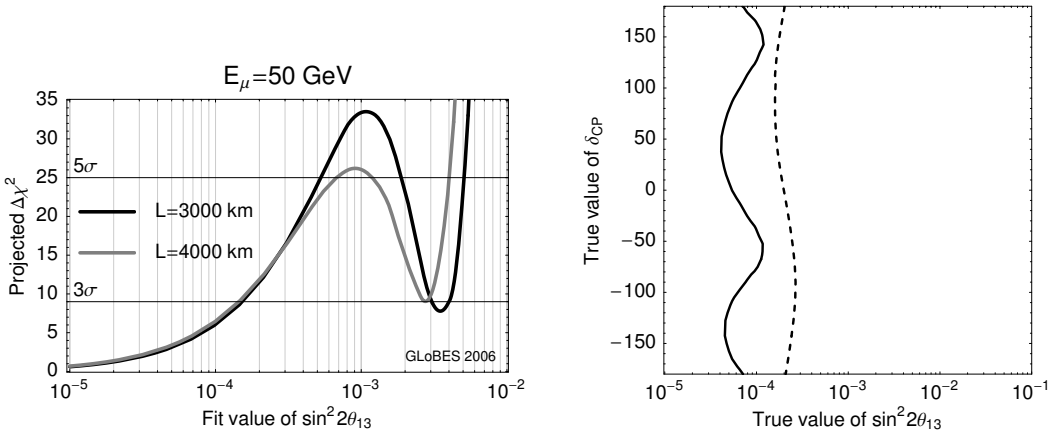

Figure 83: Left panel: Projected $\Delta\chi^2$ for the $\sin^2 2\theta_{13}$ sensitivity as a function of the fit value of $\sin^2 2\theta_{13}$ for $E_\mu = 50$ GeV and two different baselines as given in the plot legend (includes degeneracies). Right panel: 3σ θ_{13}-discovery; solid lines refer to the $L = 4000$ km Neutrino Factory; dashed lines to the $L = 7500$ km Neutrino Factory. Left panel taken with kind permission of the Physical Review from figure 4 in reference [208]. Copyrighted by the American Physical Society.

It can be seen in the figure how, for $L = 4000$ km, the $\Delta\chi^2$ at the second minimum increases and, at 3σ, the θ_{13}-sensitivity improves by one order of magnitude with respect to the case of $L = 3000$ km. However, at 5σ the degeneracy is still present for both baselines: these two cases will therefore be interpreted as qualitatively similar, as in fact they are. In the right panel of figure 83 the $\sin^2 2\theta_{13}$ discovery potential for $L = 4000$ km and $L = 7500$ km at $3\,\sigma$ is shown. Although the performance is slightly worse for the longer baseline, the δ-dependence is much weaker.

Figure 84 shows the $\sin^2 2\theta_{13}$ sensitivity at 5σ as a function of the baseline L and the parent muon energy E_μ. The different panels correspond to taking into account, successively, statistical uncertainties, systematic uncertainties, correlations, and degeneracies. The different contours represent the region within a factor of 0.5, 1, 2, 5, and 10 above the maximum sensitivity in each plot. The maximum sensitivity (obtained for the energies and baselines marked by the diamonds) are: $\sin^2 2\theta_{13} < 1.4 \cdot 10^{-5}$ (statistics), $2.8 \cdot 10^{-5}$ (systematics), $2.4 \cdot 10^{-4}$ (correlations), and $5.0 \cdot 10^{-4}$ (degeneracies), respectively.

When statistical and systematic uncertainties only are considered (i.e., δ is fixed to the value for which we get maximum sensitivity), figure 84(upper row), baselines from 1 000 to 4 000 km with as much muon energy as possible give the best sensitivity. However, when correlations and degeneracies are taken into account, the benefit of the 'magic baseline' [43] becomes more apparent. At the magic baseline all dependence on δ cancels and many of the degeneracies disappear 'by magic', thus improving the $\sin^2 2\theta_{13}$ sensitivity. This happens for $V = \sqrt{2} G_F n_e = 2\pi/L$, or, in terms of the constant matter density ρ, for approximately two nucleons per electron, equivalent to:

$$L_{\rm magic}\,[\rm km] \simeq 32\,726\ \frac{1}{\rho\,[\rm g/cm^3]}\,. \tag{298}$$

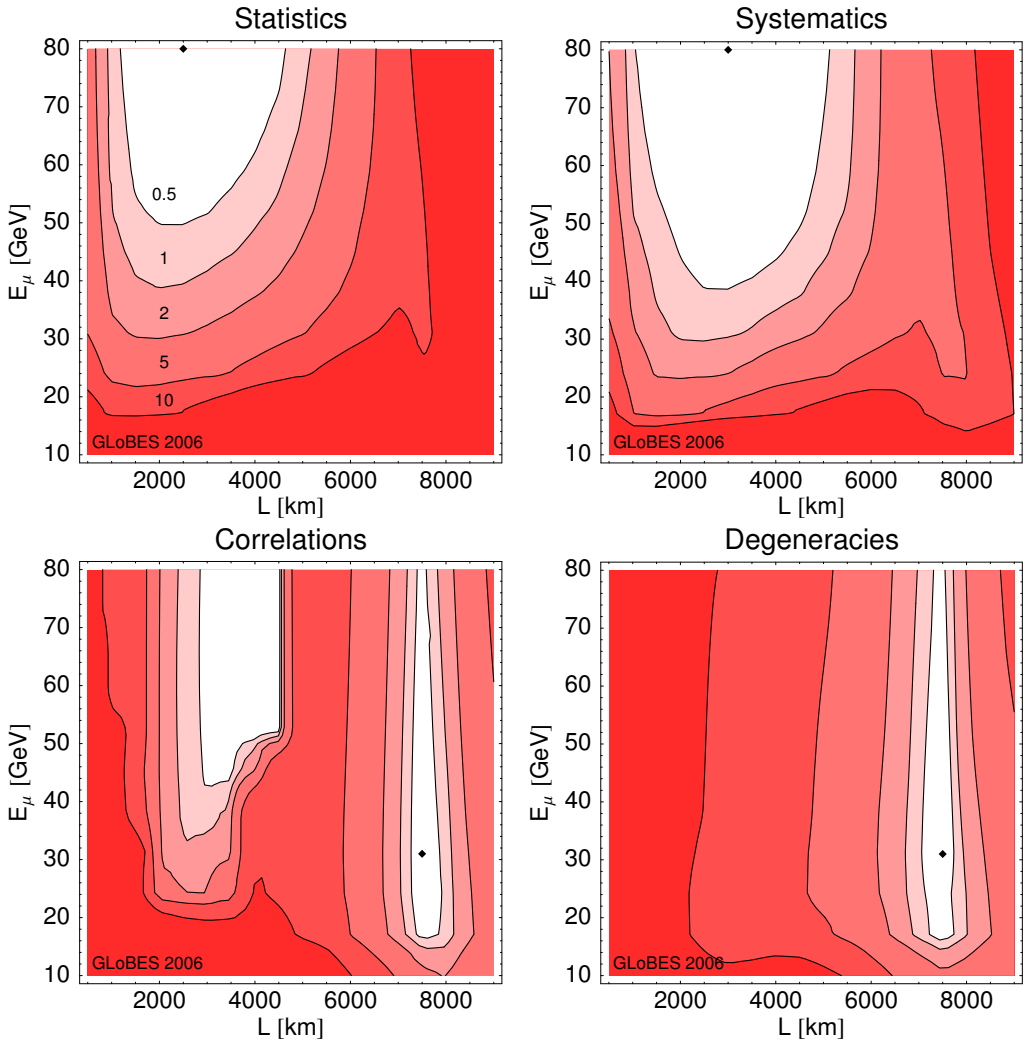

Figure 84: Sensitivity to $\sin^2 2\theta_{13}$ (5σ) relative to the optimum (white) within each plot. The different panels correspond to successively taking into account statistics, systematics, correlations, and degeneracies. The different contours represent the region within a factor of 0.5, 1, 2, 5, and 10 above the maximal sensitivity in each plot. The maximal sensitivities are $\sin^2 2\theta_{13} < 1.4 \cdot 10^{-5}$ (statistics), $2.8 \cdot 10^{-5}$ (systematics), $2.4 \cdot 10^{-4}$ (correlations), and $5.0 \cdot 10^{-4}$ (degeneracies), obtained at the energies and baselines marked by the diamonds. Taken with kind permission of the Physical Review from figure 3 in reference [208]. Copyrighted by the American Physical Society.

Numerically, it can be shown to be closer to $L_{\text{magic}} \sim 7\,250$ km for a realistic PREM [739] profile by minimising the δ-dependence in the appearance rates. At this distance, the optimal muon energy need not to be higher than 40 GeV (or even 30 GeV). The reason for this is that the $\sin^2 2\theta_{13}$ term in the appearance probability does not drop as a function of the baseline at the mantle resonance energy. Therefore, matter effects prefer lower energies, whereas higher muon energies imply higher event rates and a relative decrease of events at the mantle resonance. The optimum is determined by a balance between these two factors. The magic baseline has two obvious drawbacks: the event rate is reduced by the large distance; and it does not allow for a CP measurement.

5.4.2.2 CP-discovery potential

Figure 85 (left panel) shows the CP-discovery potential for the standard Neutrino Factory defined above for a baseline of $L = 4000$ km. No CP-discovery potential has been evaluated for the Neutrino Factory and a baseline of 7000 km; due to matter effects and the choice of the baseline (close to the magic baseline), the sensitivity to δ vanishes. The Neutrino Factory with a baseline of 4000 km is not as good as one would expect from its θ_{13}-sensitivity. This may be explained as follows: as a general rule, for small values of θ_{13} the degeneracies flow toward $\delta = 0°$ and $|\delta| = 180°$ (see references [199] and [610]), thus mimicking a non-CP violating phase. Especially problematic is the case where the data is fitted with inverted mass hierarchy, in this case it is possible to fit the data with $\delta = \pi$ for intermediate true values of $\sin^2 2\theta_{13} \sim 10^{-3}$ [1°], the so called π-transit [340]. Due to a 'parametric conspiracy' between the chosen energy and baseline and the matter effects, at the Neutrino Factory the typical value of θ_{13} for which this happens is much larger than at the SPL and or at T2HK. Therefore, although from the statistical point of view the Neutrino Factory would certainly out-perform both the SPL and T2HK, in practice for small values of θ_{13} a CP-violating phase will be difficult to distinguish from a non–CP-violating one, if the sign- and octant-degeneracies are not solved.

Figure 85 (right panel) shows the $\Delta\chi^2$ for the wrong choice of the mass hierarchy, computed for maximal CP-violation (i.e. true $\delta/2 = \pi$ or $3\pi/2$), as a function of the true θ_{13}. The $\Delta\chi^2$ is marginalised over all parameters other then δ and computed for fitted $\delta = 0$ or π. Sensitivity to maximal CP-violation is then represented (for a fixed L and E_μ) by the region of true θ_{13} for which $\Delta\chi^2$ is bigger than a given (1 dof) confidence level. For $\theta_{13} \to 0$, it becomes more and more difficult to distinguish CP-violation from CP-conservation. However, it can be seen that for $\delta = 3\pi/2$ a second minimum appears both at 3σ and at 5σ for larger θ_{13}, not present for $\delta = \pi/2$. This is the π-transit that was noted before. If the mass hierarchy is unknown, no sensitivity to maximal CP-violation is possible if $\sin^2 2\theta_{13}$ lies in this region.

The largest (rightmost) $\sin^2 2\theta_{13}$ value for which $\Delta\chi^2 \geq 9$ (or 25) represents the smallest $\sin^2 2\theta_{13}$ for which it is possible unambiguously to observe maximal CP-violation, although the sensitivity may be restored at lower values of $\sin^2 2\theta_{13}$. This value of $\sin^2 2\theta_{13}$ is labeled by an arrow in the figure. Conservatively, this value is taken as the benchmark for the (L, E_μ) optimisation. Figures will be presented at 3σ only since the results do not depend on the chosen

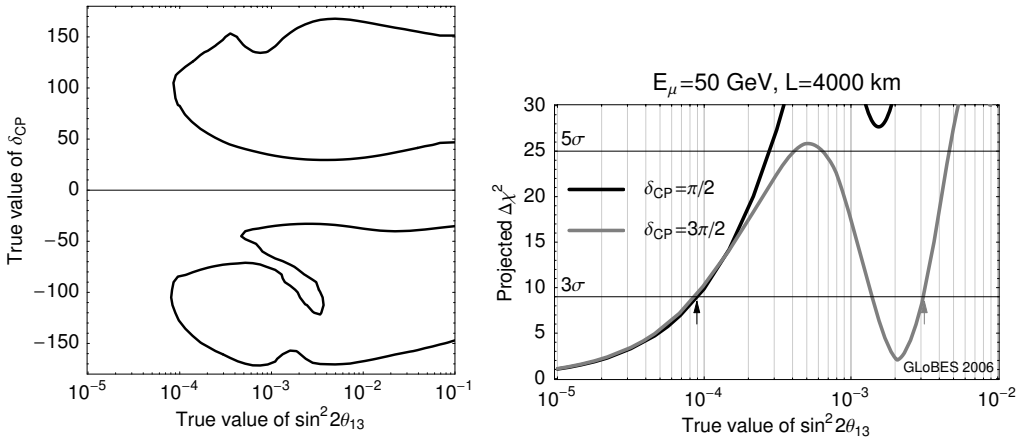

Figure 85: Left panel: 3σ CP-discovery potential for the 50 GeV Neutrino Factory at $L = 4000$ km. Right panel (Figure taken from reference [208]): Projected $\Delta\chi^2$ for the wrong choice of the hierarchy, computed for maximal CP-violation, $\delta = \pi/2$ and $\delta = 3\pi/2$, as a function of the true value of $\sin^2 2\theta_{13}$. The arrow represents the smallest $\sin^2 2\theta_{13}$ for $\delta = \pi/2$ (grey arrow) and $\delta = 3\pi/2$ (black arrow) above which CP-violation can be found for any value of $\sin^2 2\theta_{13}$. Right panel taken with kind permission of the Physical Review from figure 4 in reference [208]. Copyrighted by the American Physical Society.

confidence level.

Figure 86 shows the sensitivity to maximal CP violation (as defined above) for the two different choices of δ. For $\delta = \pi/2$, we find the optimal performance at about $3\,000 - 5\,000$ km for $E_\mu \gtrsim 30$ GeV, whereas larger energies are not required. When $\delta = 3\pi/2$, the absolute $\sin^2 2\theta_{13}$ reach is rather poor, once again the most conservative value of $\sin^2 2\theta_{13}$ above which CP violation can be determined has been chosen. In this case, degeneracies affect the CP-violation performance. It has been demonstrated in reference [700] that the magic baseline can be used to solve these degeneracies in the third and fourth quadrants of δ. If δ turned out to be in this region, to improve the sensitivity, a second baseline is needed to solve the sign-degeneracy, thus alleviating the effects of the π-transit.

5.4.2.3 Sensitivity to the mass hierarchy

The $\nu_e \to \nu_\mu$ oscillation probability in matter depends on the sign of Δm^2_{31}. A change of this sign is equivalent to a CP transformation, that is, interchanging the probability of neutrinos and anti-neutrinos. Thus, matter effects themselves induce a non-vanishing CP-odd asymmetry. The maximum sensitivity to the sign of Δm^2_{31}, using the PREM matter-density profile, is expected at a baseline $\mathcal{O}(7000)$ km. The asymmetries from different energy bins, however, peak at slightly different baselines. Therefore, spectral information can be used to improve the measurement of the sign of Δm^2_{31}.

The discovery potential for the normal 'true' mass hierarchy is shown at the 3σ confidence level in figure 87, evaluated for baselines of $L = 4000$ km and $L = 7500$ km. The sensitivity of the short and the long baselines are identical for $\delta \simeq -110°$. For this particular parameter

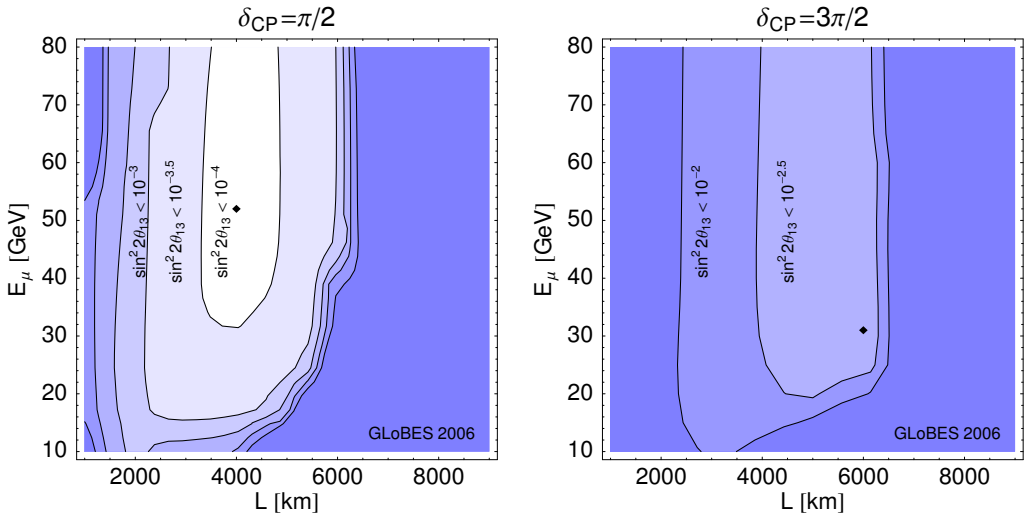

Figure 86: Sensitivity to maximal CP-violation ($\delta = \pi/2$ or $3\pi/2$) for a normal "true" mass hierarchy as a function of L and E_μ. The sensitivity is given as maximal reach in $\sin^2 2\theta_{13}$ at the 3σ 1 dof CL including correlations and degeneracies. The minima, marked by the diamonds, are $\sin^2 2\theta_{13} = 8.8{\cdot}10^{-5}$ (left panel) and $\sin^2 2\theta_{13} = 1.3{\cdot}10^{-3}$ (right panel). Taken with kind permission of the Physical Review from figure 5 in reference [208]. Copyrighted by the American Physical Society.

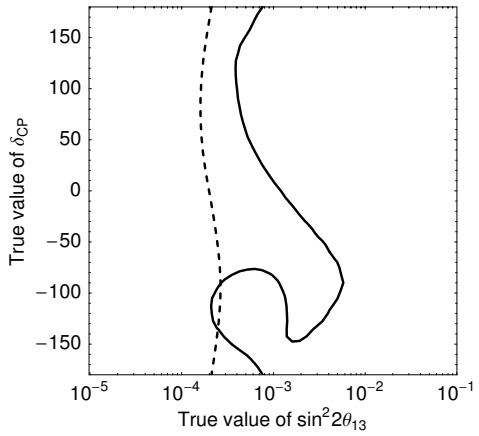

Figure 87: 3σ sensitivity to the sign(Δm^2_{31}) for normal 'true' mass hierarchy. Solid (dashed) lines refer to the $L = 4000$ km (7500 km) Neutrino Factory.

set it is also possible to lift the degeneracies at the short baseline. Compared to figure 19 of reference [218], the better sensitivity of the short baseline for $\delta \sim 100°$ depends on the efficiency function used, see section 5.4.1.1. For all other values of δ, the longer baseline has a better sensitivity.

The normal mass-hierarchy sensitivity reach in $\sin^2 2\theta_{13}$ as a function of baseline and parent muon energy is shown in figure 88 for different values of δ. The mass-hierarchy sensitivity increases with the baseline because of the matter effects. This means that for very small true values of $\sin^2 2\theta_{13}$, a very long baseline is required. The muon energy is of secondary interest, as

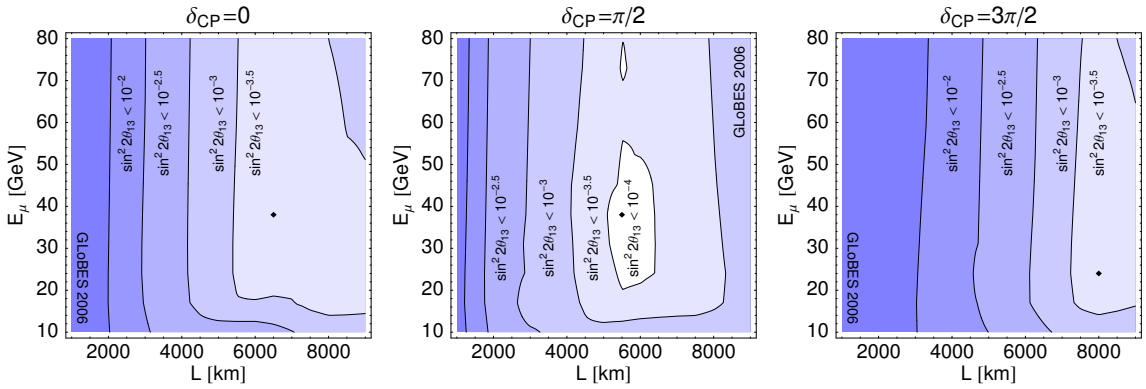

Figure 88: Sensitivity to a normal 'true' mass hierarchy for different values of δ (plot labels) as a function of L and E_μ. The sensitivity is given as the maximal reach in $\sin^2 2\theta_{13}$ at 3σ including correlations and degeneracies. The minima, marked by the diamonds, are $\sin^2 2\theta_{13} = 1.8 \cdot 10^{-4}$ (left panel), $\sin^2 2\theta_{13} = 6.7 \cdot 10^{-5}$ (middle panel), and $\sin^2 2\theta_{13} = 1.6 \cdot 10^{-4}$ (right panel). Taken with kind permission of the Physical Review from figure 6 in reference [208]. Copyrighted by the American Physical Society.

long as it is larger than about 20 GeV. In fact, for $\delta = \pi/2$ or very long baselines $L > 8\,000$ km, a muon energy larger than 50 GeV is dis-favoured because of the matter resonance at lower energies. In all cases, the magic baseline $L \simeq 7\,500$ km is near the optimum. For certain values of δ, there are 'gaps' in the $\sin^2 2\theta_{13}$ axis for which no unambiguous measurement of the hierarchy is possible, corresponding to a second minimum in $\Delta\chi^2$, as was the case in figure 85 (right panel). In figure 88, such gaps occur for $\delta = 3\pi/2$. In this case, only the largest value of $\sin^2 2\theta_{13}$ above which mass-hierarchy sensitivity can be achieved unambiguously is shown. Therefore, figure 88 (right panel) actually shows the ranges for the 'gapless' determination of the mass hierarchy. Thus, for very long baselines $L \gtrsim 7\,500$ km, the mass hierarchy can be determined over the full range of $\sin^2 2\theta_{13}$. Note that, in this case, such a baseline itself allows the degeneracies to be solved.

5.4.2.4 Measurement of the atmospheric parameters

Except for any suppressed three-flavour effects, a Neutrino Factory will be useful for the precision measurement of the leading atmospheric parameters Δm^2_{31} and θ_{23}. For simplicity, the case in which the true $\sin^2 2\theta_{13} = 0$ is considered in this section, because $\sin^2 2\theta_{13} > 0$ yields complicated correlations in the dis-appearance channel (cf., equation (33) in reference [213]). Results are presented for both hierarchies as a function of $|\Delta m^2_{31}|$ (see section 2.3 and reference [218] for a discussion of the subject). The solution for the inverted hierarchy, depending on the definition of the large mass-squared splitting, always differs somewhat from the original solution. However, there is no qualitative difference to the best-fit solution for $\sin^2 2\theta_{13} = 0$.

The ν_μ dis-appearance channel is extremely useful for the determination of the atmospheric-neutrino parameters Δm^2_{31} and $\sin^2 \theta_{23}$. An impressive accuracy can be attained, even with the standard setup. However, a better precision can be achieved with a lower muon identification threshold. This can be achieved by loosening the kinematic cuts needed for a good muon

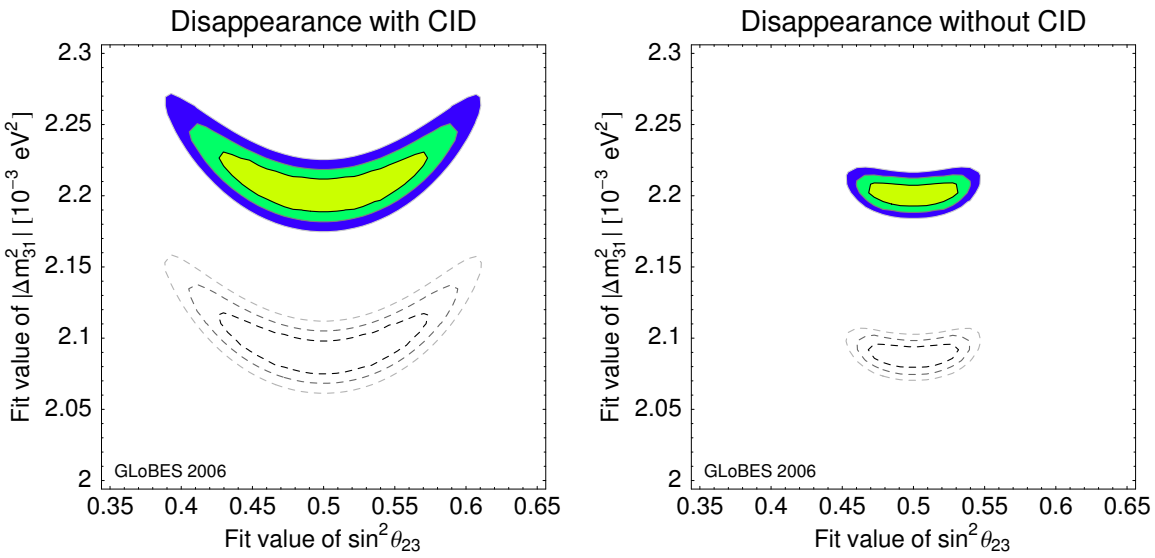

Figure 89: Comparison of (Δm^2_{31}-θ_{23})–precision between CID (left panel) and no CID (right panel) in the dis-appearance channel including all correlations (1σ, 2σ, 3σ, 2 d.o.f., $\sin^2 2\theta_{13} = 0$). The appearance information is added as usual with CID. Dashed curves correspond to the inverted hierarchy solution. Taken with kind permission of the Physical Review from figure 1 in reference [208]. Copyrighted by the American Physical Society.

charge identification. With no-CID, low-energy bins have a much higher efficiency, which in turn maximises the oscillatory signal. The price that must be paid is that neutrino and anti-neutrino rates have to be added in this case, which is not a major problem for the dis-appearance channel [588].

The raw data set is therefore split into two samples: the first with charge identification (CID), used for the appearance channel and modeled accordingly to reference [340]; the second without charge identification (no-CID). In this case the MINOS efficiencies and thresholds from references [192, 699] are used. Note that this implies two different energy-threshold functions. The fact that there are almost no events below about 4 GeV in the appearance channel is appropriately modelled. For details of the shape of the appearance channel threshold function, the efficiencies, and the model of the energy resolution, see appendix B.2 of reference [340]. By comparing the two panels of figure 89, it can be seen that it is extremely helpful not to use the CID information in the dis-appearance channel (cf. reference [740]).

Figure 90 shows the relative precision on Δm^2_{31} as a function of L and E_μ (at 1σ CL for 1 degree of freedom), including all parameter correlations, for a normal 'true' mass hierarchy. The upper end (left panel) and lower end (right panel) of the allowed region are given separately, because the $\Delta\chi^2$ is quite asymmetric in many cases. The first oscillation maximum can be found at:

$$L_{\max} \sim \left(564\,\frac{E}{\mathrm{GeV}}\right)\mathrm{km}\,, \tag{299}$$

which explains the optimum observed for $E_\mu \sim 10$ GeV at about 3 500 km (remember that the mean neutrino energy is somewhat below E_μ). For $E_\nu \geq 2$ GeV (below this energy no significant

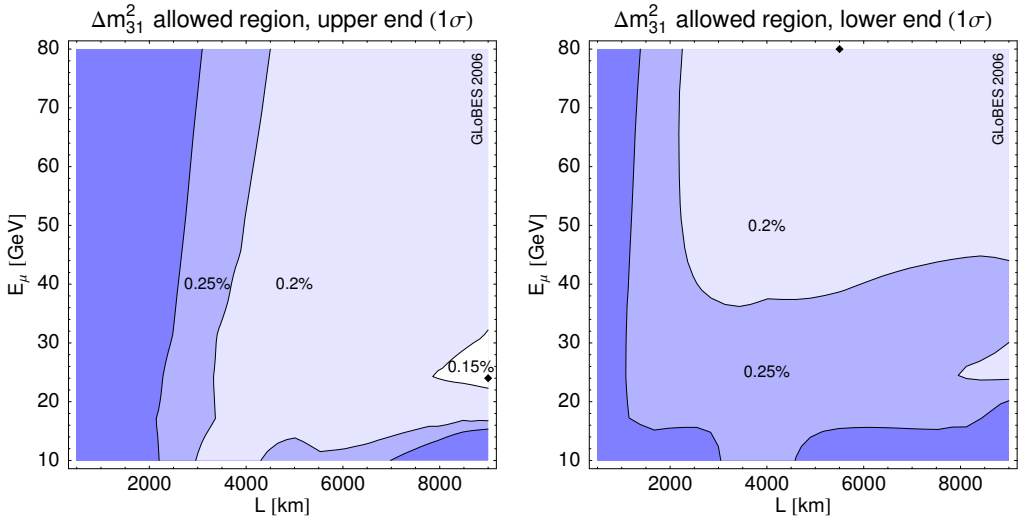

Figure 90: Relative precision on Δm^2_{31} (at 1σ) as a function of L and E_μ, including all parameter correlations for a normal mass hierarchy and $\sin^2 2\theta_{13} = 0$. The upper end (left panel) and lower end (right panel) of the allowed region are given separately because the $\Delta\chi^2$ is quite asymmetric. The minima, marked by the diamonds, occur at 0.14% (left panel) and 0.18% (right panel). Taken with kind permission of the Physical Review from figure 7 in reference [208]. Copyrighted by the American Physical Society.

rate is observed), $L \gtrsim 1\,000$ km is a necessary condition to be able to disentangle θ_{23} from Δm^2_{31}. If $L \ll L_{\max}$, θ_{23} and Δm^2_{31} are highly correlated. The separate analysis of the dataset without CID yields an extremely good (compared to, e.g., reference [741]) relative precision on Δm^2_{31} of the order of 0.2% for $L \gtrsim 3\,000$ km and $E_\mu \gtrsim 40$ GeV. This comes from the ability to resolve the oscillation maximum at low energies for long enough baselines and large enough data sets because of the lower threshold and the higher overall efficiency of the no-CID dis-appearance channel sample. Although the total rate decreases for longer baselines, more oscillation maxima can be resolved. Note that we have included sufficiently many bins at low energies to incorporate these effects.

It has been shown in reference [740] that the energy resolution has a significant influence on the accuracy on the leading parameters. In figure 91 the relative 1σ (full width) errors on $\sin^2\theta_{23}$ (left panel) and Δm^2_{31} (right panel) as a function of the baseline are shown. The different coloured lines correspond to different values of the energy resolution, σ, and the normalisation error of the signal, s. Interestingly, the signal error seems to be quite unimportant. The energy resolution, on the other hand, has a relatively large impact, especially at the shorter baselines. The dashed lines show the effect of increasing the uncertainty on the solar parameters to 10% (instead of 5%), the increased uncertainty leads to a considerable deterioration in precision. Irrespective of the error on the solar parameters and the energy resolution, longer baselines are preferred, especially for $\sin^2\theta_{23}$.

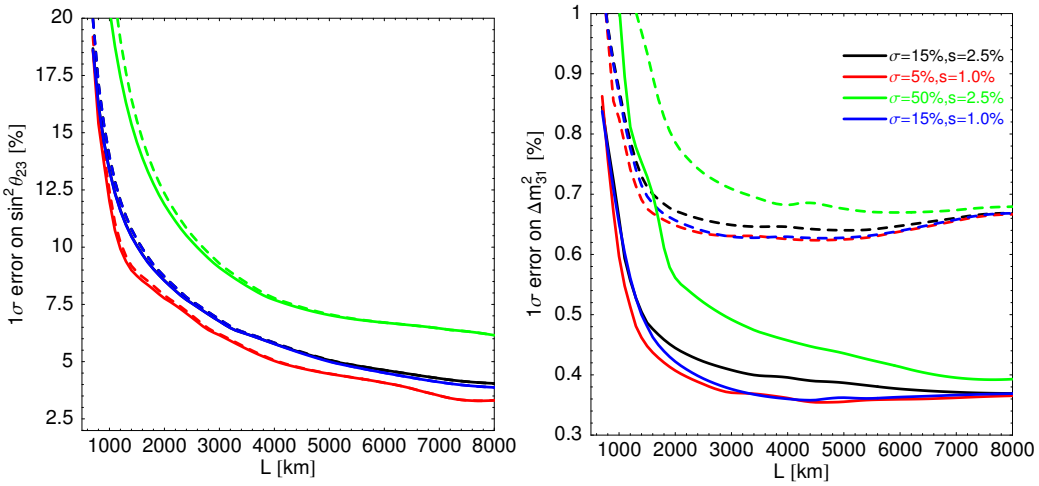

Figure 91: The relative $1\,\sigma$ (full width) errors on $\sin^2\theta_{23}$ (left panel) and Δm^2_{31} (right panel) as a function of the baseline. The result is shown for various combinations of energy resolution σ and systematic error s. The solid (dashed) lines assume an uncertainty on Δm^2_{21} and θ_{12} of 5% (10%). The results are computed for $\sin^2 2\theta_{13} \equiv 0$. Taken with kind permission of the Physical Review from figure 14 in reference [208]. Copyrighted by the American Physical Society.

5.4.2.5 Sensitivity to maximal θ_{23} and the octant-discovery potential

A natural explanation for maximal mixing ($\theta_{23} = \pi/4$) might involve a new symmetry between ν_μ and ν_τ. Therefore, the degree to which θ_{23} differs from $\pi/4$ is a powerful tool to discriminate between different neutrino-mass models [702, 742]. Figure 92 (left panel) shows the sensitivity to deviations from maximal θ_{23}. The curves have been computed for $\theta_{13} = 0$. Deviations as small as 10% of $\sin^2\theta_{23}$ from maximal mixing could be established at the $L = 4000$ km baseline for certain values of Δm^2_{31}. A better sensitivity may be obtained for $L = 7500$ km, however, in this case, the energy and baseline match the first oscillation peak in matter. The sensitivities reached are at the level of $\sin^2\theta_{23} \in [0.45 - 0.48]$ almost independent of the value of Δm^2_{31}, which means that deviations from maximal mixing of the order of 4% could be established.

Notice that, although this sensitivity is rather good, in general it is very difficult to determine the octant in which the atmospheric angle lies. It is quite difficult to break the $\theta_{23} \to \pi/2 - \theta_{23}$ symmetry induced by the leading term in the transition probability; the sub-leading terms that could help in lifting this degeneracy are strongly correlated. However, for $\theta_{13} \neq 0$, full advantage can be taken of matter effects in the muon-neutrino dis-appearance signal. The Neutrino Factory shows a certain (limited) capability to solve this degeneracy, irrespective of the baseline and the value of δ. The ability to resolve the octant is shown in figure 92 (right panel); longer baselines perform better and it is easier to resolve the octant if the true $\theta_{23} < \pi/4$.

Figure 93 shows the sensitivity to deviations from maximal mixing for a normal mass hierarchy and $\sin^2 2\theta_{13} = 0$ as a function of L and E_μ. The sensitivity is given as the relative deviation of $\sin^2\theta_{23}$ from 0.5 in per cent at 3σ, including all parameter correlations. Note that only the

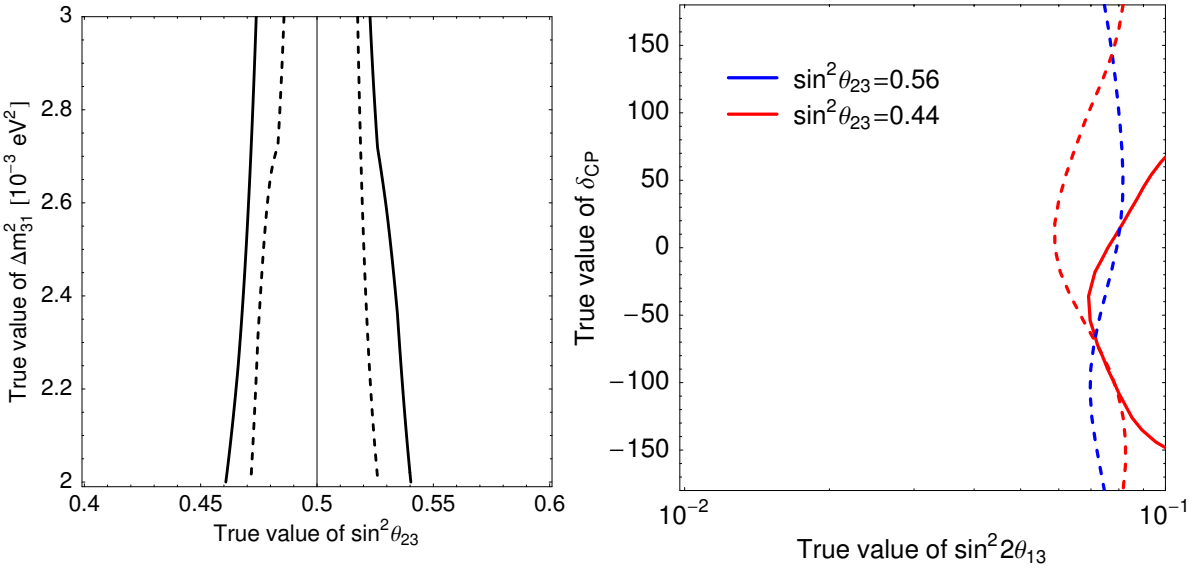

Figure 92: Left panel: 3σ sensitivity to deviations from maximal θ_{23};. Right panel: 3σ sensitivity to the θ_{23}-octant. Solid (dashed) lines refer to the $L = 4000$ km ($L = 7500$ km) Neutrino Factory.

upper branch $\sin^2\theta_{23} > 0.5$ is taken into account, because there is hardly any sensitivity to the $(\theta_{23}, \pi/2 - \theta_{23})$ ambiguity [211] and the problem is symmetric around $\theta_{23} = \pi/4$. A very similar qualitative and quantitative behaviour is found to that reported in reference [741]. However, the low-energy performance for very long baselines ($L \gtrsim 6\,000$ km) is significantly improved as the efficiencies at lower energies are better when including ν_μ dis-appearance data without CID. Most importantly, it is very hard to improve the sensitivity to deviations from maximal mixing with the standard setup, probably because of the rather large normalisation uncertainties that have been assumed. In particular, T2HK could achieve a similar quantitative performance [702].

5.4.2.6 Optimisation for large $\sin^2 2\theta_{13}$

Consider now large values of $\sin^2 2\theta_{13}$, $\sin^2 2\theta_{13} \simeq 0.1$ [$\theta_{13} \simeq 9°$], which means that it will be measured at the next generation of super-beam experiments. It is well known that for large $\sin^2 2\theta_{13}$, matter-density uncertainties affect the precision measurements of $\sin^2 2\theta_{13}$ and δ (see, e.g., references [340, 738]). Therefore, it is an interesting question whether the optimisation changes for large $\sin^2 2\theta_{13}$ depending on the matter-density uncertainty, and if the performance of conventional techniques can be exceeded.

For the mass hierarchy, the optimisation is hardly affected by the matter-density uncertainty. As a general rule, the mass hierarchy can be determined for all values of δ for $L \gtrsim 1\,000$ km almost independent of muon energy. Discovery of non-vanishing $\sin^2 2\theta_{13}$ is possible independent of δ. The CP-violation discovery potential is shown in figure 94 as a function of L and E_μ, for $\sin^2 2\theta_{13} = 0.1$ and a normal mass hierarchy, for two different values of the matter density uncertainty: 5% (left panel); and 1% (right panel).

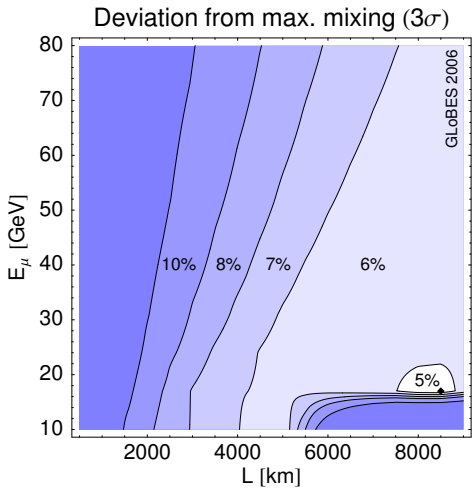

Figure 93: Sensitivity to deviations from maximal mixing for a normal mass hierarchy and $\sin^2 2\theta_{13} = 0$ as a function of L and E_μ. The sensitivity is given as relative deviation of $\sin^2 \theta_{23}$ from 0.5 in per cent at 3σ including all parameter correlations, where only the upper branch $\sin^2 \theta_{23} > 0.5$ is taken into account. The minimum, marked by a diamond, is at 4.2%. Taken with kind permission of the Physical Review from figure 8 in reference [208]. Copyrighted by the American Physical Society.

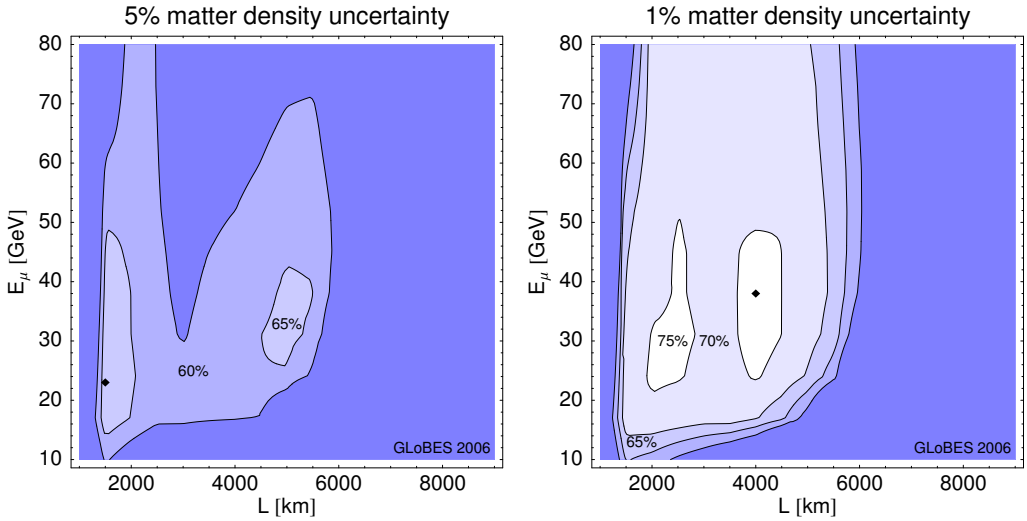

Figure 94: Fraction of (true) δ as function of L and E_μ for the measurement of CP-violation for $\sin^2 2\theta_{13} = 0.1$ and a normal mass hierarchy (3σ, including all parameter correlations and degeneracies). The left panel corresponds to a matter density uncertainty of 5%, and the right panel to a matter density uncertainty of 1%. The maxima, marked by the diamonds, are at 68% (left) and 77% (right). Taken with kind permission of the Physical Review from figure 9 in reference [208]. Copyrighted by the American Physical Society.

The maximum achievable CP-fraction depends on the matter-density uncertainty, and is only marginally affected by the choice of baseline for baselines between 1 500 and 5 500 km for small matter-density uncertainty. A very peculiar behaviour of for larger matter-density uncertainty can be observed in the left panel of figure 94. A matter density uncertainty of $\sim 5\%$ is more realistic with the present level of understanding [737, 738, 743]. In particular, the combination $L = 3\,000$ km and $E_\mu = 50$ GeV, which is often considered, performs especially badly. It is not trivial to explain this loss of sensitivity. First, smaller muon energies are preferred since matter density uncertainties hardly affect the leading $\sin^2 2\theta_{13}$-term close to the matter resonance (which is acting as a background to the δ measurement; see figure 3 of reference [738]). Second, shorter baselines are preferred since matter effects are smaller there and, therefore, the impact of density uncertainties is reduced. Third, there is a second maximum for $L \simeq 5\,000$ km, where the CP-asymmetric term is enhanced for $E \sim 10$ GeV, equation (299); remember that the mean neutrino energy is considerably below the muon energy). These factors together cause the structure in the left panel of figure 94.

Comparison of figure 94 (right panel) with figure 86(left) shows that for small values of the matter-density uncertainty, the 'usual' optimisation for CP violation is qualitatively recovered. The optimal performance for small matter density uncertainties is reached in a wide range of L and E_μ.

5.4.3 Solving degeneracies

Various solutions have been proposed to reduce the parametric correlations and degeneracies observed in the simultaneous measurement of θ_{13} and δ at the Neutrino Factory. The design of the magnetised iron detector used to measure golden-channel wrong-sign muons and the tight kinematic cuts applied to reduce the background, result in very few events being collected in the energy region below 10 GeV. This region, however, is where the first oscillation peak lies for neutrinos produced in the decay of 50 GeV muons. Unfortunately, having sufficient statistics above and below the oscillation peak has been shown to be the key to solve many of the parametric degeneracies. This is why Neutrino Factory experiments suffer from this problem more than super-beam or beta-beam experiments, for which the results are limited by statistics.

The different methods that may be used to resolve the correlations and degeneracies will be discussed under three headings:

- Combining data collected using several magnetised iron detectors of the type described in section 5.4.1.1 placed at a number of baselines;
- Combining different channels collected using the detectors described in sections 5.4.1.2 and 5.4.1.3; and
- Improving the performance of the detector described in section 5.4.1.1.

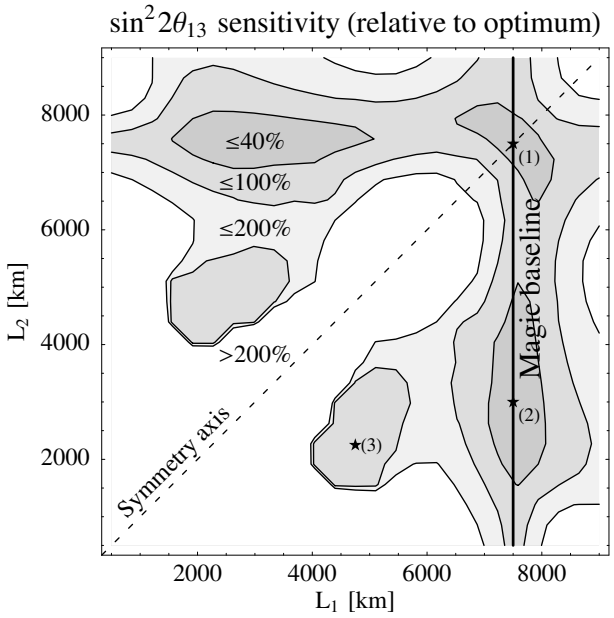

Figure 95: The $\sin^2 2\theta_{13}$ sensitivity limit relative to the optimum value of $5.9 \cdot 10^{-5}$ at $L_1 = L_2 \simeq 7\,500$ km. It is plotted at the 3σ confidence level as function of the baselines L_1 and L_2 heading from the 50 GeV Neutrino Factory towards two 25 Kton detectors. The sensitivity limit includes full correlations and degeneracies. The true parameters for this figure are $\Delta m^2_{31} = 3 \cdot 10^{-3}\,\mathrm{eV}^2$, $\theta_{23} = \pi/4$, $\Delta m^2_{21} = 7 \cdot 10^{-5}\,\mathrm{eV}^2$ and $\sin^2\theta_{12} = 0.28$. Taken with kind permission of Physical Review from figure 1 in reference [43]. Copyrighted by the American Physical Society.

5.4.3.1 Combining baselines

The first option to resolve the degeneracies is to combine golden-muon signals from experiments located at different baselines. It was recognised very early in the literature that certain types of correlations are less pronounced if data from different baselines are analysed together, see for example [205,206]. It turns out that the most useful additional baseline is around $L \sim 7500$ km, the magic baseline [43]. At this distance, matter effects completely suppress any three-flavour effect and allow for an unambiguous measurement of $\sin^2 2\theta_{13}$ and of the mass hierarchy (see also section 5.4.2.3). In figure 95, the sensitivity to $\sin^2 2\theta_{13}$ is shown for a Neutrino Factory with two baselines as a function of the two baselines. Clearly, the combination of $L_1 \sim 3\,000$ km and $L_2 = 7500$ km has a very good performance (star labeled '(2)'). The other possible choice, i.e. putting all the detector mass at $L = 7500$ km (star labeled '(1)'), is very good for $\sin^2 2\theta_{13}$ measurements but would have no sensitivity to CP-violation at all. The third possible solution '(3)' is fine tuned, as shown in figure 2 of [43].

The combination, $L \sim 3\,000$ km and $L \sim 7\,000$ km, is very effective; it allows for a clean measurement of $\sin^2 2\theta_{13}$ and of the sign of Δm^2_{31} at the magic baseline and for a good measurement of δ at the shorter baseline, where the (θ_{13}, δ) correlation is strongly reduced because θ_{13} is already constrained by the magic-baseline data. A second detector at 3 000 km in combination with the first at or around the magic baseline significantly improves the $\sin 2\theta_{13}$ sensitivity, by about an order of magnitude (the results do not change significantly if the detector is anywhere

between 3 000 km to 5 000 km). The sensitivity is not strongly affected by the exact value of the location of the first detector in the range 6 000 km to 9 000 km either [744].

5.4.3.2 Combining channels

1. *The silver channel:* In reference [44] it was noticed that muons arising from τ decay when τs are produced via a $\nu_e \to \nu_\tau$ transition show a different (θ_{13}, δ) correlation from those coming from $\nu_e \to \nu_\mu$ transitions. By using an Emulsion Cloud Chamber (ECC) capable of τ-decay vertex recognition, it is possible to use the complementarity of the information from $\nu_e \to \nu_\tau$ and from $\nu_e \to \nu_\mu$ to solve the intrinsic degeneracy. The relatively small mass of the ECC, the small ν_τ-nucleon cross section, the small $\tau \to \mu$ branching ratio, and the decay-vertex requirement, cause the statistical significance of the silver channel to be much lower than that of the golden channel. Silver muons, in combination with golden muons, are also extremely helpful in dealing with the $[\theta_{23}, \pi/2 - \theta_{23}]$ ambiguity, since the leading term in $P(\nu_e \to \nu_\tau)$ is proportional to $\cos^2\theta_{23}$, whereas the analogous term in $P(\nu_e \to \nu_\mu)$ is proportional to $\sin^2\theta_{23}$. However, the sensitivity of the silver/golden channel combination to the θ_{23}-octant strongly depends on the value of θ_{13}.

   The addition of the silver-channel data does not affect the golden-channel baseline optimisation. The golden channel suffers significantly from degeneracies at the 4 000 km baseline, in particular for true $\delta = 3\pi/2$. For $\sin^2 2\theta_{13} \sim 3 \times 10^{-3}$, the sensitivities to maximal CP-violation and to the mass hierarchy are lost, and a sensitivity gap appears.

   For a golden channel setup fixed to $\mathrm{E}_\mu = 50\,\mathrm{GeV}$ and $\mathrm{L}_{\mathrm{MID}} = 4\,000\,\mathrm{km}$, the optimal ECC baseline to close the sensitivity gap is found between 2500 and 5 000 km. It will therefore be assumed in the following that the ECC detector is located at the second golden-channel detector baseline (3 000 km).

2. *The $\nu_\mu \to \nu_\tau$ channel:* Using the ECC detector, it is possible to disentangle the (dominant) $\nu_\mu \to \nu_\tau$ appearance oscillation from the ν_μ disappearance channel. This oscillation probability, which is the main goal of the CNGS experiments, is extremely sensitive to the atmospheric parameters θ_{23} and Δm^2_{31}. In principle, it could be used to complement the information from the ν_μ disappearance channel in the MID detector to solve the octant-degeneracy.

   A detailed study of this channel at the ECC is lacking. A preliminary analysis shows that the performance of this channel is similar to the ν_μ disappearance channel at the MID detector.

3. *The platinum channel:* The platinum channel is the T-conjugate of the golden channel. Therefore, the (L, E_μ)-optimisation of the platinum channel is the same as that of the golden channel. It will be assumed that the platinum-channel detector should be sited at the same baseline as the golden-channel detector.

   As for the silver channel, the platinum channel is strongly limited by statistics. In the left panel of figure 96, $\Delta\chi^2$ (with respect to the absolute χ^2 minimum) values at the intrinsic-degeneracy and sign-degeneracy minima are shown as a function of the upper

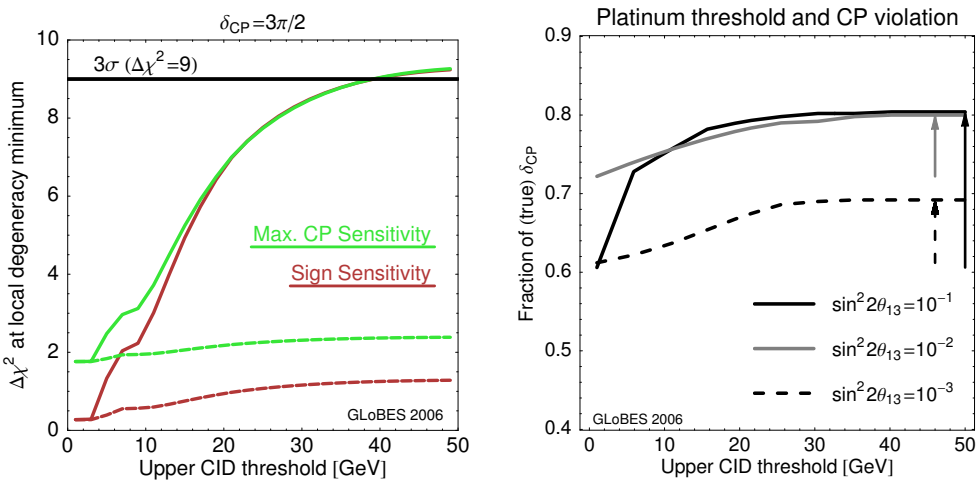

Figure 96: Left panel: Dependence of $\Delta\chi^2$ value at the intrinsic- and sign-degeneracy minima (light gray/green and dark gray/red, respectively) on the upper electron CID threshold, for input values $\sin^2 2\theta_{13} = 2.5 \times 10^{-3}$ (i.e. $\theta_{13} \sim 1.5^\circ$) and $\delta = 3\pi/2$. The baseline is assumed to be 4 000 km and $E_\mu = 50$ GeV. Solid (dashed) lines stand for the improved (standard) platinum detector, with 50 (15) Kton mass and 40% (20%) efficiency. Right panel: The fraction of (true) δ for which CP-violation can be discovered at 3σ as a function of the upper electron CID threshold (for a normal mass hierarchy), combining the 50 Kton golden detector at $L = 4\,000$ km and the improved 50 Kton platinum detector with 40% efficiency, for $E_\mu = 50$ GeV. Different curves refer to different values of $\sin^2 2\theta_{13}$. The arrows refer to the improvement in the physics potential by using the platinum channel. Taken with kind permission of the Physical Review from figures 16 and 17 in reference [208]. Copyrighted by the American Physical Society. Figures taken from reference [208].

electron/positron-charge identification threshold for $\sin^2 2\theta_{13} = 2.5 \times 10^{-3}$. Recall that, for the standard platinum-channel detector [210], the upper threshold has been fixed to 7.5 GeV. As can be seen in the figure, for a 15 Kton magnetised liquid-argon (LAr) detector the $\Delta\chi^2$ at the degenerate solutions does not change a lot. This is a severe limitation of this channel due to the small size of the available data set. On the other hand, for a 50 Kton magnetised LAr detector, both degeneracies are lifted if the upper electron CID threshold is increased above 30 GeV. In this case, the sensitivity gap can be closed completely. This means that only with both a significant increase in the detector mass and in the electron CID threshold this channel can help in solving degeneracies for low θ_{13}. The 15 Kton LAr detector, as well as the 5 Kton ECC detector, can contribute for intermediate values of θ_{13} but not for such low values.

The platinum channel may be used to solve degeneracies both for intermediate and large values of $\sin^2 2\theta_{13}$. In figure 96(right), the CP-fraction for which CP-violation can be discovered as a function of the upper CID threshold is shown. The dependence of the discovery potential on the threshold is relatively shallow for $\sin^2 2\theta_{13} \lesssim 10^{-2}$, whereas for larger $\sin^2 2\theta_{13}$ a 6 GeV upper threshold can increase the CP-fraction by about 10%. This means that if $\sin^2 2\theta_{13}$ turns out to be large, a relatively low upper threshold could be acceptable. However, if it is intended to use the platinum-channel detector as a degeneracy-solver, the threshold will need to be as high as 20 to 30 GeV.

4. **The ν_e disappearance channel** While only electron-neutrino (and anti-neutrino) appearance has been considered in this section, one could also think about implementing the ν_e disappearance channel. The impact of this channel for $\sin^2 2\theta_{13} = 0.1$ has been tested and some improvement has been observed, though it is not as beneficial as the platinum-appearance channel. If one cannot achieve CID to the assumed level, the ν_e-disappearance channel alone without CID can provide useful information. The ν_e-disappearance channel with CID performs worse than that without CID (as was the case for the ν_μ-disappearance channel). The ν_e-disappearance is not considered further in the rest of this section. If ν_e detection is eventually implemented, the disappearance-channel data should be exploited as well. The main issue determining its usefulness is, of course, how well systematic uncertainties can be controlled.

Combination of the additional channels

The combination of the data from the additional channels with golden muons is now discussed in terms of the three observables: sensitivity to $\sin^2 2\theta_{13}$; sensitivity to maximal CP-violation; and sensitivity to the mass hierarchy.

The relative contribution to the physics reach can be roughly understood by looking at the statistical significance of the various options. To this end, in table 17 the signal and background event rates (as well as the signal over the square root of the background) for two specific points in the parameter space, representing two conceptually different cases, $\sin^2 2\theta_{13} = 10^{-1}[\theta_{13} = 9^\circ]$ or $\sin^2 2\theta_{13} = 3 \times 10^{-3}[\theta_{13} = 1.6^\circ]$ are presented. For $\sin^2 2\theta_{13} = 10^{-1}$, the golden channel suffers from the matter density uncertainties. For $\sin^2 2\theta_{13} = 3 \times 10^{-3}$, on the other hand, the golden channel suffers from degeneracies. In both cases, additional channels could improve the Neutrino Factory performance (but are limited by the size of the data set). It can be seen from table 17 that the golden channel deserves its name, having the largest statistical significance for both values of $\sin^2 2\theta_{13}$. This is due to the fact that muons are relatively straightforward to detect and easy to distinguish from backgrounds. The silver channel has a much lower statistical weight and a relatively high background contamination. The event rates for the silver channel are also given at a ECC detector baseline of 732 km, the distance from CERN to Gran Sasso where the OPERA detector will be located. No data are shown for the μ^--stored phase, see reference [728]. It can be seen that the variation of the baseline does not have a big impact on the total rates. Notice that the size of the platinum-channel data set is larger when the Neutrino Factory operates in μ^--polarity, when the golden channel is weaker because of the matter effect suppression. Thus, it acts as an anti-neutrino mode without matter-effect suppression.

The performance of the golden channel can also be improved by a second detector at the magic baseline, as was stressed in section 5.4.3.1. Therefore, the golden-channel event rates are also given at the magic baseline for comparison. Despite the strong reduction in the neutrino flux, there are still a very large number of golden muons, and the signal-to-background ratio is still much better than for the silver or platinum channels. It may therefore be expected that additional channels will only be useful in those regions of the parameter space where the

$\sin^2 2\theta_{13} = 10^{-1}$	Signal	Background	$S/\sqrt{B}$
Golden	31000 (6000)	39 (73)	5000 (700)
Silver	210 (–)	32 (–)	37 (–)
Silver@732km	260 (–)	110 (–)	25 (–)
Platinum	4 (120)	140 (110)	0.3 (11)
$(\text{Golden})_{\text{MB}}$	5100 (340)	9 (17)	1700 (83)

$\sin^2 2\theta_{13} = 3 \times 10^{-3}$	Signal	Background	$S/\sqrt{B}$
Golden	1900 (450)	39 (72)	300 (53)
Silver	3 (–)	33 (–)	0.5 (–)
Silver@732km	1.7 (–)	110 (–)	0.2 (–)
Platinum	1 (5)	170 (110)	0.08 (0.5)
$(\text{Golden})_{\text{MB}}$	200 (10)	9 (17)	67 (2.4)

Table 17: The (rounded) event rates in the μ^+ (μ^-)-stored phase for the golden channel and the standard silver and platinum channels at a baseline of 4 000 km and for $E_\mu = 50\,\text{GeV}$. For comparison reasons, we also give the golden channel event rates at the magic baseline ($L = 7500$ km) and the silver channel event rates at $L = 732$ km. The upper table is calculated for $\sin^2 2\theta_{13} = 10^{-1}$ and the lower table for $\sin^2 2\theta_{13} = 3 \times 10^{-3}$. The remaining oscillation parameters are fixed as in equation (298), with $\delta = 0$.

performance of the Neutrino Factory is strongly affected by either degeneracies or correlations (i.e., for intermediate θ_{13}).

For $\sin^2 2\theta_{13} = 3 \times 10^{-3}$, the combination of the silver or platinum channel with the golden channel data is comparable, with a slightly better impact of the golden/silver combination on the sensitivity to the mass hierarchy. For $\sin^2 2\theta_{13} = 10^{-1}$, however, the golden/platinum combination has a rather larger margin of improvement with respect to the golden/silver combination. The reason for this lies in the τ production threshold which suppresses the most useful silver events around the first oscillation maximum. Thus, an increase in the size of the silver data set is not helpful. On the other hand, if one can go beyond the 15 Kton magnetised LAr detector and increase the upper electron CID threshold up to 30 GeV, the CP-discovery potential of the Neutrino Factory is significantly improved.

Although the additional channels do not improve significantly the θ_{13} sensitivity of the Neutrino Factory, they help in solving some of the degeneracies. This is shown in figure 97, where the sensitivity to the mass hierarchy (left panel) and to maximal CP-violation (right panel) are presented for different combinations of golden, silver, and platinum channels as a function of the (common) baseline. The plots refer to $\delta = 3\pi/2$, a value for which the degeneracy problem is severe. Notice that the plots (taken from reference [208]) show golden data combined with data from the silver* and platinum* detectors. The latter refers to the 50 Kton upgrade of the platinum detector described in section 5.4.1.3. The former to the silver detector with a data set 5 times as large as that assumed above. Since solving the degeneracies for intermediate θ_{13} does not rely significantly on the statistical weight of the data, the results shown would not change much using standard silver and platinum detectors.

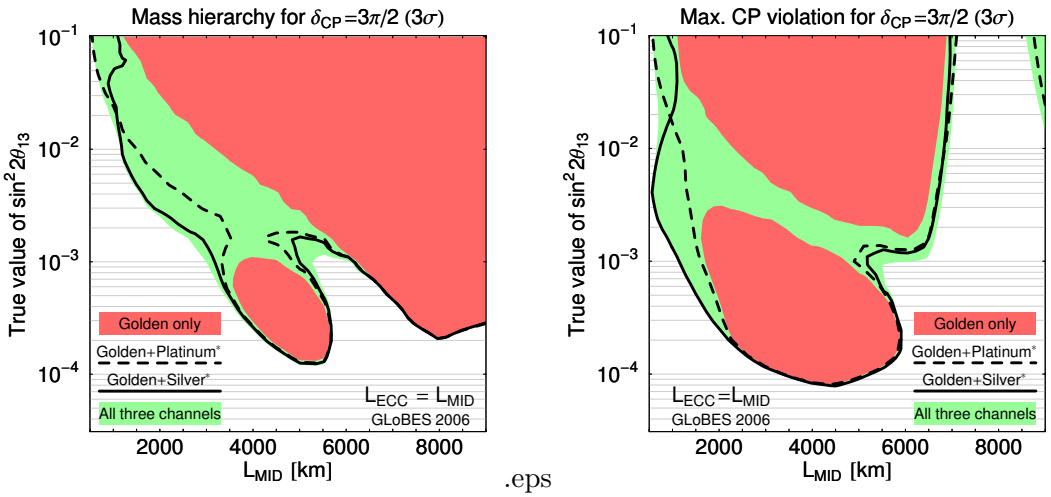

Figure 97: The sensitivity to mass hierarchy (left pane) and to maximal CP-violation (right panel) at 3σ for the combination of different channels as given in the plot legends, for $\delta = 3\pi/2$. All correlations and degeneracies are taken into account. Taken with kind permission of the Physical Review from figure 20 in reference [208]. Copyrighted by the American Physical Society.

For the sensitivity to the mass hierarchy figure 97 (left panel), the additional silver- and platinum-channel data can indeed improve the sensitivity and close the sensitivity gap between the dark shaded regions in a large range of baselines. The 4 000 km baseline with channel combination becomes as good as the magic baseline to measure the mass hierarchy, for $\delta \approx 3\pi/2$. It has been checked that the impact of the additional channels is small for $\delta = 0$ and negligible for $\delta = \pi/2$.

For the sensitivity to maximal CP-violation figure 97 (right panel), it can also be seen that the combination of silver and/or platinum channels with the golden one completely closes the degeneracy gap. For L $\approx$ 4 000 km and $\delta = 3\pi/2$, CP-violation can be determined unambiguously for $\sin^2 2\theta_{13}$ as small as $10^{-4}[\theta_{13} = 0.3^\circ]$. It has been checked that the impact of the additional channels is negligible for $\delta = \pi/2$ for baselines around 4 000 km, since the effect of degeneracies is small for that specific value of δ.

In addition to the baseline optimisation, the dependence of the sensitivities on the energy of the stored muons can be studied. As far as the sensitivity to the normal mass hierarchy is concerned, the variation of the maximal reach in (true) $\sin^2 2\theta_{13}$ is of minor importance, and even improves slightly for the choice of smaller muon energy. For the golden channel only, or golden and platinum channels combined, the maximum is approximately reached for $E_\mu \sim 30\,\mathrm{GeV}$. A sensitivity-gap for $\sin^2 2\theta_{13} \in [1,5] \times 10^{-3}$ cannot be cured by the golden channel alone, independent of E_μ. However, if combined with the silver or platinum channel, the sensitivity-gap can be closed for parent energies $E_\mu \gtrsim 20\,\mathrm{GeV}$ (golden/platinum) or larger than about $E_\mu \gtrsim 25\,\mathrm{GeV}$ (golden/silver). For the platinum combinations (or all channels combined), the additional information not only allows a lower energy neutrino beam to be used, but also favours a lower parent energy of $E_\mu \sim 30\,\mathrm{GeV}$. On the other hand, when only the silver-channel data are used, the τ-production threshold disfavours low muon energies. For the sensitivity to maximal

CP violation, qualitatively the same results as for the mass hierarchy are obtained.

5.4.3.3 Improved detector

A Neutrino Factory requires a large investment in accelerator R&D and infrastructure. A joint optimisation of both accelerator and detector, however, has been neglected so far and it is worth considering whether significant gains in performance can be achieved with an increased emphasis on the detector side of the experiment. The main problem is the lack of reliable performance predictions for large magnetic detectors. The goal of this section is not to prove the feasibility of certain detector properties or parameters, but to demonstrate the possible gain in the physics reach if certain properties can be achieved. Therefore, the following statements or assumptions about the detector performance are not to be mistaken for a claim of feasibility, but should be understood as desirable improvements; the extent to which such performance can be achieved must be determined by extensive R&D. Choices for the various factors affecting the detector performance have been made with the intention that the assumptions are not too far away from what may be possible [745]. However, the effect of varying the detector-performance assumptions on the physics performance will be discussed in some cases. These results may serve as guidelines to focus efforts in detector R&D. They should be interpreted as indicating the 'optimisation potential of the detector', rather than as the 'optimised detector' per se.

1. *Improved detector assumptions:* The main limitation of a Neutrino Factory compared to other neutrino facilities comes from the fact that the standard detector has a relatively high neutrino-energy threshold (necessary for muon charge identification), which makes the first oscillation maximum basically inaccessible (*cf.*, reference [42]). All measurements have to be performed in the high energy tail of the oscillation probability, off the oscillation maximum. This is the reason why it is the facility most affected by the eightfold-degeneracy [212, 340]. Amongst the possible solutions to this problem, the physics reach of a 'better detector' has been considered [340]. In the following, reference [340] is taken as a starting point and discuss improvements in the detection threshold and energy resolution.

   Achieving a lower threshold probably requires a finer granularity of the detector, i.e. , a higher sampling density in the calorimeter. This should at the same time improve the energy resolution of the detector. The energy resolution is parameterisation by $\sigma_E\,[\mathrm{GeV}] = [\sigma\,\sqrt{E_\nu} + 0.085]\,\mathrm{GeV}$ with $\sigma = 0.15$ for the energy resolution (as compared to $\sigma_E = 0.15\,E_\nu$ in section 5.4.1.1, corresponding to $\sigma \simeq 0.5$), where the constant part models a lower limit from Fermi motion. For definiteness, the neutrino energy threshold is taken to be 1 GeV and a constant efficiency of 0.5 is taken for all neutrino appearance events above threshold. The background model assumes that the threshold will only affect events below the threshold, not events above, i.e. , there is down-feeding of background but no up-feeding. The reason behind this assumption is that a mis-identified neutral-current event should always have a reconstructed energy which is lower than the true energy, since there is missing energy in every neutral current event. This setup of combined lower threshold, increasing background

fraction, and better energy resolution will be called 'optimal appearance'. Similar numbers are quoted for the NOνA detector [16].

The following setups will be compared:

(a) *Standard detector:* as described in section 5.4.1.1;

(b) *Optimal appearance:* $\sigma = 15\%$, $\beta = 10^{-3}$, full efficiency of 50% already reached at 1 GeV;

(c) *Better threshold:* Same as (b), but $\sigma = 50\%$ as for (a); and

(d) *Better energy resolution:* Same as (b), but old threshold from (a).

As before, it is assumed that the systematic uncertainty on the background is 20% and the corresponding uncertainty for the signal is $s = 2.5\%$ for all these setups. To a very good approximation, it is safe to say that varying s from 1% to 5% does not change the results at all. On the other hand, the weight factor β is only important so long as it does not become too large, but even an increase of a factor of 10 is not devastating. Note, however, that the error on the background is quite conservative compared to the numbers usually quoted for super-beams. Most certainly, the impact of an increased background will be strongly reduced by reducing this uncertainty. For more details see figure 13 of [208].

2. *Impact on physics reach:*

Changing the detector threshold by a significant amount certainly should affect the choice of the optimal baseline and muon energy. In the left panel of figure 98, the sensitivity to $\sin^2 2\theta_{13}$ at 5σ is shown for the optimal detector as a function of the baseline and muon energy, including the effect of degeneracies. The maximal reach, marked by the diamond, is $\sin^2 2\theta_{13} = 1.1 \cdot 10^{-4}$. It is reached for $L \sim 7\,500$ km and $E_\mu = 24$ GeV. Compared to figure 84 (lower right), a second maximum in the sensitivity is present at shorter baselines even when degeneracies are included. Energies as low as 20 GeV work reasonably well for both baselines. It is interesting to see whether the improvements are mainly due to the lower threshold or the better energy resolution. This is illustrated in figure 98(right), where different combinations of lower threshold or better energy resolution are compared with the standard setup on the basis of the sensitivity to $\sin^2 2\theta_{13}$ (in this figure, E_μ is fixed to 50 GeV). The main effect for the $\sin^2 2\theta_{13}$ sensitivity improvement clearly comes from a lower energy threshold, the better energy resolution playing a very minor role. Note that the maximum in this figure occurs at around 3 000 km for the optimal detector because the muon energy has been fixed. A comparison to figure 98(left) shows that this is not the global maximum in (L, E_μ)-space.

The behaviour of the sensitivities to CP-violation and mass hierarchy is substantially the same, as is shown in figure 99 In this figure $\delta = 3\pi/2$ was chosen, since for this value degeneracies have a larger impact than for $\delta = \pi/2$ and any improvement is more obvious. The left panel shows the sensitivity to the mass hierarchy at 3σ, where sensitivity is given within the shaded/marked areas. The red (dark) shaded regions show the results for the standard detector whereas the blue (light) shaded regions show the result for the optimal setup. Clearly, the accessible range in $\sin^2 2\theta_{13}$ improves and the constraints on the baseline

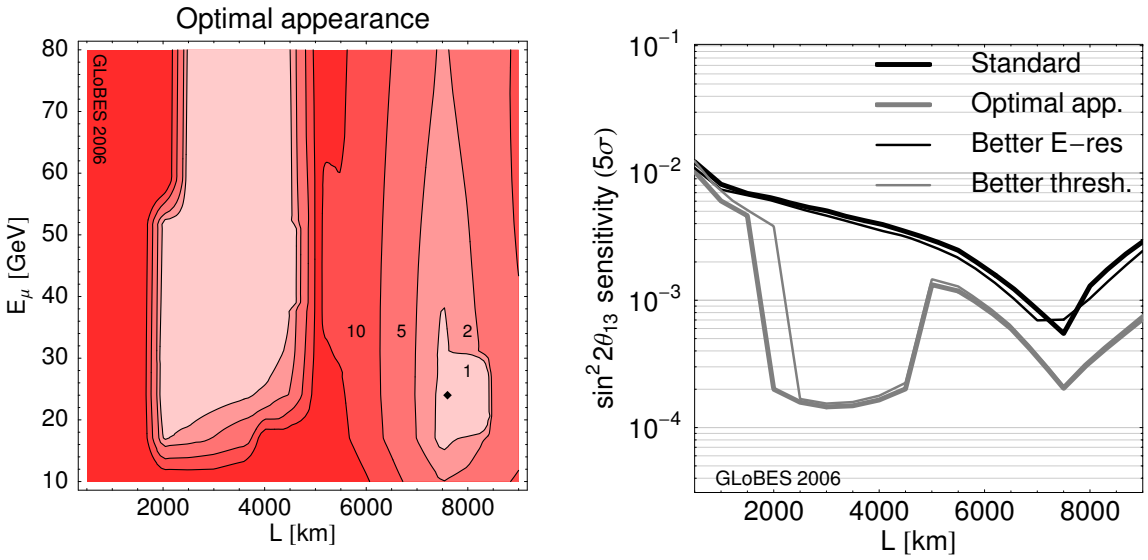

Figure 98: $\sin^2 2\theta_{13}$ sensitivity at 5σ for several improved detector options. The left hand panel shows the $\sin^2 2\theta_{13}$ sensitivity as a function of baseline and muon energy relative to the maximal reach for the 'optimal appearance' detector including degeneracies similar to figure 84 (lower right). The maximal reach, marked by a diamond, is $\sin^2 2\theta_{13} = 1.1 \cdot 10^{-4}$. The right hand panel shows the $\sin^2 2\theta_{13}$ sensitivity as a function of the baseline for different detector options (see plot legend) and fixed $E_\mu = 50\,\text{GeV}$. Note that the better energy resolution option uses a different background model, which leads to the crossing with the 'standard' curve at $L \sim 7\,500$ km. Taken with kind permission of the Physical Review from figure 10 in reference [208]. Copyrighted by the American Physical Society.

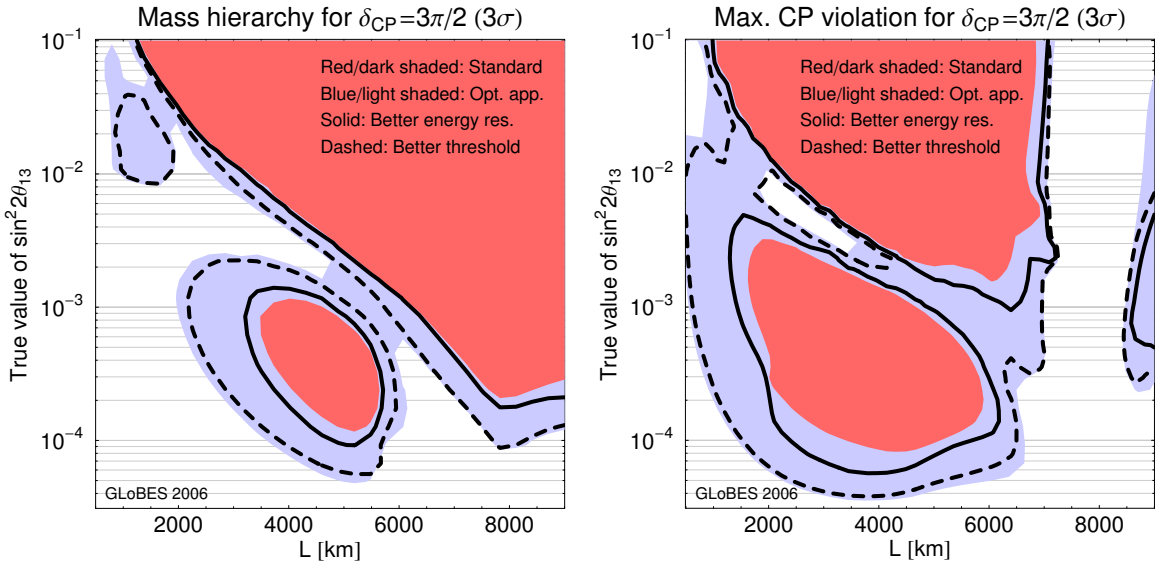

Figure 99: The normal mass hierarchy (left panel) and CP-violation (right panel) sensitivities (at 3σ) as a function of baseline and true $\sin^2 2\theta_{13}$ for a normal hierarchy and $\delta = 3\pi/2$, different detector options (see legend) and fixed $E_\mu = 50\,\mathrm{GeV}$. Sensitivity is given in the shaded/enclosed regions. Taken with kind permission of the Physical Review from figure 11 in reference [208]. Copyrighted by the American Physical Society.

become somewhat weaker for the better detector. The difference between having only a better threshold (dashed line) and only a better energy resolution (solid line) is quite large. The same happens for the sensitivity to CP-violation, figure 99 (right panel). For all the sensitivities considered, large improvements come from a lower threshold, while the improved energy resolution makes only a minor contribution. The choice of the optimal L and E_μ seems to be essentially unaffected by a better detector.

At this stage it is not clear how difficult it will be to push the threshold to lower values. The previous sections have demonstrated that the measurement of δ is the most demanding for the detector. Figure 100 shows the CP-violation discovery potential at 3σ (depicted as the CP-fraction) for several low energy thresholds, for the optimal appearance detector. Lowering the threshold to 5 GeV is enough to resolve most of the degeneracies at intermediate θ_{13}. On the other hand, a significant gain is observed for large θ_{13} for thresholds below 5 GeV.

One important issue in this context is the performance of a Neutrino Factory if $\sin^2 2\theta_{13}$ turns out to be large, $\sin^2 2\theta_{13} \sim 10^{-1}$. There will be information regarding this case from reactor experiments by around 2010 (see references [196,601] for Double Chooz). Note that $\sin^2 2\theta_{13}$ discovery and mass hierarchy measurement are rather easy for large values of $\sin^2 2\theta_{13}$, which means that the optimisation is focused on the measurement of δ.

Figure 101 shows the fraction of δ for which the sensitivity to CP violation is at or above the 3σ level as a function of the baseline for $\sin^2 2\theta_{13} = 10^{-1}$ and different combinations of experimental setup and matter-density uncertainty. For comparison the CP-fraction for

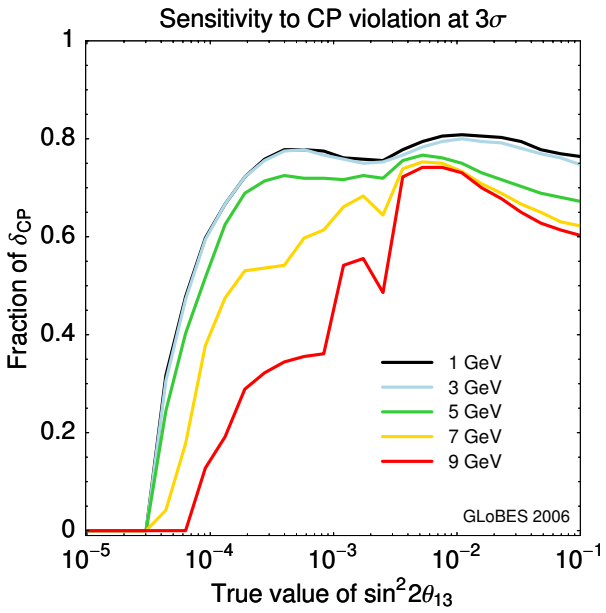

Figure 100: CP discovery reach at 3σ for the optimal appearance detector at $L = 4\,000$ km for various choices of the energy threshold as explained in the legend.

which T2HK would be sensitive to CP-violation is shown; super-beams can be competitive for large θ_{13}. In the left panel the results are shown for the canonical value of the matter-density uncertainty of 5%. Clearly, the standard Neutrino Factory setup does not perform better than the super-beam. The situation changes once better detectors are considered. The optimal setup defined previously would yield a significant improvement over the super-beam for nearly all choices of the baseline above 1500 km. It also can be seen that the improvement comes from both the lower threshold and better energy resolution. In this scenario, the detector performance is crucial in making the case for a Neutrino Factory. The right panel shows the result if the matter-density uncertainty could be reduced to 1%. Quite obviously, this would further improve the performance of the Neutrino Factory. These results for the optimal detector hold for a lower muon energy around 20 GeV as well.

In the case of large $\sin^2 2\theta_{13}$, improving the detector energy resolution and energy threshold would allow a shorter baseline of about 1500 km and a muon energy of 20 GeV to be chosen, while the option 4 000 km at 50 GeV does not mean a significant loss in sensitivity (depending on the matter-density uncertainty, the loss is about 5% to 8% in the CP-fraction). Furthermore, for one Neutrino Factory baseline only, it can be concluded that lower threshold, better energy resolution, and lower matter-density uncertainty would equally help to improve the performance.

5.4.4 The optimal Neutrino Factory

The optimised setups from the previous sections are compared below. The baseline and muon-energy optimisation is not discussed further, rather, these parameters are fixed from the earlier

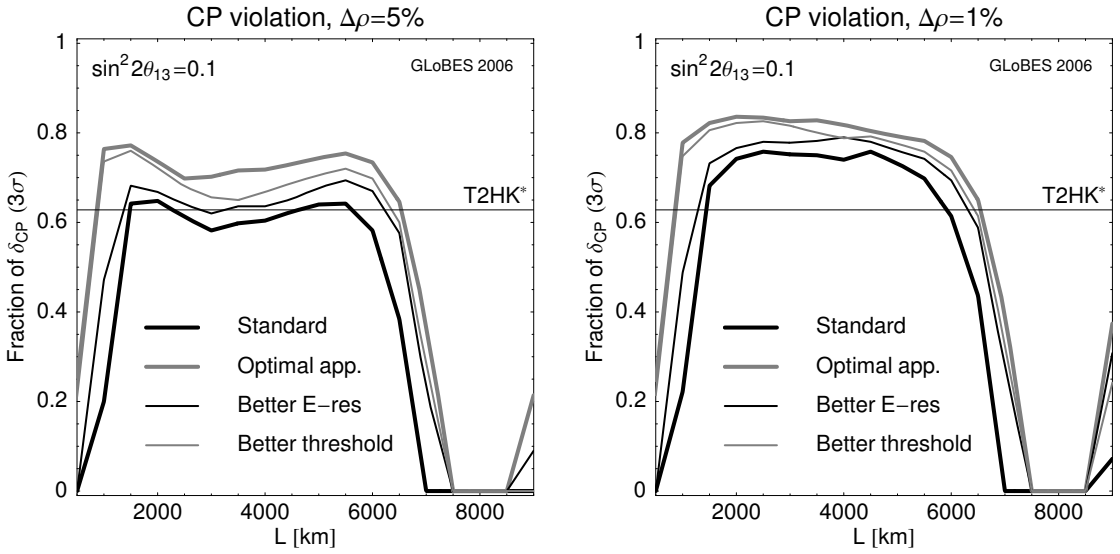

Figure 101: The CP-fraction for the sensitivity to CP-violation (at 3σ) for a normal hierarchy as function of baseline for different detector options (see legend) and $E_\mu = 50\,\mathrm{GeV}$. The left (right) panel corresponds to 5% (1%) matter density uncertainty. Taken with kind permission of the Physical Review from figure 12 in reference [208]. Copyrighted by the American Physical Society.

discussion. The muon energy is fixed, unless otherwise stated, to $E_\mu = 50\,\mathrm{GeV}$. Note that the matter-density uncertainty is assumed to be correlated among all channels at the same baseline.

For the optimal baseline, CP-violation measurements favour a baseline around 4 000 km (but baselines between 3 000 km and 5 000 km do not affect the sensitivity too much). For large values of $\sin^2 2\theta_{13}$, shorter baselines $L \gtrsim 1\,500\,\mathrm{km}$ are possible as well. Note that the short baseline ($L \lesssim 5\,000\,\mathrm{km}$) is affected by correlations and degeneracies for small and intermediate values of $\sin^2 2\theta_{13}$, which means that it has moderate $\sin^2 2\theta_{13}$ and mass hierarchy sensitivities. In addition, this result has been tested for larger values of Δm^2_{31}, and it does not change significantly (whereas the absolute physics potential increases).

As far as baseline upgrades are concerned, a degeneracy-solving baseline is necessary to improve the $\sin^2 2\theta_{13}$ sensitivity, the $\sin^2 2\theta_{13}$ discovery reach, and the mass-hierarchy discovery reach. A baseline in the range $L \sim 7\,000 - 7\,500\,\mathrm{km}$ (i.e., the magic baseline) can play this role, since the appearance probability does not depend on δ at this distance and the intrinsic-degeneracy can be solved unambiguously independent of the oscillation parameters, possibly over-estimated luminosities, confidence level, etc. (see reference [205]). Furthermore, matter effects are stronger than for the shorter baseline, which means that the magic baseline is sensitive to different physics, rather than being simply a luminosity upgrade. Moreover, it helps CP-violation measurements at large $\sin^2 2\theta_{13}$, and can establish the MSW effect in the Earth even for $\sin^2 2\theta_{13} = 0$ [746]. Since this baseline is useful in all physics scenarios, one may want to choose a Neutrino Factory setup with two such baselines from the very beginning. The second baseline will be a major challenge from the engineering point of view. However, the

physics potential of this baseline is well established and the technical feasibility should be rather predictable. In the plots of this section, the index 'MB' refers to the magic baseline.

For detector upgrades, an improvement of the golden-channel detector is certainly the main objective. In particular, lowering the detection threshold will greatly improve the physics potential in all physics scenarios and for both the mass-hierarchy and the CP-violating-phase measurements. It has been demonstrated that an improved detector would allow the use of a lower parent-muon energy, $E_\mu \sim 20\,\mathrm{GeV}$ instead of $E_\mu \sim 50\,\mathrm{GeV}$, thus reducing the effort on the accelerator side. The improvement of the detector with respect to energy resolution and threshold should be possible. Notice that an improved detector will not be able to solve all the degeneracies on its own.

Between the various additional channels, the platinum channel ($\nu_\mu \to \nu_e$) will be very useful for large $\sin^2 2\theta_{13} \gtrsim 10^{-2}$ provided the electron-charge-identification threshold can be increased up to $\sim 10 - 15\,\mathrm{GeV}$ (see the right panel of figure 96) and enough events can be collected. The reference 15 Kton magnetised LAr detector of reference [210] is statistically limited and would not improve the performance of the Neutrino Factory significantly. Platinum-channel searches may be implemented in the golden detector (thus allowing for a 50 Kton magnetised detector, something extremely difficult for the liquid-argon technique), but the electron-neutrino detection may not turn out to be technically possible at this level and might be effective only at much lower energy. It must be noted that a detector looking for the platinum channel is complementary to the improved golden detector theoretically, since a different combination of CP-violation and matter effects would be measured and it would permit the measurement of T-violation. However, it should be a secondary objective after improving the golden-channel threshold.

For intermediate values of θ_{13}, the silver and platinum channels give similar results as degeneracy-solvers, the former having a slightly larger. This channel, also, is statistically limited and any possible improvement of the detector (mass, magnetisation of the emulsions, better vertex-identification efficiency, etc.) would be extremely helpful. Notice that the silver channel is interesting for applications such as searches for physics beyond the SνM or deviations from maximal mixing; the discussion below is restricted to the measurement of the parameters of the SνM.

With the reference MID detector (with MINOS-like performance), the muon energy of a Neutrino Factory should be in the range 40 GeV to 50 GeV to be optimised for all measurements. The muon energy may not have to be as high as 50 GeV for neutrino-oscillation physics because of the matter resonance in the Earth's mantle. An improvement of the detection threshold could reduce the muon energy to 20 GeV while achieving excellent physics sensitivities, and the physics scenario 'large $\sin^2 2\theta_{13}$' may even allow for lower energies. Note that the use of the silver channel disfavours low muon energies, i.e., E_μ should be $\sim 25\,\mathrm{GeV}$ or greater.

The left panel of figure 102 summarises the outcome of this optimisation discussion by presenting the CP-fraction for the sensitivity to the mass hierarchy, successively switching on the magic baseline and the golden* improved detector. One can easily read off the excellent combined

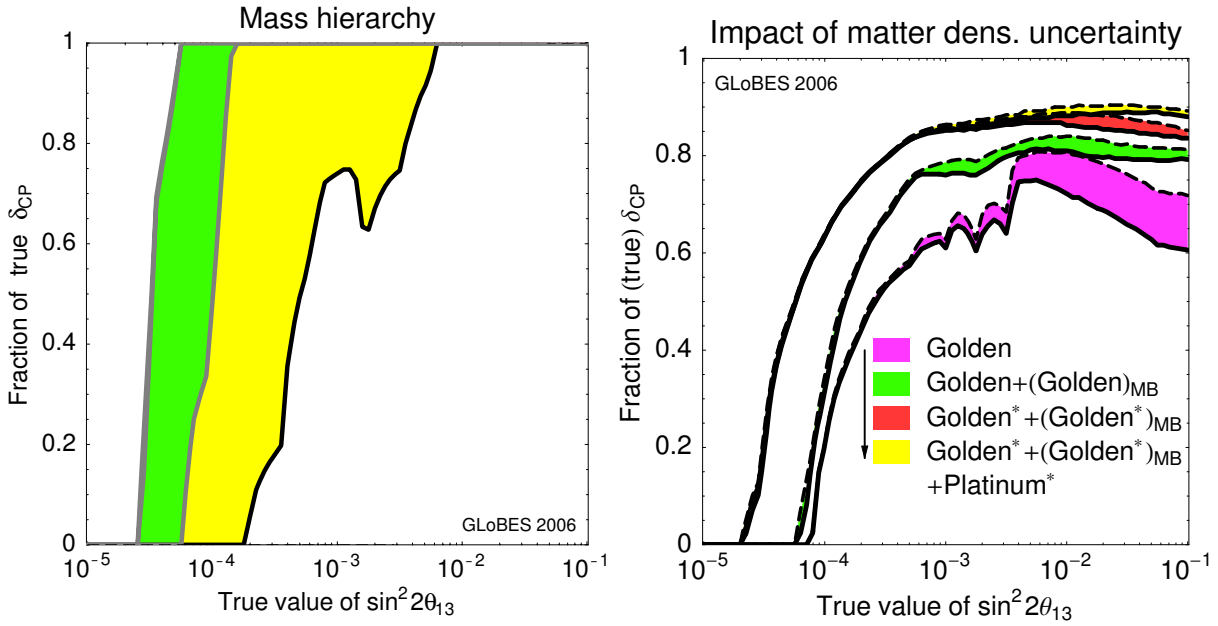

Figure 102: Left panel: CP-fraction of the sensitivity to the mass hierarchy at 3σ. The different shaded areas correspond to successively taking into account: 1) the magic baseline (yellow) and 2) an improved detector at $E_\mu = 20\,\text{GeV}$ (green). Right panel: CP-discovery potential at 3σ. The different lines correspond to successively taking into account additional optimisations as given in the legend. Solid (dashed) stands for a 5% (2%) matter density uncertainty. Shaded areas represent the improvement potential with respect to the unknown matter density profile. Notice that in going from Golden to Golden* the muon energy goes down from $E_\mu = 50\,\text{GeV}$ to $E_\mu = 20\,\text{GeV}$. Taken with kind permission of the Physical Review from figures 23 and 24 in reference [208]. Copyrighted by the American Physical Society.

potential for mass hierarchy and CP-violation of the Neutrino Factory below $\sin^2 2\theta_{13} \lesssim 10^{-2}$. Remember that none of the suggested improvements could be achieved with a simple luminosity upgrade, i.e., adding mass to the golden-channel detector.

Finally, it is well known that the matter-density uncertainty is important for $\sin^2 2\theta_{13}$ and δ measurements at large $\sin^2 2\theta_{13}$ (see, *e.g.*, references [340, 738] for the relevant regions in parameter space). Since the magic baseline and the platinum channel extract the information on $\sin^2 2\theta_{13}$ (and δ) in a different way compared to the golden channel, one may suspect that the correlation with the matter density can be partially eliminated. The impact of the matter-density uncertainty on our optimisation summary is shown in the right panel of figure 102. For the $L = 4\,000\,\text{km}$ baseline alone, it can be seen that the impact of matter density uncertainties is rather large ('Golden'). However, adding the magic baseline and (possibly) the platinum channel reduce this dependence significantly. This result is very interesting since in this case an improvement on the knowledge of the matter density profile may not be necessary anymore. Nevertheless, note that a lower matter density uncertainty cannot replace the detector, channel, and baseline improvements discussed in this section.

In conclusion, the optimal Neutrino Factory setup for oscillation parameter measurements has two baselines (at $L \sim 1500 - -4000\,\text{km}$ and one at $L \simeq 7\,500\,\text{km}$, respectively), a 'better' golden channel detector (with lower threshold and higher energy resolution) and a muon energy

of $E_\mu \sim 25\,\mathrm{GeV}$. This set of improvements exhausts the optimisation potential in most of the parameter space. The only region where an additional gain may be achieved is for large $\sin^2 2\theta_{13} \sim 10^{-1}$ (see section 5.4.5). Here, adding a high-mass platinum-channel detector (with electron CID capability) would decrease the impact of the matter density uncertainty. If, for any reason, the long baseline cannot be implemented, combination of the golden detector with a standard silver or platinum detector (with a slight preference for the former) can significantly improve the performance of the Neutrino Factory for intermediate θ_{13}.

As far as future Neutrino Factory R&D is concerned, the ability to operate two baselines as well as the lower detection threshold of the golden detector are the most critical components to the optimised physics potential. Furthermore, a better energy resolution of the golden-channel detector would improve the physics potential further.

5.4.5 Low-energy neutrino factory

In reference [41], it has been suggested that a very low energy Neutrino Factory, where the stored muons have an energy of 4.12 GeV, may be exciting if θ_{13} proves to be large ($\theta_{13} \geq 2^\circ$).

The primary neutrino-oscillation channel at a Neutrino Factory requires the identification of wrong-sign muons, and hence a detector with excellent muon-charge identification. Early studies [747] based on a MINOS-like segmented magnetised detector suggested that, to reduce the charge mis-identification rate to the 10^{-4} level while retaining a reasonable muon reconstruction efficiency, the detected muon needs to have a minimum momentum of ~ 5 GeV. The analysis obtained a 50% reconstruction efficiency for charged-current neutrino interactions exceeding ~ 20 GeV. This effectively places a lower limit of about 20 GeV on the desired energy of the muons stored in the Neutrino Factory (see section 5.4.2). Recently, a refined analysis has shown that, with more sophisticated selection criteria, high efficiencies ($> 80\%$) can be obtained for neutrino interactions exceeding ~ 10 GeV, with efficiencies dropping to $\sim 50\%$ by 5 GeV, motivating the proposed improvement in the magnetised iron detector studied in section 5.4.3.3. This new analysis suggests that a MINOS-like detector could be used at a Neutrino Factory with energy less than 20 GeV, but probably not less than 10 GeV.

Therefore, to consider a lower energy Neutrino Factory, a finer grained detector that enables reliable sign-determination with good efficiency for muons of lower energy is needed. One way to achieve this could be to use a totally active, magnetised, segmented detector, of the type proposed for the NOνA detector [16] but within a large magnetic volume. Initial studies seem to show that, for this technology, the muon reconstruction efficiency is expected to approach unity for momenta exceeding ~ 200 MeV/c, with a charge mis-identification lower than 10^{-4} (10^{-3}) for momenta exceeding approximately 400 MeV/c (300 MeV/c).

Whether these numbers are realistic must be confirmed by further and more detailed studies. Nevertheless, with a magnetised far detector concept that makes it possible to measure neutrino interactions down to about 0.8 GeV, it becomes interesting to consider a Neutrino Factory with a stored-muon energy of a few GeV. In present designs for a 25 GeV Neutrino Factory [748],

there at least two acceleration stages are required to accelerate the muons from ~ 1 GeV to 25 GeV. A Neutrino Factory for which the final muon energy is a few GeV would require only one acceleration stage.

Present Neutrino Factory studies suggest that it would be reasonable to expect, for a Neutrino Factory with (without) an ionisation-cooling channel before the pre-accelerator, about 5×10^{20} (3×10^{20}) useful positive muon decays per year and 5×10^{20} (3×10^{20}) useful negative muon decays per year in a given straight section. In reference [41] it is assumed that the same luminosity can be achieved for a 4.12 GeV Neutrino Factory. Two setups have been considered:

- *Setup A:* Five years data taking with 3×10^{20} useful muon decays per muon polarity per year; or
- *Setup B:* Ten years of data taking with 5×10^{20} useful muon decays per muon polarity per year.

In both cases, a 20 Kton fiducial mass, magnetised, totally active NOνA-type detector is considered.

Assuming the previous hypothesis on the neutrino flux and the far detector size and performances, the physics potential of this setup has been studied in reference [41] for two reference baselines: 1280 Km, the distance from Fermilab to Homestake, and 1480 Km, the distance from Fermilab to Henderson mine. Taking advantage of both the golden channel and of the $\nu_\mu \to \nu_\mu$ disappearance (but not of the silver channel, since the neutrino energy is too low to produce taus), it has been shown that:

- Maximal atmospheric neutrino mixing can be excluded at 99% CL if $\sin^2 \theta_{23} < 0.48$ ($\theta_{23} < 43.8^\circ$);
- If $\theta_{23} \neq 45^\circ$, the θ_{23}-octant is identified correctly at 99% CL if $\theta_{13} > 1^\circ$ for Setup A and $\theta_{13} > 0.6^\circ$ for Setup B, independent of the value of the CP violating phase, δ;
- The neutrino-mass hierarchy is identified at the 95% CL; and
- The CP violating phase, δ, is measured with a 95% CL error lower than 20°, if $\sin^2 2\theta_{13} > 0.01$ (i.e. $\theta_{13} > 3^\circ$) assuming the more conservative exposure scenario.

All sensitivities are computed assuming 2 degrees of freedom and a 2% overall systematic error. The statistical error is included, but no background has been considered. Finally, the detector efficiency has been assumed to be 100% above 0.8 GeV, and zero below this threshold.

5.5 Comparisons

The physics reach of second-generation super-beams, beta-beam facilities, and the Neutrino Factory have been reviewed in detail in the preceding sections. The purpose of this section is to

make a quantitative comparison of the discovery potential (as defined in section 5.2.10) of the three classes of facility for the three unknown quantities $\sin^2 2\theta_{13}$, signΔm^2_{31}, and δ.

The sensitivity of each of the proposed facilities depends on the choice of a number of parameters; optimised parameter choices may require R&D programmes to be carried out successfully. To assess the degree to which such R&D programmes can improve the physics reach, a 'conservative' and an 'optimised' set-up is assumed for each facility; the discovery reach for each facility being presented as a band, one edge of which corresponds to the conservative parameter set, the other to the optimised parameter set. For each setup, appearance and disappearance data taken using both neutrino and anti-neutrino beams are considered. In each case, the matter density is assumed to be known with an uncertainty of 2%. θ_{23} and Δm^2_{31} were assumed to be known within 10%, whereas θ_{12} and Δm^2_{21} were assumed to be known within 4%. The conservative and optimised set-ups for each of the three types of facility under consideration are summarised below.

- Second-generation super-beams: The three super-beam facilities considered, the SPL, T2HK, and the wide-band beam experiment, were defined in section 5.2.1. The aspects of these facilities that are most important to the performance comparison are summarised below:
  - T2HK is the proposed upgrade from the T2K experiment. Here a proton-beam power of 4 MW has been assumed. A megaton class water Cherenkov detector with a fiducial mass of 440 kt at a baseline of 295 km has been assumed. The running time assumed was 2 years for neutrinos and 8 years for anti-neutrinos (here, one year corresponds to 10^7 s). For more details see [27];
  - SPL is a CERN-based version of a superbeam. A proton-beam power of 4 MW a megaton class water Cherenkov detector with a fiducial mass of 440 kt at a baseline of 130 km have been assumed. The running time assumed was 2 years for neutrinos and 8 years for anti-neutrinos. For more details see [27].
  - WBB is the proposal originally put forward by BNL to use an on-axis, long baseline, wide-band neutrino beam pointed to illuminate a water Cherenkov detector. Here, a proton-beam power of 1 MW has been assumed for neutrino running and a proton-beam power of 2 MW has been assumed for anti-neutrino running. The detector assumed was a water Cherenkov detector with a fiducial mass of 300 kt at a baseline of 1300 km. The running time assumed was 5 years for neutrinos and 5 years for anti-neutrinos. For more details see [23, 691].

  The optimised parameter set corresponds to the assumption of a total systematic uncertainty of 2%. The conservative parameter set assumes a total systematic uncertainty of 5%;
- Beta-beam facilities: The beta-beam facilities were defined in section 5.3.1. The conservative option is taken to be the CERN baseline scenario with stored ^{6}He and ^{18}Ne beams at $\gamma = 100$ serving a 440 kt (fiducial) water Cherenkov detector at a baseline of 130 km. The running time assumed was is 5 years with $2.9 \cdot 10^{18}$ ^{6}He decays per year and $1.1 \cdot 10^{18}$ ^{18}Ne decays per year. A systematic uncertainty of 2% was assumed. For more details see [27].

The optimised parameter set assumes stored ^{6}He and ^{18}Ne beams at $\gamma = 350$ illuminating a 440 kt (fiducial) water Cherenkov detector at a baseline of 730 km. The running time is 5 years with $2.9 \cdot 10^{18}$ ^{6}He decays per year and $1.1 \cdot 10^{18}$ ^{18}Ne decays per year. A systematic uncertainty of 2% was assumed. For more details see [341]

- The Neutrino Factory: The Neutrino Factory setups were defined in section 5.4.1. The conservative setup assumes 10^{21} useful muon decays per year and a stored muon-beam energy of 50 GeV. The running time is 4 years with μ^+ and 4 years with μ^-. Neutrino events are recorded in a 50 kt golden detector (defined in section 5.4.1.1) at a baseline of 4000 km. This detector is assumed to have an appearance ν_μ threshold rising linearly from 0 at 4 GeV to its final value at 20 GeV. Systematic uncertainties of 2.5% on the signal and 20% on the background[18]. For more details see [208, 340].

  The optimised setup assumes a 20 GeV stored muon beam delivering 10^{21} muon decays per year and baseline. The running time assumed was 5 years with μ^+ and 5 years with μ^-. Neutrino interactions are recorded in two improved golden detectors, called golden*. Both have a mass of 50 kt. One is placed at a baseline of 4000 km, the second at a baseline of 7500 km. The improved detector has a threshold of 1 GeV, above which the effeciency is constant. Note, that the results bascially are unchanged if the threshold is raised to 3 GeV, since there is only a very small neutrino flux between 1 GeV and 3 GeV. A systematic uncertainty of 2.5% has been assumed. For more details see [208].

Figure 103 shows the discovery reach of the various facilities in $\sin^2 2\theta_{13}$. The figure shows the fraction of all possible values of the true value of the CP phase δ ('Fraction of $\delta_{\rm CP}$') for which $\sin^2 2\theta_{13} = 0$ can be excluded at the 3σ confidence level as a function of the true value of $\sin^2 2\theta_{13}$. Of the super-beam facilities, the most sensitive is the T2HK with the optimised parameter set. The SPL super-beam performance is similar to that of T2HK, while the performance of the WBB is slightly worse. The limit of sensitivity of the super-beam experiments is $\sim 5 \times 10^{-4}$; for $\sin^2 2\theta_{13} \gtrsim 10^{-3}$ the super-beam experiments can exclude $\sin^2 2\theta_{13} = 0$ at the 3σ confidence level for all values of δ. The conservative beta-beam set-up has good sensitivity to $\sin^2 2\theta_{13}$ for $\sin^2 2\theta_{13} \sim 10^{-3}$, but runs out of sensitivity for values of θ_{13} only just less than the sensitivity limit of T2HK. The optimised ($\gamma = 350$) beta-beam has significantly better performance, with a sensitivity limit of $\sin^2 2\theta_{13} \gtrsim 5 \times 10^{-5}$. Both the conservative, and the optimised Neutrino Factory set-ups have a significantly greater $\sin^2 2\theta_{13}$ discovery reach; the optimised set-up having a sensitivity limit of $\sim 1.5 \times 10^{-5}$.

Figure 104 shows the discovery reach of the various facilities in signΔm^2_{31}. The various bands shown in the figure have the same meaning as those shown in figure 103; the discovery reach is again evaluated at the 3σ confidence level. Of the super-beam set-ups considered only the WBB has significant sensitivity to the mass hierarchy with a sensitivity limit of $\sin^2 2\theta_{13} \gtrsim 3 \times 10^{-3}$. Of the beta-beam set-up only the optimised, $\gamma = 350$ option with the relatively long baseline of 730 km is competitive with the WBB, having a comparable sensitivity limit. The Neutrino

[18] The fact that the number of background events is small means that the large systematic uncertainty on the background-event rate has almost no impact on the performance

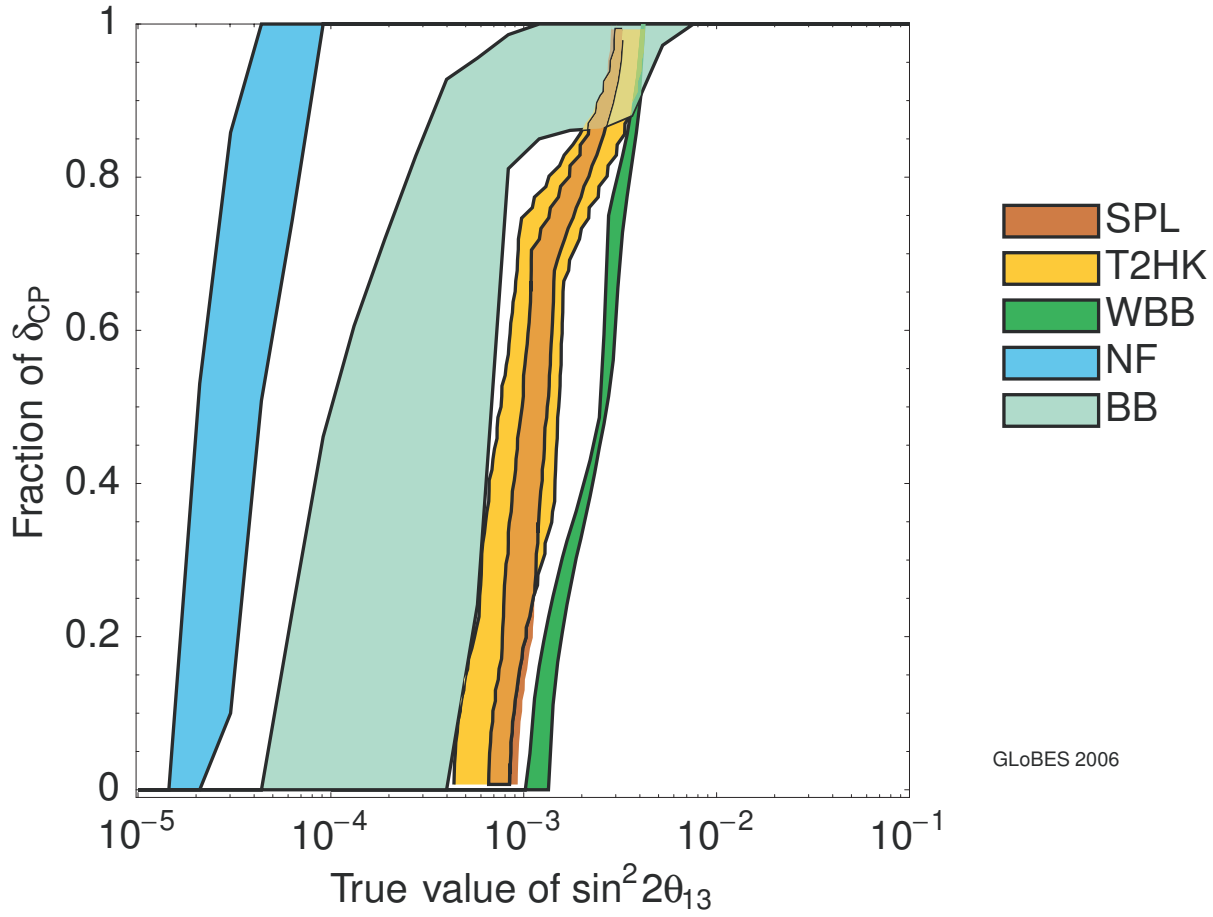

Figure 103: The discovery reach of the various proposed facilities in $\sin^2 2\theta_{13}$. In the area to the right of the bands, $\sin^2 2\theta_{13} = 0$ can be excluded at the 3σ confidence level. The discovery limits are shown as a function of the fraction of all possible values of the true value of the CP phase δ ('Fraction of $\delta_{\rm CP}$') and the true value of $\sin^2 2\theta_{13}$. The right-hand edges of the bands correspond to the conservative set-ups while the left-hand edges correspond to the optimised set-ups, as described in the text. The discovery reach of the SPL super-beam is shown as the orange band, that of T2HK as the yellow band, and that of the wide-band beam experiment as the green band. The discovery reach of the beta-beam is shown as the light green band and the Neutrino Factory discovery reach is shown as the blue band.

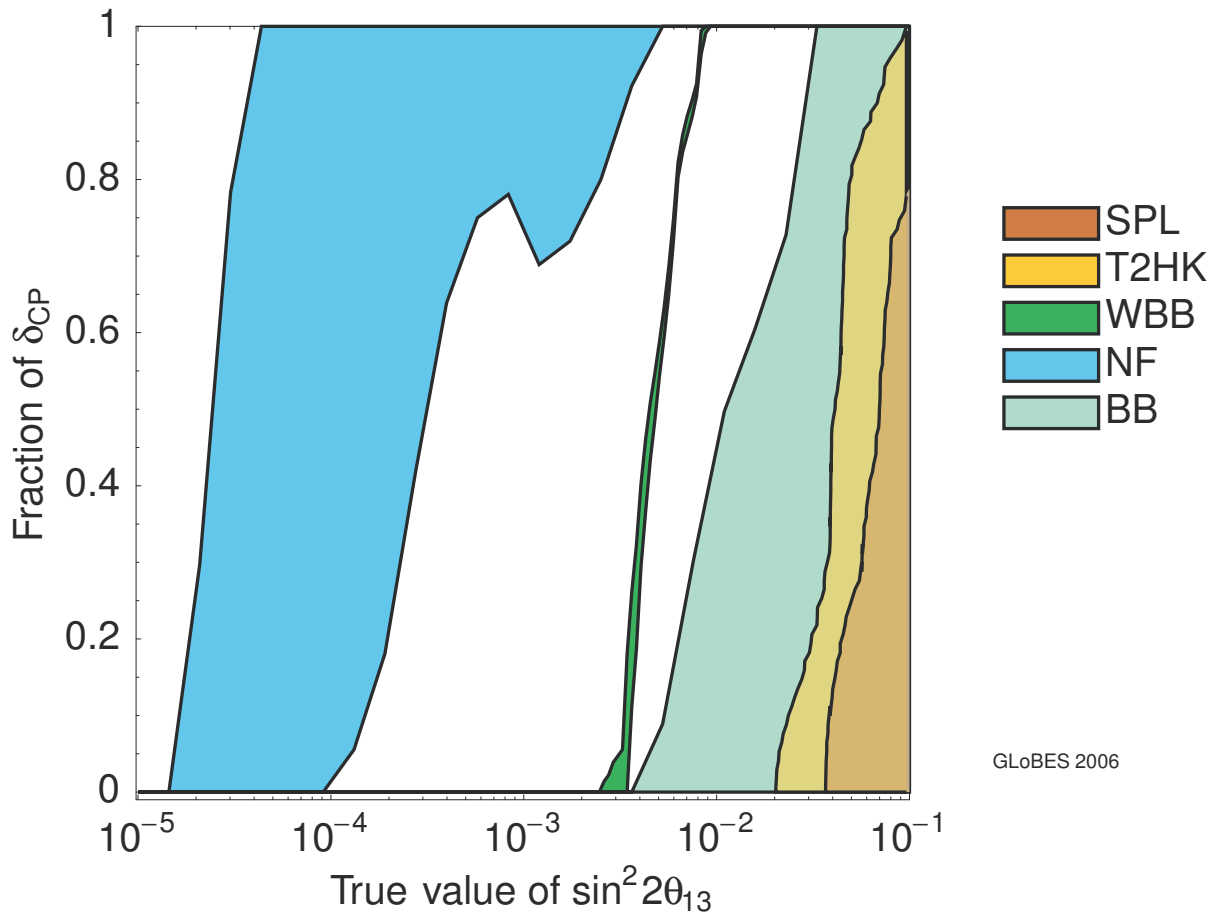

Figure 104: The discovery reach of the various proposed facilities for the discovery of the mass hierarchy. In the area to the right of the bands, signΔm^2_{31} can be established at the 3σ confidence level. The discovery limits are shown as a function of the fraction of all possible values of the true value of the CP phase δ ('Fraction of $\delta_{\rm CP}$') and the true value of $\sin^2 2\theta_{13}$. The right-hand edges of the bands correspond to the conservative set-ups while the left-hand edges correspond to the optimised set-ups, as described in the text. The discovery reach of the SPL super-beam is shown as the orange band, that of T2HK as the yellow band, and that of the wide-band beam experiment as the green band. The discovery reach of the beta-beam is shown as the light green band and the Neutrino Factory discovery reach is shown as the blue band.

Factory, benefitting from the long baseline, out-performs the other facilities. The sensitivity limit of the conservative option being $\sin^2 2\theta_{13} \gtrsim 1.5 \times 10^{-4}$, while the sensitivity limit of the optimised facility is $\sin^2 2\theta_{13} \gtrsim 1.5 \times 10^{-5}$.

Figure 105 shows the discovery reach of the various facilities in the CP phase δ. The various bands shown in the figure have the same meaning as those shown in figure 103; the discovery reach is again evaluated at the 3σ confidence level. The T2HK and the SPL super-beams show a greater sensitivity to CP violation for $\sin^2 2\theta_{13} \sim 10^{-3}$ than the WBB experiment. However, the WBB experiment has sensitivity for a larger range of values of δ that the other super-beam facilities considered for $\sin^2 2\theta_{13} \sim 10^{-1}$. The performance of the conservative ($\gamma = 100$) beta-beam is comparable to that of the optimised T2HK experiment. The optimised ($\gamma = 350$) beta-beam shows considerably better performance; a sensitivity limit of $\sim 4 \times 10^{-5}$ and a

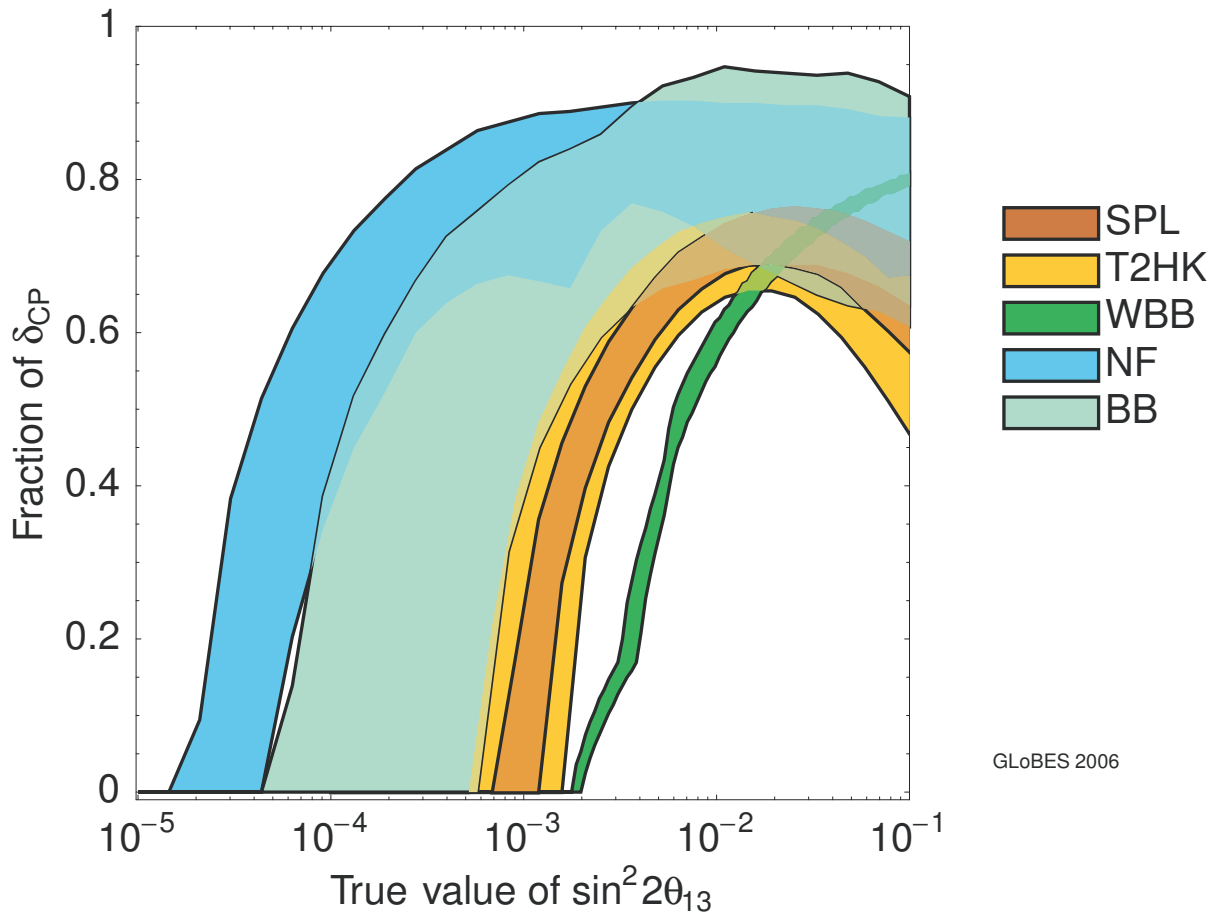

Figure 105: The discovery reach of the various proposed facilities in the CP phase δ. In the area to the right of the bands, $\delta = 0$ and $\delta = \pi$ can be excluded at the 3σ confidence level. The discovery limits are shown as a function of the fraction of all possible values of the true value of the CP phase δ ('Fraction of $\delta_{\rm CP}$') and the true value of $\sin^2 2\theta_{13}$. The right-hand edges of the bands correspond to the conservative set-ups while the left-hand edges correspond to the optimised set-ups, as described in the text. The discovery reach of the SPL super-beam is shown as the orange band, that of T2HK as the yellow band, and that of the wide-band beam experiment as the green band. The discovery reach of the beta-beam is shown as the light green band and the Neutrino Factory discovery reach is shown as the blue band.

CP coverage of around 90% for $\sin^2 2\theta_{13} \gtrsim 10^{-2}$. For low values of θ_{13} ($\sin^2 2\theta_{13} \lesssim 10^{-4}$ the conservative Neutrino Factory performance is comparable with that of the optimised beta-beam. For larger values of θ_{13}, the CP coverage of the optimised beta-beam is significantly better. The optimised Neutrino Factory out-performs the optimised beta-beam for $\sin^2 2\theta_{13} \lesssim 4 \times 10^{-3}$. For larger values of θ_{13} the optimised beta-beam has a slightly larger CP coverage.

In summary, for large values of θ_{13} ($\sin^2 2\theta_{13} \gtrsim 10^{-2}$), the three classes of facility have comparable sensitivity; the best precision on individual parameters being achieved at the Neutrino Factory. For intermediate values of θ_{13} ($5 \times 10^{-4} \lesssim \sin^2 2\theta_{13} \lesssim 10^{-2}$), the super-beams are out-performed by the beta-beam and the Neutrino Factory. For small values of θ_{13} ($\sin^2 2\theta_{13} \lesssim 5 \times 10^{-4}$), the Neutrino Factory out-performs the other options. A significant amount of conceptual design work and hardware R&D is required before the performance as-

sumed for each of the facilities can be realised. Therefore, an energetic, programme of R&D into the accelerator facilities and the neutrino detectors must be established with a view to the timely delivery of conceptual design reports for the various facilities.

6 The potential of other alternatives

6.1 Solar- and reactor-neutrino experiments

Possible future solar- and reactor-neutrino experiments are discussed together in this section. In addition, a comparative study of the sensitivity of these experiments to Δm^2_{21} and $\sin^2\theta_{12}$ is presented.

6.1.1 The Generic *pp* experiment

The present generation of solar- and reactor-neutrino experiments will not be able to determine $\sin^2\theta_{12}$ with an accuracy better than 10%–15%. To make a more precise measurement of $\sin^2\theta_{12}$ in solar-neutrino experiments it is necessary to make a precise measurement of the *pp*-neutrino flux [749], sub-MeV solar-neutrino experiments (LowNu experiments) are therefore being planned for the detection of the *pp* neutrinos using either charged-current reactions (LENS [750], MOON [751], SIREN [752]) or electron-scattering processes (XMASS [753], CLEAN [754], HERON [755], MUNU [756], GENIUS [757]) [758].

Figure 106 shows the dependence of the sensitivity of solar-neutrino measurements to $\sin^2\theta_{12}$ on the precision with which the *pp* flux is known [97]. The results are for a generic ν_e-e scattering experiment with a threshold of 50 keV. The figure shows the two-generation allowed range of $\sin^2\theta_{12}$ from the global analysis of KamLAND and solar data including the LowNu *pp* rate, as a function of the error in the *pp* measurement. Three illustrative *pp* rates of 0.68, 0.72, and 0.77 are considered and the experimental error in the *pp* measurement is varied from 1% to 5%. By adding the *pp*-flux data in the analysis, the error on $\sin^2\theta_{12}$ reduces to 14% (19%) at 3σ for a 1% (3%) uncertainty in the measured *pp* rate [97]. Performing a similar three-neutrino oscillation analysis it is found that, as a consequence of the uncertainty on $\sin^2\theta_{13}$, the error on the value of $\sin^2\theta_{12}$ increases to 17% (21%) [97].

6.1.2 The SK-Gd reactor experiment

A detector with the fiducial mass of the Super-Kamiokande (SK) detector that was sensitive to reactor neutrinos would be able to make a very precise measurement of θ_{12}. In view of this, there has been a proposal to dope SK with gadolinium (Gd) by dissolving 0.2% of gadolinium chloride in the SK water [759]. SK receives the same reactor flux as KamLAND and, in principle, could detect these reactor $\overline{\nu}_{\rm e}$ through inverse beta decay. The inverse beta-decay process produces an electron and a neutron: the electron produces Čerenkov light which can be detected; the

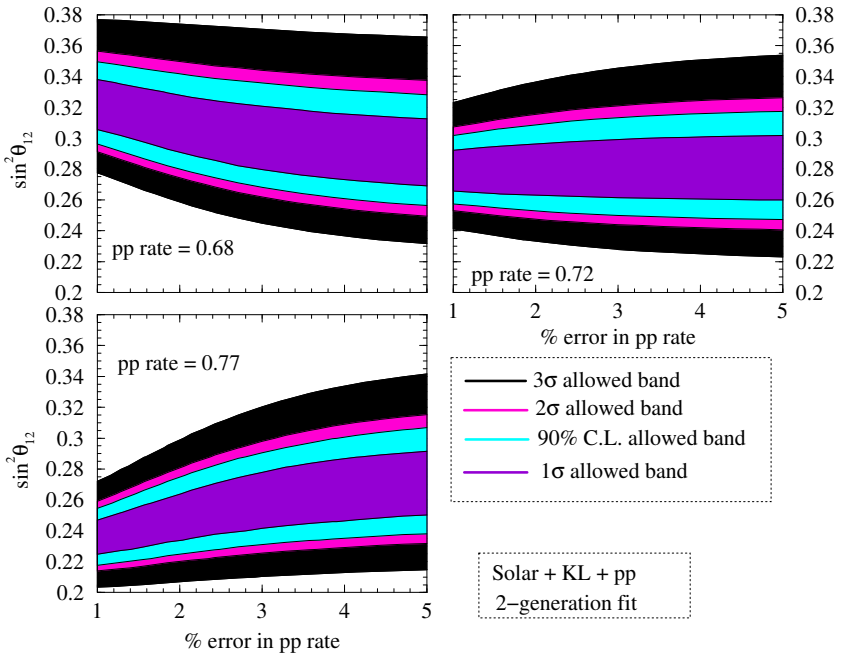

Figure 106: Sensitivity plot showing the C.L. (1 dof) allowed range of $\sin^2\theta_{12}$ as a function of the error in *pp* rate for three different values of measured *pp* rate. Adapted with kind permission of the Physical Review from figure 3 in reference [97].

neutron must be detected through neutron capture. Unfortunately, neutron capture on a proton releases a photon with an energy of only 2.2 MeV, which can not be detected in SK. The addition of Gadolinium circumvents this problem since neutron capture on gadolinium releases an 8 MeV γ cascade which is above the SK threshold. With its 22.5 kton of ultra pure water, the SK detector offers a target with 1.5×10^{33} free protons for the antineutrinos coming from the various reactors in Japan. Therefore, for the same measurement period, the SK-Gd reactor experiment may be expected to yield a data set roughly 43 times that which can be provided by the KamLAND experiment.

In [96], the reactor-$\overline{\nu}_e$ data expected in the proposed SK-Gd detector is simulated for $\Delta m^2_{21} = 8.3 \times 10^{-5}$ eV^2, $\sin^2\theta_{12} = 0.27$, and divided into 18 energy bins, with a visible-energy threshold of 3 MeV and bin width of 0.5 MeV. The precision with which the parameters Δm^2_{21} and $\sin^2\theta_{12}$ can be determined after a five-year exposure is shown in figure 107 [96]. Also shown for comparison in the figure is the 99.73% C.L. line expected from a 3 kTy exposure of KamLAND. The precision expected from SK-Gd is superior in both Δm^2_{21} and $\sin^2\theta_{12}$. The 3σ spread in Δm^2_{21} and $\sin^2\theta_{12}$ expected from five-years data taking in SK-Gd would be at the level of 2%–3% and 18% respectively [96]. This is to be compared with the corresponding spread of 6% and 32% expected from 3 kTy of KamLAND data. Results for a similar experimental set-up in Europe and the corresponding accuracy in the measurement of Δm^2_{21} and $\sin^2\theta_{12}$ has been studied recently [339].

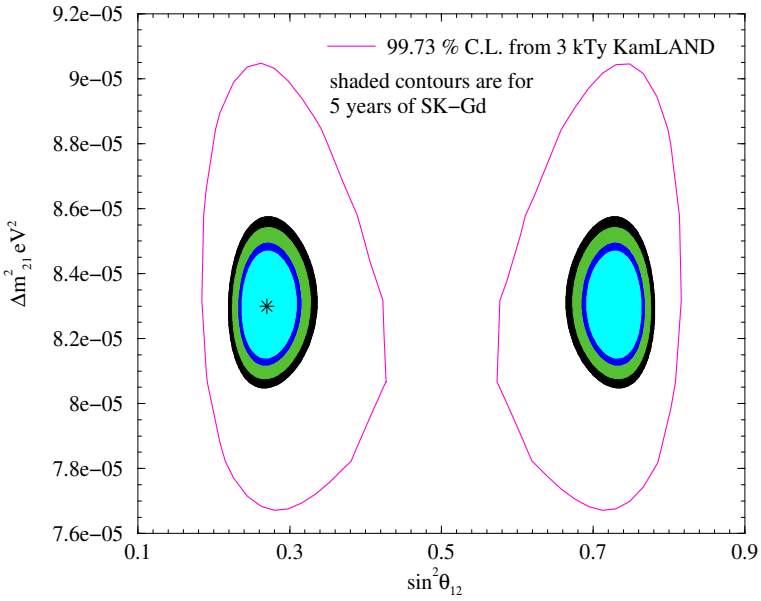

Figure 107: The 90%, 95%, 99%, 99.73% C.L. (2 dof) allowed regions in the $\Delta m^2_{21} - \sin^2\theta_{12}$ plane from an analysis of prospective data, obtained in 5 years of running of the SK-Gd detector. The open contours shows the 99.73% C.L. allowed areas expected from 3 kTy of KamLAND data. The definition of the C.L. correspond to a two parameter fit. Taken with kind permission of Springer-Verlag GMBH from reference [110]. Copyrighted by the Springer-Verlag GMBH.

6.1.3 The SPMIN reactor experiment

The solar mixing angle could be measured with great accuracy in a reactor experiment with the baseline tuned to the Survival Probability MINimum (SPMIN) [98]. Figure 108 shows the $\sin^2\theta_{12}$ sensitivity expected in a reactor experiment as a function of the baseline L [97]. The sensitivity has been evaluated on the assumption of a total systematic uncertainty of 2% and a data set corresponding to 73 GWkTy (given as a product of reactor power in GW and the exposure of the detector in kTy). The true value of $\sin^2\theta_{12}$ is assumed to be 0.27 and the positron spectrum that would be observed in the detector is simulated for four different assumed values of for Δm^2_{21}. The spectrum is thus simulated at each baseline and the range of values of $\sin^2\theta_{12}$ allowed by the experiment is plotted as a function of the baseline. The baseline at which the band of allowed values of $\sin^2\theta_{12}$ is narrowest is the ideal baseline for the SPMIN reactor experiment. The figure confirms that this ideal baseline depends critically on the true value of Δm^2_{21}. The optimal baseline for $\Delta m^2_{21} = 8.0(8.3) \times 10^{-5}$ eV^2 is 63 km (60 km). At the optimal baseline, the SPMIN reactor experiment can achieve a precision of $\sim 2(6)\%$ at $1\sigma(3\sigma)$ in the measurement of $\sin^2\theta_{12}$ [97, 583].

Figure 108 gives the impression that the optimal baseline for a given value of Δm^2_{21} is very well defined. However, note that in figure 108 Δm^2_{21} was allowed to vary freely. The uncertainty in the Δm^2_{21} measurement translates to extra uncertainty in the $\sin^2\theta_{12}$ measurement. If Δm^2_{21} could be measured to a very high precision in some other experiment, such as KamLAND or SK-Gd, then the uncertainty in $\sin^2\theta_{12}$ due to Δm^2_{21} can be reduced significantly. If Δm^2_{21} was

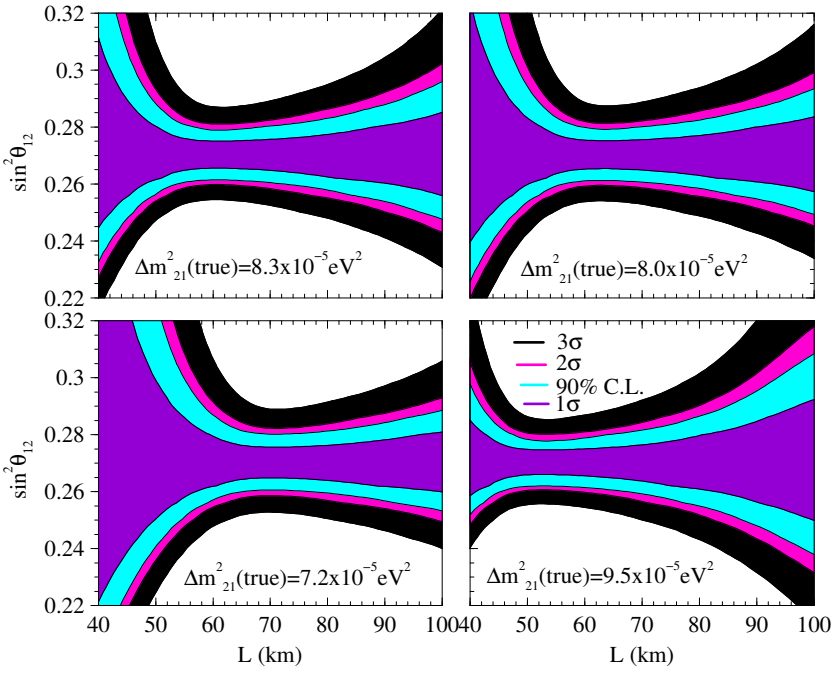

Figure 108: Sensitivity plots for the SPMIN reactor experiment showing the 1σ, 1.64σ, 2σ, and 3σ (1 dof) range of allowed values for $\sin^2\theta_{12}$ as a function of the baseline L. Taken with kind permission of the Physical Review from figure 9 in reference [97]. Copyrighted by the American Physical Society.

kept fixed, the choice of the baseline for the SPMIN experiment becomes much broader [97].

The measurement of $\sin^2\theta_{12}$ is statistics limited making a large exposure very important. For example, the sensitivity to $\sin^2\theta_{12}$ improves from 3(10)% to 2(6)% at $1\sigma(3\sigma)$ as the exposure is increased from 20 GWkTy to 60 GWkTy. The effect of systematics on the $\sin^2\theta_{12}$ measurement can be checked by repeating the analysis with a more conservative estimate of 5% for the systematic uncertainty. For $\Delta m^2_{21}(\text{true}) = 8.3 \times 10^{-5}$ eV^2, the spread in $\sin^2\theta_{12}$ at $L = 60$ km increases from 6.1% to 8.6% at 3σ, as the systematic error is increased from 2% to 5% . Finally, the impact of the error on θ_{13} on the precision of $\sin^2\theta_{12}$ is to increase the uncertainty in $\sin^2\theta_{12}$ from 6.1% to 8.7% at 3σ, for $\Delta m^2_{21}(\text{true}) = 8.3 \times 10^{-5}$ eV^2 and $L = 60$ km [97].

6.2 Atmospheric neutrino experiments

The effect of the sub-dominant terms in the Super-Kamiokande (SK) atmospheric-neutrino data is not yet statistically significant. However, the sub-dominant terms, if observed in a future high statistics atmospheric-neutrino experiment, can be used to constrain: the extent to which θ_{23} differs from 45°; the octant in θ_{23} is to be found; and sgn(Δm^2_{31}).

Assuming that the matter-density is constant, the excess of electron-type events in a water-

Čerenkov experiment such as SK is given by [100, 102, 703, 705, 760, 761]:

$$\begin{aligned}\frac{N_e}{N_e^0} - 1 &\simeq \sin^2 2\theta_{12}^M \sin^2\left(\frac{(\Delta m^2_{21})^M L}{4E}\right) \times (r\cos^2\theta_{23} - 1) \\ &+ \sin^2 2\theta_{13}^M \sin^2\left(\frac{(\Delta m^2_{31})^M L}{4E}\right) \times (r\sin^2\theta_{23} - 1) \\ &+ \sin\theta_{23}\cos\theta_{23}\ r\ Re\left[A^*_{13}A_{12}\exp(-i\delta)\right]\,, \end{aligned} \tag{300}$$

where L is the baseline, E is the energy of the neutrino, $r = N_e/N_\mu$, N_e and N_μ being the number electron and muon events respectively in the detector in the absence of oscillations, and θ_{12}^M, θ_{13}^M, $(\Delta m^2_{21})^M$ and $(\Delta m^2_{31})^M$ are the mixing angle and mass-squared differences in matter.

The first term in equation (300) is the Δm^2_{21}-driven oscillation term – which is more important for the sub-GeV neutrino sample. Since $r \simeq 0.5$ in the sub-GeV regime, this term brings an excess (depletion) of sub-GeV electron events if $\theta_{23} < \pi/4$ ($\theta_{23} > \pi/4$). It can thus be used to study the maximality and octant of θ_{23} through the sub-GeV electron sample [704, 760]. The second term is the θ_{13}-driven oscillation term. Being dependent on $\sin^2\theta_{23}$, this term goes in the opposite direction to the first term. Therefore, for sub-GeV neutrinos, larger θ_{13} would imply that the effect of the first term would be suppressed by this term. However, for multi-GeV neutrinos, there will be large matter effects inside the earth and this is the dominant term for the electron neutrinos. The $\sin^2\theta_{23}$ dependence of this term could then be used to study the maximality and the octant of θ_{23} through the multi-GeV electron sample [38, 762]. Since matter effects bring in sensitivity to the $\mathrm{sgn}(\Delta m^2_{31})$, this term can be used to study the mass hierarchy. The last term is the 'interference' term [703], which depends on δ. The effect of this term could be to dilute the effect of the first two terms and spoil the sensitivity of the experiment. However, being directly dependent on δ, this term also brings in some sensitivity to the CP phase itself [114, 703].

The depletion of muon events in the limit of $\Delta m^2_{21} = 0$ is given by:

$$1 - \frac{N_\mu}{N_\mu^0} = (P^1_{\mu\mu} + P^2_{\mu\mu}) + (P^3_{\mu\mu})' \sin^2\theta_{23}(\sin^2\theta_{23} - \frac{1}{r})\,, \tag{301}$$

where:

$$P^1_{\mu\mu} = \sin^2\theta_{13}^M \sin^2 2\theta_{23} \sin^2\frac{\left[(A + \Delta m^2_{31}) - (\Delta m^2_{31})^M\right] L}{8E}\,; \tag{302}$$

$$P^2_{\mu\mu} = \cos^2\theta_{13}^M \sin^2 2\theta_{23} \sin^2\frac{\left[(A + \Delta m^2_{31}) + (\Delta m^2_{31})^M\right] L}{8E}\,; \tag{303}$$

$$(P^3_{\mu\mu})' = \sin^2 2\theta_{13}^M \sin^2\frac{(\Delta m^2_{31})^M L}{4E}\,; \tag{304}$$

and $A = 2\sqrt{2}G_F N_e E$ is the matter potential. The approximation of a vanishing Δm^2_{21} has been made in equation (304) only for the sake of simplicity, since the main sub-dominant effect in the muon-neutrino channel comes from matter effects, which are large for multi-GeV neutrinos for which the Δm^2_{21} dependence is of less importance. The results presented in later sections

have been obtained using the full numerical solution of the three-generation equation. For small values of θ_{13}, matter effects are very small and $P^2_{\mu\mu}$ is the dominant term in the survival probability. Since this term depends on $\sin^2 2\theta_{23}$, in the absence of matter effects, sensitivity to the θ_{23} octant is not expected from experiments probing the $P_{\mu\mu}$ channel alone. However, if θ_{13} is not small, neutrinos which travel through large baselines suffer large matter effects. The mixing angle θ_{13} increases in matter and the third term $(P^3_{\mu\mu})'$ becomes important as well. Since this term has a strong dependence on $\sin^2\theta_{23}$, rather than $\sin^2 2\theta_{23}$, the $P_{\mu\mu}$ channel is expected to develop sensitivity to the octant of θ_{23} in the presence of large matter effects [763]. Also, by probing matter effects in the resultant muon signal, the neutrino-mass hierarchy can be probed [101, 761, 764–768]

High-energy (multi-GeV) neutrinos are sensitive to matter effects. Since upward-going neutrinos have a longer path length through matter than downward-going neutrinos, matter effects may be studied by evaluating the up-down asymmetry using multi-GeV atmospheric-neutrino data. In contrast to matter effects in the electron-neutrino-appearance channel, the disappearance probability, $P_{\mu\mu}$, is a function of L and E. This is illustrated in figure 109 [763], which shows the difference between the ratio of upward-going to downward-going muon events for atmospheric neutrinos (U_N/D_N) and anti-neutrinos (U_A/D_A). The rate estimates have been made for a large magnetised-iron detector, such as that proposed for the India-based Neutrino Observatory (INO) [769]. The normal mass hierarchy is assumed and the results are shown for different energy and zenith-angle bins. Since, for a given mass hierarchy, large matter effects appear either in the neutrino or in the anti-neutrino channel, the difference in the ratios for neutrinos and anti-neutrinos gives the net matter effect. The figure indicates that the matter effect is largest for neutrinos travelling $L \simeq 7000$ km with $E \sim 5$ GeV and that the net matter effect changes sign with L and E. Thus, in order to see the matter effects it is necessary to bin the data judiciously both in energy and zenith angle. The figure also shows that that $\Delta P_{\mu\mu}$ depends on the value of θ_{23}.

Magnetised-iron calorimeters are expected to have good energy and zenith-angle resolution. Therefore, fine binning would allow such detectors to observe matter effects in the muon signal. The magnetic field which allows muon-neutrino induced events to be distinguished from anti-muon-neutrino events enhances the sensitivity of these detectors to matter effects since, as noted above, matter effects appear either in the neutrino or the anti-neutrino channel. Iron calorimeters have two principal disadvantages: the neutrino energy threshold is relatively high, allowing for the detection of multi-GeV neutrinos only; and electron-neutrino induced events can not be detected.

Water Čerenkov detectors have the advantage that sub-GeV neutrinos can be detected. However, the energy resolution is worse than that of an iron calorimeter. For the results presented here, the data is binned in sub-GeV and multi-GeV bins and therefore the matter effect in the $P_{\mu\mu}$ channel is largely averaged out. This averaging implies that only a very small residual matter effect in the multi-GeV muon sample may be observed. However, matter effects in the $P_{\mu e}$ channel do not change sign over most of the relevant range of E and L in the multi-GeV regime. Therefore, the multi-GeV electron sample has large matter effects and can be used to

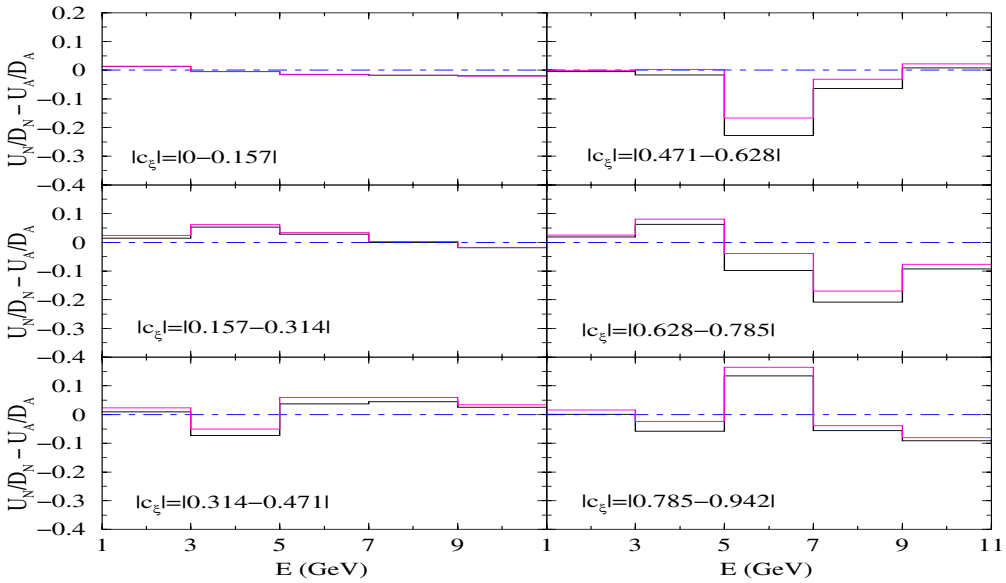

Figure 109: The difference between the up-down ratio for the neutrinos (U_N/D_N) and anti-neutrinos (U_A/D_A) shown for the various energy and zenith-angle bins. The solid black and solid magenta lines are for neutrinos/anti-neutrinos travelling in matter with $\sin^2\theta_{23} = 0.5$ and 0.36 respectively. Taken with kind permission of the Physical Review from figure 6 in reference [763]. Copyrighted by the American Physical Society.

study the deviation of θ_{23} from maximality and the θ_{23} octant, as well as the mass hierarchy.

6.2.1 Is the mixing angle θ_{23} maximal?

The measurement of both the magnitude and sign of the deviation of $\sin^2\theta_{23}$ from its maximum is of great importance. The deviation of $\sin^2\theta_{23}$ from 0.5 may be quantified by defining $D \equiv \frac{1}{2} - \sin^2\theta_{23}$. At present, the best limit $|D|$ comes from the SK experiment giving $|D| \leq 0.16$ at 3σ [116]; the sign of D is unknown at present. The potential of atmospheric-neutrino experiments to test the deviation of θ_{23} from maximality is shown in figure 110. The figure also shows the sensitivity obtained by combining data from the current and the next generation of long-baseline experiments. The combined long-baseline data set includes five years of running for each of the following: MINOS; ICARUS; OPERA; T2K; and NOνA. The middle panel shows the sensitivity to $|D|$ of atmospheric-neutrino experiments with water Čerenkov detectors with a data set corresponding to an exposure of 4.6 Megaton-years. The left panel shows the corresponding sensitivity of atmospheric-neutrino data in large magnetised-iron detectors with an exposure of 500-kiloton-years. At $\Delta m^2_{31}(\text{true}) = 2.5 \times 10^{-3}$ eV^2, it should be possible to measure $|D|$ within 19% and 25% at 3σ with atmospheric neutrinos using water and iron detectors respectively. This is slightly weaker than the sensitivity of the combined long-baseline experiments, where it should be possible to measure $|D|$ to within 14% at 3σ. However, note that all the results presented in figure 110 have been obtained assuming that the true value of θ_{13} was zero. For non-zero θ_{13}, the presence of matter effects in the $P_{\mu\mu}$ channel brings a marginal improvement in the sensitivity of atmospheric-neutrino experiments using a magnetised-iron detector. For the megaton-water

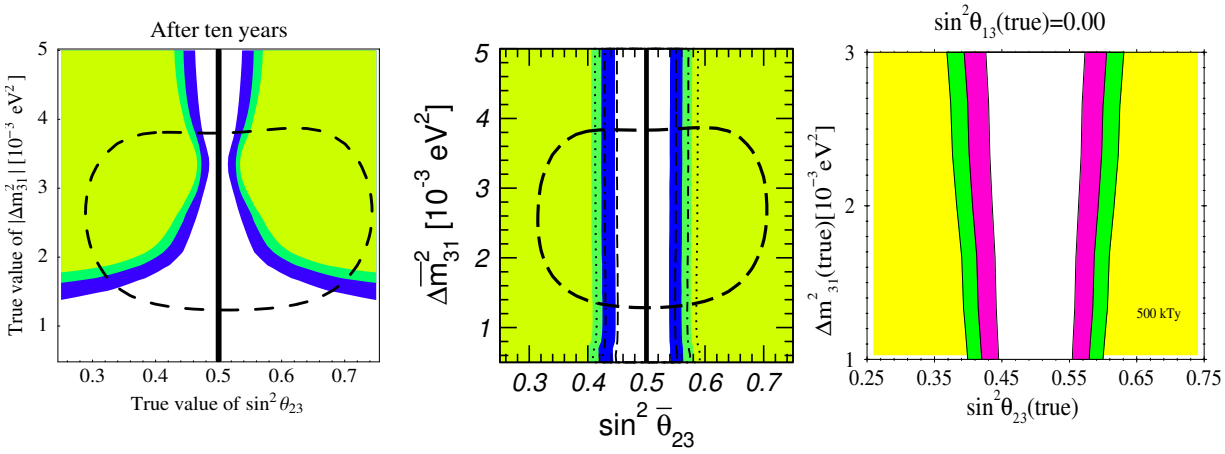

Figure 110: The regions of Δm^2_{31}(true) and $\sin^2\theta_{23}$(true) where maximal θ_{23} mixing can be rejected at 1σ (inner bands), 2σ (middle bands) and 3σ (outer bands) C.L. The sensitivity expected: the left panel (taken from [702]) shows the sensitivity expected from the combined data from the long base-line experiments. The middle panel (taken from [704]) shows the sensitivity expected with atmospheric neutrinos in a megaton water detector (SK50). The right-hand panel (taken from [762]) shows the corresponding reach expected from 500 kTy atmospheric neutrino data in large magnetised-iron detectors. The true value of θ_{13} is assumed to be zero. Middle panel taken with kind permission of the Physical Review from figure 4 in reference [704], copyrighted by the American Physical Society. Left panel taken with kind permission of the Physical Review from figure 1 in reference [702], copyrighted by the American Physical Society.

atmospheric-neutrino experiment, very large matter effects in the $P_{\mu e}$ channel bring a significant improvement in the determination of $|D|$, making this experiment comparable to, or better than, the long-baseline experiments for studying the deviation of θ_{23} from maximality [762].

6.2.2 Resolving the θ_{23} Octant Ambiguity

If the true value of θ_{23} is not 45°, then the question of whether $\theta_{23} > \pi/4$ (D positive) or $\theta_{23} < \pi/4$ (D negative) arises. This ambiguity is generally regarded as the most difficult to resolve. As discussed above, the presence of matter effects in the zenith-angle- and energy-binned atmospheric-ν_μ /$\overline{\nu}_\mu$ data opens up the possibility of probing the octant of θ_{23} in magnetised-iron detectors [763]. On the other hand, atmospheric $\nu_e/\overline{\nu}_e$ data in water Čerenkov detectors could also give information on the octant of θ_{23}, both through the Δm^2_{21}-dependent sub-dominant term in the sub-GeV sample [704,760], and through the matter effect in the multi-GeV sample [38,762]. This, therefore, opens the possibility of combining atmospheric-neutrino data with data from long-baseline experiments to resolve parameter degeneracies [27, 38].

In order to obtain the limiting value of $\sin^2\theta_{23}$(true) which could still allow for the determination of the sign of D it is convenient to define:

$$\Delta\chi^2 \equiv \chi^2(\sin^2\theta_{23}(\text{true}), \sin^2\theta_{13}(\text{true}), \text{others(true)}) - \chi^2(\sin^2\theta_{23}(\text{false}), \sin^2\theta_{13}, \text{others}), \quad (305)$$

with $\sin^2\theta_{23}$(false) restricted to the wrong octant and 'others' comprising Δm^2_{31}, Δm^2_{21}, $\sin^2\theta_{12}$, and δ. These parameters, along with $\sin^2\theta_{13}$ as well as $\sin^2\theta_{23}$(false), are allowed to vary freely

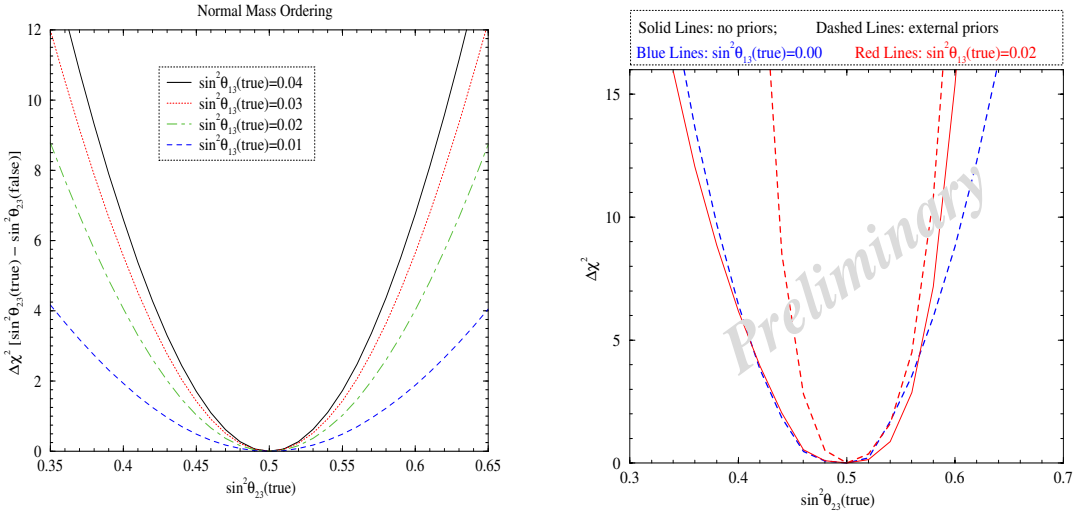

Figure 111: Plot showing the octant sensitivity as a function of $\sin^2\theta_{23}$(true), for an atmospheric neutrino experiment with large magnetised-iron calorimeter (left panel) and megaton water detector (right-hand panel). Taken from [762].

in the fit. The results of the fit are shown in figure 111 for a 500-kiloton-year exposure in a large magnetised-iron calorimeter (left panel) and a 4.6 Megaton-year exposure of a water Čerenkov experiment (right-hand panel) [762]. For the magnetised-iron detector, the results are presented using four different values of $\sin^2\theta_{13}$(true), assuming a normal mass ordering. For a given $\sin^2\theta_{13}$(true), the range of $\sin^2\theta_{23}$(true) for which $\sin^2\theta_{23}$(false) can be ruled out with atmospheric neutrinos in magnetised-iron detector is given in table 18. These results can be compared to the sensitivity that can be obtained using a water Čerenkov detector, which is shown for normal mass hierarchy in the right-hand panel of figure 111 and reported in table 18. The octant determination can be performed reasonably well even if $\sin^2\theta_{13}$(true) was zero [704]. However, if $\sin^2\theta_{13}$(true) is non-vanishing and reasonably large, the octant sensitivity of this experiments becomes significantly enhanced through earth matter effects appearing in the multi-GeV electron sample [38, 762].

6.2.3 Resolving the ambiguity in the neutrino-mass hierarchy

Large matter effects in atmospheric neutrinos can be exploited to probe the sign of Δm^2_{31}. Figure 112 shows the sensitivity to sign(Δm^2_{31}) that is expected in a magnetised-iron calorimeter with 4000 observed upward going events [768]. The simulation has been performed for both the normal and the inverted hierarchy; the curves show the χ^2, and hence the C.L., with which the wrong hierarchy can be ruled out. Fits have been carried out under the following conditions: all parameters other than the mass hierarchy are fixed (red lines); external priors have been used for the oscillation parameters (blue lines); and all oscillation parameters are allowed to vary freely in the fit (green lines). The left panel is for muon events in a detector with 15% energy and 15° zenith angle resolution, the middle panel is for muon events with 5% energy and 5° zenith angle resolution, while the right-hand panel is for electron events. For vanishing θ_{13}, the matter effects

Type of Experiment	$\sin^2\theta_{23}$(false) excluded at 3σ if:	for
Magnetised-Iron (0.5 MTy)	$\sin^2\theta_{23}(\text{true}) < 0.402$ or > 0.592	$\sin^2\theta_{13}(\text{true}) = 0.02$
	$\sin^2\theta_{23}(\text{true}) < 0.421$ or > 0.573	$\sin^2\theta_{13}(\text{true}) = 0.04$
Water Čerenkov (4.6 MTy)	$\sin^2\theta_{23}(\text{true}) < 0.383$ or > 0.600	$\sin^2\theta_{13}(\text{true}) = 0.00$
	$\sin^2\theta_{23}(\text{true}) < 0.438$ or > 0.573	$\sin^2\theta_{13}(\text{true}) = 0.02$

Table 18: A comparison of the potential of different experiments to rule out the wrong θ_{23} octant at 3σ (1 dof). The third column gives the condition on the true value of $\sin^2\theta_{13}$ needed for the θ_{23} octant resolution.

vanish giving $\chi^2 = 0$. As θ_{13} increases, matter effects increase, thereby increasing the sensitivity of the experiment to the hierarchy. For a magnetised-iron calorimeter such as INO, where the energy resolution is expected to be around 15% and the zenith angle resolution to be around 15°, the wrong hierarchy can be ruled out at $\sim 2\sigma$ using the muon events, if $\sin^2 2\theta_{13}(\text{true}) = 0.1$ and $\sin^2\theta_{23}(\text{true}) = 0.5$, and where the information from the other long-baseline experiments on the oscillation parameters have been included through the priors. Comparison of the left with the middle panel shows that the sensitivity to the hierarchy increases if the detector resolution is improved. Comparison of the left with the right-hand panel shows that the sensitivity to the hierarchy increases if the detector is able to detect electron-type events. Of course, since matter effects increase with θ_{23}, the sensitivity to the hierarchy increases as the true value of θ_{23} increases.

The sign of Δm^2_{31} can be determined using the excess in the multi-GeV electron sample that arises due to matter effects using a water Čerenkov detector [38, 762, 767, 770]. The wrong hierarchy can be ruled by a 4.6 Megaton-year exposure of such an experiment at more than 2σ if $\sin^2 2\theta_{13}(\text{true}) = 0.1$ and $\sin^2\theta_{23}(\text{true}) = 0.5$ [38, 762]. This is comparable to the sensitivity of the magnetised-iron detectors discussed above. However, since water detectors use the excess in electron events for multi-GeV neutrinos for which matter effects contribute to the probability $P_{\mu e}$, the excess is also dependent on the CP phase δ. If the value of δ is allowed to vary freely in the fit then the sensitivity decreases appreciably [762].

6.3 Neutrino Mass Hierarchy from Future $0\nu\beta\beta$ Experiments

If neutrinos are Majorana particles, it may be possible to observe the process $(A, Z) \to (A, Z-2) + 2\,e^-$, neutrinoless double-beta decay ($0\nu\beta\beta$). The effective mass that may be extracted, or bounded, in a $0\nu\beta\beta$ experiment is given by the coherent sum: $\langle m \rangle = \left|\sum_i m_i U_{ei}^2\right|$, where m_i is the mass of the i^{th} neutrino mass state, the sum is over all the light-neutrino mass states and U_{ei} are the matrix elements of the neutrino mixing matrix, i.e. $\langle m \rangle$ depends on 7 out of the 9 parameters

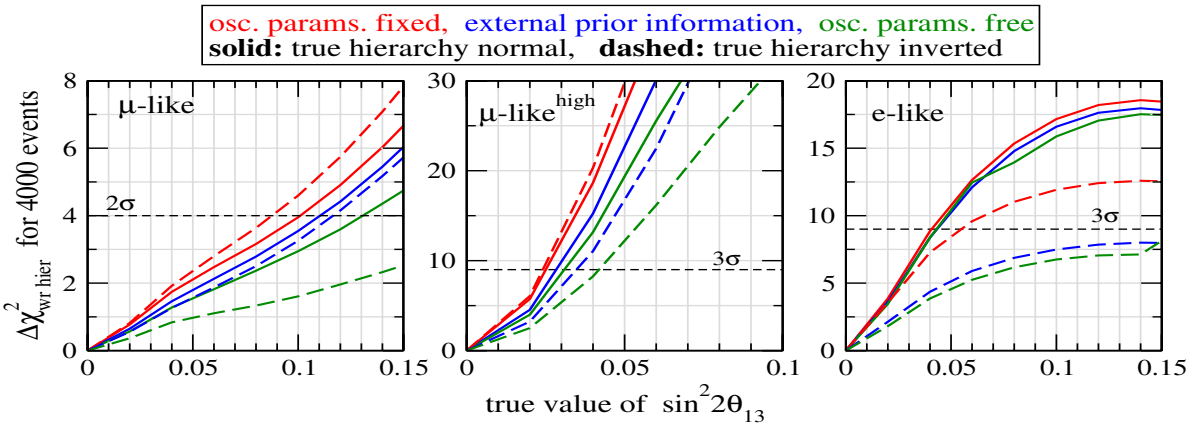

Figure 112: $\Delta\chi^2$ for the wrong hierarchy as a function of $\sin^2 2\theta_{13}$(true). See the text for the details.

contained in the neutrino-mass matrix. In particular, the effective mass that may be extracted from neutrinoless double beta decay depends on the neutrino-mass spectrum. There have been a large number of papers written on the implications of a future measurement of $\langle m \rangle$ (see for example [133]). At present, the best limit on the effective mass is given by the Heidelberg–Moscow collaboration $\langle m \rangle \leq 0.35\, z$ eV, where $z(= \mathcal{O}(1))$ indicates that there is an uncertainty in the value of the nuclear matrix elements (NME) involved in the $0\nu\beta\beta$ process [771]. Several new experiments are running, under construction, or in the planing phase [131]. It is reasonable, therefore, to expect that $\langle m \rangle$ will be probed down to $\simeq 0.04$ eV and it is pertinent to ask if such a measurement can help determine the neutrino-mass hierarchy.

For the normal-hierarchy (NH) scheme, for which $m_1 \ll m_2 \ll m_3$, and assuming that m_1 can be neglected, the effective mass may be written:

$$\langle m \rangle^{\rm NH} \simeq \left| \sqrt{\Delta m^2_{21}}\, \sin^2\theta_{12}\, \sin^2\theta_{13} + \sqrt{\Delta m^2_{31}}\, \sin^2\theta_{13}\, e^{2i(\beta-\alpha)} \right| . \tag{306}$$

For the inverted-hierarchy (IH) scheme, assuming that $m_3 \ll m_1 < m_2$, and neglecting m_3, the effective mass may be written:

$$\langle m \rangle^{\rm IH} \simeq \sqrt{|\Delta m^2_{31}|}\, \sin^2\theta_{13}\, \sqrt{1 - \sin^2 2\theta_{12}\, \sin^2\alpha} . \tag{307}$$

Any positive signal for $0\nu\beta\beta$ will be able to distinguish the IH scheme from the NH scheme if the difference between the predicted values for $\langle m \rangle$ for the IH scheme and the NH scheme is larger than the error in the measured value of $\langle m \rangle$. Among the most important errors involved is the one coming from the uncertainty in the value of the nuclear matrix elements. Figure 113 shows the difference in the predicted values of $\langle m \rangle^{\rm NH}_{\rm max}$ and $\langle m \rangle^{\rm IH}_{\rm min}$ taking into account the error in the nuclear matrix elements [152]. $\langle m \rangle^{\rm NH}_{\rm max}$ and $\langle m \rangle^{\rm IH}_{\rm min}$ are the largest and smallest values for $\langle m \rangle$ that are allowed, given the present knowledge of the oscillation parameters, in the NH and IH scheme respectively. This uncertainty is incorporated through the parameter z, which gives the factor by which the nuclear matrix elements are uncertain (see [152] for the details). It was argued in [152] that, for a given mass hierarchy, the uncertainty in the

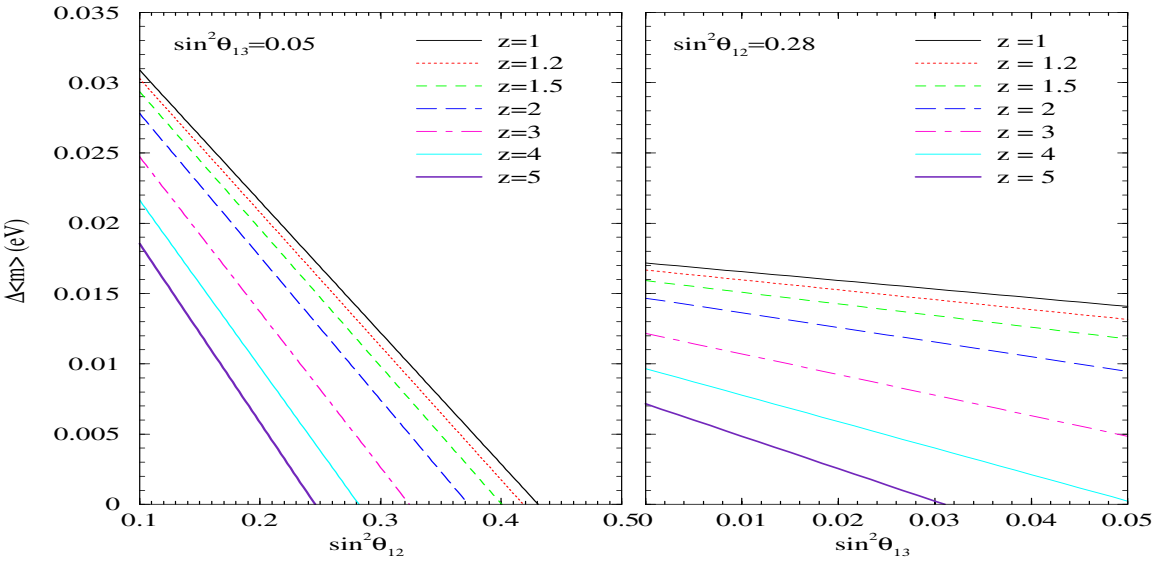

Figure 113: The difference between the minimal value of $\langle m \rangle$ for IH and the maximal value of $\langle m \rangle$ for NH for different z, as a function of $\sin^2\theta_{12}$ (left–hand panel) and $\sin^2\theta_{13}$ (right–hand panel). Taken with kind permission of Physical Review Letters from figure 4 in reference [772]. Copyrighted by the American Physical Society. Taken with kind permission of the Physical Review from figure 5 in reference [152]. Copyrighted by the American Physical Society.

prediction of $\langle m \rangle$ coming from the uncertainty in the allowed values of Δm^2_{31} and Δm^2_{21} can be neglected since these parameters are expected to be measured with very high accuracy in the immediate future. Therefore, the major uncertainty in $\langle m \rangle$ will come from the uncertainty on the values of $\sin^2\theta_{12}$ and $\sin^2\theta_{13}$. Figure 113 shows the impact of the uncertainty in the values of $\sin^2\theta_{12}$ and $\sin^2\theta_{13}$ on the sensitivity of the future $0\nu\beta\beta$ experiments to the neutrino-mass hierarchy. The figure shows that for $\sin^2\theta_{13}$ close to its current limit and assuming $z = 2$, $\sin^2\theta_{12} = 0.3$, and $\Delta\langle m \rangle \simeq 0.01$ eV it should be possible to determine the mass hierarchy if the experimental uncertainty in $\langle m \rangle$ is less than 0.01 eV. The chances of determining the hierarchy is largest when $\sin^2\theta_{13} = 0$. More importantly, while the dependence on $\sin^2\theta_{13}$ is weak, the sensitivity of the $0\nu\beta\beta$ experiments to the hierarchy is strongly dependent on $\sin^2\theta_{12}$. Therefore, a substantial reduction in the uncertainty on the allowed values of $\sin^2\theta_{12}$ is a prerequisite for the determination of the neutrino-mass hierarchy using $0\nu\beta\beta$ experiments.

So far, the assumption that the lightest neutrino mass was close to zero has been made. If the lightest neutrino had a mass $m_0 \gtrsim 0.01$ eV, it would not be possible to distinguish between the NH and IH schemes using $0\nu\beta\beta$ measurements, the mass spectrum in that case would be quasi-degenerate. However, we could still use $0\nu\beta\beta$ to put a limit on the absolute neutrino-mass scale. For a quasi-degenerate (QD) mass spectrum, with a common mass scale m_0, the limit on the neutrino mass reads [152]:

$$m_0 \leq z \, \langle m \rangle^{\rm exp}_{\rm min} \, \frac{1 + \tan^2\theta_{12}}{1 - \tan^2\theta_{12} - 2\,|U_{e3}|^2} \equiv z \, \langle m \rangle^{\rm exp}_{\rm min} \, f(\theta_{12}, \theta_{13}) \; . \tag{308}$$

Currently, the uncertainty on $f(\theta_{12}, \theta_{13})$ is around 50%, $1.9 < f(\theta_{12}, \theta_{13}) < 5.6$. It is expected

to reduce to $\sim$ 21% ($\sim$ 9%) at 3σ if a low energy pp solar-neutrino experiment (a reactor experiment at the SPMIN) should be built. The uncertainty depends only a little on the value of θ_{13}. From the current limit on the effective mass, $\langle m \rangle \leq 0.35\, z$ eV, with the accepted value of $z \simeq 3$ and our current knowledge of $f(\theta_{12}, \theta_{13})$, we can set a limit on m_0 of 5.6 eV, clearly weaker than the limit from tritium beta decay experiments. However, if $f(\theta_{12}, \theta_{13})$ was known with an uncertainty of 20%, say $2.7 < f(\theta_{12}, \theta_{13}) < 4.0$, then for $z \langle m \rangle^{\rm exp}_{\rm min} = 0.1$ eV the limit would become 0.3 eV $\lesssim m_0 \lesssim$ 0.4 eV. Of course, if there is no signal for $0\nu\beta\beta$, but just an upper limit on $z \langle m \rangle_{\rm min}$, the allowed range of m_0 will be replaced by an upper limit corresponding to the largest value in the range. The examples given above, indicate that, for the QD mass spectrum, a measurement of, or a better constraint on, $\langle m \rangle$ will lead to a stronger limit on the absolute neutrino mass scale than can currently be obtained from direct kinematic searches.

6.4 Astrophysical methods of determining the mixing parameters

Measuring the fluxes of neutrinos from astrophysical sources can help us to determine the mixing-matrix elements. The goal of this section is to discuss this method, focusing on the possibility of extracting $|U_{\mu 1}|$, arguably the most challenging element of the mixing matrix to measure. In section 4.4.2, we discussed the possibility of using neutrino beams made up either of pure or incoherent mass eigenstates to extract the moduli of the mixing-matrix elements by studying their charged-current interactions. Astrophysical sources can yield such beams through three classes of mechanisms: adiabatic conversion; neutrino decay; and decoherence. The second and third cases will be discussed in detail in sections 6.4.2 and 6.4.3. Here we comment on the case of adiabatic conversion which takes place for solar neutrinos. Propagating from central regions of the Sun, the electron neutrinos with energies $E > 10$ MeV are converted to a state which nearly coincides with ν_2 at the surface of the Sun. As a result, by studying the charged-current interactions of the solar neutrinos with $E > 10$ MeV, we can determine $|U_{e2}|$. Unfortunately, the energy of these neutrinos will be too small to allow muon production at the detectors; so, they cannot be used to extract $|U_{\mu 2}|$. However, there is a possibility that more energetic neutrinos ($E \gg m_\mu$) may be produced inside the Sun: if the dark matter is composed of Weakly Interacting Massive Particles (WIMPs), over time they can be accumulated in the core of the Sun. Thus, the WIMP-annihilation rate in the core of the Sun will increase, giving rise to a relatively high energy flux (for a recent review, see [773]). As shown in [587], for the low energy part of the spectrum $E_\nu < 5$ GeV, the transition probability in the Sun will be adiabatic and therefore the oscillation probabilities will depend only on the absolute values of the elements of U_{PMNS}. In [587], it was suggested that the value of $|U_{\mu 1}|$ could be derived by studying these neutrinos. Unfortunately, because of the high energy-threshold of large-scale neutrino detectors, this method does not seem to be feasible. There is another mechanism for production of neutrinos with $E_\nu > 1$ GeV inside the Sun: cosmic-ray collisions in the Sun can give rise to 'solar-atmospheric neutrinos'. Recently in [774], it has been shown that the oscillation probability of these neutrinos (after averaging over neutrino and anti-neutrino channels) depends only on the absolute values of the elements of the PMNS matrix. However, low statistics (only $\sim$ten events in ICECUBE per year) render this an unsuitable tool for the extraction of $|U_{\mu 1}|$.

6.4.1 General remarks about astrophysical neutrinos

The methods for extracting $|U_{\mu 1}|$ discussed here are based on the flavour-identification capability of neutrino telescopes. Since neutrino telescopes cannot distinguish between neutrino and anti-neutrino; neutrino and anti-neutrino events will therefore enter the same data sample.

In the energy range 1–100 TeV, a neutrino telescope can identify two types of neutrino events: muon-track events; and shower-like events. The muon-tracks originate from the charged current (CC) interactions of ν_μ ($\bar{\nu}_\mu$) as well as CC interactions of ν_τ ($\bar{\nu}_\tau$), with the subsequent decay of the τ (τ^+) to μ (μ^+). Shower-like events can be produced in three ways: neutral current (NC) interactions of all the active neutrinos; CC interaction of ν_e ($\bar{\nu}_e$); and CC interactions of ν_τ ($\bar{\nu}_\tau$) and the subsequent decay of τ (τ^+) through non-muonic decay modes. It is convenient to define the ratio:

$$R \equiv \frac{\text{muon} - \text{track events}}{\text{shower} - \text{like events}}. \tag{309}$$

Following the above discussion, R can be written as:

$$R = \frac{\int_{E_{th}^{\mu}} \left[\frac{dN_{\mu}^{CC}(F_{\nu_\mu}, F_{\bar{\nu}_\mu})}{dE_\mu} + B \frac{dN_{\tau\to\mu}^{CC}(F_{\nu_\tau}, F_{\bar{\nu}_\tau})}{dE_\mu} \right] \times R_\mu(E_\mu) dE_\mu}{T \int_{E_{th}^{sh}}^{E_{cut}} \left(\sum_\alpha \frac{dN^{NC}(F_{\nu_\alpha}, F_{\bar{\nu}_\alpha})}{dE} + \frac{dN^{CC}(F_{\nu_e}, F_{\bar{\nu}_e})}{dE} + (1-B) \frac{dN^{CC}(F_{\nu_\tau}, F_{\bar{\nu}_\tau})}{dE} \right) dE}, \tag{310}$$

where R_μ and T are respectively the muon range and the thickness of the detector, and $B \equiv \mathrm{Br}(\tau \to \mu \nu_\mu \nu_\tau)$. dN_α^{CC}/dE and dN_α^{NC}/dE are respectively the rates of CC and NC interactions of ν_α and $\bar{\nu}_\alpha$:

$$\frac{dN_\mu^{CC}(F, \tilde{F})}{dE_\mu} = \int^{E_{cut}} \frac{dF}{dE_\nu} \frac{d\sigma_{CC}}{dE_\mu} dE_\nu + \int^{E_{cut}} \frac{d\tilde{F}}{dE_{\bar{\nu}}} \frac{d\bar{\sigma}_{CC}}{dE_\mu} dE_{\bar{\nu}} \, ; \tag{311}$$

$$\frac{dN^{CC}(F, \tilde{F})}{dE} = \sigma_{CC} \frac{dF}{dE} + \bar{\sigma}_{CC} \frac{d\tilde{F}}{dE} \tag{312}$$

and

$$\frac{dN^{NC}(F, \tilde{F})}{dE} = \int_0^{E - E_{th}} \left[\frac{d\sigma_{NC}}{dE_{\nu_f}} \frac{dF}{dE} + \frac{d\bar{\sigma}_{NC}}{dE_{\nu_f}} \frac{d\tilde{F}}{dE} \right] dE_{\nu_f} \, . \tag{313}$$

Here σ_{CC} and $\bar{\sigma}_{CC}$ are the charged-current cross sections for ν and $\bar{\nu}$, and $d\sigma_{NC}/dE_{\nu_f}$ and $d\bar{\sigma}_{NC/dE_{\bar{\nu}_f}}$ are the partial cross sections for $\nu(E)N \to \nu_f(E_{\nu_f}) + \text{jet}$ and $\bar{\nu}(E)N \to \bar{\nu}_f(E_{\bar{\nu}_f}) + \text{jet}$, respectively. Finally,

$$\frac{dN_{\tau\to\mu}^{CC}(F, \tilde{F})}{dE_\mu} = \tag{314}$$

$$\int_0^{E_\tau} \int_0^{E_{cut}} f(E_\tau, E_\mu) \frac{d\sigma_{CC}}{dE_\tau} \frac{dF}{dE_{\nu_\tau}} dE_{\nu_\tau} dE_\tau + \int_0^{E_\tau} \int_0^{E_{cut}} f(E_\tau, E_\mu) \frac{d\bar{\sigma}_{CC}}{dE_\tau} \frac{d\tilde{F}}{dE_{\bar{\nu}_\tau}} dE_{\bar{\nu}_\tau} dE_\tau \, , \tag{315}$$

where $f(E_\tau, E_\mu)$ is the probability of the production of a muon with energy E_μ in the decay of a τ lepton with energy E_τ.

The possibility of measuring R using the ICECUBE experiment has been studied in detail in [775] and it has been found that with $E_\nu^2 dF_\nu/dE_\nu = 10^{-7}$ GeV cm^2 sec^{-1}, the ratio R can be measured with 20% accuracy after one year of data taking. Since the statistical error dominates, by increasing the data-taking time to 10 years, the uncertainty would decrease to 7%.

Notice that we have used the fact that, at this energy range ($E_{c.o.m} \gg m_\tau$), the cross sections are approximately equal for all flavours. In the above formulæ, E_{th}^{μ} ($\sim$1 TeV) and E_{th}^{sh} are respectively the thresholds for detecting muon-track and shower-like events and E_{cut} ($\sim$ 100 TeV) is the energy above which neutrinos will be absorbed in the Earth. Above E_{cut}, all the neutrinos will be absorbed in the Earth but ν_τ can re-appear as a result of the transitions $\nu_\tau \to \tau \to \nu_\tau$. Of course, the final ν_τ reaching the detector will be less energetic than the original one, which can fake a ν_τ with energy less than E_{cut}. Consequently, the ratio R will turn out to be smaller than expected if this phenomenon is not taken into account. In order to be able to extract $|U_{\mu 2}|$ with the required precision, it will be necessary to evaluate the correction due to such an effect. Estimating this correction requires some knowledge of the energy spectrum for $E > E_{cut}$ and is therefore model dependent.

Notice that before entering the detector, the upward-going neutrinos pass through the Earth. However, this will not significantly change the flavour composition because, for $E > 1$ TeV, $\Delta m_{31}^2/2E \ll \sqrt{2} G_F n_e$ and the effective flavour mixing in the Earth is therefore strongly suppressed.

6.4.2 Unstable neutrinos arriving from cosmic distances

In [587], the possibility of employing the decaying neutrinos to derive the CP-violating phase has been proposed. In a series of papers [776, 777], the idea has been further elaborated. In the following, the results will be reviewed.

In the SM, neutrinos are stable, however, in the framework of Majoron models, the rapid decay of neutrinos may become a possibility [309, 778]:[19]

$$\nu_i \to \bar{\nu}_j + J \ , \tag{316}$$

where ν_i and ν_j are mass eigenstates, and J is a Goldstone boson called the Majoron.

[19] It was shown later in ref. [252] that the decays discussed in [309, 778] are so much suppressed that these decay modes are phenomenologically irrelevant. However, majoron couplings are rather model-dependent, and it is possible to contrive models where they are sizable enough to lead to lifetimes of phenomenological interest. For more on these issues, see [76, 779]. Here we simply assume that fast invisible decays of neutrinos are possible, and ask ourselves whether such decay modes lead to interesting consequences.

If the lifetime of the neutrinos in their rest frame is finite but much larger than $\sim 10^{-3}$ sec, the solar and atmospheric neutrinos will not undergo decay; however, neutrinos from very distant sources (i.e., the gamma-ray bursters, the Active Galactic Nuclei, AGN, and supernovæ) can decay before reaching the detectors. At the detectors, the neutrino flux from the distant sources will be composed only of the lightest neutrinos, ν_1 and $\bar{\nu}_1$: F_1 and $F_{\bar{1}}$. Notice that we have assumed that the ordering of the neutrino masses is normal: $m_1 < m_2 < m_3$. As a result, regardless of the flavour composition at the source, we expect that at the detector:

$$dF_{\nu_e}/dE : dF_{\nu_\mu}/dE : dF_{\nu_\tau}/dE = |U_{e1}|^2 : |U_{\mu 1}|^2 : |U_{\tau 1}|^2 \, , \tag{317}$$

and recalling that mixing matrices of neutrinos and anti-neutrinos are the complex conjugate of of one-another, we have

$$dF_{\bar{\nu}_e}/dE : dF_{\bar{\nu}_\mu}/dE : dF_{\bar{\nu}_\tau}/dE = |U_{e1}|^2 : |U_{\mu 1}|^2 : |U_{\tau 1}|^2 \, . \tag{318}$$

Notice that this result is independent of energy. Equation (310) implies:

$$R = \frac{|U_{\mu 1}|^2 + B\xi_1 |U_{\tau 1}|^2}{\xi_2 + |U_{e1}|^2 \xi_3 + (1-B)\xi_3 |U_{\tau 1}|^2} \, , \tag{319}$$

where (see equations (311), (312), (313), and (314) for definitions):

$$\xi_1 = \frac{\int_{E^\mu_{th}} \frac{dN^{CC}_{\tau\to\mu}(F_1, F_{\bar{1}})}{dE_\mu} \times R_\mu(E_\mu) dE_\mu}{\int_{E^\mu_{th}} \frac{dN^{CC}_{\mu}(F_1, F_{\bar{1}})}{dE_\mu} R_\mu(E_\mu) dE_\mu} \, ; \tag{320}$$

and:

$$\xi_2 = \frac{T \int_{E^{sh}_{th}}^{E_{cut}} \sum_\alpha \frac{dN^{NC}(F_1, F_{\bar{1}})}{dE}}{\int_{E^\mu_{th}} \frac{dN^{CC}_{\mu}(F_1, F_{\bar{1}})}{dE_\mu} R_\mu(E_\mu) dE_\mu} \, ; \tag{321}$$

and finally:

$$\xi_3 = \frac{T \int_{E^{sh}_{th}}^{E_{cut}} \frac{dN^{CC}(F_1, F_{\bar{1}})}{dE} dE}{\int_{E^\mu_{th}} \frac{dN^{CC}_{\mu}(F_1, F_{\bar{1}})}{dE_\mu} R_\mu(E_\mu) dE_\mu} \, . \tag{322}$$

In first approximation, $F_{\nu_e} : F_{\nu_\mu} : F_{\nu_\tau} \sim 0.6 : 0.15 : 0.15$, which significantly deviates from what is expected in the case of stable neutrinos. Thus, by measuring R with a moderate precision, we can test whether neutrinos are stable or not. To extract $|U_{\mu 1}|$ precisely enough, higher accuracy in the measurement of R will be required. Though the flux arriving at the Earth is purely composed of ν_1 and $\bar{\nu}_1$, for extracting R from the data the knowledge of the dependence of the neutrino flux on energy, $F_1(E)$, is necessary since detection of processes contributing to R have different kinematics. As discussed in [775], the spectrum of neutrinos can be determined by measuring the total energy of muon-track events. The accuracy with which the spectrum can be determined, as indicated in [775], strongly depends on the overall shape of the spectrum. Another limiting factor will be the size of the data sample which depends on the, as yet unknown, neutrino luminosity at the source.

γ-ray bursts may be accompanied by a flux of energetic ($\sim$ 1 TeV) neutrinos [780]. Taking the distance of the γ-ray burster from the Earth to be of order 10^{28} cm, one finds that $\overset{(-)}{\nu}_2$ and $\overset{(-)}{\nu}_3$ will decay before reaching the detectors if their lifetimes in their rest frame, τ_{ν_i}, satisfy the following inequality:

$$\tau_{\nu_i} \lesssim 10^{16}\text{sec} \left(\frac{m_{\nu_i}}{E}\right)\left(\frac{L}{10^{28}\text{ cm}}\right). \tag{323}$$

In the case of a hierarchical spectrum $m_1 \simeq 0$, $m_3 \sim 0.05$ eV and $m_2 \sim 0.009$ eV, from equation (323) we find that in order to have en route decay of ν_2 and ν_3 coming from gamma ray bursters, their respective lifetimes have to be shorter than 10 sec and 100 sec. For the quasi-degenerate spectrum with $m_1 \simeq m_2 \simeq m_3 = 0.1$ eV, the bound is weaker: 10^3 sec. Taking the coupling of the Majoron to neutrinos to be $\mathcal{O}\left(10^{-6}\right)$ (corresponding to the bound from supernova cooling considerations [781]), we find the lifetime of neutrinos in their rest frames to be of order of 1 sec for $m_\nu = \left(\Delta m^2_{21}\right)^{1/2}$, which means neutrinos with TeV-scale energies that come from cosmic distances can decay before reaching the detectors, whereas neutrinos with TeV-scale energies produced inside our Galaxy will not have enough time to decay before reaching the Earth. If nature is so kind as to set the lifetime of neutrinos in this range, the two methods described in this section and the next may be combined to extract the value of $|U_{\mu 1}|$. All these considerations are essentially at an 'idea level' and further study is necessary to see if useful information can be obtained from the proposed measurements.

The flux of neutrinos with TeV-scale energies from an individual γ-ray burster at cosmological distance $z \sim 1$ produces $(10^{-1} - 10)$ muons in 1 km^3-size detectors [780]. Since these neutrinos are correlated in time with the γ-ray bursts and coming from the same source, they can be distinguished from background neutrino fluxes. The rate of γ-ray bursts detectable on the Earth is $\sim 10^3$/year, so the data sample is fairly large and useful information on mixings may be obtained.

6.4.3 Stable neutrinos and loss of coherence

Consider stable or meta-stable neutrinos produced by cosmological sources. For example, consider again the neutrinos with $E \sim 1$ TeV accompanying the γ-ray bursts [780] or TeV neutrinos from the center of our Galaxy ($L \sim$ 10 kpc). For such neutrinos, the oscillation length is much smaller than the distance from the source; i.e., $\Delta m^2_{21} L/E \gg 1$. As a consequence, the (anti-)neutrino beam will loose its coherence and the transition probability is therefore averaged out as:

$$P_{\alpha\beta} = \bar{P}_{\alpha\beta} = \sum_i |U_{\alpha i}|^2 |U_{\beta i}|^2 \,, \tag{324}$$

where $P_{\alpha\beta}$ and $\bar{P}_{\alpha\beta}$ are respectively the probabilities of transitions $\nu_\alpha \to \nu_\beta$ and $\bar{\nu}_\alpha \to \bar{\nu}_\beta$. To derive (324) the fact that $|\bar{U}_{\alpha i}| = |U_{\alpha i}|$ has been used. In particular:

$$P_{\mu\mu} = \sum_i |U_{\mu i}|^4 = K_{\mu\mu} - 2|U_{\mu 2}|^2 |U_{\mu 1}|^2 \,, \tag{325}$$

and:

$$P_{e\mu} = \sum_i |U_{\mu i}|^2 |U_{ei}|^2 = K_{e\mu} - |U_{\mu 2}|^2 (|U_{e1}|^2 - |U_{e2}|^2) \ , \tag{326}$$

where $K_{\mu\mu}$ and $K_{e\mu}$ are known functions of $|U_{e1}|$, $|U_{e2}|$, $|U_{e3}|$, $|U_{\mu 3}|$ which do not depend on $|U_{\mu 1}|^2$ and $|U_{\mu 2}|^2$. The probability P_{ee} does not depend on $|U_{\mu 1}|^2$ and $|U_{\mu 2}|^2$.

The probabilities in equations (324), (325), and (326) have the following properties which play a key role in the calculations: $P_{\alpha\beta} = P_{\beta\alpha}$; the probabilities for neutrinos and anti-neutrinos are equal; and the probabilities do not depend on energy.

Let us assume that at the source $F_{\nu_e} : F_{\nu_\mu} : F_{\nu_\tau} = w_e : w_\mu : w_\tau$. After traveling long distances ($\Delta m^2_{21} L/2E \gg 1$), the flavour ratio will evolve into:

$$F_{\nu_e} : F_{\nu_\mu} : F_{\nu_\tau} = \sum_{\alpha,i} w_\alpha |U_{\alpha i}|^2 |U_{ei}|^2 : \sum_{\alpha,i} w_\alpha |U_{\alpha i}|^2 |U_{\mu i}|^2 : \sum_{\alpha,i} w_\alpha |U_{\alpha i}|^2 |U_{\tau i}|^2. \tag{327}$$

Thus, the ratio R depends on $|U_{\mu 1}|$ and measuring this ratio, the value of $|U_{\mu 1}|$ can, in principle, be derived [587] (see also [782–784]). However, this ratio strongly depends on the original flavour composition. Two different processes for neutrino production have been suggested with different predictions for the flavour ratios:

1. $\pi^+ \to \mu^+ + \nu_\mu$, and then $\mu^+ \to e^+ + \nu_e + \bar{\nu}_\mu$; and the CP-conjugate of these processes. These processes yield $F^0_{\nu_e} : F^0_{\nu_\mu} : F^0_{\nu_\tau} = 1 : 2 : 0$ at the source; and
2. Decay of the neutron: $n \to p + e + \bar{\nu}_e$ which yields $F^0_{\nu_e} : F^0_{\nu_\mu} : F^0_{\nu_\tau} = 1 : 0 : 0$.

The two cases can be discriminated by a moderately accurate measurement of R. However, as shown in [785], the muon produced in pion decay can lose energy before it decays, which in turn reduces the value of $F^0_{\nu_e} : F^0_{\nu_\mu}$ at the source. Moreover, the two processes can simultaneously be at work which again will result in an unknown flavour ratio at the source. In order to extract $|U_{\mu 1}|$ with an accuracy of 10%, it is necessary to know the original flux with a precision better than 10%. As discussed in [587], if F_{ν_e}/F_{ν_μ} and F_{ν_τ}/F_{ν_μ} are separately measured, it will be possible to independently extract the original flavour ratio. Such information can be derived, if the detector can discriminate between electronic showers (resulting from the CC interactions of ν_e or the CC interaction of ν_τ and the subsequent decay of the produced τ to the electron) and hadronic showers (produced by the NC interaction of all neutrinos or the CC interaction of ν_τ and the subsequent 'hadronic' decay of the produced τ). Although such a discrimination is in principle possible but, in practice, it will be challenging [775].

6.4.4 Summary

In this section, we have discussed the possibility of extracting information on the mixing parameters by studying neutrinos from astrophysical sources. As discussed in section 4.4, measuring

the value of $|U_{\mu 1}|$ is essential for reconstructing the unitarity triangle; it is extremely challenging for the accelerator-based experiments to measure $|U_{\mu 1}|$. We have therefore focused on deriving $|U_{\mu 1}|$ from the astrophysical-neutrino data in this section.

The flavour ratio of astrophysical neutrinos can be employed to measure $|U_{\mu 1}|$. In the case of stable neutrinos, the result would suffer from the uncertainty in the flavour composition of the flux at the source. We have argued that if neutrinos decay on their way with $\tau_\nu < 10 - 10^3$ sec (depending on the neutrino-mass scheme) such an uncertainty would not affect the results. So, if there sources of sufficient luminosity to provide reasonable data samples, astrophysical neutrinos can be considered a useful means of deriving $|U_{\mu 1}|$ and thus reconstructing the unitarity triangle.

7 Muon physics

7.1 Introduction

Ever since the discovery of the muon, the study of its properties and decays have contributed to a deeper understanding of Nature at the smallest distance scale. Muon physics played a fundamental role in establishing the V–A structure of weak interactions and the validity of quantum electrodynamics. Moreover, muon physics has not yet exhausted its potential and, indeed, may provide crucial information regarding one of the most fundamental quests in modern physics: the structure of the theory which lies beyond the Standard Model of particle physics. The present 3.4 standard deviation difference between the measured [786–788] and Standard Model [789] values of the muon anomalous magnetic moment, $a_\mu = (g_\mu - 2)/2$, might be such an example.

A muon storage ring is an essential part of the Neutrino Factory idea, with the primary aim of the machine being the study of neutrino properties. The Neutrino Factory is also an ideal place to study muon properties, since they provide, necessarily, muon fluxes which are orders of magnitude larger than that which can be obtained at present. For example, at the Paul Scherrer Institut (PSI) beams of 10^8 μ/s are available. At the Japan Proton Accelerator Research Complex (J-PARC) the proposed muon intensity for the PRISM experiment is 10^{11} to 10^{12} μ/s. At a Neutrino Factory fluxes as large as 10^{13} to 10^{14} μ/s could be available. It is, therefore, imperative to understand how to take full advantage of these intense muon beams in order to improve significantly on the reach of low-energy muon experiments.

Independent of whether or not $(g-2)_\mu$ is constraining, or pointing to, new physics, it, along with the suite of muon experiments described below, will provide significant information from the precision frontier that is complementary to that expected from the Large Hadron Collider. If charged lepton-flavour-violation, or a permanent electric-dipole moment are observed, they will help clarify our understanding of the information gained at the LHC. If not observed, along with $(g-2)_\mu$, they will restrict possible interpretations of the new physics. In order to proceed to significantly greater sensitivities, the electric-dipole moment and lepton-flavour violating experiments would greatly benefit from this new, very intense muon source.

While precise measurements of the muon lifetime and Michel parameters provide tests for the theory of weak interactions and its possible extensions, one of the main interests in muon physics lies in the search for processes that violate muon number, or the observation of a permanent muon electric-dipole moment (EDM). The discovery of decays such as $\mu^+ \to e^+\gamma$, $\mu^+ \to e^+e^-e^+$, of μ^-–e^- conversion in nuclei, or the observation of a muon EDM, would be an indisputable proof of the existence of new dynamics beyond the Standard Model.

Global symmetries (like individual lepton numbers), as opposed to local symmetries, are considered not to be based on fundamental principles and are expected to be violated by gravitational effects, in the strong regime, and, more generally, by higher-dimensional effective operators which describe local interactions originating from some unknown high-energy dynamics. Baryon number conservation is another example of an abelian global symmetry of the Standard Model, which can be broken by new-physics effects.

Atmospheric- and solar-neutrino experiments have provided strong evidence for neutrino oscillations, which has now been confirmed by terrestrial experiments at accelerators and reactors. This implies violation of individual lepton numbers (L_i) and, most likely, of total lepton number (L), which is a first indication of physics beyond the Standard Model. Current neutrino data indicate values of the neutrino masses corresponding to non-renormalisable interactions at a scale $M \sim 10^{9-14}$ GeV. New lepton-number violating dynamics at the scale M cannot yield observable rates for rare muon processes, since the corresponding effects are suppressed by $(m_\mu/M)^4$. The observation of muon-number violation in muon decays would thus require new physics beyond that responsible for neutrino masses. Theoretically, however, there is no reason why L_i and L would be broken at the same energy scale. Indeed, in many frameworks, such as supersymmetry, the L_i-breaking scale can be close to the weak scale. In this case, muon processes with L_μ violation would occur with rates close to the current experimental bounds.

It is also very important to stress that the information which can be extracted from the study of rare muon processes is, in many cases, not accessible to high-energy colliders. Take supersymmetry as an example. While the LHC can significantly probe slepton masses, it cannot compete with muon-decay experiments in constraining the slepton mixing angles.

In the following section we discuss dipole moments, lepton-flavour violation and other muon-decay experiments. Many additional details can be found in the excellent report of the CERN working group [790] of 2001, on which this document is based.

7.2 The Magnetic and Electric Dipole Moments of the Muon

The electric- and magnetic-dipole moments have been an integral part of relativistic electron (lepton) theory since Dirac's famous 1928 paper, in which he pointed out that an electron in external electric and magnetic fields has "the two extra terms:

$$\frac{e\hbar}{c}\left(\sigma, \boldsymbol{H}\right) + i\frac{e\hbar}{c}\rho_1\left(\sigma, \boldsymbol{E}\right), \tag{328}$$

	$\vec{E}$	$\vec{B}$	$\vec{\mu}$ or $\vec{d}$
P	-	+	+
C	-	-	-
T	+	-	-

(a)

Particle	Present EDM Limit (e cm)	Standard Model Value (e cm)
n	2.9×10^{-26} (90%CL) [796]	10^{-31}
e^-	$\sim 1.6 \times 10^{-27}$ (90%CL) [797]	10^{-38}
μ	$< 10^{-18}$ (CERN) [798]	10^{-35}
	$\sim 10^{-19}$ † (E821)	
^{199}Hg	2.1×10^{-28} (95%CL) [799]	

†Estimated

(b)

Table 19: (a) Transformation properties of the magnetic and electric fields and dipole moments. (b) Measured limits on electric dipole moments, and their Standard Model values

. . . [which], when divided by the factor $2m$, can be regarded as the additional potential energy of the electron due to its new degree of freedom. [791]" These terms represent the magnetic-dipole (Dirac) moment and electric dipole moment interactions with the external magnetic and electric fields.

In modern notation, the magnetic dipole moment (MDM) interaction becomes:

$$\bar{u}_\mu \left[eF_1(q^2)\gamma_\beta + \frac{ie}{2m_\mu} F_2(q^2)\sigma_{\beta\delta} q^\delta \right] u_\mu \,, \tag{329}$$

where $F_1(0) = 1$, and $F_2(0) = a_\mu$, the latter being the anomalous (Pauli) moment. The electric dipole moment (EDM) interaction is:

$$\bar{u}_\mu \left[\frac{ie}{2m_\mu} F_2(q^2) - F_3(q^2)\gamma_5 \right] \sigma_{\beta\delta} q^\nu u_\mu \,, \tag{330}$$

where $F_2(0) = a_\mu$, $F_3(0) = d_\mu$, with:

$$d_\mu = \left(\frac{\eta}{2}\right)\left(\frac{e\hbar}{2mc}\right) \simeq \eta \times 4.7 \times 10^{-14}\ e\,\text{cm}. \tag{331}$$

This η, which is the EDM analogy to g for the MDM, should not be confused with the Michel parameter η.

The existence of an EDM implies that both P and T are violated [792–794]. This can be seen by considering the non-relativistic Hamiltonian for a spin one-half particle in the presence of both an electric and a magnetic field: $\mathcal{H} = -\vec{\mu}\cdot\vec{B} - \vec{d}\cdot\vec{E}$. The transformation properties of $\vec{E}$, $\vec{B}$, $\vec{\mu}$ and $\vec{d}$ are given in the table 19(a), and we see that while $\vec{\mu}\cdot\vec{B}$ is even under all three, $\vec{d}\cdot\vec{E}$ is odd under both P and T. While parity violation has been observed in many weak processes, direct T violation has only been observed in the neutral-kaon system [795]. In the context of CPT symmetry, an EDM implies CP violation, which is allowed by the Standard Model for decays in the neutral-kaon and B-meson sectors.

The identification of new sources of CP violation appears to be a crucial requirement for explaining the dominance of matter over anti-matter in the Universe. Permanent electric-dipole

moments of fundamental particles would violate both time reversal (T) and parity (P) invariance, and with the assumption of CPT conservation also the CP symmetry [793, 794]. The present limits from EDM searches are given in table 19(b).

The anomalous magnetic moment (anomaly) of the muon, $a_\mu \equiv g_\mu - 2$, has a long history of constraining models of physics beyond the Standard Model. It has now been measured to a relative precision of 0.54 parts per million [786–788]. Muons are stored in a super-ferric storage ring, and the spin difference frequency between the cyclotron frequency and the muon-spin-rotation frequency is given by:

$$\vec{\omega}_a = -\frac{e}{m}\left[a_\mu \vec{B} - \left(a_\mu - \frac{1}{\gamma^2 - 1}\right)\vec{\beta} \times \vec{E}\right]. \tag{332}$$

which is the frequency that the spin precesses relative to the momentum. At $\gamma = 29.3$ the electric field used for vertical focusing does not contribute to the spin precession for a muon on the central orbit. By counting high-energy positrons as a function of time, one observes the muon lifetime modulated by the $(g-2)$ precession, as shown in figure 114(a). Both a_{μ^+} and a_{μ^-} were measured. Assuming CPT invariance, the E821 collaboration obtained the anomalous magnetic moment [788]:

$$a_\mu(\text{Expt}) = 11\,659\,181.2(6.9) \times 10^{-10} \quad (0.54\,\text{ppm})\,. \tag{333}$$

The total uncertainty includes a 0.46 ppm statistical uncertainty and a 0.28 ppm systematic uncertainty, combined in quadrature.

The Standard Model theory value consists of well known QED and Weak contributions, plus a hadronic contribution of about 60 ppm of a_μ which dominates the uncertainty on the Standard Model value. The leading-order contributions are shown diagrammatically in figure 115.

The hadronic contribution has been the source of substantial work [800, 801], which continues to the present. The lowest order must be taken from $e^+e^- \to$ hadrons using a dispersion relation [789]:

$$a_\mu^{(\text{Had;1})} = \left(\frac{\alpha m_\mu}{3\pi}\right)^2 \int_{4m_\pi^2}^{\infty} \frac{ds}{s^2} K(s) R(s); \tag{334}$$

where:

$$R \equiv \frac{\sigma_{\text{tot}}(e^+e^- \to \text{hadrons})}{\sigma_{\text{tot}}(e^+e^- \to \mu^+\mu^-)}\,, \tag{335}$$

and $K(s)$ is a known function [789]. The only assumptions here are analyticity and the optical theorem. Recently published data on the hadronic cross sections [802–805] have significantly reduced the uncertainty on the hadronic contribution [806, 807]. The present Standard Model value is [789]:

$$a_\mu^{(\text{SM07})} = 116\,591\,785(61) \times 10^{-11}\,. \tag{336}$$

When compared with the experimental value in equation (333) one obtains 3.4 standard deviation difference between experiment and theory [789, 806, 807].

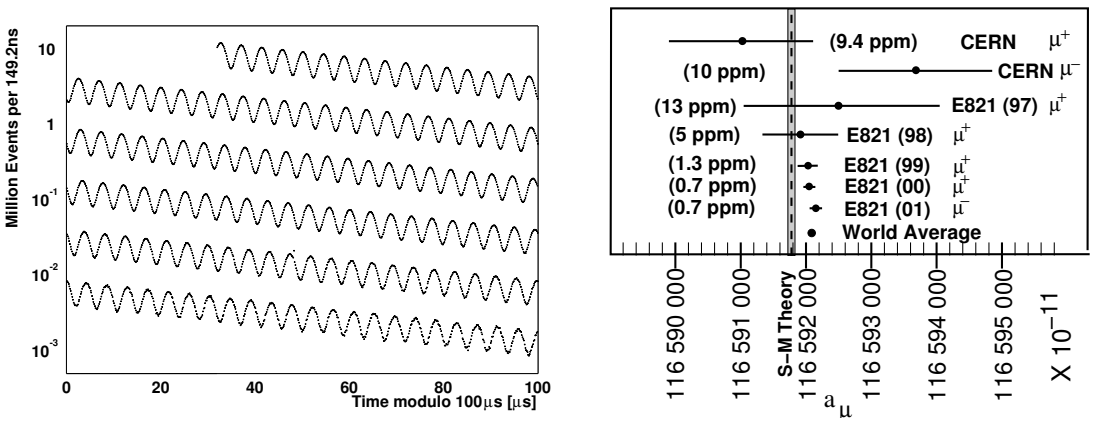

(a) (b)

Figure 114: (a)The time spectrum of 3.6×10^9 electrons with energy greater than 1.8 GeV from the 2001 E821 data set [787]. The diagonal "wiggles" displayed modulo 100 μs result from the muon spin precession in the storage ring. Adapted with kind permission of Physical Review from figure 2 in reference Bennett:2006fi. Copyrighted by the American Physical Society. (b)Measurements of the muon anomaly, indicating the value, as well as the muon's sign. As indicated in the text, to obtain the value of a_{μ^-} and the world average CPT invariance is assumed. The theory value is taken from reference [789], which uses electron-positron annihilation to determine the hadronic contribution.

It has been proposed that the hadronic contributions could also be determined from hadronic τ-decay data, using the conserved vector current (CVC) hypothesis [808]. Such an approach can only give the iso-vector part of the amplitude, i.e. the ρ but not the ω intermediate states. In contrast, the e^+e^- annihilation cross section contains both iso-vector and iso-scalar contributions, with the cusp from $\rho - \omega$ interference as a dominant feature. Since hadronic τ decay goes through the charged-ρ resonance, and e^+e^- annihilation goes through the neutral ρ, understanding the isospin corrections is essential in this approach. This use of the CVC can be checked by comparing the hadronic contribution to a_μ obtained from each method. Alternately, one can take the measured branching ratio for $\tau^- \to V^-\nu_\tau$, where V is any vector final state (*e.g.* $\pi^-\pi^0$) and compare it to that predicted using CVC and e^+e^- data, applying all the appropriate isospin corrections. At present, neither comparison gives a satisfactory result [807], and the prescription of CVC with the appropriate isospin correction seems to have aspects that are not understood. Given two consistent e^+e^- data sets and the uncertainties inherent in the required isospin corrections to the τ data, the most recent Standard Model evaluations do not use the τ data to determine $a^{(\mathrm{Had};1)}$ [789,806,807]. Additional e^+e^- data are expected to become available in the next year which should increase our confidence in the e^+e^--based evaluation.

Since the muon anomaly results from virtual particles that couple to the muon, or photon, in principle it is sensitive to all such particles, not just the known Standard Model particles. Thus the muon anomaly is sensitive to a number of potential candidates for physics beyond the Standard Model [809], e.g., new particles that couple to the muon such as the supersymmetric partners of the weak gauge bosons [810,811]; muon substructure, where the contribution depends

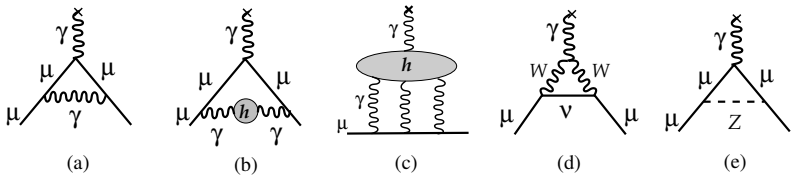

Figure 115: The Feynman graphs for: (a) Lowest-order QED (Schwinger) term; (b)Lowest-order hadronic contribution; (c) hadronic light-by-light contribution; (d)-(e) the lowest order electroweak W and Z contributions. With the present limits on m_h, the contribution from the single Higgs loop is negligible.

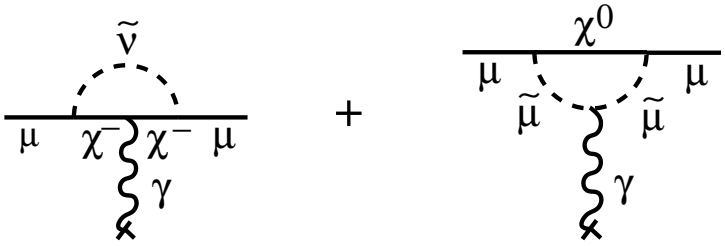

Figure 116: The lowest-order supersymmetric contributions to the muon anomaly. The χ are the superpartners of the Standard Model gauge bosons.

on the substructure scale Λ as, $\delta a_\mu(\Lambda_\mu) \simeq m_\mu^2/\Lambda_\mu^2$; W-boson substructure; and extra dimensions [812].

The potential contribution from supersymmetry has generated a lot of attention [810, 811], with the relevant diagrams shown in figure 116. A simple model with equal masses [809] gives

$$\begin{aligned} a_\mu^{(\mathrm{SUSY})} &\simeq \frac{\alpha(M_Z)}{8\pi \sin^2\theta_W} \frac{m_\mu^2}{\tilde{m}^2} \tan\beta \left(1 - \frac{4\alpha}{\pi} \ln\frac{\tilde{m}}{m_\mu}\right) \\ &\simeq (\mathrm{sgn}\mu)\ 13 \times 10^{-10}\ \tan\beta\ \left(\frac{100\ \mathrm{GeV}}{\tilde{m}}\right)^2\ ; \end{aligned} \tag{337}$$

where $\tan\beta$ is the ratio of the two vacuum expectation values of the two Higgs fields. If the SUSY mass scale were known, then $a_\mu^{(\mathrm{SUSY})}$ would provide a clean way to determine $\tan\beta$.

One candidate for the cosmic dark matter is the lightest supersymmetric partner, the neutralino, χ^0 in figure 116. In the context of a constrained minimal supersymmetric model (CMSSM), $(g-2)_\mu$ provides an orthogonal constraint on dark matter [813, 814] from that provided by the WMAP survey, as can be seen in figures 117 and 118.

The results from E821 at the Brookhaven AGS are interesting, if not definitive. Whatever the final interpretation of a_μ turns out to be, it will constrain the theories of physics beyond the Standard Model [815]. This ability is clearly demonstrated in figures 117 and 118 (see reference [815] for additional examples). An improved experiment is possible at existing facilities, and does not need the ultra high flux of muons that would be available at the Neutrino Factory. However, it is clear that the measurement needs to be further refined at BNL or a future facility.

While the MDM has a substantial Standard Model value, the Standard Model EDMs for the leptons are immeasurably small and lie orders of magnitude below the present experimental limits

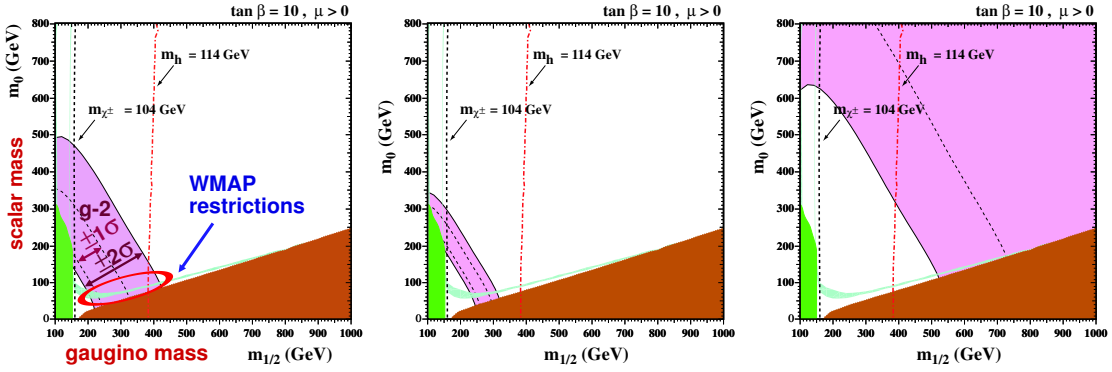

(a) (b) (c)

Figure 117: The m_0–$m_{1/2}$ plane of the CMSSM parameter space for $\tan\beta = 10$, $A_0 = 0$, sign$(\mu) = +$. (a) The $\Delta a_\mu^{(\text{today})} = 295(88) \times 10^{-11}$ between experiment and Standard Model theory is from reference [789], see text. The brown wedge on the lower right is excluded by the requirement the dark matter be neutral. Direct limits on the Higgs and chargino $\chi^\pm$ masses are indicated by vertical lines. Restrictions from the WMAP satellite data are shown as a light-blue line. The $(g-2)$ 1 and 2-standard deviation boundaries are shown in purple. The region "allowed" by WMAP and $(g-2)$ is indicated by the ellipse, which is further restricted by the limit on M_h. (b) The plot with $\Delta a_\mu = 295(39) \times 10^{-11}$, which assumes that in the future both the theory and experimental errors decrease to 22×10^{-11}. (c) The same errors as (b), but $\Delta = 0$. (Figures courtesy of K. Olive)

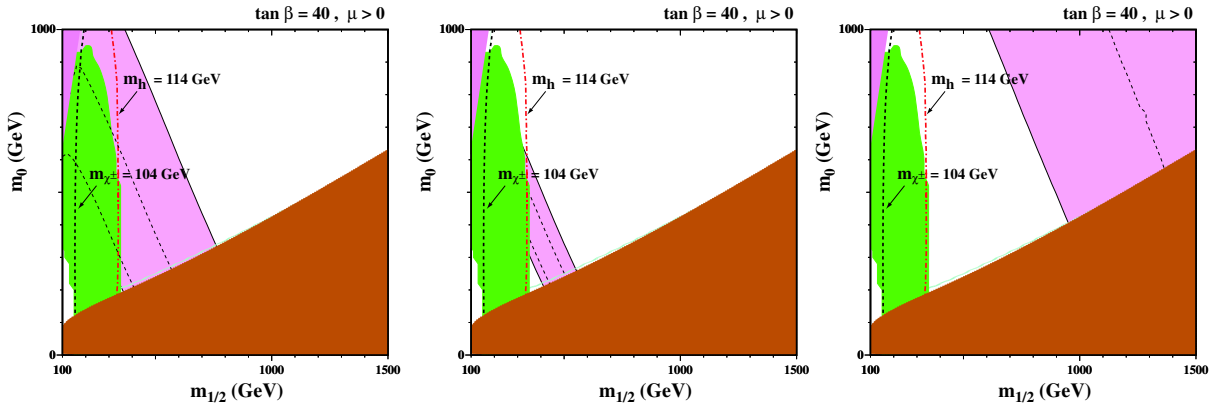

(a) (b) (c)

Figure 118: The CMSSM plots as above, but with $\tan\beta = 40$. (a) As in figure 117 but for $\tan\beta = 40$ (b) The plot with $\Delta a_\mu = 295(39) \times 10^{-11}$, which assumes that in the future both the theory and experimental errors decrease to 22×10^{-11}. (c) The same errors as (b), but $\Delta = 0$. (Figures courtesy of K. Olive)

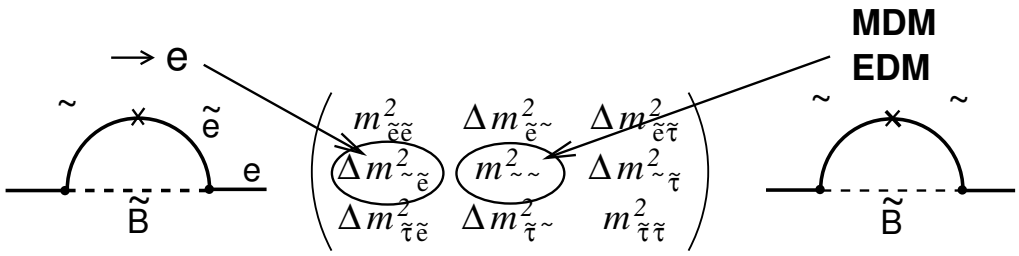

Figure 119: The supersymmetric contributions to the anomaly, and to $\mu \to e$ conversion, showing the relevant slepton mixing matrix elements. The MDM and EDM give the real and imaginary parts of the matrix element respectively.

(see table 19). Thus an EDM at a measurable level would signify physics beyond the Standard Model. SUSY models, and other dynamics at the TeV scale do predict EDMs at measurable levels [418, 816–819]. In the context of SUSY, the EDM and MDM provide information on the diagonal matrix element of the slepton mixing matrix, while muon flavour violation provides information on the off-diagonal matrix element, as indicated in figure 119.

If the muon possessed a permanent electric-dipole moment, the spin precession formula (equation (332)) is modified by the addition of a second term:

$$\vec{\omega} = -\frac{e}{m}\left[a_\mu \vec{B} - \left(a_\mu - \frac{1}{\gamma^2 - 1}\right)\frac{\vec{\beta}\times\vec{E}}{c}\right] + \frac{e}{m}\left[\frac{\eta}{2}\left(\frac{\vec{E}}{c} + \vec{\beta}\times\vec{B}\right)\right] \tag{338}$$

where $d_\mu = (\eta/2)(e\hbar/2mc) \simeq \eta \times 4.7 \times 10^{-14}$ $e-$cm and $a_\mu = (g-2)/2$. For reasonable values of β, the motional electric field $\vec{\beta}\times\vec{B}$ is much larger than electric fields that can be obtained in the laboratory and the two vector frequencies are orthogonal to each other.

A new idea optimises the EDM signal in a storage ring using the motional electric field in the rest frame of the muon interacting with the EDM to cause spin motion [820]. The dedicated experiment will be operated off of the magic γ, for example at $\sim$ 500 MeV/c, and will use a radial electric field to stop the $(g-2)$ precession. Then the spin will follow the momentum as the muons go around the ring, except for any movement (out of plane) arising from an EDM. Thus the EDM would cause a steady build-up of the spin out of the plane with time. Detectors would be placed above and below the storage region, and a time-dependent, up-down asymmetry $R = (N_{\rm up} - N_{\rm down})/(N_{\rm up} + N_{\rm down})$ would be the signal of an EDM.

Two muon EDM experiments are being discussed. Adelmann and Kirsh [821] have proposed that a sensitivity of $5 \times 10^{-23}\, e-$cm could be achieved with a small storage ring at PSI. An experiment to search for a permanent EDM of the muon with a design sensitivity of 10^{-24} e-cm has been presented to J-PARC as a letter of intent [822]. These sensitivities lie well within values predicted by some SUSY models [816]. For a dedicated muon EDM experiment, a sensitivity of 10^{-24} e cm requires the product of polarisation times detected decays to be $NP^2 = 10^{16}$, a flux only available at a the front-end of a Neutrino Factory, or other high-power proton accelerator. The sensitivity is limited by the muon flux, and it should be possible to improve significantly on the sensitivity at a higher intensity facility such as a Neutrino Factory.

If an EDM were to be discovered, one would wish to measure as many EDMs as possible to understand the nature of the interaction. The muon provides a unique opportunity to search for an EDM of a second-generation particle. While naively the muon and electron EDMs scale linearly with mass, in some theories the muon EDM is greatly enhanced relative to linear scaling relative to the electron EDM when the heavy neutrinos of the theory are non-degenerate. [418, 816, 819]

7.3 Search for muon number violation

7.3.1 Theoretical considerations

In the Standard Model (SM), muon number is exactly conserved. When neutrino masses are added and neutrino oscillations take place, muon-number violating processes involving charged leptons become possible as well. However, because of the smallness of neutrino masses, the rates for these processes are unobservable [823–828]; for instance:

$$B(\mu \to e\gamma) = \frac{3\alpha}{32\pi} \sum_i \left| V^*_{\mu i} V_{ei} \frac{m^2_{\nu_i}}{M^2_W} \right|^2 \sim 10^{-60} \left| \frac{V^*_{\mu i} V_{ei}}{10^{-2}} \right|^2 \left(\frac{m_{\nu_i}}{10^{-2}\ \mathrm{eV}} \right)^4 . \tag{339}$$

The observation of muon-number violation in charged muon decay would, therefore, serve as an unambiguous sign of new physics and indeed, a number of SM extensions may be probed sensitively by the study of rare muon decays. Here we will concentrate on supersymmetric models and models with extra dimensions, but it should be pointed out that various other SM extensions also predict observable rates for the rare μ decays: models with new Z' gauge bosons [829]; leptoquarks [830]; or Lorentz-invariance violation [555, 831–833]. For a review on muon number violation, see reference [349].

7.3.2 Model-independent analysis of rare muon processes

Although a purely model-independent analysis based on effective operators cannot make any prediction for the absolute rate of rare muon processes, it can be very useful in determining the relative rates. We will compare the rates for $\mu^+ \to e^+\gamma$, $\mu^+ \to e^+e^-e^+$, and μ^-–e^- conversion. In a large class of models, the dominant source of individual lepton number violation comes from a flavour non-diagonal magnetic-moment transition. Let us therefore consider the effective operator

$$\mathcal{L} = \frac{m_\mu}{\Lambda^2} \bar{\mu}_R \sigma^{\mu\nu} e_L F_{\mu\nu} + \mathrm{h.c.} \tag{340}$$

This interaction leads to the following results for the branching ratios of $\mu^+ \to e^+\gamma$ ($B(\mu \to e\gamma)$) and $\mu^+ \to e^+e^-e^+$ ($B(\mu \to 3e)$), and for the rate of μ^-–e^- conversion in nuclei normalised to

the nuclear capture rate ($B(\mu N \to eN)$):

$$B(\mu \to e\gamma) = \frac{3(4\pi)^2}{G_F^2 \Lambda^4} , \tag{341}$$

$$\frac{B(\mu \to 3e)}{B(\mu \to e\gamma)} = \frac{\alpha}{3\pi}\left(\ln\frac{m_\mu^2}{m_e^2} - \frac{11}{4}\right) = 6 \times 10^{-3} , \tag{342}$$

$$\frac{B(\mu N \to eN)}{B(\mu \to e\gamma)} = 10^{12}\ B(A,Z)\ \frac{2G_F^2 m_\mu^4}{(4\pi)^3 \alpha} = 2 \times 10^{-3}\ B(A,Z) . \tag{343}$$

Here $B(A,Z)$ is an effective nuclear coefficient which is of order 1 for elements heavier than aluminium [834]. The logarithm in equation 342 is an enhancement factor for $B(\mu \to 3e)$, which is a consequence of the collinear divergence of the electron-positron pair in the $m_e \to 0$ limit. Nevertheless, because of the smaller phase space and extra power of α, $B(\mu \to 3e)$ and $B(\mu N \to eN)$ turn out to be suppressed with respect to $B(\mu \to e\gamma)$ by factors of 6×10^{-3} and $(2\text{–}4) \times 10^{-3}$, respectively. See reference [790] for further discussion.

Next, let us include an effective four-fermion operator which violates individual lepton number:

$$\mathcal{L} = \frac{1}{\Lambda_F^2} \bar{\mu}_L \gamma^\mu e_L \bar{f}_L \gamma_\mu f_L + \text{h.c.} , \tag{344}$$

where f is a generic quark or lepton. The choice of the operator in equation 344 is made for concreteness, and our results do not depend significantly on the specific chiral structure of the operator. First we consider the case in which f is neither an electron nor a light quark, and therefore $\mu^+ \to e^+e^-e^+$ and μ^-–e^- conversion occur only at the loop level. Comparing the $\mu^+ \to e^+\gamma$ rate in equation 341 with the contributions from the four-fermion operator to $B(\mu \to 3e)$ and $B(\mu N \to eN)$, we find:

$$\frac{B(\mu \to 3e)}{B(\mu \to e\gamma)} = \frac{8\alpha^2 N_f^2}{9(4\pi)^4}\left(\frac{\Lambda}{\Lambda_F}\right)^4 \left[\ln\frac{\max(m_f^2, m_\mu^2)}{M_F^2}\right]^2 , \tag{345}$$

$$\frac{B(\mu N \to eN)}{B(\mu \to e\gamma)} = 10^{12}\ B(A,Z)\ \frac{32 G_F^2 m_\mu^4 N_f^2}{9(4\pi)^6}\left(\frac{\Lambda}{\Lambda_F}\right)^4 \left[\ln\frac{\max(m_f^2, m_\mu^2)}{M_F^2}\right]^2 . \tag{346}$$

Here N_f is the number of colours of the fermion f and M_F is the heavy-particle mass generating the effective operators (typically M_F is much smaller than Λ or Λ_F because of loop factors and mixing angles). The logarithms in equations 345 and 346 correspond to the anomalous dimension mixing of the operator in equation 344 with the four-fermion operator generating the relevant rare muon process [835]. If $\Lambda \sim \Lambda_F$, then the contributions from the four-fermion operator are irrelevant, since the ratios in equations 342 and 343 are larger than those in equations 345 and 346. More interesting is the case in which the four-fermion operator in equation 344 is generated at tree level, while the magnetic-moment transition in equation 340 is generated only at one loop, as in models with R-parity violation [228, 229, 836] or with leptoquarks [830]. In this case, we expect:

$$\left(\frac{\Lambda}{\Lambda_F}\right)^4 \simeq \frac{(4\pi)^3}{\alpha} . \tag{347}$$

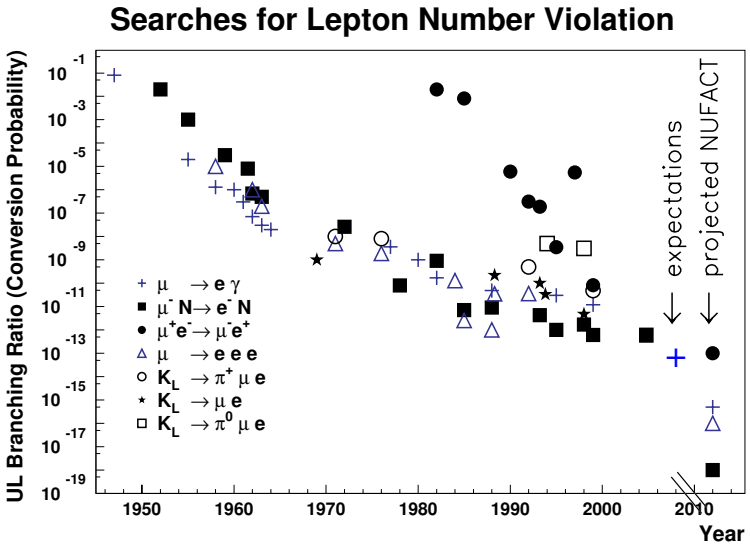

Figure 120: Historical development of the 90% C.L. upper limits (UL) on branching ratios respectively conversion probabilities of muon-number violating processes which involve muons and kaons. Sensitivities expected for planned searches are indicated in the year 2008 (see also reference [349]). The projections for a neutrino factory (NUFACT) are also shown. Taken from [790].

If equation 347 holds and if we take $M_F \simeq 1$ TeV, then the ratios in equations 345 and 346 become of order unity, so the different rare muon processes have comparable rates.

Alternatively, if the fermion f in equation 344 is an electron (or a light quark), the effective operator can mediate $\mu \to 3e$ (or $\mu^- - e^-$ conversion) at tree-level, and the corresponding process can dominate over the others [380]. For instance, we obtain:

$$\frac{B(\mu \to 3e)}{B(\mu \to e\gamma)} = \frac{1}{12(4\pi)^2} \left(\frac{\Lambda}{\Lambda_F}\right)^4 , \tag{348}$$

for the case $f = e$.

In conclusion, the various rare muon processes are all potentially very interesting. In the event of a positive experimental signal for muon-number violation, a comparison between searches in the different channels and the use of the effective-operator approach will allow us to identify quickly the correct class of models.

7.4 Experimental prospects

The experimental sensitivities achieved during the past decades in tests of muon number conservation are illustrated in figure 120, and given in table 20. Generally the tests were limited by the intensities of the available μ and K beams, but in some cases detector limitations have played a role as well.

All recent results with μ^+ beams were obtained with "surface" muon beams (see for instance [842]), that consist of muons originating in the decay of π^+'s that stopped at the surface

Table 20: Present limits on rare μ decays.

mode	upper limit (90% C.L.)	year	Exp./Lab.	reference
$\mu^+ \to e^+\gamma$	1.2×10^{-11}	2002	MEGA / LAMPF	[350, 837]
$\mu^+ \to e^+e^+e^-$	1.0×10^{-12}	1988	SINDRUM I/ PSI	[351]
$\mu^+e^- \leftrightarrow \mu^-e^+$	8.3×10^{-11}	1999	PSI	[772, 838]
μ^- Ti $\to e^-$Ti	6.1×10^{-13}	1998	SINDRUM II / PSI	[839]
μ^- Ti $\to e^+$Ca*	3.6×10^{-11}	1998	SINDRUM II / PSI	[840]
μ^- Pb $\to e^-$Pb	4.6×10^{-11}	1996	SINDRUM II / PSI	[841]
μ^- Au $\to e^-$Au	7×10^{-13}	2006	SINDRUM II / PSI	[352]

of the pion-production target, or "sub-surface" beams, in which the muons originate from the decays of π^+ stopping just below the surface. Because of the narrow momentum spread, such beams are superior to conventional pion decay channels in terms of muon stop density; they permit the use of relatively thin (typically 10 mg/cm^2) foils to stop the beam; and they offer the highest muon stop densities that can be obtained at present. Such low-mass stopping targets are required for the ultimate resolution in positron momentum and emission angle, photon yield, or the efficient production of muonium in vacuum.

In this section we indicate how far experimental searches could benefit from muon beam intensities which are 2–3 orders of magnitude higher than are presently available. Further details can be found in the CERN study of 2001 [790].

7.4.1 $\mu \to e\gamma$

Neglecting the positron mass, the 2-body decay $\mu^+ \to e^+\gamma$ of muons at rest is characterised by:

$$\begin{aligned} E_\gamma &= E_e = m_\mu c^2/2 = 52.8 \text{ MeV} ; \\ \Theta_{e\gamma} &= 180^\circ ; \text{and} \\ t_\gamma &= t_e . \end{aligned}$$

All $\mu \to e\gamma$ searches performed during the past three decades were limited by accidental coincidences between a positron from normal muon decay, $\mu \to e\nu\overline{\nu}$, and a photon produced in the decay of another muon, either by bremsstrahlung or by e^+e^- annihilation in flight. This background dominates the intrinsic background from radiative muon decay $\mu \to e\nu\overline{\nu}\gamma$. Accidental $e\gamma$ coincidences can be suppressed by testing the three conditions listed above. The vertex constraint resulting from the ability to trace back positrons and photons to an extended stopping target can further reduce background. Attempts have been made to suppress accidental coincidences by observing the low-energy positron associated with the photon, but with minimal success.

The most sensitive search to date was performed by the MEGA Collaboration at the Los Alamos Meson Physics Facility (LAMPF) [350, 837], which established an upper limit (90% C.L.) on $B_{\mu\to e\gamma}$ of 1.2×10^{-11} [350]. The MEG experiment [843] at PSI, aims at a single-event

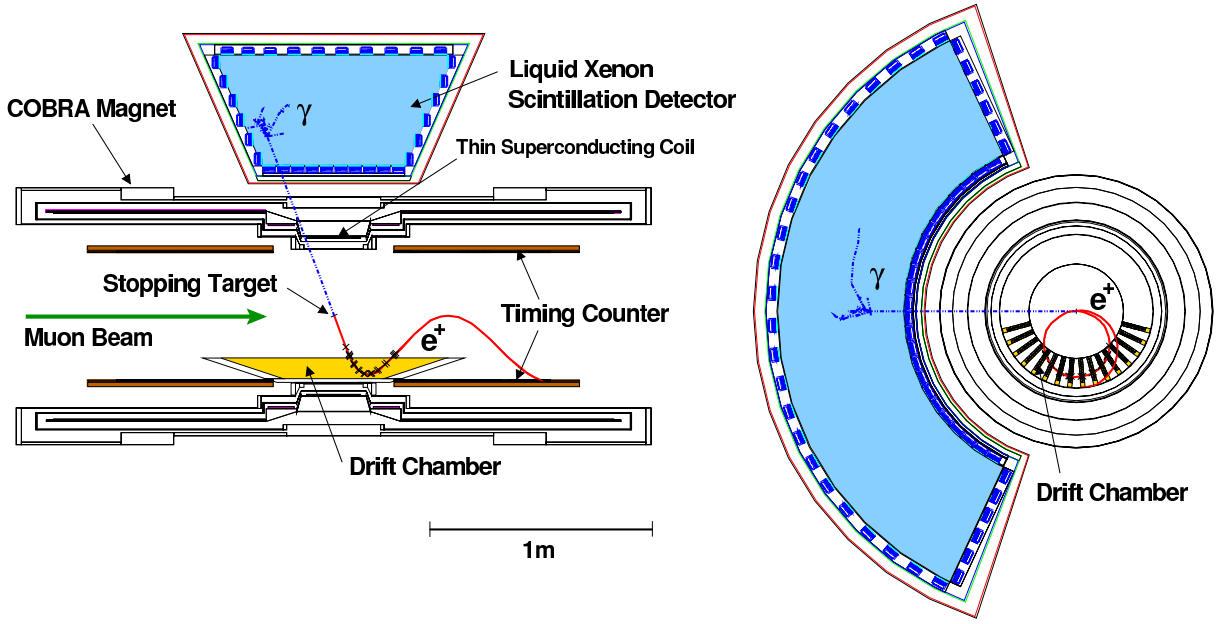

Figure 121: Side and end views of the MEG setup. The magnetic field is shaped such that positrons are quickly swept out of the tracking region thus minimising the load on the detectors. The cylindrical 0.8 m^3 single-cell LXe detector is viewed from all sides by by 846 PMTs immersed in the LXe allowing the reconstruction of photon energy, time, conversion point and direction and the efficient rejection of pile-up signals. (Figure courtesy of T. Mori)

sensitivity of $\sim 10^{-13} - 10^{-14}$, and began commissioning in early 2007. A surface muon beam is employed that reaches an intensity around $5 \times 10^8\, \mu^+/s$.

A straightforward improvement of more than an order of magnitude in suppression of accidental background results from the DC beam at PSI, as opposed to the pulsed LAMPF beam which had a macro duty cycle of 7.7% . Another order-of-magnitude improvement is achieved by superb time resolution (≈ 0.15 ns FWHM on $t_\gamma - t_e$).

The MEG setup is shown in figure 121. The MEG spectrometer magnet makes use of a unique "COBRA"(COnstant Bending RAdius) design which results in a graded magnetic field varying from 1.27 T at the centre to 0.49 T at both ends. This field distribution not only results in a constant projected bending radius for the 52.8 MeV positron, for emission angles θ with $|\cos\theta| < 0.35$, but also sweeps away positrons with low longitudinal momentum more effectively than does a solenoidal field as used by MEGA. This design significantly reduces the instantaneous rates in the drift chambers. The drift chambers are made of 12.5 μm thin foils supported by C-shaped carbon-fibre frames which are out of the way of the positrons. The foils have "vernier" cathode pads which permit the measurement of the trajectory coordinate along the anode wires with an accuracy of about 500 μm. There are two timing counters at each end of the magnet (see figure 122), each of which consists of a layer of plastic scintillating fibres and 15 plastic scintillator bars of $4 \times 4 \times 90$ cm^3. The fibres give hit positions along the beam axis and the bars measure positron timings with a precision of $\sigma = 40$ ps. The counters are placed at large radii so only high-energy positrons reach them, giving a total rate of a few$\times 10^4$/s for each bar.

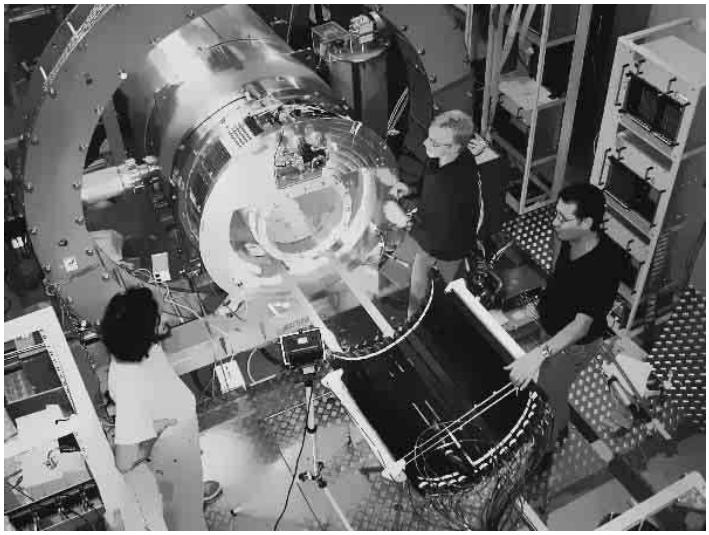

Figure 122: Installing one of the timing counters into the COBRA magnet during the pilot run of the positron spectrometer at the end of 2006. The large ring is one of two Helmholtz coils used to compensate the COBRA stray field at the locations of the photomultipliers of the LXe detector. (Figure courtesy of T. Mori)

Table 21: Performance of a prototype of the MEG LXe detector at E_γ=53 MeV.

observable	resolution (σ)
energy	1.2%
time	65 ps
conversion point	≈4 mm

High strength aluminium-stabilised conductor is used to make the magnet as thin as $0.20X_0$, so that 85% of 52.8 MeV/c gamma rays traverse the magnet without interaction before entering the gamma ray detector placed outside the magnet. Whereas MEGA used rather inefficient pair spectrometers to detect the photon, MEG developed a novel liquid-xenon scintillation detector as shown in figure 121. By viewing the scintillation light from all sides, the electromagnetic shower induced by the photon can be reconstructed which allows a precise measurement of the photon conversion point and direction [844]. Special PMTs that work at liquid-zenon (LXe) temperature (−110°C), persist under high pressures and are sensitive to the VUV scintillation light of LXe ($\lambda \approx 178$ nm) have been developed in collaboration with Hamamatsu Photonics. To identify and separate pile-up efficiently, fast waveform digitising is used for all the PMT outputs.

The performance of the detector was measured with a prototype detector. The results are shown in table 21. First data taking with the complete setup is scheduled for the second half of 2007. A sensitivity of $\mathcal{O}(10^{-13})$ for the 90% C.L. upper limit in case no candidates are found should be reached after two years.

As a next step it seems reasonable to consider experiments aiming at a sensitivity of 10^{-15} or better. However, it is not at all obvious how to reach such levels of sensitivity without running into the background of accidental $e\gamma$ coincidences. Surface-muon rates ten-times larger

than those used by MEG already can be achieved today. However, to exloit such rates, the background suppression would have to be improved by two orders of magnitude.

Accidental background, $N_{\rm acc}$, scales with the detector resolutions as:

$$N_{\rm acc} \propto \Delta E_e \cdot \Delta t \cdot (\Delta E_\gamma \cdot \Delta \Theta_{e\gamma} \cdot \Delta x_\gamma)^2 \cdot A_T^{-1} \ ,$$

with x_γ the coordinate of the photon trajectory at the target and A_T the target area. Here, it has been assumed that the photon can be traced back to the target with an uncertainty that is small compared to A_T. Since the angular resolution is dictated by the positron multiple scattering in the target, this can be written:

$$N_{\rm acc} \propto \Delta E_e \cdot \Delta t \cdot (\Delta E_\gamma \cdot \Delta x_\gamma)^2 \cdot \frac{d_T}{A_T} \ ,$$

with d_T the target thickness. When using a series of n target foils each of them could have a thickness of d_T/n and the beam would still be stopped. Since the area would increase like $n \cdot A_T$ the background could be reduced in proportion with $1/n^2$:

$$N_{\rm acc} \propto \Delta E_e \cdot \Delta t \cdot (\Delta E_\gamma \cdot \Delta x_\gamma)^2 \cdot \frac{d_T/n}{n \cdot A_T} \ ,$$

so a geometry with ten targets, 1 mg/cm^2 each, would lead to the required background suppression.

The expected number N_s of observed $\mu \to e\gamma$ decays can be written as:

$$N_s = R_\mu T \frac{\Omega}{4\pi} \epsilon_e \epsilon_\gamma \epsilon_{cut} \, B_{\mu \to e\gamma} \ , \tag{349}$$

where R_μ is the muon-stop rate, T is the total measuring time, Ω is the detector solid angle (we assume identical values for the photon and the positron detectors), ϵ_e and ϵ_γ are the positron- and photon-detection efficiencies, ϵ_{cut} is the efficiency of the selection cuts. Selection cuts can be applied on the reconstructed positron energy (E_e), photon energy (E_γ), opening angle ($\theta_{e\gamma}$) and relative timing ($t_{e\gamma}$).

In the MEG experiment at PSI, the background is dominated by accidental coincidences of a positron from normal muon decay and a photon which may originate in the decay $\mu^+ \to e^+ \nu \overline{\nu} \gamma$ or may be produced by an e^+ through external bremsstrahlung or annihilation in flight. In a DC beam the number of accidental coincidences is given by:

$$N_b = {R_\mu}^2 f_e \epsilon_e f_\gamma \epsilon_\gamma (\frac{\Omega}{4\pi})^2 \, \pi \frac{\Delta \theta_{e\gamma}^2}{\Omega} 2 \Delta t \, T \ , \tag{350}$$

where f_e (f_γ) is the e^+ (γ) yield per stopped muon within the selection window and Δt is the cut applied on the $e^+ - \gamma$ time difference. For a non-DC beam, N_b must multiplied by the inverse of the duty cycle.

Since the accidental background rises quadratically with the muon-stop rate, it will be even more problematic in future experiments using a higher beam intensity. An experiment with $R_\mu = 10^{10}\mu$/s and all the other quantities of equation (349) unchanged would yield one $\mu \to e\gamma$ event for $B_{\mu \to e\gamma} = 10^{-16}$. However, the accidental background would increase to 10^4 events. It is obvious that better detector resolutions and/or improved experimental concepts are required.

7.4.2 $\mu^+ \to e^+e^+e^-$

From an experimental point of view the decay $\mu \to 3e$ offers some important advantages compared to the more familiar $\mu \to e\gamma$ discussed in the previous section. The principal background is from accidental coincidences between positrons from normal muon decay and e^+e^- pairs originating from photon conversions or scattering of positrons off atomic electrons (Bhabha scattering). Since the final state contains only charged particles, the setup may consist of a magnetic spectrometer without the need for an electromagnetic calorimeter with its limited performance in terms of energy and directional resolution, rate capability, and event definition in general. On the other hand, of major concern are the high rates in the tracking system of a $\mu \to 3e$ setup which has to withstand the load of the full muon decay spectrum.

The present experimental limit, $B(\mu \to 3e) < 1 \times 10^{-12}$ [351], was published in 1988. Since no new proposals exist for this decay mode we shall analyse the prospects of an improved experiment with the SINDRUM experiment as a point of reference. A detailed description of the experiment may be found in reference [845].

Data were taken during six months using a 25 MeV/c sub-surface beam. The beam was brought to rest with a rate of 6×10^6 μ^+ s^{-1} in a hollow double-cone foam target (length 220 mm, diameter 58 mm, total mass 2.4 g). SINDRUM I is a solenoidal spectrometer with a relatively low magnetic field of 0.33 T corresponding to a transverse-momentum threshold around 18 MeV/c for particles crossing the tracking system. This system consists of five cylindrical MWPCs concentric with the beam axis. Three-dimensional space points are found by measuring the charges induced on cathode strips oriented $\pm 45^\circ$ relative to the sense wires. Gating times were typically 50 ns. The spectrometer acceptance for $\mu \to 3e$ was 24% of 4π sr (for a constant transition-matrix element) so the only place for a significant improvement in sensitivity would be the beam intensity.

Figure 123 shows the time distribution of the recorded $e^+e^+e^-$ triples. Apart from a prompt contribution of correlated triples one notices a dominant contribution from accidental coincidences involving low-invariant-mass e^+e^- pairs. Most of these are explained by Bhabha scattering of positrons from normal muon decay $\mu \to e\nu\overline{\nu}$. The accidental background thus scales with the target mass, but it is not obvious how to reduce this mass significantly below the 11 mg/cm^2 achieved in this search.

Figure 124 shows the vertex distribution of prompt events. One should keep in mind that most of the uncorrelated triples contain e^+e^- pairs coming from the target and their vertex distribution will thus follow the target contour as well. This 1-fold accidental background is suppressed by the ratio of the vertex resolution (couple of mm^2) and the target area. There is no reason, other than the cost of the detection system, not to choose a much larger target. Such an increase might also help to reduce the load on the tracking detectors. Better vertex resolution would help as well. At these low energies tracking errors are dominated by multiple scattering in the first detector layer but it should be possible to gain by bringing it closer to the target.

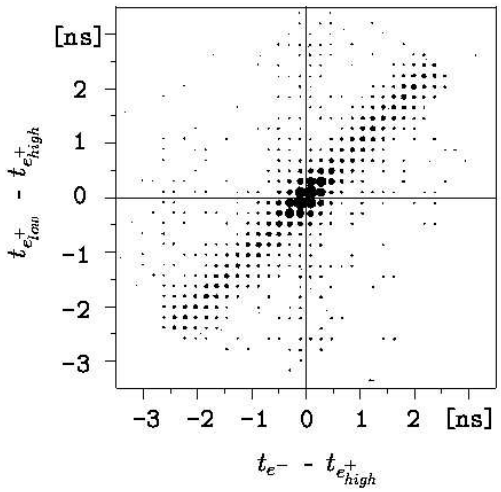

Figure 123: Relative timing of $e^+e^+e^-$ events. The two positrons are labelled according to the invariant mass when combined with the electron. One notices a contribution of correlated triples in the centre of the distribution. These events are mainly $\mu \to 3e\nu\overline{\nu}$ decays. The concentration of events along the diagonal is due to low-invariant-mass e^+e^- pairs in accidental coincidence with a positron originating in the decay of a second muon. The e^+e^- pairs are predominantly due to Bhabha scattering in the target. Taken from [790].

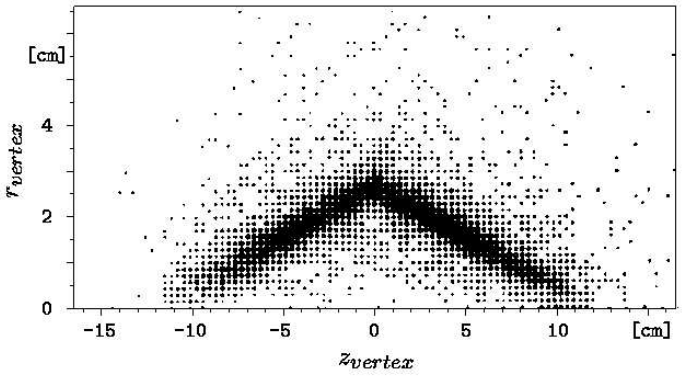

Figure 124: Spatial distribution of the vertex fitted to prompt $e^+e^+e^-$ triples. One clearly notices the double-cone target. Taken from [790].

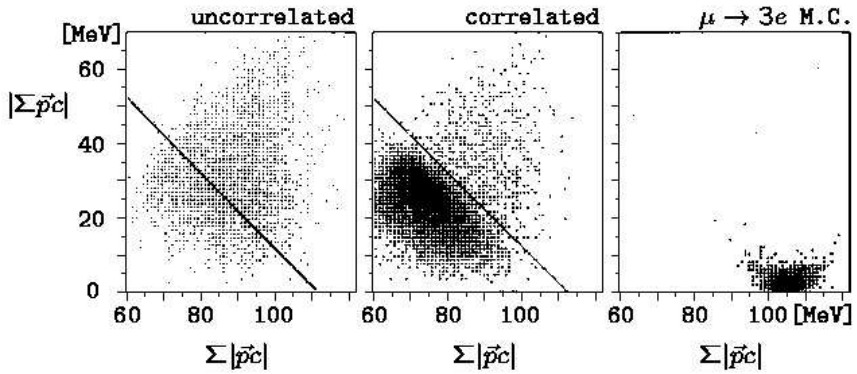

Figure 125: Total momentum versus total energy for three event classes discussed in the text. The line shows the kinematic limit (within resolution) defined by $\Sigma|\vec{p}c| + |\Sigma\vec{p}c| \leq m_\mu c^2$ for any muon decay. The enhancement in the distribution of correlated triples below this limit is due to the decay $\mu \to 3e\nu\overline{\nu}$. Taken from [790].

Finally, figure 125 shows the distribution of total momentum versus total energy for three classes of events: (i) uncorrelated $e^+e^+e^-$ triples; (ii) correlated $e^+e^+e^-$ triples; and (iii) simulated $\mu \to 3e$ decays. The distinction between uncorrelated and correlated triples has been made on the basis of relative timing and vertex as discussed above.

What would a $\mu \to 3e$ set-up look like that would aim at a single-event sensitivity around 10^{-16}, that would make use of a beam rate around 10^{10} μ^+/s? The SINDRUM I measurement was background-free at the level of 10^{-12} with a beam of 0.6×10^7 μ^+/s. Taking into account that background would have set in at 10^{-13}, the increased stop rate would raise the background level to $\approx 10^{-10}$; so six orders of magnitude in background reduction would have to be achieved. Increasing the target size and improving the tracking resolution should bring two orders of magnitude from the vertex requirement alone. Since the dominant sources of background are accidental coincidences between two decay positrons (one of which undergoes Bhabha scattering), the background rate scales with the momentum-resolution squared. Assuming an improvement by one order of magnitude, i.e., from the $\approx 10\%$ FWHM obtained by SINDRUM I to $\approx 1\%$ for a new search, one would gain two orders of magnitude from the constraint on total energy alone. The remaining factor 100 would result from the test on the collinearity of the e^+ and the e^+e^- pair.

As mentioned in reference [845], a dramatic suppression of background could be achieved by requiring a minimum opening angle (typically 30°) for both e^+e^- combinations. Depending on the mechanism for $\mu \to 3e$, such a cut might lead to a strong loss in $\mu \to 3e$ sensitivity as well.

Whereas background levels may be under control, the question remains whether detector concepts can be developed that work at the high beam rates proposed. A large modularity will be required to solve problems of pattern recognition. Also the trigger for data readout may turn out to be a great challenge.

7.4.3 $\mu \to e$ conversion

When negative muons stop in matter, they quickly get captured, form muonic atoms, and mostly reach the atomic ground ($1s$) state before decaying. The main channels are muon decay in orbit (DIO):

$$\mu^- + (A, Z) \to e^- + \overline{\nu}_e + \nu_\mu + (A, Z) \; ; \tag{351}$$

and nuclear muon capture (NMC):

$$\mu^- + (A, Z) \to \nu_\mu + (A, Z - 1) \; ; \tag{352}$$

where the final nucleus is likely to be in an excited state.

Because of the two-body final state, neutrinoless $\mu^- - e^-$ conversion in muonic atoms:

$$\mu^- + (A, Z) \to e^- + (A, Z) \; ; \tag{353}$$

with a nucleus of a mass number A and an atomic number Z, has the greatest potential for significant increases in sensitivity over present limits; potentially by as many as six orders of magnitude. The electrons produced in $\mu - e$ conversion are mono-energetic with the energy:

$$E_{\mu e} = m_\mu c^2 - B_\mu(Z) - R(A) \; , \tag{354}$$

where $B_\mu(Z)$ is the atomic binding energy of the muon, and R is the atomic recoil energy, for a muonic atom with atomic number Z and mass number A. In the lowest approximation $B_\mu(Z) \propto Z^2$ and $R(A) \propto A^{-1}$.

For conversions that leave the nucleus in its ground state, the nucleons act coherently which boosts the conversion probability relative to the rate of the dominant process of ordinary nuclear muon capture. The electron is emitted with energy $E_e \approx m_\mu c^2$, which coincides with the endpoint of muon DIO, the only intrinsic physics background. Since the energy distribution of muon decay in orbit falls steeply above $m_\mu c^2/2$ the experimental set-up may have a large signal acceptance and the detectors can still be protected against the vast majority of decay and capture background events.

The muon-electron conversion probability, $B_{\mu-e}$, varies as a function of A and Z, and with the probability that the nucleus stays in its ground state. Calculations [363, 846–850] predicted a steady rise of the branching ratio until $Z \approx 30$, from which point it was expected to drop again. For this reason most experiments were performed on medium-heavy nuclei. The nuclear-physics calculations predict the coherent fraction to be larger than 80% for all nuclear systems [851,852].

Muon decay in orbit (DIO) constitutes an intrinsic background source which can only be suppressed with sufficient electron-energy resolution. Energy distributions for DIO electrons have been calculated for a number of muonic atoms [853–855]. The process predominantly results in electrons with energy $E_{\rm DIO}$ below $m_\mu c^2/2$, the kinematic endpoint in free muon decay, with a steeply falling high-energy component reaching up to $E_{\mu e}$. In the endpoint region the

DIO rate varies as $(E_{\mu e} - E_{\rm DIO})^5$ and a resolution of $1 - 2\,$MeV (FWHM) is sufficient to keep the DIO background under control. Since the DIO endpoint rises at lower Z, great care has to be taken to avoid low-Z contaminations in and around the target.

Another background source is due to radiative muon capture (RMC):

$$\mu^-(A,Z) \rightarrow \gamma(A,Z-1)^*\nu_\mu \ , \tag{355}$$

after which the photon creates an e^+e^- pair either internally (Dalitz pair) or through $\gamma \rightarrow e^+e^-$-pair production in the target. The RMC endpoint can be kept below $E_{\mu e}$ for selected isotopes.

Most low-energy muon beams have large pion contaminations. Pions may produce background when stopping in the target through radiative pion capture (RPC) which takes place with a probability of $O(10^{-2})$. Most RPC photons have energies above $E_{\mu e}$. As in the case of RMC, these photons may produce background through $\gamma \rightarrow e^+e^-$ pair production. There are various strategies to cope with RPC background:

- One option is to keep the total number of π^- stopping in the target during the live time of the experiment below 10^{4-5}. This can be achieved with the help of a moderator in the beam, exploiting the range difference between pions and muons of given momentum or with a muon storage ring exploiting the difference in lifetime; and
- Another option is to exploit the fact that pion capture takes place in a time-scale far below a nanosecond. The background can thus be suppressed by using a pulsed beam and selecting only delayed events.

Cosmic rays (electrons, muons, photons) are a copious source of electrons with energies around $\approx 100\,$MeV. With the exception of $\gamma \rightarrow e^+e^-$ in the target, these events can be recognised by the presence of an incoming particle. Passive shielding and veto counters above the detection system also help to suppress this background.

The present best limits (see table 20) have been measured with the SINDRUM II spectrometer at PSI. Most recently, a search was performed on a gold target [352]. In this experiment (see figure 126), pion suppression is based on the the fact that the range of pions is a factor of two shorter than that of muons at the selected momentum (52 MeV/c). A simulation using the measured range distribution shows that about one in 10^6 pions cross an 8 mm thick CH_2 moderator. Since these pions are relatively slow, 99.9% of them decay before reaching the gold target which is situated some 10 m further downstream. As a result, pion stops in the target have been reduced to a negligible level. What remains are radiative pion capture in the degrader and $\pi^- \rightarrow e^-\overline{\nu}_e$ decay-in-flight shortly before entering the degrader. The resulting electrons may reach the target where they can scatter into the solid angle acceptance of the spectrometer. $\mathcal{O}(10)$ events are expected with a flat energy distribution between 80 and 100 MeV. These events are peaked in the forward direction and show a time correlation with the cyclotron RF signal. To cope with this background two event classes have been introduced based on the values of

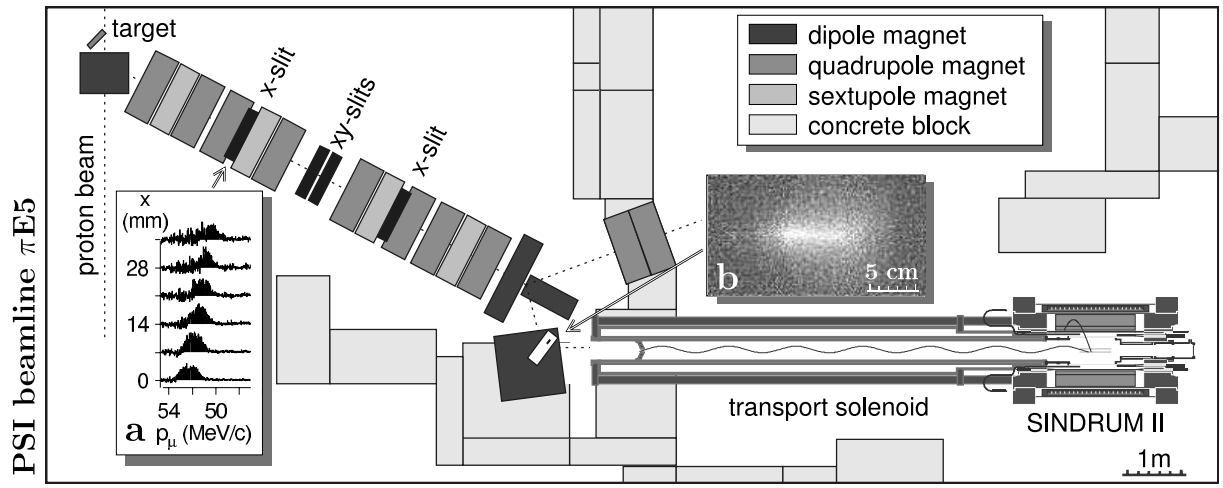

Figure 126: Plan view of the SINDRUM II experiment. The 1 MW 590 MeV proton beam hits the 40 mm carbon production target (top left of the figure). The πE5 beam line transports secondary particles (π, μ, e) emitted in the backward direction to a degrader situated at the entrance of a solenoid connected axially to the SINDRUM II spectrometer. Inset a) shows the momentum dispersion at the position of the first slit system. Inset b) shows a cross section of the beam at the position of the beam focus. Taken with kind permission of the European Physical Journal from figure 2 in reference [352]. Copyrighted by Springer Berlin/Heidelberg.

polar angle and rf phase. Figure 127 shows the corresponding momentum distributions. The spectra show no indication for $\mu - e$ conversion. The corresponding upper limit:

$$B_{\mu e} \equiv \frac{\Gamma(\mu^- \mathrm{Au} \to e^- \mathrm{Au}_{\mathrm{g.s.}})}{\Gamma_{\mathrm{capture}}(\mu^- \mathrm{Au})} < 7 \times 10^{-13} \quad 90\% \text{ C.L.}; \tag{356}$$

has been obtained with the help of a likelihood analysis of the momentum distributions shown in figure 127 taking into account: muon decay in orbit; $\mu - e$ conversion; a contribution taken from the observed positron distribution describing processes with intermediate photons, such as radiative muon capture; and a flat component from pion decay-in-flight or cosmic rays.

Based on a scheme originally developed during the eighties for the Moscow Meson Factory [856], μe-conversion experiments are being considered both in the USA and in Japan. The key elements are:

- A pulsed proton beam permits the removal of pion background by selecting events in a delayed time window. Proton extinction factors between pulses of $\leq 10^{-9}$ are needed;
- A large acceptance capture solenoid surrounding the pion-production target leads to a major increase in muon flux; and
- A bent solenoid transporting the muons to the experimental target results in a significant increase in momentum transmission compared to a conventional quadrupole channel. A bent solenoid not only removes neutral particles and photons but also separates electric charges.

Unfortunately, the MECO proposal at BNL [857] designed along these lines was stopped because of the high costs. Presently, the various possibilities are being studied to perform a

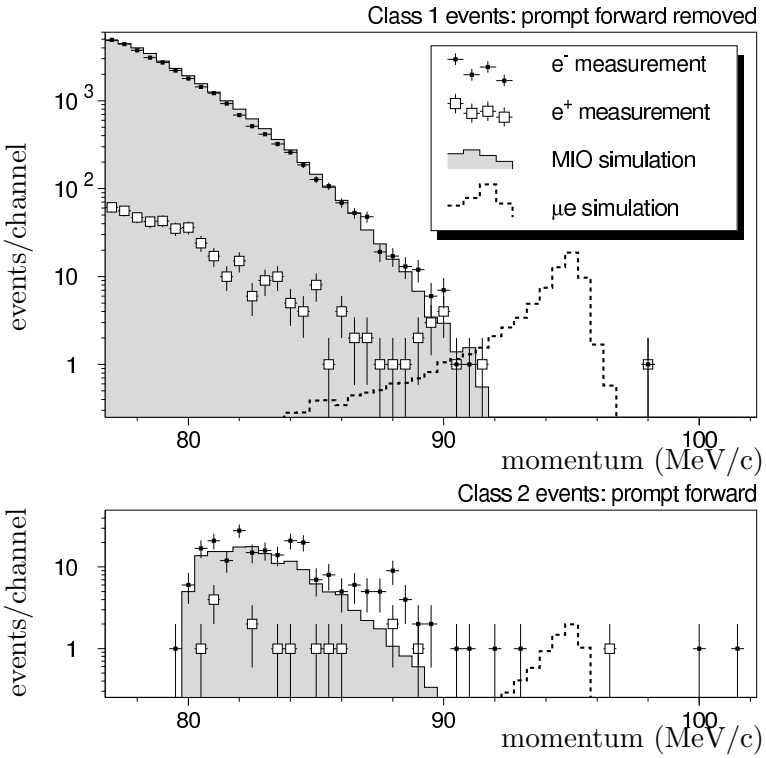

Figure 127: Momentum distributions of electrons and positrons for two event classes described in the text. Measured distributions are compared with the results of simulations of muon decay in orbit and $\mu - e$ conversion. N.b.decay in orbit is labelled "MIO" in this figure. Taken with kind permission of the European Physical Journal from figure 11 in reference [352]. Copyrighted by Springer Berlin/Heidelberg.

Table 22: $\mu - e$ conversion searches.

project	Lab	status	E_p [GeV]	p_μ [MeV/c]	μ^- stops [s^{-1}]	S [a]
SINDRUM II	PSI	finished	0.6	52±1	10^7	2×10^{-13}
MECO	BNL	cancelled	8	45±25	10^{11}	2×10^{-17}
mu2e	FNAL	under study	8	45±25	0.6×10^{10}	4×10^{-17}
PRISM/PRIME	J-PARC	LOI	40	68±3	10^{12}	5×10^{-19}

[a] value of $B_{\mu e}$ corresponding to an expectation of one observed event

MECO-type of experiment at Fermilab (mu2e). There is good hope that a proton beam with the required characteristics can be produced with minor modifications to the existing accelerator complex which will become available after the Tevatron collider stops operation in 2009. A letter of intent is in preparation.

Further improvements are being considered for an experiment at J-PARC. To exploit fully the lifetime difference to suppress pion induced background, the separation has to occur in the beamline rather than after the muon has stopped, since the lifetime of the muonic atom may be significantly shorter than the 2.2 μs lifetime of the free muon. For this purpose a muon storage ring, PRISM (Phase Rotated Intense Slow Muon source, see figure 128), is being considered [858] which makes use of large-acceptance fixed-field alternating-gradient (FFAG) magnets. A portion of the PRISM-FFAG ring is presently under construction as an R&D project. As the name suggests the ring is also used to reduce the momentum spread of the beam (from ≈30 % to ≈3 %). This is achieved by accelerating late muons and decelerating early muons in RF electric fields. The scheme requires the construction of a pulsed proton beam [859], which is under consideration by the J-PARC Laboratory Management. The low momentum spread of the muons allows the use of a relatively thin target which is an essential ingredient for high resolution in the positron momentum measurement with the PRIME detector [860]. Table 22 lists the μ^- stop rates and single-event sensitivities for the various projects discussed above.

7.4.4 Muonium-anti-muonium conversion

Muonium is the atomic bound state of a positive muon and an electron. For leptons, a spontaneous conversion of muonium (μ^+e^-) into anti-muonium (μ^-e^+) would be completely analogous to the well known $K^0 - \overline{K^0}$ oscillations in the quark sector. A search was suggested in 1957 by Pontecorvo [2,861] three years before the atom was discovered by Hughes [862,863]. The process could proceed at tree level through bi-lepton exchange or through various loops. Predictions for the process exist in a variety of speculative models including left-right symmetry, R-parity-violating supersymmetry, GUT theories, and several others [864–871].

Any possible coupling between muonium and its anti-atom will give rise to oscillations between them. For atomic s-states with principal quantum number, n, a splitting of their energy levels:

$$\delta = \frac{8G_F}{\sqrt{2}n^2\pi a_0^3}\frac{G_{M\overline{M}}}{G_F} \; ; \tag{357}$$

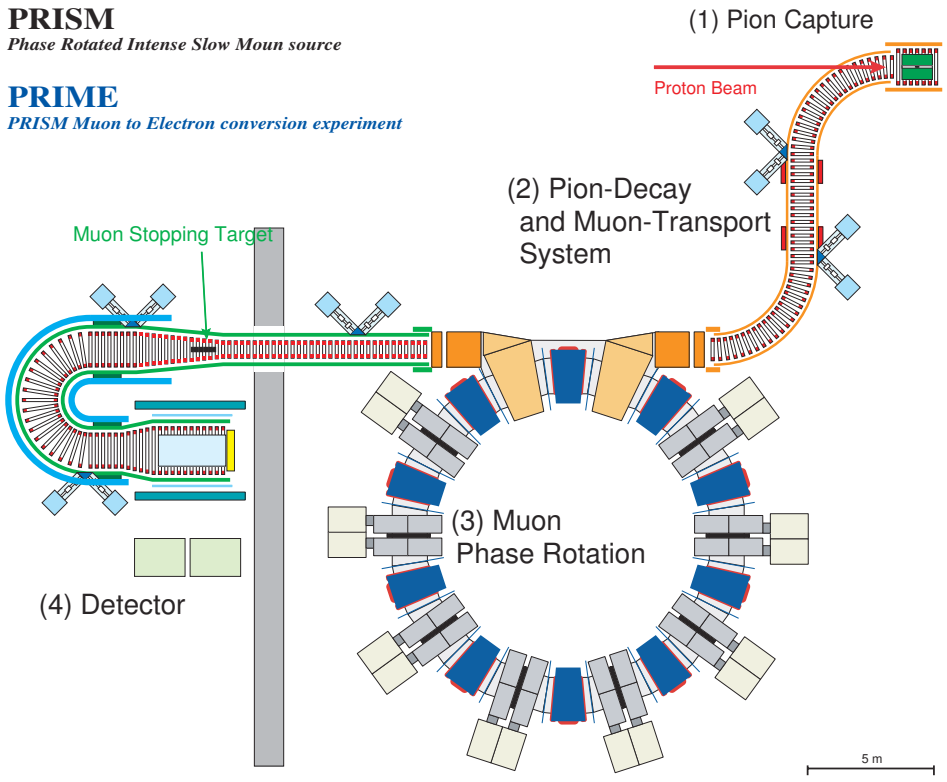

Figure 128: Layout of PRISM/PRIME. The experimental target is situated at the entrance of the 180° bent solenoid that transports decay electrons to the detection system. See text for further explanations. Reproduced with the kind permission of the PRISM/PRIME collaboration.

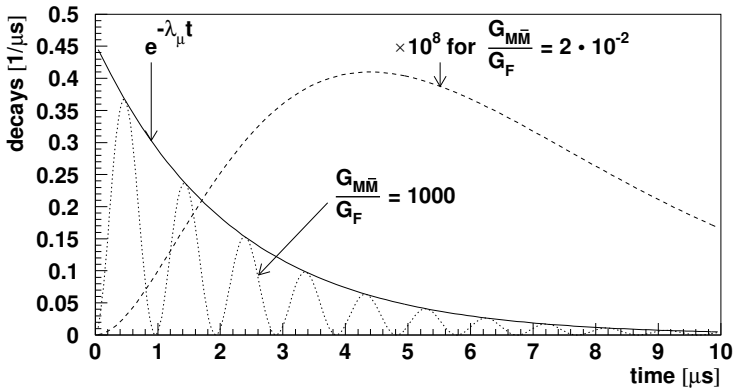

Figure 129: Time dependence of the probability to observe an anti-muonium decay for a system which was initially in a pure muonium state. The solid line represents the exponential decay of muonium in the absence of a finite coupling. The decay probability as anti-muonium is given for a coupling strength of $G_{\mathrm{M}\overline{\mathrm{M}}} = 1000 G_F$ by the dotted line and for a coupling strength small compared to the muon decay rate (dashed line). In the latter case the maximum of the probability is always at about 2 muon lifetimes. Only for strong coupling could several oscillation periods be observed. Taken with kind permission of Springer Berlin/Heidelberg from figure 2 in reference [838]. Copyrighted by the Springer Berlin/Heidelberg.

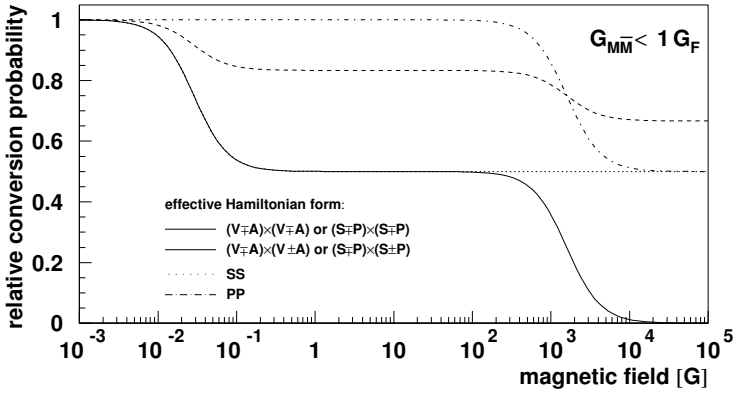

Figure 130: The muonium to anti-muonium conversion probability depends on external magnetic fields and the coupling type. Independent calculations were performed by Wong and Hou [872] and Horikawa and Sasaki [873]. Taken with kind permission of Springer Berlin/Heidelberg from figure 3 in reference [838]. Copyrighted by the Springer Berlin/Heidelberg.

is caused, where a_0 is the Bohr radius of the atom, $G_{\mathrm{M}\overline{\mathrm{M}}}$ is the coupling constant in an effective four-fermion interaction and G_{F} is the weak interaction Fermi coupling constant. For the ground state we have $\delta = 1.5 \times 10^{-12}\,\mathrm{eV} \times (G_{\mathrm{M}\overline{\mathrm{M}}}/G_{\mathrm{F}})$ which corresponds to 519 Hz for $G_{\mathrm{M}\overline{\mathrm{M}}} = G_{\mathrm{F}}$. An atomic system created at time $t = 0$ as a pure state of muonium can be expected to be observed in the anti-muonium state at a later time t with a time dependent probability of:

$$p_{\mathrm{M}\overline{\mathrm{M}}}(t) \quad = \sin^2\left(\tfrac{\delta\, t}{2\,\hbar}\right) e^{-\lambda_\mu t} \quad \approx \left(\frac{\delta\, t}{2\,\hbar}\right)^2 e^{-\lambda_\mu t}\,, \tag{358}$$

where $\lambda_\mu = 1/\tau_\mu$ is the muon decay rate (see figure 129). The approximation is valid for a weak coupling as suggested by the known experimental limits on $G_{\mathrm{M}\overline{\mathrm{M}}}$.

The degeneracy of corresponding states in the atom and its anti-atom is removed by external magnetic fields which can cause a suppression of the conversion and a reduction of the probability $p_{\mathrm{M}\overline{\mathrm{M}}}$. The influence of an external magnetic field depends on the interaction type of the process.

The reduction of the conversion probability has been calculated for all possible interaction types as a function of field strength (figure 130) [872, 873]. In the case of an observation of the conversion process, the coupling type could be revealed by measurements of the conversion probability at two different magnetic-field values.

The conversion process is strongly suppressed for muonium in contact with matter since a transfer of the negative muon in anti-muonium to any other atom is energetically favoured and breaks up the symmetry between muonium and anti-muonium by opening up an additional decay channel for the anti-atom only [874, 875] [20]. Therefore any new sensitive experiment needs to employ muonium atoms in vacuum [772, 838].

The most recent experiment, which was carried out at PSI, utilised a powerful signature in which the identification of both constituents of the anti-atom and their coincident detection after its decay. In this experiment, an energetic electron appears in the μ^- decay. The positron from the atomic shell remains with an average kinetic energy of 13.5 eV [876]. The energetic particle could be observed in a magnetic, wire-chamber spectrometer and a position-sensitive microchannel plate (MCP) served as a detector for atomic shell positrons onto which these particles could be transported in a guiding magnetic field after post-acceleration in an electrostatic device. A clean vertex reconstruction and the observation of annihilation γ's in a pure CsI detector surrounding the MCP were required in an event signature [772, 838]. Half a year of data-taking was carried out what is currently the most intense surface-muon source; the πE5 channel at PSI. The previous upper bound on the total conversion probability per muonium atom $P_{\mathrm{M}\overline{\mathrm{M}}} = \int p_{\mathrm{M}\overline{\mathrm{M}}}(t)\mathrm{d}t$ was improved by more than three orders of magnitude and yielded an upper bound of $P_{\mathrm{M}\overline{\mathrm{M}}} \leq 8.0 \times 10^{-11}/S_{\mathrm{B}}$. Here, a magnetic field correction S_{B} is included which accounts for the 0.1 T magnetic field in the experiment. S_{B} is of order unity and depends on the type of the $\mathrm{M}\overline{\mathrm{M}}$ interaction. For an assumed effective (V–A)×(V–A)-type four-fermion interaction the quoted result corresponds to an upper limit for the coupling constant of $G_{\mathrm{M}\overline{\mathrm{M}}} \leq 3.0 \times 10^{-3} G_{\mathrm{F}}$ (90 % C.L.). Several limits on model parameters were significantly improved, such as the mass of the bi-leptonic gauge boson, and some models were strongly disfavoured, such as a certain Z_8 model with radiative mass generation and the minimal version of 331 models [772, 838].

With a new and intense, pulsed beam the characteristic time dependence of the conversion process could be exploited only if the decay of atoms that have survived several muon lifetimes, τ_μ, can be observed. Whereas all beam-muon-related background decays exponentially, the anti-atom population increases quadratically with time, giving the signal an advantage over background which, for a 3-fold coincidence signature as in the PSI experiment, can be expected to decay with a time constant of $\tau_\mu/3$ (compare equation (358)). Some two orders of magnitude improvement can be envisaged [877] with no significant background arising from the $\mu \to 3e2\nu$ process or internal Bhabha scattering in which the positron from μ^+ decay would transfer its energy to the electron in the atomic shell and mimic a signal event (figure 131). The requirements for radiation hardness and rate capability of the set-up are similar to those of a $\mu \to 3e$

[20] In gases at atmospheric pressures the conversion probability is approximately five orders of magnitude smaller than in vacuum mainly due to scattering of the atoms from gas molecules. In solids the reduction amounts to 10 orders of magnitude.

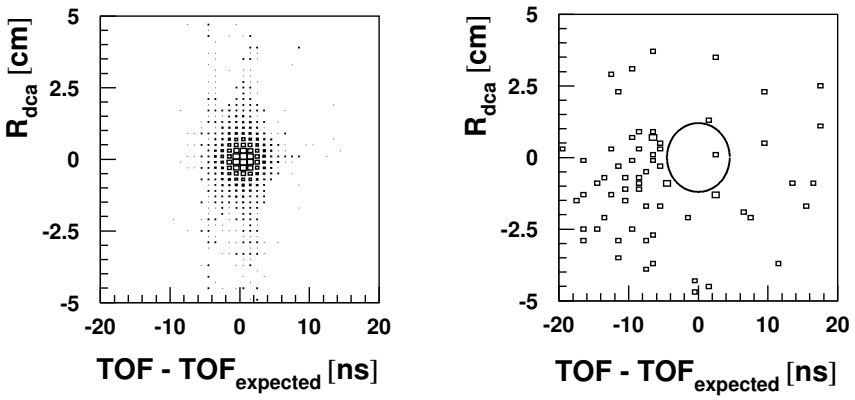

Figure 131: The distribution of the distance of closest approach (R_{dca}) between a track from an energetic particle in the magnetic spectrometer and the back projection of the position on the MCP detector versus the time of flight (TOF) of the atomic shell particle for a muonium measurement (left) and for all data recorded within 1290 h of data taking while searching for anti-muonium (right) (From reference [772]). One single event falls within 3 standard deviations region of the expected TOF and R_{dca} which is indicated by the ellipse. The events concentrated at early times and low R_{dca}correspond to a background signal from the allowed decay $\mu \rightarrow 3e2\nu$. In a new experiment such background could be suppressed significantly through the characteristically different time evolution of a potential anti-muonium signal and the background. Taken with kind permission of Physical Review Letters from figure 4 in reference [772]. Copyrighted by the American Physical Society.

experiment. As before, a common approach to these two measurements may be found.

7.5 Normal muon decay

7.5.1 Theoretical background

All measurements of normal muon decay, $\mu^- \rightarrow e^- \overline{\nu}_e \nu_\mu$, and its inverse, $\nu_\mu e^- \rightarrow \mu^- \nu_e$, are successfully described by the 'V–A' interaction, which is a particular case of the local, derivative-free, lepton-number-conserving, four-fermion interaction [878]. The 'V–A' form and the nature of the neutrinos ($\overline{\nu}_e$ and ν_e) have been determined by experiment [879, 880].

The observables in muon decay (energy spectra, polarisations and angular distributions) and in inverse muon decay (the reaction cross section) at energies well below $m_W c^2$ may be parameterised in terms of the dimensionless coupling constants $g^\gamma_{\varepsilon\mu}$ and the Fermi coupling constant G_F. The matrix element is:

$$\mathcal{M} = \frac{4G_\mathrm{F}}{\sqrt{2}} \sum_{\substack{\gamma=\mathrm{S,V,T} \\ \varepsilon,\mu=\mathrm{R,L}}} g^\gamma_{\varepsilon\mu} \langle \overline{e}_\varepsilon | \Gamma^\gamma | (\nu_e)_n \rangle \langle (\overline{\nu}_\mu)_m | \Gamma_\gamma | \mu_\mu \rangle \ . \tag{359}$$

We use here the notation of Fetscher et al., [879, 881] who in turn use the sign conventions and definitions of Scheck [882]. Here $\gamma = \mathrm{S, V, T}$ indicates a (Lorentz) scalar, vector, or tensor interaction, and the chirality of the electron or muon (right- or left-handed) is labelled by $\varepsilon, \mu = \mathrm{R, L}$. The chiralities n and m of the ν_e and the $\overline{\nu}_\mu$ are determined by given values of γ, ε and μ. The 10 complex amplitudes, $g^\gamma_{\varepsilon\mu}$, and G_F constitute 19 independent parameters to

be determined by experiment. The 'V–A' interaction corresponds to $g^{\mathrm{V}}_{\mathrm{LL}} = 1$, with all other amplitudes being 0.

With the deduction from experiments that the interaction is predominantly of the vector type and left-handed ($g^{\mathrm{V}}_{\mathrm{LL}} > 0.96$ (90 %CL)), there remain several separate routes of investigation of normal muon decay, which will be discussed in the following.

7.5.2 Muon-lifetime measurements

The measurement of the muon lifetime yields the most precise determination of the Fermi coupling constant G_{F}, which until recently was known with a relative precision of 9×10^{-6} [231]. Improving this measurement is certainly an interesting goal [876] since G_{F} is one of the fundamental parameters of the Standard Model. Until recently, the ability to extract G_{F} from τ_μ was limited by theory, the recent the radiative corrections calculated by van Ritbergen and Stuart [883–885] have removed this uncertainty.

A clean beam pulse structure with very good suppression of particles between pulses is indispensable. Presently three experiments are in progress, two of which are at PSI [886, 887] and one is located at RAL [888]. The MuLan experiment at PSI has recently released an 11 ppm measurement of τ_μ obtained from their 2004 data set [889], which gives a new world average $\tau_\mu = 2.197\,019(21)$ μs and determines the Fermi constant to be $G_F = 1.166\,371(6) \times 10^{-5}$ GeV^{-2} (± 5 ppm). The 2006 MuLan data set has 10^{12} μ^+ decays on tape which, in principle, will give a 1 ppm measurement. A final data run in 2007 should accumulate a data set of equal size. These new data should result in an improvement in the precision of τ_μ by about a factor of 20 over the previous world average [231]. An additional order of magnitude could be gained at a Neutrino Factory primarily from increased muon flux, with the major systematics being pile-up and detector timing stability.

There are two caveats, however: reducing the error on G_{F} by precise measurements of the muon lifetime would not improve the electroweak fits, because the error on the dimensionless input $G_{\mathrm{F}} M_Z^2$ is dominated by the uncertainty on M_Z^2, which is now 23×10^{-6} (or 23 ppm), where ($M_Z = (91\,187.6 \pm 2.1)$ MeV [231]). Also G_{F} is commonly determined assuming exclusively V-A interactions. A somewhat more general formula has been given by Greub et al. [890]:

$$G_{\mathrm{F}}^2 = \frac{192\pi^3\hbar}{\tau_\mu m_\mu^5}\left[1 + \frac{\alpha}{2\pi}\left(\pi^2 - \frac{25}{4}\right)\right]\left[1 - \frac{3}{5}\left(\frac{m_\mu}{m_W}\right)^2\right] \times \left[1 - 4\eta\frac{m_e}{m_\mu} - 4\lambda\frac{m_{\nu_\mu}}{m_\mu} + 8\left(\frac{m_e}{m_\mu}\right)^2 + 8\left(\frac{m_{\nu_\mu}}{m_\mu}\right)^2\right], \tag{360}$$

$$\eta = \frac{1}{2}\mathrm{Re}\left[g^{\mathrm{V}}_{\mathrm{LL}} g^{\mathrm{S}*}_{\mathrm{RR}} + g^{\mathrm{V}}_{\mathrm{RR}} g^{\mathrm{S}*}_{\mathrm{LL}} + g^{\mathrm{V}}_{\mathrm{LR}}(g^{\mathrm{S}*}_{\mathrm{RL}} + g^{\mathrm{T}*}_{\mathrm{RL}}) + g^{\mathrm{V}}_{\mathrm{RL}}(g^{\mathrm{S}*}_{\mathrm{LR}} + g^{\mathrm{T}*}_{\mathrm{LR}})\right], \tag{361}$$

$$\lambda = \frac{1}{2}\mathrm{Re}\left[g^{\mathrm{S}}_{\mathrm{LL}} g^{\mathrm{S}*}_{\mathrm{LR}} + g^{\mathrm{S}}_{\mathrm{RR}} g^{\mathrm{S}*}_{\mathrm{RL}} - 2g^{\mathrm{V}}_{\mathrm{RR}} g^{\mathrm{V}*}_{\mathrm{RL}} - 2g^{\mathrm{V}}_{\mathrm{LL}} g^{\mathrm{V}*}_{\mathrm{LR}}\right]. \tag{362}$$

Here, besides the muon lifetime and the muon mass, radiative corrections to first order and mass terms are included. Most important is the muon-decay parameter η which is 0 in the SM. If we assume that only one additional interaction contributes to muon decay, then $\eta \simeq \frac{1}{2}\mathrm{Re}g^{\mathrm{S}}_{\mathrm{RR}}$, where $g^{\mathrm{S}}_{\mathrm{RR}}$ corresponds to a scalar coupling with right-handed charged leptons. Including the experimental value of $\eta = (-7 \pm 13) \times 10^{-3}$ [891] the error on G_{F} increases by a factor of 20.

7.5.3 Precision measurement of the Michel parameters

The measurement of individual decay parameters alone generally does not give conclusive information about the decay interaction owing to the many different couplings and interference terms. An example is the spectrum Michel parameter, ϱ. A precise measurement yielding the V–A value of 3/4 by no means establishes the V–A interaction. In fact, any interaction consisting of an arbitrary combination of $g^{\mathrm{S}}_{\mathrm{LL}}$, $g^{\mathrm{S}}_{\mathrm{LR}}$, $g^{\mathrm{S}}_{\mathrm{RL}}$, $g^{\mathrm{S}}_{\mathrm{RR}}$, $g^{\mathrm{V}}_{\mathrm{RR}}$, and $g^{\mathrm{V}}_{\mathrm{LL}}$ will yield exactly $\varrho = 3/4$ [892]. This can be seen if we write ϱ in the form [893]:

$$\varrho - \tfrac{3}{4} = -\tfrac{3}{4}\left\{|g^{\mathrm{V}}_{\mathrm{LR}}|^2 + |g^{\mathrm{V}}_{\mathrm{RL}}|^2\right\} + 2\left(|g^{\mathrm{T}}_{\mathrm{LR}}|^2 + |g^{\mathrm{T}}_{\mathrm{RL}}|^2\right) + Re\left(g^{\mathrm{S}}_{\mathrm{LR}} g^{\mathrm{T}*}_{\mathrm{LR}} + g^{\mathrm{S}}_{\mathrm{RL}} g^{\mathrm{T}*}_{\mathrm{RL}}\right) . \tag{363}$$

For $\varrho = \frac{3}{4}$ and $g^{\mathrm{T}}_{\mathrm{RL}} = g^{\mathrm{T}}_{\mathrm{LR}} = 0$ (no tensor interaction) one finds $g^{\mathrm{V}}_{\mathrm{RL}} = g^{\mathrm{V}}_{\mathrm{LR}} = 0$, with all of the remaining six couplings being arbitrary. On the other hand, any deviation from the canonical value certainly would signify new physics. Tree-level new physics contributions to the Michel parameters occur in supersymmetric theories with R-parity violation or theories with left-right symmetric gauge groups. For instance, the R-parity violating interactions $\lambda_{311} L^{(3)}_{\mathrm{L}} L^{(1)}_{\mathrm{L}} \bar{E}^{(1)}_{\mathrm{R}} + \lambda_{322} L^{(3)}_{\mathrm{L}} L^{(2)}_{\mathrm{L}} \bar{E}^{(2)}_{\mathrm{R}}$ (where the index denotes the lepton generation) give the following contributions [228, 229, 836]:

$$\Delta\rho = \frac{3\epsilon^2}{16}, \quad \Delta\eta = \frac{\epsilon}{2}, \quad \Delta\xi = -\frac{\epsilon^2}{4}, \quad \Delta\delta = 0, \qquad \epsilon \equiv \frac{\lambda_{311}\lambda_{322}}{4\sqrt{2} G_{\mathrm{F}} \tilde{m}^2_{e^{(3)}_{\mathrm{L}}}} . \tag{364}$$

For a left-right model, one finds:

$$\Delta\rho = -\frac{3}{2}\vartheta^2_{W_{\mathrm{R}}}, \quad \Delta\xi = -2\vartheta^2_{W_{\mathrm{R}}} - 2\left(\frac{M_{W_1}}{M_{W_2}}\right)^4 , \tag{365}$$

where $\vartheta_{W_{\mathrm{R}}}$ is the W_{L}-W_{R} mixing angle, and M_{W_1} (M_{W_2}) is the mass of the mainly left (right) charged gauge boson. Measurements of ϱ and ξ with a precision of 10^{-4} can probe W_{R} masses of about 1 TeV (in the most unfavourable case $\vartheta_{W_{\mathrm{R}}} = 0$) and values of the R-parity violating couplings $\lambda_{311} \approx \lambda_{322} \approx 0.2$ (for a slepton mass of 200 GeV). These tests are competitive with direct searches at high-energy colliders.

There exist also observables which yield valuable information even if they assume their canonical values, all of which are related to the spin variables of the muon and the electron:

- A measurement of the decay asymmetry yields the parameters δ and $P_\mu\xi$. Especially interesting is the combination $P_\mu\xi\delta/\varrho$, which has been measured at TRIUMF [894] with a precision of $\approx 3 \times 10^{-3}$. A new, ambitious experiment of the TWIST collaboration at

TRIUMF measuring ϱ, δ and $P_\mu\xi$ has published improved results on the former two decay parameters ($\rho = 750.80 \pm 0.44_{\text{stat.}} \pm 0.93_{\text{syst.}} \pm 0.23_\eta) \times 10^{-3}$, where the last uncertainty is due to the correlation of ρ with η [895], $\delta = (749.64 \pm 0.66_{\text{stat.}} \pm 1.12_{\text{syst.}}) \times 10^{-3}$ [896] and $P_\mu\xi = (1000.3 \pm 0.6_{\text{stat.}} \pm 3.8_{\text{syst.}}) \times 10^{-3}$ [897]);

- A measurement of the longitudinal polarisation of the decay electrons P_{L} consistent with 1 yields limits for all five couplings where the electrons are right-handed. This is a difficult experiment due to the lack of highly polarised electron targets used as analysers. The present precision is $\Delta P_{\text{L}} = 45 \times 10^{-3}$;

- The angular dependence of the longitudinal polarisation of decay positrons at the endpoint energy is currently being measured at PSI by the Louvain-la-Neuve-PSI-ETH Zürich collaboration [898]. This yields the parameter ξ'' which is sensitive to the right-handed vector and the tensor currents; and

- A measurement of the transverse polarisation of the decay positrons requires a highly polarised, pulsed muon beam. From the energy dependence of the component P_{T_1} one can deduce the low-energy decay parameter η which is needed for a model-independent value of the Fermi coupling constant. The second component P_{T_2}, which is transverse to the positron momentum and the muon polarisation, is non-invariant under time reversal. A second generation experiment has been performed at PSI by the ETH Zürich-Cracow-PSI collaboration [899]. They obtained, among several other results, for the energy averaged transverse polarisation components $\langle P_{\text{T}_1} \rangle = (6.3 \pm 7.7_{\text{stat.}} \pm 3.4_{\text{syst.}}) \times 10^{-3}$, $\langle P_{\text{T}_2} \rangle = (-3.7 \pm 7.7_{\text{stat.}} \pm 3.4_{\text{syst.}}) \times 10^{-3}$ and for the decay parameter $\eta = -2.1 \pm 7.0_{\text{stat.}} \pm 1.0_{\text{syst.}}) \times 10^{-3}$ [900]. This last value has been obtained considering only terms interfering with the dominant $V - A$ interaction.

7.5.4 Experimental prospects

As mentioned above, the precision on the muon lifetime can presumably be increased over the ongoing measurements by one order of magnitude. Improvement in measurements of the decay parameters seems more difficult. Most ambitious is the TRIUMF project which has published first results on the parameters ϱ (positron energy spectrum), $P_\mu\xi$ and δ (decay asymmetry) [895–897]. Their final goal is an improvement by more than one order of magnitude. The limits on most other observables are not given by the muon rates which usually are high enough already ($\approx 3 \times 10^8$ s^{-1} at the μE1 beam at PSI, for example), but rather by effects such as positron depolarisation in matter or by the small available polarisation ($< 7\%$) of the electron targets used as analysers. The measurement of the transverse positron polarisation might be improved with a smaller phase space (lateral beam dimension of a few millimetres or better). This experiment needs a pulsed beam with high polarisation.

7.6 Muon-Physics Conclusions

The main conclusion of this study is that the physics potential of a new slow muon facility, such as the one that will become available as a necessary step on the way to building a muon storage ring (Neutrino Factory), is very rich and compelling, with a large variety of applications in many fields of basic research. Indeed, muon physics, that has already played an important role in establishing the Standard Model, may provide us with crucial information regarding the theory that lies beyond, proving itself to be still far from having exhausted its potential.

This new low-energy muon source will have unprecedented intensity, three to four orders of magnitude larger than presently available. It can have the large degree of flexibility necessary to satisfy the requirements of very different experiments, providing muon beams with a wide variety of momenta and time structures. Both continuous and pulsed beams are possible. In addition, it is capable of producing physics results at the very early stages of the muon complex, well before the completion of muon cooling, acceleration, and storage sections.

Only preliminary ideas on the design of this facility are introduced here, suggesting ways by which the muon flux could be boosted orders of magnitude above present or foreseen facilities. The tasks of detailed conceptual design of target and capture systems and of quantitative estimates of beam performances are still entirely ahead of us. The possibility of using pions/muons produced in the backward direction is actively being studied, which if feasible would permit the Neutrino Factory to take forward muons simultaneously and operate simultaneously with the muon facility.

A major interest in muon physics lies in the searches for rare processes that violate muon number conservation, or for a permanent electric-dipole moment of the muon. In many extensions of the Standard Model, such as supersymmetry, lepton flavour violation may occur at rates close to the current experimental bounds. Their discovery would have far-reaching consequences. The most interesting processes are $\mu^+ \to e^+\gamma$, $\mu^+ \to e^+e^-e^+$, and μ^-–e^- conversion in nuclei. We emphasise that all the different processes should be pursued, along with a search for a muon EDM. Indeed, the relative rates of the different modes provide a powerful tool for discriminating different manifestations of new physics.

The muon facility discussed here has enough flexibility to allow the study of different muon processes, and promises to be more sensitive by at least a few orders of magnitude, when compared with current experiments. In closing, we should mention that if such a facility existed, a number of fundamental studies with muonium and other muonic atoms would also be possible. Such studies would permit increased precision of the measurement of fundamental constants, and would serve to attract an additional community to such a facility.

Acknowledgements

We would like to thank the management of Rutherford Appleton Laboratory, CCLRC and PPARC, for their support during the study and to Professor J. Wood in particular for initiating

the study. During the course of the year, we were welcomed at a number of laboratories across the world and therefore thank the management of the CERN, KEK, RAL laboratories and the University of Irvine for hosting the ISS plenary meetings. The work of the group benefitted greatly from the Physics Working Group meetings at Imperial, Boston, and Valencia; we would like to thank the groups involved for welcoming us to their laboratories. Finally, our warm and sincere thanks go to all those who contributed to the plenary and working group meetings, either through making presentations or by contributing to the discussion, and to those who contributed to the production of this report.

The authors acknowledge the support of CARE, contract number RII3-CT-2003-506395. The work was supported by the Science and Technology Facilities Council under grant numbers PPA/G/S2003/00512, PP/B500790/1, PP/B500815/1, PP/B500882/1, and through SLAs with STFC supported laboratories. The authors also acknowledge the support of the World Premier International Research Center Initiative (WPI Initiative), MEXT, Japan. This research was partially supported by the Director, Office of Science, Office of High Energy Physics, of the U.S. Department of Energy, under contract nos. DE-AC02-05CH11231, DE-AC02-98CH10886, DE-AC02-07CH11359, and DE-AC03-76SF00098. The work was also supported by the U.S. National Science Foundation under grants PHY-0355245 and PHY-04-57315.

References

[1] J. Schechter and J. W. F. Valle, "Neutrinoless double-beta decay in SU(2) x U(1) theories," *Phys. Rev.* **D25** (1982) 2951.

[2] B. Pontecorvo, "Mesonium and antimesonium," *Sov. Phys. JETP* **6** (1957) 429.

[3] B. Pontecorvo, "Inverse beta processes and nonconservation of lepton charge," *Sov. Phys. JETP* **7** (1958) 172–173.

[4] Z. Maki, M. Nakagawa, and S. Sakata, "Remarks on the unified model of elementary particles," *Prog. Theor. Phys.* **28** (1962) 870.

[5] **Super-Kamiokande** Collaboration, Y. Fukuda *et al.*, "Evidence for oscillation of atmospheric neutrinos," *Phys. Rev. Lett.* **81** (1998) 1562–1567, `hep-ex/9807003`.

[6] B. T. Cleveland *et al.*, "Measurement of the solar electron neutrino flux with the Homestake chlorine detector," *Astrophys. J.* **496** (1998) 505–526.

[7] **SNO** Collaboration, Q. R. Ahmad *et al.*, "Measurement of the charged current interactions produced by B-8 solar neutrinos at the Sudbury Neutrino Observatory," *Phys. Rev. Lett.* **87** (2001) 071301, `nucl-ex/0106015`.

[8] **KamLAND** Collaboration, T. Araki *et al.*, "Measurement of neutrino oscillation with KamLAND: Evidence of spectral distortion," *Phys. Rev. Lett.* **94** (2005) 081801, `hep-ex/0406035`.

[9] **Super-Kamiokande** Collaboration, Y. Ashie *et al.*, "Evidence for an oscillatory signature in atmospheric neutrino oscillation," *Phys. Rev. Lett.* **93** (2004) 101801, `hep-ex/0404034`.

[10] **K2K** Collaboration, M. H. Ahn *et al.*, "Measurement of neutrino oscillation by the K2K experiment," *Phys. Rev.* **D74** (2006) 072003, `hep-ex/0606032`.

[11] **MINOS** Collaboration, D. G. Michael *et al.*, "Observation of muon neutrino disappearance with the MINOS detectors and the NuMI neutrino beam," *Phys. Rev. Lett.* **97** (2006) 191801, `hep-ex/0607088`.

[12] **OPERA** Collaboration, K. Kodama *et al.*, "A long baseline nu/tau appearance experiment in the CNGS beam from CERN to Gran Sasso. Progress report." CERN-SPSC-99-20.

[13] Y. Itow *et al.*, "The JHF-Kamioka neutrino project," `hep-ex/0106019`.

[14] M. Mezzetto, "Physics potential of the SPL super beam," *J. Phys.* **G29** (2003) 1781–1784, `hep-ex/0302005`.

[15] J. E. Campagne and A. Cazes, "The theta(13) and delta(CP) sensitivities of the SPL-Frejus project revisited," *Eur. Phys. J.* **C45** (2006) 643–657, `hep-ex/0411062`.

[16] **NOvA** Collaboration, D. S. Ayres *et al.*, "NOvA proposal to build a 30-kiloton off-axis detector to study neutrino oscillations in the Fermilab NuMI beamline," hep-ex/0503053.

[17] O. Mena Requejo, S. Palomares-Ruiz, and S. Pascoli, "Super-NOvA: A long-baseline neutrino experiment with two off-axis detectors," *Phys. Rev.* **D72** (2005) 053002, hep-ph/0504015.

[18] O. Mena, S. Palomares-Ruiz, and S. Pascoli, "Determining the neutrino mass hierarchy and CP violation in NOnuA with a second off-axis detector," *Phys. Rev.* **D73** (2006) 073007, hep-ph/0510182.

[19] M. Ishitsuka, T. Kajita, H. Minakata, and H. Nunokawa, "Resolving neutrino mass hierarchy and CP degeneracy by two identical detectors with different baselines," *Phys. Rev.* **D72** (2005) 033003, hep-ph/0504026.

[20] K. Hagiwara, N. Okamura, and K.-i. Senda, "Solving the neutrino parameter degeneracy by measuring the T2K off-axis beam in Korea," *Phys. Lett.* **B637** (2006) 266–273, hep-ph/0504061.

[21] K. Hagiwara, N. Okamura, and K.-i. Senda, "Physics potential of T2KK: An extension of the T2K neutrino oscillation experiment with a far detector in Korea," *Phys. Rev.* **D76** (2007) 093002, hep-ph/0607255.

[22] T. Kajita, H. Minakata, S. Nakayama, and H. Nunokawa, "Resolving eight-fold neutrino parameter degeneracy by two identical detectors with different baselines," *Phys. Rev.* **D75** (2007) 013006, hep-ph/0609286.

[23] M. Diwan *et al.*, "Proposal for an experimental program in neutrino physics and proton decay in the homestake laboratory," hep-ex/0608023.

[24] P. Zucchelli, "A novel concept for a anti-nu/e / nu/e neutrino factory: The beta beam," *Phys. Lett.* **B532** (2002) 166–172.

[25] J. Burguet-Castell, D. Casper, J. J. Gomez-Cadenas, P. Hernandez, and F. Sanchez, "Neutrino oscillation physics with a higher gamma beta- beam," *Nucl. Phys.* **B695** (2004) 217–240, hep-ph/0312068.

[26] M. Mezzetto, "Physics potential of the gamma = 100,100 beta beam," *Nucl. Phys. Proc. Suppl.* **155** (2006) 214–217, hep-ex/0511005.

[27] J. E. Campagne, M. Maltoni, M. Mezzetto, and T. Schwetz, "Physics potential of the CERN-MEMPHYS neutrino oscillation project," *JHEP* **04** (2007) 003, hep-ph/0603172.

[28] S. Geer, "Neutrino beams from muon storage rings: Characteristics and physics potential," *Phys. Rev.* **D57** (1998) 6989–6997, hep-ph/9712290.

[29] A. De Rujula, M. B. Gavela, and P. Hernandez, "Neutrino oscillation physics with a neutrino factory," *Nucl. Phys.* **B547** (1999) 21–38, hep-ph/9811390.

[30] **The Muon Collider and Neutrino Factory** Collaboration. See the web site `http://www.cap.bnl.gov/mumu/` which contains also references.

[31] D. Finley and N. Holtkamp, "A feasibility study of a neutrino source based on a muon storage ring," *Nucl. Instrum. Meth.* **A472** (2000) 388–394.

[32] S. Ozaki and others (ed.), "Feasibility study 2 of a muon-based neutrino source." BNL-52623.

[33] P. Gruber and others (ed.), "The study of a European Neutrino Factory complex." CERN-PS-2002-080-PP.

[34] **Muon Collider/Neutrino Factory** Collaboration, M. M. Alsharoa *et al.*, "Recent progress in neutrino factory and muon collider research within the Muon collaboration," *Phys. Rev. ST Accel. Beams* **6** (2003) 081001, `hep-ex/0207031`.

[35] M. S. Zisman, "Technical design aspects of feasibility study-II," *Nucl. Instrum. Meth.* **A503** (2003) 384–389.

[36] M. V. Diwan *et al.*, "Very long baseline neutrino oscillation experiments for precise measurements of mixing parameters and CP violating effects," *Phys. Rev.* **D68** (2003) 012002, `hep-ph/0303081`.

[37] M. V. Diwan, "The case for a super neutrino beam," *Frascati Phys. Ser.* **35** (2004) 89–109, `hep-ex/0407047`.

[38] P. Huber, M. Maltoni, and T. Schwetz, "Resolving parameter degeneracies in long-baseline experiments by atmospheric neutrino data," *Phys. Rev.* **D71** (2005) 053006, `hep-ph/0501037`.

[39] **LSND** Collaboration, C. Athanassopoulos *et al.*, "Evidence for nu/mu $\rightarrow$ nu/e neutrino oscillations from LSND," *Phys. Rev. Lett.* **81** (1998) 1774–1777, `nucl-ex/9709006`.

[40] **The MiniBooNE** Collaboration, A. A. Aguilar-Arevalo *et al.*, "A Search for electron neutrino appearance at the $\Delta m^2 \sim 1\mathrm{eV}^2$ scale," *Phys. Rev. Lett.* **98** (2007) 231801, `0704.1500`.

[41] S. Geer, O. Mena, and S. Pascoli, "A Low energy neutrino factory for large θ_{13}," *Phys. Rev.* **D75** (2007) 093001, `hep-ph/0701258`.

[42] A. Cervera, F. Dydak, and J. Gomez Cadenas, "A large magnetic detector for the neutrino factory," *Nucl. Instrum. Meth.* **A451** (2000) 123–130.

[43] P. Huber and W. Winter, "Neutrino factories and the 'magic' baseline," *Phys. Rev.* **D68** (2003) 037301, `hep-ph/0301257`.

[44] A. Donini, D. Meloni, and P. Migliozzi, "The silver channel at the neutrino factory," *Nucl. Phys.* **B646** (2002) 321–349, `hep-ph/0206034`.

[45] P. Huber, M. Lindner, and W. Winter, "Simulation of long-baseline neutrino oscillation experiments with GLoBES," *Comput. Phys. Commun.* **167** (2005) 195, hep-ph/0407333.

[46] P. Huber, J. Kopp, M. Lindner, M. Rolinec, and W. Winter, "New features in the simulation of neutrino oscillation experiments with GLoBES 3.0," *Comput. Phys. Commun.* **177** (2007) 432–438, hep-ph/0701187.

[47] **Kamiokande** Collaboration, Y. Fukuda *et al.*, "Solar neutrino data covering solar cycle 22," *Phys. Rev. Lett.* **77** (1996) 1683–1686.

[48] **SAGE** Collaboration, J. N. Abdurashitov *et al.*, "Measurement of the solar neutrino capture rate by the Russian-American gallium solar neutrino experiment during one half of the 22-year cycle of solar activity," *J. Exp. Theor. Phys.* **95** (2002) 181–193, astro-ph/0204245.

[49] **GNO** Collaboration, T. A. Kirsten, "Progress in GNO," *Nucl. Phys. Proc. Suppl.* **118** (2003) 33–38.

[50] C. Cattadori, N. Ferrari, and L. Pandola, "Results from radiochemical experiments with main emphasis on the gallium ones," *Nucl. Phys. Proc. Suppl.* **143** (2005) 3–12.

[51] **Super-Kamiokande** Collaboration, S. Fukuda *et al.*, "Determination of solar neutrino oscillation parameters using 1496 days of Super-Kamiokande-I data," *Phys. Lett.* **B539** (2002) 179–187, hep-ex/0205075.

[52] **SNO** Collaboration, Q. R. Ahmad *et al.*, "Direct evidence for neutrino flavor transformation from neutral-current interactions in the Sudbury Neutrino Observatory," *Phys. Rev. Lett.* **89** (2002) 011301, nucl-ex/0204008.

[53] **SNO** Collaboration, Q. R. Ahmad *et al.*, "Measurement of day and night neutrino energy spectra at SNO and constraints on neutrino mixing parameters," *Phys. Rev. Lett.* **89** (2002) 011302, nucl-ex/0204009.

[54] **SNO** Collaboration, S. N. Ahmed *et al.*, "Measurement of the total active B-8 solar neutrino flux at the Sudbury Neutrino Observatory with enhanced neutral current sensitivity," *Phys. Rev. Lett.* **92** (2004) 181301, nucl-ex/0309004.

[55] **KamLAND** Collaboration, K. Eguchi *et al.*, "First results from KamLAND: Evidence for reactor anti- neutrino disappearance," *Phys. Rev. Lett.* **90** (2003) 021802, hep-ex/0212021.

[56] **K2K** Collaboration, M. H. Ahn *et al.*, "Indications of neutrino oscillation in a 250-km long- baseline experiment," *Phys. Rev. Lett.* **90** (2003) 041801, hep-ex/0212007.

[57] **K2K** Collaboration, E. Aliu *et al.*, "Evidence for muon neutrino oscillation in an accelerator- based experiment," *Phys. Rev. Lett.* **94** (2005) 081802, hep-ex/0411038.

[58] B. Pontecorvo, "Neutrino experiments and the question of leptonic-charge conservation," *Sov. Phys. JETP* **26** (1968) 984–988.

[59] S. M. Bilenky and B. Pontecorvo, "Lepton Mixing and Neutrino Oscillations," *Phys. Rept.* **41** (1978) 225–261.

[60] L. Wolfenstein, "Neutrino oscillations in matter," *Phys. Rev.* **D17** (1978) 2369.

[61] S. P. Mikheev and A. Y. Smirnov, "Resonance enhancement of oscillations in matter and solar neutrino spectroscopy," *Sov. J. Nucl. Phys.* **42** (1985) 913–917.

[62] S. M. Bilenky and S. T. Petcov, "Massive neutrinos and neutrino oscillations," *Rev. Mod. Phys.* **59** (1987) 671.

[63] S. T. Petcov, "The solar neutrino problem and solar neutrino oscillations in vacuum and in matter," *Lect. Notes Phys.* **512** (1998) 281–328, `hep-ph/9806466`.

[64] M. C. Gonzalez-Garcia and Y. Nir, "Developments in neutrino physics," *Rev. Mod. Phys.* **75** (2003) 345–402, `hep-ph/0202058`.

[65] A. Bandyopadhyay, S. Choubey, S. Goswami, S. T. Petcov, and D. P. Roy, "Constraints on neutrino oscillation parameters from the SNO salt phase data," *Phys. Lett.* **B583** (2004) 134–148, `hep-ph/0309174`.

[66] V. N. Gribov and B. Pontecorvo, "Neutrino astronomy and lepton charge," *Phys. Lett.* **B28** (1969) 493.

[67] M. Maltoni, T. Schwetz, M. A. Tortola, and J. W. F. Valle, "Status of global fits to neutrino oscillations," *New J. Phys.* **6** (2004) 122, `hep-ph/0405172`. updated results in `hep-ph/0405172 (v6)`.

[68] M. Sorel, J. M. Conrad, and M. Shaevitz, "A combined analysis of short-baseline neutrino experiments in the (3+1) and (3+2) sterile neutrino oscillation hypotheses," *Phys. Rev.* **D70** (2004) 073004, `hep-ph/0305255`.

[69] S. M. Bilenky, J. Hosek, and S. T. Petcov, "On oscillations of neutrinos with Dirac and Majorana masses," *Phys. Lett.* **B94** (1980) 495.

[70] J. Schechter and J. W. F. Valle, "Neutrino Masses in SU(2) x U(1) Theories," *Phys. Rev.* **D22** (1980) 2227.

[71] M. Doi, T. Kotani, H. Nishiura, K. Okuda, and E. Takasugi, "CP violation in Majorana neutrinos," *Phys. Lett.* **B102** (1981) 323.

[72] J. Schechter and J. W. F. Valle, "Neutrino oscillation thought experiment," *Phys. Rev.* **D23** (1981) 1666.

[73] S. M. Bilenky, S. Pascoli, and S. T. Petcov, "Majorana neutrinos, neutrino mass spectrum, CP-violation and neutrinoless double beta-decay. I: The three-neutrino mixing case," *Phys. Rev.* **D64** (2001) 053010, `hep-ph/0102265`.

[74] **CHOOZ** Collaboration, M. Apollonio *et al.*, "Limits on neutrino oscillations from the CHOOZ experiment," *Phys. Lett.* **B466** (1999) 415–430, `hep-ex/9907037`.

[75] F. Boehm *et al.*, "Search for neutrino oscillations at the Palo Verde nuclear reactors," *Phys. Rev. Lett.* **84** (2000) 3764–3767, `hep-ex/9912050`.

[76] J. W. F. Valle, "Gauge theories and the physics of neutrino mass," *Prog. Part. Nucl. Phys.* **26** (1991) 91–171.

[77] A. Bandyopadhyay, S. Choubey, S. Goswami, S. T. Petcov, and D. P. Roy, "Update of the solar neutrino oscillation analysis with the 766-Ty KamLAND spectrum," *Phys. Lett.* **B608** (2005) 115–129, `hep-ph/0406328`.

[78] A. Bandyopadhyay, S. Choubey, S. Goswami, S. T. Petcov, and D. P. Roy, 2005. unpublished.

[79] T. Schwetz, "Global fits to neutrino oscillation data," *Phys. Scripta* **T127** (2006) 1–5, `hep-ph/0606060`.

[80] **Super-Kamiokande** Collaboration, J. Hosaka *et al.*, "Three flavor neutrino oscillation analysis of atmospheric neutrinos in Super-Kamiokande," *Phys. Rev.* **D74** (2006) 032002, `hep-ex/0604011`.

[81] S. T. Petcov, "Exact analytic description of two neutrino oscillations in matter with exponentially varying density," *Phys. Lett.* **B200** (1988) 373–379.

[82] S. T. Petcov, "On the oscillations of solar solar neutrinos in the Sun," *Phys. Lett.* **B214** (1988) 139–146.

[83] S. T. Petcov, "Describing analytically the matter-enhanced two-neutrino transitions in a medium," *Phys. Lett.* **B406** (1997) 355, `hep-ph/9910335`.

[84] S. T. Petcov, "An analytic description of three neutrino oscillations in matter with varying density," *Phys. Lett.* **B214** (1988) 259.

[85] W. C. Haxton, "Adiabatic conversion of solar neutrinos," *Phys. Rev. Lett.* **57** (1986) 1271–1274.

[86] S. J. Parke, "Nonadiabatic level crossing in resonant neutrino oscillations," *Phys. Rev. Lett.* **57** (1986) 1275–1278.

[87] P. I. Krastev and S. T. Petcov, "On the analytic description of two neutrino transitions of solar neutrinos in the Sun," *Phys. Lett.* **B207** (1988) 64.

[88] M. Bruggen, W. C. Haxton, and Y. Z. Qian, "Landau-Zener treatments of solar neutrino oscillations," *Phys. Rev.* **D51** (1995) 4028–4034.

[89] S. T. Petcov and J. Rich, "The effects of averaging on the matter enhanced oscillations of solar neutrinos," *Phys. Lett.* **B224** (1989) 426–432.

[90] S. M. Bilenky, C. Giunti, C. W. Kim, and S. T. Petcov, "Short-baseline neutrino oscillations and neutrinoless double-beta decay in schemes with an inverted mass spectrum," *Phys. Rev.* **D54** (1996) 4432–4444, hep-ph/9604364.

[91] S. Pascoli and S. T. Petcov, "The SNO solar neutrino data, neutrinoless double-beta decay and neutrino mass spectrum," *Phys. Lett.* **B544** (2002) 239–250, hep-ph/0205022.

[92] P. Langacker, S. T. Petcov, G. Steigman, and S. Toshev, "On the Mikheev-Smirnov-Wolfenstein (MSW) mechanism of amplification of neutrino oscillations in matter," *Nucl. Phys.* **B282** (1987) 589.

[93] S. Pascoli, S. T. Petcov, and A. Riotto, "Connecting low energy leptonic CP-violation to leptogenesis," *Phys. Rev.* **D75** (2007) 083511, hep-ph/0609125.

[94] S. Pascoli, S. T. Petcov, and A. Riotto, "Leptogenesis and low energy CP violation in neutrino physics," *Nucl. Phys.* **B774** (2007) 1–52, hep-ph/0611338.

[95] S. T. Petcov and T. Shindou, "LFV radiative decays and leptogenesis in the SUSY seesaw model," hep-ph/0605204.

[96] S. Choubey and S. T. Petcov, "Reactor anti-neutrino oscillations and gadolinium loaded Super-Kamiokande detector," *Phys. Lett.* **B594** (2004) 333–346, hep-ph/0404103.

[97] A. Bandyopadhyay, S. Choubey, S. Goswami, and S. T. Petcov, "High precision measurements of Theta(solar) in solar and reactor neutrino experiments," *Phys. Rev.* **D72** (2005) 033013, hep-ph/0410283.

[98] A. Bandyopadhyay, S. Choubey, and S. Goswami, "Exploring the sensitivity of current and future experiments to Theta(odot)," *Phys. Rev.* **D67** (2003) 113011, hep-ph/0302243.

[99] M. Chizhov, M. Maris, and S. T. Petcov, "On the oscillation length resonance in the transitions of solar and atmospheric neutrinos crossing the earth core," hep-ph/9810501.

[100] J. Bernabeu, S. Palomares Ruiz, and S. T. Petcov, "Atmospheric neutrino oscillations, theta(13) and neutrino mass hierarchy," *Nucl. Phys.* **B669** (2003) 255–276, hep-ph/0305152.

[101] S. Palomares-Ruiz and S. T. Petcov, "Three-neutrino oscillations of atmospheric neutrinos, theta(13), neutrino mass hierarchy and iron magnetized detectors," *Nucl. Phys.* **B712** (2005) 392–410, hep-ph/0406096.

[102] S. T. Petcov, "Diffractive-like (or parametric-resonance-like?) enhancement of the earth (day-night) effect for solar neutrinos crossing the earth core," *Phys. Lett.* **B434** (1998) 321–332, hep-ph/9805262.

[103] M. V. Chizhov and S. T. Petcov, "New conditions for a total neutrino conversion in a medium," *Phys. Rev. Lett.* **83** (1999) 1096–1099, hep-ph/9903399.

[104] M. V. Chizhov and S. T. Petcov, "Chizhov and Petcov Reply," *Phys. Rev. Lett.* **85** (2000) 3979, hep-ph/0504247.

[105] M. V. Chizhov and S. T. Petcov, "Enhancing mechanisms of neutrino transitions in a medium of nonperiodic constant-density layers and in the earth," *Phys. Rev.* **D63** (2001) 073003, hep-ph/9903424.

[106] **GALLEX** Collaboration, W. Hampel *et al.*, "GALLEX solar neutrino observations: Results for GALLEX IV," *Phys. Lett.* **B447** (1999) 127–133.

[107] **GNO** Collaboration, M. Altmann *et al.*, "Complete results for five years of GNO solar neutrino observations," *Phys. Lett.* **B616** (2005) 174–190, hep-ex/0504037.

[108] **Super-Kamiokande** Collaboration, M. B. Smy *et al.*, "Precise measurement of the solar neutrino day/night and seasonal variation in Super-Kamiokande-I," *Phys. Rev.* **D69** (2004) 011104, hep-ex/0309011.

[109] **SNO** Collaboration, B. Aharmim *et al.*, "Electron energy spectra, fluxes, and day-night asymmetries of B-8 solar neutrinos from the 391-day salt phase SNO data set," *Phys. Rev.* **C72** (2005) 055502, nucl-ex/0502021.

[110] S. Choubey, "Probing the neutrino mass matrix in next generation neutrino oscillation experiments," *Phys. Atom. Nucl.* **69** (2006) 1930–1939, hep-ph/0509217.

[111] S. Goswami, "Neutrino oscillations and masses," *Int. J. Mod. Phys.* **A21** (2006) 1901–1913. Talk given at *22nd International Symposium on Lepton-Photon Interactions at High Energy (LP 2005)*, Uppsala, Sweden, 30 Jun - 5 Jul 2005.

[112] A. W. P. Poon, "Review of solar and reactor neutrinos," *Int. J. Mod. Phys.* **A21** (2006) 1855–1868, hep-ex/0509024. Talk given at *22nd International Symposium on Lepton-Photon Interactions at High Energy (LP 2005)*, Uppsala, Sweden, 30 Jun - 5 Jul 2005.

[113] A. Bandyopadhyay, S. Choubey, S. Goswami, and S. T. Petcov, "On the measurement of solar neutrino oscillation parameters with KamLAND," *Phys. Lett.* **B581** (2004) 62–74, hep-ph/0309236.

[114] G. L. Fogli, E. Lisi, A. Marrone, and A. Palazzo, "Global analysis of three-flavor neutrino masses and mixings," *Prog. Part. Nucl. Phys.* **57** (2006) 742–795, hep-ph/0506083.

[115] S. Goswami and A. Y. Smirnov, "Solar neutrinos and 1-3 leptonic mixing," *Phys. Rev.* **D72** (2005) 053011, hep-ph/0411359.

[116] **Super-Kamiokande** Collaboration, Y. Ashie *et al.*, "A measurement of atmospheric neutrino oscillation parameters by Super-Kamiokande I," *Phys. Rev.* **D71** (2005) 112005, hep-ex/0501064.

[117] **Kamiokande** Collaboration, Y. Fukuda *et al.*, "Atmospheric muon-neutrino / electron-neutrino ratio in the multiGeV energy range," *Phys. Lett.* **B335** (1994) 237–245.

[118] **Kamiokande** Collaboration, S. Hatakeyama *et al.*, "Measurement of the flux and zenith angle distribution of upward through-going muons in Kamiokande II + III," *Phys. Rev. Lett.* **81** (1998) 2016–2019, `hep-ex/9806038`.

[119] **MACRO** Collaboration, M. Ambrosio *et al.*, "Atmospheric neutrino oscillations from upward throughgoing muon multiple scattering in MACRO," *Phys. Lett.* **B566** (2003) 35–44, `hep-ex/0304037`.

[120] **MACRO** Collaboration, M. Ambrosio *et al.*, "Measurements of atmospheric muon neutrino oscillations, global analysis of the data collected with MACRO detector," *Eur. Phys. J.* **C36** (2004) 323–339.

[121] **Soudan 2** Collaboration, M. C. Sanchez *et al.*, "Observation of atmospheric neutrino oscillations in Soudan 2," *Phys. Rev.* **D68** (2003) 113004, `hep-ex/0307069`.

[122] C. L. Cowan, F. Reines, F. B. Harrison, H. W. Kruse, and A. D. McGuire, "Detection of the free neutrino: A Confirmation," *Science* **124** (1956) 103–104.

[123] G. Danby *et al.*, "Observation of high-energy neutrino reactions and the existence of two kinds of neutrinos," *Phys. Rev. Lett.* **9** (1962) 36–44.

[124] K. Nishikawa *et al.*, "Proposal for a long-baseline neutrino oscillation experiment, using KEK-PS and Super-Kamiokande," 1995.

[125] P. Adamson *et al.*, "The MINOS calibration detector," *Nucl. Instrum. Meth.* **A556** (2006) 119–133.

[126] S. T. Petcov, "Towards complete neutrino mixing matrix and CP-violation," *Nucl. Phys. Proc. Suppl.* **143** (2005) 159–166, `hep-ph/0412410`.

[127] P. Minkowski, "Mu $\rightarrow$ e gamma at a rate of one out of 1-billion muon decays?," *Phys. Lett.* **B67** (1977) 421.

[128] M. Fukugita and T. Yanagida, "Baryogenesis without grand unification," *Phys. Lett.* **B174** (1986) 45.

[129] P. H. Frampton, S. T. Petcov, and W. Rodejohann, "On deviations from bimaximal neutrino mixing," *Nucl. Phys.* **B687** (2004) 31–54, `hep-ph/0401206`.

[130] A. Morales and J. Morales, "The neutrinoless double beta decay: The case for germanium detectors," *Nucl. Phys. Proc. Suppl.* **114** (2003) 141–157, `hep-ph/0211332`.

[131] C. Aalseth *et al.*, "Neutrinoless double beta decay and direct searches for neutrino mass," `hep-ph/0412300`.

[132] S. T. Petcov, "Neutrino masses, mixing, Majorana CP-violating phases and (beta beta)(0nu) decay," *New J. Phys.* **6** (2004) 109.

[133] S. T. Petcov, "Theoretical prospects of neutrinoless double beta decay," *Phys. Scripta* **T121** (2005) 94–101, hep-ph/0504166.

[134] S. Pascoli and S. T. Petcov, "Neutrino masses, mixing and (beta beta)(0nu) decay," hep-ph/0308034.

[135] S. M. Bilenky, S. Pascoli, and S. T. Petcov, "Majorana neutrinos, neutrino mass spectrum, CP-violation and neutrinoless double beta-decay. II: Mixing of four neutrinos," *Phys. Rev.* **D64** (2001) 113003, hep-ph/0104218.

[136] S. M. Bilenky, C. Giunti, W. Grimus, B. Kayser, and S. T. Petcov, "Constraints from neutrino oscillation experiments on the effective Majorana mass in neutrinoless double beta decay," *Phys. Lett.* **B465** (1999) 193–202, hep-ph/9907234.

[137] V. D. Barger and K. Whisnant, "Majorana neutrino masses from neutrinoless double beta decay and cosmology," *Phys. Lett.* **B456** (1999) 194–200, hep-ph/9904281.

[138] F. Vissani, "Signal of neutrinoless double beta decay, neutrino spectrum and oscillation scenarios," *JHEP* **06** (1999) 022, hep-ph/9906525.

[139] M. Czakon, J. Gluza, and M. Zralek, "Perspectives on finding the neutrino nature," hep-ph/0003161.

[140] H. V. Klapdor-Kleingrothaus, H. Pas, and A. Y. Smirnov, "Neutrino mass spectrum and neutrinoless double beta decay," *Phys. Rev.* **D63** (2001) 073005, hep-ph/0003219.

[141] S. Pascoli, S. T. Petcov, and L. Wolfenstein, "Searching for the CP-violation associated with Majorana neutrinos," *Phys. Lett.* **B524** (2002) 319–331, hep-ph/0110287.

[142] S. Pascoli, S. T. Petcov, and W. Rodejohann, "On the CP violation associated with Majorana neutrinos and neutrinoless double-beta decay," *Phys. Lett.* **B549** (2002) 177–193, hep-ph/0209059.

[143] S. Pascoli, S. T. Petcov, and W. Rodejohann, "On the neutrino mass spectrum and neutrinoless double-beta decay," *Phys. Lett.* **B558** (2003) 141–156, hep-ph/0212113.

[144] S. Pascoli and S. T. Petcov, "The SNO solar neutrino data, neutrinoless double beta-decay and neutrino mass spectrum. (Addendum)," *Phys. Lett.* **B580** (2004) 280–289, hep-ph/0310003.

[145] H. Murayama and C. Pena-Garay, "Neutrinoless double beta decay in light of SNO salt data," *Phys. Rev.* **D69** (2004) 031301, hep-ph/0309114.

[146] W. Rodejohann, "On cancellations in neutrinoless double beta decay," *Nucl. Phys.* **B597** (2001) 110–126, hep-ph/0008044.

[147] K. Matsuda, N. Takeda, T. Fukuyama, and H. Nishiura, "Graphical representation of CP violation effects in neutrinoless double beta decay," *Phys. Rev.* **D63** (2001) 077301, hep-ph/0007237.

[148] K. Matsuda, N. Takeda, T. Fukuyama, and H. Nishiura, "MNS parameters from neutrino oscillations, single beta decay and double beta decay," *Phys. Rev.* **D64** (2001) 013001, hep-ph/0012357.

[149] F. Feruglio, A. Strumia, and F. Vissani, "Neutrino oscillations and signals in beta and 0nu 2beta experiments," *Nucl. Phys.* **B637** (2002) 345–377, hep-ph/0201291.

[150] H. Nunokawa, W. J. C. Teves, and R. Zukanovich Funchal, "Constraining the absolute neutrino mass scale and Majorana CP violating phases by future 0nu beta beta decay experiments," *Phys. Rev.* **D66** (2002) 093010, hep-ph/0206137.

[151] S. Pascoli, S. T. Petcov, and T. Schwetz, "The absolute neutrino mass scale, neutrino mass spectrum, Majorana CP-violation and neutrinoless double-beta decay," *Nucl. Phys.* **B734** (2006) 24–49, hep-ph/0505226.

[152] S. Choubey and W. Rodejohann, "Neutrinoless double beta decay and future neutrino oscillation precision experiments," *Phys. Rev.* **D72** (2005) 033016, hep-ph/0506102.

[153] M. Lindner, A. Merle, and W. Rodejohann, "Improved limit on theta(13) and implications for neutrino masses in neutrino-less double beta decay and cosmology," *Phys. Rev.* **D73** (2006) 053005, hep-ph/0512143.

[154] V. Barger, S. L. Glashow, P. Langacker, and D. Marfatia, "No-go for detecting CP violation via neutrinoless double beta decay," *Phys. Lett.* **B540** (2002) 247–251, hep-ph/0205290.

[155] A. de Gouvea, B. Kayser, and R. N. Mohapatra, "Manifest CP violation from Majorana phases," *Phys. Rev.* **D67** (2003) 053004, hep-ph/0211394.

[156] S. Pascoli, S. T. Petcov, and C. E. Yaguna, "Quasi-degenerate neutrino mass spectrum, mu $\to$ e + gamma decay and leptogenesis," *Phys. Lett.* **B564** (2003) 241–254, hep-ph/0301095.

[157] S. T. Petcov, T. Shindou, and Y. Takanishi, "Majorana CP-violating phases, RG running of neutrino mixing parameters and charged lepton flavour violating decays," *Nucl. Phys.* **B738** (2006) 219–242, hep-ph/0508243.

[158] S. T. Petcov and T. Shindou, "Charged lepton decays l(i) $\to$ l(j) + gamma, leptogenesis CP-violating parameters and Majorana phases," *Phys. Rev.* **D74** (2006) 073006, hep-ph/0605151.

[159] L. Wolfenstein, "CP properties of Majorana neutrinos and double beta decay," *Phys. Lett.* **B107** (1981) 77.

[160] J. W. F. Valle, "Neutrinoless double-beta decay with quasi-Dirac neutrinos," *Phys. Rev.* **D27** (1983) 1672–1674.

[161] S. M. Bilenky, N. P. Nedelcheva, and S. T. Petcov, "Some implications of the CP invariance for mixing of Majorana neutrinos," *Nucl. Phys.* **B247** (1984) 61.

[162] B. Kayser, "CPT, CP, and C phases and their effects in Majorana particle processes," *Phys. Rev.* **D30** (1984) 1023.

[163] V. M. Lobashev, "The search for the neutrino mass by direct method in the tritium beta-decay and perspectives of study it in the project KATRIN," *Nucl. Phys.* **A719** (2003) 153–160.

[164] K. Eitel, "Direct neutrino mass experiments," *Nucl. Phys. Proc. Suppl.* **143** (2005) 197–204.

[165] M. Tegmark, "Cosmological neutrino bounds for non-cosmologists," *Phys. Scripta* **T121** (2005) 153–155, `hep-ph/0503257`.

[166] O. Elgaroy and O. Lahav, "Neutrino masses from cosmological probes," *New J. Phys.* **7** (2005) 61, `hep-ph/0412075`.

[167] S. Hannestad, H. Tu, and Y. Y. Y. Wong, "Measuring neutrino masses and dark energy with weak lensing tomography," *JCAP* **0606** (2006) 025, `astro-ph/0603019`.

[168] J. Lesgourgues, S. Pastor, and L. Perotto, "Probing neutrino masses with future galaxy redshift surveys," *Phys. Rev.* **D70** (2004) 045016, `hep-ph/0403296`.

[169] S. T. Petcov and A. Y. Smirnov, "Neutrinoless double beta decay and the solar neutrino problem," *Phys. Lett.* **B322** (1994) 109–118, `hep-ph/9311204`.

[170] S. Pascoli and S. T. Petcov, "Majorana Neutrinos, Neutrino Mass Spectrum and the —— 0.001 eV Frontier in Neutrinoless Double Beta Decay," *Phys. Rev.* **D77** (2008) 113003, `0711.4993`.

[171] H. V. Klapdor-Kleingrothaus, "Neutrino mass from laboratory: Contribution of double beta decay to the neutrino mass matrix," *Nucl. Phys. Proc. Suppl.* **100** (2001) 309–313, `hep-ph/0102276`.

[172] V. A. Rodin, A. Faessler, F. Simkovic, and P. Vogel, "On the uncertainty in the 0nu beta beta decay nuclear matrix elements," *Phys. Rev.* **C68** (2003) 044302, `nucl-th/0305005`.

[173] V. A. Rodin, A. Faessler, F. Simkovic, and P. Vogel, "Systematic analysis of the uncertainty in the 0nu beta beta decay nuclear matrix elements," `nucl-th/0503063`.

[174] A. Poves. Talk given at the *NDM06 International Symposium*, September 3-8, 2006, Paris.

[175] C. E. Aalseth *et al.*, "Recent results of the IGEX Ge-76 double-beta decay experiment," *Phys. Atom. Nucl.* **63** (2000) 1225–1228.

[176] H. V. Klapdor-Kleingrothaus, I. V. Krivosheina, A. Dietz, and O. Chkvorets, "Search for neutrinoless double beta decay with enriched Ge- 76 in Gran Sasso 1990-2003," *Phys. Lett.* **B586** (2004) 198–212, `hep-ph/0404088`.

[177] **the NEMO** Collaboration, R. Arnold *et al.*, "Study of 2beta-decay of Mo-100 and Se-82 using the NEMO3 detector," *JETP Lett.* **80** (2004) 377–381, hep-ex/0410021.

[178] **CUORE** Collaboration, S. Capelli *et al.*, "CUORICINO last results and CUORE R&D," hep-ex/0505045.

[179] F. T. Avignone, "Strategies for next generation neutrinoless double-beta decay experiments," *Nucl. Phys. Proc. Suppl.* **143** (2005) 233–239.

[180] A. Bandyopadhyay *et al.* unpublished.

[181] S. M. Bilenky and S. T. Petcov, "Nuclear matrix elements of 0nu beta beta-decay: Possible test of the calculations," hep-ph/0405237.

[182] A. Blondel *et al.*, "Future neutrino oscillation facilities," *Acta Phys. Polon.* **B37** (2006) 2077–2113, hep-ph/0606111.

[183] P. Vogel, "Double beta decay: Theory, experiment, and implications," nucl-th/0005020.

[184] S. R. Elliott and P. Vogel, "Double beta decay," *Ann. Rev. Nucl. Part. Sci.* **52** (2002) 115–151, hep-ph/0202264.

[185] **KATRIN** Collaboration, A. Osipowicz *et al.*, "KATRIN: A next generation tritium beta decay experiment with sub-eV sensitivity for the electron neutrino mass," hep-ex/0109033.

[186] S. M. Bilenky, C. Giunti, J. A. Grifols, and E. Masso, "Absolute values of neutrino masses: Status and prospects," *Phys. Rept.* **379** (2003) 69–148, hep-ph/0211462.

[187] A. D. Dolgov, "Neutrinos in cosmology," *Phys. Rept.* **370** (2002) 333–535, hep-ph/0202122.

[188] **LSND** Collaboration, A. Aguilar *et al.*, "Evidence for neutrino oscillations from the observation of anti-nu/e appearance in a anti-nu/mu beam," *Phys. Rev.* **D64** (2001) 112007, hep-ex/0104049.

[189] F. Arneodo *et al.*, "ICARUS: An innovative detector for underground physics," *Nucl. Instrum. Meth.* **A461** (2001) 324–326.

[190] M. Komatsu, P. Migliozzi, and F. Terranova, "Sensitivity to Theta(13) of the CERN to Gran Sasso neutrino beam," *J. Phys.* **G29** (2003) 443, hep-ph/0210043.

[191] P. Migliozzi and F. Terranova, "Next generation long baseline experiments on the path to leptonic CP violation," *Phys. Lett.* **B563** (2003) 73–82, hep-ph/0302274.

[192] **MINOS** Collaboration, E. Ables *et al.*, "P-875: A Long baseline neutrino oscillation experiment at Fermilab." FERMILAB-PROPOSAL-0875.

[193] G. Acquistapace *et al.*, "The CERN neutrino beam to Gran Sasso (NGS): Conceptual technical design." CERN-98-02.

[194] A. Guglielmi, M. Mezzetto, P. Migliozzi, and F. Terranova, "Measurement of three-family neutrino mixing and search for CP violation," hep-ph/0508034.

[195] O. Yasuda, "Parameter degeneracy and reactor experiments," hep-ph/0305295.

[196] F. Ardellier *et al.*, "Letter of intent for Double-CHOOZ: A search for the mixing angle theta(13)," hep-ex/0405032.

[197] **Double Chooz** Collaboration, F. Ardellier *et al.*, "Double Chooz: A search for the neutrino mixing angle theta(13)," hep-ex/0606025.

[198] M. Aoki *et al.*, "Letter of intent for KASKA: High accuracy neutrino oscillation measurements with anti-nu/es from Kashiwazaki- Kariwa nuclear power station," hep-ex/0607013.

[199] A. Donini, D. Meloni, and S. Rigolin, "Clone flow analysis for a theory inspired neutrino experiment planning," *JHEP* **06** (2004) 011, hep-ph/0312072.

[200] H. Minakata and H. Nunokawa, "Exploring neutrino mixing with low energy superbeams," *JHEP* **10** (2001) 001, hep-ph/0108085.

[201] H. Minakata, H. Nunokawa, and S. J. Parke, "CP and T trajectory diagrams for a unified graphical representation of neutrino oscillations," *Phys. Lett.* **B537** (2002) 249–255, hep-ph/0204171.

[202] H. Minakata, H. Nunokawa, and S. J. Parke, "Parameter degeneracies in neutrino oscillation measurement of leptonic CP and T violation," *Phys. Rev.* **D66** (2002) 093012, hep-ph/0208163.

[203] H. Minakata, H. Sugiyama, O. Yasuda, K. Inoue, and F. Suekane, "Reactor measurement of Theta(13) and its complementarity to long-baseline experiments," *Phys. Rev.* **D68** (2003) 033017, hep-ph/0211111.

[204] C. N. Leung and Y. Y. Y. Wong, "T-violation in flavour oscillations as a test for relativity principles at a neutrino factory," *Phys. Rev.* **D67** (2003) 056005, hep-ph/0301211.

[205] J. Burguet-Castell, M. B. Gavela, J. J. Gomez-Cadenas, P. Hernandez, and O. Mena, "On the measurement of leptonic CP violation," *Nucl. Phys.* **B608** (2001) 301–318, hep-ph/0103258.

[206] A. Cervera *et al.*, "Golden measurements at a neutrino factory," *Nucl. Phys.* **B579** (2000) 17–55, hep-ph/0002108.

[207] S. Rigolin, "Physics reach of beta-beams and nu-factories: The problem of degeneracies," *Nucl. Phys. Proc. Suppl.* **155** (2006) 33–37, hep-ph/0509366.

[208] P. Huber, M. Lindner, M. Rolinec, and W. Winter, "Optimization of a neutrino factory oscillation experiment," *Phys. Rev.* **D74** (2006) 073003, hep-ph/0606119.

[209] A. Donini and E. Fernandez-Martinez, "Alternating ions in a beta-beam to solve degeneracies," *Phys. Lett.* **B641** (2006) 432–439, hep-ph/0603261.

[210] A. Rubbia, "Neutrino factories: Detector concepts for studies of CP and T violation effects in neutrino oscillations," hep-ph/0106088.

[211] G. L. Fogli and E. Lisi, "Tests of three-flavor mixing in long-baseline neutrino oscillation experiments," *Phys. Rev.* **D54** (1996) 3667–3670, hep-ph/9604415.

[212] V. Barger, D. Marfatia, and K. Whisnant, "Breaking eight-fold degeneracies in neutrino CP violation, mixing, and mass hierarchy," *Phys. Rev.* **D65** (2002) 073023, hep-ph/0112119.

[213] E. K. Akhmedov, R. Johansson, M. Lindner, T. Ohlsson, and T. Schwetz, "Series expansions for three-flavor neutrino oscillation probabilities in matter," *JHEP* **04** (2004) 078, hep-ph/0402175.

[214] A. Donini, E. Fernandez-Martinez, P. Migliozzi, S. Rigolin, and L. Scotto Lavina, "Study of the eightfold degeneracy with a standard beta-beam and a super-beam facility," *Nucl. Phys.* **B710** (2005) 402–424, hep-ph/0406132.

[215] D. A. Petyt, "A Study of parameter measurement in a long baseline neutrino oscillation experiment." FERMILAB-THESIS-1998-66.

[216] H. Minakata, M. Sonoyama, and H. Sugiyama, "Determination of theta(23) in long-baseline neutrino oscillation experiments with three-flavor mixing effects," *Phys. Rev.* **D70** (2004) 113012, hep-ph/0406073.

[217] A. Donini, E. Fernandez-Martinez, and S. Rigolin, "Appearance and disappearance signals at a beta-beam and a super-beam facility," *Phys. Lett.* **B621** (2005) 276–287, hep-ph/0411402.

[218] A. Donini, E. Fernandez-Martinez, D. Meloni, and S. Rigolin, "nu/mu disappearance at the SPL, T2K-I, NOnuA and the neutrino factory," *Nucl. Phys.* **B743** (2006) 41–73, hep-ph/0512038.

[219] G. L. Fogli, E. Lisi, and A. Palazzo, "Quasiaveraged solar neutrino oscillations," *Phys. Rev.* **D65** (2002) 073019, hep-ph/0105080.

[220] A. Donini, D. Meloni, and S. Rigolin, "The impact of solar and atmospheric parameter uncertainties on the measurement of theta(13) and delta," *Eur. Phys. J.* **C45** (2006) 73–95, hep-ph/0506100.

[221] C. D. Froggatt and H. B. Nielsen, "Hierarchy of Quark Masses, Cabibbo Angles and CP Violation," *Nucl. Phys.* **B147** (1979) 277.

[222] M. Gell-Mann, P. Ramond, and R. Slansky, "Complex spinors and unified theories." Print-80-0576 (CERN).

[223] T. Yanagida, "Horizontal gauge symmetry and masses of neutrinos." In Proceedings of the Workshop on the Baryon Number of the Universe and Unified Theories, Tsukuba, Japan, 13-14 Feb 1979.

[224] M. Magg and C. Wetterich, "Neutrino mass problem and gauge hierarchy," *Phys. Lett.* **B94** (1980) 61.

[225] G. Lazarides, Q. Shafi, and C. Wetterich, "Proton lifetime and fermion masses in an SO(10) model," *Nucl. Phys.* **B181** (1981) 287.

[226] R. N. Mohapatra and G. Senjanovic, "Neutrino masses and mixings in gauge models with spontaneous parity violation," *Phys. Rev.* **D23** (1981) 165.

[227] C. Wetterich, "Neutrino masses and the scale of B-L violation," *Nucl. Phys.* **B187** (1981) 343.

[228] H. K. Dreiner, "An introduction to explicit R-parity violation," `hep-ph/9707435`.

[229] L. J. Hall and M. Suzuki, "Explicit R-Parity Breaking in Supersymmetric Models," *Nucl. Phys.* **B231** (1984) 419.

[230] R. Barbier *et al.*, "R-parity violating supersymmetry," *Phys. Rept.* **420** (2005) 1–202, `hep-ph/0406039`.

[231] **Particle Data Group** Collaboration, W. M. Yao *et al.*, "Review of particle physics," *J. Phys.* **G33** (2006) 1–1232.

[232] P. Nath and P. Fileviez Perez, "Proton stability in grand unified theories, in strings, and in branes," *Phys. Rept.* **441** (2007) 191–317, `hep-ph/0601023`.

[233] M. Nowakowski and A. Pilaftsis, "W and Z boson interactions in supersymmetric models with explicit R-parity violation," *Nucl. Phys.* **B461** (1996) 19–49, `hep-ph/9508271`.

[234] D. J. H. Chung *et al.*, "The soft supersymmetry-breaking Lagrangian: Theory and applications," *Phys. Rept.* **407** (2005) 1–203, `hep-ph/0312378`.

[235] M. A. Diaz, "R-parity breaking in minimal supergravity," `hep-ph/9712213`.

[236] M. Hirsch, M. A. Diaz, W. Porod, J. C. Romao, and J. W. F. Valle, "Neutrino masses and mixings from supersymmetry with bilinear R-parity violation: A theory for solar and atmospheric neutrino oscillations," *Phys. Rev.* **D62** (2000) 113008, `hep-ph/0004115`.

[237] G. Passarino and M. J. G. Veltman, "One Loop Corrections for e+ e- Annihilation Into mu+ mu- in the Weinberg Model," *Nucl. Phys.* **B160** (1979) 151.

[238] M. A. Diaz, M. Hirsch, W. Porod, J. C. Romao, and J. W. F. Valle, "Solar neutrino masses and mixing from bilinear R-parity broken supersymmetry: Analytical versus numerical results," *Phys. Rev.* **D68** (2003) 013009, `hep-ph/0302021`.

[239] A. Faessler, S. Kovalenko, and F. Simkovic, "Bilinear R-parity Violation in Neutrinoless Double Beta Decay," *Phys. Rev.* **D58** (1998) 055004, hep-ph/9712535.

[240] Y. Grossman and H. E. Haber, "Sneutrino mixing phenomena," *Phys. Rev. Lett.* **78** (1997) 3438–3441, hep-ph/9702421.

[241] M. A. Diaz, J. C. Romao, and J. W. F. Valle, "Minimal supergravity with R-parity breaking," *Nucl. Phys.* **B524** (1998) 23–40, hep-ph/9706315.

[242] M. A. Diaz, C. Mora, and A. R. Zerwekh, "Study of a neutrino mass texture generated in supergravity with bilinear R-parity violation," *Eur. Phys. J.* **C44** (2005) 277–286, hep-ph/0410285.

[243] M. Hirsch and W. Porod, "Neutrino properties and the decay of the lightest supersymmetric particle," *Phys. Rev.* **D68** (2003) 115007, hep-ph/0307364.

[244] F. de Campos *et al.*, "Neutrinos in anomaly mediated supersymmetry breaking with R-parity violation," *Phys. Rev.* **D71** (2005) 055008, hep-ph/0409043.

[245] F. De Campos, M. A. Diaz, O. J. P. Eboli, M. B. Magro, and P. G. Mercadante, "Anomaly mediated supersymmetry breaking without R-parity," *Nucl. Phys.* **B623** (2002) 47–72, hep-ph/0110049.

[246] E. J. Chun, "Axino-neutrino mixing in gauge-mediated supersymmetry breaking models," *Phys. Lett.* **B454** (1999) 304–308, hep-ph/9901220.

[247] E. J. Chun and S. C. Park, "Neutrino mass from R-parity violation in split supersymmetry," *JHEP* **01** (2005) 009, hep-ph/0410242.

[248] A. Abada and M. Losada, "Constraints on a general 3-generation neutrino mass matrix from neutrino data: Application to the MSSM with R-parity violation," *Nucl. Phys.* **B585** (2000) 45–78, hep-ph/9908352.

[249] D. Aristizabal Sierra, M. Hirsch, and W. Porod, "R-parity violating sneutrino decays," *JHEP* **09** (2005) 033, hep-ph/0409241.

[250] S. Weinberg, "Varieties of baryon and lepton nonconservation," *Phys. Rev.* **D22** (1980) 1694.

[251] J. W. F. Valle, "Neutrino physics overview," *J. Phys. Conf. Ser.* **53** (2006) 473–505, hep-ph/0608101.

[252] J. Schechter and J. W. F. Valle, "Neutrino decay and spontaneous violation of lepton number," *Phys. Rev.* **D25** (1982) 774.

[253] N. Arkani-Hamed, S. Dimopoulos, and G. R. Dvali, "The hierarchy problem and new dimensions at a millimeter," *Phys. Lett.* **B429** (1998) 263–272, hep-ph/9803315.

[254] I. Antoniadis, N. Arkani-Hamed, S. Dimopoulos, and G. R. Dvali, "New dimensions at a millimeter to a Fermi and superstrings at a TeV," *Phys. Lett.* **B436** (1998) 257–263, hep-ph/9804398.

[255] I. Antoniadis, "A Possible new dimension at a few TeV," *Phys. Lett.* **B246** (1990) 377–384.

[256] I. Antoniadis and K. Benakli, "Limits on extra dimensions in orbifold compactifications of superstrings," *Phys. Lett.* **B326** (1994) 69–78, hep-th/9310151.

[257] J. D. Lykken, "Weak Scale Superstrings," *Phys. Rev.* **D54** (1996) 3693–3697, hep-th/9603133.

[258] K. R. Dienes, E. Dudas, and T. Gherghetta, "Light neutrinos without heavy mass scales: A higher- dimensional seesaw mechanism," *Nucl. Phys.* **B557** (1999) 25, hep-ph/9811428.

[259] N. Arkani-Hamed, S. Dimopoulos, G. R. Dvali, and J. March-Russell, "Neutrino masses from large extra dimensions," *Phys. Rev.* **D65** (2002) 024032, hep-ph/9811448.

[260] A. E. Faraggi and M. Pospelov, "Phenomenological issues in TeV scale gravity with light neutrino masses," *Phys. Lett.* **B458** (1999) 237–244, hep-ph/9901299.

[261] G. R. Dvali and A. Y. Smirnov, "Probing large extra dimensions with neutrinos," *Nucl. Phys.* **B563** (1999) 63–81, hep-ph/9904211.

[262] R. N. Mohapatra, S. Nandi, and A. Perez-Lorenzana, "Neutrino masses and oscillations in models with large extra dimensions," *Phys. Lett.* **B466** (1999) 115–121, hep-ph/9907520.

[263] R. Barbieri, P. Creminelli, and A. Strumia, "Neutrino oscillations from large extra dimensions," *Nucl. Phys.* **B585** (2000) 28–44, hep-ph/0002199.

[264] A. Ioannisian and J. W. F. Valle, "Brane-inspired four-neutrino models," *Phys. Rev.* **D63** (2001) 073002, hep-ph/9911349.

[265] S. Weinberg, "Causality, anti-particles and the spin statistics connection in higher dimensions," *Phys. Lett.* **B143** (1984) 97.

[266] K. Shimizu, "C, P and T transformations in higher dimensions," *Prog. Theor. Phys.* **74** (1985) 610.

[267] C. Wetterich, "Discrete symmetries in Kaluza-Klein theories," *Nucl. Phys.* **B234** (1984) 413.

[268] R. Finkelstein and M. Villasante, "Majorana spinors in higher dimensional theories," *Phys. Rev.* **D31** (1985) 425.

[269] L. E. Ibanez, F. Marchesano, and R. Rabadan, "Getting just the Standard Model at intersecting branes," *JHEP* **11** (2001) 002, hep-th/0105155.

[270] I. Antoniadis, E. Kiritsis, J. Rizos, and T. N. Tomaras, "D-branes and the Standard Model," *Nucl. Phys.* **B660** (2003) 81–115, hep-th/0210263.

[271] A. Sagnotti, "A Note on the Green-Schwarz mechanism in open string theories," *Phys. Lett.* **B294** (1992) 196–203, hep-th/9210127.

[272] L. E. Ibanez, R. Rabadan, and A. M. Uranga, "Anomalous U(1)'s in type I and type IIB D = 4, N = 1 string vacua," *Nucl. Phys.* **B542** (1999) 112–138, hep-th/9808139.

[273] E. Poppitz, "On the one loop Fayet-Iliopoulos term in chiral four dimensional type I orbifolds," *Nucl. Phys.* **B542** (1999) 31–44, hep-th/9810010.

[274] I. Antoniadis, E. Kiritsis, and J. Rizos, "Anomalous U(1)s in type I superstring vacua," *Nucl. Phys.* **B637** (2002) 92–118, hep-th/0204153.

[275] C. D. Hoyle *et al.*, "Sub-millimeter tests of the gravitational inverse-square law," *Phys. Rev.* **D70** (2004) 042004, hep-ph/0405262.

[276] J. C. Long and J. C. Price, "Current short-range tests of the gravitational inverse square law," *Comptes Rendus Physique* **4** (2003) 337–346, hep-ph/0303057.

[277] R. S. Decca *et al.*, "Constraining new forces in the Casimir regime using the isoelectronic technique," *Phys. Rev. Lett.* **94** (2005) 240401, hep-ph/0502025.

[278] S. J. Smullin *et al.*, "New constraints on Yukawa-type deviations from Newtonian gravity at 20-microns," *Phys. Rev.* **D72** (2005) 122001, hep-ph/0508204.

[279] G. Altarelli and F. Feruglio, "Theoretical models of neutrino masses and mixings," *Springer Tracts Mod. Phys.* **190** (2003) 169–207, hep-ph/0206077.

[280] I. Antoniadis and C. Bachas, "Branes and the gauge hierarchy," *Phys. Lett.* **B450** (1999) 83–91, hep-th/9812093.

[281] H. Davoudiasl, P. Langacker, and M. Perelstein, "Constraints on large extra dimensions from neutrino oscillation experiments," *Phys. Rev.* **D65** (2002) 105015, hep-ph/0201128.

[282] P. Langacker, "TeV physics from the top down," hep-ph/0308033.

[283] M. Dine, V. Kaplunovsky, M. L. Mangano, C. Nappi, and N. Seiberg, "Superstring model building," *Nucl. Phys.* **B259** (1985) 549–571.

[284] J. D. Breit, B. A. Ovrut, and G. C. Segre, "E(6) symmetry breaking in the superstring theory," *Phys. Lett.* **B158** (1985) 33.

[285] E. Witten, "New issues in manifolds of SU(3) holonomy," *Nucl. Phys.* **B268** (1986) 79.

[286] A. Font, L. E. Ibanez, F. Quevedo, and A. Sierra, "The construction of 'realistic' four-dimensional strings through orbifolds," *Nucl. Phys.* **B331** (1990) 421–474.

[287] D. Mochinaga, "Particle contents in the Calabi-Yau superstring model with the solar neutrino problem," *Phys. Lett.* **B312** (1993) 405–410.

[288] S. Nandi and U. Sarkar, "A solution to the neutrino mass problem in superstring E6 theory," *Phys. Rev. Lett.* **56** (1986) 564.

[289] R. N. Mohapatra and J. W. F. Valle, "Neutrino mass and baryon-number nonconservation in superstring models," *Phys. Rev.* **D34** (1986) 1642.

[290] G. Cleaver, M. Cvetic, J. R. Espinosa, L. L. Everett, and P. Langacker, "Intermediate scales, mu parameter, and fermion masses from string models," *Phys. Rev.* **D57** (1998) 2701–2715, `hep-ph/9705391`.

[291] P. Langacker, "A mechanism for ordinary-sterile neutrino mixing," *Phys. Rev.* **D58** (1998) 093017, `hep-ph/9805281`.

[292] M. Cvetic and P. Langacker, "Neutrino masses within the minimal supersymmetric standard model," *Phys. Rev.* **D46** (1992) 2759–2763, `hep-th/9205029`.

[293] N. Haba, C. Hattori, M. Matsuda, T. Matsuoka, and D. Mochinaga, "A Large Majorana mass from Calabi-Yau superstring models," *Phys. Lett.* **B337** (1994) 63–68, `hep-ph/9311298`.

[294] N. Haba, C. Hattori, M. Matsuda, T. Matsuoka, and D. Mochinaga, "How can we obtain a large Majorana mass in Calabi-Yau models?," *Prog. Theor. Phys.* **92** (1994) 153–174, `hep-ph/9401332`.

[295] A. E. Faraggi and E. Halyo, "Neutrino masses in superstring derived standard - like models," *Phys. Lett.* **B307** (1993) 311–317, `hep-th/9303060`.

[296] R. Blumenhagen, M. Cvetic, P. Langacker, and G. Shiu, "Toward realistic intersecting D-brane models," *Ann. Rev. Nucl. Part. Sci.* **55** (2005) 71–139, `hep-th/0502005`.

[297] C. Coriano and A. E. Faraggi, "String inspired neutrino mass textures in light of KamLAND and WMAP," *Phys. Lett.* **B581** (2004) 99–110, `hep-ph/0306186`.

[298] J. R. Ellis, G. K. Leontaris, S. Lola, and D. V. Nanopoulos, "Fermion mass textures in an M-inspired flipped SU(5) model derived from string," *Phys. Lett.* **B425** (1998) 86–96, `hep-ph/9711476`.

[299] J. R. Ellis, G. K. Leontaris, S. Lola, and D. V. Nanopoulos, "Neutrino textures in the light of Super-Kamiokande data and a realistic string model," *Eur. Phys. J.* **C9** (1999) 389–408, `hep-ph/9808251`.

[300] J. E. Kim, "Trinification with sin**2(theta(W)) = 3/8 and seesaw neutrino mass," *Phys. Lett.* **B591** (2004) 119–126, `hep-ph/0403196`.

[301] T. Kobayashi, S. Raby, and R.-J. Zhang, "Searching for realistic 4d string models with a Pati-Salam symmetry: Orbifold grand unified theories from heterotic string compactification on a Z(6) orbifold," *Nucl. Phys.* **B704** (2005) 3–55, hep-ph/0409098.

[302] J. Giedt, G. L. Kane, P. Langacker, and B. D. Nelson, "Massive neutrinos and (heterotic) string theory," *Phys. Rev.* **D71** (2005) 115013, hep-th/0502032.

[303] L. E. Ibanez, C. Munoz, and S. Rigolin, "Aspects of type I string phenomenology," *Nucl. Phys.* **B553** (1999) 43–80, hep-ph/9812397.

[304] S. Antusch, O. J. Eyton-Williams, and S. F. King, "Dirac neutrinos and hybrid inflation from string theory," *JHEP* **08** (2005) 103, hep-ph/0505140.

[305] P. Langacker and B. D. Nelson, "String-inspired triplet see-saw from diagonal embedding of SU(2)L in SU(2)A x SU(2)B," *Phys. Rev.* **D72** (2005) 053013, hep-ph/0507063.

[306] R. N. Mohapatra *et al.*, "Theory of neutrinos: A white paper," *Rept. Prog. Phys.* **70** (2007) 1757–1867, hep-ph/0510213.

[307] M. Cvetic and P. Langacker, "New grand unified models with intersecting D6-branes, neutrino masses, and flipped SU(5)," *Nucl. Phys.* **B776** (2007) 118–137, hep-th/0607238.

[308] R. N. Mohapatra and G. Senjanovic, "Neutrino mass and spontaneous parity nonconservation," *Phys. Rev. Lett.* **44** (1980) 912.

[309] G. B. Gelmini and M. Roncadelli, "Left-Handed Neutrino Mass Scale and Spontaneously Broken Lepton Number," *Phys. Lett.* **B99** (1981) 411.

[310] A. Zee, "A Theory of Lepton Number Violation, Neutrino Majorana Mass, and Oscillation," *Phys. Lett.* **B93** (1980) 389.

[311] K. S. Babu, "Model of 'Calculable' Majorana Neutrino Masses," *Phys. Lett.* **B203** (1988) 132.

[312] S. T. Petcov, "Remarks on the Zee model of neutrino mixing (mu → e gamma, heavy neutrino → light neutrino gamma, etc.)," *Phys. Lett.* **B115** (1982) 401–406.

[313] J. C. Pati and A. Salam, "Lepton number as the fourth color," *Phys. Rev.* **D10** (1974) 275–289.

[314] N. G. Deshpande, J. F. Gunion, B. Kayser, and F. I. Olness, "Left-right symmetric electroweak models with triplet Higgs," *Phys. Rev.* **D44** (1991) 837–858.

[315] V. Cirigliano, A. Kurylov, M. J. Ramsey-Musolf, and P. Vogel, "Lepton flavor violation without supersymmetry," *Phys. Rev.* **D70** (2004) 075007, hep-ph/0404233.

[316] T. P. Cheng and L.-F. Li, "Neutrino Masses, Mixings and Oscillations in SU(2) x U(1) Models of Electroweak Interactions," *Phys. Rev.* **D22** (1980) 2860.

[317] E. J. Chun, K. Y. Lee, and S. C. Park, "Testing Higgs triplet model and neutrino mass patterns," *Phys. Lett.* **B566** (2003) 142–151, hep-ph/0304069.

[318] A. G. Akeroyd and M. Aoki, "Single and pair production of doubly charged Higgs bosons at hadron colliders," *Phys. Rev.* **D72** (2005) 035011, hep-ph/0506176.

[319] K. R. S. Balaji, W. Grimus, and T. Schwetz, "The solar LMA neutrino oscillation solution in the Zee model," *Phys. Lett.* **B508** (2001) 301–310, hep-ph/0104035.

[320] C. H. Albright and M.-C. Chen, "Model predictions for neutrino oscillation parameters," *Phys. Rev.* **D74** (2006) 113006, hep-ph/0608137.

[321] R. N. Mohapatra, "theta(13) as a probe of mu $\leftrightarrow$ tau symmetry for leptons," *JHEP* **10** (2004) 027, hep-ph/0408187.

[322] S. T. Petcov, "On pseudodirac neutrinos, neutrino oscillations and neutrinoless double beta decay," *Phys. Lett.* **B110** (1982) 245–249.

[323] J. Schechter and J. W. F. Valle, "Majorana neutrinos and magnetic fields," *Phys. Rev.* **D24** (1981) 1883–1889. Err. D25, 283 (1982).

[324] S. F. King, "Atmospheric and solar neutrinos from single right-handed neutrino dominance and U(1) family symmetry," *Nucl. Phys.* **B562** (1999) 57–77, hep-ph/9904210.

[325] S. Antusch and S. F. King, "Sequential dominance," *New J. Phys.* **6** (2004) 110, hep-ph/0405272.

[326] M.-C. Chen and K. T. Mahanthappa, "Fermion masses and mixing and CP-violation in SO(10) models with family symmetries," *Int. J. Mod. Phys.* **A18** (2003) 5819–5888, hep-ph/0305088.

[327] M.-C. Chen and K. T. Mahanthappa, "From CKM matrix to MNS matrix: A model based on supersymmetric SO(10) x U(2)F symmetry," *Phys. Rev.* **D62** (2000) 113007, hep-ph/0005292.

[328] C. H. Albright and S. M. Barr, "Realization of the large mixing angle solar neutrino solution in an SO(10) supersymmetric grand unified model," *Phys. Rev.* **D64** (2001) 073010, hep-ph/0104294.

[329] R. N. Mohapatra, M. K. Parida, and G. Rajasekaran, "High scale mixing unification and large neutrino mixing angles," *Phys. Rev.* **D69** (2004) 053007, hep-ph/0301234.

[330] S. F. King, "Predicting neutrino parameters from SO(3) family symmetry and quark-lepton unification," *JHEP* **08** (2005) 105, hep-ph/0506297.

[331] S. Antusch and S. F. King, "Charged lepton corrections to neutrino mixing angles and CP phases revisited," *Phys. Lett.* **B631** (2005) 42–47, hep-ph/0508044.

[332] I. Masina, "A maximal atmospheric mixing from a maximal CP violating phase," *Phys. Lett.* **B633** (2006) 134–140, hep-ph/0508031.

[333] V. D. Barger, S. Pakvasa, T. J. Weiler, and K. Whisnant, "Bi-maximal mixing of three neutrinos," *Phys. Lett.* **B437** (1998) 107–116, hep-ph/9806387.

[334] P. F. Harrison, D. H. Perkins, and W. G. Scott, "Tri-bimaximal mixing and the neutrino oscillation data," *Phys. Lett.* **B530** (2002) 167, hep-ph/0202074.

[335] L. Wolfenstein, "Oscillations among three neutrino types and CP violation," *Phys. Rev.* **D18** (1978) 958–960.

[336] S. F. King and G. G. Ross, "Fermion masses and mixing angles from SU(3) family symmetry and unification," *Phys. Lett.* **B574** (2003) 239–252, hep-ph/0307190.

[337] I. de Medeiros Varzielas and G. G. Ross, "SU(3) family symmetry and neutrino bi-tri-maximal mixing," *Nucl. Phys.* **B733** (2006) 31–47, hep-ph/0507176.

[338] S. Antusch, P. Huber, S. F. King, and T. Schwetz, "Neutrino mixing sum rules and oscillation experiments," *JHEP* **04** (2007) 060, hep-ph/0702286.

[339] S. T. Petcov and T. Schwetz, "Precision measurement of solar neutrino oscillation parameters by a long-baseline reactor neutrino experiment in Europe," *Phys. Lett.* **B642** (2006) 487–494, hep-ph/0607155.

[340] P. Huber, M. Lindner, and W. Winter, "Superbeams versus neutrino factories," *Nucl. Phys.* **B645** (2002) 3–48, hep-ph/0204352.

[341] J. Burguet-Castell, D. Casper, E. Couce, J. J. Gomez-Cadenas, and P. Hernandez, "Optimal beta-beam at the CERN-SPS," *Nucl. Phys.* **B725** (2005) 306–326, hep-ph/0503021.

[342] A. Datta, L. Everett, and P. Ramond, "Cabibbo haze in lepton mixing," *Phys. Lett.* **B620** (2005) 42–51, hep-ph/0503222.

[343] L. L. Everett, "Viewing lepton mixing through the Cabibbo haze," *Phys. Rev.* **D73** (2006) 013011, hep-ph/0510256.

[344] L. Wolfenstein, "Parametrization of the Kobayashi-Maskawa matrix," *Phys. Rev. Lett.* **51** (1983) 1945.

[345] P. Ramond, "Neutrinos: Windows to Planck physics," hep-ph/0401001.

[346] P. Ramond, "Chasing CHOOZ," *Int. J. Mod. Phys.* **A20** (2005) 1234–1243, hep-ph/0405176.

[347] P. Ramond, "Neutrinos: Key to new physics," *Nucl. Phys. Proc. Suppl.* **137** (2004) 317–324, hep-ph/0411009.

[348] P. Ramond, "Seesaw and the riddle of mass," hep-ph/0411010.

[349] Y. Kuno and Y. Okada, "Muon decay and physics beyond the Standard Model," *Rev. Mod. Phys.* **73** (2001) 151–202, hep-ph/9909265.

[350] **MEGA** Collaboration, M. L. Brooks *et al.*, "New limit for the family-number non-conserving decay mu+ → e+ gamma," *Phys. Rev. Lett.* **83** (1999) 1521–1524, hep-ex/9905013.

[351] **SINDRUM** Collaboration, U. Bellgardt *et al.*, "Search for the Decay mu+ → e+ e+ e-," *Nucl. Phys.* **B299** (1988) 1.

[352] W. Bertl *et al.*, "Search for muon - electron conversion on gold," *Eur. Phys. J.* **C47** (2006) 337–346.

[353] **Belle** Collaboration, K. Hayasaka *et al.*, "New search for tau → mu gamma and tau → e gamma decays at Belle," *Phys. Lett.* **B666** (2008) 16–22, 0705.0650.

[354] **BELLE** Collaboration, Y. Miyazaki *et al.*, "Search for lepton flavor violating tau- decays into l- eta, l- eta' and l- pi0," *Phys. Lett.* **B648** (2007) 341–350, hep-ex/0703009.

[355] **BELLE** Collaboration, Y. Miyazaki *et al.*, "Search for lepton flavor violating tau- decays with a K0(S) meson," *Phys. Lett.* **B639** (2006) 159–164, hep-ex/0605025.

[356] **Belle** Collaboration, Y. Yusa *et al.*, "Search for neutrinoless decays tau → 3l," *Phys. Lett.* **B589** (2004) 103–110, hep-ex/0403039.

[357] **BABAR** Collaboration, B. Aubert *et al.*, "Search for lepton flavor violating decays tau+- → l+- pi0, l+- eta, l+- eta'," *Phys. Rev. Lett.* **98** (2007) 061803, hep-ex/0610067.

[358] **BABAR** Collaboration, B. Aubert *et al.*, "Search for lepton flavor violation in the decay $\tau^{\pm} \to e^{\pm}\gamma$," *Phys. Rev. Lett.* **96** (2006) 041801, hep-ex/0508012.

[359] **BaBar** Collaboration, B. Aubert *et al.*, "Search for lepton-flavor and lepton-number violation in the decay $\tau^- \to \ell^{\mp} h^{\pm} h'^-$," *Phys. Rev. Lett.* **95** (2005) 191801, hep-ex/0506066.

[360] **BABAR** Collaboration, B. Aubert *et al.*, "Search for lepton flavor violation in the decay $\tau \to \mu\gamma$," *Phys. Rev. Lett.* **95** (2005) 041802, hep-ex/0502032.

[361] **BABAR** Collaboration, B. Aubert *et al.*, "Search for lepton flavor violation in the decay $\tau^- \to \ell^-\ell^+\ell^-$," *Phys. Rev. Lett.* **92** (2004) 121801, hep-ex/0312027.

[362] Y. Okada, K.-i. Okumura, and Y. Shimizu, "mu → e gamma and mu → 3e processes with polarized muons and supersymmetric grand unified theories," *Phys. Rev.* **D61** (2000) 094001, hep-ph/9906446.

[363] R. Kitano, M. Koike, and Y. Okada, "Detailed calculation of lepton flavor violating muon electron conversion rate for various nuclei," *Phys. Rev.* **D66** (2002) 096002, hep-ph/0203110.

[364] L. J. Hall, V. A. Kostelecky, and S. Raby, "New flavor violations in supergravity models," *Nucl. Phys.* **B267** (1986) 415.

[365] F. Borzumati and A. Masiero, "Large muon and electron number violations in supergravity theories," *Phys. Rev. Lett.* **57** (1986) 961.

[366] R. Barbieri and L. J. Hall, "Signals for supersymmetric unification," *Phys. Lett.* **B338** (1994) 212–218, hep-ph/9408406.

[367] R. Barbieri, L. J. Hall, and A. Strumia, "Violations of lepton flavor and CP in supersymmetric unified theories," *Nucl. Phys.* **B445** (1995) 219–251, hep-ph/9501334.

[368] J. Hisano, T. Moroi, K. Tobe, M. Yamaguchi, and T. Yanagida, "Lepton flavor violation in the supersymmetric standard model with seesaw induced neutrino masses," *Phys. Lett.* **B357** (1995) 579–587, hep-ph/9501407.

[369] J. Hisano, T. Moroi, K. Tobe, and M. Yamaguchi, "Lepton-Flavor Violation via Right-Handed Neutrino Yukawa Couplings in Supersymmetric Standard Model," *Phys. Rev.* **D53** (1996) 2442–2459, hep-ph/9510309.

[370] J. Hisano and D. Nomura, "Solar and atmospheric neutrino oscillations and lepton flavor violation in supersymmetric models with the right- handed neutrinos," *Phys. Rev.* **D59** (1999) 116005, hep-ph/9810479.

[371] K. S. Babu and C. Kolda, "Higgs-mediated tau $\rightarrow$ 3mu in the supersymmetric seesaw model," *Phys. Rev. Lett.* **89** (2002) 241802, hep-ph/0206310.

[372] M. Sher, "tau $\rightarrow$ mu eta in supersymmetric models," *Phys. Rev.* **D66** (2002) 057301, hep-ph/0207136.

[373] A. Dedes, J. R. Ellis, and M. Raidal, "Higgs mediated B/(s,d)0 $\rightarrow$ mu tau, e tau and tau $\rightarrow$ 3mu, e mu mu decays in supersymmetric seesaw models," *Phys. Lett.* **B549** (2002) 159–169, hep-ph/0209207.

[374] R. Kitano, M. Koike, S. Komine, and Y. Okada, "Higgs-mediated muon electron conversion process in supersymmetric seesaw model," *Phys. Lett.* **B575** (2003) 300–308, hep-ph/0308021.

[375] K. Hasegawa, C. S. Lim, and K. Ogure, "Escape from washing out of baryon number in a two-zero- texture general Zee model compatible with the LMA-MSW solution," *Phys. Rev.* **D68** (2003) 053006, hep-ph/0303252.

[376] R. Kitano, "Lepton flavor violation in the Randall-Sundrum model with bulk neutrinos," *Phys. Lett.* **B481** (2000) 39–44, hep-ph/0002279.

[377] M. Kakizaki, Y. Ogura, and F. Shima, "Lepton flavor violation in the triplet Higgs model," *Phys. Lett.* **B566** (2003) 210–216, hep-ph/0304254.

[378] O. M. Boyarkin, G. G. Boyarkina, and T. I. Bakanova, "Estimations of heavy neutrino masses and mixing in models with an extended Higgs sector," *Phys. Rev.* **D70** (2004) 113010.

[379] A. G. Akeroyd, M. Aoki, and Y. Okada, "Lepton Flavour Violating tau Decays in the Left-Right Symmetric Model," *Phys. Rev.* **D76** (2007) 013004, hep-ph/0610344.

[380] A. de Gouvea, S. Lola, and K. Tobe, "Lepton flavor violation in supersymmetric models with trilinear R-parity violation," *Phys. Rev.* **D63** (2001) 035004, hep-ph/0008085.

[381] S. Hannestad, "New constraint on the cosmological background of relativistic particles," *JCAP* **0601** (2006) 001, astro-ph/0510582.

[382] S. Hannestad and G. G. Raffelt, "Neutrino masses and cosmic radiation density: Combined analysis," *JCAP* **0611** (2006) 016, astro-ph/0607101.

[383] P. Crotty, J. Lesgourgues, and S. Pastor, "Measuring the cosmological background of relativistic particles with WMAP," *Phys. Rev.* **D67** (2003) 123005, astro-ph/0302337.

[384] E. Pierpaoli, "Constraints on the cosmic neutrino background," *Mon. Not. Roy. Astron. Soc.* **342** (2003) L63, astro-ph/0302465.

[385] U. Seljak, A. Slosar, and P. McDonald, "Cosmological parameters from combining the Lyman-alpha forest with CMB, galaxy clustering and SN constraints," *JCAP* **0610** (2006) 014, astro-ph/0604335.

[386] G. Mangano, A. Melchiorri, O. Mena, G. Miele, and A. Slosar, "Present bounds on the relativistic energy density in the Universe from cosmological observables," *JCAP* **0703** (2007) 006, astro-ph/0612150.

[387] J. Hamann, S. Hannestad, G. G. Raffelt, and Y. Y. Y. Wong, "Observational bounds on the cosmic radiation density," *JCAP* **0708** (2007) 021, arXiv:0705.0440 [astro-ph].

[388] J. Lesgourgues and S. Pastor, "Massive neutrinos and cosmology," *Phys. Rept.* **429** (2006) 307–379, astro-ph/0603494.

[389] **WMAP** Collaboration, D. N. Spergel *et al.*, "Wilkinson Microwave Anisotropy Probe (WMAP) three year results: Implications for cosmology," *Astrophys. J. Suppl.* **170** (2007) 377, astro-ph/0603449.

[390] **The 2dFGRS** Collaboration, S. Cole *et al.*, "The 2dF Galaxy Redshift Survey: Power-spectrum analysis of the final dataset and cosmological implications," *Mon. Not. Roy. Astron. Soc.* **362** (2005) 505–534, astro-ph/0501174.

[391] **SDSS** Collaboration, M. Tegmark *et al.*, "The 3D power spectrum of galaxies from the SDSS," *Astrophys. J.* **606** (2004) 702–740, astro-ph/0310725.

[392] M. Tegmark *et al.*, "Cosmological Constraints from the SDSS Luminous Red Galaxies," *Phys. Rev.* **D74** (2006) 123507, astro-ph/0608632.

[393] **SDSS** Collaboration, D. J. Eisenstein *et al.*, "Detection of the Baryon Acoustic Peak in the Large-Scale Correlation Function of SDSS Luminous Red Galaxies," *Astrophys. J.* **633** (2005) 560–574, astro-ph/0501171.

[394] P. McDonald *et al.*, "The Lyman-alpha Forest Power Spectrum from the Sloan Digital Sky Survey," *Astrophys. J. Suppl.* **163** (2006) 80–109, astro-ph/0405013.

[395] S. Hannestad, "Global neutrino parameter estimation using Markov Chain Monte Carlo," arXiv:0710.1952 [hep-ph].

[396] See http://sci.esa.int/science-e/www/area/index.cfm?fareaid=17.

[397] See http://universe.gsfc.nasa.gov/program/inflation.html.

[398] S. Wang, Z. Haiman, W. Hu, J. Khoury, and M. May, "Weighing neutrinos with galaxy cluster surveys," *Phys. Rev. Lett.* **95** (2005) 011302, astro-ph/0505390.

[399] S. Hannestad and Y. Y. Y. Wong, "Neutrino mass from future high redshift galaxy surveys: Sensitivity and detection threshold," *JCAP* **0707** (2007) 004, astro-ph/0703031.

[400] A. D. Sakharov, "Violation of CP invariance, C asymmetry, and baryon asymmetry of the universe," *Pisma Zh. Eksp. Teor. Fiz.* **5** (1967) 32–35.

[401] V. A. Kuzmin, V. A. Rubakov, and M. E. Shaposhnikov, "On the anomalous electroweak baryon number nonconservation in the early universe," *Phys. Lett.* **B155** (1985) 36.

[402] J. A. Harvey and M. S. Turner, "Cosmological baryon and lepton number in the presence of electroweak fermion number violation," *Phys. Rev.* **D42** (1990) 3344–3349.

[403] M. A. Luty, "Baryogenesis via leptogenesis," *Phys. Rev.* **D45** (1992) 455–465.

[404] M. Flanz, E. A. Paschos, and U. Sarkar, "Baryogenesis from a lepton asymmetric universe," *Phys. Lett.* **B345** (1995) 248–252, hep-ph/9411366.

[405] M. Plumacher, "Baryogenesis and lepton number violation," *Z. Phys.* **C74** (1997) 549–559, hep-ph/9604229.

[406] L. Covi, E. Roulet, and F. Vissani, "CP violating decays in leptogenesis scenarios," *Phys. Lett.* **B384** (1996) 169–174, hep-ph/9605319.

[407] M. Flanz, E. A. Paschos, U. Sarkar, and J. Weiss, "Baryogenesis through mixing of heavy Majorana neutrinos," *Phys. Lett.* **B389** (1996) 693–699, hep-ph/9607310.

[408] L. Covi and E. Roulet, "Baryogenesis from mixed particle decays," *Phys. Lett.* **B399** (1997) 113–118, hep-ph/9611425.

[409] A. Pilaftsis, "CP violation and baryogenesis due to heavy Majorana neutrinos," *Phys. Rev.* **D56** (1997) 5431–5451, hep-ph/9707235.

[410] W. Buchmuller and M. Plumacher, "CP asymmetry in Majorana neutrino decays," *Phys. Lett.* **B431** (1998) 354–362, hep-ph/9710460.

[411] A. Abada *et al.*, "Flavour matters in leptogenesis," *JHEP* **09** (2006) 010, hep-ph/0605281.

[412] S. Antusch, S. F. King, and A. Riotto, "Flavour-dependent leptogenesis with sequential dominance," *JCAP* **0611** (2006) 011, hep-ph/0609038.

[413] S. Pascoli, S. T. Petcov, and W. Rodejohann, "On the connection of leptogenesis with low energy CP violation and LFV charged lepton decays," *Phys. Rev.* **D68** (2003) 093007, hep-ph/0302054.

[414] J. A. Casas and A. Ibarra, "Oscillating neutrinos and mu → e, gamma," *Nucl. Phys.* **B618** (2001) 171–204, hep-ph/0103065.

[415] S. Davidson and A. Ibarra, "Determining seesaw parameters from weak scale measurements?," *JHEP* **09** (2001) 013, hep-ph/0104076.

[416] J. R. Ellis, J. Hisano, S. Lola, and M. Raidal, "CP violation in the minimal supersymmetric seesaw model," *Nucl. Phys.* **B621** (2002) 208–234, hep-ph/0109125.

[417] G. C. Branco, R. Gonzalez Felipe, F. R. Joaquim, and M. N. Rebelo, "Leptogenesis, CP violation and neutrino data: What can we learn?," *Nucl. Phys.* **B640** (2002) 202–232, hep-ph/0202030.

[418] J. R. Ellis and M. Raidal, "Leptogenesis and the violation of lepton number and CP at low energies," *Nucl. Phys.* **B643** (2002) 229–246, hep-ph/0206174.

[419] P. H. Frampton, S. L. Glashow, and T. Yanagida, "Cosmological sign of neutrino CP violation," *Phys. Lett.* **B548** (2002) 119–121, hep-ph/0208157.

[420] S. Davidson and A. Ibarra, "Leptogenesis and low-energy phases," *Nucl. Phys.* **B648** (2003) 345–375, hep-ph/0206304.

[421] G. C. Branco *et al.*, "Minimal scenarios for leptogenesis and CP violation," *Phys. Rev.* **D67** (2003) 073025, hep-ph/0211001.

[422] S. F. King, "Leptogenesis - MNS link in unified models with natural neutrino mass hierarchy," *Phys. Rev.* **D67** (2003) 113010, hep-ph/0211228.

[423] A. H. Guth, "The inflationary universe: a possible solution to the horizon and flatness problems," *Phys. Rev.* **D23** (1981) 347–356.

[424] K. Sato, "First order phase transition of a vacuum and expansion of the universe," *Mon. Not. Roy. Astron. Soc.* **195** (1981) 467–479.

[425] A. A. Starobinsky, "Dynamics of phase transition in the new inflationary universe scenario and generation of perturbations," *Phys. Lett.* **B117** (1982) 175–178.

[426] A. D. Linde, "Chaotic inflation," *Phys. Lett.* **B129** (1983) 177–181.

[427] J. R. Ellis, M. Raidal, and T. Yanagida, "Sneutrino inflation in the light of WMAP: Reheating, leptogenesis and flavor-violating lepton decays," *Phys. Lett.* **B581** (2004) 9–18, hep-ph/0303242.

[428] H. Murayama, H. Suzuki, T. Yanagida, and J. Yokoyama, "Chaotic inflation and baryogenesis by right-handed sneutrinos," *Phys. Rev. Lett.* **70** (1993) 1912–1915.

[429] K. Hamaguchi, H. Murayama, and T. Yanagida, "Leptogenesis from sneutrino-dominated early universe," *Phys. Rev.* **D65** (2002) 043512, hep-ph/0109030.

[430] M. Kawasaki, K. Kohri, and T. Moroi, "Big-bang nucleosynthesis and hadronic decay of long-lived massive particles," *Phys. Rev.* **D71** (2005) 083502, astro-ph/0408426.

[431] W. Buchmuller, P. Di Bari, and M. Plumacher, "Leptogenesis for pedestrians," *Ann. Phys.* **315** (2005) 305–351, hep-ph/0401240.

[432] S. Antusch and A. M. Teixeira, "Towards constraints on the SUSY seesaw from flavour-dependent leptogenesis," *JCAP* **0702** (2007) 024, hep-ph/0611232.

[433] H. Murayama, H. Suzuki, T. Yanagida, and J. Yokoyama, "Chaotic inflation and baryogenesis in supergravity," *Phys. Rev.* **D50** (1994) 2356–2360, hep-ph/9311326.

[434] K. Kadota and J. Yokoyama, "D-term inflation and leptogenesis by right-handed sneutrino," *Phys. Rev.* **D73** (2006) 043507, hep-ph/0512221.

[435] J. R. Ellis, Z. Lalak, S. Pokorski, and K. Turzynski, "The price of WMAP inflation in supergravity," *JCAP* **0610** (2006) 005, hep-th/0606133.

[436] See, *e.g.*, http://bolo.berkeley.edu/polarbear/.

[437] S. Antusch, M. Bastero-Gil, S. F. King, and Q. Shafi, "Sneutrino hybrid inflation in supergravity," *Phys. Rev.* **D71** (2005) 083519, hep-ph/0411298.

[438] **LHC/LC Study Group** Collaboration, G. Weiglein *et al.*, "Physics interplay of the LHC and the ILC," *submitted to Phys. Rept.* (2004) hep-ph/0410364.

[439] M. E. Peskin and T. Takeuchi, "A New constraint on a strongly interacting Higgs sector," *Phys. Rev. Lett.* **65** (1990) 964–967.

[440] M. E. Peskin and T. Takeuchi, "Estimation of oblique electroweak corrections," *Phys. Rev.* **D46** (1992) 381–409.

[441] T. Appelquist and R. Shrock, "Neutrino masses in theories with dynamical electroweak symmetry breaking," *Phys. Lett.* **B548** (2002) 204–214, hep-ph/0204141.

[442] T. Appelquist and R. Shrock, "Dynamical symmetry breaking of extended gauge symmetries," *Phys. Rev. Lett.* **90** (2003) 201801, hep-ph/0301108.

[443] T. Appelquist, M. Piai, and R. Shrock, "Fermion masses and mixing in extended technicolor models," *Phys. Rev.* **D69** (2004) 015002, hep-ph/0308061.

[444] T. Appelquist, N. D. Christensen, M. Piai, and R. Shrock, "Flavor-changing processes in extended technicolor," *Phys. Rev.* **D70** (2004) 093010, hep-ph/0409035.

[445] R. Foot, H. Lew, and R. R. Volkas, "A Model with fundamental improper space-time symmetries," *Phys. Lett.* **B272** (1991) 67–70.

[446] R. Foot, H. Lew, and R. R. Volkas, "Possible consequences of parity conservation," *Mod. Phys. Lett.* **A7** (1992) 2567–2574.

[447] R. Foot, "Neutrino oscillations and the exact parity model," *Mod. Phys. Lett.* **A9** (1994) 169–180, hep-ph/9402241.

[448] R. Foot and R. R. Volkas, "Neutrino physics and the mirror world: How exact parity symmetry explains the solar neutrino deficit, the atmospheric neutrino anomaly and the LSND experiment," *Phys. Rev.* **D52** (1995) 6595–6606, hep-ph/9505359.

[449] Z. G. Berezhiani and R. N. Mohapatra, "Reconciling present neutrino puzzles: Sterile neutrinos as mirror neutrinos," *Phys. Rev.* **D52** (1995) 6607–6611, hep-ph/9505385.

[450] Z. G. Berezhiani, A. D. Dolgov, and R. N. Mohapatra, "Asymmetric Inflationary Reheating and the Nature of Mirror Universe," *Phys. Lett.* **B375** (1996) 26–36, hep-ph/9511221.

[451] R. N. Mohapatra and V. L. Teplitz, "Structures in the mirror universe," *Astrophys. J.* **478** (1997) 29–38, astro-ph/9603049.

[452] Z. Berezhiani, D. Comelli, and F. L. Villante, "The early mirror universe: Inflation, baryogenesis, nucleosynthesis and dark matter," *Phys. Lett.* **B503** (2001) 362–375, hep-ph/0008105.

[453] K. Benakli and A. Y. Smirnov, "Neutrino-modulino mixing," *Phys. Rev. Lett.* **79** (1997) 4314–4317, hep-ph/9703465.

[454] Z. Chacko and R. N. Mohapatra, "Sterile neutrinos in E(6) and a natural understanding of vacuum oscillation solution to the solar neutrino puzzle," *Phys. Rev.* **D61** (2000) 053002, hep-ph/9905388.

[455] M. Frank, I. Turan, and M. Sher, "Neutrino masses in effective rank-5 subgroups of E(6). I: Non-SUSY case," *Phys. Rev.* **D71** (2005) 113001, hep-ph/0412090.

[456] M. Frank, I. Turan, and M. Sher, "Neutrino masses in the effective rank-5 subgroups of E(6): Supersymmetric case," *Phys. Rev.* **D71** (2005) 113002, hep-ph/0503084.

[457] R. N. Mohapatra and A. Perez-Lorenzana, "Sterile neutrino as a bulk neutrino," *Nucl. Phys.* **B576** (2000) 466–478, hep-ph/9910474.

[458] G. Cacciapaglia, M. Cirelli, and A. Romanino, "Signatures of supernova neutrino oscillations into extra dimensions," *Phys. Rev.* **D68** (2003) 033013, hep-ph/0302246.

[459] M. Cirelli, G. Marandella, A. Strumia, and F. Vissani, "Probing oscillations into sterile neutrinos with cosmology, astrophysics and experiments," *Nucl. Phys.* **B708** (2005) 215–267, hep-ph/0403158.

[460] A. Atre *et al.* in preparation.

[461] R. E. Shrock, "New tests for, and bounds on, neutrino masses and lepton mixing," *Phys. Lett.* **B96** (1980) 159.

[462] R. E. Shrock, "General theory of weak leptonic and semileptonic decays. 1. leptonic pseudoscalar meson decays, with associated tests for, and bounds on, neutrino masses and lepton mixing," *Phys. Rev.* **D24** (1981) 1232.

[463] R. E. Shrock, "General theory of weak processes involving neutrinos. 2. pure leptonic decays," *Phys. Rev.* **D24** (1981) 1275.

[464] A. Kusenko, S. Pascoli, and D. Semikoz, "New bounds on MeV sterile neutrinos based on the accelerator and super-Kamiokande results," *JHEP* **11** (2005) 028, hep-ph/0405198.

[465] L. S. Littenberg and R. E. Shrock, "Upper bounds on lepton number violating meson decays," *Phys. Rev. Lett.* **68** (1992) 443–446.

[466] R. Appel *et al.*, "Search for lepton flavor violation in K+ decays," *Phys. Rev. Lett.* **85** (2000) 2877–2880, hep-ex/0006003.

[467] J. H. Missimer, R. N. Mohapatra, and N. C. Mukhopadhyay, "A Muonic analog of the nuclear double beta decay: A New window for the lepton number conservation," *Phys. Rev.* **D50** (1994) 2067–2070.

[468] A. Weir *et al.*, "Upper limits on D+- and B+- decays to two leptons plus pi+- or K+-," *Phys. Rev.* **D41** (1990) 1384.

[469] L. S. Littenberg and R. E. Shrock, "Upper bounds on Delta L = 2 decays of baryons," *Phys. Rev.* **D46** (1992) 892–894.

[470] **HyperCP** Collaboration, D. Rajaram *et al.*, "Search for the lepton-number-violating decay Xi- → p mu- mu-," *Phys. Rev. Lett.* **94** (2005) 181801, hep-ex/0505025.

[471] R. H. Cyburt, B. D. Fields, K. A. Olive, and E. Skillman, "New BBN limits on physics beyond the Standard Model from He-4," *Astropart. Phys.* **23** (2005) 313–323, astro-ph/0408033.

[472] Y.-Z. Chu and M. Cirelli, "Sterile neutrinos, lepton asymmetries, primordial elements: How much of each?," *Phys. Rev.* **D74** (2006) 085015, astro-ph/0608206.

[473] V. Barger, J. P. Kneller, H.-S. Lee, D. Marfatia, and G. Steigman, "Effective number of neutrinos and baryon asymmetry from BBN and WMAP," *Phys. Lett.* **B566** (2003) 8–18, hep-ph/0305075.

[474] K. Kainulainen, J. Maalampi, and J. T. Peltoniemi, "Inert neutrinos in supernovae," *Nucl. Phys.* **B358** (1991) 435–446.

[475] K. Abazajian, G. M. Fuller, and M. Patel, "Sterile neutrino hot, warm, and cold dark matter," *Phys. Rev.* **D64** (2001) 023501, astro-ph/0101524.

[476] S. Dodelson and L. M. Widrow, "Sterile-neutrinos as dark matter," *Phys. Rev. Lett.* **72** (1994) 17–20, hep-ph/9303287.

[477] A. D. Dolgov and S. H. Hansen, "Massive sterile neutrinos as warm dark matter," *Astropart. Phys.* **16** (2002) 339–344, hep-ph/0009083.

[478] T. Asaka, S. Blanchet, and M. Shaposhnikov, "The nuMSM, dark matter and neutrino masses," *Phys. Lett.* **B631** (2005) 151–156, hep-ph/0503065.

[479] M. Viel, J. Lesgourgues, M. G. Haehnelt, S. Matarrese, and A. Riotto, "Constraining warm dark matter candidates including sterile neutrinos and light gravitinos with WMAP and the Lyman- alpha forest," *Phys. Rev.* **D71** (2005) 063534, astro-ph/0501562.

[480] U. Seljak, A. Makarov, P. McDonald, and H. Trac, "Can sterile neutrinos be the dark matter?," *Phys. Rev. Lett.* **97** (2006) 191303, astro-ph/0602430.

[481] M. Viel, J. Lesgourgues, M. G. Haehnelt, S. Matarrese, and A. Riotto, "Can sterile neutrinos be ruled out as warm dark matter candidates?," *Phys. Rev. Lett.* **97** (2006) 071301, astro-ph/0605706.

[482] X.-d. Shi and G. M. Fuller, "A new dark matter candidate: Non-thermal sterile neutrinos," *Phys. Rev. Lett.* **82** (1999) 2832–2835, astro-ph/9810076.

[483] T. Asaka, A. Kusenko, and M. Shaposhnikov, "Opening a new window for warm dark matter," *Phys. Lett.* **B638** (2006) 401–406, hep-ph/0602150.

[484] A. Kusenko, "Sterile neutrinos, dark matter, and the pulsar velocities in models with a Higgs singlet," *Phys. Rev. Lett.* **97** (2006) 241301, hep-ph/0609081.

[485] K. Abazajian, G. M. Fuller, and W. H. Tucker, "Direct detection of warm dark matter in the X-ray," *Astrophys. J.* **562** (2001) 593–604, astro-ph/0106002.

[486] A. Boyarsky, A. Neronov, O. Ruchayskiy, and M. Shaposhnikov, "Constraints on sterile neutrino as a dark matter candidate from the diffuse X-ray background," *Mon. Not. Roy. Astron. Soc.* **370** (2006) 213–218, astro-ph/0512509.

[487] A. Boyarsky, A. Neronov, O. Ruchayskiy, and M. Shaposhnikov, "The masses of active neutrinos in the nuMSM from X-ray astronomy," *JETP Lett.* **83** (2006) 133–135, hep-ph/0601098.

[488] A. Boyarsky, A. Neronov, O. Ruchayskiy, and M. Shaposhnikov, "Restrictions on parameters of sterile neutrino dark matter from observations of galaxy clusters," *Phys. Rev.* **D74** (2006) 103506, astro-ph/0603368.

[489] P. L. Biermann and A. Kusenko, "Relic keV sterile neutrinos and reionization," *Phys. Rev. Lett.* **96** (2006) 091301, astro-ph/0601004.

[490] A. Kusenko and G. Segre, "Pulsar kicks from neutrino oscillations," *Phys. Rev.* **D59** (1999) 061302, astro-ph/9811144.

[491] G. M. Fuller, A. Kusenko, I. Mocioiu, and S. Pascoli, "Pulsar kicks from a dark-matter sterile neutrino," *Phys. Rev.* **D68** (2003) 103002, astro-ph/0307267.

[492] M. Barkovich, J. C. D'Olivo, and R. Montemayor, "Active-sterile neutrino oscillations and pulsar kicks," *Phys. Rev.* **D70** (2004) 043005, hep-ph/0402259.

[493] A. D. Dolgov, S. H. Hansen, G. Raffelt, and D. V. Semikoz, "Heavy sterile neutrinos: Bounds from big-bang nucleosynthesis and SN 1987A," *Nucl. Phys.* **B590** (2000) 562–574, hep-ph/0008138.

[494] G. Gelmini, S. Palomares-Ruiz, and S. Pascoli, "Low reheating temperature and the visible sterile neutrino," *Phys. Rev. Lett.* **93** (2004) 081302, astro-ph/0403323.

[495] M. Maltoni and T. Schwetz, "Sterile neutrino oscillations after first MiniBooNE results," *Phys. Rev.* **D76** (2007) 093005, 0705.0107.

[496] **KARMEN** Collaboration, B. Armbruster *et al.*, "Upper limits for neutrino oscillations anti-nu/mu → anti- nu/e from muon decay at rest," *Phys. Rev.* **D65** (2002) 112001, hep-ex/0203021.

[497] E. D. Church, K. Eitel, G. B. Mills, and M. Steidl, "Statistical analysis of different anti-nu/mu → anti-nu/e searches," *Phys. Rev.* **D66** (2002) 013001, hep-ex/0203023.

[498] **MiniBooNE** Collaboration, J. Monroe, "Latest results from the MiniBooNE experiment and updated nu/mu → nu/e sensitivity," hep-ex/0406048.

[499] J. T. Peltoniemi, D. Tommasini, and J. W. F. Valle, "Reconciling dark matter and solar neutrinos," *Phys. Lett.* **B298** (1993) 383–390.

[500] D. O. Caldwell and R. N. Mohapatra, "Neutrino mass explanations of solar and atmospheric neutrino deficits and hot dark matter," *Phys. Rev.* **D48** (1993) 3259–3263.

[501] J. T. Peltoniemi and J. W. F. Valle, "Reconciling dark matter, solar and atmospheric neutrinos," *Nucl. Phys.* **B406** (1993) 409–422, hep-ph/9302316.

[502] M. Maltoni, T. Schwetz, M. A. Tortola, and J. W. F. Valle, "Ruling out four-neutrino oscillation interpretations of the LSND anomaly?," *Nucl. Phys.* **B643** (2002) 321–338, hep-ph/0207157.

[503] A. Strumia, "Interpreting the LSND anomaly: Sterile neutrinos or CPT- violation or...?," *Phys. Lett.* **B539** (2002) 91–101, hep-ph/0201134.

[504] M. Maltoni, T. Schwetz, and J. W. F. Valle, "Status of four-neutrino mass schemes: A global and unified approach to current neutrino oscillation data," *Phys. Rev.* **D65** (2002) 093004, hep-ph/0112103.

[505] C. Giunti, M. C. Gonzalez-Garcia, and C. Pena-Garay, "Four-neutrino oscillation solutions of the solar neutrino problem," *Phys. Rev.* **D62** (2000) 013005, hep-ph/0001101.

[506] M. C. Gonzalez-Garcia, M. Maltoni, and C. Pena-Garay, "Solar and atmospheric four-neutrino oscillations," *Phys. Rev.* **D64** (2001) 093001, hep-ph/0105269.

[507] F. Dydak *et al.*, "A search for muon-neutrino oscillations in the Delta m**2 range 0.3-eV**2 to 90-eV**2," *Phys. Lett.* **B134** (1984) 281.

[508] Y. Declais *et al.*, "Search for neutrino oscillations at 15-meters, 40-meters, and 95-meters from a nuclear power reactor at Bugey," *Nucl. Phys.* **B434** (1995) 503–534.

[509] M. Maltoni and T. Schwetz, "Testing the statistical compatibility of independent data sets," *Phys. Rev.* **D68** (2003) 033020, hep-ph/0304176.

[510] H. Pas, L.-g. Song, and T. J. Weiler, "The hidden sterile neutrino and the (2+2) sum rule," *Phys. Rev.* **D67** (2003) 073019, hep-ph/0209373.

[511] S. M. Bilenky, C. Giunti, and W. Grimus, "Neutrino mass spectrum from the results of neutrino oscillation experiments," *Eur. Phys. J.* **C1** (1998) 247–253, hep-ph/9607372.

[512] N. Okada and O. Yasuda, "A sterile neutrino scenario constrained by experiments and cosmology," *Int. J. Mod. Phys.* **A12** (1997) 3669–3694, hep-ph/9606411.

[513] V. D. Barger, S. Pakvasa, T. J. Weiler, and K. Whisnant, "Variations on four-neutrino oscillations," *Phys. Rev.* **D58** (1998) 093016, hep-ph/9806328.

[514] S. M. Bilenky, C. Giunti, W. Grimus, and T. Schwetz, "Four-neutrino mass spectra and the Super-Kamiokande atmospheric up-down asymmetry," *Phys. Rev.* **D60** (1999) 073007, hep-ph/9903454.

[515] O. L. G. Peres and A. Y. Smirnov, "(3+1) spectrum of neutrino masses: A chance for LSND?," *Nucl. Phys.* **B599** (2001) 3, hep-ph/0011054.

[516] C. Giunti and M. Laveder, "Large nu/mu → nu/tau and nu/e → nu/tau transitions in short baseline experiments?," *JHEP* **02** (2001) 001, hep-ph/0010009.

[517] W. Grimus and T. Schwetz, "4-neutrino mass schemes and the likelihood of (3+1)-mass spectra," *Eur. Phys. J.* **C20** (2001) 1–11, hep-ph/0102252.

[518] M. Maltoni, T. Schwetz, and J. W. F. Valle, "Cornering (3+1) sterile neutrino schemes," *Phys. Lett.* **B518** (2001) 252–260, hep-ph/0107150.

[519] M. Apollonio *et al.*, "Search for neutrino oscillations on a long base-line at the CHOOZ nuclear power station," *Eur. Phys. J.* **C27** (2003) 331–374, hep-ex/0301017.

[520] **NOMAD** Collaboration, P. Astier *et al.*, "Search for nu/mu → nu/e oscillations in the NOMAD experiment," *Phys. Lett.* **B570** (2003) 19–31, hep-ex/0306037.

[521] S. Dodelson, A. Melchiorri, and A. Slosar, "Is cosmology compatible with sterile neutrinos?," *Phys. Rev. Lett.* **97** (2006) 04301, astro-ph/0511500.

[522] G. Karagiorgi *et al.*, "Leptonic CP violation studies at MiniBooNE in the (3+2) sterile neutrino oscillation hypothesis," *Phys. Rev.* **D75** (2007) 013011, hep-ph/0609177.

[523] I. E. Stockdale *et al.*, "Limits on muon neutrino oscillations in the mass range 55- eV**2 < Delta m**2 < 800-eV**2," *Phys. Rev. Lett.* **52** (1984) 1384.

[524] M. C. Gonzalez-Garcia and M. Maltoni, "Atmospheric neutrino oscillations and new physics," *Phys. Rev.* **D70** (2004) 033010, hep-ph/0404085.

[525] **MiniBooNE** Collaboration, A. A. Aguilar-Arevalo *et al.*, "The MiniBooNE Run Plan," 2003. available at http://www-boone.fnal.gov/publicpages/.

[526] Webpage of C. Giunti and M. Laveder. http://www.nu.to.infn.it/Neutrino_SBL/.

[527] V. Barger, D. Marfatia, and K. Whisnant, "LSND anomaly from CPT violation in four-neutrino models," *Phys. Lett.* **B576** (2003) 303–308, hep-ph/0308299.

[528] H. Pas, S. Pakvasa, and T. J. Weiler, "Sterile - active neutrino oscillations and shortcuts in the extra dimension," *Phys. Rev.* **D72** (2005) 095017, hep-ph/0504096.

[529] S. Palomares-Ruiz, S. Pascoli, and T. Schwetz, "Explaining LSND by a decaying sterile neutrino," *JHEP* **09** (2005) 048, hep-ph/0505216.

[530] R. Fardon, A. E. Nelson, and N. Weiner, "Dark energy from mass varying neutrinos," *JCAP* **0410** (2004) 005, astro-ph/0309800.

[531] R. Takahashi and M. Tanimoto, "Model of mass varying neutrinos in SUSY," *Phys. Lett.* **B633** (2006) 675–680, hep-ph/0507142.

[532] R. Fardon, A. E. Nelson, and N. Weiner, "Supersymmetric theories of neutrino dark energy," *JHEP* **03** (2006) 042, hep-ph/0507235.

[533] R. D. Peccei, "Neutrino models of dark energy," *Phys. Rev.* **D71** (2005) 023527, hep-ph/0411137.

[534] D. B. Kaplan, A. E. Nelson, and N. Weiner, "Neutrino oscillations as a probe of dark energy," *Phys. Rev. Lett.* **93** (2004) 091801, hep-ph/0401099.

[535] K. M. Zurek, "New matter effects in neutrino oscillation experiments," *JHEP* **10** (2004) 058, hep-ph/0405141.

[536] V. Barger, P. Huber, and D. Marfatia, "Solar mass-varying neutrino oscillations," *Phys. Rev. Lett.* **95** (2005) 211802, hep-ph/0502196.

[537] N. Weiner and K. M. Zurek, "New matter effects and BBN constraints for mass varying neutrinos," *Phys. Rev.* **D74** (2006) 023517, hep-ph/0509201.

[538] A. Ringwald and Y. Y. Y. Wong, "Gravitational clustering of relic neutrinos and implications for their detection," *JCAP* **0412** (2004) 005, hep-ph/0408241.

[539] V. Barger, S. L. Glashow, D. Marfatia, and K. Whisnant, "Neutrinoless double beta decay can constrain neutrino dark matter," *Phys. Lett.* **B532** (2002) 15–18, hep-ph/0201262.

[540] N. Afshordi, M. Zaldarriaga, and K. Kohri, "On the stability of dark energy with mass-varying neutrinos," *Phys. Rev.* **D72** (2005) 065024, astro-ph/0506663.

[541] R. Takahashi and M. Tanimoto, "Speed of sound in the mass varying neutrinos scenario," *JHEP* **05** (2006) 021, astro-ph/0601119.

[542] M. C. Gonzalez-Garcia, P. C. de Holanda, and R. Zukanovich Funchal, "Effects of environment dependence of neutrino mass versus solar and reactor neutrino data," *Phys. Rev.* **D73** (2006) 033008, hep-ph/0511093.

[543] V. Barger, D. Marfatia, and K. Whisnant, "Testing the LMA solution with solar neutrinos independently of solar models," *Phys. Lett.* **B617** (2005) 78–86, hep-ph/0501247.

[544] V. D. Barger, D. Marfatia, and K. Whisnant, "Piecing the solar neutrino puzzle together at SNO," *Phys. Lett.* **B509** (2001) 19–29, hep-ph/0104166.

[545] V. Barger, D. Marfatia, and K. Whisnant, "Confronting mass-varying neutrinos with MiniBooNE," *Phys. Rev.* **D73** (2006) 013005, hep-ph/0509163.

[546] K. Anderson *et al.*, "White paper report on using nuclear reactors to search for a value of theta(13)," hep-ex/0402041.

[547] F. Suekane, K. Inoue, T. Araki, and K. Jongok, "Precise measurement of sin**2(2theta(13)) using Japanese reactors," hep-ex/0306029.

[548] S. Berridge *et al.*, "Proposal for U.S. participation in double-CHOOZ: A new Theta(13) experiment at the Chooz reactor," hep-ex/0410081.

[549] V. D. Barger *et al.*, "Neutrino oscillation parameters from MINOS, ICARUS and OPERA combined," *Phys. Rev.* **D65** (2002) 053016, hep-ph/0110393.

[550] T. Schwetz and W. Winter, "Testing mass-varying neutrinos with reactor experiments," *Phys. Lett.* **B633** (2006) 557–562, hep-ph/0511177.

[551] P.-H. Gu, X.-J. Bi, B. Feng, B.-L. Young, and X. Zhang, "Detecting dark energy in long baseline neutrino oscillations," hep-ph/0512076.

[552] V. A. Kostelecky and S. Samuel, "Spontaneous breaking of Lorentz symmetry in string theory," *Phys. Rev.* **D39** (1989) 683.

[553] D. Colladay and V. A. Kostelecky, "Lorentz-violating extension of the Standard Model," *Phys. Rev.* **D58** (1998) 116002, hep-ph/9809521.

[554] D. Colladay and V. A. Kostelecky, "CPT violation and the Standard Model," *Phys. Rev.* **D55** (1997) 6760–6774, hep-ph/9703464.

[555] S. R. Coleman and S. L. Glashow, "High-energy tests of Lorentz invariance," *Phys. Rev.* **D59** (1999) 116008, hep-ph/9812418.

[556] O. W. Greenberg, "CPT violation implies violation of Lorentz invariance," *Phys. Rev. Lett.* **89** (2002) 231602, hep-ph/0201258.

[557] V. D. Barger, S. Pakvasa, T. J. Weiler, and K. Whisnant, "CPT odd resonances in neutrino oscillations," *Phys. Rev. Lett.* **85** (2000) 5055–5058, hep-ph/0005197.

[558] H. Murayama and T. Yanagida, "LSND, SN1987A, and CPT violation," *Phys. Lett.* **B520** (2001) 263–268, hep-ph/0010178.

[559] G. Barenboim, L. Borissov, J. D. Lykken, and A. Y. Smirnov, "Neutrinos as the messengers of CPT violation," *JHEP* **10** (2002) 001, hep-ph/0108199.

[560] G. Barenboim, L. Borissov, and J. D. Lykken, "CPT violating neutrinos in the light of KamLAND," hep-ph/0212116.

[561] M. C. Gonzalez-Garcia, M. Maltoni, and T. Schwetz, "Status of the CPT violating interpretations of the LSND signal," *Phys. Rev.* **D68** (2003) 053007, hep-ph/0306226.

[562] D. Hooper, D. Morgan, and E. Winstanley, "Lorentz and CPT invariance violation in high-energy neutrinos," *Phys. Rev.* **D72** (2005) 065009, hep-ph/0506091.

[563] J. N. Bahcall, V. Barger, and D. Marfatia, "How accurately can one test CPT conservation with reactor and solar neutrino experiments?," *Phys. Lett.* **B534** (2002) 120–123, hep-ph/0201211.

[564] S. M. Bilenky, M. Freund, M. Lindner, T. Ohlsson, and W. Winter, "Tests of CPT invariance at neutrino factories," *Phys. Rev.* **D65** (2002) 073024, hep-ph/0112226.

[565] V. A. Kostelecky and M. Mewes, "Lorentz and CPT violation in neutrinos," *Phys. Rev.* **D69** (2004) 016005, hep-ph/0309025.

[566] V. A. Kostelecky and M. Mewes, "Lorentz and CPT violation in the neutrino sector," *Phys. Rev.* **D70** (2004) 031902, hep-ph/0308300.

[567] A. Datta, R. Gandhi, P. Mehta, and S. Uma Sankar, "Atmospheric neutrinos as a probe of CPT and Lorentz violation," *Phys. Lett.* **B597** (2004) 356–361, hep-ph/0312027.

[568] H. Murayama, "CPT tests: Kaon vs neutrinos," *Phys. Lett.* **B597** (2004) 73–77, hep-ph/0307127.

[569] A. de Gouvea and C. Pena-Garay, "Probing new physics by comparing solar and KamLAND data," *Phys. Rev.* **D71** (2005) 093002, hep-ph/0406301.

[570] S. R. Coleman and S. L. Glashow, "Cosmic ray and neutrino tests of special relativity," *Phys. Lett.* **B405** (1997) 249–252, hep-ph/9703240.

[571] R. Foot, C. N. Leung, and O. Yasuda, "Atmospheric neutrino tests of neutrino oscillation mechanisms," *Phys. Lett.* **B443** (1998) 185–190, hep-ph/9809458.

[572] V. A. Kostelecky and M. Mewes, "Lorentz violation and short-baseline neutrino experiments," *Phys. Rev.* **D70** (2004) 076002, hep-ph/0406255.

[573] G. Battistoni *et al.*, "Search for a Lorentz invariance violation contribution in atmospheric neutrino oscillations using MACRO data," *Phys. Lett.* **B615** (2005) 14–18, hep-ex/0503015.

[574] M. Gasperini, "Testing the principle of equivalence with neutrino oscillations," *Phys. Rev.* **D38** (1988) 2635–2637.

[575] A. Halprin and C. N. Leung, "Can the sun shed light on neutrino gravitational interactions?," *Phys. Rev. Lett.* **67** (1991) 1833–1835.

[576] J. T. Pantaleone, A. Halprin, and C. N. Leung, "Neutrino mixing due to a violation of the equivalence principle," *Phys. Rev.* **D47** (1993) 4199–4202, hep-ph/9211214.

[577] J. N. Bahcall, P. I. Krastev, and C. N. Leung, "Solar neutrinos and the principle of equivalence," *Phys. Rev.* **D52** (1995) 1770–1779, hep-ph/9410353.

[578] A. M. Gago, H. Nunokawa, and R. Zukanovich Funchal, "The solar neutrino problem and gravitationally induced long-wavelength neutrino oscillation," *Phys. Rev. Lett.* **84** (2000) 4035–4038, hep-ph/9909250.

[579] S. L. Glashow, A. Halprin, P. I. Krastev, C. N. Leung, and J. T. Pantaleone, "Remarks on neutrino tests of special relativity," *Phys. Rev.* **D56** (1997) 2433–2434, hep-ph/9703454.

[580] T. Schwetz, "Status of neutrino oscillations. II: How to reconcile the LSND result?," hep-ph/0311217.

[581] J. W. F. Valle, "Resonant oscillations of massless neutrinos in matter," *Phys. Lett.* **B199** (1987) 432.

[582] H. Nunokawa, Y. Z. Qian, A. Rossi, and J. W. F. Valle, "Resonant conversion of massless neutrinos in supernovae," *Phys. Rev.* **D54** (1996) 4356–4363, hep-ph/9605301.

[583] H. Minakata, H. Nunokawa, W. J. C. Teves, and R. Zukanovich Funchal, "Reactor measurement of theta(12): Principles, accuracies and physics potentials," *Phys. Rev.* **D71** (2005) 013005, hep-ph/0407326.

[584] **Super-Kamiokande** Collaboration, C. Saji, "SK atmospheric neutrino." Prepared for 5th Workshop on Neutrino Oscillations and their Origin (NOONE2004), Tokyo, Japan, 11-15 Feb 2004.

[585] M. C. Gonzalez-Garcia, F. Halzen, and M. Maltoni, "Physics reach of high-energy and high-statistics Icecube atmospheric neutrino data," *Phys. Rev.* **D71** (2005) 093010, hep-ph/0502223.

[586] J. A. Aguilar-Saavedra and G. C. Branco, "Unitarity triangles and geometrical description of CP violation with Majorana neutrinos," *Phys. Rev.* **D62** (2000) 096009, hep-ph/0007025.

[587] Y. Farzan and A. Y. Smirnov, "Leptonic unitarity triangle and CP-violation," *Phys. Rev.* **D65** (2002) 113001, hep-ph/0201105.

[588] M. Freund, P. Huber, and M. Lindner, "Extracting matter effects, masses and mixings at a neutrino factory," *Nucl. Phys.* **B585** (2000) 105–123, hep-ph/0004085.

[589] V. D. Barger, S. Geer, R. Raja, and K. Whisnant, "Short-baseline neutrino oscillations at a neutrino factory," *Phys. Rev.* **D63** (2001) 033002, hep-ph/0007181.

[590] T.-K. Kuo and J. T. Pantaleone, "T nonconservation in three neutrino oscillations," *Phys. Lett.* **B198** (1987) 406.

[591] H. Fritzsch and Z.-z. Xing, "Mass and flavor mixing schemes of quarks and leptons," *Prog. Part. Nucl. Phys.* **45** (2000) 1–81, hep-ph/9912358.

[592] J. Sato, "Neutrino oscillation and CP violation," *Nucl. Instrum. Meth.* **A472** (2001) 434–439, hep-ph/0008056.

[593] K. Dick, M. Freund, M. Lindner, and A. Romanino, "CP-violation in neutrino oscillations," *Nucl. Phys.* **B562** (1999) 29–56, hep-ph/9903308.

[594] P. F. Harrison and W. G. Scott, "mu - tau reflection symmetry in lepton mixing and neutrino oscillations," *Phys. Lett.* **B547** (2002) 219–228, hep-ph/0210197.

[595] W. Grimus and L. Lavoura, "A non-standard CP transformation leading to maximal atmospheric neutrino mixing," *Phys. Lett.* **B579** (2004) 113–122, hep-ph/0305309.

[596] H. Zhang and Z.-z. Xing, "Leptonic unitarity triangles in matter," *Eur. Phys. J.* **C41** (2005) 143–152, hep-ph/0411183.

[597] J. D. Bjorken, P. F. Harrison, and W. G. Scott, "Simplified unitarity triangles for the lepton sector," *Phys. Rev.* **D74** (2006) 073012, hep-ph/0511201.

[598] G. Ahuja and M. Gupta, "Constructing the leptonic unitarity triangle," *Phys. Rev.* **D77** (2008) 057301, hep-ph/0702129.

[599] E. K. Akhmedov, "Matter effects in short-baseline neutrino oscillations," *Phys. Lett.* **B503** (2001) 133–139, hep-ph/0011136.

[600] O. Yasuda, "Vacuum mimicking phenomena in neutrino oscillations," *Phys. Lett.* **B516** (2001) 111–115, hep-ph/0106232.

[601] P. Huber, J. Kopp, M. Lindner, M. Rolinec, and W. Winter, "From Double Chooz to Triple Chooz: Neutrino physics at the Chooz reactor complex," *JHEP* **05** (2006) 072, hep-ph/0601266.

[602] X.-G. He, T. Li, X.-Q. Li, and Y.-M. Wang, "PQCD calculation for Lambda/b → Lambda gamma in the standard model," *Phys. Rev.* **D74** (2006) 034026, hep-ph/0606025.

[603] J. Cao, "Daya Bay neutrino experiment," *Nucl. Phys. Proc. Suppl.* **155** (2006) 229–230, hep-ex/0509041.

[604] C.-S. Lim, "Resonant solar neutrino oscillation versus laboratory neutrino oscillation experiments." Presented at BNL Neutrino Workshop, Upton, N.Y., Feb 5-7, 1987.

[605] A. Y. Smirnov, "Status of the MSW-solution of the solar neutrino problem," *Front. Phys.* **5** (1993) 105–115.

[606] A. Strumia and F. Vissani, "Which solar neutrino experiment after KamLAND and Borexino?," *JHEP* **11** (2001) 048, hep-ph/0109172.

[607] D. Beavis *et al.*, "Neutrino oscillation experiments for precise measurements of oscillation parameters and search for nu/mu → nu/e appearance and CP violation," hep-ex/0205040.

[608] Z.-z. Xing and H. Zhang, "Reconstruction of the neutrino mixing matrix and leptonic unitarity triangles from long-baseline neutrino oscillations," *Phys. Lett.* **B618** (2005) 131–140, hep-ph/0503118.

[609] Z.-z. Xing, "Flavor mixing and CP violation of massive neutrinos," *Int. J. Mod. Phys.* **A19** (2004) 1–80, hep-ph/0307359.

[610] J. Burguet-Castell, M. B. Gavela, J. J. Gomez-Cadenas, P. Hernandez, and O. Mena, "Superbeams plus neutrino factory: The golden path to leptonic CP violation," *Nucl. Phys.* **B646** (2002) 301–320, hep-ph/0207080.

[611] S. Antusch, C. Biggio, E. Fernandez-Martinez, M. B. Gavela, and J. Lopez-Pavon, "Unitarity of the leptonic mixing matrix," *JHEP* **10** (2006) 084, hep-ph/0607020.

[612] W.-l. Guo and Z.-z. Xing, "Unitarity quadrangles of four neutrino mixing," *Phys. Rev.* **D66** (2002) 097302, hep-ph/0209017.

[613] V. Barger, S. Geer, and K. Whisnant, "Neutral currents and tests of three-neutrino unitarity in long-baseline experiments," *New J. Phys.* **6** (2004) 135, hep-ph/0407140.

[614] P. Langacker and D. London, "Mixing between ordinary and exotic fermions," *Phys. Rev.* **D38** (1988) 886.

[615] E. Nardi, E. Roulet, and D. Tommasini, "Global analysis of fermion mixing with exotics," *Nucl. Phys.* **B386** (1992) 239–266.

[616] E. Nardi, E. Roulet, and D. Tommasini, "Limits on neutrino mixing with new heavy particles," *Phys. Lett.* **B327** (1994) 319–326, hep-ph/9402224.

[617] P. Langacker and D. London, "Lepton number violation and massless nonorthogonal neutrinos," *Phys. Rev.* **D38** (1988) 907.

[618] S. M. Bilenky and C. Giunti, "Seesaw type mixing and muon-neutrino → tau-neutrino oscillations," *Phys. Lett.* **B300** (1993) 137–140, hep-ph/9211269.

[619] M. Czakon, J. Gluza, and M. Zralek, "Nonunitary neutrino mixing matrix and CP violating neutrino oscillations," *Acta Phys. Polon.* **B32** (2001) 3735–3744, hep-ph/0109245.

[620] B. Bekman, J. Gluza, J. Holeczek, J. Syska, and M. Zralek, "Matter effects and CP violating neutrino oscillations with non-decoupling heavy neutrinos," *Phys. Rev.* **D66** (2002) 093004, hep-ph/0207015.

[621] **NOMAD** Collaboration, P. Astier *et al.*, "Final NOMAD results on nu/mu → nu/tau and nu/e → nu/tau oscillations including a new search for nu/tau appearance using hadronic tau decays," *Nucl. Phys.* **B611** (2001) 3–39, hep-ex/0106102.

[622] **KARMEN** Collaboration, K. Eitel, "Latest results of the KARMEN2 experiment," *Nucl. Phys. Proc. Suppl.* **91** (2001) 191–197, hep-ex/0008002.

[623] **MINOS** Collaboration, D. A. Petyt, "First MINOS Results from the NuMI Beam." http://www-numi.fnal.gov/.

[624] M. C. Gonzalez-Garcia, "Global analysis of neutrino data," *Phys. Scripta* **T121** (2005) 72–77, hep-ph/0410030.

[625] **CERN working group on Super Beams** Collaboration, J. J. Gomez-Cadenas *et al.*, "Physics potential of very intense conventional neutrino beams," hep-ph/0105297.

[626] M. C. Gonzalez-Garcia, Y. Grossman, A. Gusso, and Y. Nir, "New CP violation in neutrino oscillations," *Phys. Rev.* **D64** (2001) 096006, hep-ph/0105159.

[627] T. Ota, J. Sato, and N.-a. Yamashita, "Oscillation enhanced search for new interaction with neutrinos," *Phys. Rev.* **D65** (2002) 093015, hep-ph/0112329.

[628] T. Ota and J. Sato, "Signature of the minimal supersymmetric standard model with right-handed neutrinos in long baseline experiments," *Phys. Rev.* **D71** (2005) 096004, hep-ph/0502124.

[629] Y. Grossman, "Nonstandard neutrino interactions and neutrino oscillation experiments," *Phys. Lett.* **B359** (1995) 141–147, hep-ph/9507344.

[630] T. Ota and J. Sato, "Can ICARUS and OPERA give information on a new physics?," *Phys. Lett.* **B545** (2002) 367–372, hep-ph/0202145.

[631] M. C. Gonzalez-Garcia, Y. Grossman, A. Gusso, and Y. Nir, "Models with New CP violation in neutrino oscillations," 2006 (in preparation).

[632] F. Cuypers and S. Davidson, "Bileptons: Present limits and future prospects," *Eur. Phys. J.* **C2** (1998) 503–528, hep-ph/9609487.

[633] S. P. Martin, "A supersymmetry primer," hep-ph/9709356 (v4-June 2006).

[634] Y. Grossman and S. Rakshit, "Neutrino masses in R-parity violating supersymmetric models," *Phys. Rev.* **D69** (2004) 093002, hep-ph/0311310.

[635] T. Banks, Y. Grossman, E. Nardi, and Y. Nir, "Supersymmetry without R-parity and without lepton number," *Phys. Rev.* **D52** (1995) 5319–5325, hep-ph/9505248.

[636] L. Randall and R. Sundrum, "A large mass hierarchy from a small extra dimension," *Phys. Rev. Lett.* **83** (1999) 3370–3373, hep-ph/9905221.

[637] Y. Grossman and M. Neubert, "Neutrino masses and mixings in non-factorizable geometry," *Phys. Lett.* **B474** (2000) 361–371, hep-ph/9912408.

[638] D. Tommasini, G. Barenboim, J. Bernabeu, and C. Jarlskog, "Nondecoupling of heavy neutrinos and lepton flavor violation," *Nucl. Phys.* **B444** (1995) 451–467, hep-ph/9503228.

[639] Y. Chikashige, R. N. Mohapatra, and R. D. Peccei, "Are there real Goldstone bosons associated with broken lepton number?," *Phys. Lett.* **B98** (1981) 265.

[640] Z. Chacko, L. J. Hall, T. Okui, and S. J. Oliver, "CMB signals of neutrino mass generation," *Phys. Rev.* **D70** (2004) 085008, hep-ph/0312267.

[641] H. Davoudiasl, R. Kitano, G. D. Kribs, and H. Murayama, "Models of neutrino mass with a low cutoff scale," *Phys. Rev.* **D71** (2005) 113004, hep-ph/0502176.

[642] A. Lukas and A. Romanino, "A brane-world explanation of the KARMEN anomaly," hep-ph/0004130.

[643] A. Lukas, P. Ramond, A. Romanino, and G. G. Ross, "Solar neutrino oscillation from large extra dimensions," *Phys. Lett.* **B495** (2000) 136–146, hep-ph/0008049.

[644] R. N. Mohapatra and A. Perez-Lorenzana, "Three flavour neutrino oscillations in models with large extra dimensions," *Nucl. Phys.* **B593** (2001) 451–470, hep-ph/0006278.

[645] A. Lukas, P. Ramond, A. Romanino, and G. G. Ross, "Neutrino masses and mixing in brane-world theories," *JHEP* **04** (2001) 010, hep-ph/0011295.

[646] H. Nunokawa, V. B. Semikoz, A. Y. Smirnov, and J. W. F. Valle, "Neutrino conversions in a polarized medium," *Nucl. Phys.* **B501** (1997) 17–40, hep-ph/9701420.

[647] S. Bergmann, Y. Grossman, and E. Nardi, "Neutrino propagation in matter with general interactions," *Phys. Rev.* **D60** (1999) 093008, hep-ph/9903517.

[648] N. Fornengo, M. C. Gonzalez-Garcia, and J. W. F. Valle, "On the interpretation of the atmospheric neutrino data in terms of flavor changing neutrino interactions," *JHEP* **07** (2000) 006, hep-ph/9906539.

[649] A. Friedland and C. Lunardini, "Two modes of searching for new neutrino interactions at MINOS," *Phys. Rev.* **D74** (2006) 033012, hep-ph/0606101.

[650] Z. Berezhiani and A. Rossi, "Limits on the non-standard interactions of neutrinos from e+ e- colliders," *Phys. Lett.* **B535** (2002) 207–218, hep-ph/0111137.

[651] S. Davidson, C. Pena-Garay, N. Rius, and A. Santamaria, "Present and future bounds on non-standard neutrino interactions," *JHEP* **03** (2003) 011, hep-ph/0302093.

[652] S. Bergmann, "The solar neutrino problem in the presence of flavor- changing neutrino interactions," *Nucl. Phys.* **B515** (1998) 363–383, hep-ph/9707398.

[653] S. Bergmann, Y. Grossman, and D. M. Pierce, "Can lepton flavor violating interactions explain the atmospheric neutrino problem?," *Phys. Rev.* **D61** (2000) 053005, hep-ph/9909390.

[654] S. Bergmann, M. M. Guzzo, P. C. de Holanda, P. I. Krastev, and H. Nunokawa, "Status of the solution to the solar neutrino problem based on non-standard neutrino interactions," *Phys. Rev.* **D62** (2000) 073001, hep-ph/0004049.

[655] A. De Gouvea, G. F. Giudice, A. Strumia, and K. Tobe, "Phenomenological implications of neutrinos in extra dimensions," *Nucl. Phys.* **B623** (2002) 395–420, hep-ph/0107156.

[656] M. Campanelli and A. Romanino, "Effects of new physics in neutrino oscillations in matter," *Phys. Rev.* **D66** (2002) 113001, hep-ph/0207350.

[657] Z. Berezhiani, R. S. Raghavan, and A. Rossi, "Probing non-standard couplings of neutrinos at the Borexino detector," *Nucl. Phys.* **B638** (2002) 62–80, hep-ph/0111138.

[658] E. Ma and P. Roy, "Neutrino oscillation data versus three light neutrino flavors," *Phys. Rev. Lett.* **80** (1998) 4637–4640, hep-ph/9706309.

[659] S. Bergmann and Y. Grossman, "Can lepton flavor violating interactions explain the LSND results?," *Phys. Rev.* **D59** (1999) 093005, hep-ph/9809524.

[660] S. Mansour and T.-K. Kuo, "Supernova neutrinos in the light of FCNC," *Phys. Rev.* **D58** (1998) 013012, hep-ph/9711424.

[661] M. Honda, N. Okamura, and T. Takeuchi, "Matter effect on neutrino oscillations from the violation of universality in neutrino neutral current interactions," hep-ph/0603268.

[662] A. M. Gago, M. M. Guzzo, H. Nunokawa, W. J. C. Teves, and R. Zukanovich Funchal, "Probing flavor changing neutrino interactions using neutrino beams from a muon storage ring," *Phys. Rev.* **D64** (2001) 073003, hep-ph/0105196.

[663] P. Huber and J. W. F. Valle, "Non-standard interactions: Atmospheric versus neutrino factory experiments," *Phys. Lett.* **B523** (2001) 151–160, hep-ph/0108193.

[664] P. Huber, T. Schwetz, and J. W. F. Valle, "How sensitive is a neutrino factory to the angle Theta(13)?," *Phys. Rev. Lett.* **88** (2002) 101804, hep-ph/0111224.

[665] P. Huber, T. Schwetz, and J. W. F. Valle, "Confusing non-standard neutrino interactions with oscillations at a neutrino factory," *Phys. Rev.* **D66** (2002) 013006, hep-ph/0202048.

[666] V. D. Barger, R. J. N. Phillips, and K. Whisnant, "Solar neutrino solutions with matter enhanced flavor changing neutral current scattering," *Phys. Rev.* **D44** (1991) 1629–1643.

[667] **CHARM** Collaboration, J. Dorenbosch *et al.*, "Experimental verification of the universality of electron- neutrino and muon-neutrino coupling to the neutral weak current," *Phys. Lett.* **B180** (1986) 303.

[668] **CHARM-II** Collaboration, P. Vilain *et al.*, "Precision measurement of electroweak parameters from the scattering of muon-neutrinos on electrons," *Phys. Lett.* **B335** (1994) 246–252.

[669] **LSND** Collaboration, L. B. Auerbach *et al.*, "Measurement of electron-neutrino electron elastic scattering," *Phys. Rev.* **D63** (2001) 112001, hep-ex/0101039.

[670] **NuTeV** Collaboration, G. P. Zeller *et al.*, "A precise determination of electroweak parameters in neutrino nucleon scattering," *Phys. Rev. Lett.* **88** (2002) 091802, hep-ex/0110059.

[671] A. Friedland and C. Lunardini, "Neutrino flavor conversion in a neutrino background: Single- versus multi-particle description," *Phys. Rev.* **D68** (2003) 013007, hep-ph/0304055.

[672] E. Roulet, "Mikheyev-Smirnov-Wolfenstein effect with flavor-changing neutrino nteractions," *Phys. Rev.* **D44** (1991) 935–938.

[673] M. M. Guzzo, A. Masiero, and S. T. Petcov, "On the MSW effect with massless neutrinos and no mixing in the vacuum," *Phys. Lett.* **B260** (1991) 154–160.

[674] N. Fornengo, M. Maltoni, R. T. Bayo, and J. W. F. Valle, "Probing neutrino non-standard interactions with atmospheric neutrino data," *Phys. Rev.* **D65** (2002) 013010, hep-ph/0108043.

[675] A. Friedland, C. Lunardini, and C. Pena-Garay, "Solar neutrinos as probes of neutrino - matter interactions," *Phys. Lett.* **B594** (2004) 347, hep-ph/0402266.

[676] M. M. Guzzo, P. C. de Holanda, and O. L. G. Peres, "Effects of non-standard neutrino interactions on MSW-LMA solution," *Phys. Lett.* **B591** (2004) 1–6, hep-ph/0403134.

[677] O. G. Miranda, M. A. Tortola, and J. W. F. Valle, "Are solar neutrino oscillations robust?," *JHEP* **10** (2006) 008, hep-ph/0406280.

[678] A. de Gouvea, A. Friedland, and H. Murayama, "The dark side of the solar neutrino parameter space," *Phys. Lett.* **B490** (2000) 125–130, hep-ph/0002064.

[679] A. Friedland, "MSW effects in vacuum oscillations," *Phys. Rev. Lett.* **85** (2000) 936–939, hep-ph/0002063.

[680] R. Engel, T. K. Gaisser, and T. Stanev, "Pion production in proton collisions with light nuclei: Implications for atmospheric neutrinos," *Phys. Lett.* **B472** (2000) 113–118, hep-ph/9911394.

[681] A. Friedland, C. Lunardini, and M. Maltoni, "Atmospheric neutrinos as probes of neutrino matter interactions," *Phys. Rev.* **D70** (2004) 111301, hep-ph/0408264.

[682] A. Friedland and C. Lunardini, "A test of tau neutrino interactions with atmospheric neutrinos and K2K," *Phys. Rev.* **D72** (2005) 053009, hep-ph/0506143.

[683] **MINOS** Collaboration, First Oscillation Results, March 2006. http://www-numi.fnal.gov/talks/results06.html.

[684] **MINOS** Collaboration, P. Adamson *et al.*, "Measurement of Neutrino Oscillations with the MINOS Detectors in the NuMI Beam," 0806.2237.

[685] N. Kitazawa, H. Sugiyama, and O. Yasuda, "Will MINOS see new physics?," hep-ph/0606013.

[686] J. Kopp, M. Lindner, T. Ota, and J. Sato, "Non-standard neutrino interactions in reactor and superbeam experiments," *Phys. Rev.* **D77** (2008) 013007, 0708.0152.

[687] J. Kopp, M. Lindner, and T. Ota, "Discovery reach for non-standard interactions in a neutrino factory," *Phys. Rev.* **D76** (2007) 013001, hep-ph/0702269.

[688] O. Yasuda. Talk at *The 3rd Plenary Meeting of the International Scoping Study of a Future Neutrino Factory and Superbeam Facility*, Rutherford Appleton Laboratory, April 24 – 28, 2006, http://www.hep.ph.ic.ac.uk/uknfic/iss0406/physics.html.

[689] M. Mezzetto, "Future European neutrino programs, accelerator based." Proceedings of Neutrino Telescopes 2007, Venice, Italy, 6-9 Mar 2007, p. 271-292.

[690] P. Huber, M. Lindner, M. Rolinec, and W. Winter, "Physics and optimization of beta-beams: From low to very high gamma," *Phys. Rev.* **D73** (2006) 053002, hep-ph/0506237.

[691] V. Barger *et al.*, "Precision physics with a wide band super neutrino beam," *Phys. Rev.* **D74** (2006) 073004, hep-ph/0607177.

[692] B. Autin *et al.*, "Conceptual design of the SPL, a high-power superconducting H- linac at CERN." CERN-2000-012.

[693] M. Apollonio *et al.*, "Oscillation physics with a neutrino factory. ((G)) ((U))," hep-ph/0210192.

[694] R. Garoby, "The SPL at CERN," *AIP Conf. Proc.* **773** (2005) 239–243.

[695] O. Mena and S. J. Parke, "Physics potential of the Fermilab NuMI beamline," *Phys. Rev.* **D72** (2005) 053003, hep-ph/0505202.

[696] C. K. Jung, "Feasibility of a next generation underground water Cherenkov detector: UNO," *AIP Conf. Proc.* **533** (2000) 29–34, hep-ex/0005046.

[697] A. de Bellefon *et al.*, "MEMPHYS: A large scale water Cerenkov detector at Frejus," hep-ex/0607026.

[698] P. Huber, M. Lindner, and W. Winter, "Synergies between the first-generation JHF-SK and NuMI superbeam experiments," *Nucl. Phys.* **B654** (2003) 3–29, hep-ph/0211300.

[699] P. Huber, M. Lindner, M. Rolinec, T. Schwetz, and W. Winter, "Prospects of accelerator and reactor neutrino oscillation experiments for the coming ten years," *Phys. Rev.* **D70** (2004) 073014, hep-ph/0403068.

[700] P. Huber, M. Lindner, and W. Winter, "From parameter space constraints to the precision determination of the leptonic Dirac CP phase," *JHEP* **05** (2005) 020, hep-ph/0412199.

[701] C. Yanagisawa. Talk at *Workshop on Long Baseline Neutrino Experiments*, Fermilab, March 6 – 7, 2006, http://www.fnal.gov/directorate/DirReviews/Neutrino_Wrkshp.html.

[702] S. Antusch, P. Huber, J. Kersten, T. Schwetz, and W. Winter, "Is there maximal mixing in the lepton sector?," *Phys. Rev.* **D70** (2004) 097302, hep-ph/0404268.

[703] O. L. G. Peres and A. Y. Smirnov, "Atmospheric neutrinos: LMA oscillations, U(e3) induced interference and CP-violation," *Nucl. Phys.* **B680** (2004) 479–509, hep-ph/0309312.

[704] M. C. Gonzalez-Garcia, M. Maltoni, and A. Y. Smirnov, "Measuring the deviation of the 2-3 lepton mixing from maximal with atmospheric neutrinos," *Phys. Rev.* **D70** (2004) 093005, hep-ph/0408170.

[705] E. K. Akhmedov, "Parametric resonance of neutrino oscillations and passage of solar and atmospheric neutrinos through the earth," *Nucl. Phys.* **B538** (1999) 25–51, hep-ph/9805272.

[706] C. W. Kim and U. W. Lee, "Comment on the possible electron-neutrino excess in the Super-Kamiokande atmospheric neutrino experiment," *Phys. Lett.* **B444** (1998) 204–207, hep-ph/9809491.

[707] T. Kajita. Talk at *NNN05*, Aussois, Savoie, France, April 7–9, 2005, http://nnn05.in2p3.fr/.

[708] A. Donini, "NUFACT'03: The fate of the clones," *AIP Conf. Proc.* **721** (2004) 219–222, hep-ph/0310014.

[709] O. Mena, "Unveiling Neutrino Mixing and Leptonic CP Violation," *Mod. Phys. Lett.* **A20** (2005) 1–17, hep-ph/0503097.

[710] C. Rubbia, A. Ferrari, Y. Kadi, and V. Vlachoudis, "Beam cooling with ionisation losses," *Nucl. Instrum. Meth.* **A568** (2006) 475–487, hep-ph/0602032.

[711] M. Mezzetto, "Physics reach of the beta beam," *J. Phys.* **G29** (2003) 1771–1776, hep-ex/0302007.

[712] J. Bouchez, M. Lindroos, and M. Mezzetto, "Beta beams: Present design and expected performances," *AIP Conf. Proc.* **721** (2004) 37–47, hep-ex/0310059.

[713] C. Rubbia, "Ionization cooled ultra pure beta-beams for long distance nu/e → nu/mu transitions, theta(13) phase and CP- violation," hep-ph/0609235.

[714] B. Autin *et al.*, "The acceleration and storage of radioactive ions for a neutrino factory," *J. Phys.* **G29** (2003) 1785–1796, physics/0306106.

[715] Eurisol Beta-beam task group. http://beta-beam.web.cern.ch/beta-beam/task/index.asp.

[716] A. Donini *et al.*, "A beta beam complex based on the machine upgrades of the LHC," *Eur. Phys. J.* **C48** (2006) 787–796, hep-ph/0604229.

[717] **MONOLITH** Collaboration, N. Y. Agafonova *et al.*, "MONOLITH: A massive magnetized iron detector for neutrino oscillation studies." LNGS-P26-2000.

[718] S. K. Agarwalla, S. Choubey, and A. Raychaudhuri, "Neutrino mass hierarchy and theta(13) with a magic baseline beta-beam experiment," *Nucl. Phys.* **B771** (2007) 1–27, hep-ph/0610333.

[719] J. Bernabeu, J. Burguet-Castell, C. Espinoza, and M. Lindroos, "Monochromatic neutrino beams," *JHEP* **12** (2005) 014, hep-ph/0505054.

[720] J. Bernabeu, J. Burguet-Castell, C. Espinoza, and M. Lindroos, "Physics reach with a monochromatic neutrino beam from electron capture," *Pos* **HEP2005** (2006) 182, hep-ph/0512297.

[721] B. Autin, A. Blondel, and J. R. E. . Ellis, "Prospective study of muon storage rings at CERN." CERN-99-02.

[722] Y. Kuno *et al.*, "A feasibility study of a neutrino factory in Japan." http://www-prism.kek.jp/nufactj/index.html.

[723] A. Blondel (Ed.) *et al.*, "ECFA/CERN studies of a European neutrino factory complex." CERN-2004-002.

[724] A. Blondel, "Muon polarisation in the neutrino factory," *Nucl. Instrum. Meth.* **A451** (2000) 131–137.

[725] A. Broncano and O. Mena, "Corrections to the fluxes of a neutrino factory," *Eur. Phys. J.* **C29** (2003) 197–206, hep-ph/0203052.

[726] S. Geer, "Neutrino factories: Physics," *Comments Nucl. Part. Phys.* **A2** (2002) 284–308, hep-ph/0008155.

[727] A. Donini, M. B. Gavela, P. Hernandez, and S. Rigolin, "Neutrino mixing and CP-violation," *Nucl. Phys.* **B574** (2000) 23–42, hep-ph/9909254.

[728] D. Autiero *et al.*, "The synergy of the golden and silver channels at the Neutrino Factory," *Eur. Phys. J.* **C33** (2004) 243–260, hep-ph/0305185.

[729] A. Bueno, M. Campanelli, and A. Rubbia, "Physics potential at a neutrino factory: Can we benefit from more than just detecting muons?," *Nucl. Phys.* **B589** (2000) 577–608, hep-ph/0005007.

[730] A. Ereditato and A. Rubbia, "Conceptual design of a scalable multi-kton superconducting magnetized liquid argon TPC," *Nucl. Phys. Proc. Suppl.* **155** (2006) 233–236, hep-ph/0510131.

[731] A. Badertscher, M. Laffranchi, A. Meregaglia, A. Muller, and A. Rubbia, "First results from a liquid argon time projection chamber in a magnetic field," *Nucl. Instrum. Meth.* **A555** (2005) 294–309, physics/0505151.

[732] **INO** Collaboration, D. Indumathi, "India-based Neutrino Observatory (INO)," *Pramana* **63** (2004) 1283–1293.

[733] A. Bueno, M. Campanelli, S. Navas, and A. Rubbia, "On the energy and baseline optimization to study effects related to the delta-phase (CP-/T-violation) in neutrino oscillations at a neutrino factory," *Nucl. Phys.* **B631** (2002) 239–284, hep-ph/0112297.

[734] **MINOS** Collaboration, M. Diwan *et al.*, "A study of $\nu_\mu \to \nu_e$ sensitivity in MINOS," Tech. Rep. NuMI-L-714, 2001.

[735] G. L. Fogli, E. Lisi, A. Marrone, and D. Montanino, "Status of atmospheric nu/mu → nu/tau oscillations and decoherence after the first K2K spectral data," *Phys. Rev.* **D67** (2003) 093006, hep-ph/0303064.

[736] J. N. Bahcall, M. C. Gonzalez-Garcia, and C. Pena-Garay, "Solar neutrinos before and after Neutrino 2004," *JHEP* **08** (2004) 016, hep-ph/0406294.

[737] R. J. Geller and T. Hara, "Geophysical aspects of very long baseline neutrino experiments," *Nucl. Instrum. Meth.* **A503** (2001) 187–191, hep-ph/0111342.

[738] T. Ohlsson and W. Winter, "The role of matter density uncertainties in the analysis of future neutrino factory experiments," *Phys. Rev.* **D68** (2003) 073007, hep-ph/0307178.

[739] A. M. Dziewonski and D. L. Anderson, "Preliminary reference earth model," *Phys. Earth Planet. Interiors* **25** (1981) 297–356.

[740] A. de Gouvea and W. Winter, "What would it take to determine the neutrino mass hierarchy if theta(13) were too small?," *Phys. Rev.* **D73** (2006) 033003, hep-ph/0509359.

[741] M. Freund, P. Huber, and M. Lindner, "Systematic exploration of the neutrino factory parameter space including errors and correlations," *Nucl. Phys.* **B615** (2001) 331–357, hep-ph/0105071.

[742] G. Altarelli and F. Feruglio, "Phenomenology of neutrino masses and mixings," hep-ph/0306265.

[743] S. V. Panasyuk, "REM (Reference Earth Model) web page," 2000. http://cfauvcs5.harvard.edu/lana/rem/index.htm.

[744] R. Gandhi and W. Winter, "Physics with a very long neutrino factory baseline," *Phys. Rev.* **D75** (2007) 053002, hep-ph/0612158.

[745] ISS detector working group. private communication.

[746] W. Winter, "Direct test of the MSW effect by the solar appearance term in beam experiments," *Phys. Lett.* **B613** (2005) 67–73, hep-ph/0411309.

[747] C. Albright *et al.*, "Physics at a neutrino factory," hep-ex/0008064.

[748] S. Geer and M. S. Zisman, "Neutrino factories: Realization and physics potential." FERMILAB-PUB-06-454-E.

[749] J. N. Bahcall and C. Pena-Garay, "Global analyses as a road map to solar neutrino fluxes and oscillation parameters," *JHEP* **11** (2003) 004, hep-ph/0305159.

[750] The LENS collaboration. http://lens.in2p3.fr/.

[751] The MOON collaboration. http://ewi.npl.washington.edu/moon/index.html.

[752] I. Liubarsky *et al.*, "The SIREN solar neutrino experiment." Prepared for 3rd International Workshop on the Identification of Dark Matter (IDM2000), York, England, 18- 22 Sep 2000.

[753] **XMASS** Collaboration, T. Namba, "XMASS." Prepared for 5th Workshop on Neutrino Oscillations and their Origin (NOONE2004), Tokyo, Japan, 11-15 Feb 2004.

[754] J. A. Nikkel, W. H. Lippincott, and D. N. McKinsey, "Neutrino and dark matter detection with CLEAN: Preliminary studies," *Int. J. Mod. Phys.* **A20** (2005) 3113–3114.

[755] R. E. Lanou, "Update on HERON," *Nucl. Phys. Proc. Suppl.* **138** (2005) 98–101.

[756] The MUNU collaboration. http://www.unine.ch/phys/corpus/MUNU/MUNU2.html.

[757] The GENIUS collaboration. http://www.mpi-hd.mpg.de/non_acc/genius.html.

[758] Y. Suzuki. Talk at *Neutrino 2004*, June 14 – 19, 2004, Paris, France.

[759] J. F. Beacom and M. R. Vagins, "GADZOOKS! Antineutrino spectroscopy with large water Cherenkov detectors," *Phys. Rev. Lett.* **93** (2004) 171101, hep-ph/0309300.

[760] O. L. G. Peres and A. Y. Smirnov, "Testing the solar neutrino conversion with atmospheric neutrinos," *Phys. Lett.* **B456** (1999) 204–213, hep-ph/9902312.

[761] J. Bernabeu, S. Palomares-Ruiz, A. Perez, and S. T. Petcov, "The earth mantle-core effect in matter-induced asymmetries for atmospheric neutrino oscillations," *Phys. Lett.* **B531** (2002) 90–98, hep-ph/0110071.

[762] S. Choubey, "What we can learn from atmospheric neutrinos," hep-ph/0609182.

[763] S. Choubey and P. Roy, "Probing the deviation from maximal mixing of atmospheric neutrinos," *Phys. Rev.* **D73** (2006) 013006, hep-ph/0509197.

[764] D. Indumathi and M. V. N. Murthy, "A question of hierarchy: Matter effects with atmospheric neutrinos and anti-neutrinos," *Phys. Rev.* **D71** (2005) 013001, hep-ph/0407336.

[765] R. Gandhi, P. Ghoshal, S. Goswami, P. Mehta, and S. Uma Sankar, "Large matter effects in nu/mu → nu/tau oscillations," *Phys. Rev. Lett.* **94** (2005) 051801, hep-ph/0408361.

[766] R. Gandhi, P. Ghoshal, S. Goswami, P. Mehta, and S. Uma Sankar, "Earth matter effects at very long baselines and the neutrino mass hierarchy," *Phys. Rev.* **D73** (2006) 053001, hep-ph/0411252.

[767] R. Gandhi, P. Ghoshal, S. Goswami, P. Mehta, and S. Uma Sankar, "Probing the nu mass hierarchy via atmospheric nu/mu + anti- nu/mu survival rates in Megaton water Cerenkov detectors," hep-ph/0506145.

[768] S. T. Petcov and T. Schwetz, "Determining the neutrino mass hierarchy with atmospheric neutrinos," *Nucl. Phys.* **B740** (2006) 1–22, hep-ph/0511277.

[769] **INO** Collaboration, M. S. Athar *et al.*, "India-based Neutrino Observatory: Project Report. Volume I." A Report of the INO Feasibility Study. Updated from the earlier Interim Report of May 1, 2005.

[770] R. Gandhi *et al.*, "Mass Hierarchy Determination via future Atmospheric Neutrino Detectors," *Phys. Rev.* **D76** (2007) 073012, 0707.1723.

[771] H. V. Klapdor-Kleingrothaus *et al.*, "Latest results from the Heidelberg-Moscow double-beta-decay experiment," *Eur. Phys. J.* **A12** (2001) 147–154, hep-ph/0103062.

[772] L. Willmann *et al.*, "New bounds from searching for muonium to antimuonium conversion," *Phys. Rev. Lett.* **82** (1999) 49–52, hep-ex/9807011.

[773] F. Halzen and D. Hooper, "Prospects for detecting dark matter with neutrino telescopes in light of recent results from direct detection experiments," *Phys. Rev.* **D73** (2006) 123507, hep-ph/0510048.

[774] G. L. Fogli, E. Lisi, A. Mirizzi, D. Montanino, and P. D. Serpico, "Oscillations of solar atmosphere neutrinos," *Phys. Rev.* **D74** (2006) 093004, hep-ph/0608321.

[775] J. F. Beacom, N. F. Bell, D. Hooper, S. Pakvasa, and T. J. Weiler, "Measuring flavor ratios of high-energy astrophysical neutrinos," *Phys. Rev.* **D68** (2003) 093005, hep-ph/0307025.

[776] J. F. Beacom, N. F. Bell, D. Hooper, S. Pakvasa, and T. J. Weiler, "Decay of high-energy astrophysical neutrinos," *Phys. Rev. Lett.* **90** (2003) 181301, hep-ph/0211305.

[777] J. F. Beacom, N. F. Bell, D. Hooper, S. Pakvasa, and T. J. Weiler, "Sensitivity to Theta(13) and delta in the decaying astrophysical neutrino scenario," *Phys. Rev.* **D69** (2004) 017303, hep-ph/0309267.

[778] Y. Chikashige, R. N. Mohapatra, and R. D. Peccei, "Spontaneously broken lepton number and cosmological constraints on the neutrino mass spectrum," *Phys. Rev. Lett.* **45** (1980) 1926.

[779] S. Pakvasa and J. W. F. Valle, "Neutrino properties before and after KamLAND," *Proc. Indian Natl. Sci. Acad.* **70A** (2004) 189–222, hep-ph/0301061.

[780] P. Meszaros and E. Waxman, "TeV neutrinos from bursting and choked fireballs," *Phys. Rev. Lett.* **87** (2001) 171102, astro-ph/0103275.

[781] Y. Farzan, "Bounds on the coupling of the Majoron to light neutrinos from supernova cooling," *Phys. Rev.* **D67** (2003) 073015, hep-ph/0211375.

[782] P. D. Serpico and M. Kachelriess, "Measuring the 13-mixing angle and the CP phase with neutrino telescopes," *Phys. Rev. Lett.* **94** (2005) 211102, hep-ph/0502088.

[783] P. D. Serpico, "Probing the 2-3 leptonic mixing at high-energy neutrino telescopes," *Phys. Rev.* **D73** (2006) 047301, hep-ph/0511313.

[784] W. Winter, "How astrophysical neutrino sources could be used for early measurements of neutrino mass hierarchy and leptonic CP phase," *Phys. Rev.* **D74** (2006) 033015, hep-ph/0604191.

[785] T. Kashti and E. Waxman, "Flavoring astrophysical neutrinos: Flavor ratios depend on energy," *Phys. Rev. Lett.* **95** (2005) 181101, astro-ph/0507599.

[786] **Muon g-2** Collaboration, G. W. Bennett *et al.*, "Measurement of the positive muon anomalous magnetic moment to 0.7-ppm," *Phys. Rev. Lett.* **89** (2002) 101804, hep-ex/0208001.

[787] **Muon g-2** Collaboration, G. W. Bennett *et al.*, "Measurement of the negative muon anomalous magnetic moment to 0.7-ppm," *Phys. Rev. Lett.* **92** (2004) 161802, hep-ex/0401008.

[788] **Muon G-2** Collaboration, G. W. Bennett *et al.*, "Final report of the muon E821 anomalous magnetic moment measurement at BNL," *Phys. Rev.* **D73** (2006) 072003, hep-ex/0602035.

[789] J. P. Miller, E. de Rafael, and B. L. Roberts, "Muon g-2: Review of Theory and Experiment," *Rept. Prog. Phys.* **70** (2007) 795, hep-ph/0703049.

[790] J. Aysto *et al.*, "Physics with low-energy muons at a neutrino factory complex," hep-ph/0109217.

[791] P. A. M. Dirac, "The Quantum theory of electron," *Proc. Roy. Soc. Lond.* **A117** (1928) 610–624. Eq. (328) uses Dirac's original notation.

[792] E. M. Purcell and N. F. Ramsey, "On the Possibility of Electric Dipole Moments for Elementary Particles and Nuclei," *Phys. Rev.* **78** (1950) 807.

[793] L. D. Landau, "On the conservation laws for weak interactions," *Nucl. Phys.* **3** (1957) 127–131.

[794] N. F. Ramsey, "Time Reversal, Charge Conjugation, Magnetic Pole Conjugation, and Parity," *Phys. Rev.* **109** (1958) 225.

[795] **CPLEAR** Collaboration, A. Angelopoulos *et al.*, "First direct observation of time-reversal non-invariance in the neutral kaon system," *Phys. Lett.* **B444** (1998) 43–51.

[796] C. A. Baker *et al.*, "An improved experimental limit on the electric dipole moment of the neutron," *Phys. Rev. Lett.* **97** (2006) 131801, hep-ex/0602020.

[797] B. C. Regan, E. D. Commins, C. J. Schmidt, and D. DeMille, "New limit on the electron electric dipole moment," *Phys. Rev. Lett.* **88** (2002) 071805.

[798] **CERN-Mainz-Daresbury** Collaboration, J. Bailey *et al.*, "Final report on the cern muon storage ring including the anomalous magnetic moment and the electric dipole moment of the muon, and a direct test of relativistic time dilation," *Nucl. Phys.* **B150** (1979) 1 and references therein.

[799] M. V. Romalis, W. C. Griffith, and E. N. Fortson, "A new limit on the permanent electric dipole moment of Hg- 199," *Phys. Rev. Lett.* **86** (2001) 2505–2508, hep-ex/0012001.

[800] M. Davier, S. Eidelman, A. Hocker, and Z. Zhang, "Updated estimate of the muon magnetic moment using revised results from e+ e- annihilation," *Eur. Phys. J.* **C31** (2003) 503–510, hep-ph/0308213.

[801] M. Davier and W. J. Marciano, "The theoretical prediction for the muon anomalous magnetic moment," *Ann. Rev. Nucl. Part. Sci.* **54** (2004) 115–140 and references therein.

[802] **KLOE** Collaboration, A. Aloisio *et al.*, "Measurement of sigma(e+ e- → pi+ pi- gamma) and extraction of sigma(e+ e- → pi+ pi-) below 1-GeV with the KLOE detector," *Phys. Lett.* **B606** (2005) 12–24, hep-ex/0407048.

[803] R. R. Akhmetshin *et al.*, "Measurement of the e+ e- → pi+ pi- cross section with the CMD-2 detector in the 370-MeV - 520-MeV cm energy range," *JETP Lett.* **84** (2006) 413–417, hep-ex/0610016.

[804] **CMD-2** Collaboration, R. R. Akhmetshin *et al.*, "High-statistics measurement of the pion form factor in the rho-meson energy range with the CMD-2 detector," *Phys. Lett.* **B648** (2007) 28–38, hep-ex/0610021.

[805] M. N. Achasov *et al.*, "Update of the e+ e- → pi+ pi- cross section measured by SND detector in the energy region 400-MeV < s**(1/2) < 1000-MeV," *J. Exp. Theor. Phys.* **103** (2006) 380–384, hep-ex/0605013.

[806] K. Hagiwara, A. D. Martin, D. Nomura, and T. Teubner, "Improved predictions for g-2 of the muon and alpha(QED)(M(Z)**2)," *Phys. Lett.* **B640** (2007) 173–179, hep-ph/0611102.

[807] M. Davier, "The hadronic contribution to (g-2)(mu)," *Nucl. Phys. Proc. Suppl.* **169** (2007) 288–296, hep-ph/0701163.

[808] R. Alemany, M. Davier, and A. Hocker, "Improved determination of the hadronic contribution to the muon (g-2) and to alpha(M(Z)**2) using new data from hadronic tau decays," *Eur. Phys. J.* **C2** (1998) 123–135, hep-ph/9703220.

[809] A. Czarnecki and W. J. Marciano, "The muon anomalous magnetic moment: A harbinger for 'new physics'," *Phys. Rev.* **D64** (2001) 013014, hep-ph/0102122.

[810] S. P. Martin and J. D. Wells, "Super-conservative interpretation of muon g-2 results applied to supersymmetry," *Phys. Rev.* **D67** (2003) 015002, hep-ph/0209309.

[811] D. Stockinger, "The muon magnetic moment and supersymmetry," *J. Phys.* **G34** (2007) R45–R92, hep-ph/0609168.

[812] T. Appelquist and B. A. Dobrescu, "Universal extra dimensions and the muon magnetic moment," *Phys. Lett.* **B516** (2001) 85–91, hep-ph/0106140.

[813] J. R. Ellis, K. A. Olive, Y. Santoso, and V. C. Spanos, "Supersymmetric dark matter in light of WMAP," *Phys. Lett.* **B565** (2003) 176–182, hep-ph/0303043.

[814] J. R. Ellis, K. A. Olive, Y. Santoso, and V. C. Spanos, "Update on the direct detection of supersymmetric dark matter," *Phys. Rev.* **D71** (2005) 095007 and references therein, hep-ph/0502001.

[815] D. W. Hertzog, J. P. Miller, E. de Rafael, B. Lee Roberts, and D. Stockinger, "The Physics Case for the New Muon (g-2) Experiment," arXiv:0705.4617 [hep-ph].

[816] K. S. Babu, B. Dutta, and R. N. Mohapatra, "Enhanced electric dipole moment of the muon in the presence of large neutrino mixing," *Phys. Rev. Lett.* **85** (2000) 5064–5067, hep-ph/0006329.

[817] J. L. Feng, K. T. Matchev, and Y. Shadmi, "Theoretical expectations for the muon's electric dipole moment," *Nucl. Phys.* **B613** (2001) 366–381, hep-ph/0107182.

[818] J. L. Feng, K. T. Matchev, and Y. Shadmi, "The measurement of the muon's anomalous magnetic moment isn't," *Phys. Lett.* **B555** (2003) 89–91, hep-ph/0208106.

[819] J. R. Ellis, J. Hisano, M. Raidal, and Y. Shimizu, "Lepton electric dipole moments in non-degenerate supersymmetric seesaw models," *Phys. Lett.* **B528** (2002) 86–96, hep-ph/0111324.

[820] F. J. M. Farley *et al.*, "A new method of measuring electric dipole moments in storage rings," *Phys. Rev. Lett.* **93** (2004) 052001, hep-ex/0307006.

[821] A. Adelmann and K. Kirch, "Search for the muon electric dipole moment using a compact storage ring," hep-ex/0606034.

[822] Y. Kuno, J. Miller, Y. Semertzidis, *et al.*, "Search for a Permanent Muon Electric Dipole Moment at the 10^{-24} e·cm Level." J-PARC Letter of Intent, January 2003.

[823] S. T. Petcov, "The processes mu → e gamma, mu → e e anti-e, neutrino' → neutrino gamma in the Weinberg-Salam model with neutrino mixing," *Sov. J. Nucl. Phys.* **25** (1977) 340.

[824] S. M. Bilenky, S. T. Petcov, and B. Pontecorvo, "Lepton mixing, mu → e + gamma decay and neutrino oscillations," *Phys. Lett.* **B67** (1977) 309.

[825] T.-P. Cheng and L.-F. Li, "Muon number nonconservation in gauge theories." Talk at *Coral Gables 1977*, Proceedings, Deeper Pathways In High- energy Physics, New York 1977, p. 659-681.

[826] W. J. Marciano and A. I. Sanda, "Exotic decays of the muon and heavy leptons in gauge theories," *Phys. Lett.* **B67** (1977) 303.

[827] B. W. Lee, S. Pakvasa, R. E. Shrock, and H. Sugawara, "Muon and Electron Number Nonconservation in a V-A Six Quark Model," *Phys. Rev. Lett.* **38** (1977) 937.

[828] B. W. Lee and R. E. Shrock, "Natural Suppression of Symmetry Violation in Gauge Theories: Muon - Lepton and Electron Lepton Number Nonconservation," *Phys. Rev.* **D16** (1977) 1444.

[829] J. Bernabeu, E. Nardi, and D. Tommasini, "mu - e conversion in nuclei and Z-prime physics," *Nucl. Phys.* **B409** (1993) 69–86, `hep-ph/9306251`.

[830] S. Davidson, D. C. Bailey, and B. A. Campbell, "Model independent constraints on leptoquarks from rare processes," *Z. Phys.* **C61** (1994) 613–644, `hep-ph/9309310`.

[831] R. Bluhm, V. A. Kostelecky, and C. D. Lane, "CPT and Lorentz tests with muons," *Phys. Rev. Lett.* **84** (2000) 1098–1101, `hep-ph/9912451`.

[832] H. Dehmelt, R. Mittleman, J. van Dyck, R. S., and P. Schwinberg, "Past electron positron g-2 experiments yielded sharpest bound on CPT violation," *Phys. Rev. Lett.* **83** (1999) 4694–4696, `hep-ph/9906262`.

[833] V. W. Hughes *et al.*, "Test of CPT and Lorentz invariance from muonium spectroscopy," *Phys. Rev. Lett.* **87** (2001) 111804, `hep-ex/0106103`.

[834] A. Czarnecki, W. J. Marciano, and K. Melnikov, "Coherent muon electron conversion in muonic atoms," *AIP Conf. Proc.* **435** (1998) 409–418, `hep-ph/9801218`.

[835] M. Raidal and A. Santamaria, "mu e conversion in nuclei versus mu → e gamma: An effective field theory point of view," *Phys. Lett.* **B421** (1998) 250–258, `hep-ph/9710389`.

[836] V. D. Barger, G. F. Giudice, and T. Han, "Some New Aspects of Supersymmetry R-Parity Violating Interactions," *Phys. Rev.* **D40** (1989) 2987.

[837] **MEGA** Collaboration, M. Ahmed *et al.*, "Search for the lepton-family-number nonconserving decay mu+ → e+ gamma," *Phys. Rev.* **D65** (2002) 112002, `hep-ex/0111030`.

[838] L. Willmann and K. Jungmann. Lecture Notes in Physics, Vol. 499 (1997) pg 43ff and references therein.

[839] P. Wintz, "Results of the SINDRUM-II experiment." Prepared for *29th International Conference on High-Energy Physics (ICHEP 98)*, Vancouver, Canada, 23-29 Jul 1998.

[840] **SINDRUM II** Collaboration, J. Kaulard *et al.*, "Improved limit on the branching ratio of mu- → e+ conversion on titanium," *Phys. Lett.* **B422** (1998) 334–338.

[841] **SINDRUM II** Collaboration, W. Honecker *et al.*, "Improved limit on the branching ratio of mu → e conversion on lead," *Phys. Rev. Lett.* **76** (1996) 200–203.

[842] A. E. Pifer, T. Bowen, and K. R. Kendall, "A high stopping density mu+ beam," *Nucl. Instrum. Meth.* **135** (1976) 39–46.

[843] L. Barkov *et al.*, "Search for $\mu \to e\,\gamma$ down to 10^{-14} branching ratio." available at `http://www.icepp.s.u-tokyo.ac.jp/meg`.

[844] S. Mihara *et al.*, "Development of a liquid-xenon photon detector - towards the search for a muon rare decay mode at Paul Scherrer Institute," *Cryogenics* **44** (2004) 223–228.

[845] **SINDRUM** Collaboration, W. Bertl *et al.*, "Search for the Decay mu+ → e+ e+ e-," *Nucl. Phys.* **B260** (1985) 1.

[846] G. Feinberg and S. Weinberg, "Electromagnetic Transitions Between Meson and Electron," *Phys. Rev. Lett.* **3** (1959) 111.

[847] T. S. Kosmas and J. D. Vergados, "Sum rules for the inclusive mu e conversion exotic reaction," *Phys. Lett.* **B217** (1989) 19–24.

[848] T. S. Kosmas and J. D. Vergados, "Study of the flavor violating (mu-, e-) conversion in nuclei," *Nucl. Phys.* **A510** (1990) 641–670.

[849] T. S. Kosmas and I. E. Lagaris, "On the muon nucleus integrals entering the neutrinoless mu- → e- conversion rates," *J. Phys.* **G28** (2002) 2907–2920.

[850] A. Czarnecki, W. J. Marciano, and K. Melnikov, "Muon electron conversion in nuclei," *AIP Conf. Proc.* **549** (2002) 938–941.

[851] H. C. Chiang, E. Oset, T. S. Kosmas, A. Faessler, and J. D. Vergados, "Coherent and incoherent (mu-, e-) conversion in nuclei," *Nucl. Phys.* **A559** (1993) 526–542.

[852] T. S. Kosmas, A. Faessler, F. Simkovic, and J. D. Vergados, "State-by-state calculations for all channels of the exotic (mu-,e-) conversion process," *Phys. Rev.* **C56** (1997) 526–534, `nucl-th/9704021`.

[853] O. Shanker, "Z dependence of coherent mu e conversion rate in anomalous neutrinoless muon capture," *Phys. Rev.* **D20** (1979) 1608.

[854] F. Herzog and K. Alder, "Decay electron spectra of bound muons," *Helv. Phys. Acta* **53** (1980) 53–76.

[855] R. Watanabe, M. Fukui, H. Ohtsubo, and M. Morita, "Angular distribution of electrons in bound muon decay," *Prog. Theor. Phys.* **78** (1987) 114–122.

[856] R. M. Dzhilkibaev and V. M. Lobashev, "On the search for mu → e conversion process in a nucleus," *Sov. J. Nucl. Phys.* **49** (1989) 384–385.

[857] **MECO** Collaboration, M. Bachman *et al.* BNL proposal AGS P940 (1997).

[858] "The PRISM Project – A Muon Source of the World Highest Brightness by Phase Rotation –," 2003. Letter of Intent to J-PARC, L24.

[859] "Request for a Pulsed Proton Beam Facility at J-PARC." Letter of Intent to J-PARC, L26.

[860] "An Experimental Search for the $\mu^- - e^-$ Conversion Process at an Ultimate Sensitivity of the Order of 10^{-18} with PRISM." Letter of Intent to J-PARC, L25.

[861] G. Feinberg and S. Weinberg, "Conversion of Muonium into Antimuonium," *Phys. Rev.* **123** (1961) 1439.

[862] V. W. Hughes, D. W. McColm, and K. Ziock, "Formation of Muonium and Observation of its Larmor Precession," *Phys. Rev. Lett.* **5** (1960) 63.

[863] V. W. Hughes and G. zu Putlitz. in *Quantum Electrodynamics*, Ed. T. Kinoshita, World Scientific, Singapore, (1990) p. 822.

[864] P. Herczeg and R. N. Mohapatra, "Muonium to anti-muonium conversion and the decay mu+ → e+ anti-neutrino neutrino in left-right symmetric models," *Phys. Rev. Lett.* **69** (1992) 2475–2478.

[865] A. Halprin, "Neutrinoless double beta decay and muonium - anti-muonium transitions," *Phys. Rev. Lett.* **48** (1982) 1313–1316.

[866] R. N. Mohapatra, "Rare muon decays and physics beyond the Standard Model," *Z. Phys.* **C56** (1992) S117–S128.

[867] G.-G. Wong and W.-S. Hou, "Weak scale radiative lepton mass," *Phys. Rev.* **D50** (1994) 2962–2965.

[868] A. Halprin and A. Masiero, "Muonium - anti-muonium oscillations and exotic muon decay in broken R-parity SUSY models," *Phys. Rev.* **D48** (1993) 2987–2989.

[869] H. Fujii, Y. Mimura, K. Sasaki, and T. Sasaki, "Muonium, hyperfine structure and the decay mu+ → e+ + anti-electron-neutrino + muon-neutrino in models with dilepton gauge baryons," *Phys. Rev.* **D49** (1994) 559–562, `hep-ph/9309287`.

[870] P. H. Frampton and M. Harada, "Constraints from precision electroweak data on leptoquarks and bileptons," *Phys. Rev.* **D58** (1998) 095013, hep-ph/9711448.

[871] V. Pleitez, "A remark on the muonium to antimuonium conversion in a 331 model," *Phys. Rev.* **D61** (2000) 057903, hep-ph/9905406.

[872] W.-S. Hou and G.-G. Wong, "Magnetic field dependence of muonium - anti-muonium conversion," *Phys. Lett.* **B357** (1995) 145–150, hep-ph/9505300.

[873] K. Horikawa and K. Sasaki, "Muonium - anti-muonium conversion in models with dilepton gauge bosons," *Phys. Rev.* **D53** (1996) 560–563, hep-ph/9504218.

[874] D. L. Morgan and V. W. Hughes, "Atomic processes involved in matter-antimatter annihilation," *Phys. Rev.* **D2** (1970) 1389–1399.

[875] D. L. Morgan and V. W. Hughes, "Atom-Antiatom Interactions," *Phys. Rev.* **A7** (1973) 1811–1825.

[876] W. J. Marciano, "Fermi constants and 'new physics'," *Phys. Rev.* **D60** (1999) 093006, hep-ph/9903451.

[877] K. P. Jungmann, "Experiments searching for lepton number violation," *AIP Conf. Proc.* **539** (2000) 341–354.

[878] L. Michel, "Interaction between four half spin particles and the decay of the mu meson," *Proc. Phys. Soc.* **A63** (1950) 514–531.

[879] W. Fetscher, H. J. Gerber, and K. F. Johnson, "Muon decay: complete determination of the interaction and comparison with the Standard Model," *Phys. Lett.* **B173** (1986) 102.

[880] P. Langacker, "Is the Standard Model unique?," *Comments Nucl. Part. Phys.* **19** (1989) 1.

[881] W. Fetscher and H. J. Gerber, "Muon decay parameters," *Eur. Phys. J.* **C15** (2000) 316–318.

[882] F. Scheck, "Electroweak and strong interactions: An introduction to theoretical particle physics." Berlin, Germany: Springer (1996) p. 499.

[883] T. van Ritbergen and R. G. Stuart, "On the precise determination of the Fermi coupling constant from the muon lifetime," *Nucl. Phys.* **B564** (2000) 343–390 and references therein, hep-ph/9904240.

[884] T. van Ritbergen and R. G. Stuart, "Hadronic contributions to the muon lifetime," *Phys. Lett.* **B437** (1998) 201–208, hep-ph/9802341.

[885] T. van Ritbergen and R. G. Stuart, "Complete 2-loop quantum electrodynamic contributions to the muon lifetime in the Fermi model," *Phys. Rev. Lett.* **82** (1999) 488–491, hep-ph/9808283.

[886] D. Hertzog *et al.* PSI Experiment R99.07.01.

[887] J. Kirkby *et al.* PSI proposal R-99-06 (1999).

[888] K. Nagamine *et al.* RIKEN-RAL muon lifetime experiment (1998).

[889] **MuLan** Collaboration, D. B. Chitwood *et al.*, "Improved Measurement of the Positive Muon Lifetime and Determination of the Fermi Constant," *Phys. Rev. Lett.* **99** (2007) 032001, 0704.1981.

[890] C. Greub, D. Wyler, and W. Fetscher, "Effects of nonstandard couplings, radiative corrections and neutrino masses on the lepton spectra in mu and tau decays," *Phys. Lett.* **B324** (1994) 109–116, hep-ph/9312301.

[891] H. Burkard *et al.*, "Muon decay: measurement of the transverse positron polarization and general analysis," *Phys. Lett.* **B160** (1985) 343.

[892] W. Fetscher, "Leptonic tau decays: How to determine the Lorentz structure of the charged leptonic weak interaction by experiment," *Phys. Rev.* **D42** (1990) 1544–1567.

[893] H. J. Gerber, "Lepton properties." Given at the International Europhysics Conference on High Energy Physics, Uppsala, Sweden, Jun 25 - Jul 1, 1987.

[894] A. Jodidio *et al.*, "Search for right-handed currents in muon decay," *Phys. Rev.* **D34** (1986) 1967.

[895] **TWIST** Collaboration, J. R. Musser, "Measurement of the Michel parameter rho in muon decay," *Phys. Rev. Lett.* **94** (2005) 101805, hep-ex/0409063.

[896] **TWIST** Collaboration, A. Gaponenko *et al.*, "Measurement of the muon decay parameter delta," *Phys. Rev.* **D71** (2005) 071101, hep-ex/0410045.

[897] **TWIST** Collaboration, B. Jamieson *et al.*, "Measurement of P(mu) xi in polarized muon decay," hep-ex/0605100.

[898] J. Prieels *et al.* PSI experiment R-97-06 (1997).

[899] I. C. Barnett *et al.*, "An apparatus for the measurement of the transverse polarization of positrons from the decay of polarized muons," *Nucl. Instrum. Meth.* **A455** (2000) 329–345.

[900] N. Danneberg *et al.*, "Muon decay: Measurement of the transverse polarization of the decay positrons and its implications for the Fermi coupling constant and time reversal invariance," *Phys. Rev. Lett.* **94** (2005) 021802.

A Origin of the ISS and its Committees

Further information on the activities that took place during the course of the International Scoping Study of a future Neutrino Factory and super-beam facility (the ISS) and links to the working groups can be found at: `http://www.hep.ph.ic.ac.uk/iss/`.

A.1 Origin

The international scoping study of a future Neutrino Factory and super-beam facility (the ISS) was carried by the international community between NuFact05, (the 7$^{\text{th}}$ International Workshop on Neutrino Factories and Superbeams, Laboratori Nazionali di Frascati, Rome, June 21–26, 2005) and NuFact06 (Ivine, California, 24–30 August 2006).

The physics case for the facility was evaluated and options for the accelerator complex and the neutrino detection systems were studied. The principal objective of the study was to lay the foundations for a full conceptual-design study of the facility. The plan for the scoping study was prepared in collaboration by the international community that wished to carry it out; the ECFA/BENE network in Europe, the Japanese NuFact-J collaboration, the US Neutrino Factory and Muon Collider collaboration, and the UK Neutrino Factory collaboration. STFC's Rutherford Appleton Laboratory was the host laboratory for the study.

The study was directed by a Programme Committee advised by a Stakeholders Board. The work of the study was carried out by three working groups: the Physics Group; the Accelerator Group; and the Detector Group. Four plenary meetings at CERN, KEK, RAL, and Irvine were held during the study period; workshops on specific topics were organised by the individual working groups in between the plenary meetings. The conclusions of the study were presented at NuFact06. This document, which presents the Physics Group's conclusions, was prepared as the physics section of the ISS study group.

A.2 Committee

Programme Committee

Chairman:	Peter Dornan,	Imperial College London
Physics convener:	Yorikiyo Nagashima,	Osaka University
Accelerator convener:	Michael S. Zisman,	Lawrence Berkeley National Laboratory
Detector convener:	Alain Blondel,	University of Geneva

Physics Working Subgroup Conveners

Theoretical:	Steve King,	University of Southampton
Phenomenological:	Osamu Yasuda,	Tokyo Metropolitan University
Experimental:	Ken Long,	Imperial College London
Muon:	B.L. Roberts,	Boston University

Council Members of the Physics Working Group

Deborah A. Harris,	Fermilab
Pilar Hernandez,	University of Valencia
Steve King,	University of Southampton
Manfred Lindner,	Max-Planck-Institut für Kernphysik
Ken Long,	Imperial College London
William Marciano,	Brookhaven National Laboratory
Mauro Mezzetto,	INFN Padova
Hitoshi Murayama,	Lawrence Berkeley National Laboratory
Yorikiyo Nagashima,	Osaka University
Kenzo Nakamura,	KEK
B.L. Roberts,	Boston University
Osamu Yasuda,	Tokyo Metropolitan University